

**Ruthenium Complexes with Non-Innocent Quinonoid, Quinoline-5,8-dione and Iminoquinone Ligands: Synthesis, Structure, Redox Properties and Electron Distribution**

Von der Fakultät Chemie der Universität Stuttgart  
Zur Erlangung der Würde eines  
Doktors der Naturwissenschaften  
(Dr. rer. nat.)  
genehmigte Abhandlung

vorgelegt von  
**Hari Sankar Das**  
aus Hooghly (Indien)

|                             |                           |
|-----------------------------|---------------------------|
| Hauptberichter:             | Prof. Dr. Biprajit Sarkar |
| Mitberichter:               | Prof. Dr. D. Gudat        |
| Tag der mündlichen Prüfung: | 20.06.2012                |

**Institut für Anorganische Chemie der Universität Stuttgart**  
**2012**



*To my elder brother*

*Sib Sankar Das*



## Acknowledgements

This work was completed from October 2008 to April 2012 at the Institute of Inorganic Chemistry, University of Stuttgart.

I would like to acknowledge all those who supported and encouraged me to complete this work and the final writing of this thesis. Without them, it would have never been possible.

First I would like to express my sincere gratitude to my supervisor Prof. Dr. Biprajit Sarkar for giving me such an opportunity with working in his well established research group, under his supervision and extreme guidance, for all his scientific knowledge, thinking and fruitful discussions throughout my entire research work. I am honoured to be his first Ph.D. student.

Next I would like to thank Prof W. Kaim, who provides me the laboratory and all the instrumental facilities along with all required chemicals that I needed to complete my doctoral studies. Throughout the time he inspired me in a lot of ways so that I could reach my final destination.

Prof. S. Sarkar, from IIT-Kanpur India, played an important role to train me in the field of coordination chemistry during my Master's thesis.

Prof G.K. Lahiri, from IIT-Bombay India, for his helpful suggestion, mental support and fruitful scientific discussions.

I would like to thank

Dr. J. Fiedler from J. Heyrovsky Institute of Physical Chemistry in Prague, Czech Republic, Mr. Fritz Weißer and Dr. Ralph Hübner for the spectroelectrochemical measurements,

Prof. C.-Y. Su from Sun Yat-Sen University, China, Dr. S. M. Mobin from Indian Institute of Technology in Bombay, India, Dr. R. Pattacini from Université de Strasbourg, France, Dr. W. Frey, Dr. D. Bubrin, Dr.F. Lissner, Dr. I. Hartenbach and Mr. S. Hohloch for the crystallographic data collection and solving crystal structures,

Mr. D. Schweinfurth and Ms. A. Paretzki for the EPR measurements, Dr. L. Bogani from Institute of Physical chemistry, University of Stuttgart for SQUID-magnetometric measurement,

Dr. S. Zálíš from J. Heyrovsky Institute of Physical Chemistry in Prague, Czech Republic and again Mr D. Schweinfurth for the DFT calculations,

Ms. K. Török for the NMR measurements,

Ms. B. Förtsch for the elemental analysis,

Ms. Sumati Panicker-Otto and Ms. A. Winkelmann for helping me out with burocratic problems and Mr M. krafft for translating the summary.

I would also like to thank

Mr. Negelein, Mr. Wesch, Mr. Lenz and Mr. Münch for their help related to chemicals, glasswares and solving the electronic problems,

Mr. O. Sarper and again Mr M. krafft for solving computer problems,

Dr. B. N. Ghosh, Mr. A. N. Mondal, Mr. M. Rahman, Dr. R. K. Jana, Mr. K.M. Jewel, Mr. B. Khan, Mr. M. Ahmed and Mr. N. Alam for making my life much easier in Stuttgart with their friendly support and help.

A special thanks to my parents, Tinkari Das and Ranibala Das, for all their love and encouragement. The last but not the least my elder brother, Mr. Sib Sankar Das, for his mental, financial support throughout my entire student life and it is only due to him that I first became interested in science when I was young. Without his contribution this thesis would certainly not existed. That's why I am dedicating my thesis to my elder brother.

I also gratefully acknowledge Institut für Anorganische Chemie, Universität Stuttgart for the financial support.

Finally I would like to thank all the past and present members of Institut für Anorganische Chemie, Universität Stuttgart, especially, the research group of Prof. Kaim's for creating a nice environment to work and making much easier and enjoyable stay at this institute.

# ***CONTENTS***

|   |              |
|---|--------------|
| <b>1. Introduction</b>  | <b>1-7</b>   |
| <b>2. Structural, redox, electronic and spectroscopic properties of mono- &amp; dinuclear ruthenium(II) complexes with noninnocent zwitterionic quinonoid ligands</b>                                       | <b>8-29</b>  |
| 2.1. Introduction   | 8            |
| 2.2. Syntheses and characterization   | 9            |
| 2.3. X-ray crystal structure  | 10           |
| 2.4. Electrochemistry   | 16           |
| 2.5. UV-Vis-NIR spectroelectrochemistry   | 19           |
| 2.6. EPR spectroscopy   | 26           |
| 2.7 Conclusion  | 29           |
| <b>3. One-pot synthesis of symmetric and asymmetric substituted <i>p</i>-quinone ligands and their structural, redox, electronic and spectroscopic properties in mono and dinuclear ruthenium complexes</b> | <b>30-69</b> |
| 3.1. Introduction   | 30           |
| 3.2. Syntheses and characterization   | 33           |
| 3.3. X-ray crystal structure  | 38           |
| 3.4. Electrochemistry   | 42           |
| 3.5. EPR spectroscopy   | 48           |
| 3.6. UV-Vis-NIR spectroelectrochemistry   | 54           |
| 3.7 Conclusion  | 69           |
| <b>4. Syntheses, electron transfer and metal-metal coupling in rare dinuclear paramagnetic symmetric and asymmetric ruthenium mixed valence complexes</b>   | <b>70-94</b> |
| 4.1. Introduction   | 70           |
| 4.2. Syntheses and characterization   | 71           |
| 4.3. X-ray crystal structure  | 73           |
| 4.4. Electrochemistry   | 75           |
| 4.5. EPR spectroscopy   | 77           |
| 4.6. UV-Vis-NIR spectroelectrochemistry   | 82           |
| 4.7 SQUID Magnetometry  | 93           |
| 4.8 Conclusion  | 94           |

**5. Charge distribution, redox properties, structures and bonding in the substitution series  $[\text{Ru}(\text{L-H})_n(\text{acac})_{3-n}]$  ( $n = 0-3$ ;  $\text{L} = N,N'$ -diisopropyl-2-amino-5-alcoholate-1,4-benzoquinonemonoiminium) 95-113**

|   |     |
|---|-----|
| 5.1. Introduction                       | 95  |
| 4.2. Syntheses and characterization     | 95  |
| 4.3. X-ray crystal structure            | 97  |
| 5.4. Electrochemistry                   | 102 |
| 5.5. EPR spectroscopy                   | 103 |
| 5.6. UV-Vis-NIR spectroelectrochemistry | 105 |
| 5.7. Conclusion                         | 113 |

**6. Isomeric forms separation and their valence and spin situations in different redox state of a  $[\text{Ru}(\text{bpy})(\text{L-H})_2]$  system;  $\text{L} = N,N'$ -diisopropyl-2-amino-5-alcoholate-1,4-benzoquinonemonoiminium and 2,5-bis(isopropylamino)-1,4-benzoquinone 114-126**

|   |     |
|---|-----|
| 6.1. Introduction                       | 114 |
| 6.2. Syntheses and characterization     | 115 |
| 6.3. X-ray crystal structure            | 116 |
| 6.4. Electrochemistry                   | 120 |
| 5.5. UV-Vis-NIR spectroelectrochemistry | 121 |
| 6.6. EPR spectroscopy                   | 124 |
| 6.7. Conclusion                         | 126 |

**7. Synthesis of dinuclear ruthenium arene complexes with symmetric and asymmetric *p*-quinone ligands and their unprecedented substituent induced reactivity 127-136**

|   |     |
|---|-----|
| 7.1. Introduction   | 127 |
| 7.2. Syntheses of <i>p</i> -quinone ligands   | 128 |
| 7.3. Synthesis of dinuclear ruthenium arene complexes   | 129 |
| 7.4. X-ray crystal structure  | 130 |
| 7.5. Reaction of dinuclear ruthenium arene complexes with $\text{AgClO}_4$ in MeCN                            | 132 |
| 7.6. Explanation for the release of Cymene  | 134 |
| 7.7. Substitution reaction of complex $[(\text{MeCN})_3\text{Ru}(\mu\text{-L})\text{Ru}(\text{MeCN})_3]^{2+}$ | 135 |
| 7.8. Conclusion   | 136 |



|  |                |
|--|----------------|
| <b>8. Molecular coupling of three non-innocent ligands and two redox-active metal centers in a super redox-rich system</b>   | <b>137-157</b> |
| 8.1. Introduction  | 137            |
| 8.2. Syntheses and characterization  | 139            |
| 8.3. X-ray crystal structure   | 139            |
| 8.4. Electrochemistry  | 141            |
| 8.5. EPR Spectroscopy  | 143            |
| 8.6. UV/Vis/NIR Spectroelectrochemistry  | 146            |
| 8.7. DFT calculation   | 151            |
| 8.8. Conclusions   | 157            |
| <br>   |                |
| <b>9. A mononuclear ruthenium complex with noninnocent <i>N</i>-(2-methyl-5,8-dioxo-5,8-dihydroquinolin-7-yl)acetamide ligand and acetylacetonato terminal ligands</b> | <b>158-171</b> |
| 9.1. Introduction  | 158            |
| 9.2. Syntheses and characterization  | 159            |
| 9.3. Electrochemistry  | 161            |
| 9.4. IR Spectroelectrochemistry  | 162            |
| 9.5. UV/Vis/NIR Spectroelectrochemistry  | 166            |
| 9.6. EPR Spectroscopy  | 169            |
| 9.7. Discussion of Combined Spectroscopic Results  | 170            |
| 9.8. Conclusions   | 171            |
| <br>   |                |
| <b>10. Experimental</b>  | <b>172-205</b> |
| 10.1. Instrumentation  | 172            |
| 10.2. Solvents and working conditions  | 173            |
| 10.3. Syntheses  |                |
| 10.3.1. Commercially available compounds   | 174            |
| 10.3.2. Syntheses of reported compounds  | 174            |
| 10.3.3. Synthesis of mono- and dinuclear complexes derived from zwitterionic quinonoid ligands (L)   |                |
| 10.3.3.1. Synthesis of mono- and dinuclear complexes with bipyridine ancillary ligands   |                |
| [Ru(bpy) <sub>2</sub> L <sub>-H</sub> ](ClO <sub>4</sub> )   | 174            |
| [Ru(bpy)(L <sub>-H</sub> ) <sub>2</sub> ]  | 175            |

|  |     |
|--|-----|
| [ $\{\text{Ru}(\text{bpy})_2\}_2(\mu\text{-L}_{\text{-H}_2})\](\text{ClO}_4)_2$  | 176 |
| [ $\{\text{Ru}(\text{bpy})_2\}_2(\mu\text{-L}'_{\text{-H}_2})\](\text{ClO}_4)_2$   | 177 |
| 10.3.3.2. Synthesis of mono- and dinuclear complexes with acetylacetonato ancillary ligands                                  |     |
| [ $\text{Ru}(\text{acac})_2\text{L}$ ]   | 177 |
| [ $\text{Ru}(\text{acac})(\text{L})_2$ ]   | 177 |
| [ $\{\text{Ru}(\text{acac})_2\}_2(\mu\text{-L}_{\text{-H}_2})$ ]   | 178 |
| 10.3.3.3. Synthesis of mononuclear complex with three quinonoid terminal ligands   |     |
| $\text{RuL}_3$   | 178 |
| 10.3.3.4. Synthesis of an asymmetric dinuclear complex with acetylacetonato and bipyridine ancillary ligands                 |     |
| [ $\text{Ru}(\text{bpy})_2(\mu\text{-L}_{\text{-H}_2})\text{Ru}(\text{acac})_2$ ]  | 179 |
| 10.3.4 Synthesis of symmetric and asymmetric quinonoid ligands   |     |
| 10.3.4.1. General procedure for preparing mono- and di-alkyl derivatives of 2,5-diamino 1,4-benzoquinone                     | 180 |
| 2-amino-5-(isopropylamino)-1,4-benzoquinone  | 180 |
| 2,5-bis(isopropylamino)-1,4-benzoquinone   | 180 |
| 10.3.4.2. General procedure for preparing symmetric and asymmetric quinonoid ligands from 2,5-dihydroxy 1,4-benzoquinone     | 181 |
| 2,5-bis(isopropylamino)-1,4-benzoquinone   | 181 |
| 2,5-bis(benzylamino)-1,4-benzoquinone  | 181 |
| 2,5-bis(2,4,6-trimethylanilino)-1,4-benzoquinone   | 181 |
| 2-(isopropylamino)-5-hydroxy-1,4-benzoquinone  | 182 |
| 2-(benzylamino)-5-hydroxy-1,4-benzoquinone   | 182 |
| 2-(2,4,6-trimethylanilino)-5-hydroxy-1,4-benzoquinone  | 182 |
| 2-[2-(Methylthio)-anilino]-5-hydroxy-1,4-benzoquinone  | 182 |
| 10.3.5 Synthesis of mono- and dinuclear complexes of symmetric quinonoid ligands (L)   |     |
| 10.3.5.1. Mono-nuclear complexes with bipyridine ancillary and 2,5-bis(isopropylamino)-1,4-benzoquinone (L) terminal ligands |     |
| [ $\text{Ru}(\text{bpy})_2\text{L}](\text{ClO}_4)$   | 183 |
| [ $\text{Ru}(\text{bpy})(\text{L}_{\text{-H}})_2$ ]  | 183 |
| 10.3.5.2. Dinuclear complexes with bipyridine ancillary ligand   |     |

|  |   |     |
|--|---|-----|
| $[\{\text{Ru}(\text{bpy})_2\}_2(\mu\text{-L}_{-2\text{H}})](\text{ClO}_4)_2$ ;   | L = 2,5-bis(isopropylamino)-1,4-          |     |
| benzoquinonen  |   | 185 |
| $[\{\text{Ru}(\text{bpy})_2\}_2(\mu\text{-L}_{-2\text{H}})](\text{ClO}_4)_2$ ;   | L = 2,5-bis(benzylamino)-1,4-benzoquinone | 185 |
| $[\{\text{Ru}(\text{bpy})_2\}_2(\mu\text{-L}^3_{-2\text{H}})](\text{ClO}_4)_2$ ; | L = 2,5-bis(2,4,6-trimethylanilino)-1,4-  |     |
| benzoquinone   |   | 186 |

#### 10.3.5.3. dinuclear complex with acetylacetonato ancillary ligand.

|  |  |     |
|--|--|-----|
| $\{\text{Ru}(\text{acac})_2\}_2(\mu\text{-L}_{-2\text{H}})$                    | L = 2,5-bis(isopropylamino)-1,4-benzoquinone | 186 |
| $[\text{Ru}(\text{bpy})_2(\mu\text{-L}_{\text{H}_2})\text{Ru}(\text{acac})_2]$ | L = 2,5-bis(isopropylamino)-1,4-benzoquinone | 186 |

### 10.3.6 Synthesis of mono- and dinuclear complexes of asymmetric quinonoid ligands

#### 10.3.6.1. Synthesis of mono-nuclear complex with bipyridine ancillary ligands

|   |   |     |
|---|---|-----|
| $[\text{Ru}(\text{bpy})_2\text{L}](\text{ClO}_4)$ ; | L = 2-(isopropylamino)-5-hydroxy-1,4-benzoquinone | 187 |
|---|---|-----|

#### 10.3.6.2. Synthesis of dinuclear complex with bipyridine ancillary ligand.

|  |   |     |
|--|---|-----|
| $[\{\text{Ru}(\text{bpy})_2\}_2(\mu\text{-L}_{-2\text{H}})](\text{ClO}_4)_2$ ; | L = 2-(isopropylamino)-5-hydroxy-1,4-         |     |
| benzoquinone   |   | 187 |
| $[\{\text{Ru}(\text{bpy})_2\}_2(\mu\text{-L}_{-2\text{H}})](\text{ClO}_4)_2$ ; | L = 2-(isopropylamino)-5-hydroxy-1,4-         |     |
| benzoquinone   |   | 187 |
| $[\{\text{Ru}(\text{bpy})_2\}_2(\mu\text{-L}_{-2\text{H}})](\text{ClO}_4)_2$ ; | L = 2-(2,4,6-trimethylanilino)-5-hydroxy-1,4- |     |
| benzoquinone   |   | 188 |

### 10.3.7. Synthesis of Cymene complexes

#### 10.3.7.1. Dinuclear ruthenium complex with symmetric bridging ligand.

|   |                                  |     |
|---|----------------------------------|-----|
| Synthesis of $[\{\text{Cl}(\eta^6\text{-Cym})\text{Ru}\}_2(\mu\text{-L}_{-2\text{H}})]$ ; | L = 2,5-di-[2-(trifluoromethyl)- |     |
| anilino]-1,4-benzoquinone   |                                  | 188 |

#### 10.3.7.2. Dinuclear ruthenium complex with asymmetric bridging ligand.

|   |   |     |
|---|---|-----|
| Synthesis of $[\{\text{Cl}(\eta^6\text{-Cym})\text{Ru}\}_2(\mu\text{-L}_{-2\text{H}})]$ ; | L = 2-[2-(trifluoromethyl)-anilino]-5-        |     |
| hydroxy-1,4-benzoquinone  |   | 189 |
| $[\{\text{Cl}(\eta^6\text{-Cym})\text{Ru}\}_2(\mu\text{-L}_{-2\text{H}})]$ ;              | L = 2-[2-(methylthio)-anilino]-5-hydroxy-1,4- |     |
| benzoquinone  |   | 189 |

### 10.3.8. Substitution of cym/Cl by acetonitrile solvents molecules.

|   |   |     |
|---|---|-----|
| $[\{(\text{CH}_3\text{CN})(\eta^6\text{-Cym})\text{Ru}\}_2(\mu\text{-L}_{-2\text{H}})](\text{ClO}_4)_2$ ; | L = 2,5-di-[2-(trifluoromethyl)-anilino]- |     |
| 1,4-benzoquinone  |   | 190 |
| $[\{(\text{CH}_3\text{CN})(\eta^6\text{-Cym})\text{Ru}\}_2(\mu\text{-L}_{-2\text{H}})](\text{ClO}_4)_2$ ; | L = 2,5-di-[2-(trifluoromethyl)-anilino]- |     |
| 1,4-benzoquinone  |   | 190 |

|   |     |
|---|-----|
| [(CH <sub>3</sub> CN)(η <sup>6</sup> -Cym)Ru(μ-L <sub>2H</sub> )Ru(CH <sub>3</sub> CN) <sub>3</sub> ][ClO <sub>4</sub> ] <sub>2</sub> ; L = 2-[2-(methylthio)-anilino]-5-hydroxy-1,4-benzoquinone   | 190 |
| 10.3.9. Substitution of coordinated acetonitrile in the [(CH <sub>3</sub> CN) <sub>3</sub> Ru] <sub>2</sub> (μ-L <sub>2H</sub> )[ClO <sub>4</sub> ] <sub>2</sub> complex (L = 2-[2-(methylthio)-anilino]-5-hydroxy-1,4-benzoquinone)  |     |
| 10.3.9.1. Synthesis of [(CH <sub>3</sub> CN)(PPh <sub>3</sub> ) <sub>2</sub> Ru] <sub>2</sub> (μ-L <sub>2H</sub> )[ClO <sub>4</sub> ] <sub>2</sub>  | 191 |
| 10.3.9.2. Synthesis of the complex [(Q)Ru] <sub>2</sub> (μ-L <sub>2H</sub> )[ClO <sub>4</sub> ] <sub>2</sub> (Q = 4,6-di- <i>tert</i> -butyl- <i>N</i> -( <i>o</i> -methylthiophenyl)- <i>o</i> -iminobenzoquinone)   | 191 |
| 10.3.9.2.1. Synthesis of complex [(Q)Ru] <sub>2</sub> (μ-L <sub>2H</sub> )[ClO <sub>4</sub> ] <sub>2</sub>  | 192 |
| 10.3.10. Ruthenium complex of quinolin-5,8-dione ligand   |     |
| [Ru(acac) <sub>2</sub> L]; L = <i>N</i> -(2-methyl-5,8-dioxo-5,8-dihydroquinolin-7-yl)acetamide   | 192 |
| 10.4 Crystallography  |     |
| 10.4.1. [Ru(bpy) <sub>2</sub> L <sub>H</sub> ][ClO <sub>4</sub> ] (L = <i>N,N'</i> -diisopropyl-2-amino-5-alcoholate-1,4-benzoquinonemonoiminium ligand)  | 195 |
| 10.4.2. [(Ru(bpy) <sub>2</sub> ) <sub>2</sub> (μ-L <sub>H2</sub> )](ClO <sub>4</sub> ) <sub>2</sub> (L = <i>N,N'</i> -diisopropyl-2-amino-5-alcoholate-1,4-benzoquinonemonoiminium ligand)  | 196 |
| 10.4.3. [(Ru(bpy) <sub>2</sub> ) <sub>2</sub> (μ-L' <sub>H2</sub> )](ClO <sub>4</sub> ) <sub>2</sub> (L' = <i>N,N'</i> -dibenzyl-2-amino-5-alcoholate-1,4-benzoquinonemonoiminium)  | 197 |
| 10.4.4. [Ru(bpy) <sub>2</sub> L <sub>H</sub> ][ClO <sub>4</sub> ] (L = 2,5-bis(isopropylamino)-1,4-benzoquinone)  | 198 |
| 10.4.5. [(Ru(bpy) <sub>2</sub> ) <sub>2</sub> (μ-L <sub>H2</sub> )](ClO <sub>4</sub> ) <sub>2</sub> (L = 2,5-bis(isopropylamino)-1,4-benzoquinone)  | 199 |
| 10.4.6. [Ru(bpy)(L <sub>H</sub> ) <sub>2</sub> ] (L = 2,5-bis(isopropylamino)-1,4-benzoquinone)   | 200 |
| 10.4.7. [Ru(acac) <sub>2</sub> L <sub>H</sub> ] (L = <i>N,N'</i> -Diisopropyl-2-amino-5-alcoholate-1,4-benzoquinonemonoiminium ligand)  | 201 |
| 10.4.8. [Ru(L <sub>H</sub> ) <sub>3</sub> ] (L = <i>N,N'</i> -Diisopropyl-2-amino-5-alcoholate-1,4-benzoquinonemonoiminium ligand)  | 202 |
| 10.4.9. [(Ru(acac) <sub>2</sub> ) <sub>2</sub> (μ-L <sub>H2</sub> )] (L = 2,5-bis(isopropylamino)-1,4-benzoquinone)   | 203 |
| 10.4.10. [(Cl(η <sup>6</sup> -Cym)Ru) <sub>2</sub> (μ-L <sub>2H</sub> )] (L = 2,5-di-[2-(trifluoromethyl)-anilino]-1,4-benzoquinone)  | 204 |
| 10.4.11. [(Q) <sup>-</sup> Ru <sup>III</sup> (μ-L <sub>2H</sub> ) <sup>2-</sup> Ru <sup>III</sup> (Q) <sup>-</sup> ](ClO <sub>4</sub> ) <sub>2</sub> ; (L = 2,5-di-[2-(methylthio)-anilino]-1,4-benzoquinone, Q = 4,6-di- <i>tert</i> -butyl- <i>N</i> -( <i>o</i> -methylthiophenyl)- <i>o</i> -iminobenzoquinone) | 205 |

**11. Summary** **206-216**

**12. Zusammenfassung** **217-227**

**Appendix**

Bibliography

Abbreviations

Curriculum Vitae

## CHAPTER 1

### 1.1. Introduction

Quinones are naturally occurring redox active molecules that function in vital electron-transport processes, often in conjugation with a transition-metal centre.<sup>[1]</sup> The transition metal complexes with non-innocent quinonoid ligands play important roles in a variety of fields such as homogenous catalysis,<sup>[2]</sup> supramolecular chemistry,<sup>[3-4]</sup> coordination polymers,<sup>[5-6]</sup> non-covalent interactions,<sup>[7-8]</sup> magnetic materials<sup>[9-11]</sup> and metal-metal coupling.<sup>[12-15]</sup> The phenomenon of metal-metal coupling has gained tremendous attention in recent years because of its potential use in information transfer<sup>[16-18]</sup> and energy-relevant research<sup>[19-20]</sup> and has revolved primarily around ruthenium complexes because of their facile and well-defined electron transfer properties.<sup>[21-24]</sup> The ruthenium complexes with non-innocent 2,5-dihydroxy-1,4-benzoquinone<sup>[25]</sup> or 2,5-diamino-1,4-benzoquinone<sup>[26]</sup> bridging ligands show strong metal-metal coupling in the mixed valence state and also display valence ambiguity and redox reactivity. In case of 2,5-dihydroxy-1,4-benzoquinone bridging ligand, the only possible way to tune the steric and electronic character is the replacement of C-H protons by R groups (R = alkyl or aryl) whereas there are two possibilities (replacement of C-H protons and N-H protons by R groups) in case of 2,5-diamino-1,4-benzoquinone bridging ligand and the replacement of N-H protons are potentially better than the C-H protons because the nitrogen atoms coordinate directly to the metal centers. Another important factor is that oxygen is isoelectronic to strong Lewis basic NR (R = alkyl or aryl) group. The replacement of oxygen by -NR group in 2,5-Dihydroxy-1,4-benzoquinone leads to the possibilities of tuning the steric and electronic nature of the bridging ligand.

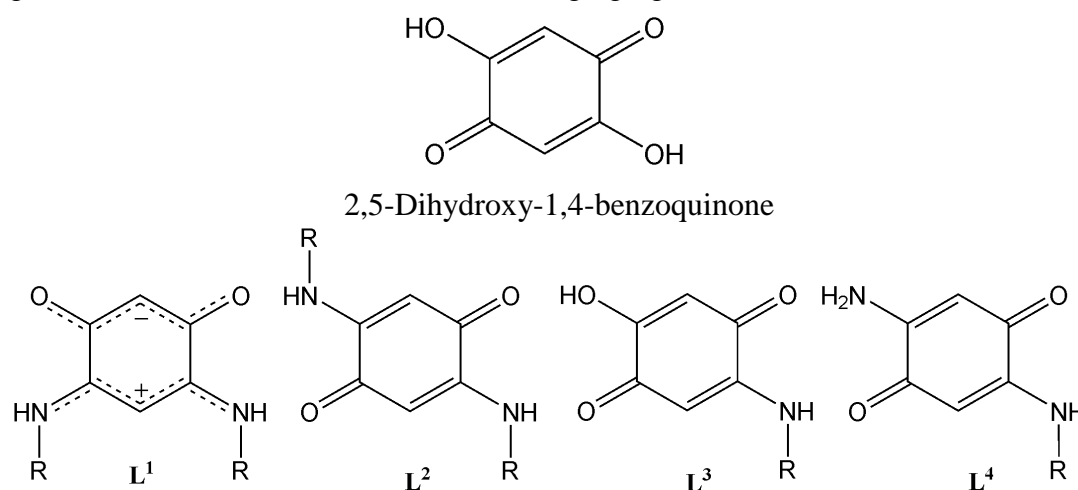


**Figure 1.1.** Molecular formulae of symmetric (**L<sup>1</sup>** and **L<sup>2</sup>**) and asymmetric (**L<sup>3</sup>** and **L<sup>4</sup>**) substituted quinonoid ligands.

This doctoral thesis clearly demonstrates the following aims for the development of the above research fields, particularly metal-metal interaction and valence ambiguity.

- (1) Systematic replacement of –OH group of 2,5-dihydroxy-1,4-benzoquinone by -NR group to tune the steric and electronic properties of the quinonoid bridging ligand and their metal complexes.
- (2) Control of the position and intensity of NIR absorptions through quinonoid bridge variation in mixed-valence state of diruthenium complexes
- (3) Comparison of metal complexes containing *m*-quinonoid ( $\mathbf{L}^1_{\cdot\text{H}}$  and  $\mathbf{L}^1_{\cdot 2\text{H}}$ ), *p*-quinonoid ( $\mathbf{L}^2_{\cdot\text{H}}$  and  $\mathbf{L}^2_{\cdot 2\text{H}}$ ) and asymmetric quinonoid ( $\mathbf{L}^3_{\cdot\text{H}}$  and  $\mathbf{L}^3_{\cdot 2\text{H}}$ ) bridging ligands.
- (4) Isolation of rare mono-nuclear complexes with potentially quinonoid bridging ligands.
- (5) Ligand centered mixed-valency in metal complexes of the form  $[\text{Ru}(\mathbf{L}')_n(\mathbf{L})_m]$ ;  $n = 0-1$ ,  $m = 2-3$ ,  $\mathbf{L}' =$  bidentate ligand and  $\mathbf{L} =$  mono-deprotonated quinonoid ligand.
- (6) Effect of the replacement of ancillary ligands on metal-metal and ligand-ligand coupling in the mixed-valence state.
- (7) Coordination induced reactivity in the ruthenium arene systems that contain quinonoid bridges with additional donor atoms.
- (8) Preparation of super redox rich systems by combining bridging and ancillary quinonoid ligands.

The methods EPR (Electron Paramagnetic Resonance) spectroscopy, UV/Vis/NIR spectroelectrochemistry, IR spectroscopy, DFT, SQUID-magnetometry and X-ray crystallography have been used for the investigation of electron transfer,  $d\pi(\text{Ru})-\pi^*$  (quinonoid) mixing, metal-metal interaction, delocalization of the  $\pi$ -systems in the quinonoid ligands and valence and spin distribution in redox rich ruthenium complexes containing quinonoid bridging ligands.

Total work about the above projects has been separated into the following chapters:-

**Chapter 2** describes the experimental and theoretical studies of mono- and dinuclear ruthenium-bipyridine complexes with zwitterionic non-innocent quinonoid  $N,N'$ -dialkyl-2-amino-5-alcoholate-1,4-benzoquinonemonoiminium ligands. The complexes have been characterized by single-crystal X-ray crystallography and delocalization of the  $\pi$  systems with the quinonoid ligands in mono- and dinuclear ruthenium complexes have been investigated. The redox properties, metal-metal coupling in mixed-valence state, charge distribution and valence ambiguity have been investigated by electrochemical and spectroelectrochemical methods (UV/Vis/NIR, IR, and X-band EPR). The tuning of redox properties of such systems by varying the alkyl groups in **L** is also presented.

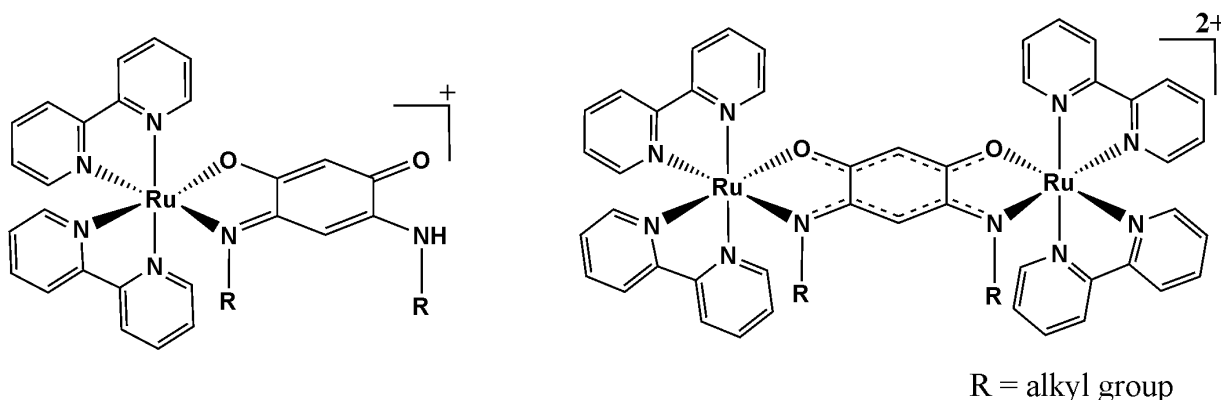


**Figure 1.2.** Molecular formulae of mono- and dinuclear ruthenium(II)-bipyridine complexes with zwitterionic quinonoid ligand.

**Chapter 3** describes one-pot, green synthesis of biologically relevant rare asymmetrically and symmetrically substituted  $p$ -quinone ligands, isolation of a key intermediate and use of these compounds as ligands in mono- and diruthenium complexes. The complexes were characterized by single-crystal X-ray crystallography to investigate the bonding pattern of  $\pi$  systems of  $p$ -quinonoid ligand in mono- and dinuclear ruthenium complexes. The tuning of the redox properties and NIR bands in mixed-valent state of such compounds have also been investigated by varying the R groups in **L**. Absorption in the NIR region is relevant to artificial photosynthesis<sup>[27-31]</sup> and molecular electronic devices.<sup>[32-35]</sup>



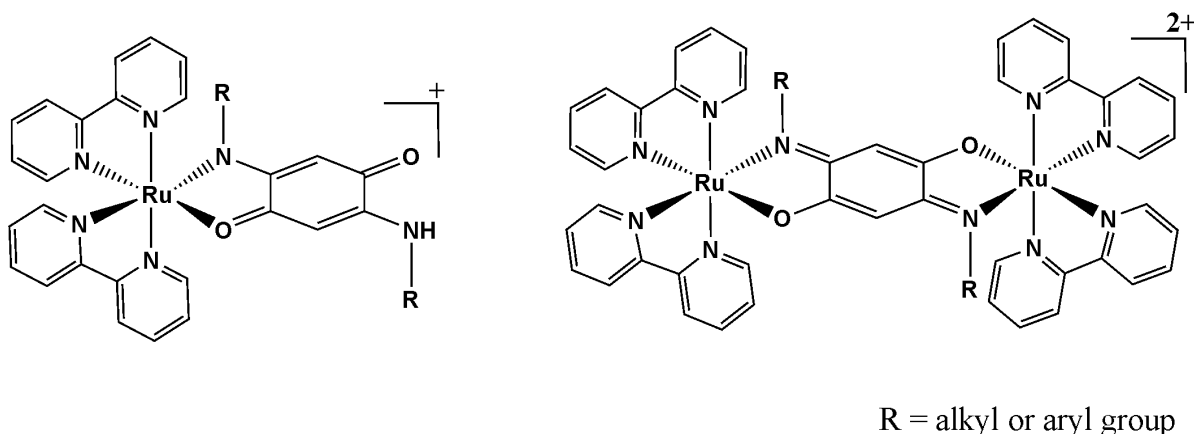


**Figure 1.3.** Molecular formula of mono- and dinuclear ruthenium(II)-bipyridine complexes with symmetric *p*-quinonoid ligand.

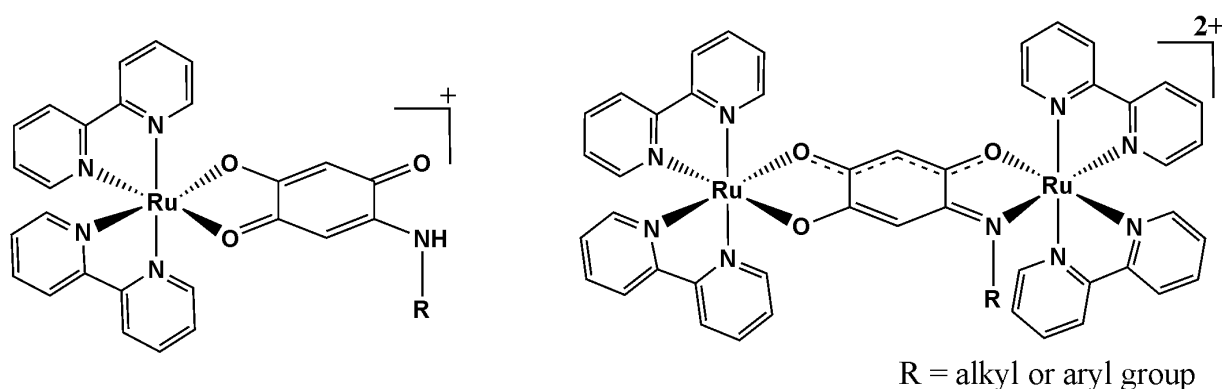


**Figure 1.4.** Molecular formula of mono- and dinuclear ruthenium(II)-bipyridine complexes with asymmetric *p*-quinonoid ligand.

**Chapter 4** presents the results obtained on quinonoid bridge symmetric dinuclear paramagnetic ruthenium complexes and asymmetric dinuclear paramagnetic ruthenium mixed valence complexes in native state. Quinonoid bridge ruthenium-bipyridine mixed-valence complexes exhibit strong metal-metal coupling in their mixed-valence states through the effective overlap with suitably placed ligand  $\pi$  or  $\pi^*$  orbitals in the quinonoid bridge<sup>[36-38]</sup> and the NIR band could be control by the use of different quinonoid ligands (chapter 2 and 3). This metal-metal coupling and the NIR absorption can also be controlled by replacing the ancillary ligands around the ruthenium centres.<sup>[26]</sup> In this context we replaced the bipyridine (electron withdrawing) ancillary ligands by acetylacetonato (electron donating) ligands and this leads to the change of oxidation state ( $\text{Ru}^{\text{II}}$  to  $\text{Ru}^{\text{III}}$ ) and NIR absorption band. We have also synthesized asymmetric native  $\text{Ru}^{\text{II}}$ - $\text{Ru}^{\text{III}}$  mixed valent complexes using bipyridine as ancillary ligands to stabilize  $\text{Ru}^{\text{II}}$  and acetylacetonato ancillary ligands to stabilize  $\text{Ru}^{\text{III}}$  to learn more about the metal-metal coupling through this type of quinonoid bridge ligands. The

redox properties, metal-metal coupling in the mixed valent state, charge distribution and valence ambiguity arising in different oxidation states of these complexes have been also investigated by using various spectroscopic methods (UV/Vis/NIR, X-band EPR and SQUID-magnetometry).

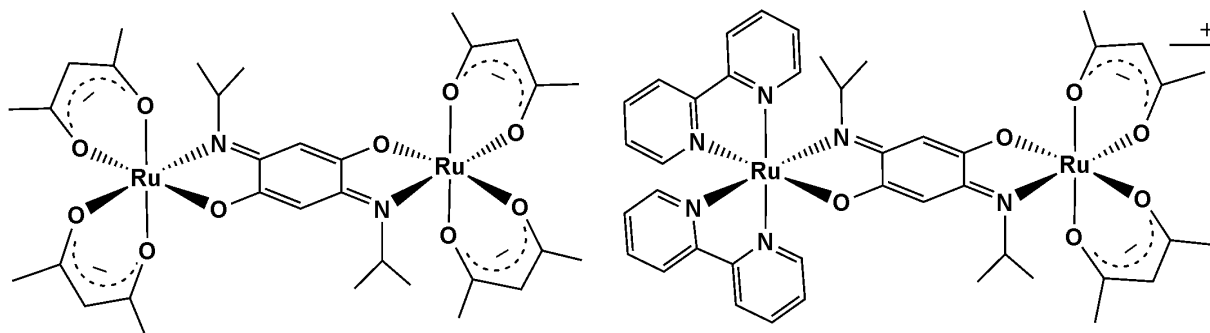


**Figure 1.5.** Molecular formula of a symmetric ( $\text{Ru}^{\text{III}}\text{-Ru}^{\text{III}}$ ) (left) and an asymmetric ( $\text{Ru}^{\text{II}}\text{-Ru}^{\text{III}}$ ) (right) quinonoid bridge ruthenium complex.

**Chapter 5** deals with a new substitution series  $[\text{Ru}(\text{L}^1\text{-H})_n(\text{acac})_{3-n}]$ ,  $n = 0\text{-}3$ ;  $\text{L}^1 = N,N'$ -diisopropyl-2-amino-5-alcoholate-1,4benzoquinonemonoiminium ligand; acac = acetylacetonato ligand. The three neutral complexes  $[\text{Ru}(\text{acac})_2(\text{L}^1\text{-H})]$ ,  $[\text{Ru}(\text{acac})(\text{L}^1\text{-H})_2]$  and  $[\text{Ru}(\text{L}^1\text{-H})_3]$  have been isolated in the paramagnetic form and were characterized by X-ray crystallography and also by EPR spectroscopic technique. Redox properties, non-covalent interactions, structures and bondings and mixing of metal and ligand based frontier orbitals have been investigated to evaluate the electronic structure within these types of complexes.

**Chapter 6** deals with two mono-nuclear ruthenium complexes, each containing one bipyridine ancillary ligand and two non-innocent quinonoid terminal ligands. The combination between ruthenium and quinone-type ligands has received much attention because of exceptional metal-to-ligand charge-transfer transition and the presence of N—H acidic protons that some time shows non-covalent interaction which plays an important role in bio-inhibitors.<sup>[8, 39-41]</sup> The complexes were characterized by spectroscopic techniques and by single-crystal X-ray crystallography. A detailed study of isomerisation, structure and bonding, redox-properties and metal-to-ligand charge-transfer transition arising in different oxidation states are presented.

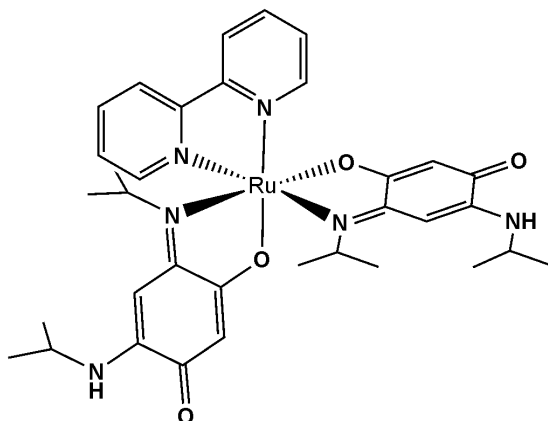


**Figure 1.6.** Molecular formula of a mono-nuclear ruthenium complex with one bipyridine and two quinonoid ligands.

**Chapter 7** presents one pot synthesis of some new symmetric and asymmetric quinonoid ligands (**L**) with and without extra coordinating groups and their complexes with ruthenium-cymene moiety. The complexes of the form  $[\{\text{Cl}(\eta^6\text{-Cym})\text{Ru}\}_2(\mu\text{-L}_{2\text{H}})]$  have been structurally characterized by X-ray crystallography to get the structural and bonding information in this types of systems and finally reacted with  $\text{AgClO}_4$  to remove the chloride in coordinating solvent such as  $\text{CH}_3\text{CN}$  to obtain dechlorofied products of the form  $[\{\text{CH}_3\text{CN}(\eta^6\text{-Cym})\text{Ru}\}_2(\mu\text{-L}_{2\text{H}})](\text{ClO}_4)_2$ , those have extensive uses for the synthesis of supramolecular assemblies<sup>[42,43]</sup> and to see the intramolecular coordinating power of extra coordinating groups.

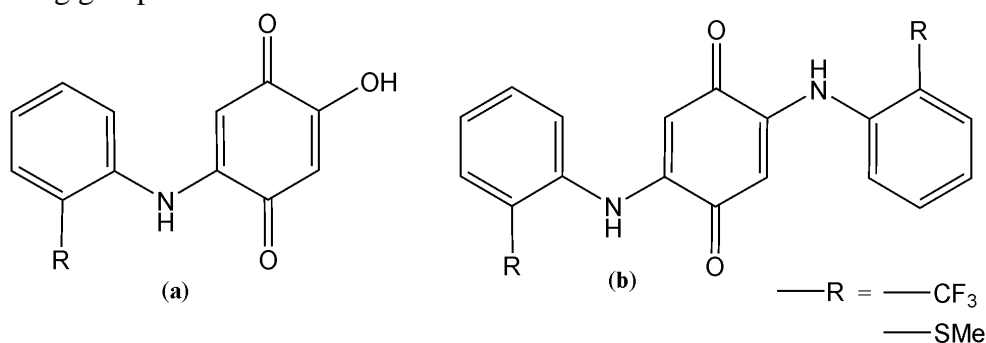


**Figure 1.7.** Molecular formulae of asymmetric (a) and symmetric (b) ligands (**L**) with extra coordinating ( $-\text{SMe}$ ) and extra non-coordinating ( $-\text{CF}_3$ ) groups.

**Chapter 8** deals with a dinuclear ruthenium complex containing non-innocent redox-active terminal and bridging ligands,  $[(\text{Q})\text{Ru}(\mu\text{-L})\text{Ru}(\text{Q})]^n$  where  $\text{Q}^0$  is 4,6-di-*tert*-butyl-*N*-(*o*-methylthiophenyl)-*o*-iminobenzoquinone and  $\text{L}^{2-}$  is the doubly deprotonated form of 2,5-di-[2-(methylthio)-anilino]-1,4-benzoquinone. The complex contains five redox active components  $[\text{Q}^n\text{-Ru}^m\text{-L}^x\text{-Ru}^{m'}\text{-Q}^n]$  was studied by cyclic voltametry to see how many redox process are there and monitored by UV/Vis/NIR spectroelectrochemistry and EPR

spectroscopy in order to assign the oxidation state of each of five components in the accessible redox states. In addition the complex of the form  $[(Q)Ru(\mu-L)Ru(Q)](ClO_4)_2$  was characterized structurally. Structure-based theoretical DFT calculations were also done to verify the oxidation state of each of five components in the accessible redox states obtained from spectroscopic results. The metal-metal, metal-ligand, ligand-metal and ligand-ligand interactions are also discussed in the accessible redox states.

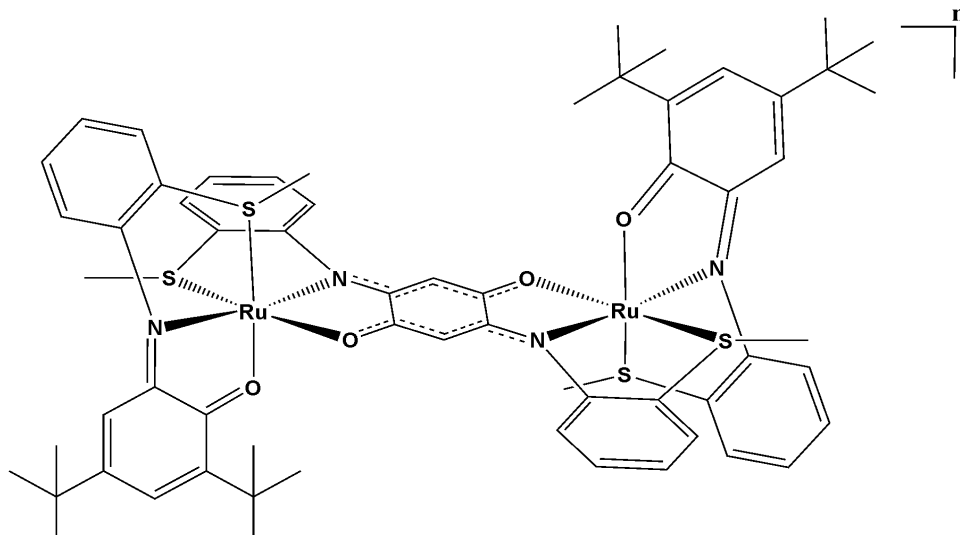


**Figure 1.8.** Molecular formulae of the dinuclear complex  $[(Q)Ru(\mu-L)Ru(Q)]^n$ .

**Chapter 9** presents the synthesis of stable ruthenium complex with a derivative of natural bio-active non-innocent nucleus quinoline-5,8-dione<sup>[44]</sup> which has antitumor, antifungal activities.<sup>[45-49]</sup> The derivative *N*-(2-methyl-5,8-dioxo-5,8-dihydroquinolin-7-yl)acetamide ligand (**L**) was reacted with electronically different ruthenium moieties to get the information about the required electronic nature of ruthenium moiety to make a stable complex with it. A stable ruthenium complex of this ligand  $[Ru(acac)_2L]$  was isolated and studied by cyclic voltammetry, EPR spectroscopy, UV/Vis and IR spectroelectrochemistry in order to investigate the redox property, non-innocent behaviour and mixing of ligand- and metal-centered frontier orbitals.

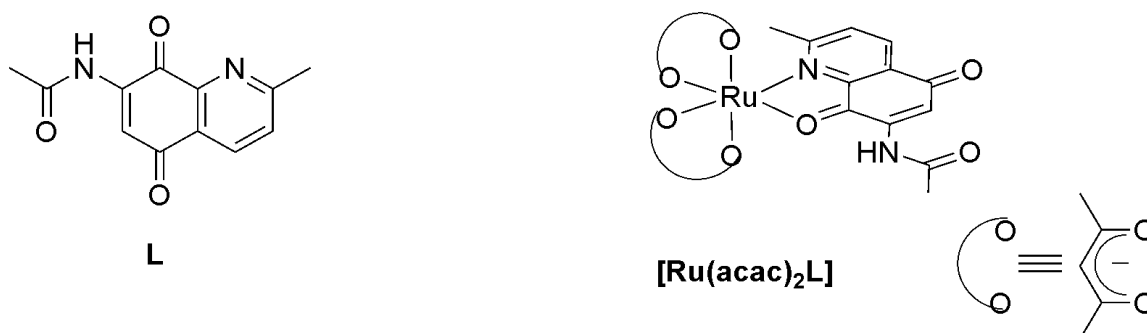


**Figure 1.9.** Molecular formulae of the substituted quinoline-5,8-diones ligand and the metal complex of it.

## CHAPTER 2

# Structural, Redox, Electronic and Spectroscopic Properties of Mono- & Dinuclear Ruthenium(II) Complexes with Noninnocent Zwitterionic Quinonoid Ligands

### 2.1. Introduction

Quinonoid ligands have fascinated chemists over the decades for a variety of reasons including their redox non-innocence.<sup>[50-51]</sup> The study of mixed-valent compounds has great importance for the design of molecular electronic devices<sup>[52-54]</sup> and has revolved primarily around ruthenium complexes because of their facile and well-defined electron transfer properties.<sup>[55-59]</sup> Recent years have seen some ‘unconventional’<sup>[60]</sup> developments in this field with concepts such as Class II/III borderline<sup>[58]</sup> and ‘charge transfer isomers’<sup>[61]</sup> being invoked and the questions of metal vs. ligand centered processes being answered using a variety of spectroscopic techniques.<sup>[62]</sup> The use of quinonoid ligands in mononuclear ruthenium complexes is challenging because of the energetically close lying  $d\pi$  ruthenium based orbitals and quinonoid based  $\pi^*$  orbitals.<sup>[63]</sup> Using quinonoid ligands as bridges in dinuclear ruthenium complexes can raise ambiguity regarding the site of electron transfer with the quinonoid bridge sometimes dominating the redox processes as opposed to metal centered processes which would lead to mixed-valent forms.<sup>[64-65]</sup>

The quinonoid ligands such as **L** belong to a unique class of molecules where the zwitterionic form is more stable than its canonical form and the two delocalized  $\pi$ -systems are separated by C–C  $\sigma$ -bonds.<sup>[66]</sup>

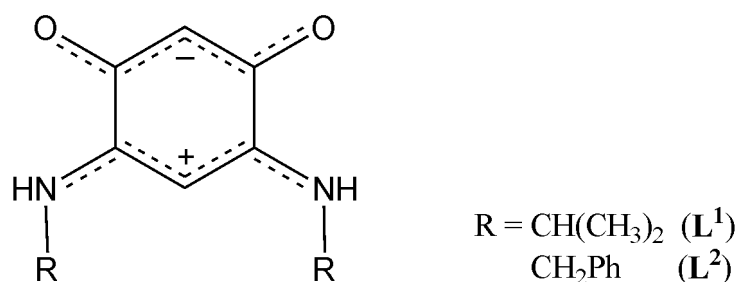


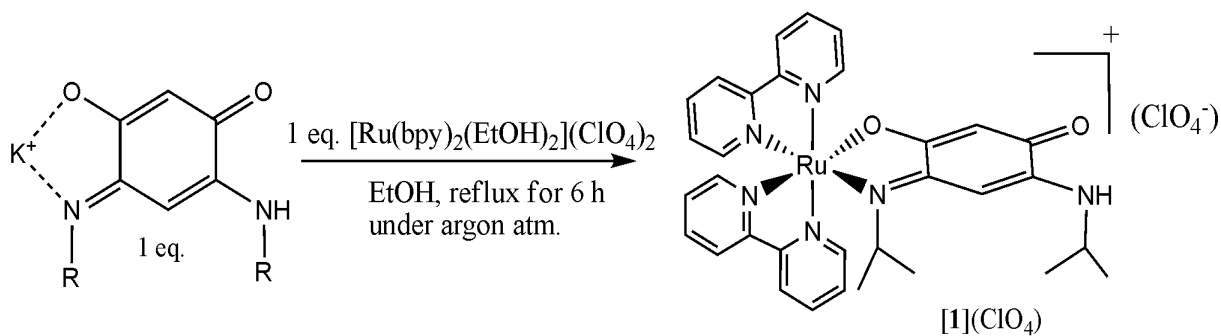
**Figure. 2.1.1.** Molecular formula of zwitterionic quinonoid ligand (**L**).

Such a *N,N'*-disubstituted ligand related to **L** was recently found to be a remarkably good facilitator of electronic communication between two quadruply bonded dimolybdenum units and provided record values for comproportionation constants<sup>[67]</sup> and such type of ligand was also used recently in connection with dinickel(II)-catalyzed olefin polymerization.<sup>[68]</sup>

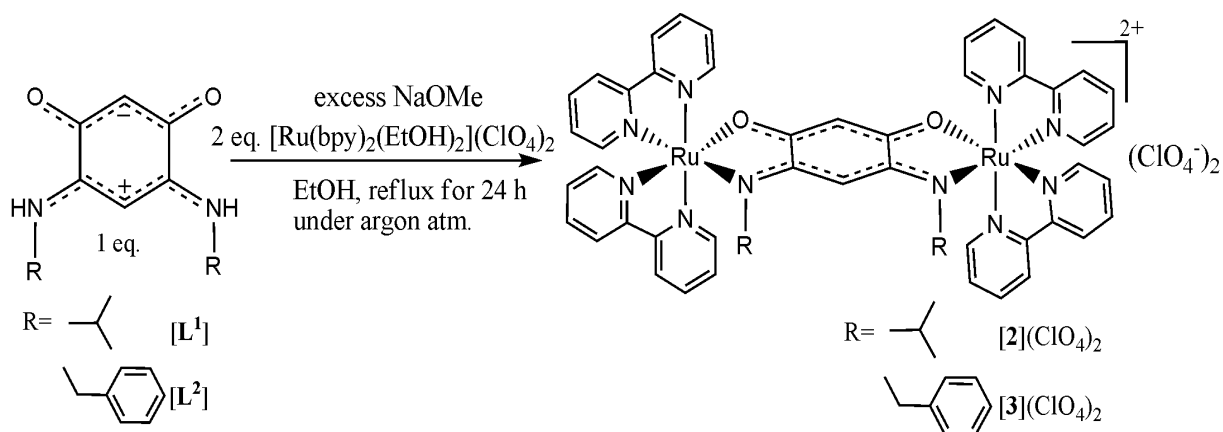
In this chapter, structural, electrochemical and UV/Vis/NIR and EPR spectroelectrochemical investigations are reported on the mononuclear ruthenium complex  $[\text{Ru}(\text{bpy})_2\text{L}^1_{-\text{H}}](\text{ClO}_4)$ , **1**(ClO<sub>4</sub>) and dinuclear ruthenium complexes  $[\{\text{Ru}(\text{bpy})_2\}_2(\mu\text{-L}^1_{-2\text{H}})](\text{ClO}_4)_2$ , **2**(ClO<sub>4</sub>)<sub>2</sub> and  $[\{\text{Ru}(\text{bpy})_2\}_2(\mu\text{-L}^2_{-2\text{H}})](\text{ClO}_4)_2$ , **3**(ClO<sub>4</sub>)<sub>2</sub> (bpy = 2,2'-bipyridine, **L**<sup>1</sup> = *N,N'*-diisopropyl-2-amino-5-alcoholate-1,4-benzoquinonemonoiminium and **L**<sup>2</sup> = *N,N'*-dibenzyl-2-amino-5-alcoholate-1,4-benzoquinonemonoiminium) (Scheme 2.2.1-2.2.2) in order to determine localization vs. delocalization of the  $\pi$ -system in **L**, the site of electron transfer in these complexes and the general utility of such ligands in mixed-valence chemistry. Two different *N*-substituted ligands were used to tune metal-metal coupling in the mixed-valent state and redox potentials.

## 2.2. Synthesis and characterization

The ligands **L**<sup>1</sup> and **L**<sup>2</sup> were prepared as reported.<sup>[69]</sup> The mononuclear complex **1**(ClO<sub>4</sub>) was synthesized by the reaction of  $[\text{Ru}(\text{bpy})_2(\text{EtOH})_2](\text{ClO}_4)_2$  with the monodeprotonated form of **L**<sup>1</sup><sup>[17]</sup> in a 1:1 ratio in refluxing ethanol (Scheme 2.2.1). The dinuclear complexes **2**(ClO<sub>4</sub>)<sub>2</sub> and **3**(ClO<sub>4</sub>)<sub>2</sub> were synthesized in a one-pot reaction by reacting two equivalents of  $[\text{Ru}(\text{bpy})_2(\text{EtOH})_2](\text{ClO}_4)_2$  with one equivalent of the corresponding quinonoid ligand (**L**) in presence of excess sodium methoxide in refluxing ethanol (Scheme 2.2.2). All the complexes were purified by column chromatography using neutral alumina column and characterized by <sup>1</sup>H NMR, electrospray mass spectroscopy and elemental analysis (see experimental section). The <sup>1</sup>H NMR spectrum of dinuclear complexes **2**(ClO<sub>4</sub>)<sub>2</sub> and **3**(ClO<sub>4</sub>)<sub>2</sub> showed two sets of signals that indicate the formation of both isomers under our reaction conditions (see experimental section)



**Scheme 2.2.1.** Synthesis of mononuclear ruthenium complex  $\mathbf{1}(\text{ClO}_4)$ .



**Scheme 2.2.2.** Synthesis of dinuclear ruthenium complexes  $\mathbf{2}(\text{ClO}_4)_2$  and  $\mathbf{3}(\text{ClO}_4)_2$ .

## 2.3 Crystal structures

The complexes could be crystallized as  $\mathbf{1}(\text{ClO}_4) \cdot \text{CH}_2\text{Cl}_2$  (Figure 2.3.1), *meso*- $\mathbf{2}(\text{ClO}_4)_2 \cdot 2\text{CH}_2\text{Cl}_2$  (Figure 2.3.2) and *meso*- $\mathbf{3}(\text{ClO}_4)_2$  (Figure 2.3.3-2.3.4) by layering their dichloromethane solution with excess *n*-hexene (1:2, slow diffusion).  $\mathbf{1}(\text{ClO}_4) \cdot \text{CH}_2\text{Cl}_2$  crystallizes in the  $P2_1/c$  space group, complex  $\mathbf{2}(\text{ClO}_4)_2 \cdot 2\text{CH}_2\text{Cl}_2$  crystallizes in the  $P-1$  space group and complex  $\mathbf{3}(\text{ClO}_4)_2$  crystallizes in the  $P2_1/n$  space group. Selected bond lengths of the complexes are given in Tables 2.3.1-2.3.2. The bond lengths of  $\text{L}^1$  are also included in table 2.3.1 for comparison.

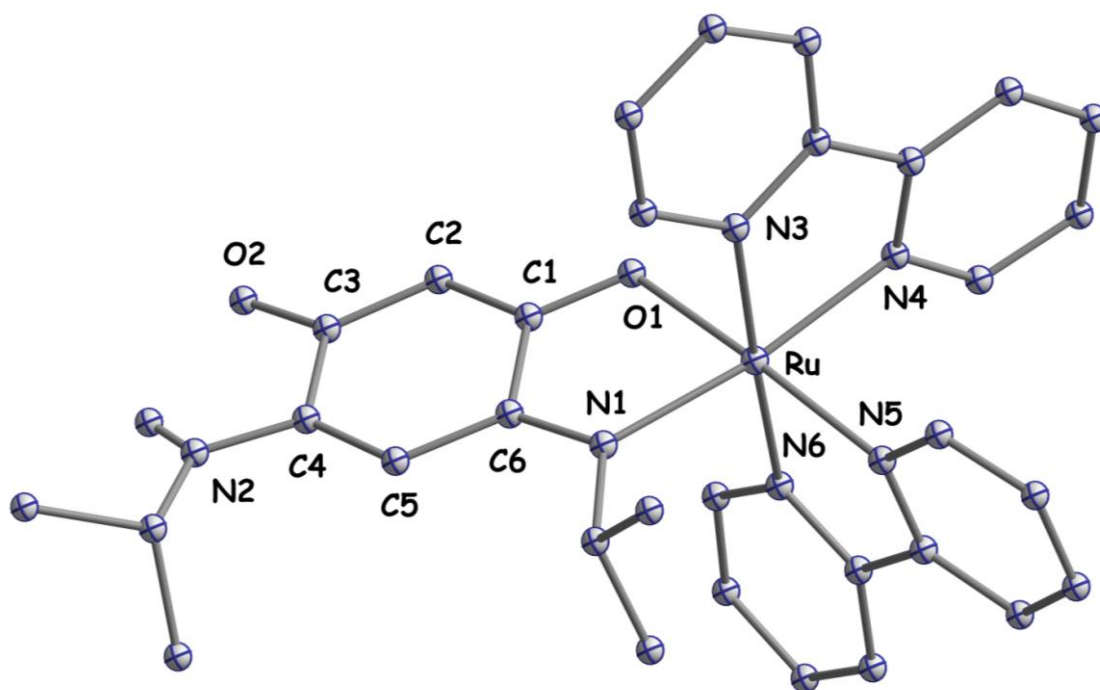


**Figure 2.3.1.** Molecular structure of the cation in the crystal structure of  $1(\text{ClO}_4)\cdot\text{CH}_2\text{Cl}_2$ . Ellipsoids include 50% of the electron density. Hydrogen atoms, except H1N are omitted for clarity.

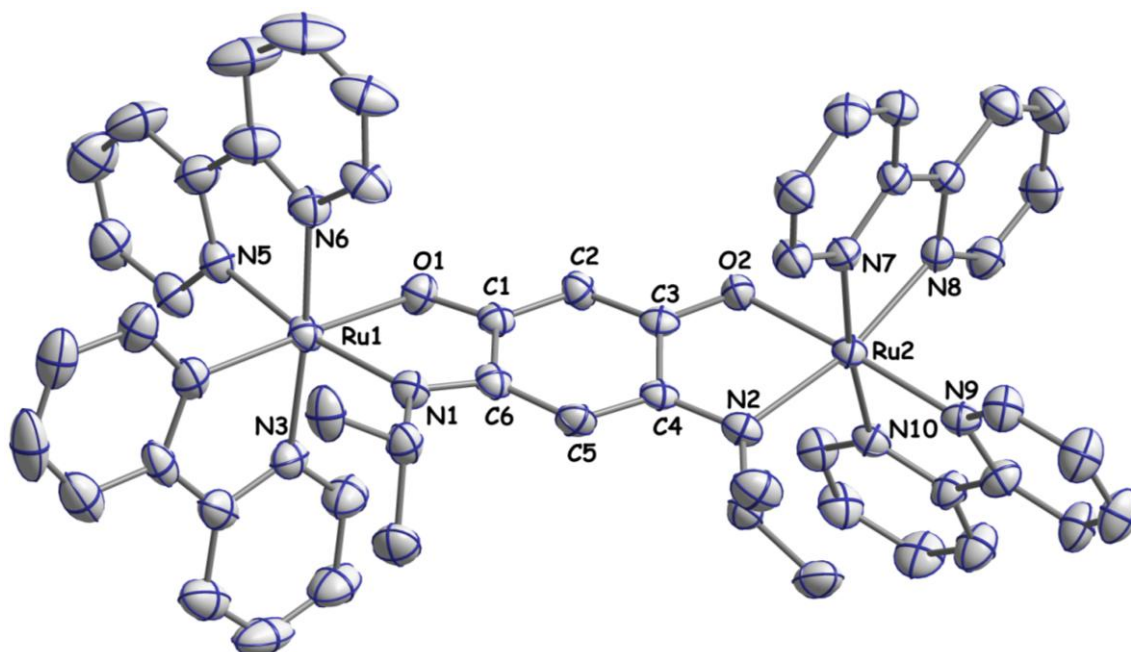


**Figure 2.3.2.** Molecular structure of the dication in the crystal structure of *meso*- $2(\text{ClO}_4)_2\cdot 2\text{CH}_2\text{Cl}_2$ . Ellipsoids include 50% of the electron density. Hydrogen atoms are omitted for clarity.



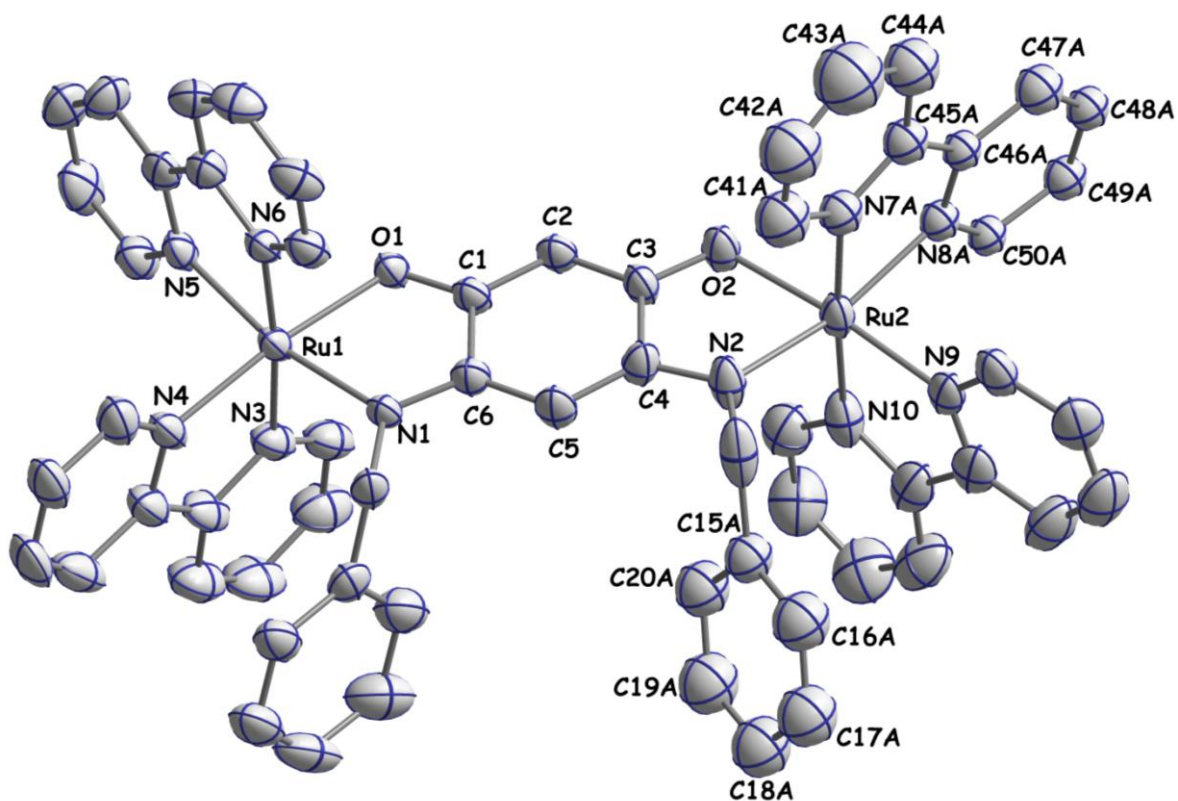


**Figure 2.3.3.** Molecular structure of the dication in the crystal structure of *meso*-3A(ClO<sub>4</sub>)<sub>2</sub>. Ellipsoids include 50% of the electron density. Hydrogen atoms are omitted for clarity.

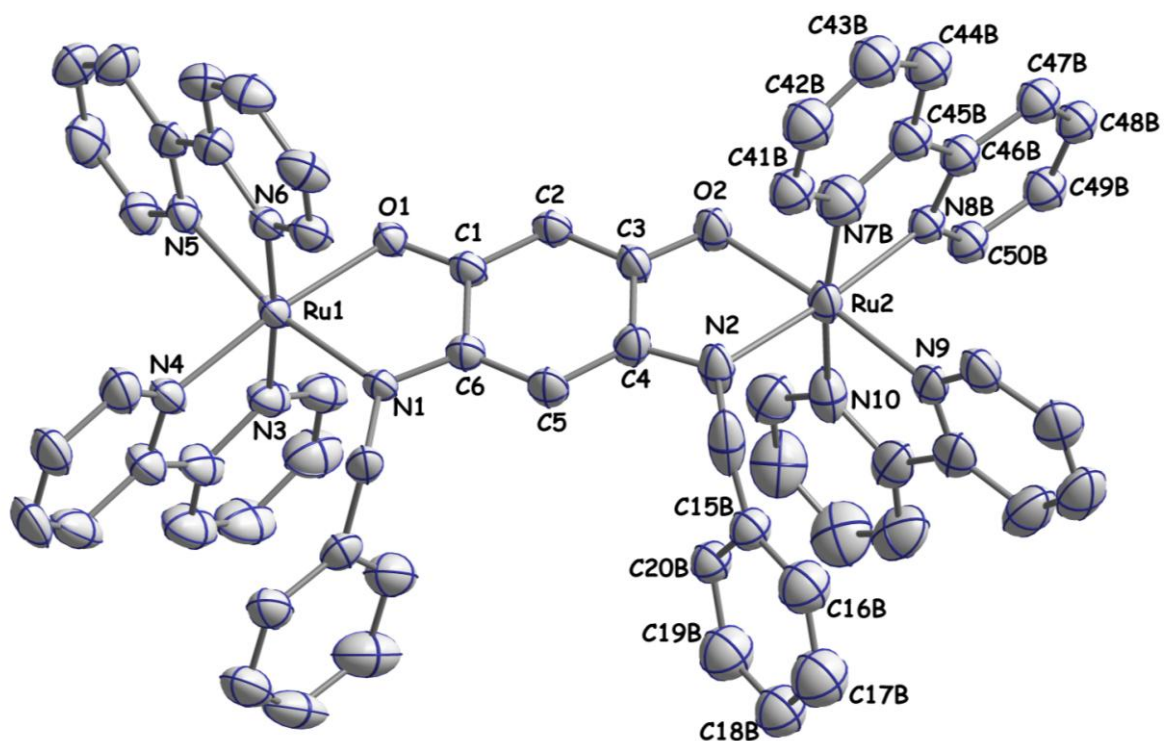


**Figure 2.3.4.** Molecular structure of the dication in the crystal structure of *meso*-3B(ClO<sub>4</sub>)<sub>2</sub>. Ellipsoids include 50% of the electron density. Hydrogen atoms are omitted for clarity.

The ruthenium center in **1**(ClO<sub>4</sub>) exhibits a distorted octahedral coordination being bonded to four nitrogen atoms from the two bipyridine ligands and the nitrogen and oxygen atoms from the mono-deprotonated form of **L**<sup>1</sup>. The ruthenium centres in the dinuclear complexes **2**(ClO<sub>4</sub>)<sub>2</sub> and **3**(ClO<sub>4</sub>)<sub>2</sub> also have a distorted octahedral coordinated geometry with the bis-deprotonated form of **L**<sup>1</sup> and **L**<sup>2</sup> respectively bridging the metal centres in a double chelating O,N; O,N fashion; the remaining coordination sites being taken up by the nitrogen atoms from the bipyridine ligands. In the crystal lattice, complex **3**(ClO<sub>4</sub>)<sub>2</sub> exhibits a perfectly statistical disorder with one bipyridine and one phenyl ring in **L**<sup>2</sup>-<sub>2H</sub> ligands occupying two sets of positions around the same Ru center {**3A**(ClO<sub>4</sub>)<sub>2</sub> and **3B**(ClO<sub>4</sub>)<sub>2</sub>}.

**Table 2.3.1.** Metal-ligand bond lengths in [Å] for **1**(ClO<sub>4</sub>), **2**(ClO<sub>4</sub>)<sub>2</sub> and **3**(ClO<sub>4</sub>)<sub>2</sub>.

|         | <b>1</b> (ClO <sub>4</sub> ) | <b>2</b> (ClO <sub>4</sub> ) <sub>2</sub> | <b>3A</b> (ClO <sub>4</sub> ) <sub>2</sub> |
|---------|------------------------------|---|--|
| Ru1-O1  | 2.071(2)                     | 2.066(3)                                  | 2.081(4)                                   |
| Ru1-N1  | 2.071(2)                     | 2.091(4)                                  | 2.053(5)                                   |
| Ru1-N3  | 2.065(2)                     | 2.044(4)                                  | 2.051(5)                                   |
| Ru1-N4  | 2.070(2)                     | 2.029(4)                                  | 2.047(5)                                   |
| Ru1-N5  | 2.052(2)                     | 2.058(4)                                  | 2.058(5)                                   |
| Ru1-N6  | 2.048(2)                     | 2.050(4)                                  | 2.036(5)                                   |
| Ru2-O2  |                              | 2.065(3)                                  | 2.080(4)                                   |
| Ru2-N2  |                              | 2.091(4)                                  | 2.036(5)                                   |
| Ru2-N7  |                              | 2.067(3)                                  |  |
| Ru2-N8  |                              | 2.061(4)                                  |  |
| Ru2-N9  |                              | 2.028(4)                                  | 2.035(5)                                   |
| Ru2-N10 |                              | 2.034(3)                                  | 2.028(6)                                   |
| Ru2-N7A |                              |   | 2.108(13)                                  |
| Ru2-N8A |                              |   | 2.068(11)                                  |

**Table 2.3.2.** Comparison of selected bond lengths in [Å] for **1**(ClO<sub>4</sub>), **2**(ClO<sub>4</sub>)<sub>2</sub> and **3**(ClO<sub>4</sub>)<sub>2</sub> and **L**<sup>1[66]</sup>.

|       | <b>L</b> <sup>1[66]</sup> | <b>1</b> (ClO <sub>4</sub> ) | <b>2</b> (ClO <sub>4</sub> ) <sub>2</sub> | <b>3</b> (ClO <sub>4</sub> ) <sub>2</sub> |
|-------|---------------------------|------------------------------|---|---|
| C1-C2 | 1.390(4)                  | 1.385(4)                     | 1.386(6)                                  | 1.390(8)                                  |
| C2-C3 | 1.391(4)                  | 1.412(4)                     | 1.378(6)                                  | 1.375(8)                                  |
| C3-C4 | 1.526(5)                  | 1.503(4)                     | 1.500(6)                                  | 1.495(8)                                  |
| C4-C5 | 1.387(4)                  | 1.376(4)                     | 1.394(6)                                  | 1.400(8)                                  |
| C5-C6 | 1.391(4)                  | 1.429(4)                     | 1.408(6)                                  | 1.396(8)                                  |
| C6-C1 | 1.529(4)                  | 1.492(4)                     | 1.495(6)                                  | 1.501(7)                                  |
| O1-C1 | 1.253(4)                  | 1.291(3)                     | 1.287(5)                                  | 1.294(7)                                  |
| C3-O2 | 1.252(4)                  | 1.254(3)                     | 1.286(5)                                  | 1.277(7)                                  |
| N1-C6 | 1.316(4)                  | 1.314(3)                     | 1.336(6)                                  | 1.331(7)                                  |
| N2-C4 | 1.316(4)                  | 1.348(4)                     | 1.337(6)                                  | 1.329(7)                                  |

The metal–donor distances in mono- and dinuclear complexes are typical of Ru–N and Ru–O bonds (Table 2.3.1). On comparing the bond distances within the coordinated ligand **L**<sup>1</sup> in **1**(ClO<sub>4</sub>), **2**(ClO<sub>4</sub>)<sub>2</sub>, **3**(ClO<sub>4</sub>)<sub>2</sub> and the free form of **L**<sup>1</sup> one sees some remarkable trends. The free ligand **L**<sup>1</sup> has a non-crystallographic C<sub>2v</sub> symmetry (see the similar lengths of e.g., O1–C1 and O2–C3 in Table 2.3.2). Upon coordination to one metal centre in **1**(ClO<sub>4</sub>), an asymmetrization of the  $\pi$  bonding over the O1–C1–C2–C3–O2 and N1–C6–C5–C4–N2 groups occurs with, e.g., O1–C1 [1.291(3) Å] becoming significantly longer than O2–C3 [1.254(3) Å], the latter value being similar to those observed in free **L**<sup>1</sup>. While the N1–C6 bond remains similar in **1**(ClO<sub>4</sub>), with respect to free **L**<sup>1</sup>, the uncoordinated N2–C4 bond elongates, confirming the electronic communication between the two moieties. These changes have consequences also on the C–C bonds within the two aforementioned delocalized groups. The symmetry is restored when a second metal is coordinated by the quinonoid ligand in **2**(ClO<sub>4</sub>)<sub>2</sub> (see the similar lengths of e.g., O1–C1 [1.287(5) Å] and O2–C3 [1.286(5) Å]). So the two  $\pi$  systems O1–C1–C2–C3–O2 and N1–C6–C5–C4–N2 of coordinated bridging ligand in **2**(ClO<sub>4</sub>)<sub>2</sub> are completely delocalized and separated by authentic C–C single bonds like free **L**<sup>1</sup>. In **2**(ClO<sub>4</sub>)<sub>2</sub>, at variance with **L**<sup>1</sup> and **1**(ClO<sub>4</sub>), the quinonoid moiety is not planar; a slight twisting occurs around the C2–C5 line (Figure 2.3.5). This is allowed by the single bond nature of C1–C6 and C3–C4, which remains *ca.* 1.5 Å in all the complexes. The O1, C1, C2,

C3 and O2 atoms are almost coplanar (maximum deviation from the mean plane: 0.027(4) Å for C3) as well as the N1, C6, C5, C4 and N2 (maximum deviation from the mean plane: 0.059(4) Å for C6). The two planes form an angle of 9.0(1)°.

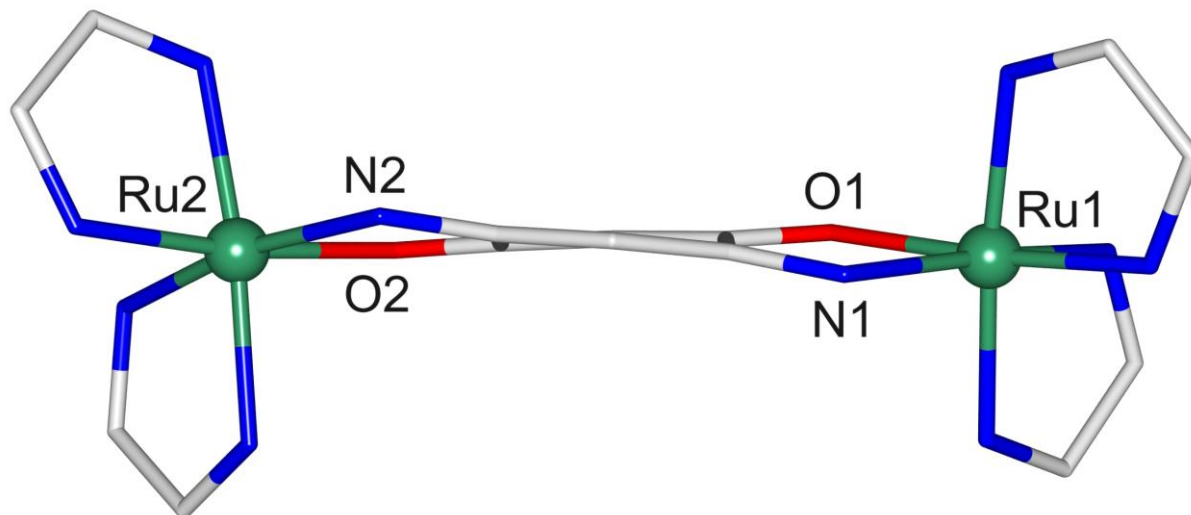


**Table 2.3.5.** Structural diagram of the cation in *meso*- $2(\text{ClO}_4)_2 \cdot 2\text{CH}_2\text{Cl}_2$ , emphasizing the twisting of the quinonoid ligand. Only the chelation rings are depicted for the pyridine ligands, hydrogen atoms and isopropyl groups are omitted for clarity.

The crystal structure of  $3(\text{ClO}_4)_2$  shows similar bond lengths as observed in *meso*- $2(\text{ClO}_4)_2$  (Figure 2.3.3-2.3.4 and Table 2.3.2). The two  $\pi$  systems O1–C1–C2–C3–O2 and N1–C6–C5–C4–N2 are also delocalized in  $3(\text{ClO}_4)_2$  as expected. The quinonoid moiety is also twisted around C2–C5 just like in  $2(\text{ClO}_4)_2$ .

To summarize, on coordination of one metal centre,  $\pi$ -bonding becomes more localized. However, on double metallation, the delocalization is restored again. Hence we have here a rare example of metallation-controlled delocalization of the  $\pi$ -system. The Ru–Ru distance in the dinuclear complexes  $2(\text{ClO}_4)_2$  and  $3(\text{ClO}_4)_2$  are 7.996 Å and 7.986 Å respectively.

## 2.4. Electrochemistry

The electrochemistry of the complexes  $1(\text{ClO}_4)$ ,  $2(\text{ClO}_4)_2$  and  $3(\text{ClO}_4)_2$  have been studied by cyclic voltammetry in order to investigate their redox properties (Figure 2.4.1). Ferrocene was used as an internal standard and all the redox potentials are referenced with respect to ferrocenium /ferrocene ( $\text{Fc}^+/\text{Fc}$ ) couple. The potential values (oxidations and reductions) for all the complexes are summarized in Table 2.4.1.

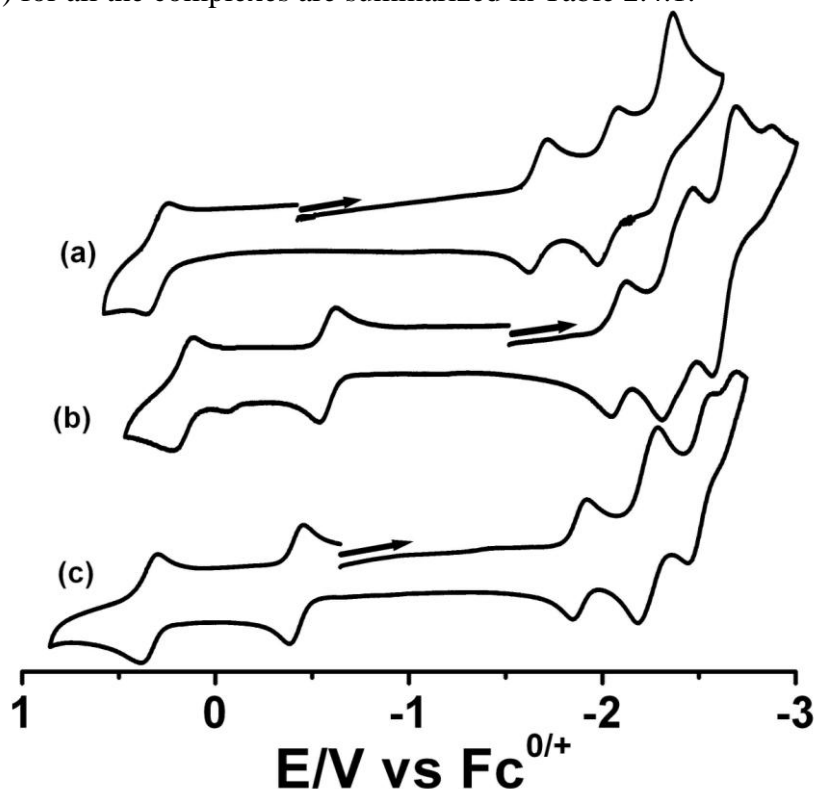


**Figure 2.4.1.** Cyclic voltammograms of complexes  $1^+$  (a),  $2^{2+}$  (b) and  $3^{2+}$  (c) in  $\text{CH}_3\text{CN}/0.1 \text{ M}$   $\text{Bu}_4\text{NPF}_6$  at 295 K.

**Table 2.4.1.** Redox potentials of the complexes.<sup>[a]</sup>

| Complex    | $E_{1/2}^{ox2}(\Delta E_p)^{[b]}$ | $E_{1/2}^{ox1}(\Delta E_p)^{[b]}$ | $E_{1/2}^{red1}(\Delta E_p)^{[b]}$ | $E_{1/2}^{red2}(\Delta E_p)^{[b]}$ | $E_{1/2}^{red3}(\Delta E_p)^{[b]}$ |
|------------|-----------------------------------|-----------------------------------|------------------------------------|------------------------------------|------------------------------------|
| $[1]^+$    |                                   | +0.19 (117)                       | -1.65 (90)                         | -2.01 (104)                        | -2.31 (116)                        |
| $[2]^{2+}$ | +0.17 (95)                        | -0.58 (82)                        | -2.10 (72)                         | -2.40 (155)                        | -2.65 (113)                        |
| $[3]^{2+}$ | +0.34 (78)                        | -0.42 (64)                        | -1.88 (69)                         | -2.24 (98)                         | -2.50 (113)                        |

<sup>[a]</sup> Electrochemical potentials in V from cyclic voltammetry in  $\text{CH}_3\text{CN} / 0.1 \text{ M}$   $\text{Bu}_4\text{NPF}_6$  at 298 K. Scan Rate: 100 mV/s. Ferrocene / Ferrocenium was used as internal standard.

<sup>[b]</sup>  $\Delta E_p$ : difference between peak potentials in mV.

The complex  $1^+$  shows one quasi-reversible oxidation at 0.19 V vs. ferrocene/ferrocenium in  $\text{CH}_3\text{CN}/0.1 \text{ M Bu}_4\text{NPF}_6$  and several reduction processes. The first reduction could be either coordinated  $\text{L}^1_{\text{H}}$  centred or bipyridine centred. The coordinated  $\text{L}^1_{\text{H}}$  in  $1^+$  contains an N-H group and a carbonyl group in the metal free side which could interact strongly with the solvent molecules. If the first reduction is  $\text{L}^1_{\text{H}}$  centred then the reduction potential could change remarkably on solvent variation. In this regard the cyclic voltammogram of  $1^+$  has been investigated in several solvents with different polarity to assign the first reduction.

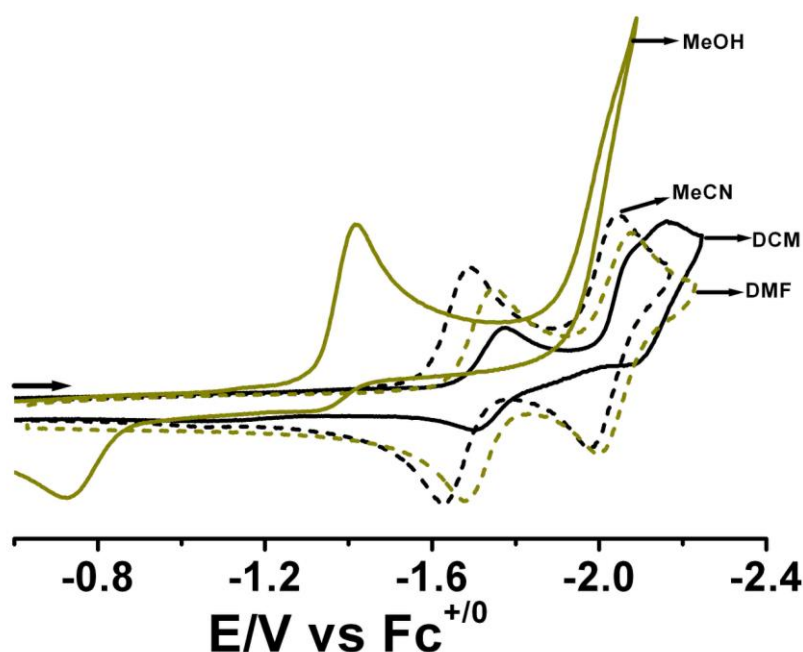


**Figure 2.4.2.** Cyclic voltammograms of  $1^+$  in different solvents containing 0.1 M  $\text{Bu}_4\text{NPF}_6$  at 295 K.

**Table 2.4.1:** Redox potentials of the complex  $1^+$  in different solvents.<sup>[a]</sup>

| Solvent | $E_{1/2}^{red1}$<br>( $\Delta E_p$ ) <sup>[b]</sup> | $E_{1/2}^{red2}$<br>( $\Delta E_p$ ) <sup>[b]</sup> |
|---------|---|---|
| DCM     | -1.74 (re)<br>(72)                                  | -2.12 (ir)<br>(88)                                  |
| DMF     | -1.71 (re)<br>(63)                                  | -2.04 (re)<br>(76)                                  |
| MeCN    | -1.65 (re)<br>(58)                                  | -2.01 (re)<br>(67)                                  |
| MeOH    | -1.41 (ir)  |   |

<sup>[a]</sup> Electrochemical potentials in V from cyclic voltammetry in different solvents / 0.1 M  $\text{Bu}_4\text{NPF}_6$  at 298 K. Scan Rate: 100 mV/s. Ferrocene / Ferrocenium was used as internal standard. <sup>[b]</sup>  $\Delta E_p$ : difference between peak potentials in mV.

The first reduction potential of  $1^+$  shifts remarkably with changing solvent polarity (Figure 2.4.2 and Table 2.4.2). In protic solvents such as methanol, the first reduction become completely irreversible that suggest  $L^1_{-H}$  centred reduction. Similarly, the oxidation step can also be assigned by the solvent influence on the oxidation potential. The first oxidation potential has also been measured in several solvents (Figure 2.4.3). The potential values are listed in Table 2.4.3. The oxidation potential has also been shifted remarkably with the change of solvent polarity and that indicates  $L^1_{-H}$  centred oxidation.

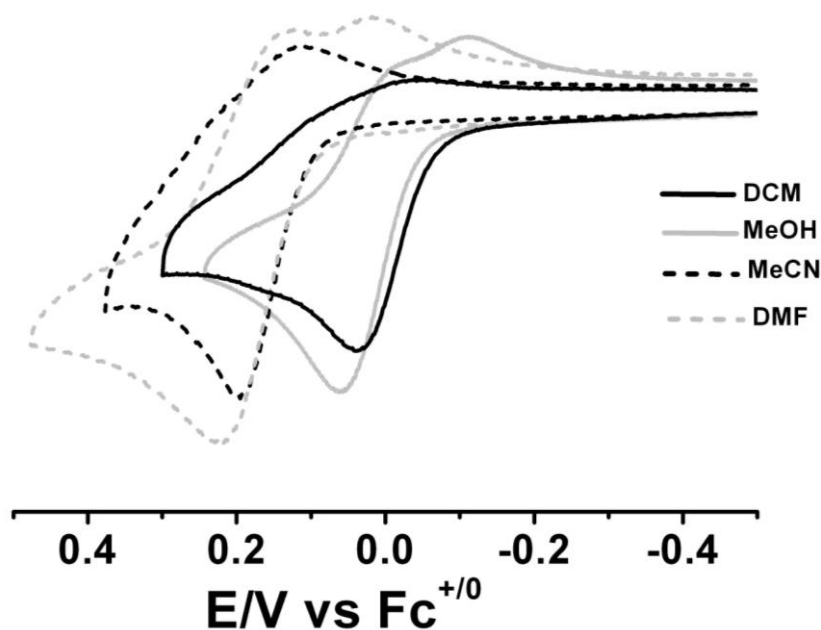


**Figure 2.4.3.** Cyclicvoltammogram of the complex the  $1^+$  in different solvents / 0.1 M  $Bu_4NPF_6$  at 298 K. Scan Rate: 100 mV/s.

**Table 2.4.3:** Oxidation potentials of the complex  $1^+$  in different solvents.<sup>[a]</sup>

| Solvent | $E^{oxdI}$ |
|---------|------------|
| DCM     | +0.04 (ir) |
| MeOH    | +0.06 (ir) |
| MeCN    | +0.19 (ir) |
| DMF     | +0.22 (ir) |

<sup>[a]</sup> Electrochemical potentials in V from cyclic voltammetry in different solvents / 0.1 M  $Bu_4NPF_6$  at 298 K. Scan Rate: 100 mV/s. Ferrocene / Ferrocenium was used as internal standard.

The complex  $\mathbf{2}^{2+}$  and  $\mathbf{3}^{2+}$  also show several reduction processes in  $\text{CH}_3\text{CN}/0.1 \text{ M Bu}_4\text{NPF}_6$ , which are assigned to successive reductions of bridge **L** and the bipyridine units (Figure 2.4.1). The  $\mathbf{3}^{2+}$  reduces at comparatively lower potentials than  $\mathbf{2}^{2+}$  (Table 2.4.1). This shift of redox potentials are caused by the presence of electron withdrawing groups  $-\text{CH}_2\text{Ph}$  in  $\mathbf{3}^{2+}$  as compared to than electron donating groups  $-\text{CH}_2(\text{CH}_3)_2$  in  $\mathbf{2}^{2+}$ . The oxidation processes for  $\mathbf{2}^{2+}$  occur at remarkably low potentials ( $-0.58$  and  $0.17 \text{ V}$ , respectively, vs. ferrocene/ferrocenium) (Figure 2.4.1). The difference between the two oxidation potentials of  $750 \text{ mV}$ , translates into exceptionally large comproportionation constant,<sup>[70]</sup>  $K_c$  of the order of  $10^{13}$ . Similarly the oxidation processes for  $\mathbf{3}^{2+}$  occur also at remarkably low potentials ( $-0.42$  and  $0.34 \text{ V}$ , respectively, vs. ferrocene/ferrocenium) (Figure 2.4.1) but the potentials are marginally shifted to the higher potentials as expected due to the electron withdrawing nature of  $-\text{CH}_2\text{Ph}$  group. The difference between the two oxidation potentials for  $\mathbf{3}^{2+}$  is  $760 \text{ mV}$ , and this translates into a comproportionation constant,  $K_c$  of the same order of  $10^{13}$ . Such large values of  $K_c$  are unprecedented in quinonoid-bridged dinuclear  $[\text{Ru}(\text{bpy})_2]$  complexes, suggests high stability of the mixed-valent state. For comparison, the complex  $\{[\text{Ru}(\text{bpy})_2]_2(\mu\text{-L}^3)\}^{2+}$  ( $\text{L}^3 =$  dianion of 2,5-dihydroxy-1,4 benzoquinone)<sup>[64]</sup> has a  $K_c$  of the order of  $10^5$  and the complex  $\{[\text{Ru}(\text{bpy})_2]_2(\mu\text{-L}^4)\}^{2+}$  ( $\text{L}^4 =$  dianion of 2,5-dihydroxy-1,4-iminobenzoquinone)<sup>[71]</sup> has a  $K_c$  of the order of  $10^8$ . The strongly delocalized bonding situation in the ligand  $\text{L}_{\text{2H}}$  in  $\mathbf{2}^{2+}$  and  $\mathbf{3}^{2+}$  (vide supra) as opposed to a more localized one in the bridging ligand of the other quinonoid-bridged complexes<sup>[71]</sup> is probably responsible for such large  $K_c$  value.

## 2.5. UV/Vis/NIR spectroelectrochemistry

In order to determine the metal-metal electronic coupling in dinuclear complexes and electronic distribution in various accessible redox processes, UV/Vis/NIR spectroelectrochemical changes of all three complexes  $\mathbf{1}^+$ ,  $\mathbf{2}^{2+}$  and  $\mathbf{3}^{2+}$  were monitored using an optically transparent Thin Layer Electrochemical (OTTLE) cell. The data are summarized in Table 2.5.1.

The UV/Vis spectrum of  $\mathbf{1}^+$  is dominated by an intense broad band at  $528 \text{ nm}$  ( $\epsilon = 15000 \text{ M}^{-1} \text{ cm}^{-1}$ ) (Figure 2.5.1) which can be assigned as mixed MLCT ( $\text{Ru}^{\text{II}} \rightarrow \text{bpy}$ ) and ( $\text{Ru}^{\text{II}} \rightarrow \text{L}^1_{\text{H}}$ ) transitions. The  $\text{Ru}^{\text{II}} \rightarrow \text{L}^1_{\text{H}}$  transition can be tune by varying the polarity of solvents. The bands are separated in protic solvents such as methanol or ethanol (Figure



2.5.2). This is because of energy lowering of  $L^1_{-H}$  centred  $\pi^*$  orbitals through hydrogen bonds with protic solvents.

One electron oxidation of  $1^+$  to  $1^{2+}$  in  $CH_3CN/0.1 M Bu_4NPF_6$  leads to slight decomposition of the complex and the MLCT transitions are red shifted to 621 and 578 nm with substantial decrease in intensity (Figure 2.5.3) that suggest  $L^1_{-H}$  centred oxidation.

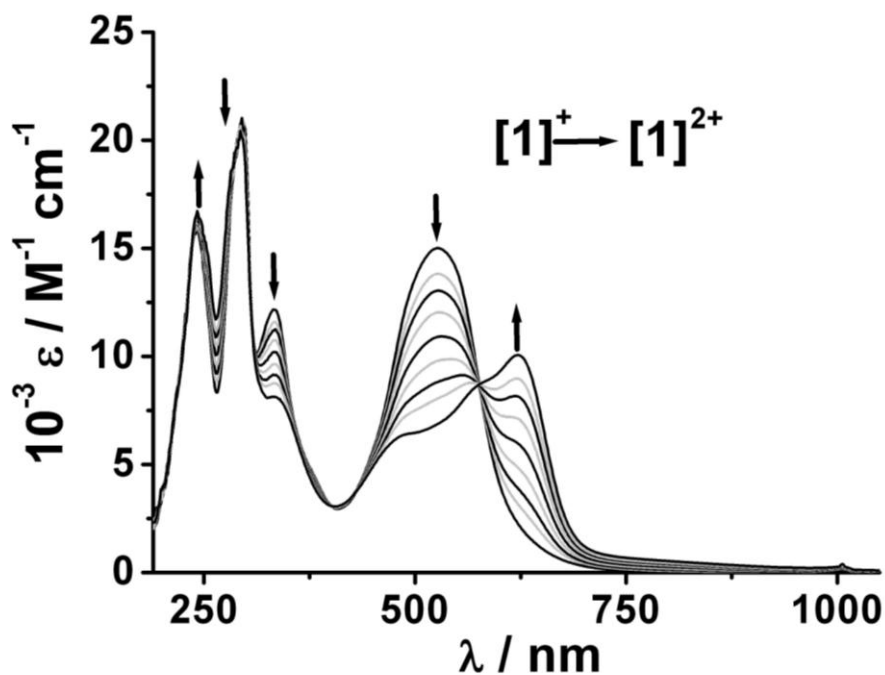


**Figure 2.5.1.** UV-Vis-NIR spectroelectrochemistry of the conversion  $[1]^{(1+) \rightarrow (2+)}$  in  $CH_3CN / 0.1 M Bu_4NPF_6$ .

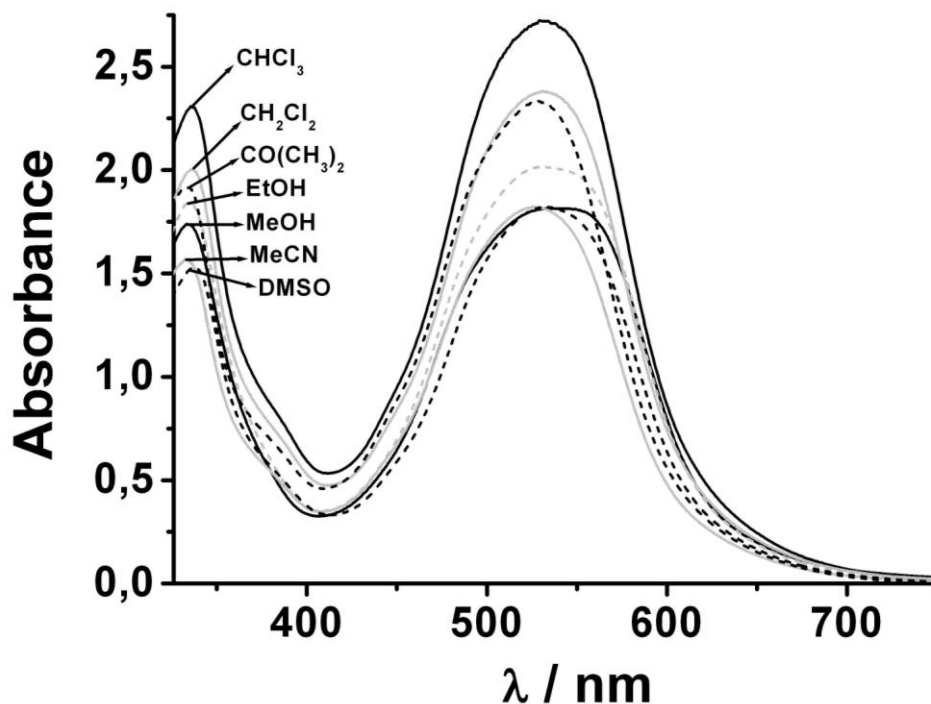


**Figure 2.5.2.** Change of UV-Vis spectra of the complex  $1^+$  in different solvents.

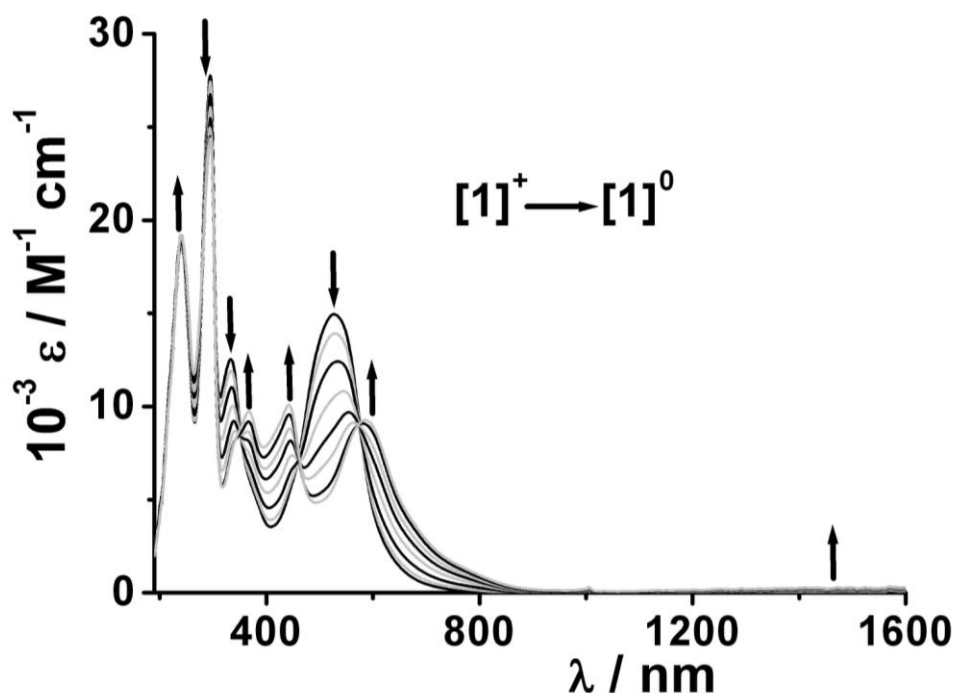


**Figure 2.5.3.** UV-Vis-NIR spectroelectrochemistry of the conversion  $[1]^{(+)} \rightarrow [1]^{(0)}$  in  $\text{CH}_3\text{CN} / 0.1 \text{ M Bu}_4\text{NPF}_6$ .

On one-electron reduction  $1^+ \rightarrow 1^0$  form, the broad  $\text{Ru}^{\text{II}}$ -based MLCT transitions band at about 528 nm are splitted in to two bands at about 443 nm and 587 nm (Figure 2.5.3). So one MLCT transition is red-shifted and another one is blue shifted. This probably occurs by one electron reduction of  $\text{L}^1_{\text{-H}}$  which results in a red-shift of the  $\text{Ru}^{\text{II}} \rightarrow \text{bpy}$  transition and a blue shift of  $\text{Ru}^{\text{II}} \rightarrow \text{L}^1_{\text{-H}}$  transition. Thus the first reduction takes place on  $\text{L}^1_{\text{-H}}$  centre leading to the configuration  $[\text{Ru}^{\text{II}}(\text{bpy})_2(\text{L}^1_{\text{-H}})^-]$  after the first reduction.

The UV-Vis spectrum of  $2^{2+}$  is dominated by intense bands at 623 ( $\epsilon = 21700 \text{ M}^{-1}\text{cm}^{-1}$ ) and 543 nm ( $\epsilon = 19100 \text{ M}^{-1}\text{cm}^{-1}$ ) with a shoulder at about 809 nm (Figure 2.5.4). These are tentatively assigned to  $\text{Ru}^{\text{II}} \rightarrow \text{L}^1_{\text{-H}}$  and  $\text{Ru}^{\text{II}} \rightarrow \text{bpy}$  MLCT transitions. Spectroelectrochemical oxidation of  $2^{2+}$  to the  $2^{3+}$  form in  $\text{CH}_3\text{CN}/0.1 \text{ M Bu}_4\text{NPF}_6$  shows the emergence of bands in the NIR region (Figure 2.5.4). The band at 1560 nm ( $\epsilon = 2100 \text{ M}^{-1}\text{cm}^{-1}$ ) appears during the first oxidation processes but disappears on further oxidation to the  $2^{4+}$  state (Figure 2.5.5) which could be attributed to the intervalence charge transfer (IVCT) transition for the configuration  $\text{Ru}^{\text{II}}-\text{L}^1_{\text{-2H}}-\text{Ru}^{\text{III}}$  for  $2^{3+}$ . The experimental line-width of the IVCT band ( $\Delta\nu_{1/2}$ ) of about  $1670 \text{ cm}^{-1}$  for the IVCT band at 1560 nm is much smaller than that calculated using the Hush formula<sup>[72]</sup>  $\Delta\nu_{1/2}(\text{calc}) = (2310\nu_{\text{IVCT}})^{1/2} \approx 3850 \text{ cm}^{-1}$ . The second oxidation to  $2^{4+}$  is likely to produce  $\text{Ru}^{\text{III}}-\text{L}^1_{\text{-2H}}-\text{Ru}^{\text{III}}$  and that is why the MLCT charge

transfer transitions are blue-shifted and the IVCT transition disappears. On spectroelectrochemical one-electron reduction of  $2^{2+}$  to  $2^+$  in  $\text{CH}_3\text{CN}$ -0.1 M  $\text{Bu}_4\text{NPF}_6$  the  $\text{Ru}^{\text{II}} \rightarrow \text{L}^{\text{I-H}}$  MLCT band at 623 nm is blue shifted to 594 nm and the  $\text{Ru}^{\text{II}} \rightarrow \text{bpy}$  MLCT band at 543 nm is red shifted to 549 nm with substantial decrease in intensity (Figure 2.5.6) that suggest  $\text{L}^{\text{I-H}}$  centered reduction. In addition there is also a new band appearing at 1032 nm ( $\epsilon = 2800 \text{ M}^{-1} \text{ cm}^{-1}$ ) which probably corresponds to intra ligand  $\text{L}^{\text{I-H}}$  centered SOMO  $\rightarrow$  LUMO transition.<sup>[71]</sup>

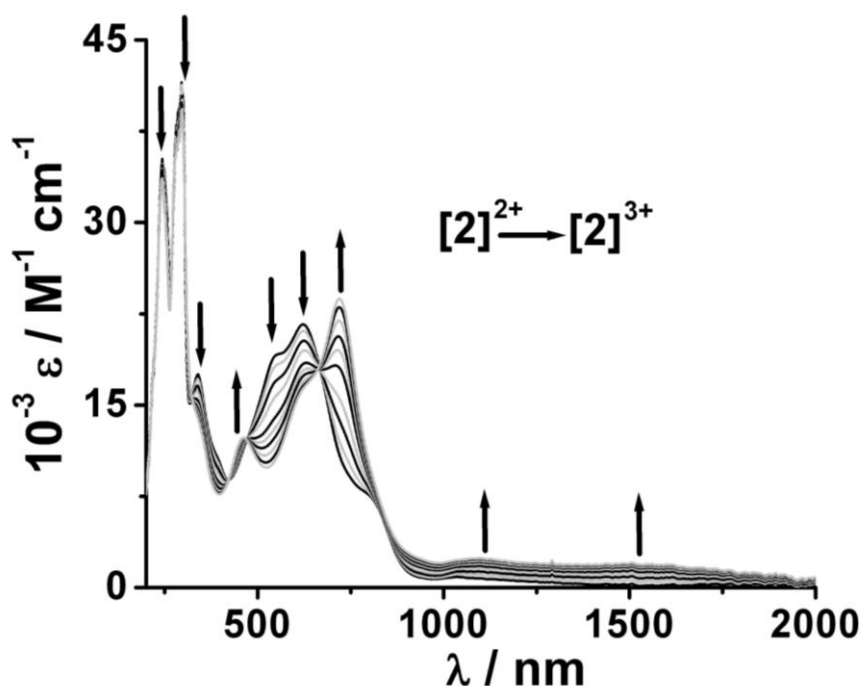


**Figure 2.5.4.** UV-Vis-NIR spectroelectrochemistry of the conversion  $[2]^{(2+) \rightarrow (3+)}$  in  $\text{CH}_3\text{CN}$  / 0.1 M  $\text{Bu}_4\text{NPF}_6$ .

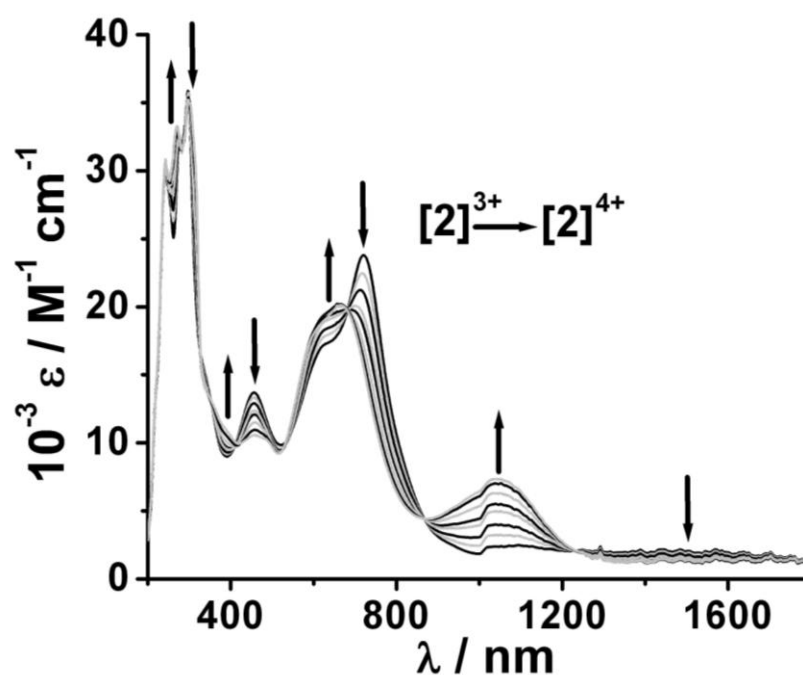


**Figure 2.5.5.** UV-Vis-NIR spectroelectrochemistry of the conversion  $[2]^{(3+) \rightarrow (4+)}$  in  $\text{CH}_3\text{CN}$  / 0.1 M  $\text{Bu}_4\text{NPF}_6$ .

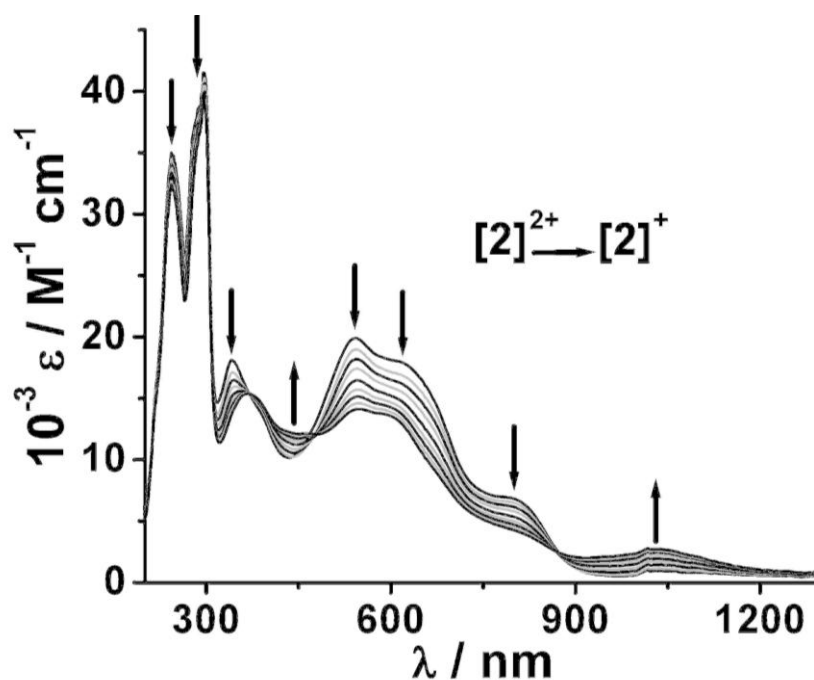


**Figure 2.5.6.** UV-Vis-NIR spectroelectrochemistry of the conversion  $[2]^{(2+) \rightarrow (+)}$  in  $\text{CH}_3\text{CN} / 0.1 \text{ M Bu}_4\text{NPF}_6$ .

In case of *N*-benzyl substituted quinonoid bridge dinuclear complex  $3^{2+}$ , the MLCT bands appear at 554 ( $\epsilon = 25300 \text{ M}^{-1}\text{cm}^{-1}$ ), 626 ( $\epsilon = 26500 \text{ M}^{-1}\text{cm}^{-1}$ ) and 812 nm ( $\epsilon = 14100 \text{ M}^{-1}\text{cm}^{-1}$ ). On comparison with  $2^{2+}$  the MLCT bands are slightly red-shifted. This is due to the electron withdrawing nature of the  $-\text{CH}_2\text{Ph}$  groups that lowers the energy of  $\text{L}_{2\text{H}}$  centered  $\pi^*$  orbitals. Spectroelectrochemical oxidation of  $3^{2+}$  to the  $3^{3+}$  form in  $\text{CH}_3\text{CN}/0.1 \text{ M Bu}_4\text{NPF}_6$  shows broad intervalence charge transfer (IVCT) transition in the NIR region for the electronic configuration  $\text{Ru}^{\text{II}}-\text{L}_{2\text{H}}-\text{Ru}^{\text{III}}$  and disappears on further oxidation (Figure 2.5.7 and 2.5.8) as observed in case of  $2^{2+}$ . The broad IVCT band appears at about at about 1340 nm which is much blue-shifted compared to broad IVCT band for  $2^{2+}$ . On spectroelectrochemical reduction of  $3^{2+}$  to the  $3^+$  form in  $\text{CH}_3\text{CN}/0.1 \text{ M Bu}_4\text{NPF}_6$ , the  $\text{Ru}^{\text{II}} \rightarrow \text{L}_{2\text{H}}$  transitions are slightly blue shifted with decrease in intensity and  $\text{Ru}^{\text{II}} \rightarrow \text{bpy}$  transitions are remain almost unchanged indicate quinonoid centered reduction. However the intra ligand quinonoid centered SOMO  $\rightarrow$  LUMO transition observed at about 1032 nm for the reduction of  $2^{2+}$  to  $2^+$  is absent in this case (Figure 2.5.9). May be in this case the intensity of quinonoid centered SOMO  $\rightarrow$  LUMO transition is very weak. The first reduction of electron donating *N*-isopropyl substituted dinuclear complex  $2^{2+}$  is completely quinonoid bridging ligand centered which is confirmed also by EPR spectroscopy (see later). Whereas in case of  $3^{2+}$ , the bridging ligand contains  $-\text{CH}_2\text{Ph}$  electron withdrawing groups. Thus the first reduction should be quinonoid centered.

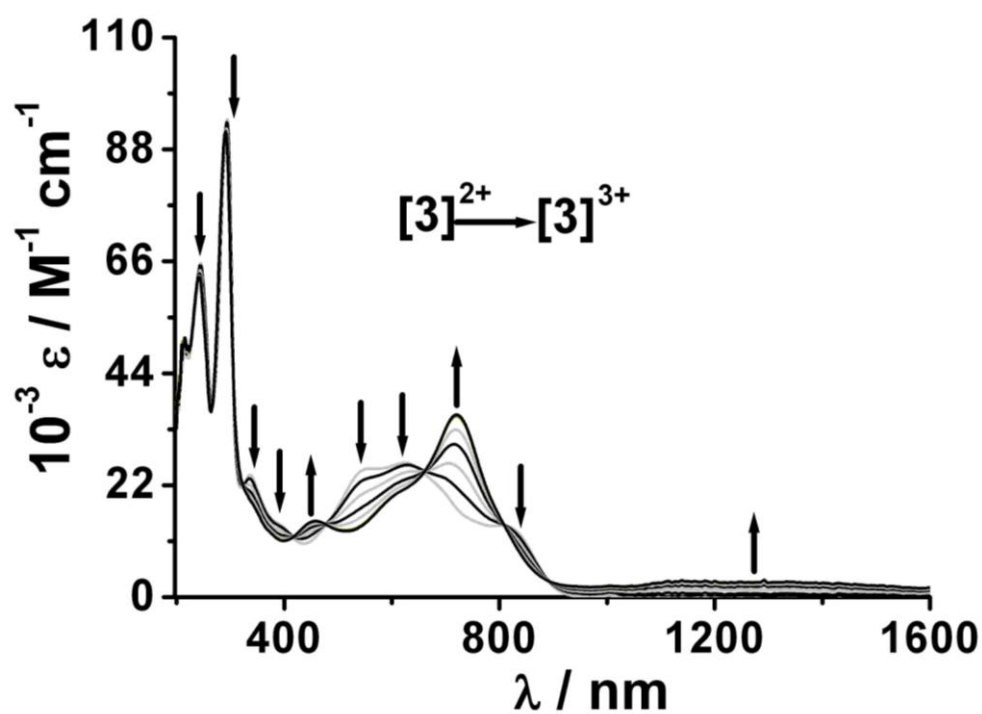


**Figure 2.5.7.** UV-Vis-NIR spectroelectrochemistry of the conversion  $[3]^{(2+) \rightarrow (3+)}$  in  $\text{CH}_3\text{CN}$  / 0.1 M  $\text{Bu}_4\text{NPF}_6$ .

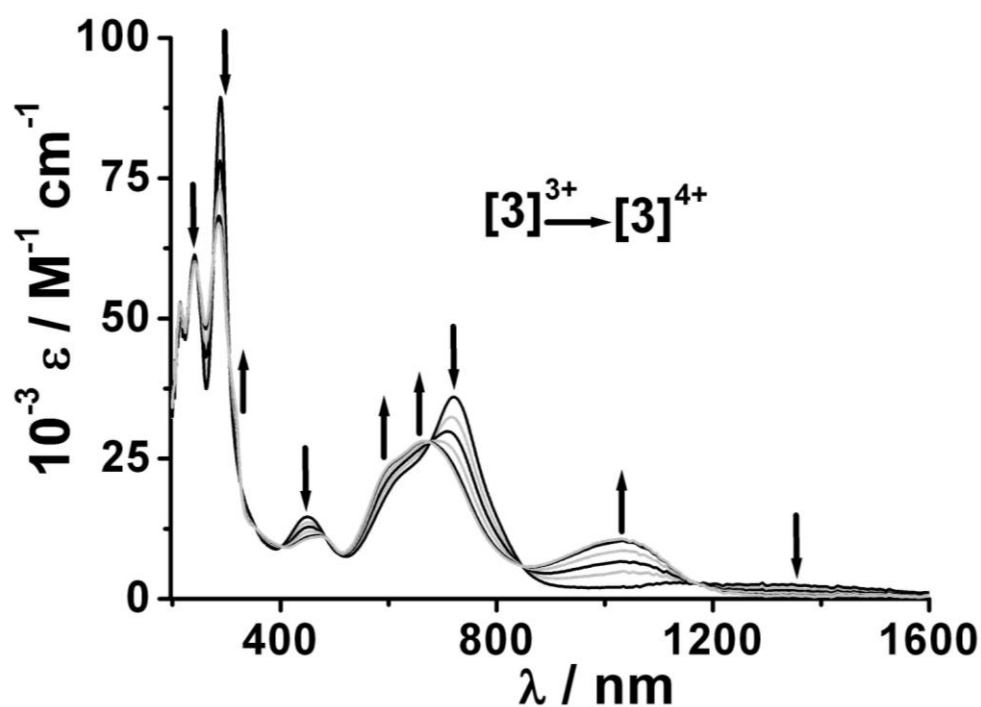


**Figure 2.5.8.** UV-Vis-NIR spectroelectrochemistry of the conversion  $[3]^{(3+) \rightarrow (4+)}$  in  $\text{CH}_3\text{CN}$  / 0.1 M  $\text{Bu}_4\text{NPF}_6$ .

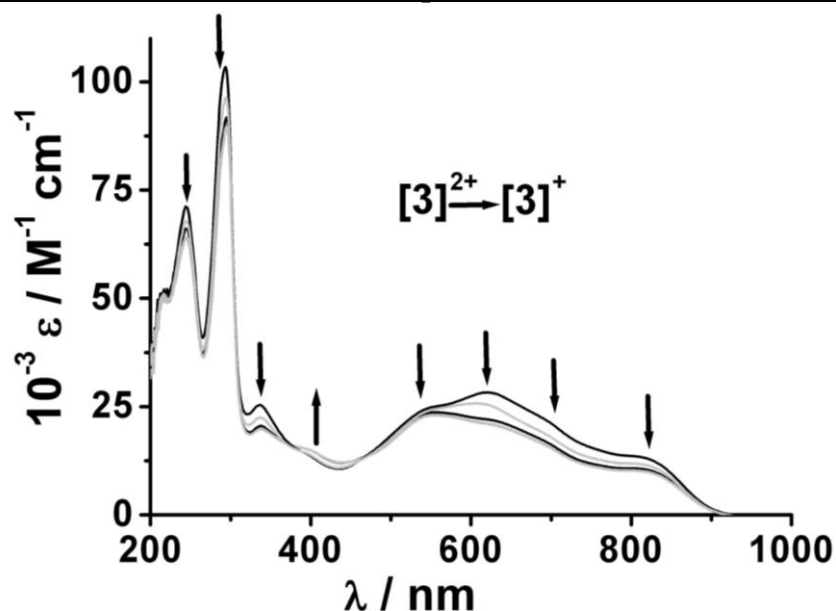


**Figure 2.5.9.** UV-Vis-NIR spectroelectrochemistry of the conversion  $[3]^{(2+) \rightarrow (+)}$  in  $\text{CH}_3\text{CN} / 0.1 \text{ M Bu}_4\text{NPF}_6$ .

**Table 2.5.1.** Absorption data of complexes.<sup>[a]</sup>

| Complex  | $\lambda_{\text{max}}$ [nm] ( $10^3 \epsilon$ [ $\text{M}^{-1} \text{cm}^{-1}$ ])            |
|----------|--|
| $1^+$    | 242 (19.2), 295 (27.9), 333 (12.6), 528 (15.0)   |
| $1^{2+}$ | 242 (19.6), 292 (20.3), 332 (8.2), 492 (6.4), 578 (sh), 621 (10.1)                           |
| $1^0$    | 242 (19.3), 295 (24.5), 341 (8.2), 368 (9.8), 443 (10.1), 587 (9.3), 1473 (0.3)              |
| $2^+$    | 243 (32.3), 287 (sh), 296 (39.1), 368 (15.4), 549 (14.1), 594 (13.4), 795 (sh), 1032 (2.8)   |
| $2^{2+}$ | 243 (35.2), 295 (41.5), 340 (17.5), 393 (10.6), 543 (19.1), 623 (21.7), 809 (sh), 1044 (0.8) |
| $2^{3+}$ | 243 (33.6), 295 (39.1), 334 (sh), 458 (12.4), 642 (sh), 719 (23.8), 1098 (2.5), 1506 (2.1)   |
| $2^{4+}$ | 243 (30.7), 270 (33.4), 301 (35.0), 315 (sh), 458 (10.6), 661 (20.2), 1043 (7.3)             |
| $3^+$    | 244 (63.7), 295 (89.1), 339 (19.8), 398 (sh), 552 (23.0), 633 (sh), 692 (sh), 820 (10.0),    |
| $3^{2+}$ | 245 (65.7), 294 (94.1), 337 (24.1), 391 (sh), 554 (25.3), 626 (26.5), 692 (sh), 812 (14.1)   |
| $3^{3+}$ | 241 (62.7), 291 (91.1), 337 (sh), 456 (15.1), 608 (sh), 721 (36.0), 1140 (3.2), 1337 (3.0)   |
| $3^{4+}$ | 242 (59.8), 285 (66.6), 318 (sh), 475 (11.3), 602 (24.1), 667 (28.4), 1031 (10.8)            |

<sup>[a]</sup> From spectroelectrochemistry in  $\text{CH}_3\text{CN} / 0.1 \text{ M Bu}_4\text{NPF}_6$  at 298 K.

## 2.6. EPR spectroscopy

The EPR investigations were performed on the mononuclear complex  $\mathbf{1}^+$  and dinuclear complexes  $\mathbf{2}^{2+}$  and  $\mathbf{3}^{2+}$  to determine the electronic configuration and the sites of the redox processes in this type of systems. The mononuclear complex  $\mathbf{1}^+$  and dinuclear complexes  $\mathbf{2}^{2+}$  and  $\mathbf{3}^{2+}$  are diamagnetic in native state and EPR inactive. EPR active odd electron species were generated by in situ electrolysis for the EPR spectroscopic measurements.

### 2.6.1. Complex $\mathbf{1}^+$

One-electron reduction of the diamagnetic complex  $\mathbf{1}^+$  results in a broad and line-rich unsymmetrical EPR signal with  $g_{av} = 2.001$  at 295 K (Figure 2.6.1.1) in  $\text{CH}_3\text{CN}/0.1 \text{ M Bu}_4\text{NPF}_6$  suggesting ligand centered reduction. From the splitting of the spectrum it is difficult to say whether reduction is  $\text{L}^{\text{1-H}}$  centered or bipyridine centered. May be both bipyridine and  $\text{L}^{\text{1-H}}$  have contribution to the SOMO of  $\mathbf{1}^0$  in acetonitrile and shows such broad EPR spectrum with coupling to several protons because in acetonitrile it is observed that the  $\text{L}^{\text{1-H}}$  centred  $\pi^*$  orbitals and bipyridine centred  $\pi^*$  orbitals are energetically very close in native state (Figure 2.5.2). Together with the solvent dependence of the cyclic voltammetry data and the UV-Vis absorption (Figures 2.4.2 and 2.5.2), the one electron reduced form  $\mathbf{1}^0$  is thus best formulated as  $[(\text{bpy})_2\text{Ru}^{\text{II}}(\text{L}^{\text{1-H}})^{2-}]$ .

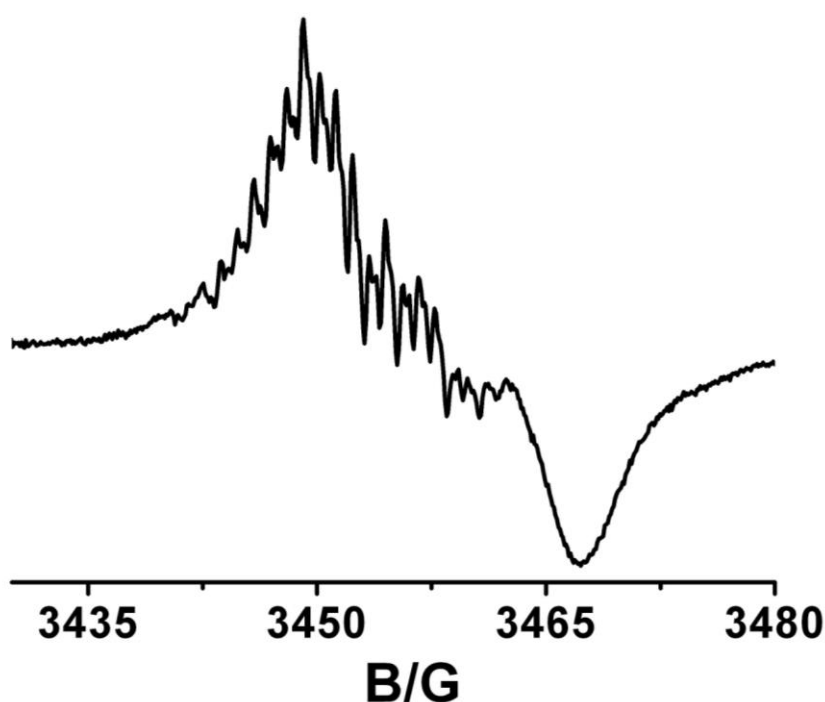


**Figure 2.6.1.1.** EPR spectrum of electrochemically generated  $\mathbf{1}^+$  at RT in  $\text{CH}_3\text{CN} / 0.1 \text{ M Bu}_4\text{NPF}_6$ .

### 2.6.2. Complex $2^{2+}$

The one-electron oxidation of diamagnetic di-nuclear complex  $2^{2+}$  to  $2^{3+}$  in  $\text{CH}_3\text{CN}/0.1(\text{M}) \text{Bu}_4\text{NPF}_6$  at 110 K exhibits EPR signals with  $g_1 = 2.139$ ,  $g_2 = 2.070$  and  $g_3 = 2.004$  ( $g_{\text{av}} = 2.072$ ,  $\Delta g = 0.135$ ) (Figure 2.6.2.1). The  $g_{\text{av}}$  value of  $2^{3+}$  is greater than the  $g_{\text{av}}$  value of organic-radicals (2.0023) whereas the  $g$ -anisotropy is very small (0.135). Hexacoordinated  $\text{Ru}^{\text{III}}$  centered EPR signals usually show a large  $g$ -anisotropy, whereas radical-bound  $\text{Ru}^{\text{II}}$  species show EPR signals that have  $g$  values much closer to the free electron  $g$  value with small  $g$  anisotropy.<sup>[73-74]</sup> The present EPR spectrum of  $2^{3+}$  points to a situation where the unpaired electron is delocalized over the whole system. The complex  $2^{3+}$  also shows intervalence charge transfer transition in the NIR region for the electronic configuration  $\text{Ru}^{\text{II}}\text{-L}_{2\text{H}}\text{-Ru}^{\text{III}}$ . These results point to a valence averaged situation and hence the species  $2^{3+}$  belongs to the strongly coupled Class III mixed-valent systems.

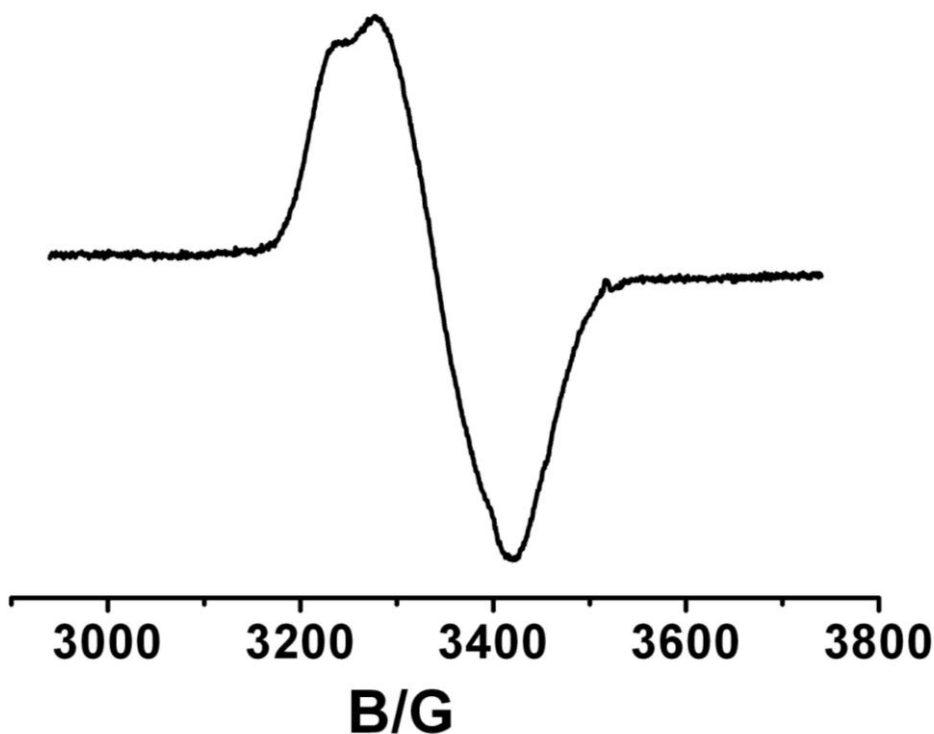


**Figure 2.6.2.1.** EPR spectrum of electrochemically generated  $2^{3+}$  at 110 K in  $\text{CH}_3\text{CN} / 0.1 \text{ M} \text{Bu}_4\text{NPF}_6$ .

In contrast to the one-electron oxidized forms, the one-electron reduced form  $2^+$  generated in situ in  $\text{CH}_3\text{CN}/0.1\text{M}\text{Bu}_4\text{NPF}_6$  shows an isotropic EPR signal with hyperfine coupling at 295 K that have  $g_{\text{av}} = 2.002$  which is very much closer to the free electron  $g$  value (Figure 2.6.2.2). The  $g_{\text{av}}$  value of the spectrum strongly suggest ligand centered reduction and direct evidence for the quinonoid bridge-centered reduction comes from the hyperfine



coupling of the unpaired electron with the two equivalent nitrogen atoms ( $^{14}\text{N}$ ,  $I = 1$ ) of the quinonoid bridge. Thus, the EPR spectrum of the one-electron reduced form  $2^+$  generated in  $\text{CH}_3\text{CN}/0.1\text{MBu}_4\text{NPF}_6$  shows a quintet signal ( $2nI + 1$ ;  $n =$  equivalent nuclei, each with a spin of  $I$ ).

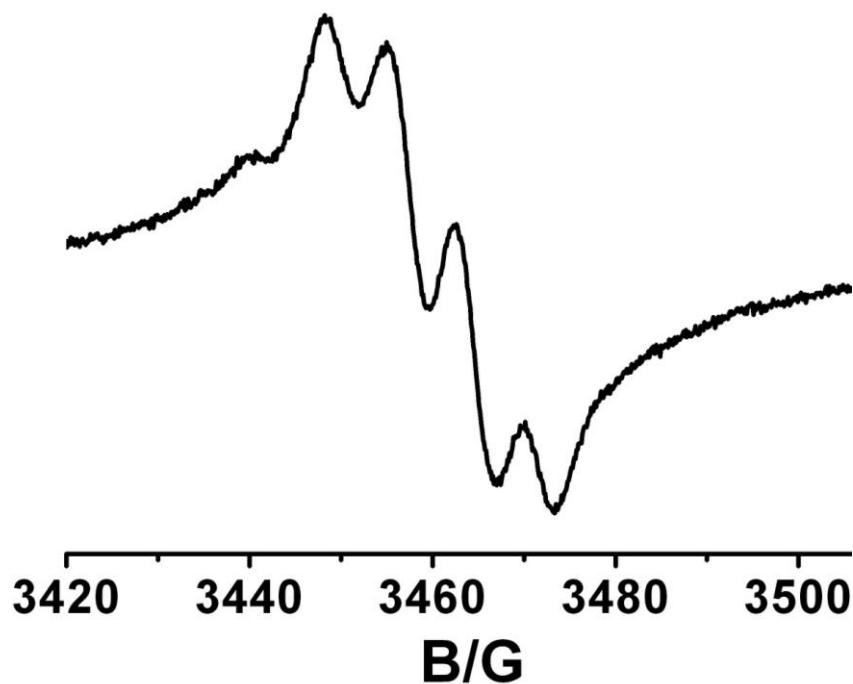


**Figure 2.6.2.2.** EPR spectrum of electrochemically generated  $2^+$  at RT in  $\text{CH}_3\text{CN} / 0.1 \text{ M Bu}_4\text{NPF}_6$ .

### 2.6.3. Complex $3^{2+}$

The one-electron oxidized di-nuclear species  $3^{3+}$  generated in situ from  $3^{2+}$  in  $\text{CH}_3\text{CN}/0.1(\text{M}) \text{Bu}_4\text{NPF}_6$  at 110 K exhibits EPR signals with  $g_1 = 2.110$ ,  $g_2 = 2.061$  and  $g_3 = 2.025$  ( $g_{\text{av}} = 2.066$ ,  $\Delta g = 0.085$ ) (Figure 2.6.3.1a). The  $g_{\text{av}}$  (2.066) value {greater than the  $g_{\text{av}}$  value of organic-radicals (2.002)} and very small  $g$ -anisotropy (0.085) suggest delocalization of the unpaired electron over the whole system like the unpaired electron in di-nuclear oxidized species  $2^{3+}$ . The one-electron reduced form  $3^+$  generated in situ in  $\text{CH}_3\text{CN}/0.1\text{MBu}_4\text{NPF}_6$  shows a sharp isotropic ligand centered EPR signal ( $g_{\text{av}} = 1.998$ ) even in dilute concentration instead of quintet signal observed in case of similar complex  $2^+$  at 295 K (Figure 2.6.2.2 and 2.6.3.1b). The narrow line width, appearance of the signal in fluid solution at 295 K and the  $g$ -value are all indicative of a ligand centered reduction. The expected hyperfine coupling for the nitrogen atoms of  $\text{L}^2_{\cdot 2\text{H}}$  ligand is not observed in this case. Sometime the expected hyperfine coupling to the nitrogen atoms of  $\text{L}^2_{\cdot 2\text{H}}$  ligand is in all likelihood not well resolved due to unfavorable line width to hyperfine coupling constant ratios.<sup>[122]</sup>

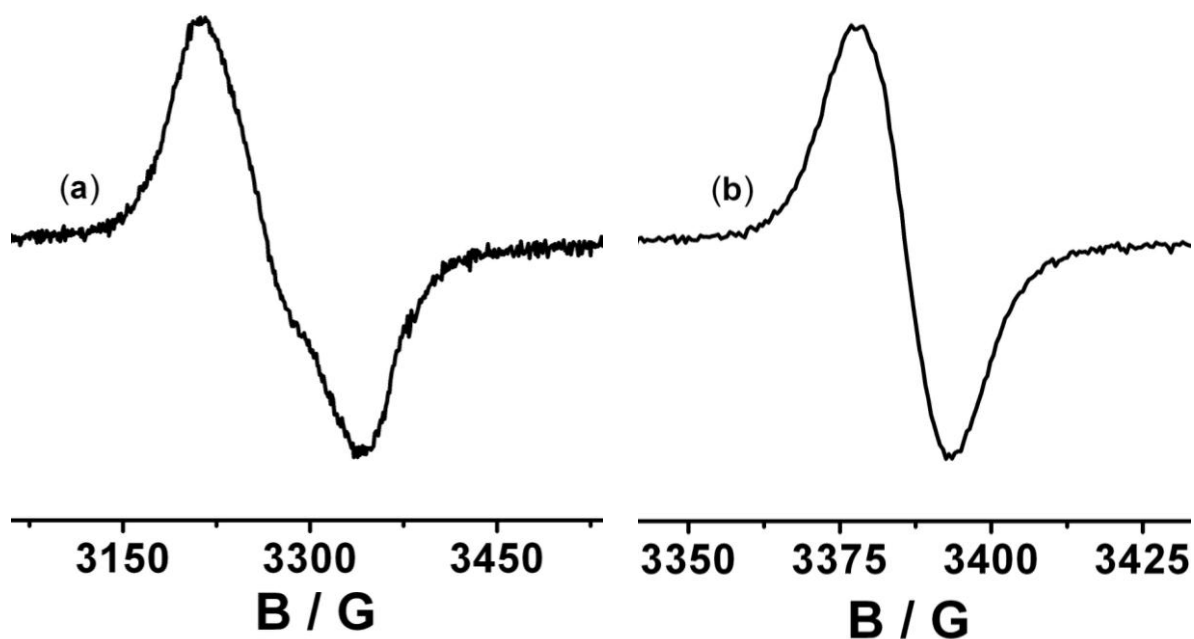


**Figure 2.6.3.1.** (a) EPR spectrum of electrochemically generated  $3^{3+}$  at 110 K in  $\text{CH}_3\text{CN} / 0.1$  M  $\text{Bu}_4\text{NPF}_6$  and (b) EPR spectrum of electrochemically generated  $3^{3+}$  at RT in  $\text{CH}_3\text{CN} / 0.1$  M  $\text{Bu}_4\text{NPF}_6$ .

## 2.6. Conclusion

In summary, the synthesis, characterization, structural and electronic properties of mono- and dinuclear ruthenium complexes with zwitterionic quinonoid ligands have been reported here. The successive metallations of zwitterionic ligand **L** lead first to a localization of the  $\pi$ -system in the mononuclear complex  $1^+$  and further 're'-delocalization in the dinuclear complexes  $2^{2+}$  and  $3^{2+}$ . Complexes  $1^+$ ,  $2^{2+}$  and  $3^{2+}$  are rare example where quinonoid bridged mono- and dinuclear  $[\text{Ru}(\text{bpy})_2]$ -type complexes have been structurally characterized.<sup>[65]</sup> All the complexes show redox rich chemistry. The one electron oxidized forms,  $2^{3+}$  and  $3^{3+}$  show properties that are typical of valence-averaged mixed-valent species. This proves the utility of ligands such as **L** as strong mediators of 'metal-metal coupling' in mixed-valence chemistry. The redox potentials and metal-metal coupling of the quinonoid bridge dinuclear complex is tuned remarkably by varying the R groups in **L**. The one electron reduction of dinuclear complex  $2^{2+}$  is completely bridging ligand centered because of the appearance of quintet EPR signal for the two equivalent  $^{14}\text{N}$  ( $I = 1/2$ ) nuclei in **L**.

## CHAPTER 3

# One-Pot Synthesis of Symmetric and Asymmetric substituted *p*-Quinone Ligands and Their Structural, Redox, Electronic and Spectroscopic Properties in Mono and Dinuclear Ruthenium Complexes

## 3.1. Introduction

### 3.1.1. *p*-Quinones

Quinones are ubiquitous in biological systems, being part of vital processes such as cellular respiration and photosynthesis.<sup>[75-77]</sup> Owing to their facile electron transfer properties, they are often found in combination with transition metal centers in biological systems.<sup>[77,78]</sup> *p*-Quinones, such as vitamin K derivatives, ubiquinones or plastoquinones, play important roles in photosynthesis, respiration, and information-transfer processes.<sup>[79,80]</sup> They are also usually found in the paradoxical role of mutagenic agents as well as effective antitumor agents.<sup>[81]</sup> The biological activity of quinone molecules is often related to the presence of acidic protons in these molecules.<sup>[82-84]</sup> Quinones of the form **L** (Figure 3.1.1) containing an OH substituent play an important role as inhibitors of tumors<sup>[85]</sup> and of hydroxyphenyl pyruvate dioxygenase.<sup>[86]</sup> Despite intensive research efforts in that direction, straightforward one-pot and green synthetic routes for access to such molecules are, to the best of our knowledge, nonexistent in the literature, with the existing procedures requiring multistep synthesis, extraction from natural products, or involved purification steps.<sup>[85-93]</sup>

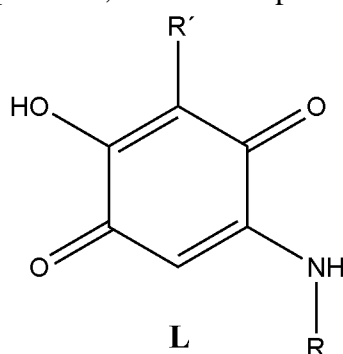


**Figure 3.1.1.** Quinone containing -OH substituent.

Another type of *p*-quinones such as 2,5-Diamino-1,4-benzoquinone **L'**<sup>[94]</sup> and its substituted derivatives<sup>[21, 22]</sup> have been known for decades. The synthesis of **L'** has previously been

reported and such syntheses are rarely straightforward one-pot reactions.<sup>[24, 97]</sup> Some years back Braunstein et al. reported a straightforward and “green” synthesis of a new class of molecules that occurs through transamination.<sup>[98, 99]</sup> Such molecules, which are isomers of  $L'$  and its derivatives, are best described as zwitterions,  $L^1$ .<sup>[98, 99]</sup> Inspired by this process we looked for an elegant synthesis for the parent compound  $L'$  and for possible intermediates formed during the transamination process.



**Figure 3.1.2.** Molecular formulae of 2,5-Diamino-1,4-benzoquinone ( $L'$ ) and its zwitterionic isomer ( $L^1$ ).

Herein we have reported straightforward one-pot and green synthesis of substituted symmetric *p*-quinonoid ligands ( $L^2$ ) and asymmetric biologically relevant *p*-quinonoid ligands ( $L^3$ ) like  $L$  (Scheme 3.2.1.1). In addition, straightforward one-pot synthesis of  $L'$  and its mono- and dialkyl derivatives of the forms  $L^4$  and  $L^2$  respectively are also reported in this chapter (Scheme 3.2.1.2).

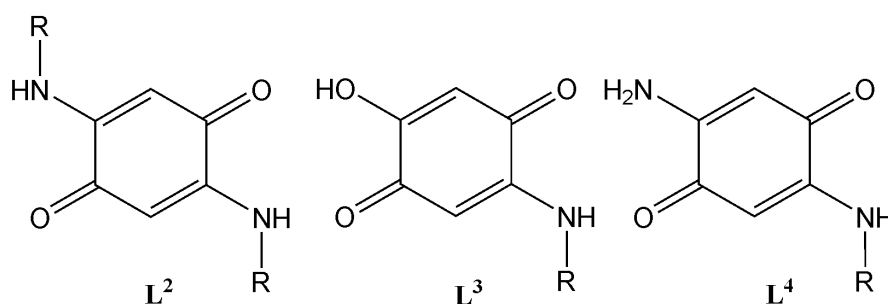


**Figure 1.1.** Molecular formulae of symmetric ( $L^2$ ) and asymmetric ( $L^3$  and  $L^4$ ) substituted *p*-quinonoid ligands.

### 3.1.1. Metal complexes of quinones

The quinones have been extensively used as ligands in coordination chemistry in recent years.<sup>[100–102]</sup> The ability of quinones and related ligands to exist in various redox states in their metal complexes has led to the use of the term non-innocent ligands for such molecules.<sup>[103–104]</sup> The interaction between ruthenium centers and non-innocent ligands have fascinated chemists because of the valence ambiguity arising in such complexes as a result of

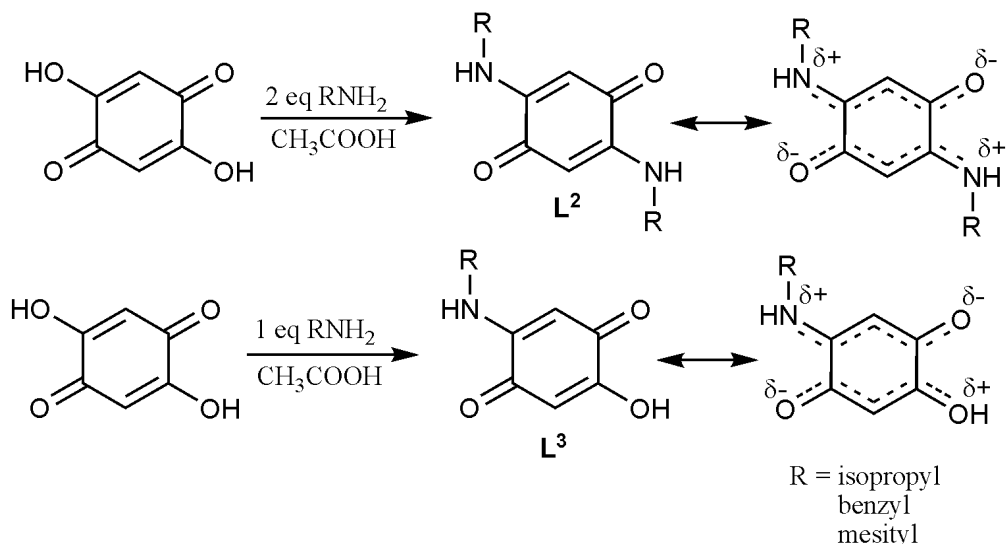
the close proximity of metal  $d\pi$  and ligand based  $\pi$  orbitals.<sup>[105-107]</sup> Such proximity of metal and ligand based orbitals in these complexes makes the exact description of electronic states experimentally challenging.<sup>[103-104]</sup> Non-innocent character of ligands has led to the concept of their use as electron-reservoirs.<sup>[108]</sup> This concept has been made use of in ruthenium complexes of non-innocent ligands and such complexes have been used as catalysts for water oxidation<sup>[109]</sup> and in dye-sensitized solar cells.<sup>[110]</sup> The doubly deprotonated form of 2,5-dihydroxy-1,4-benzoquinone has been extensively used as a bridging ligand in coordination chemistry.<sup>[111-113]</sup> However, tuning of steric and electronic properties in that ligand is limited only to substitution at the C3 and C6 positions of the six-membered ring. In synthesizing these ligands, our aim has been to substitute [O] with the isoelectronic [NR] groups (Scheme 3.2.1.1). Such a substitution makes the tuning of the steric and electronic properties of the complexes possible through the R-groups of [NR].

In this chapter, we have presented the synthesis of mononuclear complexes of the form  $[(bpy)_2Ru(\mathbf{BL}_{-H})](ClO_4)$  and dinuclear ruthenium complexes of the form  $[(bpy)_2Ru(\mu-\mathbf{BL}_{-2H})Ru(bpy)_2](ClO_4)_2$  ( $\mathbf{BL}$  =  $p$ -quinonoid bridging ligands) with the symmetric and asymmetric  $p$ -quinonoid bridging ligands ( $\mathbf{L}^2$  and  $\mathbf{L}^3$ ) and compared their electronic properties. Mononuclear complexes of the form  $[(bpy)_2Ru(\mathbf{L}^2_{-H})](ClO_4)$  are extremely rare in the literature because symmetric nature of the  $\mathbf{L}^2$  ligands leads to comparable acidities of both the protons. The mononuclear complexes of the form  $[(bpy)_2Ru(\mathbf{L}^3_{-H})](ClO_4)$  are also extremely rare in the literature though the acidity of two protons in  $\mathbf{L}^3$  are slightly different. A consequence of this is the difficulty of targeted synthesis and isolation of mononuclear complexes with such ligands. In the present case, the mononuclear complex of the form  $[(bpy)_2Ru(\mathbf{L}^2_{-H})](ClO_4)$  and  $[(bpy)_2Ru(\mathbf{L}^3_{-H})](ClO_4)$  will be used as a standard to discuss the properties of the dinuclear complexes. Structural data of  $[(bpy)_2Ru(\mathbf{L}^2_{-H})](ClO_4)$  and  $[(bpy)_2Ru(\mu-\mathbf{L}^2_{-2H})Ru(bpy)_2](ClO_4)_2$  will be presented and these data will be used to elucidate the bonding situation inside the ligands in these complexes. A combination of cyclic voltammetry, UV-vis-NIR and EPR spectroelectrochemistry will be used to elucidate the electronic structure of the compounds and determine the site of electron transfer. Solvent dependence of the electrochemical properties of  $[(bpy)_2Ru(\mathbf{L}^2_{-H})](ClO_4)$  will be reported. Comparisons will be made between the complexes reported here with the parent compound  $[(bpy)_2Ru(\mu-DHBQ^{2-})Ru(bpy)_2]^{2+}$ ,  $\mathbf{5}^{2+}$  (DHBQ = 2,5-dihydroxy-1,4-benzoquinone). Such comparisons will elucidate the effect on the electrochemical and spectroscopic properties of the metal complexes on substituting [O] with the isoelectronic [NR] groups in such  $p$ -quinone ligands.

## 3.2. Synthesis and characterization

### 3.2.1 Synthesis and characterization of substituted symmetric ( $\mathbf{L}^2$ ) and asymmetric ( $\mathbf{L}^3$ and $\mathbf{L}^4$ ) *p*-quinonoid ligands

One of the reports on the synthesis of (aromatic)aminosubstituted *p*-quinones deals with the reaction of the commercially available and relatively inexpensive 2,5-dihydroxy-1,4-benzoquinone with aromatic amines in *m*-cresol under reflux at temperatures of over 100 C° in the presence of catalytic amounts of trifluoroacetic acid.<sup>[114]</sup> This reaction, which is often used in the literature even up to now,<sup>[115]</sup> deals with *m*-cresol as a solvent, a substance that is highly toxic, and whose health hazards are well documented.<sup>[116]</sup> Additionally, polymer formation is often a problem while using the above-mentioned synthetic method.<sup>52</sup> In trying to unveil the possible mechanism of this reaction, we reasoned that the critical points in its functioning are relatively high temperatures and acid catalysis. Similar acid catalyzed reactions are found in several enzymatic processes which function in water.<sup>[117]</sup> Hence, we carried out the same reaction with nontoxic and environmentally benign acetic acid as a solvent. Gratifyingly, the reaction in acetic acid worked as good as or even better than that using *m*-cresol. No problems with polymer formation were observed, and we were able to isolate alkyl and aryl substituted symmetric *p*-quinonoid ( $\mathbf{L}^2$ ) compounds (Scheme 3.2.1.1) in high yields after just a one-step chromatographic purification. To our surprise, repeating the same reactions with equimolar amounts of 2,5-dihydroxy-1,4-benzoquinone and the corresponding amine under the same conditions as stated above resulted in the formation of asymmetric *p*-quinone ( $\mathbf{L}^3$ ) compounds (Scheme 3.2.1.1). There are no reports in the literature of the synthesis of such compounds in *m*-cresol, as has been mentioned above for symmetrically amino-substituted *p*-quinones. Such compounds containing an additional –OH group are very closely related to many biologically active *p*-quinones which function as bioinhibitors, and a simple and straightforward synthesis of such molecules has been rare and elusive up to now, to the best of our knowledge. The asymmetric *p*-quinone ( $\mathbf{L}^3$ ) could be obtained in high yields with our method of using acetic acid as a solvent. Using our method we have synthesized *N*-isopropyl, *N*-benzyl and *N*-mesityl substituted symmetric and asymmetric *p*-quinonoid compounds with high yield (Scheme 3.2.1.1).

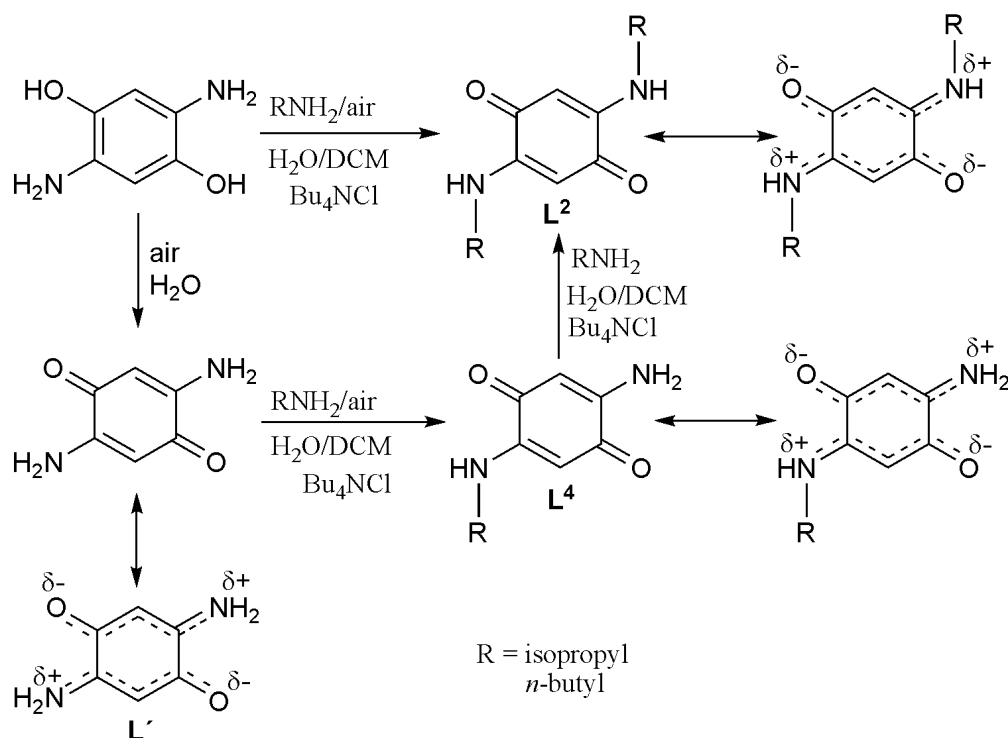


**Scheme 3.2.1.1.** One-pot synthesis of symmetric ( $L^2$ ) and asymmetric ( $L^3$ ) quinonoid ligands.

The symmetric ( $L^2$ ) compounds are well soluble in organic solvents except *N*-mesityl substituted compounds whereas all the asymmetric ( $L^3$ ) compounds are very poor soluble in organic solvents after purification. For this reason we have characterized *N*-isopropyl and *N*-benzyl substituted symmetric ( $L^2$ ) compounds by  $^1\text{H}$ - and  $^{13}\text{C}$  NMR spectroscopy, elemental analysis and mass spectrometry whereas the others (symmetric and asymmetric) are characterized by only elemental analysis and mass spectrometry. The formations of the asymmetric ligands of the form  $L^3$  are also confirmed by the characterization of their metal complexes which are more soluble in organic solvents (see section 3.2.2).

The symmetric *N*-alkyl substituted quinonoid ligands ( $L^2$ ) can be synthesized easily by a straightforward transamination reaction (Scheme 3.2.1.2). Reaction of 2,5-diamino-1,4-dihydroxybenzene in water with air leads to the formation of  $L'$ . This is a one-pot reaction and, in stark contrast to the synthetic procedures known in the literature for  $L'$ , does not require any further purification.<sup>[94, 97]</sup> When the same reaction was carried out in the presence of alkylamine such as isopropylamine or *n*-butylamine<sup>[118]</sup> we observed “double” transamination leading to the formation of symmetric disubstituted products of the form  $L^2$  (Scheme 3.2.1.2). Such transamination reactions have been observed previously, but this is only the second example of transamination reactions in quinonoid chemistry.<sup>[112]</sup> However, in contrast to reference [119] the yield of disubstituted products were unsatisfactory. Careful examination of the reaction mixture showed that the formation of the parent compound  $L'$ , which is poorly soluble in water, is extremely fast and its precipitation limits the yield of the transamination. To circumvent this problem, we carried out the transamination reactions in a mixture of water, dichloromethane, and THF with  $\text{Bu}_4\text{NCl}$  as a phase-transfer catalyst (see

experimental section). These reaction conditions not only led to higher yields, but also to the formation of a second product. Analysis of the products showed it to be a mixture of monosubstituted products of the form  $L^4$  and disubstituted products of the form  $L^2$ . Thus, the monosubstituted compounds of the form  $L^4$  are key intermediates in the transamination reactions leading to the formation of the disubstituted products of the form  $L^2$ , as has been proposed for the formation of compounds of type  $L^1$ . However, in these cases they could not be isolated due to the extremely fast second transamination reaction leading to the disubstituted products.<sup>[119-120]</sup> To the best of our knowledge, examples of asymmetrically substituted *p*-quinones of the form  $L^4$ , are extremely rare in the literature.<sup>[121]</sup>



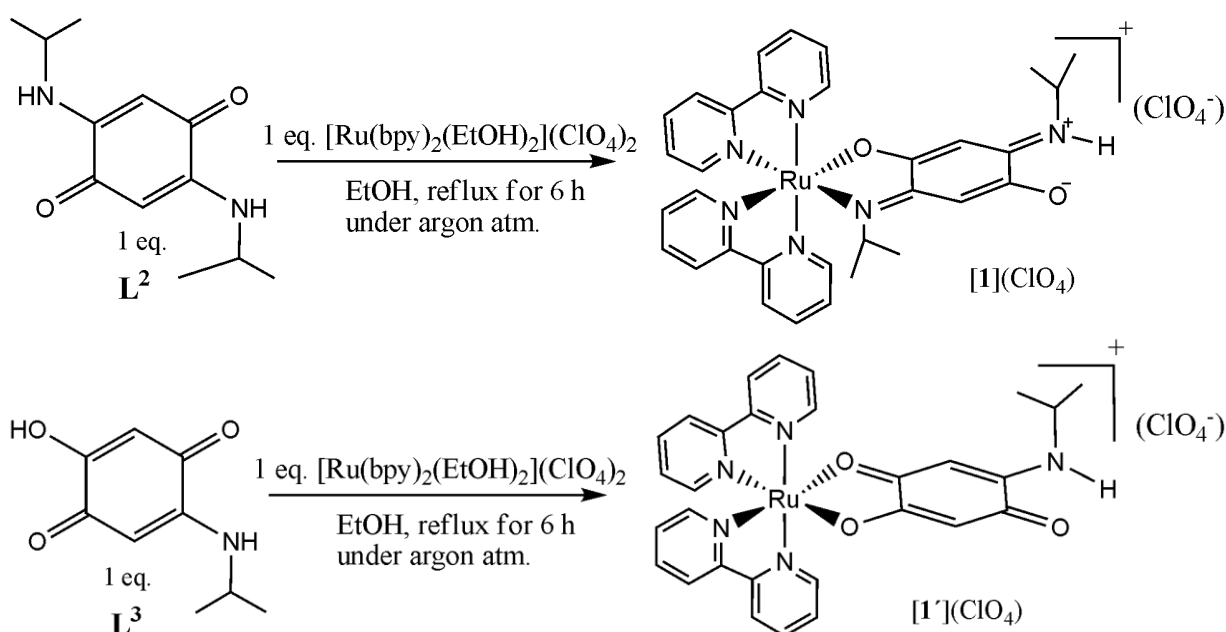
**Scheme 3.2.1.2.** One-pot synthesis of  $L'$  and its mono ( $L^4$ ) and dialkyl ( $L^2$ ) derivatives.

The symmetric ( $L^2$ ) and asymmetric compounds ( $L^4$ ) were characterized by  $^1\text{H}$ - and  $^{13}\text{C}$  NMR spectroscopy, elemental analysis and mass spectrometry. Whereas symmetric ligands of the form  $L^2$  show only one signal corresponding to the *p*-quinone ring C-H protons in their  $^1\text{H}$  NMR spectra owing to symmetry equivalence, asymmetric ligands of the form  $L^4$  show two different signals for the now inequivalent *p*-quinone ring C-H protons (see the Experimental Section), and this was the first indication for the formation of such asymmetrically substituted *p*-quinones. In the  $^{13}\text{C}$  NMR spectra for  $L^2$ , only one signal is seen for the “C=O” carbon; for  $L^4$  two different signals are observed owing to their inequivalence.



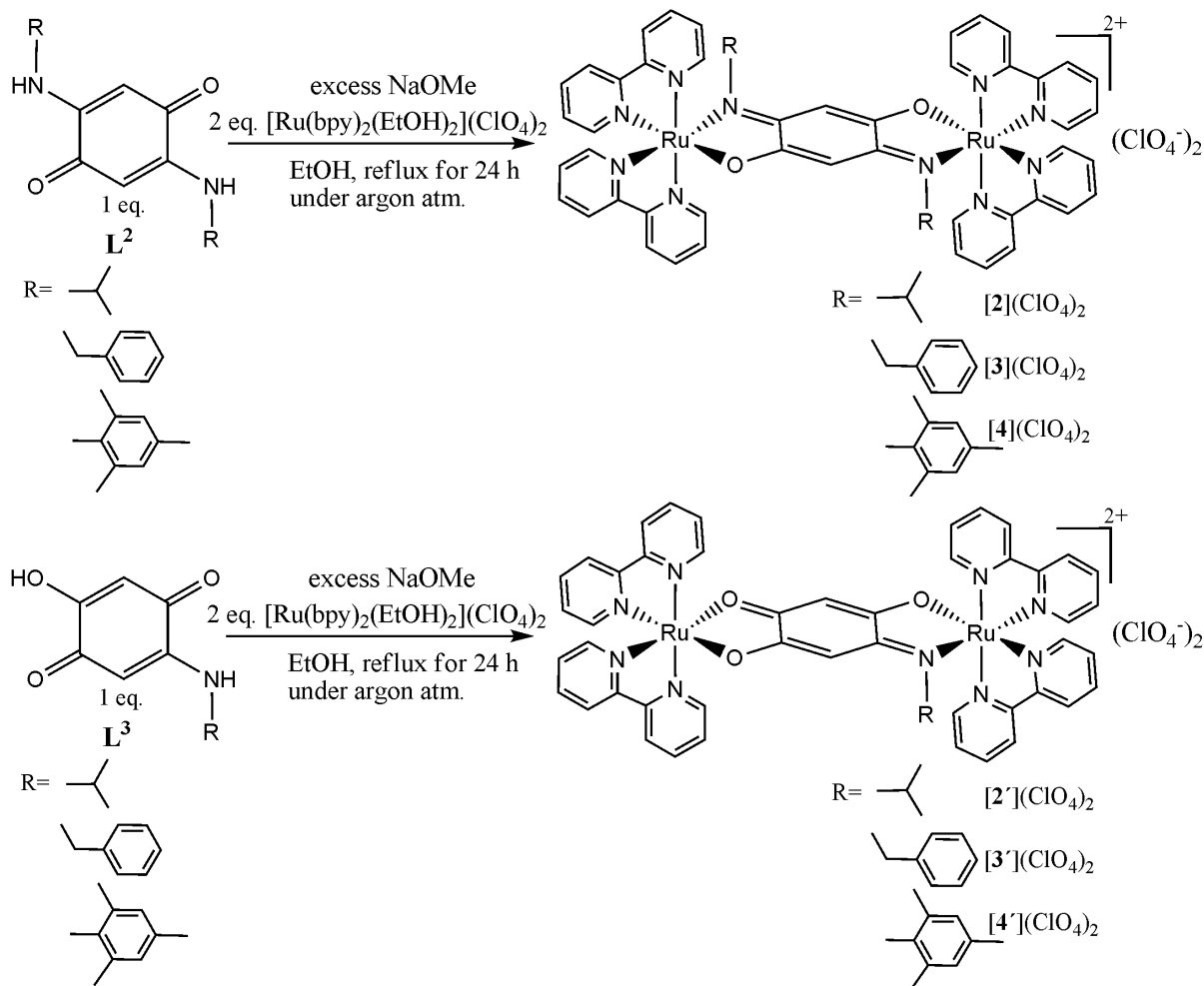
### 3.2.2. Synthesis and characterization of mono and dinuclear ruthenium complexes of substituted symmetric ( $L^2$ ) and asymmetric ( $L^3$ and $L^4$ ) *p*-quinonoid ligands

The mono and dinuclear ruthenium complexes of the zwitterionic *m*-quinone ligands are shown in the pervious chapter (Chapter 2). Herein we have reported mono and dinuclear ruthenium complexes of symmetric ( $L^2$ ) and asymmetric ( $L^3$ ) *p*-quinone ligands. The mononuclear complexes  $[1](ClO_4)$  and  $[1'](ClO_4)$  were synthesized in an one-pot reaction by reacting of  $[Ru(bpy)_2(EtOH)_2](ClO_4)_2$  with the corresponding *p*-quinonoid ligand in the presence of an excess of sodium methoxide in a 1:1 ratio in refluxing ethanol (Scheme 3.2.2.1).



**Scheme 3.2.2.1.** Synthesis of mononuclear complexes  $[1](ClO_4)$  (top) and  $[1'](ClO_4)$  (bottom) of symmetric ( $L^2$ ) and asymmetric ( $L^3$ ) *p*-quinone ligands.

All the dinuclear complexes with the symmetric ( $L^2$ ) and asymmetric ( $L^3$ ) *p*-quinone ligands  $[2](ClO_4)_2$ ,  $[3](ClO_4)_2$ ,  $[4](ClO_4)_2$ ,  $[2'](ClO_4)_2$ ,  $[3'](ClO_4)_2$  and  $[4'](ClO_4)_2$  were synthesized also in an one-pot reaction by reacting two equivalents of  $[Ru(bpy)_2(EtOH)_2](ClO_4)_2$  with one equivalent of the corresponding quinonoid ligand in the presence of an excess of sodium methoxide in refluxing ethanol (Scheme 3.2.2.2).



**Scheme 3.2.2.2.** Synthesis of dinuclear complexes  $[2](ClO_4)_2$ ,  $[3](ClO_4)_2$  and  $[4](ClO_4)_2$  (top) with symmetric ( $L^2$ )  $p$ -quinone ligands and  $[2'](ClO_4)_2$ ,  $[3'](ClO_4)_2$  and  $[4'](ClO_4)_2$  (bottom) with asymmetric ( $L^3$ )  $p$ -quinone ligands.

All the mono and dinuclear complexes were purified by column chromatography using neutral alumina column and characterized by  $^1H$  NMR, electrospray mass spectroscopy and elemental analysis (see experimental section). The symmetric ( $L^2$ - $2H$ )  $p$ -quinonoid bridge dinuclear complexes  $[2](ClO_4)_2$ ,  $[3](ClO_4)_2$  and  $[4](ClO_4)_2$  show only one signal corresponding to the  $p$ -quinone ring C-H protons in their  $^1H$  NMR spectra owing to symmetry equivalence whereas asymmetric ( $L^3$ - $2H$ )  $p$ -quinonoid bridge dinuclear complexes  $[2'](ClO_4)_2$ ,  $[3'](ClO_4)_2$  and  $[4'](ClO_4)_2$  show two different signals for the now inequivalent  $p$ -quinone ring C-H protons (see the Experimental Section), and this is also an evidence for the formation of such asymmetrically substituted  $p$ -quinones in the above reaction (Scheme 3.2.1.1). The  $^1H$  NMR spectrum of all the dinuclear complexes showed two sets of signals that indicate the formation of both *rac* and *meso* diastereomers under our reaction conditions (see experimental section). No attempts were made to separate these isomers and all further studies were carried out with a mixture of diastereomers.

### 3.3 Crystal structures

The complexes  $1(\text{ClO}_4)$  and  $2(\text{ClO}_4)_2$  could be crystallized by slow diffusion of a dichloromethane solution layered with *n*-hexane (1/2) at ambient temperatures. The crystal structures of the complexes are depicted in Figures 3.3.1 and 3.3.4. Selected bond lengths and bond angles of the complexes are given in Tables 5.3.1-5.3.3, while X-ray diffraction parameters and crystallographic data are reported in Chapter 10.

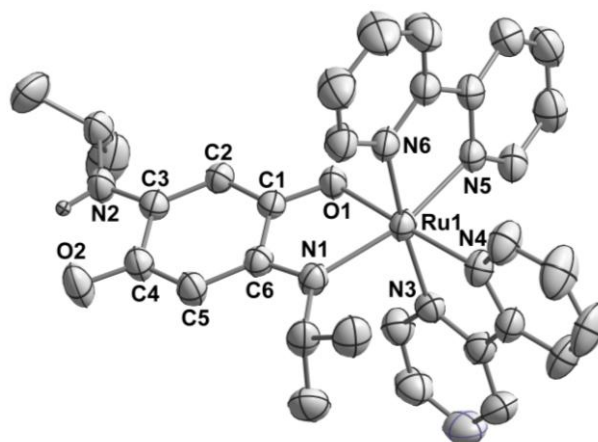


**Figure 3.3.1.** Molecular structure of the cation in the crystal structure of  $1(\text{ClO}_4)$ . Ellipsoids include 50% of the electron density. Hydrogen atoms are omitted for clarity.

**Table 3.3.1:** Selected bond lengths [Å] and bond angles [°] for  $[1]\text{ClO}_4$ .

| Bond lengths | [Å]      | Bond angles | [°]        |
|--------------|----------|-------------|------------|
| C1-C2        | 1.387(4) | N1-Ru1-N6   | 95.97(10)  |
| C2-C3        | 1.388(4) | N4-Ru1-N6   | 95.73(11)  |
| C3-C4        | 1.519(5) | N5-Ru1-N6   | 78.77(10)  |
| C4-C5        | 1.387(5) | O1-Ru1-N6   | 87.94(10)  |
| C5-C6        | 1.413(4) | N1-Ru1-N3   | 87.41(10)  |
| C6-C1        | 1.491(4) | N3-Ru1-N4   | 78.69(11)  |
| O1-C1        | 1.280(4) | N3-Ru1-N5   | 99.09(10)  |
| C4-O2        | 1.257(4) | O1-Ru1-N3   | 97.48(10)  |
| N1-C6        | 1.328(4) | N1-Ru1-O1   | 77.83(9)   |
| N2-C3        | 1.309(4) | N1-Ru1-N4   | 106.18(10) |
| Ru1-O1       | 2.050(2) | N4-Ru1-N5   | 88.41(10)  |
| Ru1-N1       | 2.103(3) | O1-Ru1-N5   | 87.89(9)   |
|              |          | N1-Ru1-N5   | 165.00(10) |
|              |          | O1-Ru1-N4   | 174.19(10) |
|              |          | N3-Ru1-N6   | 174.13(10) |

**1**(ClO<sub>4</sub>) crystallizes in the monoclinic *C2/c* space group. The ruthenium center in **1**(ClO<sub>4</sub>) is in a distorted octahedral environment, being coordinated by an oxygen and a nitrogen atom from **L**<sup>2</sup><sub>H</sub> and from four nitrogen atoms of the two bpy ligands (Figure 3.3.1). The Ru-N and Ru-O bond lengths are in the expected range (Table 3.3.1). Bond length analyses within the **L**<sup>2</sup><sub>H</sub> ligand show relatively long C1-O1 and C4-O2 bond lengths of 1.280(4) and 1.257(4) Å respectively. The C6-N1 and C3-N2 bond lengths of 1.328(4) and 1.309(4) Å on the other hand are relatively short. The C-C bonds, particularly the C4-C5 at 1.387(5) Å and C5-C6 at 1.413 Å shows alternation of one short and one long bond. The C1-C6 and C3-C4 bonds lengths of 1.491(4) and 1.519(5) Å lie in the range of authentic C-C single bonds. Thus, the bond length analyses of coordinated **L**<sup>2</sup><sub>H</sub> in complex **1**(ClO<sub>4</sub>) suggest that the mono deprotonated ligand **L**<sup>2</sup><sub>H</sub> acting as a bis(phenolate)-*p*-diimine type donor (Figure 3.3.3). The ruthenium center is then coordinated through an O<sup>-</sup> and a neutral imine donor from **L**<sup>2</sup><sub>H</sub>. Such type of preferred coordination has been previously observed for dinuclear ruthenium complexes with substituted *p*-quinone ligands.<sup>[122]</sup> We have presented here structural evidence for a mononuclear complex with such ligands. This structural motive is additionally stabilized by strong intermolecular hydrogen bonding between the non-coordinated, formally iminium type nitrogen and the non-coordinated, formally phenolate type O<sup>-</sup> (Figure 3.3.2) (hydrogen bond distance was found to be 2.073 Å, which is much shorter than the sum of the van der waals radii of hydrogen and oxygen (2.72 Å)).

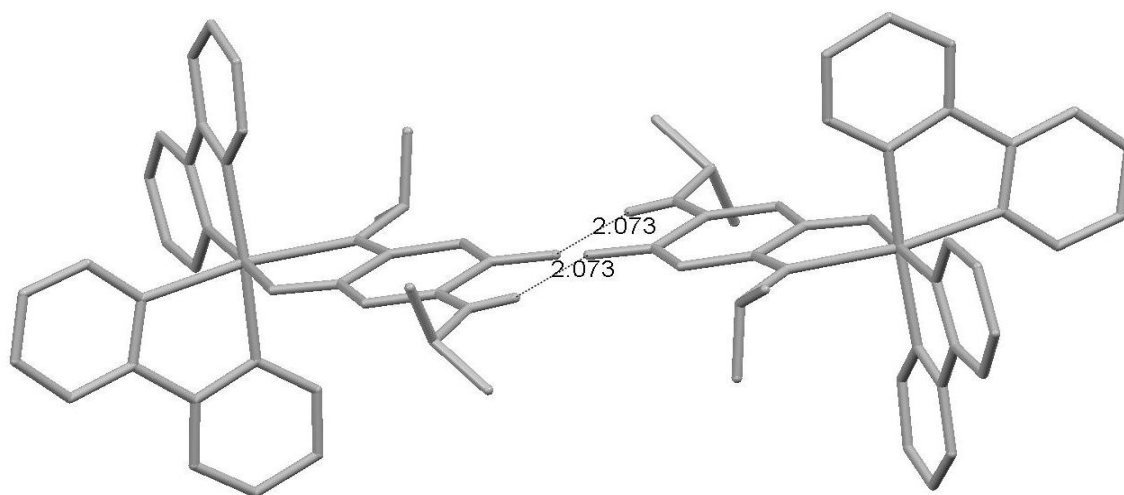


**Figure 3.3.2.** Intermolecular hydrogen bonding in the crystal structure of **1**(ClO<sub>4</sub>).

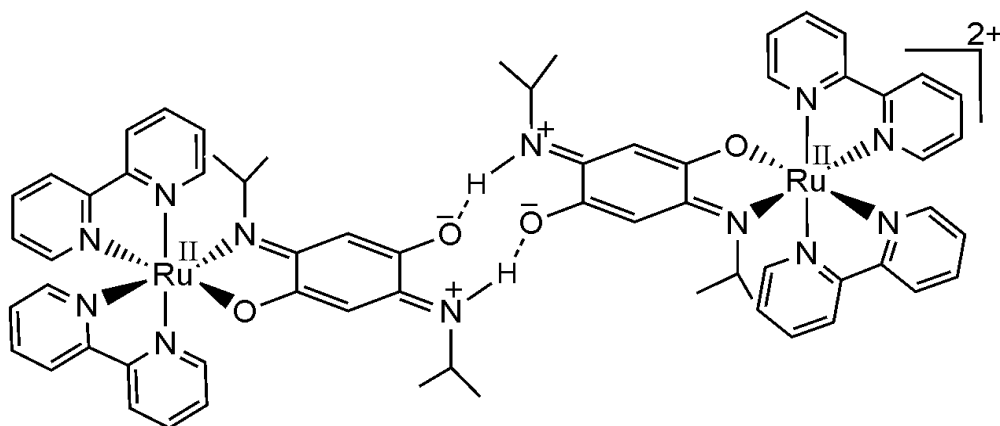


**Figure 3.3.3.** Molecular formula of the complexes  $1(\text{ClO}_4)$  with intermolecular H-bonding showing the orientation of  $\pi$ -systems in coordinated quinonoid ligand.

The dinuclear complex  $2(\text{ClO}_4)_2$  could also be crystallized. The quality of the diffraction data is unfortunately not very high. This precludes the detailed discussion of bond lengths within that complex. However, the connectivity pattern is clearly seen (Figure 3.3.4). As expected, each ruthenium center is coordinated through four N atoms of the two bipyridine rings and through the oxygen and nitrogen atoms of the bridging ligand  $\text{L}^2\text{-2H}$ . Of the two diastereomers observed in solution through  $^1\text{H}$  NMR spectroscopy, the meso isomers crystallizes preferentially as can be seen from the ORTEP plot in Figure 3.3.4. Given the literature precedence of related compounds and the mononuclear complex  $1^+$  discussed above, it is to be expected that the bridging ligand  $\text{L}^2\text{-2H}$  binds to the metal centers through  $\text{O}^-$  and an neutral imine nitrogen.

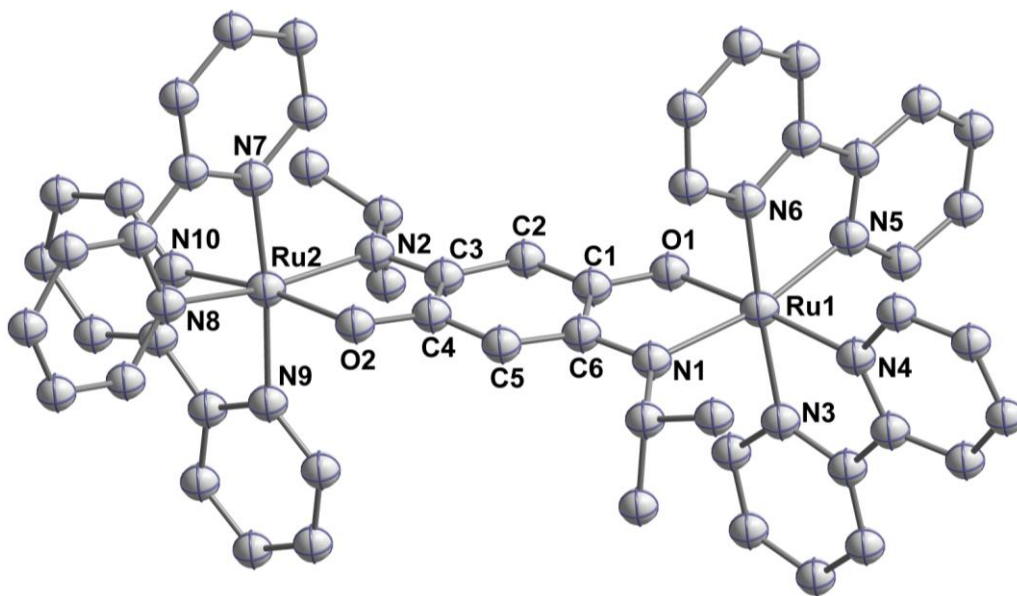


**Figure 3.3.4.** Molecular structure of the dication in the crystal structure of  $2(\text{ClO}_4)_2$ . Balls include  $0.3 \text{ \AA}$  radius of the atom. Hydrogen atoms are omitted for clarity.

**Table 3.3.2:** Selected bond lengths [Å] for [2](ClO<sub>4</sub>)<sub>2</sub>.

|       |           |         |           |
|-------|-----------|---------|-----------|
| C1-C2 | 1.434(17) | N1-C6   | 1.330(13) |
| C2-C3 | 1.414(19) | N2-C3   | 1.370(15) |
| C3-C4 | 1.497(19) | Ru1-O1  | 2.041(8)  |
| C4-C5 | 1.342(17) | Ru2-O2  | 2.068(8)  |
| C5-C6 | 1.349(16) | Ru1-N1  | 2.070(10) |
| C6-C1 | 1.397(16) | Ru2-N2  | 2.094(12) |
| O1-C1 | 1.316(15) | Ru1-Ru2 | 7.963     |
| C4-O2 | 1.285(15) |         |           |

**Table 3.3.3:** Selected bond angles [°] for [2](ClO<sub>4</sub>)<sub>2</sub>.

|           |          |            |          |
|-----------|----------|------------|----------|
| N1-Ru1-N6 | 92.8(5)  | N2-Ru2-N7  | 95.7(8)  |
| N4-Ru1-N6 | 96.9(4)  | N8-Ru2-N7  | 72.2(8)  |
| N5-Ru1-N6 | 80.5(6)  | N10-Ru2-N7 | 98.0(5)  |
| O1-Ru1-N6 | 90.6(4)  | O2-Ru2-N7  | 88.0(4)  |
| N1-Ru1-N3 | 87.9(4)  | N2-Ru2-N9  | 89.7(5)  |
| N3-Ru1-N4 | 78.3(4)  | N8-Ru2-N9  | 102.6(6) |
| N3-Ru1-N5 | 99.5(5)  | N10-Ru2-N9 | 79.6(5)  |
| O1-Ru1-N3 | 94.2(4)  | O2-Ru2-N9  | 94.0(5)  |
| N1-Ru1-O1 | 76.8(4)  | N2-Ru2-O2  | 80.4(4)  |
| N1-Ru1-N4 | 105.9(3) | N2-Ru2-N10 | 103.9(4) |
| N4-Ru1-N5 | 85.6(3)  | N8-Ru2-N10 | 83.5(3)  |
| O1-Ru1-N5 | 92.5(3)  | O2-Ru2-N8  | 93.6(4)  |
| N1-Ru1-N5 | 167.4(4) | N2-Ru2-N8  | 166.7(6) |
| O1-Ru1-N4 | 171.9(4) | O2-Ru2-N10 | 172.2(5) |
| N3-Ru1-N6 | 175.2(4) | N7-Ru2-N9  | 174.5(7) |

### 3.4. Electrochemistry

All the complexes  $1(\text{ClO}_4)$ ,  $2(\text{ClO}_4)_2$ ,  $3(\text{ClO}_4)_2$ ,  $4(\text{ClO}_4)_2$ ,  $1'(\text{ClO}_4)$ ,  $2'(\text{ClO}_4)_2$ ,  $3'(\text{ClO}_4)_2$  and  $4'(\text{ClO}_4)_2$  have been studied by cyclic voltammetry in order to investigate their electron-transfer properties. The cyclic voltammetry experiments were carried out in a  $\text{CH}_3\text{CN}$  solution of  $\text{Bu}_4\text{NPF}_6$  (0.1 mol). Ferrocene was used as an internal standard and all the redox potentials are referenced with respect to ferrocenium /ferrocene ( $\text{Fc}^+/\text{Fc}$ ) couple. The reductions and the oxidations of all the complexes are shown in figure 3.4.1.1 and 3.4.2.1 and the potential values are summarized in Table 3.4.1.2 and 3.4.2.1.

#### 3.4.1. Electrochemistry of complexes $1(\text{ClO}_4)$ , $2(\text{ClO}_4)_2$ , $3(\text{ClO}_4)_2$ and $4(\text{ClO}_4)_2$ containing symmetric *p*-quinonoid ligands.

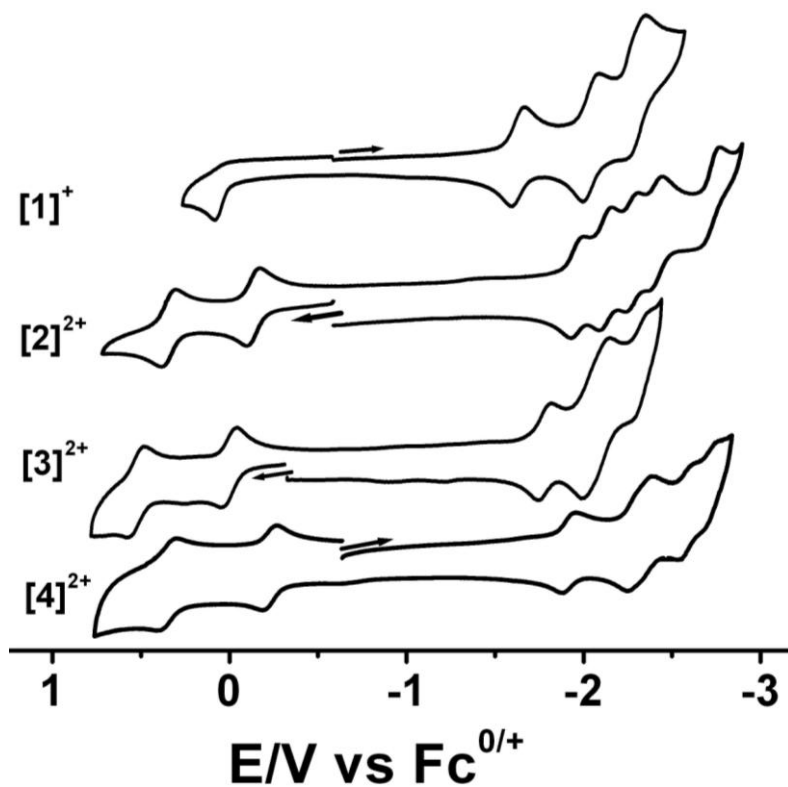


**Figure 3.4.1.1.** Cyclic voltammogram of  $1(\text{ClO}_4)$ ,  $2(\text{ClO}_4)_2$ ,  $3(\text{ClO}_4)_2$  and  $4(\text{ClO}_4)_2$  in  $\text{CH}_3\text{CN}$  / 0.1 M  $\text{Bu}_4\text{NPF}_6$  at 295 K.

The four complexes containing symmetric *p*-quinonoid ligands show redox rich chemistry. The mononuclear complex  $1^+$  shows one oxidation (+0.09 V) and several reduction steps, the first of which occur at -1.62 V in  $\text{CH}_3\text{CN}$  / 0.1 M  $\text{Bu}_4\text{NPF}_6$  at 295 K (Figure 3.4.1.1 and Table 3.4.1.2). Since the mononuclear complex has free N-H and O groups on the non-coordinated side of the ligand  $\text{L}^2_{\text{-H}}$  and since the complex shows strong intermolecular hydrogen bonding in the solid state, we decided to study the solvent dependence of the redox

potentials of  $\mathbf{1}^+$ . The redox potentials do not show very significant shifts on changing the polarity of the solvent from dichloromethane to acetonitrile to dimethylformamide {Figure 3.4.1.2 (right) and Table 3.4.1.1}. However, on using a protic solvent such as methanol the first reduction potential shifts significantly to -1.06 V. The effect of the protic solvent on the second reduction potential of  $\mathbf{1}^+$  is comparatively much less (Table 3.4.1.1). Reduction of the ruthenium center can be ruled out because of the instability of the ruthenium(I) state with the ligands reported herein. The O-H group of methanol is likely to participate in hydrogen bonding with the N-H and O (non-coordinating) groups of  $\mathbf{L}^2_{\text{-H}}$  in  $\mathbf{1}^+$ . Such a phenomenon is responsible for the large shift in the first reduction potential of  $\mathbf{1}^+$  on moving from acetonitrile to methanol and also indicates that the first reduction step is based on  $\mathbf{L}^2_{\text{-H}}$ . Since the shift of the second reduction potential is much less on changing the solvent from acetonitrile to methanol, this step is likely to be centered on the bpy ligand. Use of methanol as a solvent also renders the first reduction step electrochemically irreversible with the peak to peak difference being more than 500 mV (Figure 3.4.1.2). This probably occurs because methanol changes the chemical composition of  $\mathbf{1}^+$  by participating in hydrogen bonding with it. As compared to the first reduction potential the first oxidation potential shows only a marginal shift on changing the solvent from acetonitrile to methanol {Figure 3.4.1.2 (left), Table 3.4.1.1}. Such a small shift is a first indication that the first oxidation step is not exclusively centered on the  $\mathbf{L}^2_{\text{-H}}$  ligand in  $\mathbf{1}^+$  (*vide infra*).

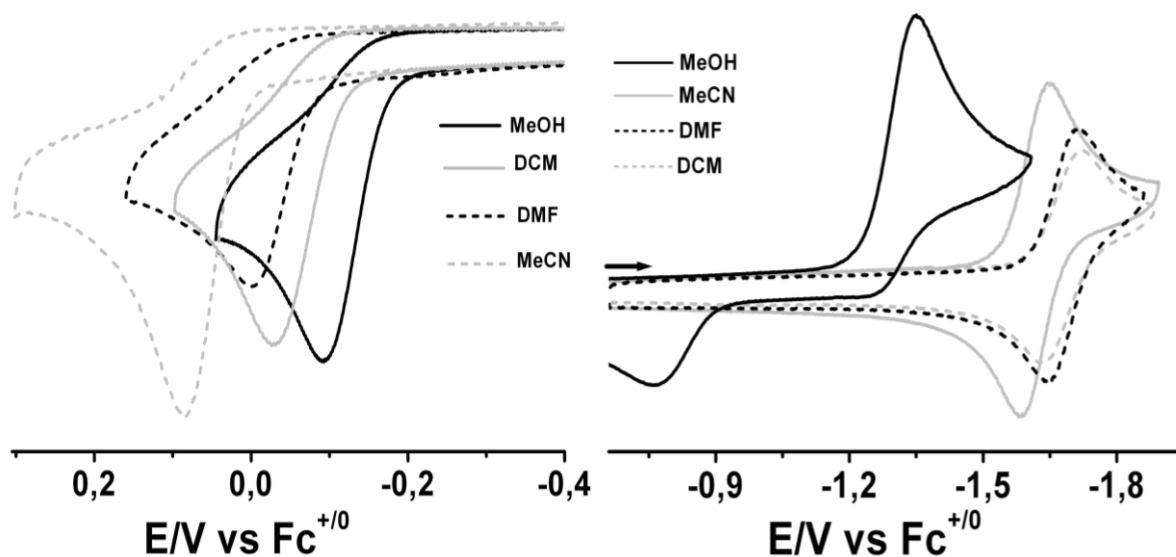


**Figure 3.4.1.2.** Change of first oxidation potential (left) and first reduction potential (right) of the complex  $\mathbf{1}^+$  in different solvents containing 0.1 M  $\text{Bu}_4\text{NPF}_6$  at 295 K.



**Table 3.4.1.1:** Redox potentials of the complex  $\mathbf{1}^+$  in different solvents.<sup>[a]</sup>

| Solvent | $E_{1/2}^{ox1}$ | $E_{1/2}^{red1}$ |
|---------|-----------------|------------------|
| DCM     | -0.03 (ir)      | -1.67 (re)       |
| DMF     | 0.00 (ir)       | -1.68 (re)       |
| MeCN    | +0.09 (ir)      | -1.61 (re)       |
| MeOH    | -0.09 (ir)      | -1.35 (ir)       |

<sup>[a]</sup> Electrochemical potentials in V from cyclic voltammetry in different solvents / 0.1 M  $\text{Bu}_4\text{NPF}_6$  at 298 K. Scan Rate: 100 mV/s. Ferrocene / Ferrocenium was used as internal standard.

**Table 3.4.1.2.** Redox potentials of the complexes.<sup>[a]</sup>

| Complex             | $E_{1/2}^{ox2}$<br>( $\Delta E_p$ ) <sup>[b]</sup> | $E_{1/2}^{ox1}$<br>( $\Delta E_p$ ) <sup>[b]</sup> | $E_{1/2}^{red1}$<br>( $\Delta E_p$ ) <sup>[b]</sup> | $E_{1/2}^{red2}$<br>( $\Delta E_p$ ) <sup>[b]</sup> | $E_{1/2}^{red3}$<br>( $\Delta E_p$ ) <sup>[b]</sup> | $E_{1/2}^{red4}$<br>( $\Delta E_p$ ) <sup>[b]</sup> | $E_{1/2}^{red5}$<br>( $\Delta E_p$ ) <sup>[b]</sup> |
|---------------------|--|--|---|---|---|---|---|
| $\mathbf{[1]}^+$    |  | +0.09<br>(92)                                      | -1.62<br>(69)                                       | -2.05<br>(91)                                       | -2.32<br>(104)                                      |   |   |
| $\mathbf{[2]}^{2+}$ | +0.34<br>(78)                                      | -0.14<br>(68)                                      | -1.96<br>(73)                                       | -2.12<br>(68)                                       | -2.27<br>(63)                                       | -2.40<br>(68)                                       | -2.69<br>(130)                                      |
| $\mathbf{[3]}^{2+}$ | +0.53<br>(95)                                      | +0.00<br>(84)                                      | -1.76<br>(75)                                       | -2.05<br>[2e red]                                   | -2.31<br>(85)                                       |   |   |
| $\mathbf{[4]}^{2+}$ | +0.35<br>(95)                                      | -0.23<br>(78)                                      | -1.92<br>(73)                                       | -2.32<br>[2e red]                                   | -2.59<br>(90)                                       | -2.75<br>(95)                                       |   |

<sup>[a]</sup> Electrochemical potentials in V from cyclic voltammetry in  $\text{CH}_3\text{CN}$  / 0.1 M  $\text{Bu}_4\text{NPF}_6$  at 298 K. Scan Rate: 100 mV/s. Ferrocene / Ferrocenium was used as internal standard.

<sup>[b]</sup>  $\Delta E_p$ : difference between peak potentials in mV.

The dinuclear complex  $\mathbf{2}^{2+}$  displays two oxidation processes at -0.14 V and 0.34 V in  $\text{CH}_3\text{CN}$  / 0.1 M  $\text{Bu}_4\text{NPF}_6$  at 295 K (Figure 3.4.1.1 and Table 3.4.1.2). Thus coordination of a second  $\text{Ru}(\text{bpy})_2$  center to  $\mathbf{1}^+$  and removal of a proton from  $\mathbf{L}^2_{\text{-H}}$  results in a cathodic shift of the first oxidation potential and the emergence of a second oxidation step within the acetonitrile solvent window. The removal of a proton and coordination of a second metal center shifts the Highest Occupied Molecular Orbital (HOMO) of the complex to higher energy. The difference between the two oxidation potentials translate to a comproportion constant ( $K_c$ ) value of the order of  $10^8$  (Table 3.4.1.2) for the odd electron  $\mathbf{2}^{3+}$  form. The first

reduction potential is shifted from -1.62 V in  $1^+$  to -1.96 V in  $2^{2+}$ . Similar to the oxidation potential, the reduction potentials also show a cathodic shift on moving from the mononuclear to the dinuclear complex. Additionally, several other reduction steps appear for  $2^{2+}$  in comparison to  $1^+$ . This is a result of the reduction of the additional bpy ligands that are bound to the second Ru(bpy)<sub>2</sub> center in  $2^{2+}$ .

Changing the substituents on the nitrogen atoms of the bridging ligands from isopropyl ( $2^{2+}$ ) to benzyl ( $3^{2+}$ ) result in a positive shift of all the redox potentials (Table 3.4.1.2). This is a result of changing the isopropyl groups with their positive inductive effect with the aromatic phenyl ring. On moving further to  $4^{2+}$  that has mesityl substituents on the nitrogen atoms of the bridge, a reverse trend is observed. All redox potentials of  $4^{2+}$  are negatively shifted compared to both  $2^{2+}$  and  $3^{2+}$ . The effect of introducing a phenyl substituent directly on the nitrogen donor atoms seems to be overcompensated by the three methyl substituents on the phenyl ring with their strong positive inductive effect. The order of the  $K_c$  values for the one-electron oxidized forms  $3^{3+}$  and  $4^{3+}$  are in a range comparable to that of  $2^{3+}$  (Table 3.4.1.2).

The literature known parent compound  $5^{2+}$  containing the all oxygen [O,O,O,O] donor set in the bridge has its oxidation potentials at 0.36 and 0.70 V and the first reduction potential at -1.05 V.<sup>[123]</sup> Thus on moving from the [O,O,O,O] donor set in the bridge of  $5^{2+}$  to the [O,N,O,N] donor set for  $2^{2+}$ - $4^{2+}$  in the present case, the redox potentials are all significantly shifted in the negative direction. Thus the oxidation steps occur are lower positive (or even negative) potentials for  $2^{2+}$ - $4^{2+}$  as compared to  $5^{2+}$  and the reduction processes occur at higher negative potential. This effect is related to the higher electronegativity of the [O] donors compared to their [NR] counterparts that results in stabilization of orbitals in  $5^{2+}$  as compared to  $2^{2+}$ - $4^{2+}$ . The  $K_c$  value for  $5^{3+}$  is only of the order of  $10^5$  as compared to the range of  $10^8$  for  $2^{3+}$ - $4^{3+}$ . Thus the thermodynamic stability of the one-electron oxidized forms of the complexes increases significantly on moving from a [O,O,O,O] donor set to a [O,N,O,N] donor set.

### 3.4.2. Electrochemistry of complexes $1'(\text{ClO}_4)$ , $2'(\text{ClO}_4)_2$ , $3'(\text{ClO}_4)_2$ and $4'(\text{ClO}_4)_2$ containing asymmetric *p*-quinonoid ligands.

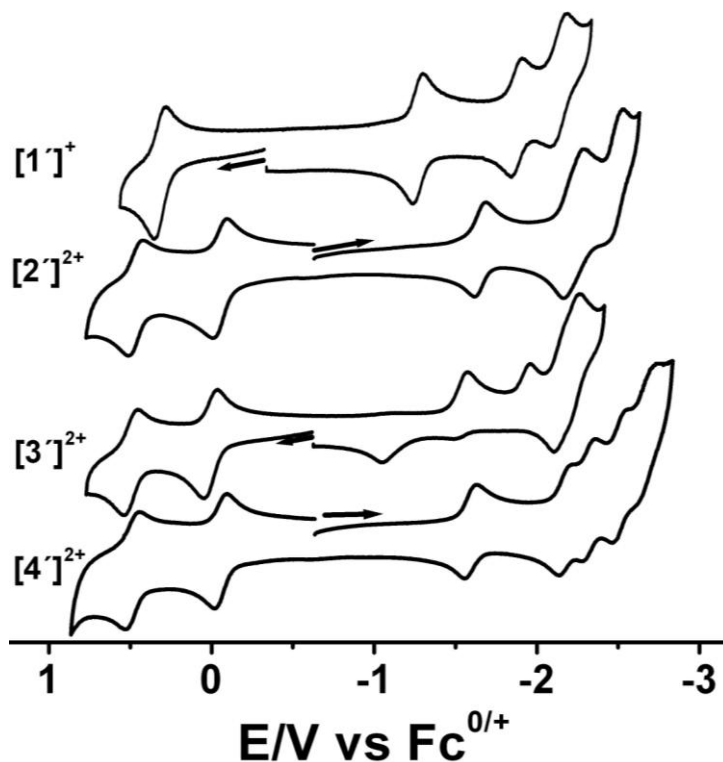


**Figure 3.4.2.1.** Cyclic voltammogram of  $1'(\text{ClO}_4)$ ,  $2'(\text{ClO}_4)_2$ ,  $3'(\text{ClO}_4)_2$  and  $4'(\text{ClO}_4)_2$  in  $\text{CH}_3\text{CN} / 0.1 \text{ M Bu}_4\text{NPF}_6$  at 295 K.

The four complexes containing asymmetric *p*-quinonoid ligands also show similar redox rich chemistry like the complexes containing symmetric *p*-quinonoid ligands. The mononuclear complex  $1^{+\bullet}$  shows one oxidation (+0.32 V) and several reduction steps, the first of which occur at -1.26 V in  $\text{CH}_3\text{CN} / 0.1 \text{ M Bu}_4\text{NPF}_6$  at 295 K (Figure 3.4.2.1 and Table 3.4.2.1). On moving from  $1^+$  to  $1^{+\bullet}$ , all the redox potentials are positively shifted significantly because the one less electronegative [NR] group is replaced by more electronegative [O] atom in the quinonoid ligand (Table 3.4.1.2 and 3.4.2.1). The first reduction potential of  $1^{+\bullet}$  shifted more (0.36 V) towards the less negative potential than the other reduction potentials (0.18 and 0.19 V) clearly indicate quinonoid centered ( $\text{L}^3_{\text{H}}$ ) first reduction and bpy centered second and third reductions. The reversible nature of the first oxidation process and marginal shift of oxidation potential (0.23 V) compared to the first reduction potential (0.32 V) clearly indicates ruthenium centered oxidation. That's why we did not measure the solvent dependence of the redox potentials of  $1^{+\bullet}$  to verify the redox processes.

**Table 3.4.2.1.** Redox potentials of the complexes.<sup>[a]</sup>

| Complex                         | $E_{1/2}^{ox2}$<br>( $\Delta E_p$ ) <sup>[b]</sup> | $E_{1/2}^{ox1}$<br>( $\Delta E_p$ ) <sup>[b]</sup> | $E_{1/2}^{red1}$<br>( $\Delta E_p$ ) <sup>[b]</sup> | $E_{1/2}^{red2}$<br>( $\Delta E_p$ ) <sup>[b]</sup> | $E_{1/2}^{red3}$<br>( $\Delta E_p$ ) <sup>[b]</sup> | $E_{1/2}^{red4}$<br>( $\Delta E_p$ ) <sup>[b]</sup> | $E_{1/2}^{red3}$<br>( $\Delta E_p$ ) <sup>[b]</sup> |
|---------------------------------|--|--|---|---|---|---|---|
| [1 <sup>+</sup> ] <sup>+</sup>  |  | +0.32<br>(73)                                      | -1.26<br>(60)                                       | -1.87<br>(61)                                       | -2.13<br>(105)                                      |   |   |
| [2 <sup>+</sup> ] <sup>2+</sup> | +0.46<br>(84)                                      | -0.06<br>(82)                                      | -1.66<br>(68)                                       | -2.24<br>[2e red]                                   | -2.49<br>(106)                                      |   |   |
| [3 <sup>+</sup> ] <sup>2+</sup> | +0.49<br>(85)                                      | 0.00<br>(84)                                       | -1.859<br>(ir)                                      | -1.97<br>(ir)                                       | -2.20<br>[2e red]                                   |   |   |
| [4 <sup>+</sup> ] <sup>2+</sup> | +0.49(79)  | -0.06<br>(72)                                      | -1.59<br>(73)                                       | -2.17<br>(73)                                       | -2.32<br>(73)                                       | -2.51<br>(80)                                       | -2.68<br>(129)                                      |

<sup>[a]</sup> Electrochemical potentials in V from cyclic voltammetry in CH<sub>3</sub>CN / 0.1 M Bu<sub>4</sub>NPF<sub>6</sub> at 298 K. Scan Rate: 100 mV/s. Ferrocene / Ferrocenium was used as internal standard.

<sup>[b]</sup>  $\Delta E_p$ : difference between peak potentials in mV.

The dinuclear complex **2**<sup>2+</sup> displays two oxidation processes at comparatively higher potentials (-0.06 V and 0.46 V in CH<sub>3</sub>CN / 0.1 M Bu<sub>4</sub>NPF<sub>6</sub> at 295 K [Figure 3.4.2.1 and Table 3.4.2.1]) than the dinuclear complex **2**<sup>2+</sup> as expected. The coordination of a second Ru(bpy)<sub>2</sub> center to **1**<sup>+</sup> and removal of a proton from **L**<sup>3-H</sup> results in a cathodic shift of the first oxidation potential and the emergence of a second oxidation step within the acetonitrile solvent window like the coordination of a second Ru(bpy)<sub>2</sub> center to **1**<sup>+</sup>. The removal of a proton and coordination of a second metal center shifts the Highest Occupied Molecular Orbital (HOMO) of the complex to higher energy. In this case, on coordination of a second Ru(bpy)<sub>2</sub> center to **1**<sup>+</sup> the first oxidation potential shifts more compared to the previous case, suggest very large energy shifts of HOMO in this case. The difference between the two oxidation potentials translate to a comproportion constant ( $K_c$ ) value of the order of 10<sup>9</sup> (Table 3.4.2.1) for the odd electron **2**<sup>3+</sup> form. The first reduction potential is shifted from -1.26 V in **1**<sup>+</sup> to -1.66 V in **2**<sup>2+</sup>. Similar to the oxidation potential, the reduction potentials also show a cathodic shift on moving from the mononuclear to the dinuclear complex.

Changing the substituent on the nitrogen atom of the bridging ligands from isopropyl (**2**<sup>2+</sup>) to benzyl (**3**<sup>2+</sup>) and mesityl (**4**<sup>2+</sup>) result marginal shift of all the redox potentials (Table 3.4.2.1) and show similar trend like previous observation in the section 3.4.1. In the previous case, on moving from **2**<sup>2+</sup> to **4**<sup>2+</sup>, all the redox potential shifts remarkably (Table 3.4.1.2) than moving from **2**<sup>2+</sup> to **4**<sup>2+</sup>. This is because of the electronic nature of the asymmetric bridging ligands (**L**<sup>3</sup>) in the complexes **2**<sup>2+</sup>, **3**<sup>2+</sup> and **4**<sup>2+</sup> are guided by only one N-R group where as the electronic nature of the symmetric bridging ligands (**L**<sup>2</sup>) in the complexes **2**<sup>2+</sup>, **3**<sup>2+</sup> and **4**<sup>2+</sup>

are guided by two N-R groups. The order of the  $K_c$  values for the one-electron oxidized forms  $\mathbf{3}^{3+}$  and  $\mathbf{4}^{3+}$  are in a range comparable to that of  $\mathbf{2}^{3+}$  (Table 3.4.2.1). Another important fact is that the first reduction of asymmetric  $p$ -[O,O,O,N] bridged  $N$ -benzyl substituted dinuclear complex  $\mathbf{3}^{2+}$  is completely irreversible whereas the  $p$ -[O,N,O,N] bridged  $N$ -benzyl substituted dinuclear complex  $\mathbf{3}^{2+}$  is completely reversible. This may be due to the more acidic nature of the benzyl protons in the complex  $\mathbf{3}^{2+}$  than  $\mathbf{3}^{2+}$ . (See the  $^1\text{H}$  NMR in the experimental section). The presence of more electronegative oxygen atoms in the asymmetric  $p$ -[O,O,O,N] bridged dinuclear complex  $\mathbf{3}^{2+}$  could be the reason for high acidity of benzyl protons.

On comparison with the [O,O,O,O] donor set in the bridge of  $\mathbf{5}^{2+}$  and the [O,O,O,N] donor set for  $\mathbf{2}^{2+}$ - $\mathbf{4}^{2+}$  in the present case, the redox potentials are all significantly shifted in the negative direction (Section 3.4.1 and Table 3.4.3). The oxidation steps occur at lower positive (or even negative) potentials for  $\mathbf{2}^{2+}$ - $\mathbf{4}^{2+}$  as compared to  $\mathbf{5}^{2+}$  and the reduction processes occur at higher negative potential as expected due to the higher electronegativity of the [O] donors compared to their [NR] counterparts that results in stabilization of orbitals in  $\mathbf{5}^{2+}$  as compared to  $\mathbf{2}^{2+}$ - $\mathbf{4}^{2+}$ .

### 3.5. EPR spectroscopy

The one-electron oxidized as well as reduced states of all the complexes were probed by EPR spectroscopy in order to shed light on their electronic structures. The EPR of mono- and dinuclear complexes ( $\mathbf{1}^+$ - $\mathbf{4}^{2+}$ ) with symmetric quinonoid ligands ( $\mathbf{L}^2$ ) and ( $\mathbf{1}^+$ - $\mathbf{4}^{2+}$ ) with asymmetric quinonoid ligands ( $\mathbf{L}^3$ ) are discussed in separate sections.

#### 3.5.1. The Complexes $\mathbf{1}^+$ - $\mathbf{4}^{2+}$

The *in-situ* generated one-electron reduced form  $\mathbf{1}^\cdot$  of the mononuclear complex shows a narrow signal in  $\text{CH}_3\text{CN} / 0.1 \text{ M Bu}_4\text{NPF}_6$  at 295 K with a peak to peak separation of about 18 G (Figure 4.5.1.1a, Table 3.5.1.1). The signal is centered at  $g = 2.000$ . The narrow line width, appearance of the signal in fluid solution at 295 K and the  $g$ -value are all indicative of a ligand centered reduction. Together with the solvent dependence of the cyclic voltammetry data the one electron reduced form  $\mathbf{1}^\cdot$  is thus best formulated as  $[(\text{bpy})_2\text{Ru}^{\text{II}}(\mathbf{L}^2_{\text{H}})^{2\cdot-}]$ . The expected hyperfine coupling to the nitrogen atoms of  $\mathbf{L}^2_{\text{H}}$  ligand is in all likelihood not well resolved due to unfavorable line width to hyperfine coupling constant ratios. Such a phenomenon has precedence in the literature for related ruthenium complexes with quinone ligands.<sup>[122]</sup>

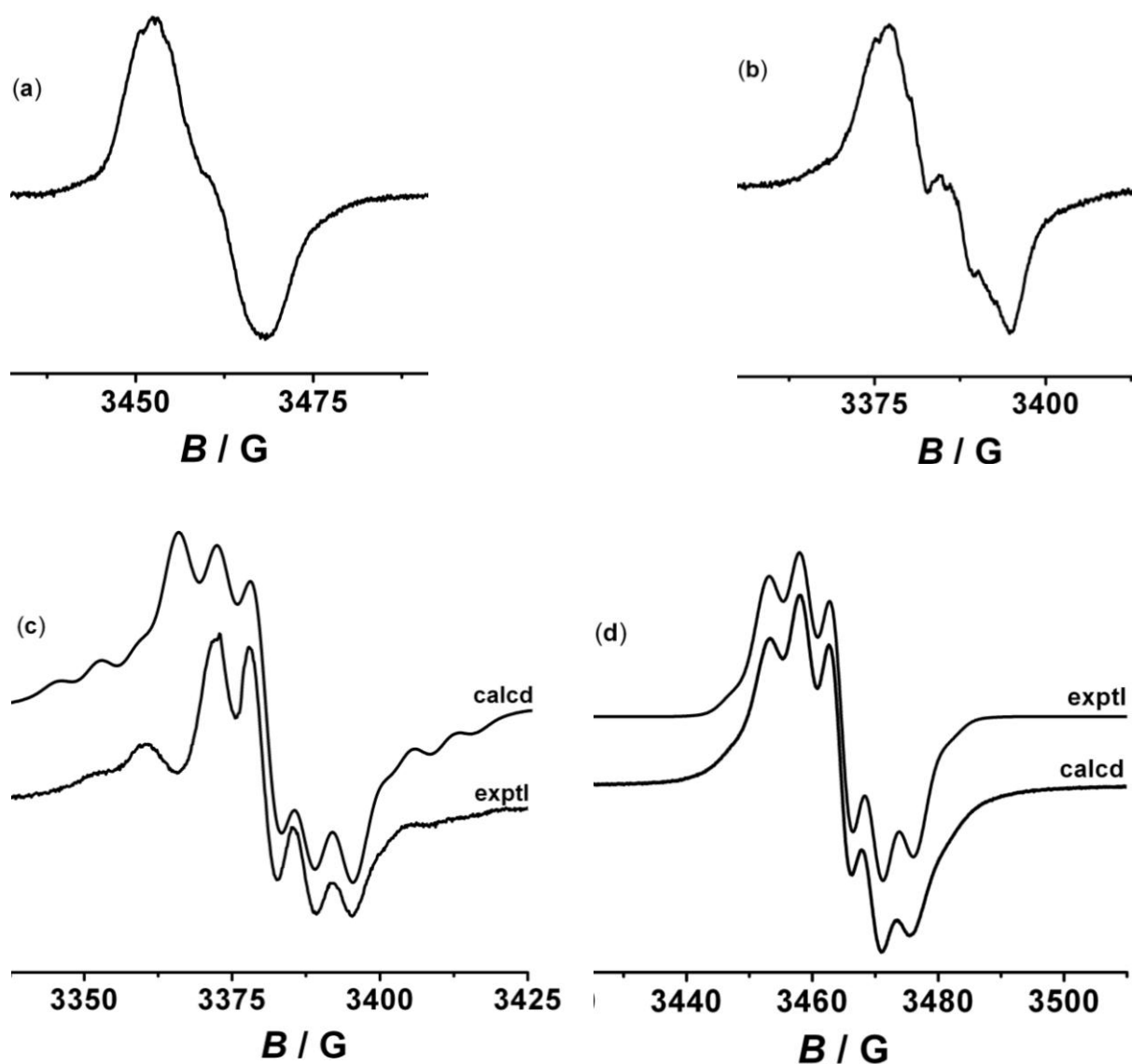


**Figure 3.5.1.1.** EPR spectra of electrochemically generated  $1^\bullet$  (a),  $2^+$  (b),  $3^+$  (c) and  $4^+$  (d) at RT in  $\text{CH}_3\text{CN} / 0.1 \text{ M Bu}_4\text{NPF}_6$ .

The *in-situ* electrochemically generated one electron reduced forms of the dinuclear complexes  $2^+$ - $4^+$  in  $\text{CH}_3\text{CN} / 0.1 \text{ M Bu}_4\text{PF}_6$  displays well resolved EPR signals at 295 K. Thus the signal of  $4^+$  is a well resolved quintet centered at  $g = 1.998$  due to the hyperfine coupling of the unpaired electron with the two equivalent  $^{14}\text{N}$  atoms ( $I = 1$ ) of  $(\text{L}^2\text{-2H})^\bullet$  (Figure 3.5.1.1d). Additionally, ruthenium satellites are observed at both the extremities of the main signal. The spectrum could be simulated with parameters of 4.8 G for  $^{14}\text{N}$  and 2.4 G for  $^{103,105}\text{Ru}$ . The other two dinuclear complexes show similar spectrum. The data for the one electron reduced forms of all the complexes are summarized in Table 3.5.1.1. The EPR data thus clearly point to a reduction of the bridging ligand in these dinuclear complexes and the one-electron reduced forms are thus best formulated as  $[(\text{bpy})_2\text{Ru}^{\text{II}}(\mu\text{-L}^2\text{-2H})^{3-}\text{Ru}^{\text{II}}(\text{bpy})_2]^+$ .

**Table 3.5.1.1.** EPR data of one-electron reduced form of the complexes  $1^+$ - $4^{2+}$ .<sup>[a]</sup>

| complex | $g_{av}$ (exptl) | $g_{av}$ (calcd) | $A$ ( $^{99,101}\text{Ru}$ ) <sup>[b]</sup> | $A$ ( $^{14}\text{N}$ ) <sup>[b]</sup> |
|---------|------------------|------------------|---|--|
| $1^+$   | 2.000            | -                | -   | -                                      |
| $2^+$   | 2.000            | -                | -   | -                                      |
| $3^+$   | 2.003            | 2.002            | 8   | 6.2                                    |
| $4^+$   | 1.998            | 1.997            | 2.4   | 4.8                                    |

<sup>[a]</sup> EPR data of species generated by in situ electrolysis in  $\text{CH}_3\text{CN}/0.1\text{m Bu}_4\text{NPF}_6$ . The spectra were recorded at 295 K. <sup>[b]</sup> Hyperfine coupling constant in Gauss obtained from simulation.

In contrast to the one electron reduced forms, the one electron oxidized forms of the dinuclear complexes  $2^{3+}$ - $4^{3+}$  in  $\text{CH}_3\text{CN}$  were EPR silent at 295 K. The reason for this is fast relaxation in fluid solution and is already an indication of possible ruthenium participation in the singly occupied molecular orbital (SOMO). On cooling down the samples to 110 K, an anisotropic signal with rhombicity is observed (Figure 3.5.1.2, Table 3.5.1.2). The spectrum obtained for  $4^{3+}$  could be simulated with the parameters  $g_1 = 2.315$ ,  $g_2 = 2.105$  and  $g_3 = 1.880$ . The  $g_{av}$  is 2.100 and  $g$ -anisotropy,  $\Delta g = 0.435$ . Such a large deviation of the  $g$  value from the free electron value of 2.0023 and the large anisotropy observed are indications of substantial metal contribution to the SOMO. The complexes  $2^{3+}$  and  $3^{3+}$  show very similar spectra and parameters (Table 3.5.1.2). The one-electron oxidized forms of these complexes are thus best described as  $[(\text{bpy})_2\text{Ru}^{\text{II}}(\mu\text{-L}^2\text{-2H})^2\text{-Ru}^{\text{III}}(\text{bpy})_2]^{3+}$  or more appropriately  $[(\text{bpy})_2\text{Ru}^{2.5}(\mu\text{-L}^2\text{-2H})^2\text{-Ru}^{2.5}(\text{bpy})_2]^{3+}$  (*vide infra*). The  $g$  values are less extreme as compared to a “pure” Ru(III) case because of an orbital reduction factor  $< 1$  that is to partial electron delocalization onto the ligand.

**Table 3.5.1.2.** EPR data and  $K_c$  value of one-electron oxidized form of the complexes  $2^{3+}$ - $4^{3+}$ .<sup>[a]</sup>

| complex  | $g_x$ <sup>[a]</sup> | $g_y$ <sup>[a]</sup> | $g_z$ <sup>[a]</sup> | $g_{av}$ <sup>[a]</sup> | $g_x$ <sup>[b]</sup> | $g_y$ <sup>[b]</sup> | $g_z$ <sup>[b]</sup> | $g_{av}$ <sup>[b]</sup> | $K_c$              |
|----------|----------------------|----------------------|----------------------|-------------------------|----------------------|----------------------|----------------------|-------------------------|--------------------|
| $2^{3+}$ | 2.230                | 2.065                | 1.912                | 2.069                   | 2.280                | 2.070                | 1.900                | 2.083                   | $1.16 \times 10^8$ |
| $3^{3+}$ | 2.272                | 2.119                | 1.905                | 2.099                   | 2.210                | 2.100                | 1.900                | 2.070                   | $8.55 \times 10^8$ |
| $4^{3+}$ | 2.280                | 2.118                | 1.887                | 2.095                   | 2.315                | 2.105                | 1.880                | 2.100                   | $4.73 \times 10^9$ |

<sup>[a]</sup> EPR data of species generated by chemically in  $\text{CH}_3\text{CN}$ . The spectra were recorded at 110 K. <sup>[b]</sup> Hyperfine coupling constant in Gauss obtained from simulation.

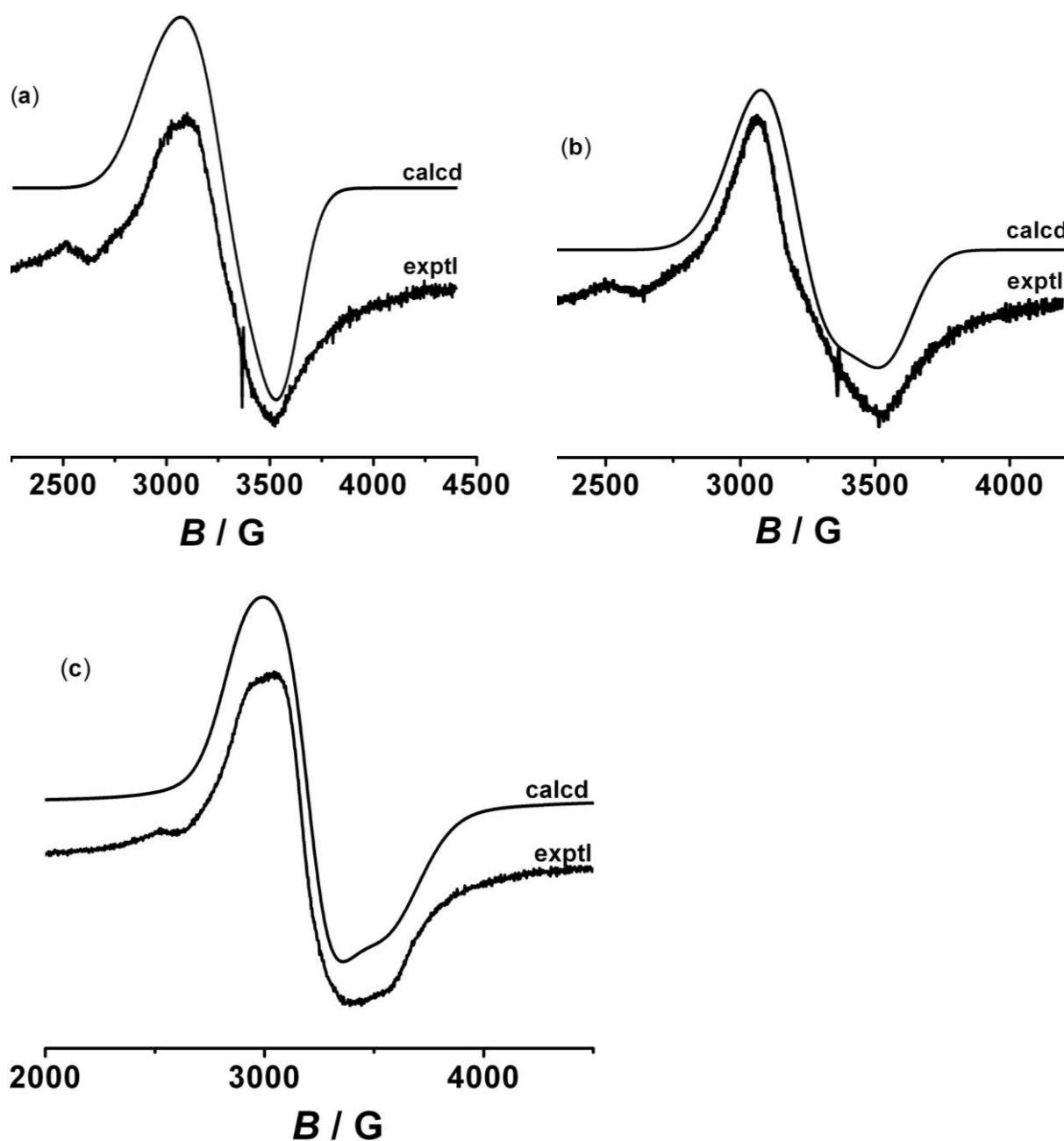


**Figure 3.5.1.2.** EPR spectra of chemically generated  $2^{3+}$  (a),  $3^{3+}$  (b) and  $4^{3+}$  (c) at 110 K in  $\text{CH}_3\text{CN}$ .

### 3.5.2. The Complexes $1^{+}$ - $4^{2+}$

The one-electron reduced form  $1^{\cdot-}$  generated *in situ* in  $\text{CH}_3\text{CN}/0.1\text{MBu}_4\text{NPF}_6$  shows an isotropic EPR signal with hyperfine coupling at 295 K having  $g_{\text{av}} = 2.002$  which is very much closer to the free electron  $g$  value (Figure 3.5.2.1a). The  $g_{\text{av}}$  value of the spectrum strongly suggests ligand centered reduction and direct evidence for the quinonoid bridge-centered reduction which comes from the hyperfine coupling. The hyperfine coupling of the unpaired electron with nitrogen atom ( $^{14}\text{N}$ ,  $I = 1$ ) of the asymmetric quinonoid bridge results as triplet signal.<sup>[122]</sup> Whereas in this case, we have observed some more splitting (quintet).



The appearance of more splitted signal may be either due to the hyperfine coupling of the unpaired electron with one nitrogen atom ( $^{14}\text{N}$ ,  $I = 1$ ) and two ring-hydrogen atoms ( $^1\text{H}$ ,  $I = 1/2$ ) of the asymmetric quinonoid bridge or two nitrogen atoms ( $^{14}\text{N}$ ,  $I = 1$ ) for a hydrogen-bonded dimer where the unpaired electron is delocalized over the two hydrogen-bonded quinonoid moieties. The delocalization of the unpaired electron over the hydrogen-bonded two quinonoid moieties is more logical because the presence of two nitrogen atoms (one from each) which are responsible for quintet signal.

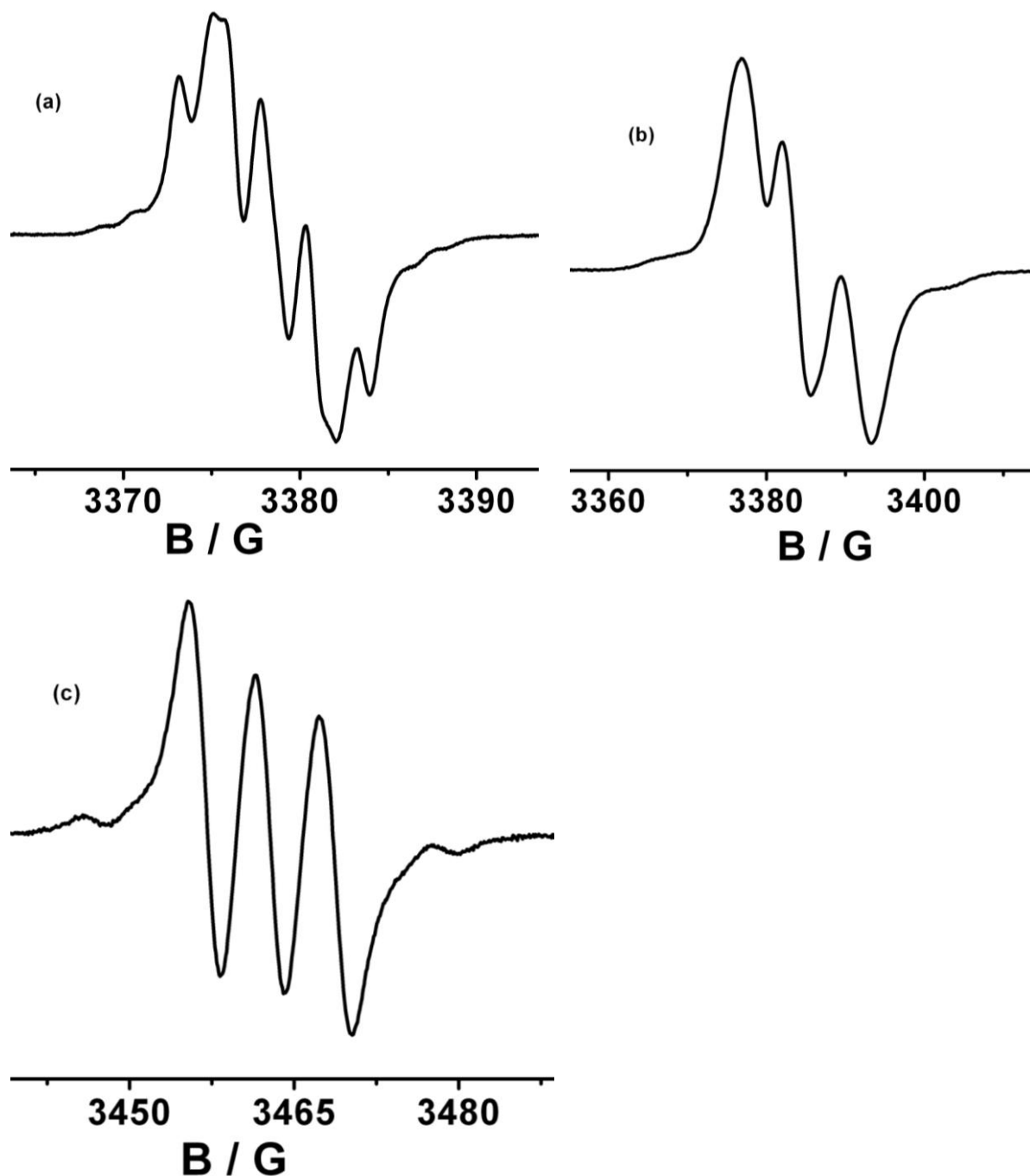


**Figure 3.5.2.1.** EPR spectra of electrochemically generated  $1^{\cdot-}$  (a),  $2^{+\cdot}$  (b), and  $4^{+\cdot}$  (d) at RT in  $\text{CH}_3\text{CN} / 0.1 \text{ M Bu}_4\text{NPF}_6$ .

The *in-situ* electrochemically generated one electron reduced form of the dinuclear complexes  $2^{+}$  and  $4^{+}$  in  $\text{CH}_3\text{CN} / 0.1 \text{ M Bu}_4\text{PF}_6$  displays well resolved ligand centered ( $g_{\text{av}} = 2.000$  and  $1.998$ , close to free electron  $g$  value) EPR signals at 295 K (Figure 3.5.2.1b and 3.5.2.1c). The direct evidence for the quinonoid bridge-centered reduction comes from the hyperfine coupling of the unpaired electron with the nitrogen atom ( $^{14}\text{N}$ ,  $I = 1$ ) of the quinonoid bridge. Thus, the EPR spectrum of the one-electron reduced forms  $2^{+}$  and  $4^{+}$  generated in  $\text{CH}_3\text{CN}/0.1\text{MBu}_4\text{NPF}_6$  showed triplet signals ( $2nI + 1$ ;  $n =$  equivalent nuclei, each with a spin of  $I$ ). In addition, ruthenium satellites are also observed at both the extremities of the main signal. The EPR data thus clearly point to a reduction of the bridging ligand in these dinuclear complexes and the one-electron reduced forms are thus best formulated as  $[(\text{bpy})_2\text{Ru}^{\text{II}}(\mu\text{-L}^3\text{-2H})^{3-}\text{Ru}^{\text{II}}(\text{bpy})_2]^+$  like the similar symmetric quinonoid bridged dinuclear complexes  $2^+-4^+$ . We did not measure the EPR of one electron reduced form of  $3^{2+}$  because of its irreversible nature during the reduction.

In contrast to the EPR of one electron reduced forms, the EPR of one electron oxidized forms of the mononuclear complex  $1^{+}$  and dinuclear complexes  $2^{2+}$ - $4^{2+}$  were also measured. All the one-electron oxidized species  $1^{2+}$ - $4^{3+}$  were EPR silent at 295 K in  $\text{CH}_3\text{CN}$  due to the fast relaxation in fluid solution which is an indication of possible ruthenium participation in the singly occupied molecular orbital (SOMO). On cooling down the samples to 110 K, an anisotropic signal with rhombicity is observed (Figure 3.5.2.2). The EPR spectra of all the species ( $1^{2+}$ - $4^{3+}$ ) show  $g_{\text{av}}$  value greater than the  $g_{\text{av}}$  value of organic-radicals (2.0023) and large  $g$ -anisotropy (Table 3.5.2.1) suggest ruthenium centered spin. Thus the one electron oxidized mononuclear species  $1^{2+}$  can be formulated as  $[(\text{bpy})_2\text{Ru}^{\text{III}}\text{L}^3\text{-H}]^{2+}$  and all the one electron oxidized dinuclear species ( $2^{3+}$ - $4^{3+}$ ) can be formulated as  $[(\text{bpy})_2\text{Ru}^{\text{II}}(\mu\text{-L}^3\text{-2H})^{2-}\text{Ru}^{\text{III}}(\text{bpy})_2]^{3+}$  or more appropriately  $[(\text{bpy})_2\text{Ru}^{2.5}(\mu\text{-L}^3\text{-2H})^{2-}\text{Ru}^{2.5}(\text{bpy})_2]^{3+}$  (*vide infra*) like the species  $2^{3+}$ - $4^{3+}$  (Section 3.5.1).

**Table 3.5.2.1.** EPR data and  $K_c$  value of one-electron oxidized form of the complexes.<sup>[a]</sup>

| complex    | $g_x^{[a]}$ | $g_y^{[a]}$ | $g_z^{[a]}$ | $g_{\text{av}}^{[a]}$ | $K_c$              |
|------------|-------------|-------------|-------------|-----------------------|--------------------|
| $[1]^{3+}$ | 2.623       | 2.104       | 1.922       | 2.236                 |                    |
| $[2]^{3+}$ | 2.428       | 2.063       | 1.903       | 2.143                 | $6.27 \times 10^8$ |
| $[3]^{3+}$ | 2.408       | 2.181       | 1.912       | 2.176                 | $2.65 \times 10^8$ |
| $[4]^{3+}$ | 2.295       | 2.145       | 1.887       | 1.907                 | $1.53 \times 10^9$ |

<sup>[a]</sup> EPR data of one electron oxidized species generated chemically by ferrocenium hexafluorophosphate.

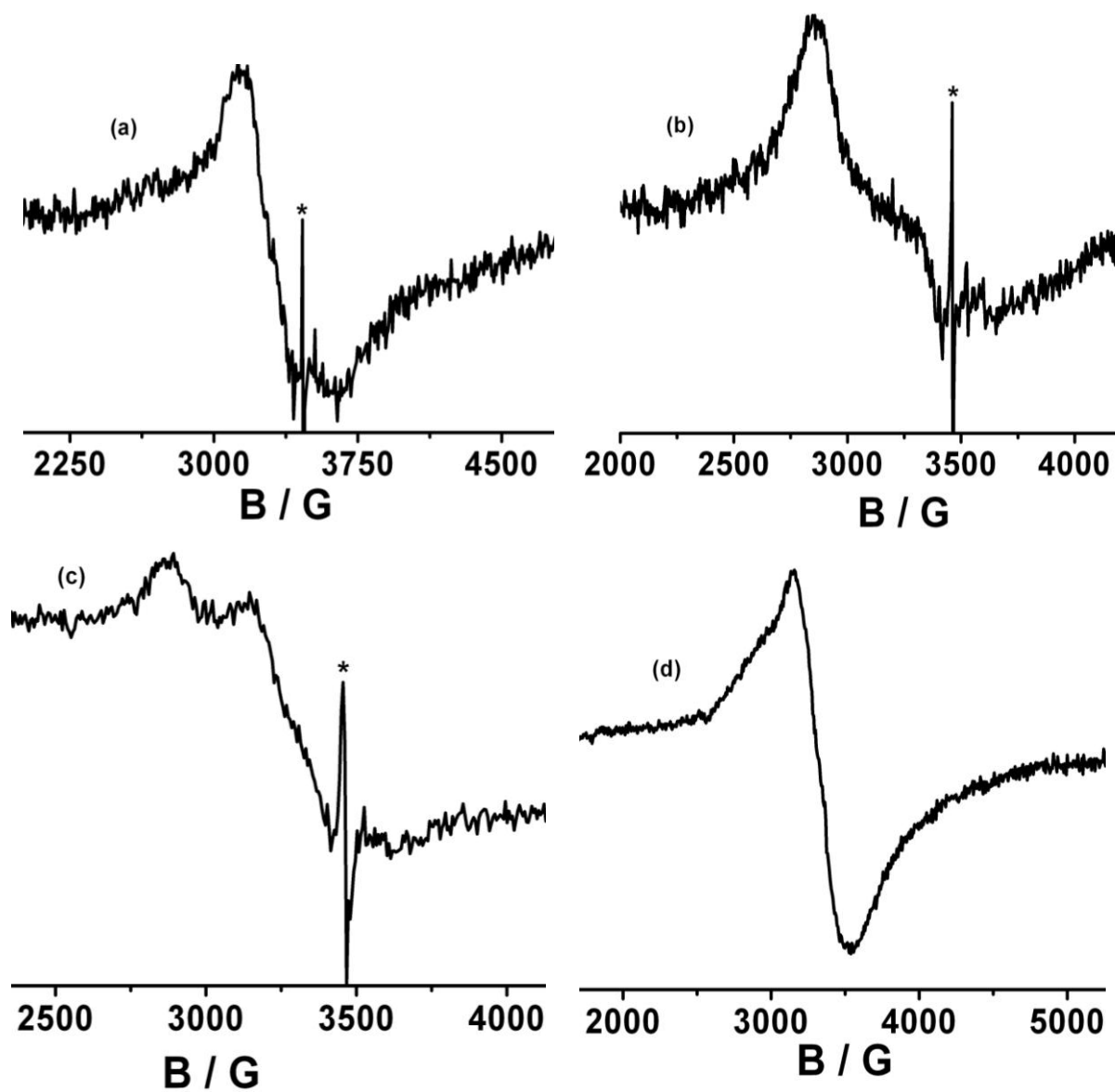


**Figure 3.5.2.2.** EPR spectra of chemically generated  $1^{2+}$  (a),  $2^{3+}$  (b),  $3^{3+}$  (c) and  $4^{3+}$  (d) at 110 K in  $\text{CH}_3\text{CN}$ .

### 3.6. UV/Vis/NIR spectroelectrochemistry

In order to verify the electronic distribution in various accessible redox processes and determine the metal-metal electronic coupling in dinuclear complexes, UV/Vis/NIR spectroelectrochemical changes of all the complexes were monitored using an optically transparent Thin Layer Electrochemical (OTTLE) cell. The data are summarized in Table 3.6.1 and 3.6.2.

The mononuclear complex  $1^+$  with symmetric quinonoid ligand ( $L^2$ ) displays two low energy bands at 560 and 528 nm in  $\text{CH}_3\text{CN} / 0.1 \text{ M Bu}_4\text{NPF}_6$  which are assigned to  $d\pi$  (Ru(II)) to  $\pi^*$  ( $L^2_{-H}$ ) and  $d\pi$  (Ru(II)) to  $\pi^*$  (bpy) metal to ligand charge transfer (MLCT)

transitions respectively (Figure 3.6.1). The higher energy bands are most likely ligand centered in nature. The  $\text{Ru}^{\text{II}} \rightarrow \text{L}^2_{\cdot\text{H}}$  MLCT transition can be tuned by varying the polarity of solvents. The  $\text{Ru}^{\text{II}} \rightarrow \text{L}^2_{\cdot\text{H}}$  band appears at comparatively higher wavelengths in protic solvents (methanol, ethanol) or highly polar solvents (DMSO) than in non protic non polar solvents (Figure 3.6.1). This is because of energy lowering of  $\text{L}^2_{\cdot\text{H}}$  centred  $\pi^*$  orbitals through hydrogen bonds with protic solvents.

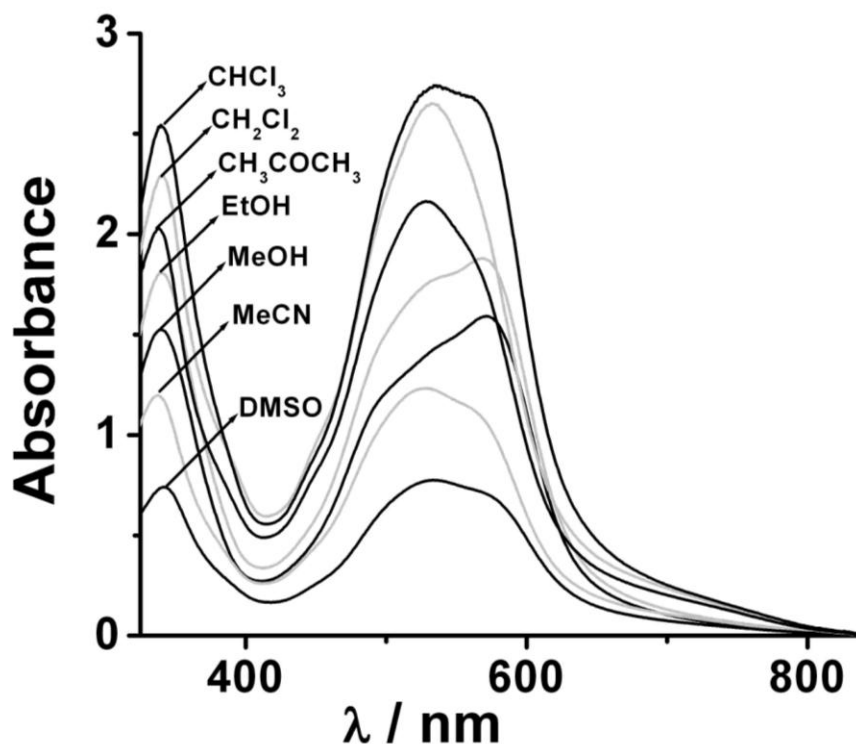


**Figure 3.6.1.** Change of UV-Vis spectra of the complex  $\mathbf{1}^+$  in different solvents.

On one electron reduction to the  $\mathbf{1}^\cdot$  form using an optically transparent thin layer electrochemical (OTTLE) cell, the MLCT bands shift in energy and new bands appear in the NIR region at 1520 and 845 nm (Figure 3.6.2). These bands are tentatively assigned to SOMO ( $\text{L}^2_{\cdot\text{H}}$ ) to LUMO (bpy) ligand to ligand charge transfer (LLCT) transitions in the one electron reduced form  $\mathbf{1}^\cdot$ . Further reduction to the  $\mathbf{1}^-$  form leads to a slight shift of the LLCT bands and an increase of their intensity (Figure 3.6.3, Table 3.6.1).

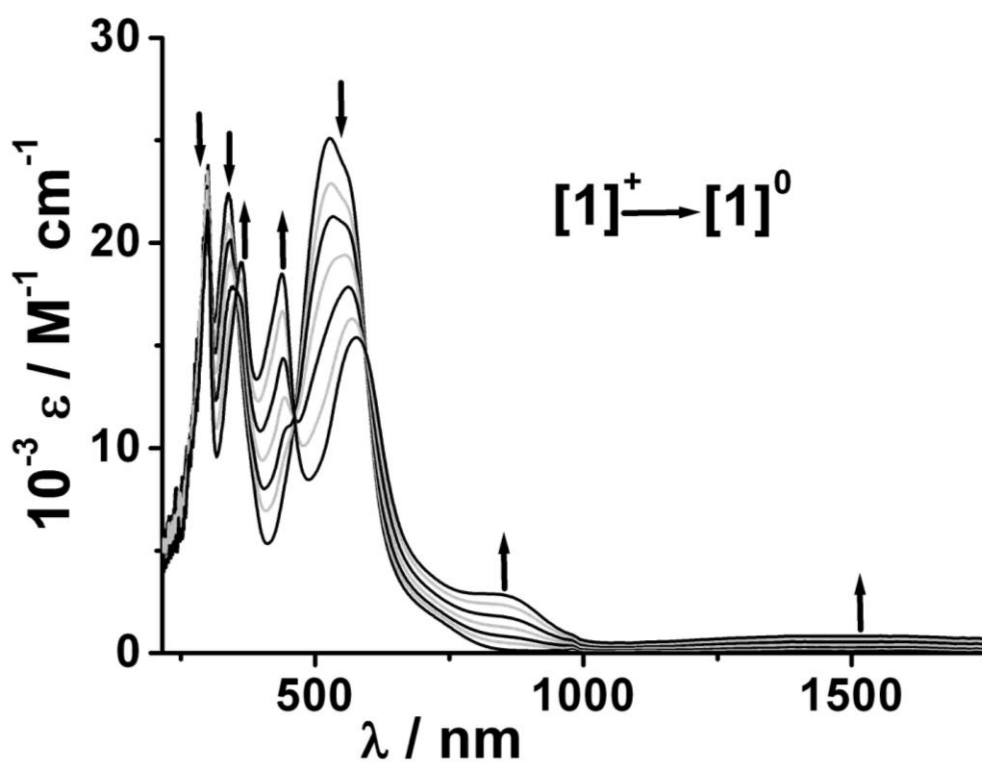


**Figure 3.6.2.** UV-Vis-NIR spectroelectrochemistry of the conversion  $[1]^{(1+) \rightarrow (0)}$  in  $\text{CH}_3\text{CN}$  / 0.1 M  $\text{Bu}_4\text{NPF}_6$ .

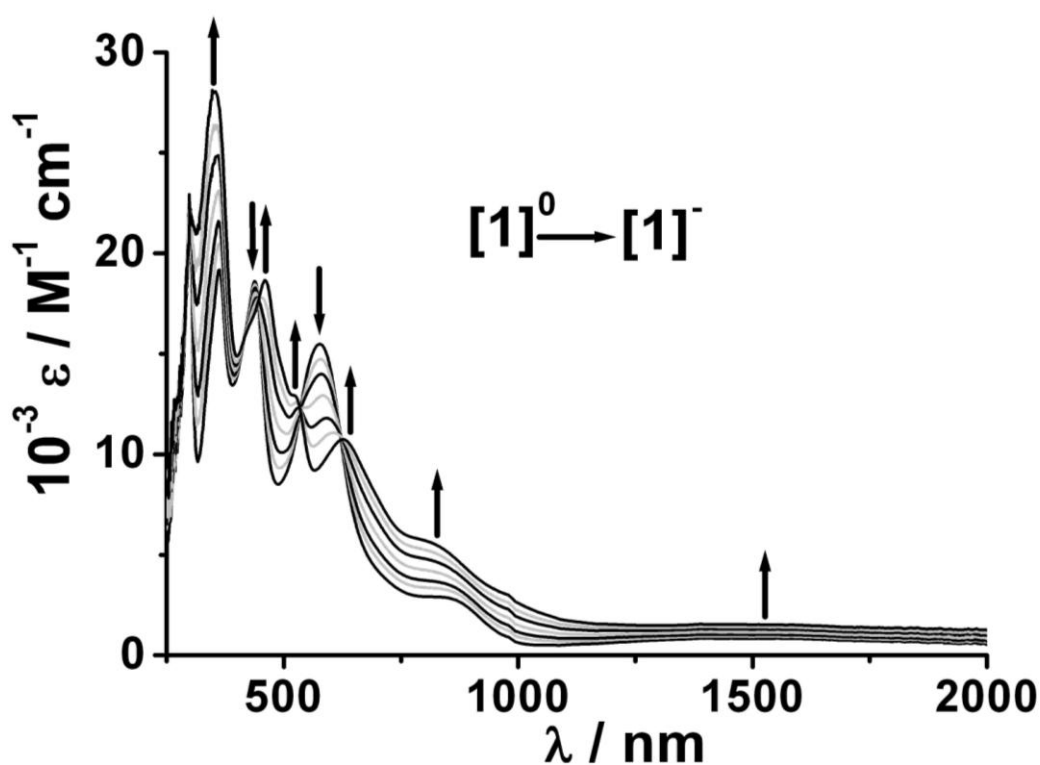


**Figure 3.6.3.** UV-Vis-NIR spectroelectrochemistry of the conversion  $[1]^{(1+) \rightarrow (0)}$  in  $\text{CH}_3\text{CN}$  / 0.1 M  $\text{Bu}_4\text{NPF}_6$ .

The mononuclear complex  $\mathbf{1}^{+}$  with asymmetric quinonoid ligand ( $\mathbf{L}^3$ ) displays similar absorption band like  $\mathbf{1}^+$ . The two low energy MLCT bands  $\{d\pi(\text{Ru(II)}) \rightarrow \pi^*(\mathbf{L}^2_{\cdot\text{H}})$  and  $d\pi(\text{Ru(II)}) \rightarrow \pi^*(\text{bpy})\}$  appear at 570 and 511 nm respectively in  $\text{CH}_3\text{CN} / 0.1 \text{ M Bu}_4\text{NPF}_6$  (Figure 3.6.4). On one electron reduction to the  $\mathbf{1}'$  form, the MLCT bands shift in energy and new bands appear in the NIR region at 1060 nm and in the visible region at 405 nm with shoulder (Figure 3.6.4). The new NIR band at 1060 nm and visible band at 405 nm can be tentatively assigned to SOMO ( $\mathbf{L}^3_{\cdot\text{H}}$ ) to LUMO (bpy) ligand to ligand charge transfer (LLCT) transitions and ( $\mathbf{L}^3_{\cdot\text{H}}$ ) to Ru(II) ligand to metal (LMCT) transition respectively in the one electron reduced form  $\mathbf{1}'$ . On one electron oxidation to the  $\mathbf{1}'^{2+}$  two MLCT bands at 570 and 511 nm are blue shifted with large decrease in intensity and two new bands with moderate intensity appeared at 430 and 369 nm (Figure 3.6.5). These two bands are tentatively assigned to LMCT transitions ( $\mathbf{L}^3_{\cdot\text{H}} \rightarrow \text{Ru(III)}$ ) and  $\text{bpy} \rightarrow \text{Ru(III)}$ ) respectively for the ruthenium centered oxidized species  $[(\text{bpy})_2\text{Ru}^{\text{III}}(\mathbf{L}^3_{\cdot\text{H}})]^{2+}$ .

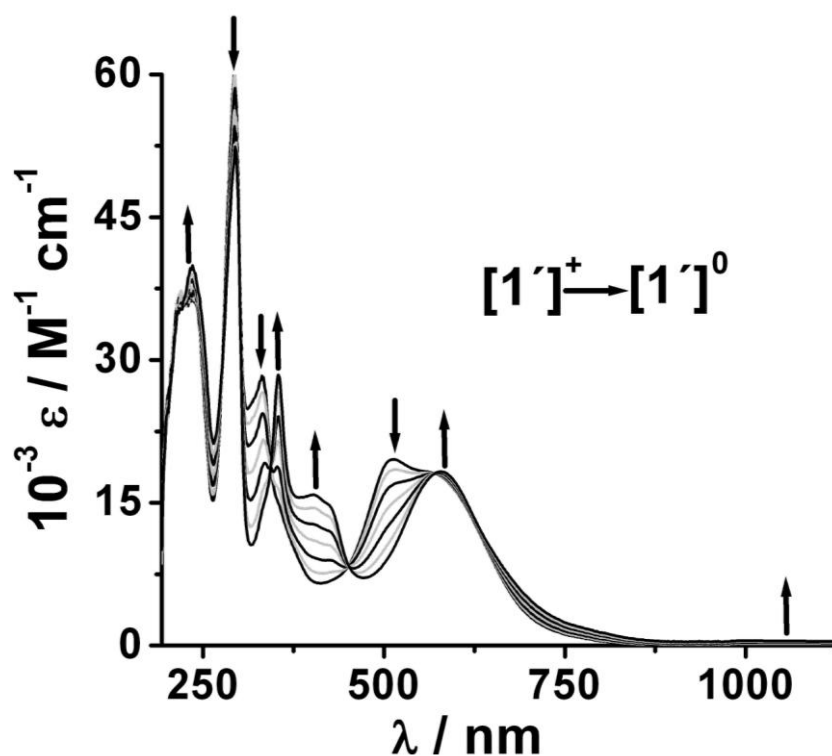


**Figure 3.6.4.** UV-Vis-NIR spectroelectrochemistry of the conversion  $[\mathbf{1}']^{(+)\rightarrow(0)}$  in  $\text{CH}_3\text{CN} / 0.1 \text{ M Bu}_4\text{NPF}_6$ .

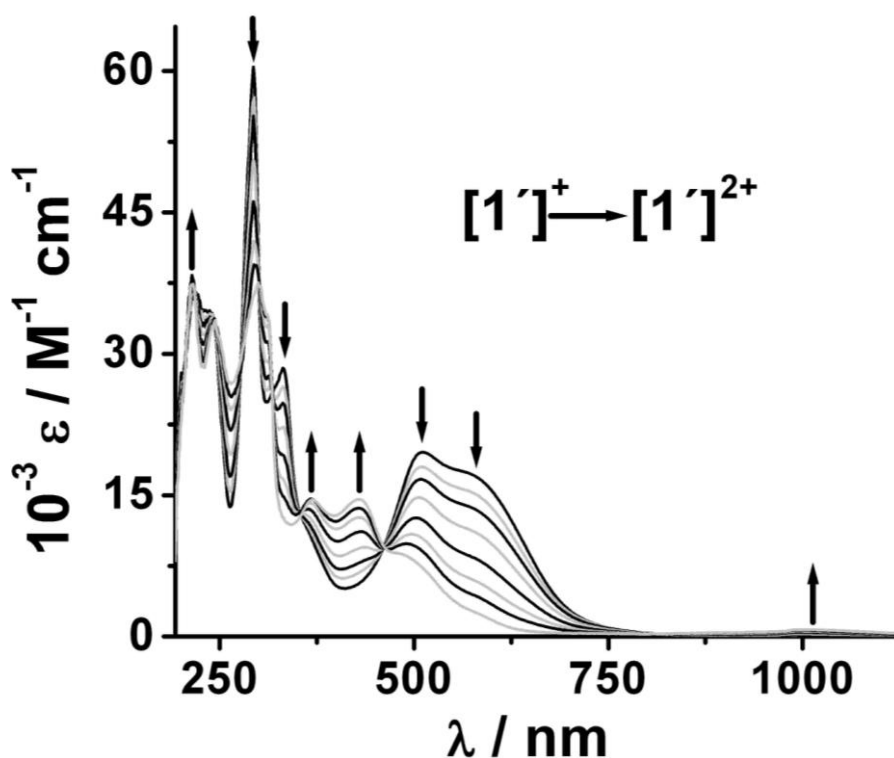


**Figure 3.6.5.** UV-Vis-NIR spectroelectrochemistry of the conversion  $[1']^{(+)\rightarrow(2+)}$  in  $\text{CH}_3\text{CN} / 0.1 \text{ M Bu}_4\text{NPF}_6$ .

The dinuclear complex  $2^{2+}$  with symmetric quinonoid ligand ( $L^2$ ) and  $2'^{2+}$  with asymmetric quinonoid ligand ( $L^3$ ) show two strong bands in the visible region (Figure 3.6.6 and 3.6.9). The complex  $2^{2+}$  shows two strong bands at 615 and 552 nm whereas for  $2'^{2+}$  shows at 650 and 528 nm in  $\text{CH}_3\text{CN} / 0.1 \text{ M Bu}_4\text{NPF}_6$ . These two bands are assigned to  $d\pi(\text{Ru(II)}) \rightarrow \pi^*(L_{-2H})$  {where  $L_{-2H}$  = symmetric ( $L^2_{-2H}$ ) or asymmetric ( $L^3_{-2H}$ ) quinonoid ligands} and  $d\pi(\text{Ru(II)}) \rightarrow \pi^*(\text{bpy})$  MLCT transitions respectively. Additional bands at higher energy observed in both cases are ligand centered in origin. For comparison, the lowest energy MLCT band in the case of  $5^{2+}$  appears at 721 nm in  $\text{CH}_3\text{CN}$ . The low energy shift of this band for  $5^{2+}$  as compared to  $2^{2+}-4^{2+}$  and  $2'^{2+}-4'^{2+}$  is consistent with the lower difference between the first oxidation and reduction potentials for  $5^{2+}$  as compared to  $2^{2+}-4^{2+}$  and  $2'^{2+}-4'^{2+}$  (Table 3.4.1.2 and 3.4.2.1). Similarly due to the same reason the  $d\pi(\text{Ru(II)}) \rightarrow \pi^*(L_{-2H})$  MLCT transition band for complex  $2'^{2+}$  appears at low energy (650 nm) as compared to  $2^{2+}$  (615 nm). The complexes  $3^{2+}$  and  $4^{2+}$  display three low energy bands each (Figures 3.6.7-3.6.8 and Table 3.6.1). Whereas complexes  $3'^{2+}$  and  $4'^{2+}$  display two low energy bands like  $2'^{2+}$  (Figures 3.6.10-3.6.11). These are all MLCT in origin. Multiple MLCT bands are to be expected because of the presence of various empty target orbitals ( $L_{-2H}$  and bpy's) in these compounds (see cyclic voltammetry section).

On one-electron oxidation, the MLCT bands are shifted to lower energies and a new band around 1400 nm appears in the NIR region for all three symmetric dinuclear complexes  $2^{2+}$ - $4^{2+}$  (Figures 3.6.6-3.6.8). On one-electron oxidation, the asymmetric complexes  $2^{2+}$ - $4^{2+}$  also show an intense band at around 1400 nm together with a comparatively less intense band at around 1900 nm (Figures 3.6.9-3.6.11). The position of the NIR band at around 1400 nm is more or less same for all six compounds (Figure 3.6.12 and Table 3.6.1 and 3.6.2). However, the intensity of this band for  $3^{3+}$  is much higher compared to those for  $2^{3+}$ ,  $2^{3+}$ ,  $3^{3+}$ ,  $4^{3+}$  and  $4^{3+}$  indicating higher oscillator strength and better orbital overlap for the NIR bands in case of  $3^{3+}$  as compared to the other four complexes. The experimental band width at half height is much smaller compared to that calculated using the Hush formalution (Table 3.6.3). Together with the results obtained from EPR spectroscopy (metal centered spin) the one electron oxidized form of the dinuclear complexes can be classified as strongly coupled class III mixed valent species and the NIR bands as  $\pi$  to  $\pi^*$  transitions in the strongly coupled class III mixed valent state. The more intense NIR band for  $3^{3+}$  is also narrower compared to the NIR bands of  $2^{3+}$ ,  $2^{3+}$ ,  $3^{3+}$ ,  $4^{3+}$  and  $4^{3+}$  (Figure 3.6.12). The NIR bands at about 1400 nm for symmetric and asymmetric complexes ( $2^{2+}$ - $4^{2+}$  and  $2^{2+}$ - $4^{2+}$ ) and NIR bands at about 1900 nm for asymmetric complexes ( $2^{2+}$ - $4^{2+}$ ) disappear on further oxidation to the  $2^{4+}$ - $4^{4+}$  and  $2^{4+}$ - $4^{4+}$  forms for all the dinuclear complexes as would be expected for a homo valent complex (Figures 3.6.13-3.6.18). The complexes  $2^{4+}$ - $4^{4+}$  and  $2^{4+}$ - $4^{4+}$  show a low energy band at about 1100 nm which is assigned to an LMCT transition from  $L_{2H}$  to Ru(III). The NIR band observed here for the one-electron oxidized form was absent in the case of  $5^{3+}$  showing the importance of incorporating NR groups into the bridging ligands.<sup>[123]</sup>

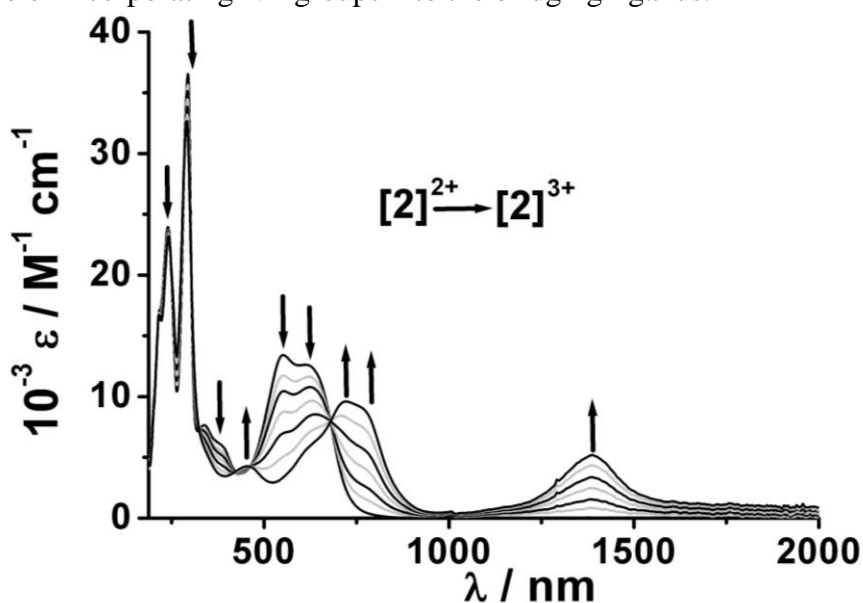


**Figure 3.6.6.** UV-Vis-NIR spectroelectrochemistry of the conversion  $[2]^{(2+) \rightarrow (3+)}$  in  $CH_3CN / 0.1 M Bu_4NPF_6$ .



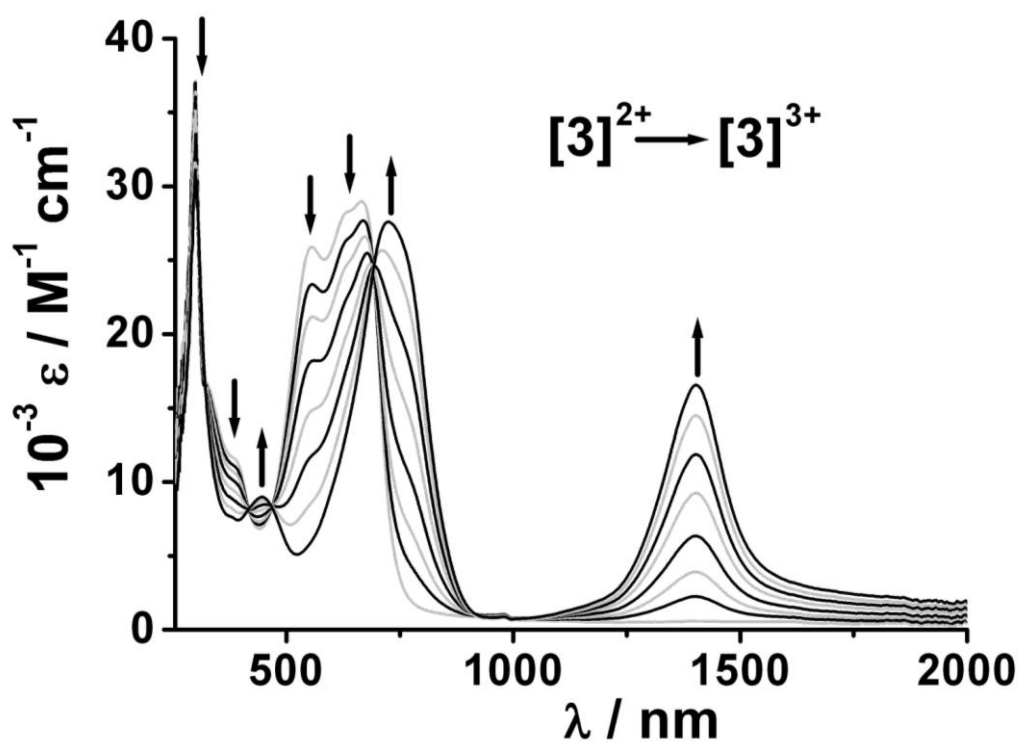


**Figure 3.6.7.** UV-Vis-NIR spectroelectrochemistry of the conversion  $[3]^{(2+) \rightarrow (3+)}$  in  $\text{CH}_3\text{CN}$  / 0.1 M  $\text{Bu}_4\text{NPF}_6$ .

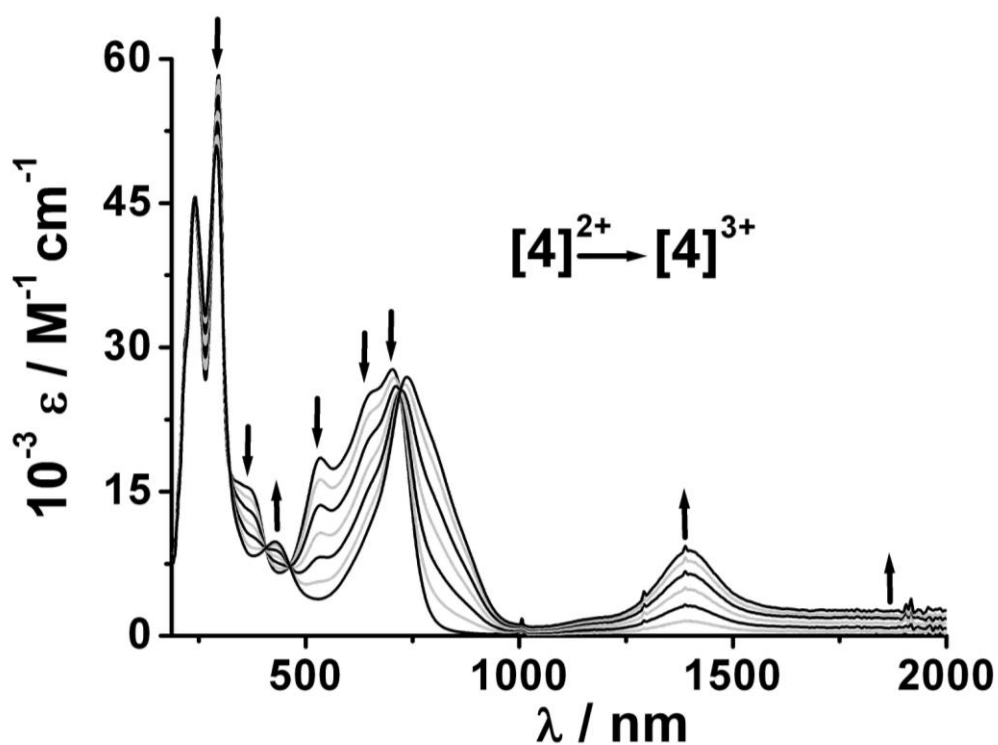


**Figure 3.6.8.** UV-Vis-NIR spectroelectrochemistry of the conversion  $[4]^{(2+) \rightarrow (3+)}$  in  $\text{CH}_3\text{CN}$  / 0.1 M  $\text{Bu}_4\text{NPF}_6$ .

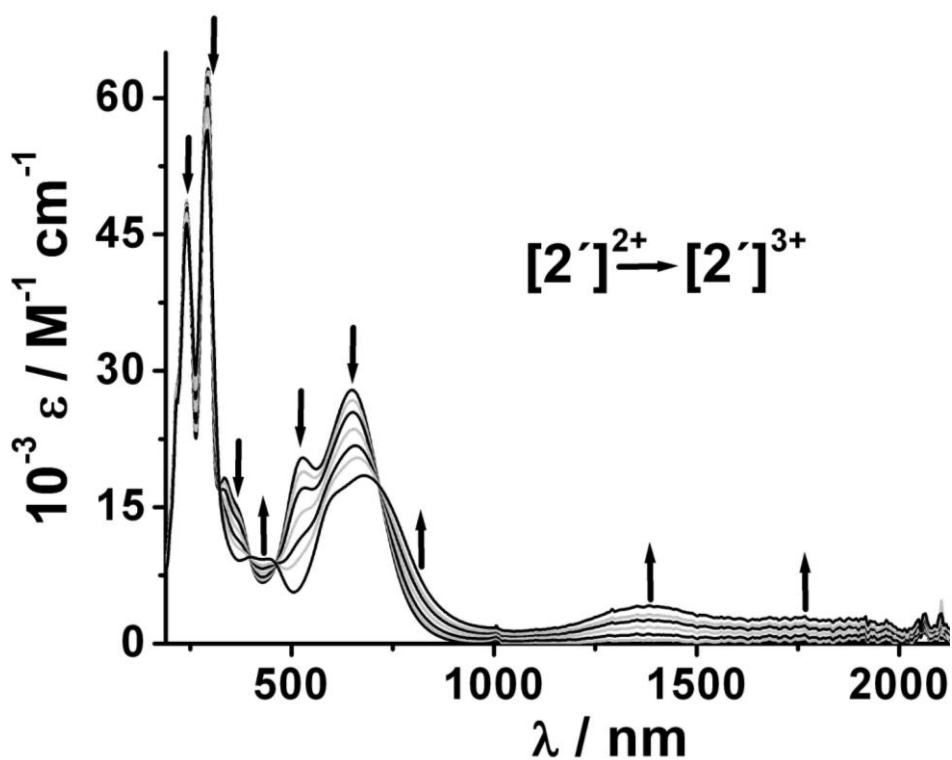


**Figure 3.6.9.** UV-Vis-NIR spectroelectrochemistry of the conversion  $[2']^{(2+) \rightarrow (3+)}$  in  $\text{CH}_3\text{CN}$  / 0.1 M  $\text{Bu}_4\text{NPF}_6$ .

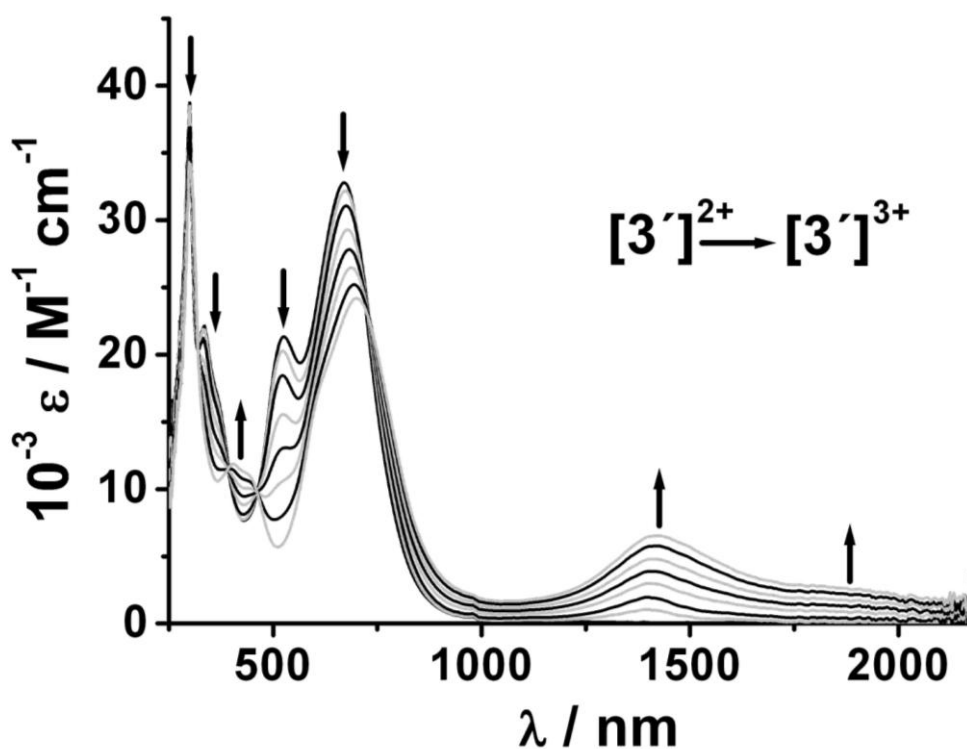


**Figure 3.6.10.** UV-Vis-NIR spectroelectrochemistry of the conversion  $[3']^{(2+) \rightarrow (3+)}$  in  $\text{CH}_3\text{CN}$  / 0.1 M  $\text{Bu}_4\text{NPF}_6$ .

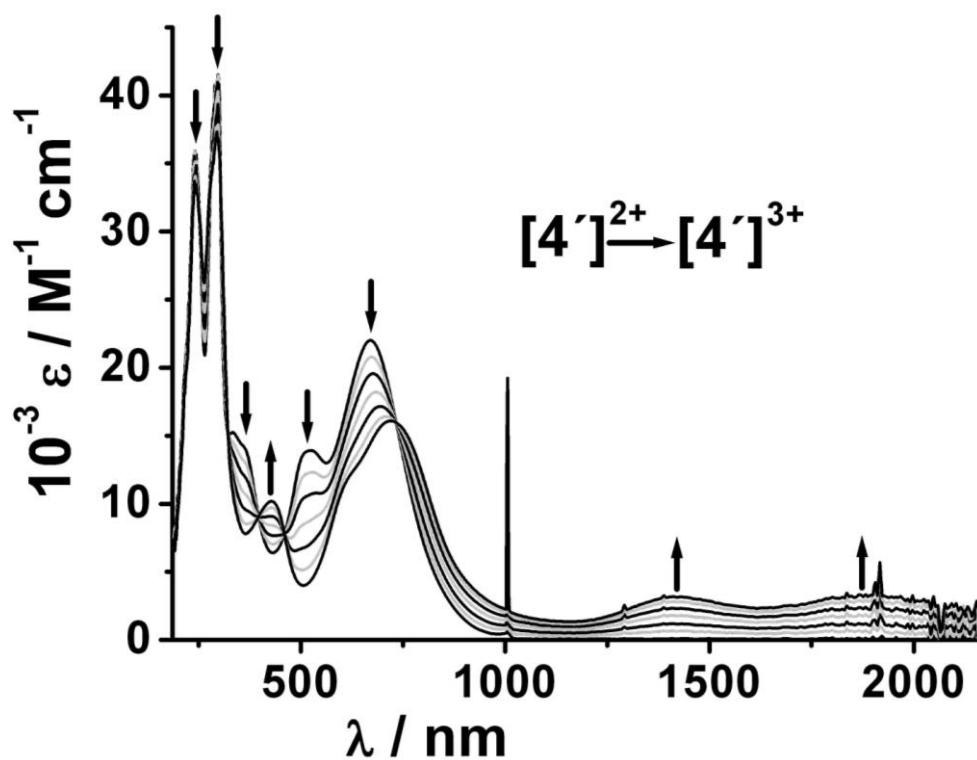


**Figure 3.6.11.** UV-Vis-NIR spectroelectrochemistry of the conversion  $[4']^{(2+) \rightarrow (3+)}$  in  $\text{CH}_3\text{CN}$  / 0.1 M  $\text{Bu}_4\text{NPF}_6$ .

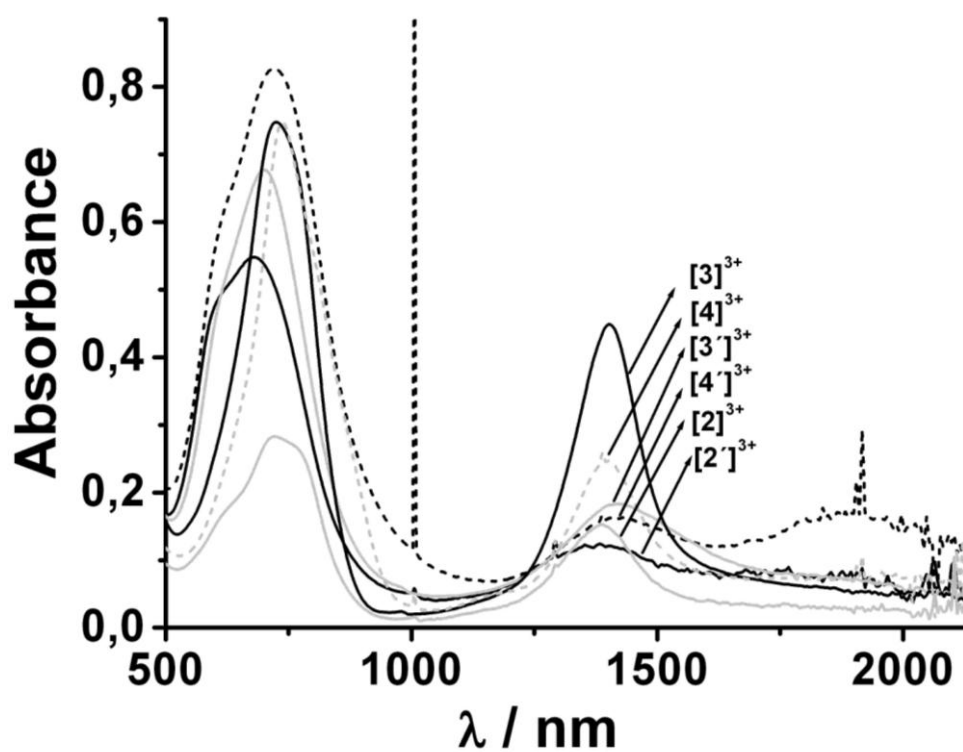


**Figure 3.6.12.** Change of NIR band on replacement of bridging ligands.

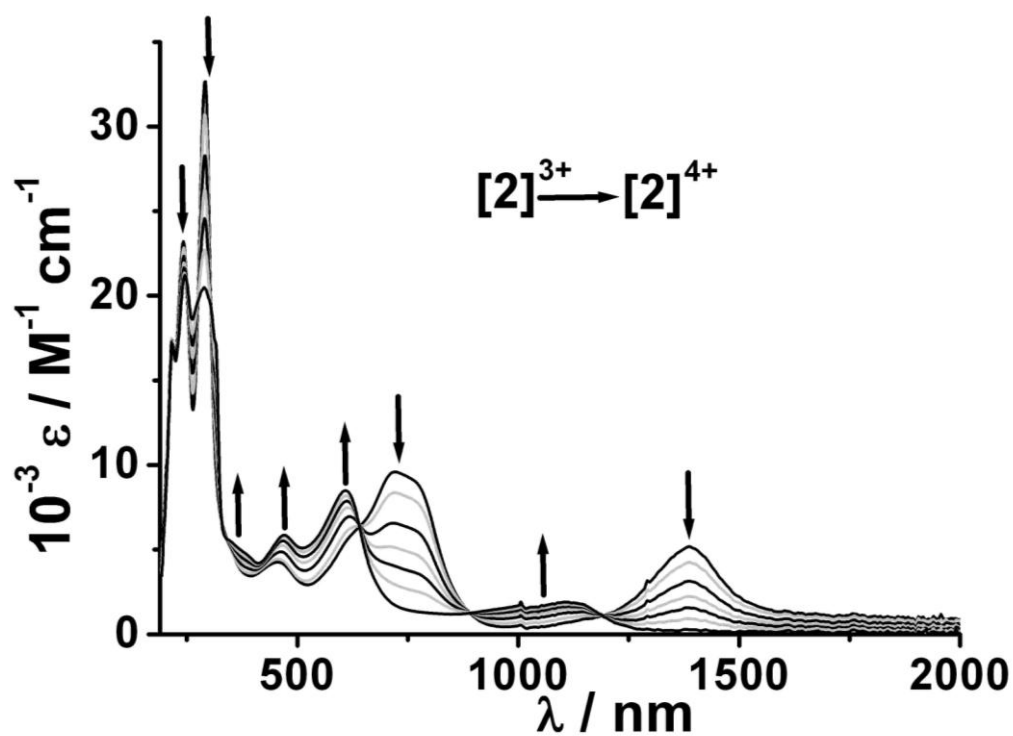


**Figure 3.6.13.** UV-Vis-NIR spectroelectrochemistry of the conversion  $[2]^{(3+) \rightarrow (4+)}$  in  $\text{CH}_3\text{CN}$  / 0.1 M  $\text{Bu}_4\text{NPF}_6$ .

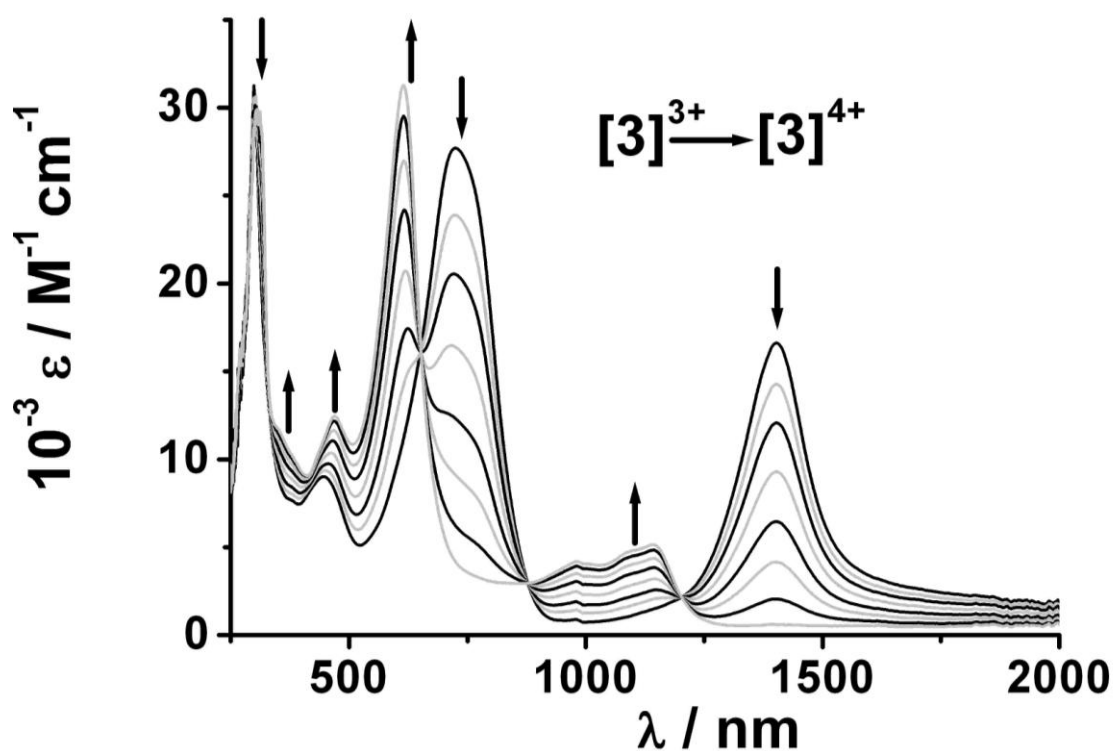


**Figure 3.6.14.** UV-Vis-NIR spectroelectrochemistry of the conversion  $[3]^{(3+) \rightarrow (4+)}$  in  $\text{CH}_3\text{CN}$  / 0.1 M  $\text{Bu}_4\text{NPF}_6$ .

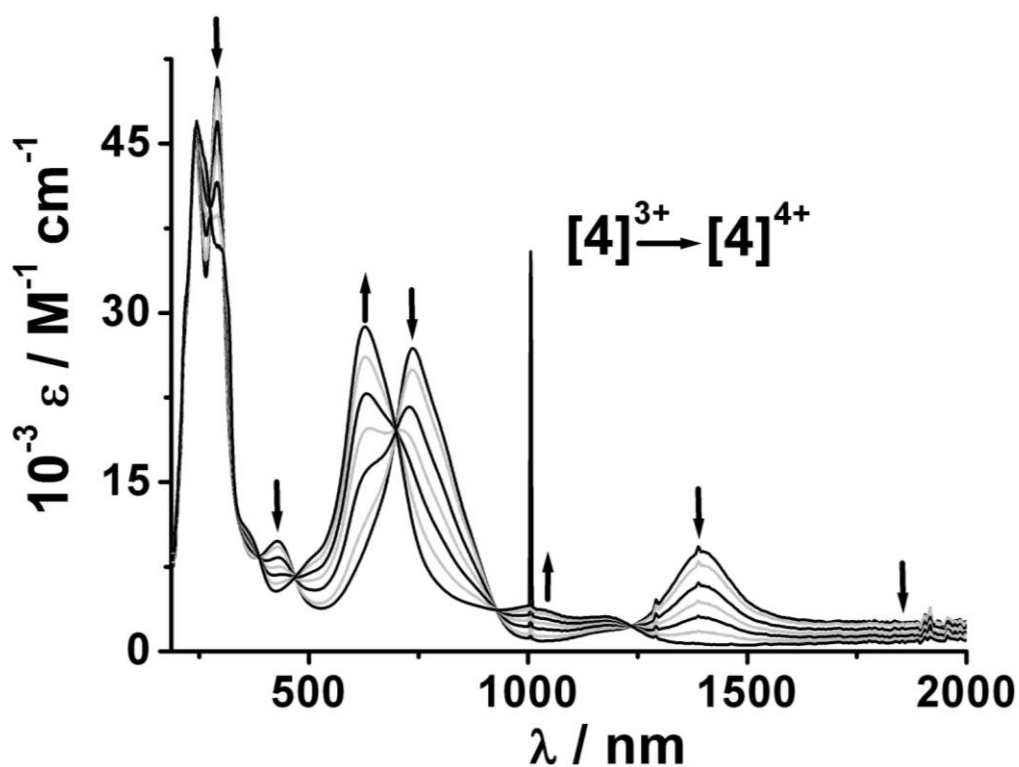


**Figure 3.6.15.** UV-Vis-NIR spectroelectrochemistry of the conversion  $[4]^{(3+) \rightarrow (4+)}$  in  $\text{CH}_3\text{CN}$  /  $0.1 \text{ M Bu}_4\text{NPF}_6$ .

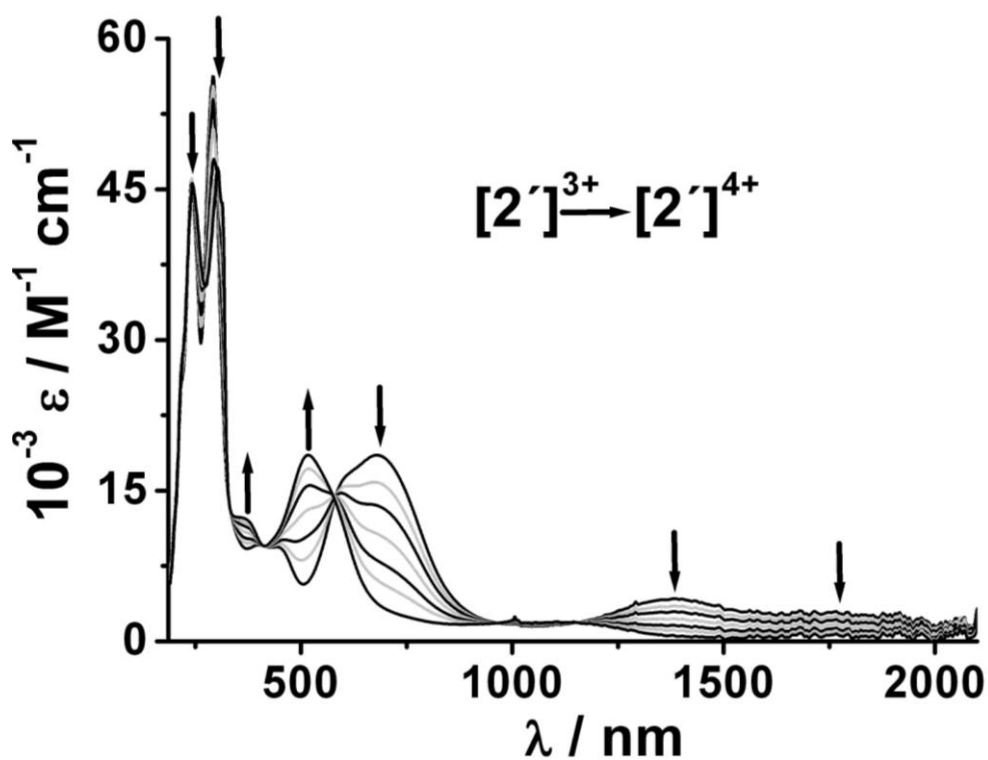


**Figure 3.6.16.** UV-Vis-NIR spectroelectrochemistry of the conversion  $[2']^{(3+) \rightarrow (4+)}$  in  $\text{CH}_3\text{CN}$  /  $0.1 \text{ M Bu}_4\text{NPF}_6$ .

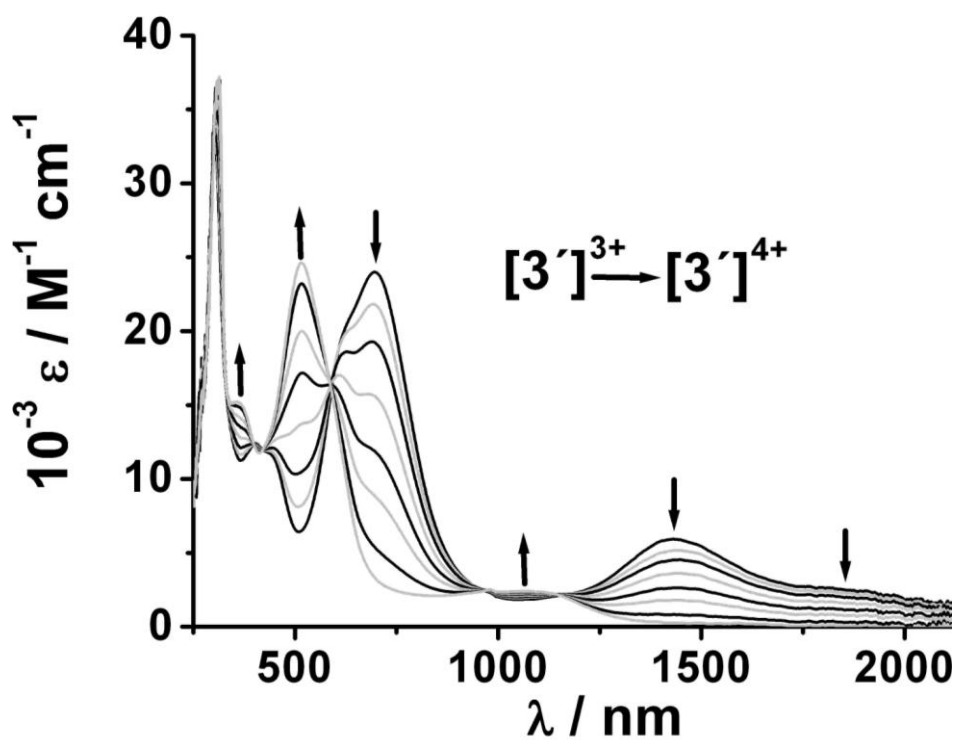


**Figure 3.6.17.** UV-Vis-NIR spectroelectrochemistry of the conversion  $[3']^{(3+) \rightarrow (4+)}$  in  $\text{CH}_3\text{CN}$  / 0.1 M  $\text{Bu}_4\text{NPF}_6$ .

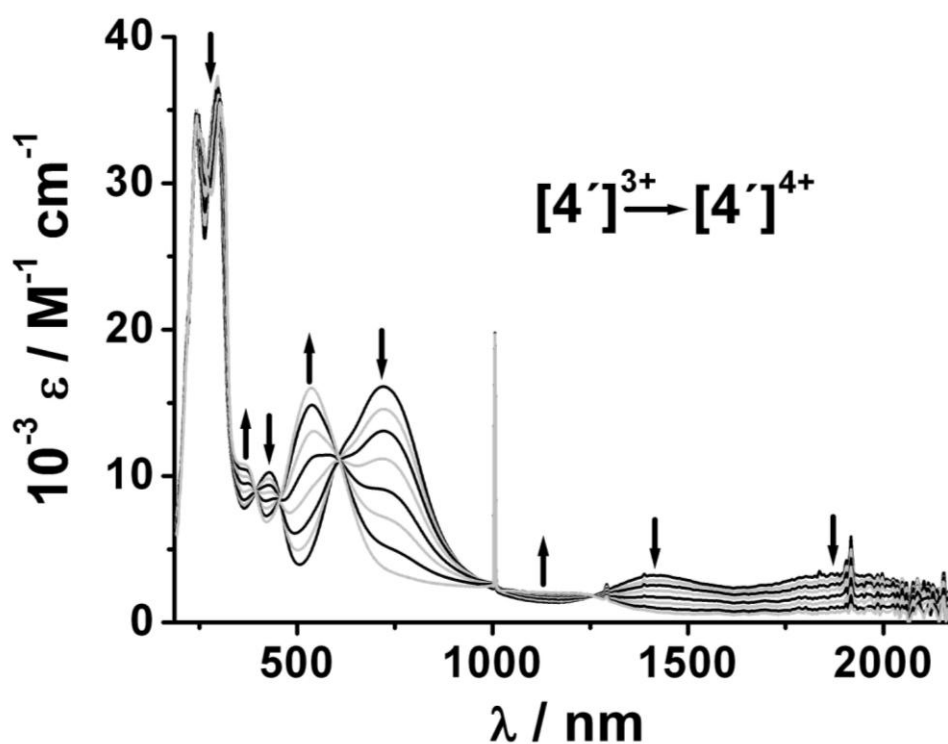


**Figure 3.6.18.** UV-Vis-NIR spectroelectrochemistry of the conversion  $[4']^{(3+) \rightarrow (4+)}$  in  $\text{CH}_3\text{CN}$  / 0.1 M  $\text{Bu}_4\text{NPF}_6$ .

On reduction of the dinuclear symmetric and asymmetric complexes to the  $2^+-4^+$ ,  $2^+$  and  $4^+$  forms two distinct bands appear in the NIR region for all six complexes (Figures 3.6.18-3.6.19, Table 3.6.1 and 3.6.2). These bands are reminiscent of the NIR bands observed for the one electron reduced form of the mononuclear complex  $1^{\cdot}$  and  $1^{\cdot-}$ . Similar to the mononuclear complex, these NIR bands are also assigned to a LLCT transition from SOMO ( $L_{-2H}$ ) to LUMO (bpy). The presence of multiple target orbitals makes the appearance of multiple LLCT transitions possible.

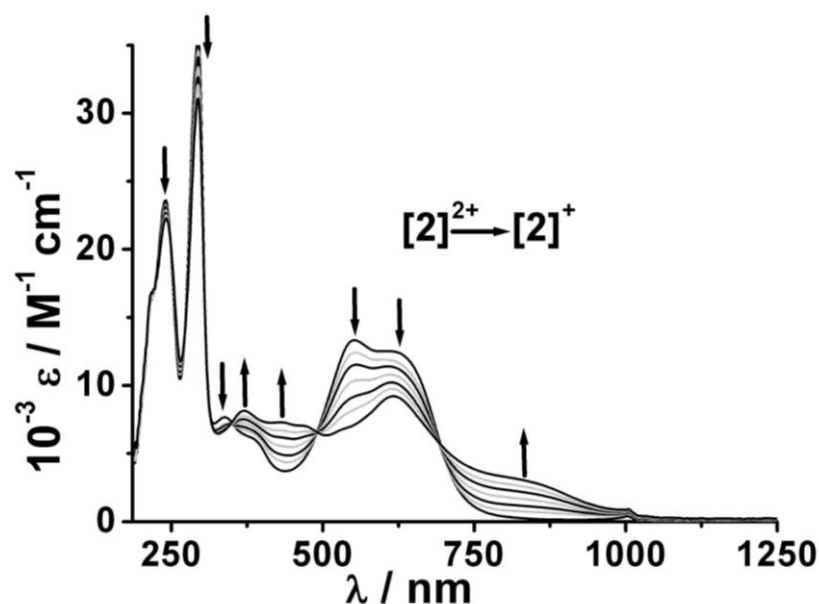


**Figure 3.6.18.** UV-Vis-NIR spectroelectrochemistry of the conversion  $[2]^{(2+) \rightarrow (+)}$  in  $\text{CH}_3\text{CN}$  /  $0.1 \text{ M Bu}_4\text{NPF}_6$ .

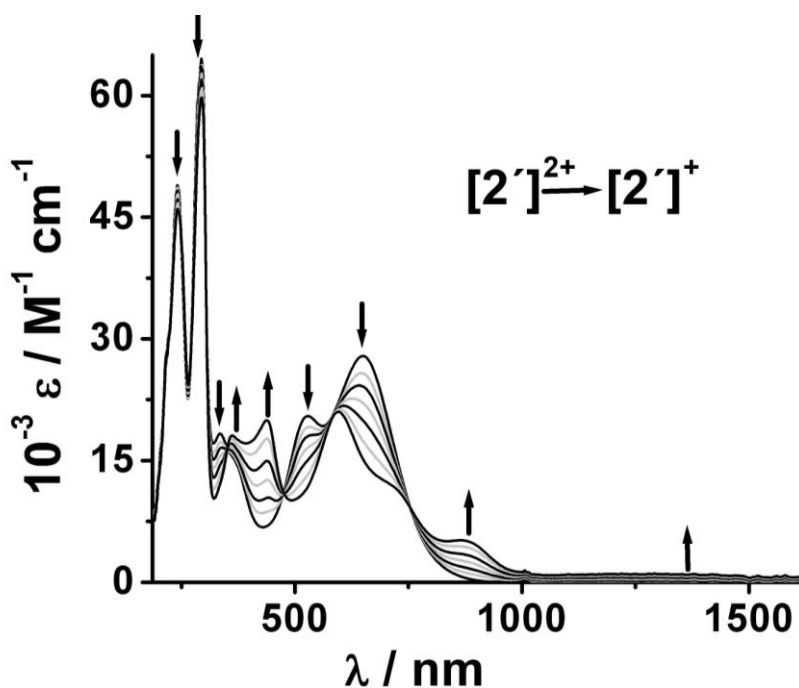


**Figure 3.6.19.** UV-Vis-NIR spectroelectrochemistry of the conversion  $[2']^{(2+) \rightarrow (+)}$  in  $\text{CH}_3\text{CN}$  /  $0.1 \text{ M Bu}_4\text{NPF}_6$ .

**Table 3.6.1.** Spectroelectrochemical data of the symmetric complexes.<sup>[a]</sup>

| Compound              | $\lambda_{\max}$ [nm] ( $10^{-3} \epsilon$ [ $M^{-1} \text{ cm}^{-1}$ ])                     |
|-----------------------|--|
| <b>1<sup>+</sup></b>  | 560 (sh), 528 (25.2), 337 (22.4), 301 (23.8)   |
| <b>1<sup>0</sup></b>  | 1520 (0.9), 845 (3.0), 578 (15.4), 439 (18.5), 363 (19.1), 300 (21.5),                       |
| <b>1<sup>-</sup></b>  | 1530 (1.6), 814 (5.7), 629 (10.9), 522 (13.0), 460 (18.7), 426 (sh), 352 (28.1), 303 (21.8)  |
| <b>2<sup>4+</sup></b> | 1112 (2.0), 610 (8.5), 468 (5.9), 355 (sh), 288 (20.3), 245 (21.1)                           |
| <b>2<sup>3+</sup></b> | 1386 (5.3), 770 (sh), 721 (9.7), 627 (sh), 456 (4.4), 291 (32.5), 242 (23.0)                 |
| <b>2<sup>2+</sup></b> | 615 (12.6), 552 (13.4), 386 (6.2), 341 (7.8), 294 (36.3), 240 (23.8)                         |
| <b>2<sup>+</sup></b>  | 818 (32.7), 666 (9.2), 536 (sh), 466 (7.1), 430 (7.4), 370 (8.2), 294 (31.09), 241 (22.3)    |
| <b>3<sup>4+</sup></b> | 1145 (5.2), 1095 (sh), 982 (4.3), 616 (31.3), 470 (12.5), 366 (sh), 308 (29.6)               |
| <b>3<sup>3+</sup></b> | 1402 (16.7), 724 (27.7), 446 (9.0), 299 (31.1)   |
| <b>3<sup>2+</sup></b> | 666 (29.0), 633 (28.3), 553 (26.0), 390 (11.6), 327 (sh), 299 (37.1)                         |
| <b>3<sup>+</sup></b>  | 1855 (1.9), 840 (10.2), 618 (18.4), 442 (17.4), 366 (16.4), 300 (31.0)                       |
| <b>4<sup>4+</sup></b> | 1870 (0.7), 1176 (3.1), 1006 (4.1), 626 (28.9), 362 (sh), 296 (35.9), 242 (47.1)             |
| <b>4<sup>3+</sup></b> | 1870 (2.8), 1390 (9.1), 1176 (1.9), 737 (27.0), 431 (9.9), 290 (51.0), 240 (45.7)            |
| <b>4<sup>2+</sup></b> | 702 (27.8), 654 (25.5), 534 (18.5), 360 (sh), 294 (58.5), 240 (45.6)                         |
| <b>4<sup>+</sup></b>  | 1796 (1.7), 860 (10.7), 596 (14.6), 456 (sh), 418 (16.3), 371 (17.8), 295 (49.2), 238 (43.5) |

<sup>[a]</sup> From spectroelectrochemistry in CH<sub>3</sub>CN / 0.1 M Bu<sub>4</sub>NPF<sub>6</sub> at 298 K.



**Table 3.6.2.** Spectroelectrochemical data of the asymmetric complexes.<sup>[a]</sup>

| Complex           | $\lambda_{\max}$ [nm] ( $10^3 \epsilon$ [ $M^{-1} \text{cm}^{-1}$ ])                          |
|-------------------|---|
| [1] <sup>+</sup>  | 218 (36.5), 241 (34.2), 294 (60.6), 332 (28.6), 362 (sh), 511 (19.8), 570 (17.5)              |
| [1] <sup>2+</sup> | 214 (37.6), 244 (33.6), 300 (37.4), 312 (34.2), 369 (14.6), 430 (14.6), 481 (8.9), 1007 (0.9) |
| [1] <sup>0</sup>  | 217 (sh), 235 (39.8), 295 (52.1), 353 (28.5), 405 (15.8), 426 (sh), 580 (18.4), 1060 (0.7)    |
| [2] <sup>+</sup>  | 242 (45.8), 294 (59.8), 362 (18.3), 438 (20.1), 596 (21.0), 713 (12.1), 868 (5.3), 1290 (1.2) |
| [2] <sup>2+</sup> | 241 (48.6), 294 (63.4), 335 (18.3), 368 (sh), 528 (20.6), 650 (28.1)                          |
| [2] <sup>3+</sup> | 241 (46.1), 291 (56.3), 402 (9.6), 441 (9.5), 604 (sh), 677 (18.7), 1380 (4.3), 1759 (2.9)    |
| [2] <sup>4+</sup> | 243 (45.4), 304 (47.0), 365 (12.3), 516 (18.7), 1068 (2.1)                                    |
| [3] <sup>+</sup>  | 298 (36.6), 357 (22.5), 442 (19.7), 591 (23.6), 682 (16.0), 748 (13.4), 891 (5.7), 1232 (1.3) |
| [3] <sup>2+</sup> | 299 (38.8), 337 (22.2), 527 (21.4), 672 (32.8)  |
| [3] <sup>3+</sup> | 301 (33.9), 405 (11.9), 435 (sh), 700 (24.), 1420 (6.6), 1840 (sh)                            |
| [3] <sup>4+</sup> | 313 (37.3), 357 (15.3), 517 (24.8), 1056 (2.5)  |
| [4] <sup>+</sup>  | 238 (33.1), 298 (36.7), 368 (16.8), 433 (14.7), 585 (16.0), 705 (10.8), 916 (5.2), 1368 (1.4) |
| [4] <sup>2+</sup> | 241 (35.8), 297 (41.4), 336 (15.4), 362 (14.4), 514 (13.9), 672 (22.1)                        |
| [4] <sup>3+</sup> | 238 (33.5), 294 (37.1), 428 (10.1), 624 (sh), 1418 (3.2), 1910 (3.2)                          |
| [4] <sup>4+</sup> | 243 (34.5), 303 (35.3), 369 (10.8), 536 (16.0), 1137 (2.1)                                    |

<sup>[a]</sup> From spectroelectrochemistry in CH<sub>3</sub>CN / 0.1 M Bu<sub>4</sub>NPF<sub>6</sub> at 298 K.

**Table 3.6.3.** Analysis of the NIR bands of the complexes.

| Complex           | $\lambda$ [nm] | $\Delta\nu_{1/2(\text{expt})}$ <sup>[a]</sup> | $\Delta\nu_{1/2(\text{calcd})}$ <sup>[b]</sup> | $\Gamma$ <sup>[c]</sup> |
|-------------------|----------------|---|--|-------------------------|
| [2] <sup>3+</sup> | 1386           | 1060  | 4082   | 0.74                    |
| [3] <sup>3+</sup> | 1402           | 874   | 4059   | 0.78                    |
| [4] <sup>3+</sup> | 1390           | 1004  | 4077   | 0.75                    |
| [2] <sup>3+</sup> | 1380           | 1802  | 4091   | 0.56                    |
| [3] <sup>3+</sup> | 1420           | 1600  | 4033   | 0.60                    |
| [4] <sup>3+</sup> | 1418           | 2000  | 4036   | 0.50                    |

<sup>[a]</sup> From OTTLE spectroelectrochemistry in CH<sub>3</sub>CN / 0.1 M Bu<sub>4</sub>NPF<sub>6</sub>.

<sup>[b]</sup>  $\Delta\nu_{1/2(\text{calcd})} = \sqrt{(2310\nu_{\max})}$ . <sup>[c]</sup>  $\Gamma = 1 - \Delta\nu_{1/2(\text{expt})} / \Delta\nu_{1/2(\text{calcd})}$ .

### 3.7. Conclusion

We have reported here on a straightforward one-pot and green synthesis of symmetrically ( $L^2$ ) and rare asymmetrically ( $L^3$ ) substituted biologically relevant *p*-quinone ligands. We have also reported one-pot, synthetic route to  $L'$  and its transaminated analogues symmetric ( $L^2$ ) *p*-quinone ligands. In addition we also detected asymmetrically substituted *p*-quinone compounds ( $L^4$ ) as key intermediates in the transamination reaction step. Using the isoelectronic analogy of [O] and [NR] we have also reported here on a rare example of mononuclear ruthenium complexes using these symmetrically ( $L^2$ ) and asymmetrically ( $L^3$ ) substituted *p*-quinone ligands and various dinuclear complexes. The substituted symmetrically ( $L^2$ ) *p*-quinone ligands bind to the metal centers through a phenolate O- and an imine type neutral nitrogen donor. The consequence of this is the appearance of strong hydrogen bonding in the solid state for the mononuclear complex. The ruthenium complexes with symmetric ( $L^2$ ) and asymmetric ( $L^3$ ) show various redox processes. The redox potentials can be varied by varying the substituents on the bridge. For the dinuclear complexes the one-electron oxidized forms show absorptions in the NIR region that can be tuned by substituting [O] for [NR] in the bridging ligands. Such absorptions are absent from the homovalent forms of these complexes. EPR spectroscopy supports the mixed-valent assignment through the large anisotropic signals. The one-electron reduced forms on the other hand show narrow well resolved EPR signals as is expected for metal bound organic radicals. The one-electron reduced forms of the mono and dinuclear complexes show absorptions in the NIR region that are LLCT in nature. Thus the complexes presented here show switchable NIR absorptions. The NIR bands can be switched on and off by a simple electron transfer. The position, shape and intensity of the NIR bands can be varied by changing the substituents on the nitrogen atoms of the bridge or by choosing the redox potentials (oxidation or reduction). The complexes presented here are intriguing examples of metal complexes that show NIR bands in both their one electron oxidized and their one electron reduced forms.

## CHAPTER 4

# Syntheses, Electron Transfer and Metal-Metal Coupling in Rare Dinuclear Paramagnetic Symmetric and Asymmetric Ruthenium Mixed Valence Complexes

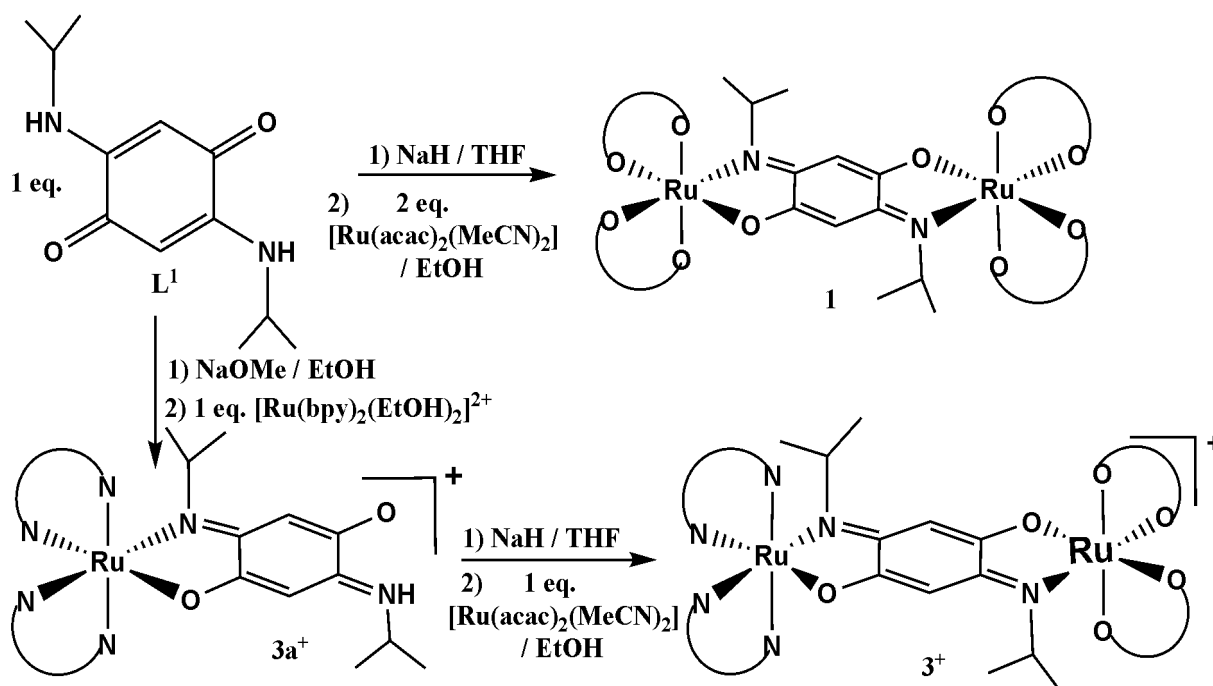
### 4.1. Introduction

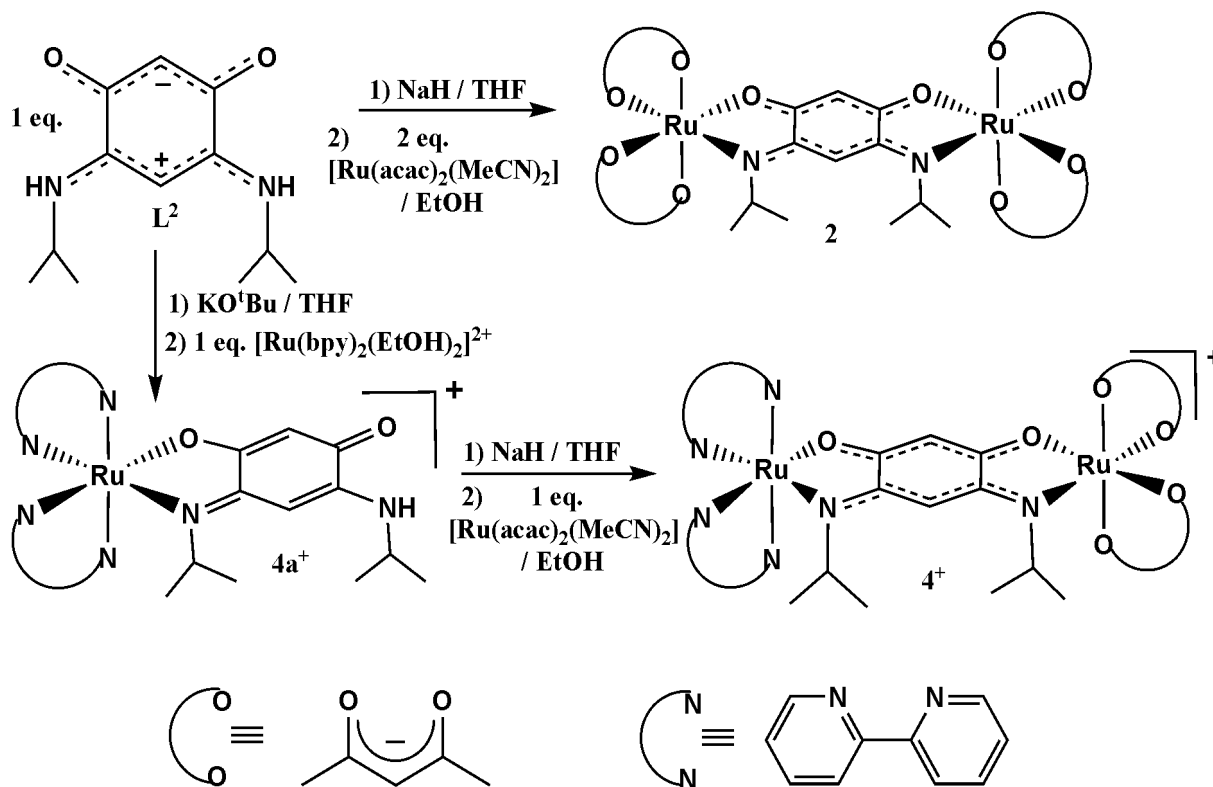
Ligand-bridge mixed-valent complexes of ruthenium are of considerable current research interest to develop a detailed understanding of the localized-to-delocalized (class II to class III in the Robin–Day classification scheme) transition.<sup>[123-127]</sup> This is primarily due to their potential applications in artificial photosynthesis,<sup>[128-130]</sup> molecular electronic devices<sup>[131-132]</sup> and as photoactive DNA cleavage agents for therapeutic purposes.<sup>[133-135]</sup> Quinonoid bridge ruthenium polypyridine mixed-valence complexes have been extensively discussed in the previous two chapters and exhibit strong metal-metal electronic coupling in their mixed-valence states through the effective overlap of ruthenium  $d\pi$  orbitals with suitably placed ligand  $\pi$  or  $\pi^*$  orbitals in the quinonoid bridge. It has also observed that the metal-metal electronic coupling can be tuned substantially by varying the electronic nature of the bridging quinonoid ligands or by altering ancillary ligands which affects the electronic environment around the ruthenium centers.<sup>[136-140]</sup>

In this regard symmetric and asymmetric dinuclear ruthenium complexes of 2,2'-bipyridyl and acetylacetonato ancillary ligands have been investigated where ruthenium metal centers are bridged by doubly negatively charged quinonoid ligand. Systems that contain two different ruthenium centres as redox active metals remain rare in the literature. This chapter describes the syntheses, characterization and spectroscopic studies of two dinuclear symmetric ruthenium complexes [ $\{(\text{acac})_2\text{Ru}^{\text{III}}\}_2(\mu\text{-L}^1\text{-}_{2\text{H}})$ ] (**1**) and [ $\{(\text{acac})_2\text{Ru}^{\text{III}}\}_2(\mu\text{-L}^2\text{-}_{2\text{H}})$ ] (**2**) and two dinuclear asymmetric ruthenium complexes [ $(\text{bpy})_2\text{Ru}^{\text{II}}(\mu\text{-L}_{-2\text{H}}^1)\text{Ru}^{\text{III}}(\text{acac})_2(\text{ClO}_4)$ ] (**3**[ClO<sub>4</sub>]) and [ $(\text{bpy})_2\text{Ru}^{\text{II}}(\mu\text{-L}^2\text{-}_{2\text{H}})\text{Ru}^{\text{III}}(\text{acac})_2(\text{ClO}_4)$ ] (**4**[ClO<sub>4</sub>]) (where bpy = 2,2'-bipyridine, acac<sup>-</sup> = acetylacetonato, L<sup>1</sup> = 2,5-bis(isopropylamino)-1,4-benzoquinone L<sup>2</sup> = N,N'-diisopropyl-2-amino-5-alcoholate-1,4-benzoquinonemonoiminium (Scheme 4.2.1).

## 4.2. Synthesis and characterization

The symmetric dinuclear complexes  $[\{(acac)_2Ru^{III}\}_2(\mu-L^1_{-2H})]$  (**1**) and  $[\{(acac)_2Ru^{III}\}_2(\mu-L^2_{-2H})]$  (**2**) were synthesized by the reaction of 2 eq. of  $[(acac)_2Ru(CH_3CN)_2]$  with 1 eq. of quinonoid ligand in presence of NaH as a base in EtOH under refluxing conditions (see Scheme 4.2.1). On the other hand, the asymmetric dinuclear ruthenium complexes  $[(bpy)_2Ru^{II}(\mu-L^1_{-2H})Ru^{III}(acac)_2](ClO_4)$  (**3** $[ClO_4]$ ) and  $[(bpy)_2Ru^{II}(\mu-L^2_{-2H})Ru^{III}(acac)_2](ClO_4)$  (**4** $[ClO_4]$ ) were synthesized from the corresponding mononuclear complexes  $[(bpy)_2Ru^{II}L^1_{-H}](ClO_4)$  (**3a** $[ClO_4]$ ) and  $[(bpy)_2Ru^{II}L^2_{-H}](ClO_4)$  (**4a** $[ClO_4]$ ), respectively (Scheme 4.2.1). The syntheses of **3a** $[ClO_4]$  and **4a** $[ClO_4]$  were reported in Chapters 3 and 2 respectively. The asymmetric dinuclear complexes can also be synthesized from the corresponding mononuclear ruthenium complexes  $[(acac)_2Ru^{III}L^1_{-H}]$  and  $[(acac)_2Ru^{III}L^2_{-H}]$ ; however, the difficulty arises in the removal of N-H proton as the acidity of N-H proton in the acetylacetonato complexes is much lower compared to that in the corresponding mononuclear bipyridine complexes **3a** $[ClO_4]$  and **4a** $[ClO_4]$ . The +2 oxidation state of ruthenium ion in the precursor complex  $[Ru^{II}(bpy)_2(EtOH)_2]^{2+}$  is retained in **3a** $[ClO_4]$  and **4a** $[ClO_4]$ . On the other hand, the +2 oxidation state of ruthenium ion in the precursor complex  $[Ru^{II}(acac)_2(CH_3CN)_2]$  is changed from +2 to +3 state upon binding to quinonoid ligand in **1**, **2**, **3a** $[ClO_4]$  and **4a** $[ClO_4]$ . The presence of electron-rich  $acac^-$  ancillary ligands as opposed to the  $\pi$ -acidic  $bpy$  facilitates the stabilization of  $Ru^{III}$  state as compared to  $Ru^{II}$  state.





**Scheme 4.2.1.** Syntheses of symmetric and asymmetric dinuclear ruthenium complexes

The different electronic nature of the bipyridine and  $acac^-$  ancillary ligands leads to a mixed-valent  $Ru^{II}-Ru^{III}$  situation in asymmetric complexes **3<sup>+</sup>** and **4<sup>+</sup>** and iso-valent  $Ru^{III}-Ru^{III}$  in symmetric complexes **1** and **2**. The complexes were purified by column chromatography on an alumina column and characterized by elemental analysis and electrospray mass spectrometry (see experimental section). Each of the complexes can exist in two diastereoisomeric forms; however, the diastereoisomers were separable only in the case of **2** (**2a** {less polar} and **2b** {more polar}).

### 4.3. X-ray crystal structure of **1**

The single crystal of **1** was obtained by the slow evaporation of its dichloromethane solution at room temperature. It is crystallized in the  $P2_1/c$  space group with monoclinic crystal system. The X-ray diffraction parameters and crystallographic data of **1** are reported in Chapter 10. The crystal structure of **1** is shown in Figures 4.3.1-4.3.2. The selected bond lengths of **1** and the reported free ligand  $L^{[14]}$  are given in Table 4.3.1.

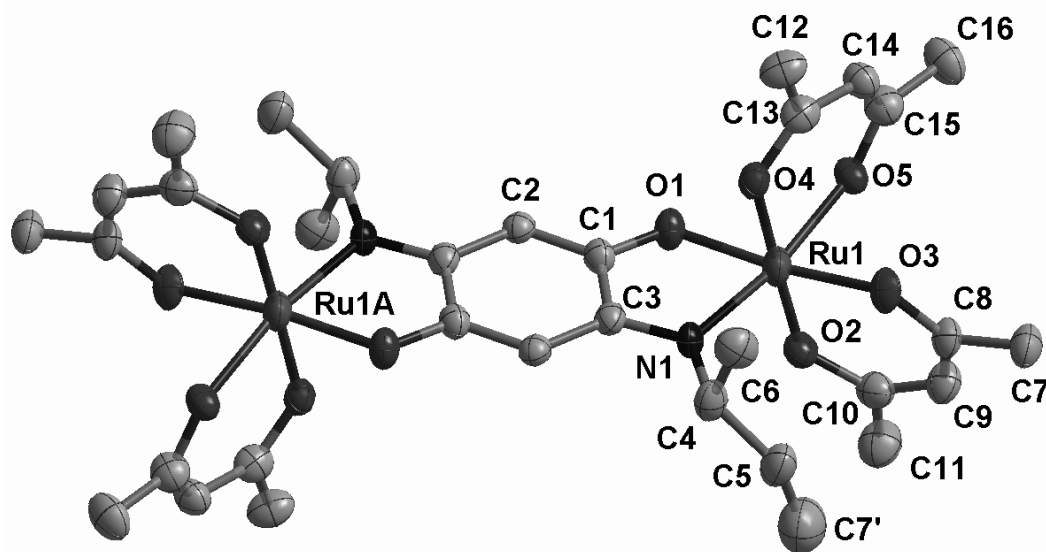


**Figure 4.3.1:** Molecular structure of **1** in the crystal. (Occupancy of each set of ligands assigned to 50 %).

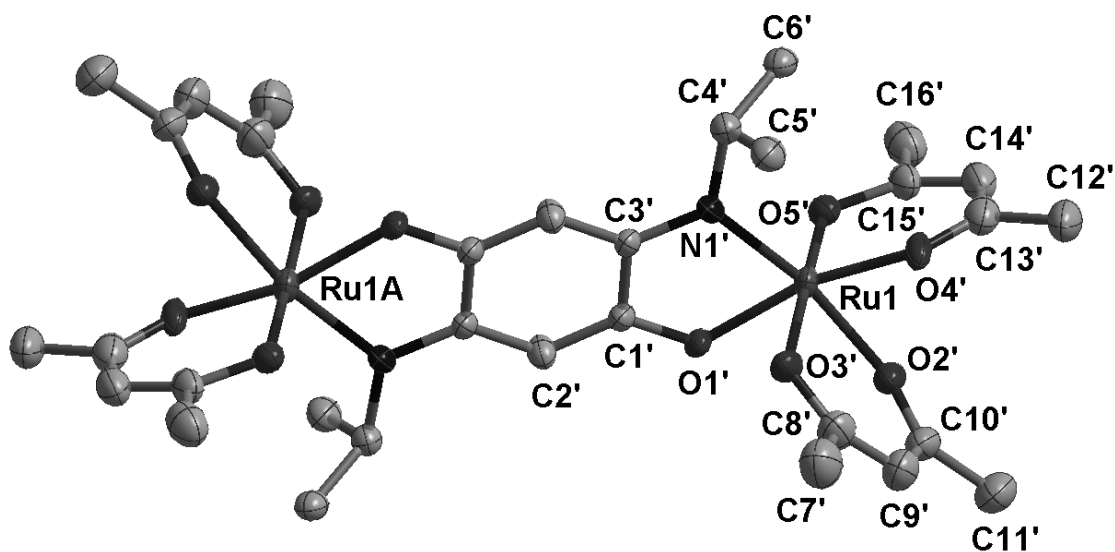


**Figure 4.3.2:** Molecular structure of **1'** in the crystal. (Occupancy of each set of ligands assigned to 50 %).

**Table 4.3.1:** Selected bond lengths [Å] for **L**<sup>1</sup> and **1**.

|        | <b>L</b> <sup>1</sup> [141] | <b>1</b>  | <b>1'</b> |
|--------|-----------------------------|-----------|-----------|
| C1-O1  | 1.246(2)                    | 1.315(19) | 1.34(2)   |
| C3-N1  | 1.333(2)                    | 1.308(14) | 1.348(14) |
| C1-C2  | 1.411(2)                    | 1.38(2)   | 1.35(2)   |
| C2-C3  | 1.379(2)                    | 1.415(15) | 1.389(16) |
| C1-C3  | 1.519(2)                    | 1.48(3)   | 1.46(2)   |
| Ru1-O1 |                             | 1.952(8)  | 2.071(9)  |
| Ru1-N1 |                             | 2.066(8)  | 1.953(9)  |
| Ru1-O2 |                             | 1.898(7)  | 2.123(9)  |
| Ru1-O3 |                             | 2.10(2)   | 2.041(10) |
| Ru1-O4 |                             | 2.098(7)  | 1.93(2)   |
| Ru1-O5 |                             | 2.039(8)  | 1.992(9)  |
| Ru-Ru  |                             | 7.840(1)  | 7.840(1)  |

The crystal structure of **1** shows a dimeric form with two Ru<sup>III</sup> centers bridged by a doubly deprotonated bis-bidentate **L**<sup>1</sup><sub>·2H</sub> ligand. The remaining coordination sites at ruthenium center are occupied by donors from *acac*<sup>-</sup> ligands. There is a crystallographically imposed inversion center located in the middle of the **L**<sup>1</sup><sub>·2H</sub> ring; therefore, the dimer **1** exists in a *meso*-form with two octahedral Ru<sup>III</sup> centers displaying opposite chirality. In the crystal lattice, complex **1** exhibits a perfectly statistic disorder with all *acac*<sup>-</sup> and **L**<sup>1</sup><sub>·2H</sub> ligands occupying two sets of positions around the same Ru center.

A look at the bond distances within **1** (Figure 4.3.2) shows that there is an extensive delocalization within the O1-C1-C2-C3'-N1' and N1-C3-C2'-C1'-O1' parts of the molecule and these are connected by authentic C-C single bonds with C1-C3 distances of 1.519(2) Å (Table 4.3.1). These molecules can thus be considered as two merocyanine units connected by C-C single bonds as has been observed before.<sup>[142]</sup> The bond lengths of bridging ligand **L**<sup>1</sup><sub>·2H</sub> in **1** shows higher localization of the double bonds as compared to the free ligand **L**<sup>1</sup> (Table 4.3.1), possibly as a result of the aforementioned delocalization of Ru(III) electrons.<sup>[143]</sup> The C1-C3 bond at 1.48(3) (1.46(2)) Å remains an authentic single bond as in the case of the free ligand **L**<sup>1</sup>. Such localization of bonds within a substituted *p*-quinone ligand has been observed

previously with the doubly deprotonated form of unsubstituted *p*-quinone ligand.<sup>[144]</sup> The bridging ligand thus binds to the Ru centers through O<sup>-</sup> and imino nitrogen donors. The Ru-Ru distance in **1** is 7.840(1) Å.

#### 4.4. Electrochemistry

The electrochemistry of the complexes **1**, **2a**, **2b**, **3<sup>+</sup>** and **4<sup>+</sup>** have been studied by cyclic voltammetry in order to investigate their redox properties (Figure 4.4.1). Ferrocene was used as an internal standard and all the redox potentials are referenced with respect to ferrocenium/ferrocene (Fc<sup>+</sup>/Fc) couple. The redox potentials for all the complexes are summarized in Table 4.4.1.

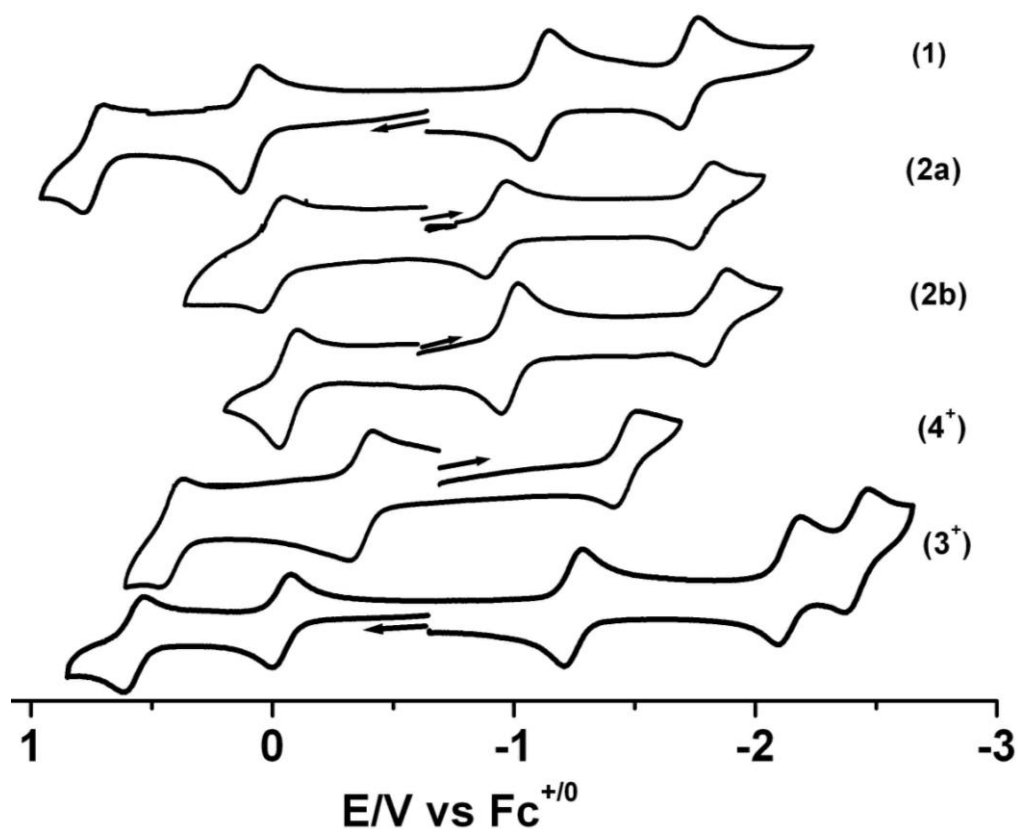


**Figure 4.4.1.** Cyclic voltammograms of complexes **1**, **2a**, **2b**, **3<sup>+</sup>** and **4<sup>+</sup>** in CH<sub>3</sub>CN/0.1 M Bu<sub>4</sub>NPF<sub>6</sub> at 295 K



**Table 4.4.1:** Redox potentials of the complexes.<sup>[a]</sup>

| Complex          | $E_{1/2}^{ox2}$<br>( $\Delta E_p$ ) <sup>[b]</sup> | $E_{1/2}^{ox1}$<br>( $\Delta E_p$ ) <sup>[b]</sup> | $E_{1/2}^{red1}$<br>( $\Delta E_p$ ) <sup>[b]</sup> | $E_{1/2}^{red2}$<br>( $\Delta E_p$ ) <sup>[b]</sup> | $E_{1/2}^{red3}$<br>( $\Delta E_p$ ) <sup>[b]</sup> |
|------------------|--|--|---|---|---|
| [1]              | +0.76<br>(79)                                      | +0.11<br>(70)                                      | -1.10<br>(70)                                       | -1.72<br>(74)                                       |   |
| [2a]             |  | -0.01<br>(101)                                     | -0.94<br>(110)                                      | -1.79<br>(89)                                       |   |
| [2b]             |  | -0.07<br>(79)                                      | -0.99<br>(71)                                       | -1.84<br>(97)                                       |   |
| [3] <sup>+</sup> | +0.57<br>(84)                                      | -0.04<br>(73)                                      | -1.25<br>(79)                                       | -2.14<br>(91)                                       | -2.42<br>(90)                                       |
| [4] <sup>+</sup> | +0.42<br>(94)                                      | -0.36<br>(89)                                      | -1.45<br>(97)                                       |   |   |

<sup>[a]</sup> Electrochemical potentials in V from cyclic voltammetry in CH<sub>3</sub>CN / 0.1 M Bu<sub>4</sub>NPF<sub>6</sub> at 298 K. Scan Rate: 100 mV/s. Ferrocene / Ferrocenium was used as internal standard.

<sup>[b]</sup>  $\Delta E_p$ : difference between peak potentials in mV.

Cyclic voltammetry of complex **1** in CH<sub>3</sub>CN with 0.1 M Bu<sub>4</sub>NPF<sub>6</sub> reveals two oxidation and two reduction processes (Figure 4.4.1) that are all completely reversible. The difference between the two oxidation potentials of 650 mV translates to a comproportionation constant  $K_c$  ( $K_c=10^{\Delta E/59}$  at 298 K)<sup>[145]</sup> of the order of  $10^{11}$  for the one-electron oxidized species. The corresponding difference in the reduction potentials is 630 mV (Table 4.4.1) and the  $K_c$  value is of the order of  $10^{10}$ . The two diastereomers of symmetric complex **2** show only one one-electron reversible oxidation and two one-electron reversible reductions in identical condition (Figure 4.4.1) and the potential values for **2a** are marginally shifted to the higher potential compared to **2b**. The redox property of complex **2** is comparatively same as **1** except second oxidation (reversible for **1** and irreversible for **2**). The difference between the reduction potentials in **2** is 860 mV and the corresponding  $K_c$  value is of the order of  $10^{14}$  which is higher compared to **1** ( $K_c=10^{10}$ ). This is most probably due to higher delocalization inside the bridging quinonoid ligand in **2** as compared to **1**. The cyclic voltammetry of asymmetric complex **3**<sup>+</sup> in CH<sub>3</sub>CN / 0.1 M Bu<sub>4</sub>NPF<sub>6</sub> at 298 K shows two reversible one electron oxidation processes and three reversible one electron reduction processes (Figure 4.4.1). On the other hand, cyclic voltammetry of similar asymmetric complex **4**<sup>+</sup> shows two reversible one electron oxidations and only one reversible reduction in identical condition (Figure 4.4.1). Both the asymmetric complexes are present in mixed-valence state. The

potentials difference between the first oxidation and first reduction for  $3^+$  and  $4^+$  are 1210 mV and 1090 mV, respectively. The corresponding  $Kc$  value for  $3^+$  and  $4^+$  are of the order of  $10^{20}$  and  $10^{18}$ , respectively. The high stability of the mixed-valence state is due to the presence of electron donating ancillary ligands around one  $Ru^{III}$  centre and electron withdrawing ancillary ligands around another  $Ru^{II}$  centre.

## 4.5. EPR spectroscopy

To assign the ground state electronic configuration and the sites of the redox processes, the X-band EPR were measured for all four paramagnetic complexes. The EPR of symmetric dinuclear complexes (**1** and **2**) and asymmetric dinuclear complexes ( $3^+$  and  $4^+$ ) are discussed in separate sections.

### 4.5.1. The Complexes 1 and 2

The EPR spectra of all the species of complex **1** showed no signal at room temperature. This is because fast relaxation makes the system EPR silent until the solution is frozen. At 110 K the EPR spectrum of **1** showed a very weak signal (Figure 4.5.1.1a) and could be simulated using  $g_1 = 2.33$ ,  $g_2 = 2.24$  and  $g_3 = 1.91$  ( $g_{av} = 2.16$ ), in overall agreement with the susceptibility extracted value. Hyperfine interaction with the  $^{99}Ru$  and  $^{101}Ru$  isotopes (natural abundances of 13 and 17%, respectively) was considered for the simulation with  $A_{//}=260$  MHz and  $A_{\perp}=150$  MHz values, similar to reported literature values.<sup>[146]</sup> The weakness of the signal likely indicates the detection of the fraction  $P$  of single  $Ru^{III}$  centers in defective dimers, which would otherwise be silent due to antiferromagnetic coupling (like in the case of Cu-acetate).<sup>[147]</sup>

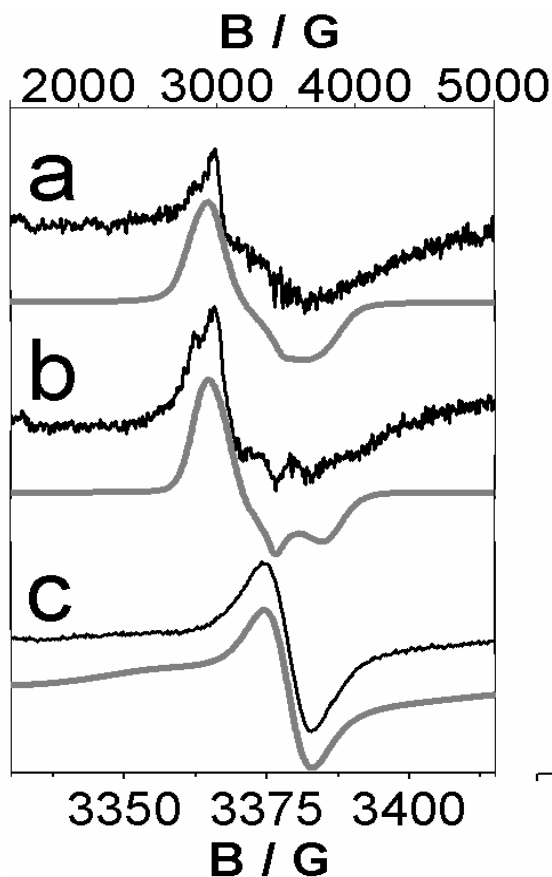


**Figure 4.5.1.1.** EPR investigation of the compounds, with the upper scale referring to spectra a) and b) and the bottom one to spectrum c). All spectra have been vertically shifted for clarity and the gray lines are the corresponding simulations. a) EPR spectrum of **1** in  $\text{CH}_2\text{Cl}_2$  at 110K; b) EPR spectrum of **1**<sup>+</sup> in  $\text{CH}_2\text{Cl}_2 / 0.1 \text{ M Bu}_4\text{NPF}_6$  at 110K; EPR spectrum of **1**<sup>-</sup> in  $\text{CH}_2\text{Cl}_2 / 0.1 \text{ M Bu}_4\text{NPF}_6$  at 110K.

The EPR signal of **1**<sup>+</sup> at 110 K (Figure 4.5.1.1b) is very similar to that of **1**, strengthening the hypothesis of the detection of defective dimers for **1**. The spectrum can be simulated well with the same  $g$  and  $A$  parameters by using a narrower linewidth. The high  $g$  anisotropy and increase in the strength of the signal indicate metal centered oxidation  $\text{Ru}^{\text{III}} \rightarrow \text{Ru}^{\text{IV}}$  leading to the formation of the mixed-valent form  $\text{Ru}^{\text{III}}\text{-Ru}^{\text{IV}}$  and it is proved farther by UV-vis-NIR spectroelectrochemistry (see later). The one-electron reduced form **1**<sup>-</sup> at 110 K (Figure 4.5.1.1c) shows a strong quinone signal that shadows the much weaker  $\text{Ru}^{\text{III}}$  line. The spectrum is well reproduced by using an isotropic signal with  $g = 2.004$ , and considering hyperfine coupling to the N nuclei. This points to a reduction of the bridging ligand leading to a three-spin situation,  $\text{Ru}^{\text{III}}\text{-(L}^1\text{-2H)}^-\text{-Ru}^{\text{III}}$ , ( $\uparrow, \uparrow, \downarrow$ ), with antiferromagnetic coupling between the  $\text{Ru}^{\text{III}}$  spins. This contrasts with what has been observed for the reduced state of the compound, analogous to **1**<sup>-</sup>, with the doubly deprotonated form of 2,5-diamino

1,4-benzoquinone as the bridging ligand. In that case the metal-centered spin was observed by EPR spectroscopy.<sup>[148]</sup> This shows the subtle changes in orbital coupling pattern that can be brought about by simple substitutions on the nitrogen atoms of *p*-quinones.

The paramagnetic complex **2** is also EPR silent at room temperature but shows an axial signal with  $g_{\perp} = 2.288$  and  $g_{\parallel} = 1.786$  in frozen solution at 110 K (Figure 4.5.1.2). The large  $g$  anisotropy ( $\Delta g = g_{\perp} - g_{\parallel}$ ) of 0.502 and the  $g_{av}$  value of 2.134 indicates ruthenium-centered spin. The fast relaxation makes the system EPR silent until the solution is frozen which is a characteristic of low spin  $d^5$  centres like  $\text{Ru}^{\text{III}}$ .

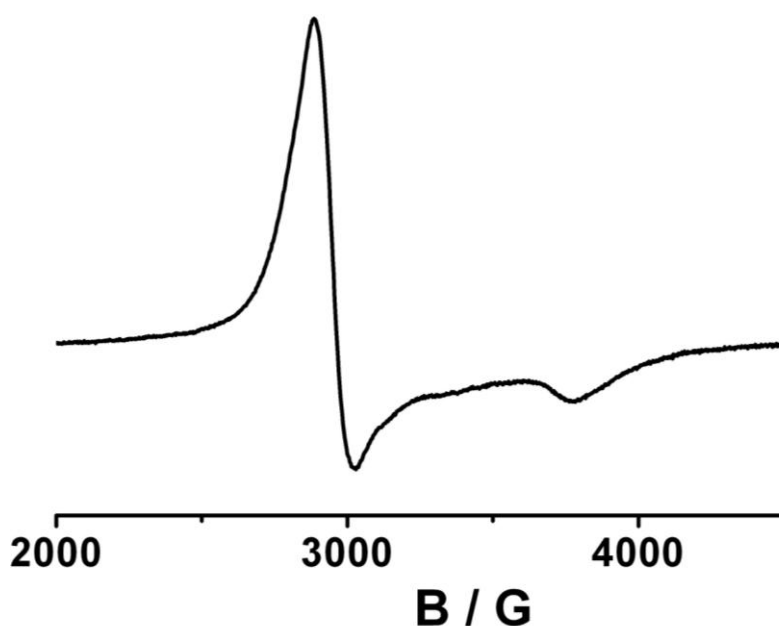


**Figure 4.5.1.2.** EPR spectrum of **2** at 110 K in  $\text{CH}_3\text{CN}$ .

The one electron oxidized form  $\mathbf{2}^+$  shows an EPR signal at 110 K with  $g_{av}$  value of 2.010 (Figure 4.5.1.3). Usually  $\text{Ru}^{\text{III/IV}}$  centered EPR signals show a large  $g$ -anisotropy and large  $g_{av}$  value with respect to the  $g_{av}$  value of organic radicals. The decrease of  $g_{av}$  value with respect to ground state ( $g_{av} = 2.134$ ) and some ligand centered splitting indicates the one electron oxidised form  $\mathbf{2}^+$  is in three-spin arrangements,  $\text{Ru}^{\text{III}}-(\text{L}^1\text{-2H})^{\cdot-}-\text{Ru}^{\text{III}}$ . ( $\uparrow, \uparrow, \downarrow$ ), with antiferromagnetic coupling between the  $\text{Ru}^{\text{III}}$  spins, whereas similar compound  $\mathbf{1}^+$  shows completely metal-centered spin (Figure 4.5.1.1b). This substantial change in orbital coupling pattern probably has to do with the delocalized  $\pi$ -system of quinonoid bridging ligand in **2** (chapter 2) as compared to **1**.

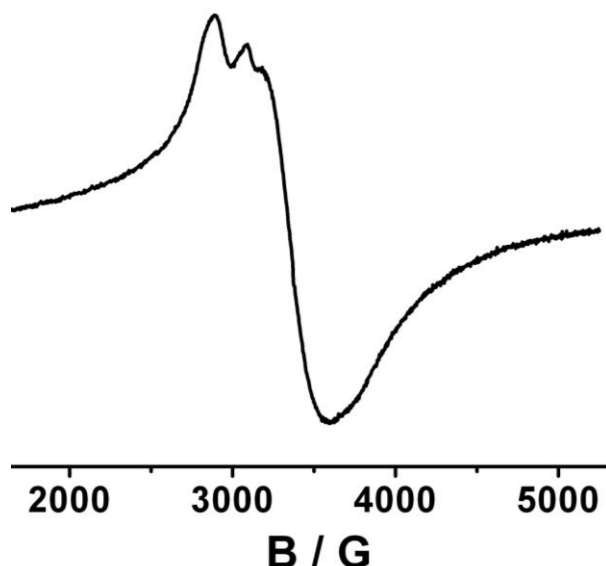


**Figure 4.5.1.3.** EPR spectrum of chemically generated  $2^+$  at 110 K in  $\text{CH}_3\text{CN}$ .

The chemically generated one electron reduced form  $2^-$  shows EPR signals at 110 K with three  $g$  values ( $g_1 = 2.044$ ,  $g_2 = 2.008$  and  $g_3 = 1.984$ ) having  $g_{\text{av}} = 2.012$  and  $\Delta g = 0.06$  (Figure 4.5.1.4). The  $g_{\text{av}}$  value of 2.012 (Figure 4.5.4.4) is much closed to the  $g_{\text{av}}$  value (2.0023) of organic radicals and the  $g$ -anisotropy is also very small (0.06).  $\text{Ru}^{\text{III}}$  centered EPR signals usually show  $g_{\text{av}} \gg g_{\text{av}}$  of organic radicals and large  $g$ -anisotropy e.g. the native state  $\text{Ru}^{\text{III}}-(\text{L}^2\text{-2H})\text{-Ru}^{\text{III}}$  ( $g_{\text{av}} = 2.134$  and  $\Delta g = 0.502$ ). The present EPR spectrum of  $2^-$  suggests both  $\text{Ru}^{\text{III}}$  centered spin and  $\text{L}^2\text{-2H}$  centered spin. Thus the one electron reduction of  $2$  to  $2^-$  leads to a three-spin arrangements  $\text{Ru}^{\text{III}}-(\text{L}^2\text{-2H})^{\cdot-}\text{-Ru}^{\text{III}}$ . The weakening of the  $\text{Ru}^{\text{III}}$  centred signal may be due to the antiferromagnetic coupling with the  $\text{L}^2\text{-2H}^{\cdot-}$  centred spin ( $\uparrow, \downarrow, \uparrow$ ).

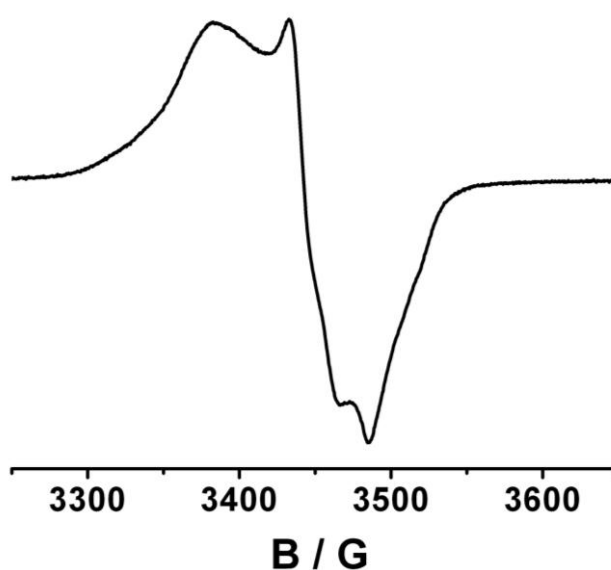


**Figure 4.5.1.4.** EPR spectrum of electrochemically generated  $2^-$  at 110 K in  $\text{CH}_3\text{CN} / 0.1 \text{ M Bu}_4\text{NPF}_6$ .

### 4.5.2. The Complexes $3^+$ and $4^+$

The paramagnetic complexes  $3^+$  and  $4^+$  are EPR silent at room temperature but show EPR signals in frozen solution at 110 K. The complex  $3^+$  exhibits EPR parameters of  $g_1 = 2.445$ ,  $g_2 = 2.280$  and  $g_3 = 1.706$  ( $g_{av} = 2.167$ ,  $\Delta g = g_1 - g_3 = 0.739$ ) and the complex  $4^+$  exhibits EPR parameters of  $g_1 = 2.420$ ,  $g_2 = 2.198$  and  $g_3 = 1.771$  ( $g_{av} = 2.147$ ,  $\Delta g = g_1 - g_3 = 0.649$ ) (Figure 4.5.2.1). The large  $g$  anisotropy and the  $g_{av}$  value of greater than 2.0023 ( $g$  value for free electron), reflects the presence of  $Ru^{III}$ -centered spin.

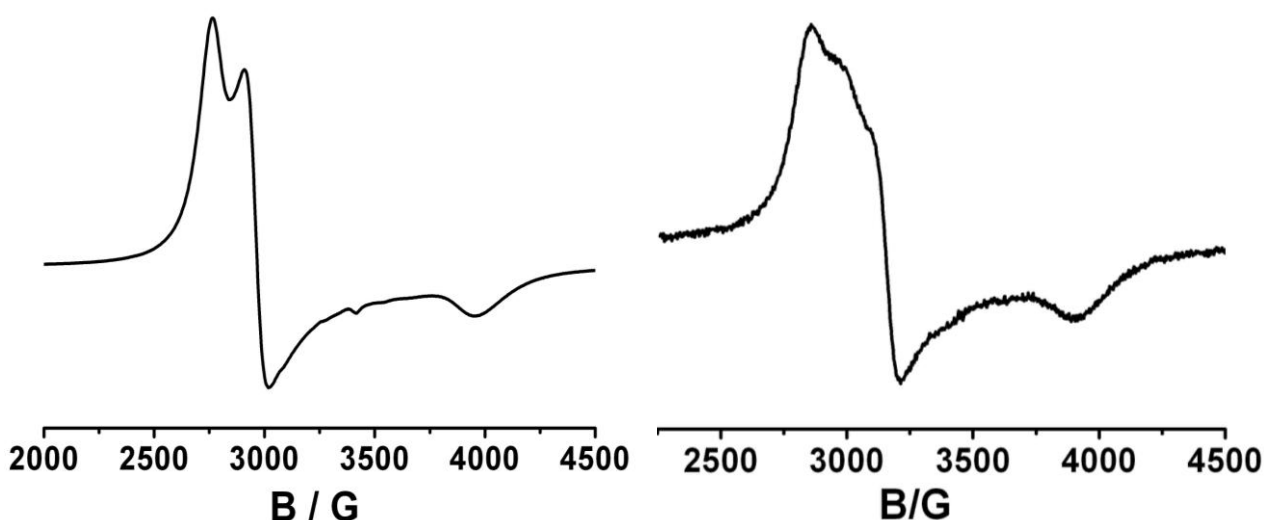


**Figure 4.5.2.1.** EPR spectra of  $3^+$  (left) and  $4^+$  (right) at 110 K in  $CH_3CN$ .

The one electron oxidized species  $3^{2+}$  shows EPR signal at 110 K with unusual splitting. The spectrum contain a strong signal at  $g = 2.263$  and some line rich signal at about  $g = 2.005$  (Figure 4.5.2.2 [left]). The EPR spectrum of  $3^{2+}$  can be explained by the two non-interacting parallel spin  $Ru^{III}/(L^1\text{-}2H)^+$  ( $\uparrow, \uparrow$ ). Thus the first oxidation of  $3^+$  [ $Ru^{III}-(L^1\text{-}2H)-Ru^{II}$ ] is bridging ligand centred and produce  $Ru^{III}-(L^1\text{-}2H)^+-Ru^{II}$  electronic configuration. Similarly, the first oxidation of  $4^+$  [ $Ru^{III}-(L^2\text{-}2H)-Ru^{II}$ ] is also bridging ligand centered and produce  $Ru^{III}-(L^2\text{-}2H)^+-Ru^{II}$  electronic configuration. The  $Ru^{III}$  centred spin appears at about  $g = 2.287$  and the  $(L^2\text{-}2H)^+$  centred spin appears at about  $g = 2.005$  as a broad signal (Figure 4.5.2.2 [wright]). The UV-vis-NIR spectroelectrochemistry also supports the ligand centered oxidation (see later). The one-electron reduction of the paramagnetic complexes  $3^+$  and  $4^+$  lead to EPR silent diamagnetic form [ $Ru^{II}-(L\text{-}2H)-Ru^{II}$ ].

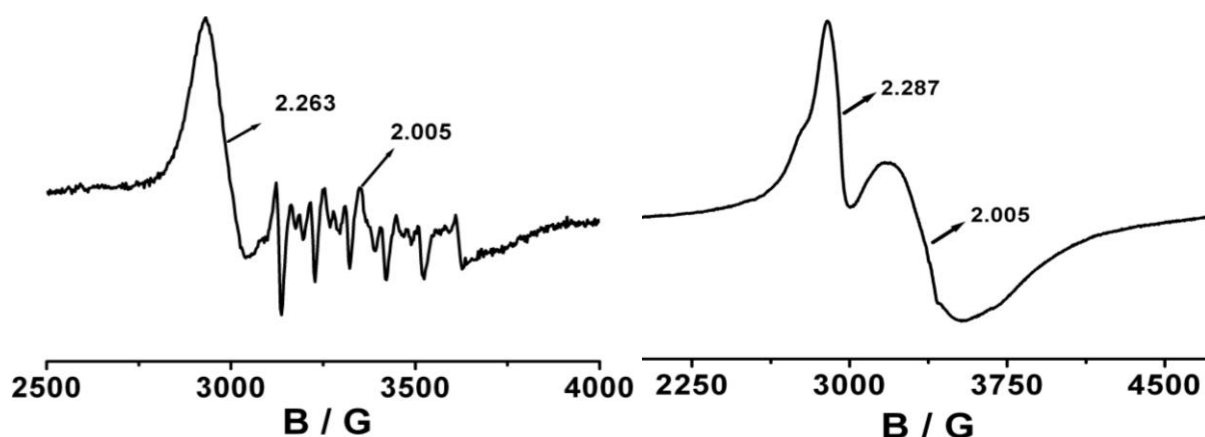


**Figure 4.5.2.2.** EPR spectra of chemically generated  $3^{2+}$  (left) and  $4^{2+}$  (right) at 110 K in  $\text{CH}_3\text{CN}$ .

## 4.6 UV/Vis/NIR Spectroelectrochemistry

To obtain information about the metal-metal electron coupling and electronic distribution of the complexes **1**, **2**,  $3^+$  and  $4^+$  in various accessible redox processes, UV-Vis-NIR spectroelectrochemical changes of all the four complexes were monitored using an OTTLE cell. The spectral results are summarized in Table 4.6.1.

### 4.6.1. Complex 1

The native  $\text{Ru}^{\text{III}}\text{-Ru}^{\text{III}}$  species **1** shows an intense LMCT ( $\text{L}^1\text{-}_{2\text{H}} \rightarrow \text{Ru}^{\text{III}}$ ) transition at 534 nm ( $\epsilon=19900 \text{ M}^{-1} \text{ cm}^{-1}$ ) (Figure 4.6.1.1). In addition, there are further ligand-centered transitions in the UV region. In the one-electron oxidized form  $1^+$  the LMCT band is red shifted to 708 nm with the intensity remaining almost unchanged. In addition, there is a new band growing in the NIR region at 1515 nm with  $\epsilon$  of  $5000 \text{ M}^{-1} \text{ cm}^{-1}$ , which disappears on second oxidation (Figure 4.6.1.1 and 4.6.1.2). The UV-vis-NIR measurements of  $1^+$  thus point to a mixed-valent situation leading to the formation of a  $\text{Ru}^{\text{III}}\text{-Ru}^{\text{IV}}$  species on one electron oxidation. The  $\Delta\nu_{1/2}$  of the IVCT band at 1515 nm is measured at about  $1475 \text{ cm}^{-1}$ . The Hush formulation gives  $\Delta\nu_{1/2} = (2310\nu_{\text{IVCT}})^{1/2} \approx 3905 \text{ cm}^{-1}$ .<sup>[72]</sup> This points to a delocalized situation in the mixed-valent form and hence  $1^+$  belongs to the strongly-coupled Class III system.

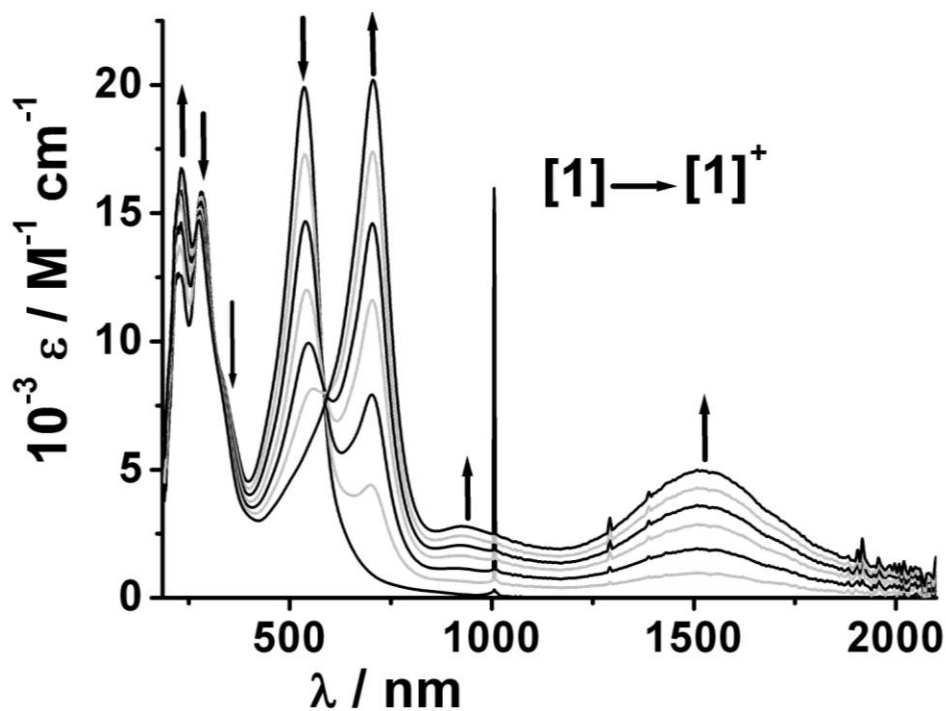


**Figure 4.6.1.1.** UV-Vis-NIR spectroelectrochemistry of the conversion  $[1]^{(0) \rightarrow (+)}$  in  $\text{CH}_3\text{CN} / 0.1 \text{ M Bu}_4\text{NPF}_6$ .

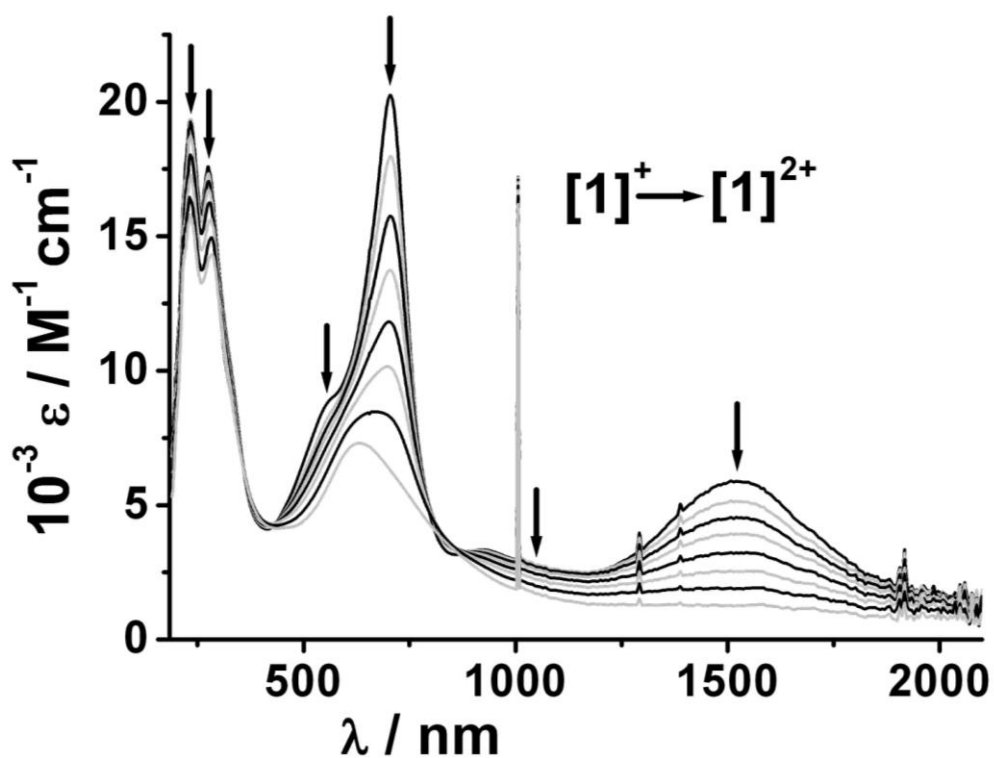


**Figure 4.6.1.2.** UV-Vis-NIR spectroelectrochemistry of the conversion  $[1]^{(+ \rightarrow (2+))}$  in  $\text{CH}_3\text{CN} / 0.1 \text{ M Bu}_4\text{NPF}_6$ .



The one-electron reduced form  $\mathbf{1}^-$  shows a very strong band at 750 nm ( $\epsilon=31700 \text{ M}^{-1} \text{ cm}^{-1}$ ). In addition, this species also shows absorptions in the NIR region at 1725 nm ( $\epsilon=1100 \text{ M}^{-1} \text{ cm}^{-1}$ ). On further reduction the NIR absorption band at 1725 nm is disappeared and the strong band at 750 nm is red shifted to 844 nm with slightly decreased intensity (Figure 4.6.1.3). Since the starting  $\text{Ru}^{\text{III}}\text{-Ru}^{\text{III}}$  compound can in principle be reduced to the  $\text{Ru}^{\text{III}}\text{-Ru}^{\text{II}}$  form, such NIR bands could be taken as evidence for a mixed-valent species. However, EPR spectrum of  $\mathbf{1}^-$  at 110 K indicates ligand centered reduction (Figure 4.5.1) and that leads to a three-spin situation,  $\text{Ru}^{\text{III}}(\text{L}^1\text{-}2\text{H}^{\bullet})\text{Ru}^{\text{III}}$  ( $\uparrow, \uparrow, \downarrow$ ) with antiferromagnetic coupling between the  $\text{Ru}^{\text{III}}$  spins. The combined UV-vis-NIR and EPR spectroelectrochemistry studies revealed that the first reduction is ligand centered.

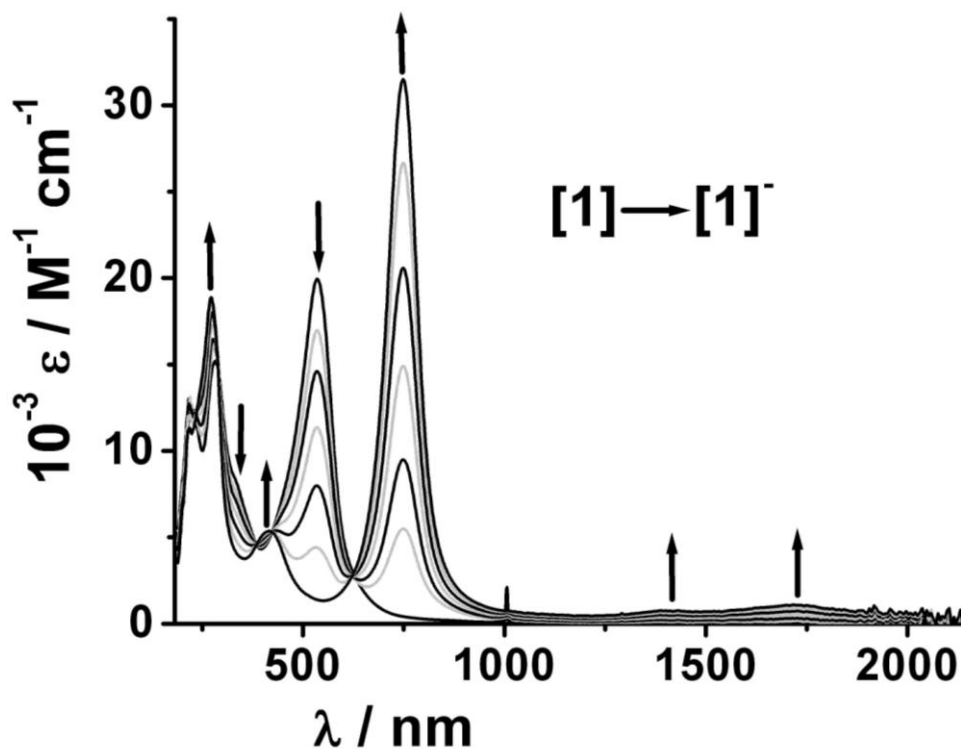


**Figure 4.6.1.3.** UV-Vis-NIR spectroelectrochemistry of the conversion  $[\mathbf{1}]^{(0)-}$  in  $\text{CH}_3\text{CN} / 0.1 \text{ M Bu}_4\text{NPF}_6$ .

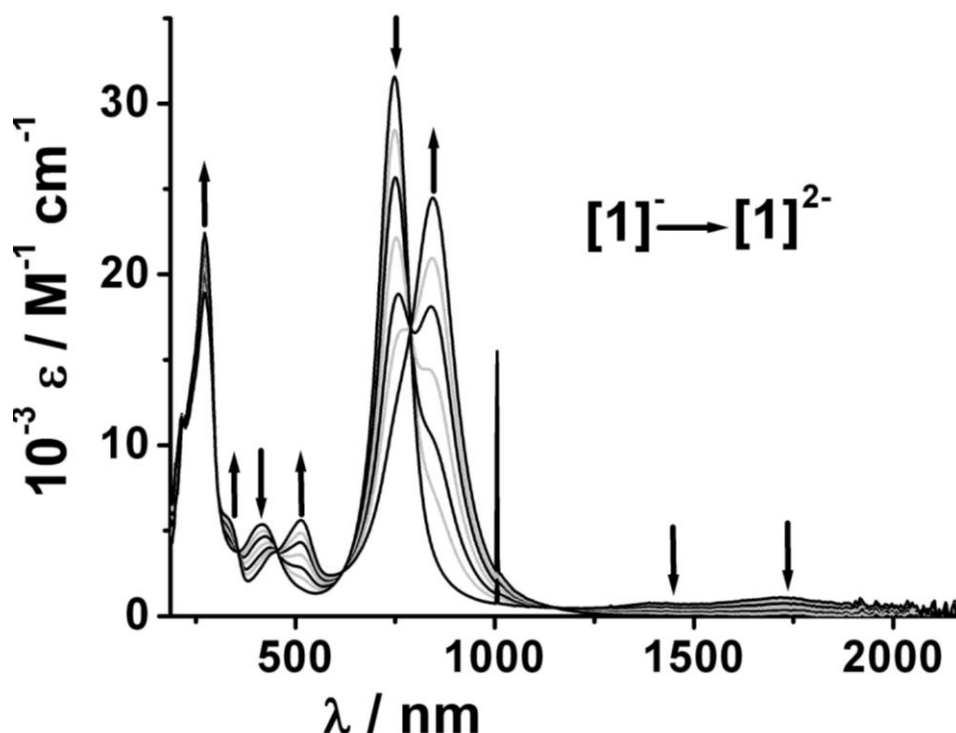


**Figure 4.6.1.4.** UV-Vis-NIR spectroelectrochemistry of the conversion  $[1]^{(-)} \rightarrow [1]^{(2-)}$  in  $\text{CH}_3\text{CN} / 0.1 \text{ M Bu}_4\text{NPF}_6$ .

#### 4.6.2. Complex 2

The complex **2** exists in two diastereomeric forms, **2a** (less polar) and **2b** (more polar). Both the forms show almost similar absorption bands in different redox states and have similarity with the redox states of **1**. Each of **2a** and **2b** shows intense LMCT ( $\text{L}^{2-}_{2\text{H}} \rightarrow \text{Ru}^{\text{III}}$ ) transition at around 635 nm (Figures 4.6.2.1 and Table 4.6.1) in addition to ligand centered signals in the UV region. However, in the one-electron oxidized form (**2a**<sup>+</sup> and **2b**<sup>+</sup>), the LMCT band is red shifted to 700 nm with slightly decreased intensity. In addition, there is a new band growing in the NIR region at around 1060 nm with a very less intense broad shoulder at around 1400 nm (Figure 4.6.2.1 and Table 4.6.1). The band at around 1060 nm could be intraligand  $\pi \rightarrow \pi^*$  (SOMO  $\rightarrow$  LUMO) charge transfer transitions.<sup>[26-28]</sup> The EPR spectrum of **2**<sup>+</sup> at low temperature (110 K) also supports ligand centered oxidation (Figure 4.5.3). However the appearance of NIR band at around 1400 nm can be taken as evidence for a mixed-valent species  $\text{Ru}^{\text{III}}(\text{L}^1_{2\text{H}})\text{Ru}^{\text{IV}}$ . Thus the one electron oxidized form **2**<sup>+</sup> is a radical bridge mixed-valent species.

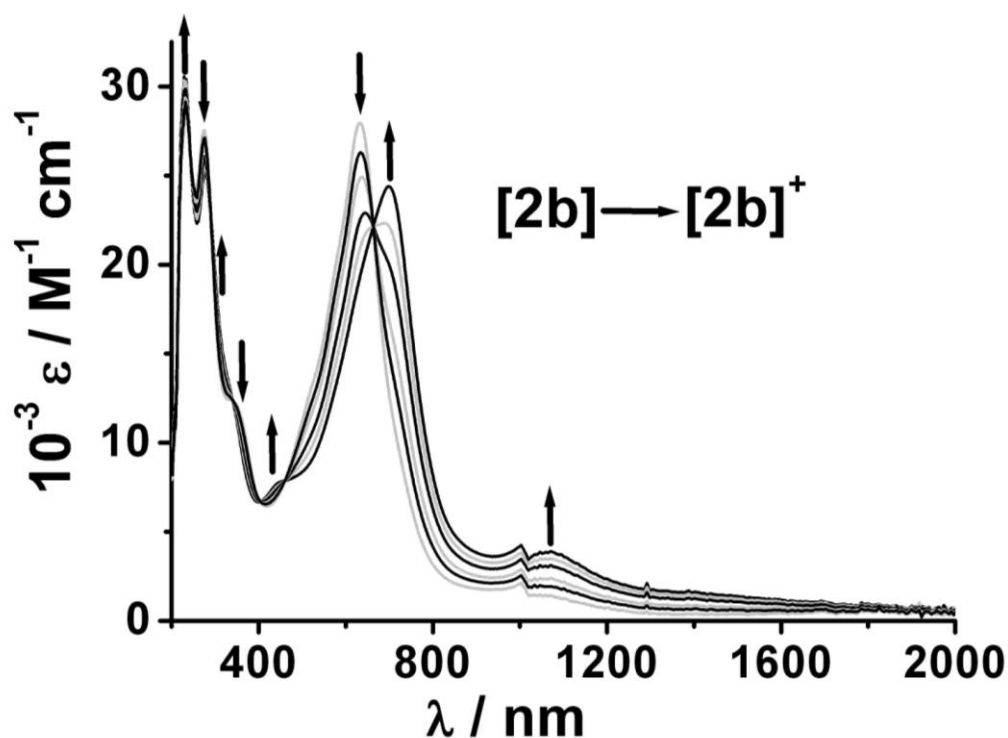


**Figure 4.6.2.1.** UV-Vis-NIR spectroelectrochemistry of the conversion  $[2b]^{(0) \rightarrow (+)}$  in  $\text{CH}_3\text{CN} / 0.1 \text{ M Bu}_4\text{NPF}_6$ .

Each of the one-electron reduced form  $2a^-$  and  $2b^-$  shows a strong LMCT absorption band at about 740 nm and a weak absorption band at about 1400 nm similar to the absorption of  $1^-$  (Figures 4.6.2.2 and Table 4.6.1). On further reduction, the strong LMCT band is red shifted to about 890 nm with slightly decreased intensity whereas the NIR absorption band at about 1400 nm is disappeared completely (Figures 4.6.2.2-4.6.2.3 and Table 4.6.1). Since the starting  $\text{Ru}^{\text{III}}\text{-Ru}^{\text{III}}$  compound (**2**) can, in principle, be reduced to the  $\text{Ru}^{\text{III}}\text{-Ru}^{\text{II}}$  form, the NIR bands at about 1400 nm can be taken as evidence for a mixed-valent species. However, strong intense LMCT band at about 740 nm and the EPR spectroscopic results suggest reduction of bridging ligand. So, the one electron reduction of complex **2** is bridging ligand centred that leading to a three-spin situation,  $\text{Ru}^{\text{III}}(\text{L}^2\text{-}2\text{H}^{\cdot-})\text{Ru}^{\text{III}}$  ( $\uparrow, \uparrow, \downarrow$ ) with antiferromagnetic coupling between the  $\text{Ru}^{\text{III}}$  spins.

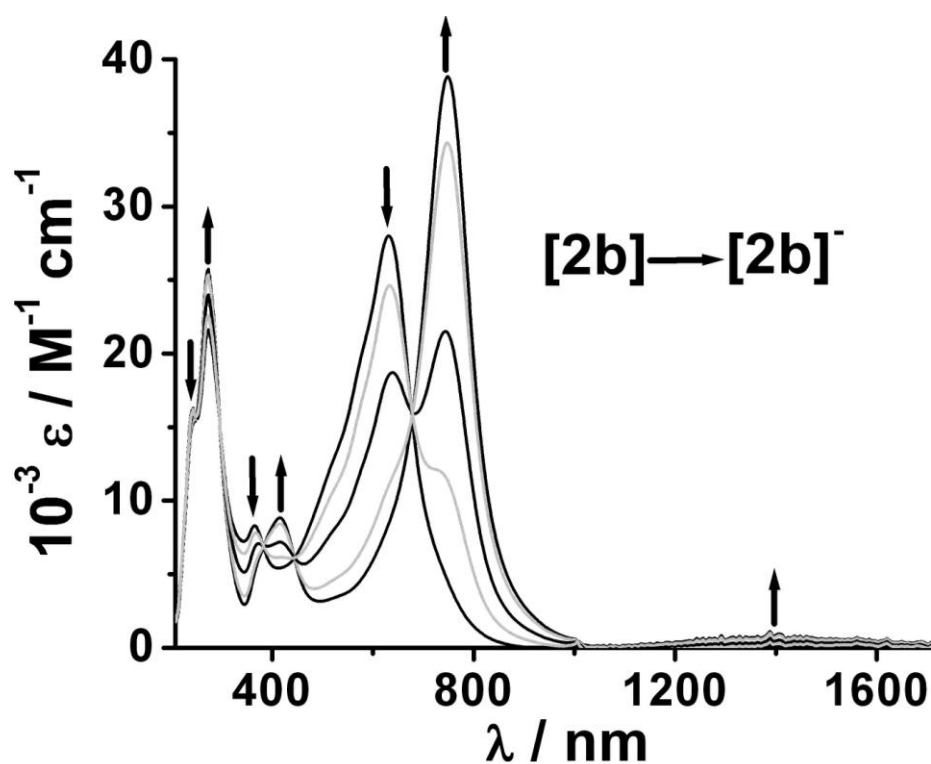


**Figure 4.6.2.2.** UV-Vis-NIR spectroelectrochemistry of the conversion  $[2b]^{(0) \rightarrow (-)}$  in  $\text{CH}_3\text{CN} / 0.1 \text{ M Bu}_4\text{NPF}_6$ .

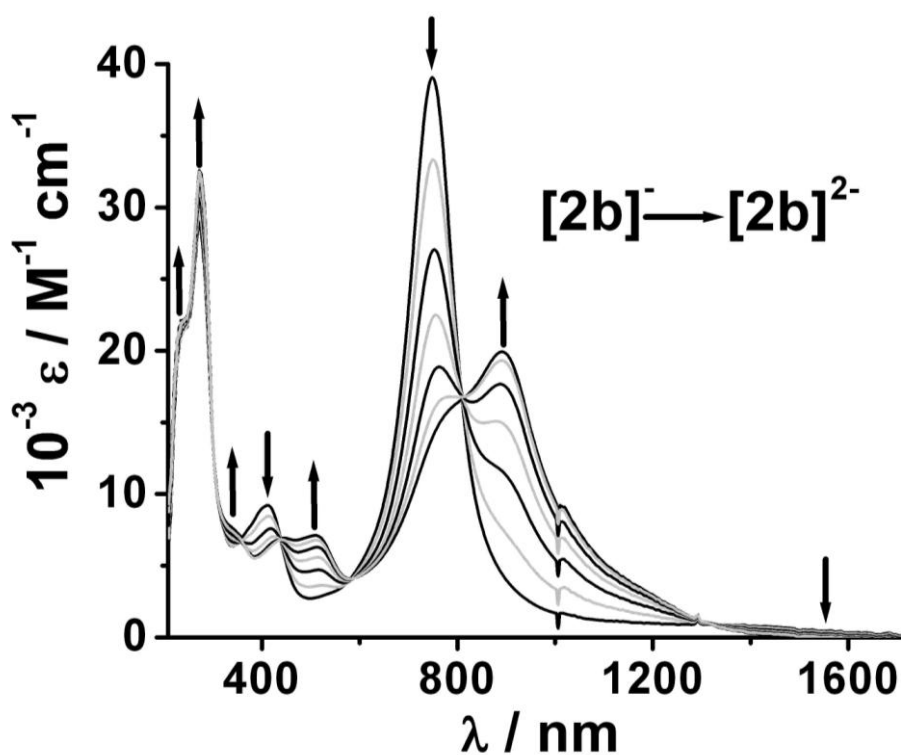


**Figure 4.6.2.3.** UV-Vis-NIR spectroelectrochemistry of the conversion  $[2b]^{(-) \rightarrow (2-)}$  in  $\text{CH}_3\text{CN} / 0.1 \text{ M Bu}_4\text{NPF}_6$ .

### 4.6.3. Complex $3^+$ and $4^+$

The native asymmetric mixed-valent species  $[(bpy)_2Ru^{II}(\mu-L^1_{-2H})Ru^{III}(acac)_2]^+$  ( $3^+$ ) and  $[(bpy)_2Ru^{II}(\mu-L^2_{-2H})Ru^{III}(acac)_2]^+$  ( $4^+$ ) show only two lowest energy charge-transfer bands at around 600 nm. These are tentatively assigned to mixed MLCT ( $Ru^{II} \rightarrow bpy$  and  $Ru^{II} \rightarrow L_{-2H}$ ) / LMCT ( $L_{-2H} \rightarrow Ru^{III}$ ) ( $L$  = bridging ligand) transitions (Figure 4.6.3.1 and 4.6.3.3). Metal to metal ( $Ru^{II} \rightarrow Ru^{III}$ ) IVCT transitions are not observed in the NIR region in native state. The reason for this may be the native complexes  $3^+$  and  $4^+$  are class I species or relatively weakly interacting class II species, in which case the IVCT band would be of low intensity. In the one-electron oxidized form  $3^{2+}$  the MLCT ( $Ru^{II} \rightarrow L^1_{-2H}$ ) band is red shifted to 705 nm with almost unchanged intensity. In addition, there is a new intense band growing up in the NIR region at 1346 nm ( $\epsilon$  of  $5700 M^{-1}cm^{-1}$ ,  $\Delta\nu_{1/2} = 1350 cm^{-1}$ ) (Figure 4.6.3.1). The emergence of NIR band could be either due to a metal to metal ( $Ru^{II} \rightarrow Ru^{III}$ ) IVCT transitions or  $\pi \rightarrow \pi^*$  (SOMO  $\rightarrow$  LUMO) intraligand charge transfer transitions for organic radical  $(L^1_{-2H})^{\cdot+}$ .<sup>[14,26]</sup> Both possibilities suggest mixed-valent configuration  $[(bpy)_2Ru^{II}(\mu-L^1_{-2H})^{\cdot+}Ru^{III}(acac)_2]^{2+}$  for  $3^{2+}$ . On further oxidation to  $3^{3+}$  the intense NIR band (at 1346 nm) disappears and  $Ru^{II} \rightarrow (L^1_{-2H})^{\cdot+}$  (MLCT) transitions are blue shifted (Figure 4.6.3.2) with substantial decrease in intensity, clearly indicate  $Ru^{II} \rightarrow Ru^{III}$  oxidation which leads to the configuration  $[(bpy)_2Ru^{III}(\mu-L^1_{-2H})^{\cdot+}Ru^{III}(acac)_2]^{3+}$  for  $3^{3+}$ . On the other hand, one electron oxidation of  $4^+$  to  $4^{2+}$  leads to a red shift of the MLCT band ( $Ru^{II} \rightarrow L^2_{-2H}$ ) to 694 nm and a broad NIR band appears at around 1170 nm (Figure 4.6.3.3) suggesting bridge-centered oxidation like  $3^{2+}$ . The EPR spectra of  $3^{2+}$  and  $4^{2+}$  provide direct evidence for bridge-centered oxidation (Figure 4.5.2.2). On further oxidation to  $4^{3+}$ , the NIR band remain unchanged while a new broad band appears at around 1500 nm (Figure 4.6.3.5) which is totally absent in case of  $3^{3+}$ . The MLCT bands are also blue shifted with substantial reduction in intensity (Figure 4.6.3.4), suggesting  $Ru^{II} \rightarrow Ru^{III}$  oxidation but presence of NIR band (at around 1500 nm) suggest further ligand centered oxidation. Thus the two electrons oxidized species  $4^{3+}$  can be express as a mixed of  $[(bpy)_2Ru^{III}(\mu-L^2_{-2H})^{\cdot+}Ru^{III}(acac)_2]^{3+}$  and diradical bridge mixed species  $[(bpy)_2Ru^{II}(\mu-L^2_{-2H})^{2\cdot+}Ru^{III}(acac)_2]^{3+}$ , indicate one unpaired electron is delocalized over  $(bpy)_2Ru^{III}$  moiety and  $(L^2_{-2H})^{\cdot+}$  moiety.

On one electron reduction of each complex  $3^+$  and  $4^+$  to  $3^0$  and  $4^0$  the intensity of MLCT bands at around 600 nm are substantially decreased and a new band at around 780 nm is appeared with high intensity (Figure 4.6.3.5-4.6.3.6 and Table 4.6.1). Since the starting complex  $[(bpy)_2Ru^{II}(\mu-L_{-2H})Ru^{III}(acac)_2]^+$  can reduced to either  $[(bpy)_2Ru^{II}(\mu-L^-_{-2H})Ru^{III}(acac)_2]$  or  $[(bpy)_2Ru^{II}(\mu-L_{-2H})Ru^{II}(acac)_2]$ , this new band could be  $L^-_{-2H} \rightarrow Ru^{III}$

LMCT or  $\text{Ru}^{\text{II}} \rightarrow \text{L}_{-2\text{H}}$  MLCT transitions. However the one electron reduced forms  $3^0$  and  $4^0$  are EPR silent that clearly indicate ruthenium centered reduction. So the band appeared at around 780 nm is due to the  $\text{Ru}^{\text{II}} \rightarrow \text{L}_{-2\text{H}}$  MLCT transitions for the electronic configuration  $[(\text{bpy})_2\text{Ru}^{\text{II}}(\mu\text{-L}_{-2\text{H}})\text{Ru}^{\text{II}}(\text{acac})_2]$ .

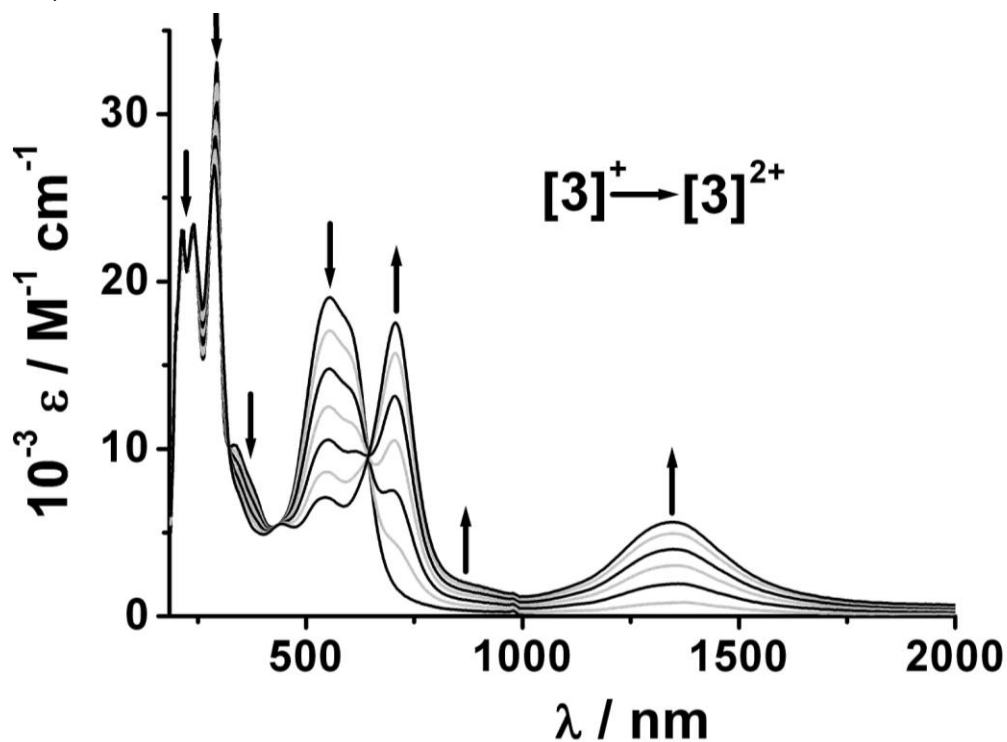


**Figure 4.6.3.1.** UV-Vis-NIR spectroelectrochemistry of the conversion  $[3]^{(+)} \rightarrow [3]^{(2+)}$  in  $\text{CH}_3\text{CN} / 0.1 \text{ M Bu}_4\text{NPF}_6$ .

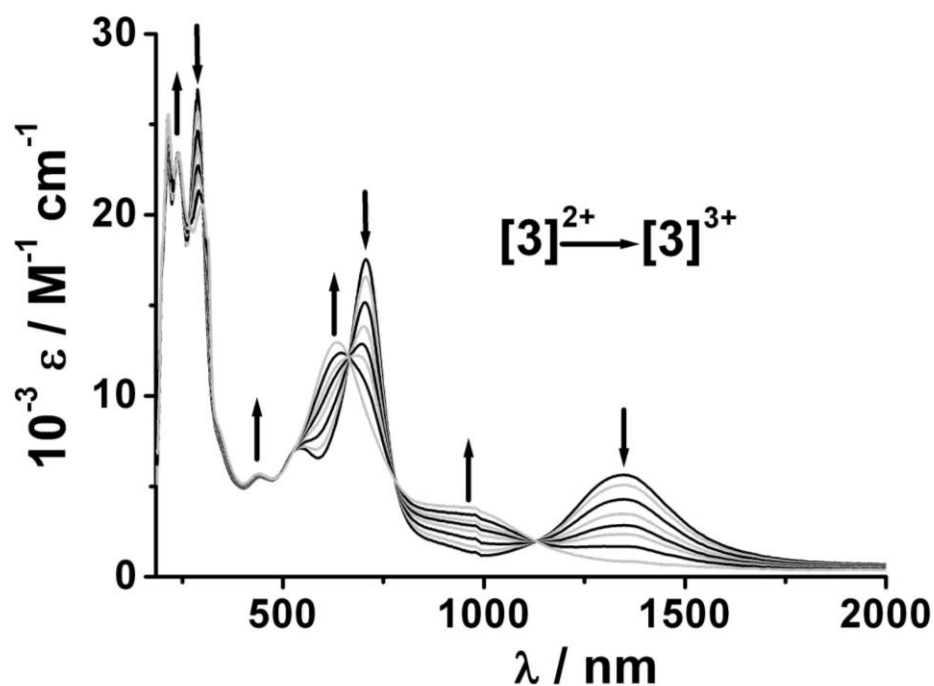


**Figure 4.6.3.2.** UV-Vis-NIR spectroelectrochemistry of the conversion  $[3]^{(2+)} \rightarrow [3]^{(3+)}$  in  $\text{CH}_3\text{CN} / 0.1 \text{ M Bu}_4\text{NPF}_6$ .

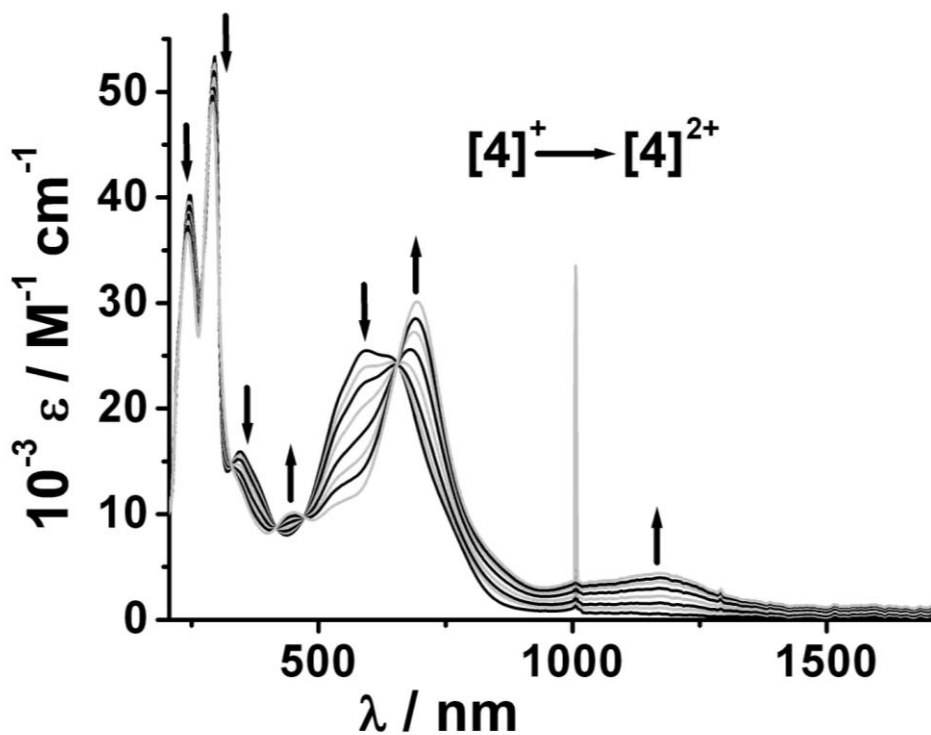


**Figure 4.6.3.3.** UV-Vis-NIR spectroelectrochemistry of the conversion  $[4]^{(+)\rightarrow(2+)}$  in  $\text{CH}_3\text{CN} / 0.1 \text{ M Bu}_4\text{NPF}_6$ .

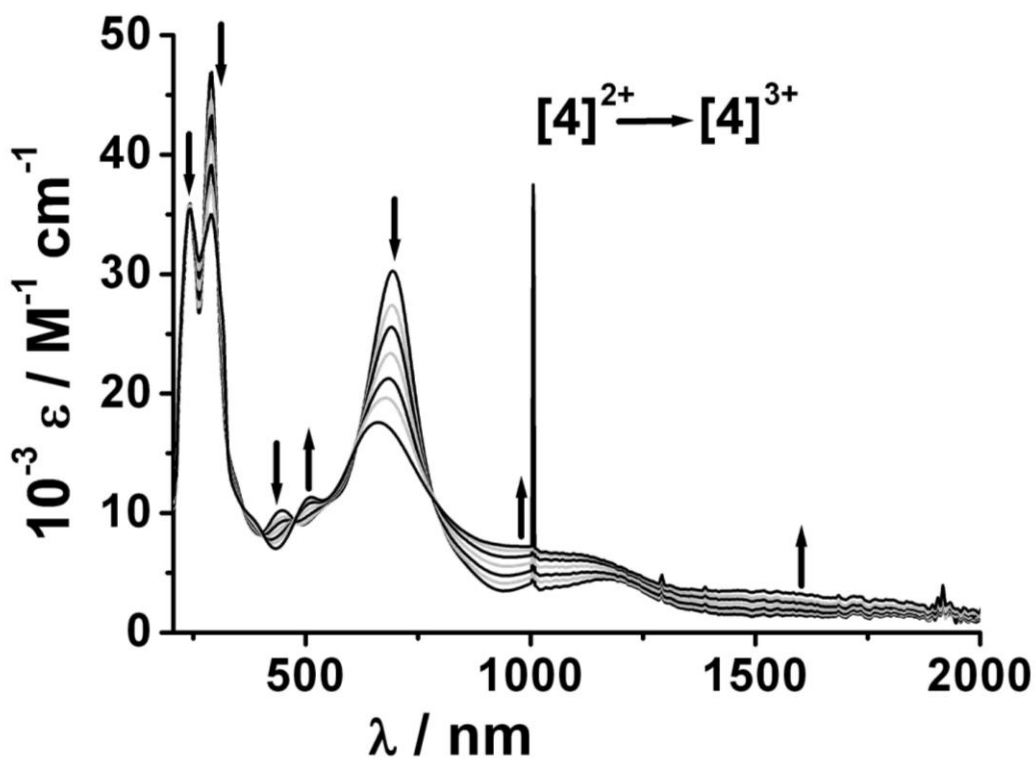


**Figure 4.6.3.4.** UV-Vis-NIR spectroelectrochemistry of the conversion  $[4]^{(2+)\rightarrow(3+)}$  in  $\text{CH}_3\text{CN} / 0.1 \text{ M Bu}_4\text{NPF}_6$ .

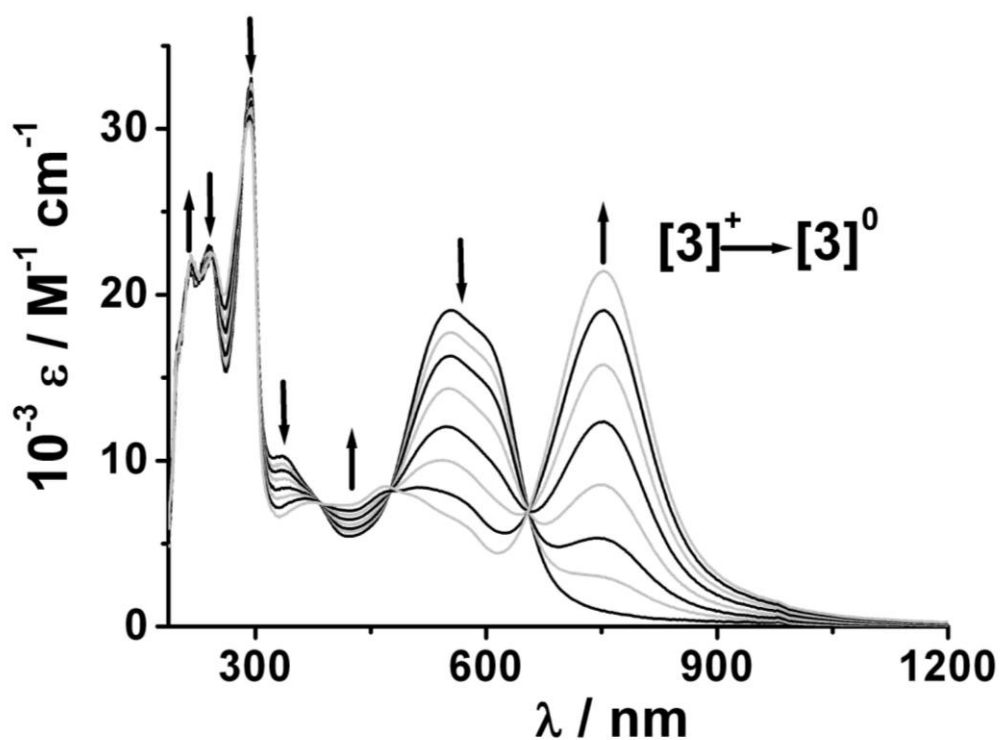


**Figure 4.6.3.5.** UV-Vis-NIR spectroelectrochemistry of the conversion  $[3]^{(+)\rightarrow(0)}$  in  $\text{CH}_3\text{CN} / 0.1 \text{ M Bu}_4\text{NPF}_6$ .

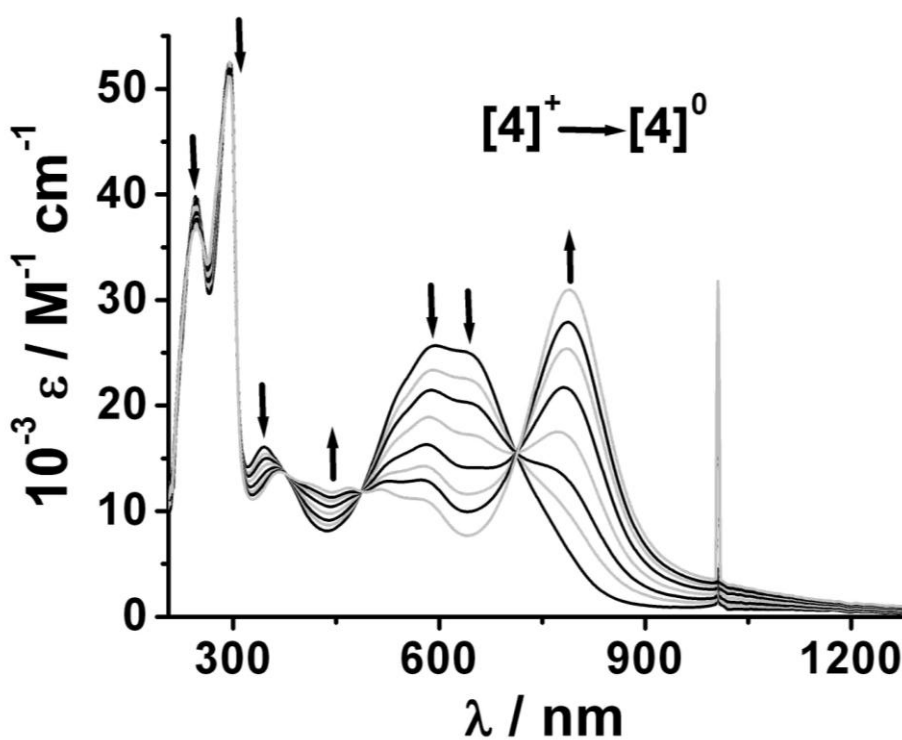


**Figure 4.6.3.2.** UV-Vis-NIR spectroelectrochemistry of the conversion  $[3]^{(+)\rightarrow(0)}$  in  $\text{CH}_3\text{CN} / 0.1 \text{ M Bu}_4\text{NPF}_6$ .



**Table 4.6.1.** Absorption data from UV/Vis/NIR spectroelectrochemistry.<sup>[a]</sup>

| Compound           | $\lambda_{\max}$ [nm] ( $\epsilon$ [ $\text{m}^{-1}\text{cm}^{-1}$ ])              |
|--------------------|--|
| [1]                | 223 (12.7), 280 (15.9), 340 (sh), 535 (20.0)                                       |
| [1] <sup>+</sup>   | 230 (16.8), 275 (14.7), 325 (sh), 570 (sh), 704 (20.2), 925 (2.9), 1518 (5.0)      |
| [1] <sup>2+</sup>  | 233 (15.7), 284 (14.3), 627 (7.3), 1542 (1.3)                                      |
| [1] <sup>-</sup>   | 216 (11.3), 272 (18.9), 418 (5.4), 746 (31.6), 1398 (0.8), 1722 (1.2)              |
| [1] <sup>2-</sup>  | 215 (11.8), 272 (22.4), 332 (5.8), 447 (3.7), 515 (5.7), 844 (24.6)                |
| [2a]               | 242 (25.0), 273 (25.8), 350 (13.0), 634 (29.2), 1058 (3.8)                         |
| [2a] <sup>+</sup>  | 235 (26.0), 277 (23.1), 240 (sh), 446 (sh), 702 (25.1), 1056 (6.46), 1427 (3.9)    |
| [2a] <sup>-</sup>  | 210 (30.5), 274 (36.2), 409 (10.4), 740 (43.8), 1365 (1.3)                         |
| [2a] <sup>2-</sup> | 215 (30.7), 273 (44.4), 506 (9.4), 774 (sh), 892 (28.9)                            |
| [2b]               | 233 (28.5), 274 (27.7), 343 (sh), 633 (28.0), 1052 (1.5)                           |
| [2b] <sup>+</sup>  | 231 (30.5), 276 (25.3), 339 (sh), 440 (sh), 700 (24.5), 1071 (4.0), 1390 (1.8)     |
| [2b] <sup>-</sup>  | 247 (15.5), 272 (25.8), 380 (sh), 416 (8.9), 746 (39.0), 1400 (1.1),               |
| [2b] <sup>2-</sup> | 236 (22.2), 272 (32.6), 337 (sh), 443 (7.1), 509 (7.2), 805 (sh), 890 (20.0)       |
| [3] <sup>+</sup>   | 214 (23.1), 240 (23.5), 293 (33.1), 336 (10.3), 553 (19.2), 595 (sh)               |
| [3] <sup>2+</sup>  | 215 (21.8), 240 (23.0), 288 (26.7), 440 (5.5), 541 (7.1), 705 (17.6), 1346 (5.7)   |
| [3] <sup>3+</sup>  | 216 (25.6), 241 (23.5), 302 (20.6), 441 (5.8), 634 (13.1), 954 (3.9)               |
| [3] <sup>0</sup>   | 216 (22.3), 244 (22.4), 292 (30.2), 377 (7.5), 468 (8.5), 565 (sh), 752 (21.5)     |
| [4] <sup>+</sup>   | 248 (40.2), 293 (53.4), 345 (16.1), 543 (sh), 591 (25.8), 636 (25.1)               |
| [4] <sup>2+</sup>  | 240 (36.3), 290 (48.4), 446 (10.3), 547 (sh), 694 (30.2), 1172 (4.65)              |
| [4] <sup>3+</sup>  | 241 (35.1), 290 (34.8), 505 (11.4), 662 (17.8), 987 (sh), 1514 (3.6)               |
| [4] <sup>0</sup>   | 247 (37.0), 295 (51.1), 367 (13.7), 467 (12.4), 516 (12.2), 575 (11.3), 790 (31.1) |

<sup>[a]</sup> From spectroelectrochemistry in CH<sub>3</sub>CN / 0.1 M Bu<sub>4</sub>NPF<sub>6</sub> at 298 K.

## 4.7 SQUID Magnetometry

The complexes **1** and **2** are paramagnetic with the quinonoid ligand bridging two Ru<sup>III</sup> centers. The Ru<sup>III</sup> complexes of this family are known to show temperature-independent paramagnetism (TIP).<sup>[148, 152]</sup> The magnetic susceptibility of compound **1** was measured with a SQUID setup (Figure 4.7.1).

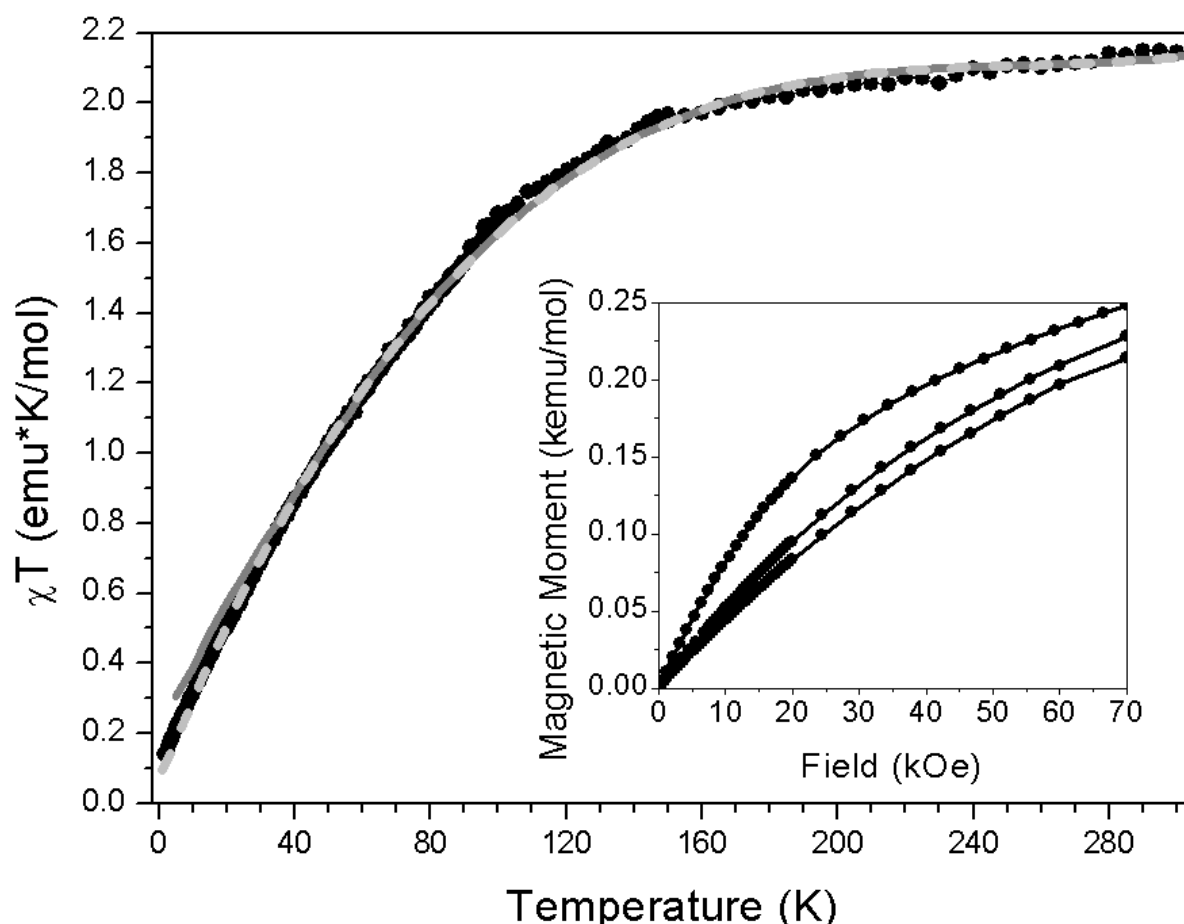


**Figure 4.7.1.** Magnetic behavior of compound **1**. The data were recorded with a SQUID magnetometer and corrected for diamagnetic contributions of the sample and sample holder, as independently determined. The gray line represents the fit to the data, using intradimer interactions only, as described in the text. The low-temperature discrepancy, visible below 30K, is probably due to the contemporary presence of depopulation of higher energy levels and interdimer interactions, and better agreement is obtained by including an interdimer interaction  $J'$  (dashed line).<sup>[148, 153, 154]</sup> The inset shows the low temperature magnetization curves, recorded at 5, 4 and 2 K.

As in previously reported cases,<sup>[25, 29, 30]</sup> the spectrum was fitted by considering the system as composed of dimers with a small fraction,  $P$ , of defective paramagnetic sites<sup>[155, 156]</sup> and using  $g$ , TIP, and the magnetic exchange,  $J$ , as free parameters; this yielded  $\text{TIP}=0.01\pm 0.01 \text{ cm}^3 \text{ mol}^{-1}$ ,  $g = 2.1\pm 0.1$ , and  $J = -19\pm 3 \text{ cm}^{-1}$ . This antiferromagnetic behavior is in agreement with previous reports<sup>[148, 155]</sup> and is also visible from the nonsaturated value attained by the low-temperature  $M$  versus  $H$  curves. The obtained value is comparable to those previously reported for similar compounds and its slightly diminished magnitude can probably be attributed to the reduced twisting induced by the isopropyl substituents on the imino nitrogen atoms. The discrepancy from the fit at lower temperatures can probably be attributed to the presence of either the onset of interdimer interactions or a zero-field splitting effect.<sup>[157]</sup> While the latter case cannot be excluded, our attempt at a fit with the same parameters as above, but adding interdimer interactions,  $J'$ , obtained satisfactory agreement at low T when  $J' = -4\pm 1 \text{ cm}^{-1}$ . The magnetic interaction pathway for  $J'$  is not purely dipolar in origin, since its magnitude is higher than that expected for a dipolar interaction transmitted by the interdimer  $\text{Ru}^{\text{III}}\text{-Ru}^{\text{III}}$  distance of  $7.649(1) \text{ \AA}$ . However this can be considered an indicative value, since single-crystal measurements would be needed for a complete determination of the local anisotropic axes of  $\text{Ru}^{\text{III}}$  and an accurate evaluation of the interdimer interactions.

#### 4.8. Conclusion

The two symmetric dinuclear complexes  $[\{(\text{acac})_2\text{Ru}^{\text{III}}\}_2(\mu\text{-L}^1\text{-2H})]$  (**1**) and  $[\{(\text{acac})_2\text{Ru}^{\text{III}}\}_2(\mu\text{-L}^2\text{-2H})]$  (**2**) and two rare asymmetric dinuclear complexes  $[(\text{bpy})_2\text{Ru}^{\text{II}}(\mu\text{-L}^1\text{-2H})\text{Ru}^{\text{III}}(\text{acac})_2](\text{ClO}_4)$  (**3** $[\text{ClO}_4]$ ) and  $[(\text{bpy})_2\text{Ru}^{\text{II}}(\mu\text{-L}^2\text{-2H})\text{Ru}^{\text{III}}(\text{acac})_2](\text{ClO}_4)$  (**4** $[\text{ClO}_4]$ ) have been synthesized and isolated in paramagnetic form  $\text{Ru}^{\text{III}}\text{-Ru}^{\text{III}}$  (for **1** and **2**) and paramagnetic mixed-valent form  $\text{Ru}^{\text{III}}\text{-Ru}^{\text{II}}$  (for **3**<sup>+</sup> and **4**<sup>+</sup>). The oxidation of the symmetric compounds (**1** and **2**) leads to  $\text{Ru}^{\text{III}}\text{-Ru}^{\text{IV}}$  mixed-valent species and shows strong metal-metal coupling in the NIR region, whereas reduction leads to a quinonoid radical-containing  $\text{Ru}^{\text{III}}\text{-Ru}^{\text{III}}$  species. The native mixed-valent  $\text{Ru}^{\text{III}}\text{-Ru}^{\text{II}}$  species **3**<sup>+</sup> and **4**<sup>+</sup> does not show IVCT bands in the NIR region. One electron oxidation of **3**<sup>+</sup> and **4**<sup>+</sup> leads to quinonoid radical-containing  $\text{Ru}^{\text{III}}\text{-Ru}^{\text{II}}$  species while one electron reduction of **3**<sup>+</sup> and **4**<sup>+</sup> leads to  $\text{Ru}^{\text{II}}\text{-Ru}^{\text{II}}$  species. The substitution of localized quinonoid ligand  $\text{L}^1$  by  $\text{L}^2$  in these complexes helps in tuning the redox properties, metal-metal coupling and charge distributions in different oxidation states substantially.

## CHAPTER 5

# Charge Distribution, Redox Properties, Structures and Bonding in the Substitution Series $[\text{Ru}(\text{L-H})_n(\text{acac})_{3-n}]$ ( $n = 0-3$ ; $\text{L} = \text{N,N}'$ -Diisopropyl-2-amino-5-alcoholate-1,4-benzoquinonemonoiminium)

### 5.1. Introduction

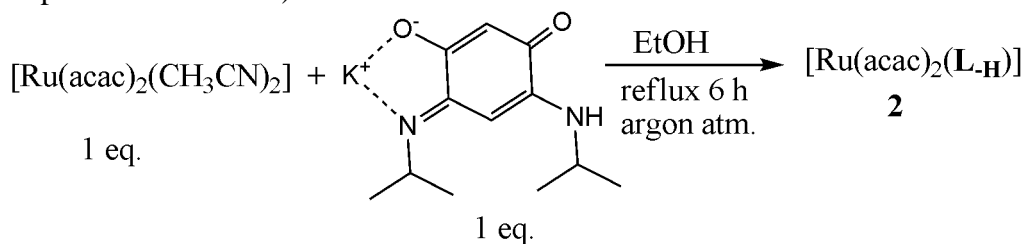
Transition metal complexes containing quinonoid ligands are of general interest in the investigation of ligand centered redox reactions,<sup>[158-161]</sup> intriguing electronic properties,<sup>[158-161]</sup> noncovalent interactions<sup>[162]</sup> and as models for metallo-biochemical process.<sup>[163]</sup> The combination between redox-active ruthenium and noninnocent quinonoid ligands leads to an interesting array of redox-rich compounds and shows considerable mixing of metal and ligand based frontier orbitals and valence ambiguity.<sup>[164-166]</sup> The mixing of metal and ligand based frontier orbitals can be controlled by replacing the ancillary ligands. Non-covalent interactions in mononuclear quinonoid complexes often depend on the acidity of the N—H proton. A large number of natural quinonoid compounds are available. Some of these compounds contain acidic protons which play important roles as bioinhibitors<sup>[167-170]</sup> through hydrogen bonding.<sup>[171-173]</sup>

In this regard the syntheses of a complete substitution series  $[\text{Ru}(\text{L-H})_n(\text{acac})_{3-n}]$   $\{n = 0$  (Complex **1**),  $n = 1$  (Complex **2**),  $n = 2$  (Complex **3**),  $n = 3$  (Complex **4**),  $\text{L} = \text{N,N}'$ -diisopropyl-2-amino-5-alcoholate-1,4-benzoquinonemonoiminium $\}$  complexes are reported and their redox properties, charge distribution, non-covalent interactions, structures and bonding have been investigated.

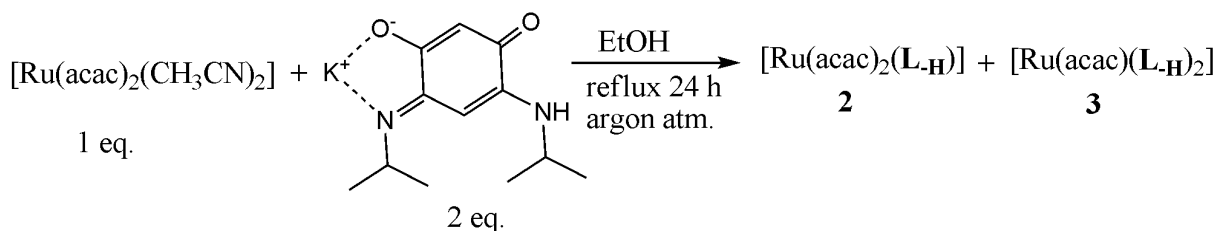
### 5. 2. Syntheses and characterization

The complex **1** was synthesized according to a reported procedure.<sup>[174]</sup> The ligand **L** was deprotonated by 1 eq. <sup>t</sup>BuOK in THF under inert atmosphere. The para-magnetic complexes **2** and **3** were synthesized by the reactions of  $[\text{Ru}(\text{acac})_2(\text{CH}_3\text{CN})_2]$  with mono-deprotonated quinonoid ligand (**L-H**) in EtOH (Scheme 5.2.1-5.2.2) and purified by column chromatography using an alumina column. Refluxing of  $[\text{Ru}(\text{acac})_2(\text{CH}_3\text{CN})_2]$  with 1 eq. **L-H** for 6 h results only in complex **2**, while reaction of  $[\text{Ru}(\text{acac})_2(\text{CH}_3\text{CN})_2]$  with 2 eq. **L-H**

(condition: 24 h reflux) leads to the formation of both complexes **2** and **3**. The complexes **2** and **3** were characterized by elemental analysis and electrospray mass spectrometry (see the Experimental Section).

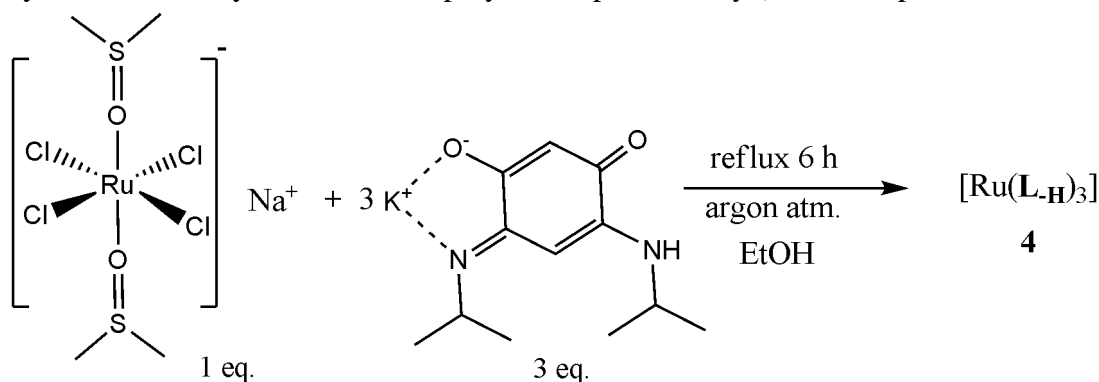


**Scheme 5.2.1.** Synthetic scheme for complex **2**.



**Scheme 5.2.2.** Synthetic scheme for complex **3**.

The paramagnetic complex **4** was synthesized by the reaction of  $[\text{Na}][\text{RuCl}_4(\text{DMSO})_2]$  with 3 eq. of  $\text{L}_\text{H}$  under an inert atmosphere (Scheme 5.2.3). The compound was purified by column chromatography using alumina column and characterized by elemental analysis and electrospray mass spectrometry (see the Experimental Section).



**Scheme 5.2.3.** Synthetic scheme for complex **4**.

Each of the four complexes **1-4** can exist in different isomeric forms. Complexes **1-2** can form a pair of enantiomers. For complex **3**, three positional isomers are possible as in the case of  $[\text{Ru}(\text{bpy})(\text{L}_\text{H})_2]$  (Chapter 6). However, in the present case only a single isomer was isolated by column chromatography. On the other hand, complex **4** can exist in the *fac* (facial) and *mer* (meridional) isomeric forms; however, only one isomer was isolated by column chromatography and its identity as the *mer* isomer was confirmed by single crystal X-ray diffraction studies (Figure 5.3.2). The formation of only *mer* isomer may be rationalised in

terms of the steric influences as *fac* isomer suffers more steric constraints due to the presence of three close *N*-isopropyl groups inside the moiety (Figure 5.2.1). Analogues complexes of ruthenium(III), cobalt(III) and iron(III) with three related quinonoid ligands were also reported in *mer* form.<sup>[164, 175-176]</sup>

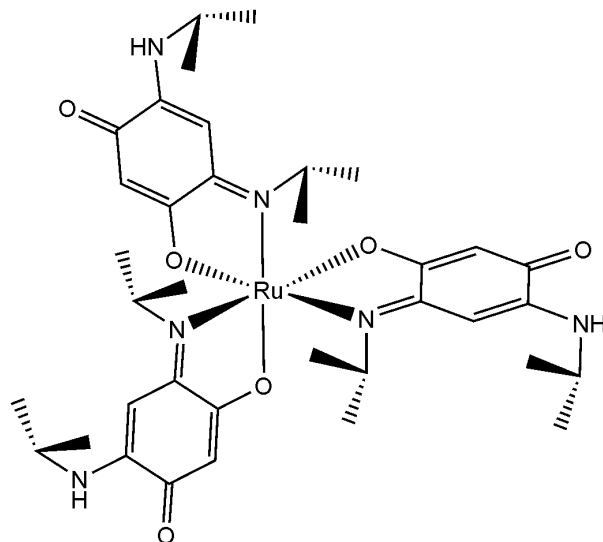


**Figure 5.2.1.** The orientation of isopropyl groups in *fac* isomeric form.

## 5. 2. X-ray crystallographic characterization of 2 and 4

In order to establish the structure of isomers, single crystal X-ray diffraction studies of **2** and **4** were carried out. The single crystals of complexes **2** and **4** were obtained by slow evaporation of their dichloromethane solution at room temperature. Both the complexes crystallize in the monoclinic  $P2_1/c$  space group with monoclinic crystal system. The crystal structures of the complexes are depicted in Figures 5.3.1-5.3.2. Selected bond lengths and bond angles of the complexes are given in Tables 5.3.1-5.3.3, while X-ray diffraction parameters and crystallographic data are reported in Chapter 10.

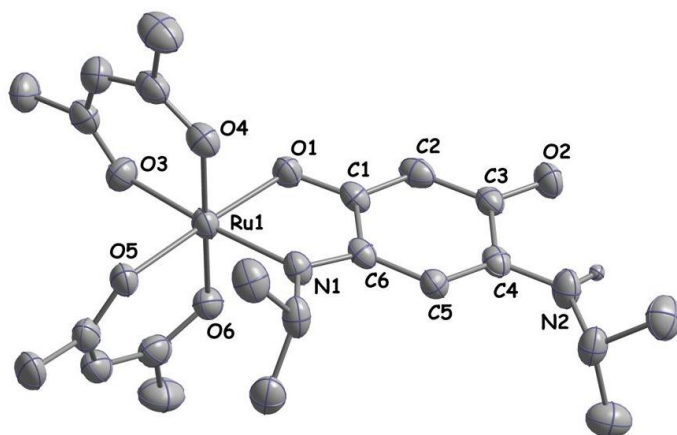


**Figure 5.3.1.** Molecular structure of complex **2** in the crystal. Thermal ellipsoids are drawn at 50% probability. Hydrogen atoms, except H2N2 have been omitted for clarity.

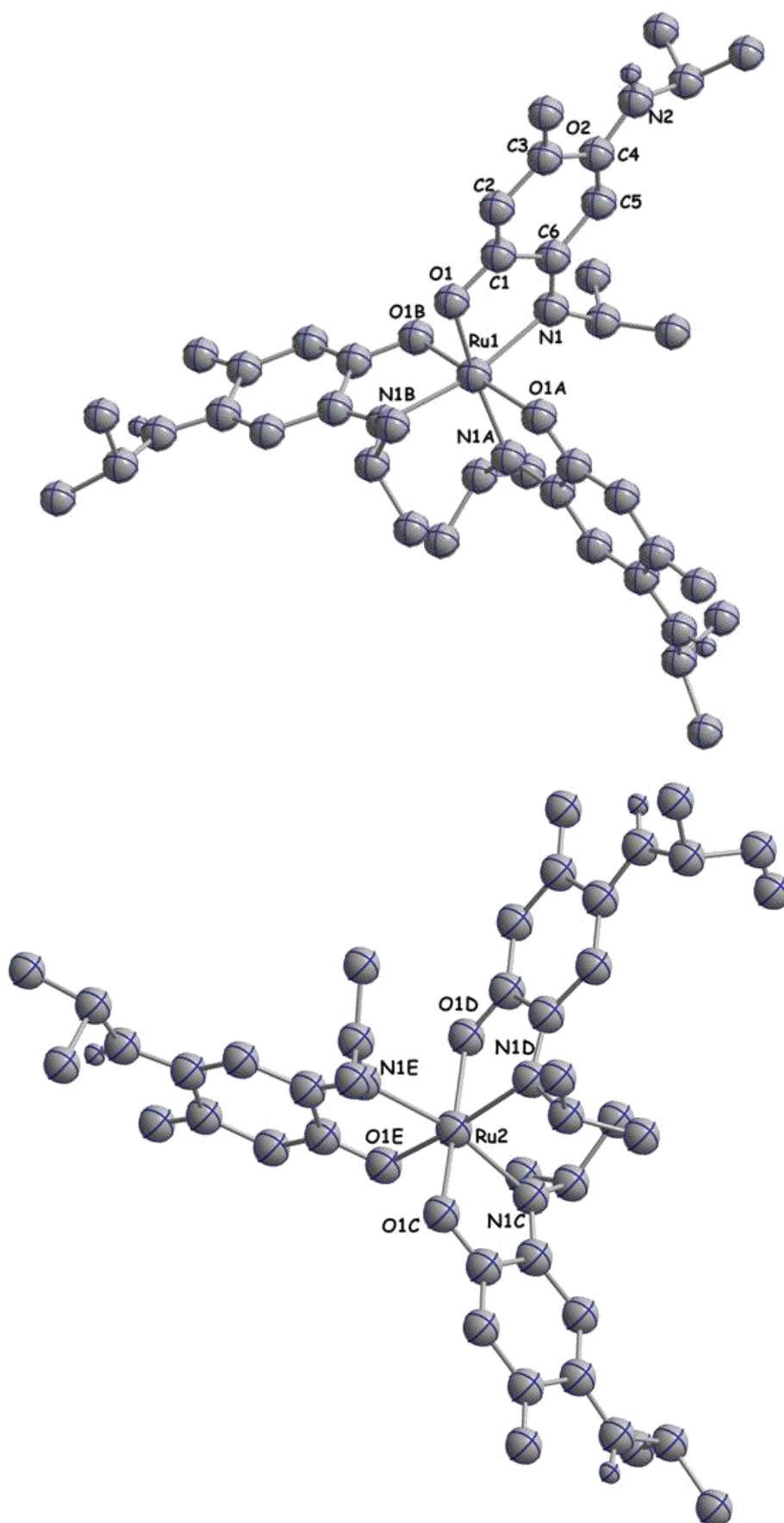


**Figure 5.3.2.** Molecular structure of two enantiomers  $\Delta$  (top) and  $\Lambda$  (bottom) of *mer*-isomer of **4**. Thermal ellipsoids are drawn at 50% probability. Hydrogen atoms, except HN have been omitted for clarity.

The crystal structures of complexes **2** and **4** reveal a distorted octahedral geometry around the ruthenium centre. In complex **2**, the ruthenium center is coordinated by four oxygen atoms from the two acac ligands and one nitrogen and one oxygen atom from the mono-deprotonated form of **L**. On the other hand, in the case of complex **4**, three oxygen atoms and three nitrogen atoms from the three mono-deprotonated form of **L** coordinate to the ruthenium center. The crystal structure of **4** also confirms the existence of meridional isomer.

**Table 5.3.1.** Selected bond lengths [Å] for **2**, **4** and **L**.<sup>[172]</sup>

| Compound | <b>2</b> | <b>4</b> ( $\Delta$ -enantiomer) | <b>L</b> |
|----------|----------|----------------------------------|----------|
| C1-C2    | 1.361(5) | 1.340(8)                         | 1.390(4) |
| C2-C3    | 1.412(6) | 1.394(8)                         | 1.391(4) |
| C3-C4    | 1.508(6) | 1.526(8)                         | 1.526(5) |
| C4-C5    | 1.374(5) | 1.360(8)                         | 1.387(4) |
| C5-C6    | 1.413(5) | 1.428(8)                         | 1.391(4) |
| C6-C1    | 1.492(5) | 1.482(7)                         | 1.529(4) |
| O1-C1    | 1.301(5) | 1.317(6)                         | 1.253(4) |
| C3-O2    | 1.243(4) | 1.235(7)                         | 1.252(4) |
| N1-C6    | 1.318(5) | 1.300(7)                         | 1.316(4) |
| N2-C4    | 1.335(5) | 1.331(8)                         | 1.316(4) |
| Ru1-O1   | 1.998(3) | 2.003(4)                         |          |
| Ru1-N1   | 2.047(3) | 2.066(5)                         |          |



**Table 5.3.2.** Selected bond angles (°) for the complex **2**.

|           |           |           |            |
|-----------|-----------|-----------|------------|
| O1-Ru1-N1 | 79.99(12) | O1-Ru1-O6 | 86.62(11)  |
| O1-Ru1-O3 | 93.16(11) | O3-Ru1-O6 | 86.30(11)  |
| O3-Ru1-O5 | 87.89(11) | O5-Ru1-O6 | 91.10(11)  |
| N1-Ru1-O5 | 98.88(12) | N1-Ru1-O6 | 91.68(13)  |
| O1-Ru1-O4 | 91.39(11) | O1-Ru1-O5 | 177.42(11) |
| O3-Ru1-O4 | 92.12(12) | N1-Ru1-O3 | 172.98(12) |
| O4-Ru1-O5 | 90.92(11) | O4-Ru1-O6 | 177.38(11) |
| N1-Ru1-O4 | 89.64(13) |           |            |

**Table 5.3.3.** Selected bond angles (°) for the  $\Delta$  isomer of complex **4**.

|             |           |             |            |
|-------------|-----------|-------------|------------|
| O1A-Ru1-N1  | 84.94(19) | N1-Ru1-N1A  | 99.37(18)  |
| O1A-Ru1-N1B | 90.66(15) | N1A-Ru1-O1A | 77.71(16)  |
| N1B-Ru1-O1B | 79.10(17) | N1A-Ru1-N1B | 91.58(17)  |
| N1-Ru1-O1B  | 93.0(2)   | N1A-Ru1-O1B | 97.57(16)  |
| N1-Ru1-O1   | 79.78(16) | O1A-Ru1-O1B | 174.42(15) |
| O1-Ru1-O1A  | 91.50(15) | N1-Ru1-N1B  | 167.28(19) |
| O1-Ru1-N1B  | 90.66(15) | O1-Ru1-N1A  | 169.21(17) |
| O1-Ru1-O1B  | 93.22(16) |             |            |

The metal–ligand ( $L_H$ ) distances in both complexes (**2** and **4**) are of typical Ru–N and Ru–O bonds. The Ru–N and Ru–O distances in both complexes are comparatively shorter than in the mono-nuclear complex  $[(bpy)_2Ru^{II}(L_H)](ClO_4)$  (chapter 2), because of the oxidation state change from Ru<sup>II</sup> to Ru<sup>III</sup> in the complexes **2** and **4**. Comparison of bond distances within the coordinated ligand  $L_H$  in **2**, **4**, and the free ligand **L** shows some changes in terms of bond lengths (for example, see O1–C1 and O2–C3 bond lengths in Table 5.3.1).

Upon coordination to the metal center in **2** and **4**, an asymmetrization of the  $\pi$  bonding over the O1–C1–C2–C3–O2 and N1–C6–C5–C4–N2 groups occurs. As a result, some C–O {e.g. C1–O1 [1.301(5) Å in **2** and 1.317(6) Å in **4**]} and C–N {e.g. C4–N2 [1.335(5) Å in **2** and 1.331(6) Å in **4**]} bonds become longer on metal coordination and others {e.g. C3–O2 [1.243(4) Å in **2** and 1.235 (7) Å in **4**] and C6–N1 [1.318(5) Å in **2** and 1.300 (7) Å in **4**]} become shorter. Similarly some C–C {e.g. C2–C3 [1.412(6) Å in **2** and 1.394(8) Å in **4**]} bonds become longer and others {e.g. C2–C3 [1.361(5) Å in **2** and 1.340(8) Å in **4**]} bonds become shorter on metal coordination. Therefore, the two  $\pi$ -systems O1–C1–C2–C3–O2 and N1–C6–C5–C4–N2 separated by C–C single bonds are delocalized in free ligand **L** but localized in **2** and **4**.

The crystal packing of **4** also contains some additional features. NH- group of one moiety forms intermolecular hydrogen bond with the carbonyl oxygen of another moiety (see Figure 5.3.3) (hydrogen bond distance was found to be 2.499 Å, which is less than the sum of the van der waals radii of hydrogen and oxygen (2.72 Å)), thereby leading to the formation of polymeric frameworks.

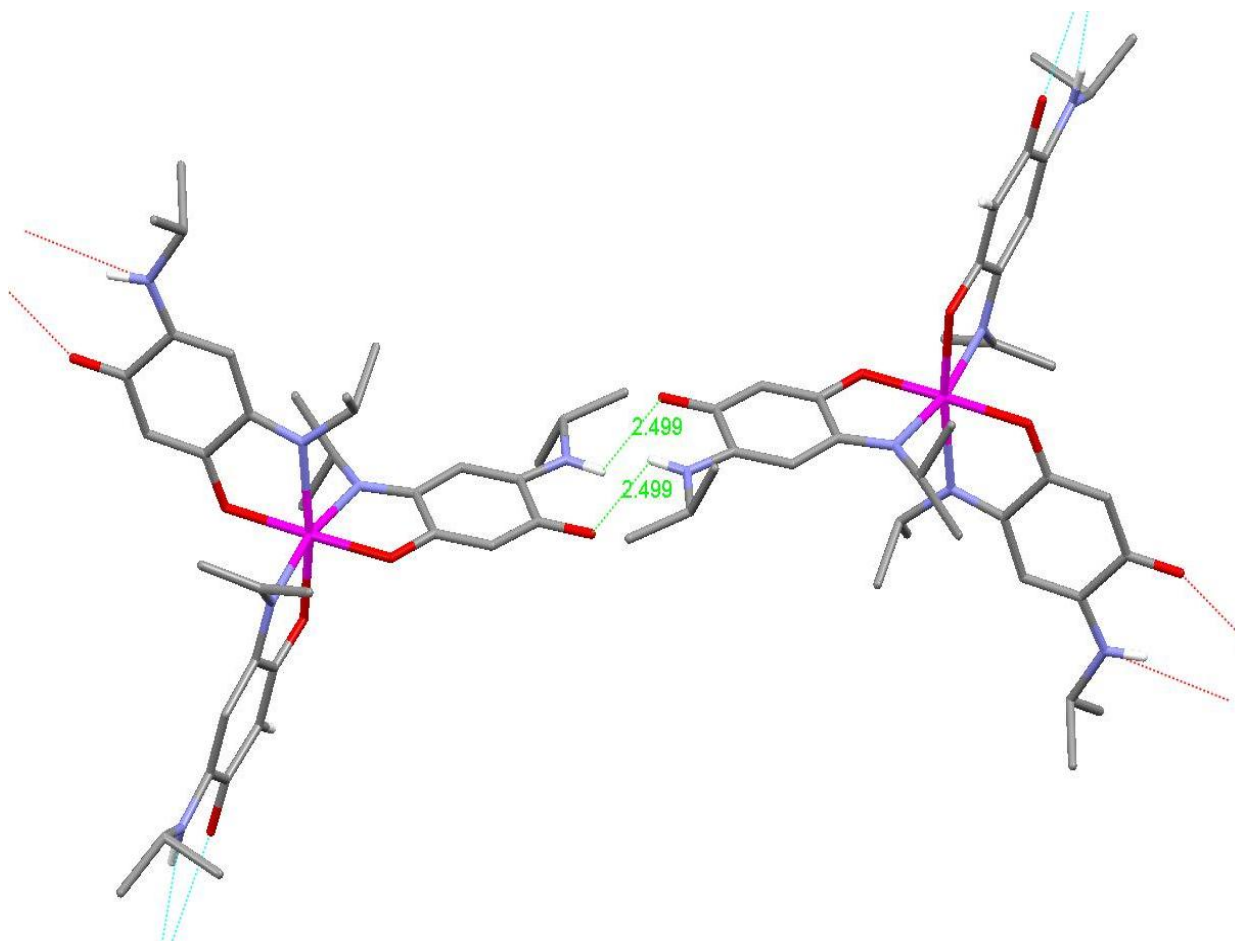


**Figure 5.3.3.** Intermolecular hydrogen bonding in the crystal structure of **4**.

## 5.4. Electrochemistry

The electrochemistry of the complexes **2**, **3** and **4** were studied by cyclic voltammetry in  $\text{CH}_2\text{Cl}_2/0.1 \text{ m Bu}_4\text{NPF}_6$  at 295 K to investigate their redox properties. Ferrocene was used as an internal standard and all the redox potentials are referenced with respect to the ferrocenium/ferrocene ( $\text{Fc}^+/\text{Fc}$ ) couple. The cyclic voltammograms are shown in Figure 6.4.1, while the redox potentials of the complexes are summarized in Table 5.4.1.

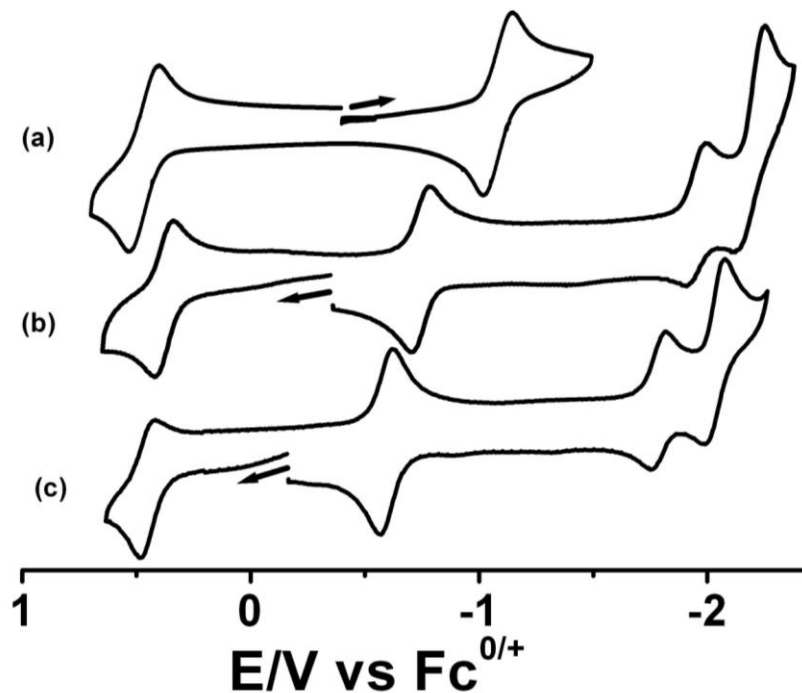


**Figure 5.4.1.** Cyclic voltammograms of **2** (a), **3** (b) and **4** (c) in  $\text{CH}_2\text{Cl}_2/0.1 \text{ m Bu}_4\text{NPF}_6$  at 295 K.

Both the complexes **1** and **2** display one one-electron reversible oxidation and one one-electron reversible reduction (Figure 5.4.1).<sup>[177]</sup> On the other hand, the complexes **3** and **4** undergo one one-electron reversible oxidation and three one-electron reductions within the solvent window (Figure 5.4.1). The third reduction for **3** was found to be an irreversible process, while for **4** it was quasireversible process. For **1**, the redox processes are ruthenium centered,  $\text{Ru}^{\text{III}} \rightarrow \text{Ru}^{\text{IV}}$  (oxidation) and  $\text{Ru}^{\text{III}} \rightarrow \text{Ru}^{\text{II}}$  (reduction).<sup>[177]</sup> For **2**, **3** and **4**, the first oxidation and first reduction could be either ruthenium centred or  $\text{L}_\text{H}$  centred because  $\text{L}_\text{H}$  can also be potentially oxidized or reduced. If the successive replacement of electron donating  $\text{acac}^-$  ligands of **1** by electron withdrawing  $\text{L}_\text{H}$  ligands happen then it will successively increase electron deficiency around the ruthenium centre much more compared to  $\text{L}_\text{H}$ . So, if the first oxidation and first reduction of **2**, **3** and **4** are ruthenium centred then the oxidation

potential should increase successively and the reduction potential should decrease successively from complex **1** to **4**. Whereas if both the process for **2**, **3** and **4** are  $L_{-H}$  centred then the potentials should remain almost unchanged from complex **2** to **4**. For complexes **2**, **3** and **4**, the first oxidation potentials are remain almost unchanged whereas the first reduction potentials are decreased successively which indicate first oxidation is  $L_{-H}$  centred and the first reduction is ruthenium centred (Figure 5.4.1). To verify this hypothesis, UV/Vis/NIR spectroelectrochemistry studies of the complexes **2**, **3** and **4** have been also done (see section 5.6). The separation in peak potential between the first oxidation (ox1) and first reduction (red1) for complexes **1**, **2**, **3** and **4**,  $\Delta E = 1.76, 1.55, 1.11$  and  $1.04$  V translates to comproportionation constants  $K_c = 10^{29.8}, 10^{26.3}, 10^{18.8}$  and  $10^{17.6}$  respectively implying the inherent stability of the Ru(III) state in such complexes.

**Table 5.4.1.** Redox potentials of the complexes **1**, **2**, **3** and **4**.<sup>[a]</sup>

| Complex  | $E_{1/2}^{ox1}$<br>( $\Delta E_p$ ) <sup>[b]</sup> | $E_{1/2}^{red1}$<br>( $\Delta E_p$ ) <sup>[b]</sup> | $E_{1/2}^{red2}$<br>( $\Delta E_p$ ) <sup>[b]</sup> | $E_{1/2}^{red3}$<br>( $\Delta E_p$ ) <sup>[b]</sup> | $K_c=10^{\Delta E/59}$ |
|----------|--|---|---|---|------------------------|
| <b>1</b> | +0.60  | -1.16   |   |   | $6.3 \times 10^{29}$   |
| <b>2</b> | +0.48 (129)  | -1.07 (128)   |   |   | $2 \times 10^{26}$     |
| <b>3</b> | +0.37 (84)   | -0.74 (79)  | -1.94 (84)  | -2.17 (125)   | $6.3 \times 10^{18}$   |
| <b>4</b> | +0.45 (63)   | -0.59 (57)  | -1.79 (70)  | -2.03 (92)  | $4.0 \times 10^{17}$   |

<sup>[a]</sup> Electrochemical potentials in V from cyclic voltammetry in  $CH_2Cl_2/0.1$  M  $Bu_4NPF_6$  at 298 K. Scan Rate: 100 mV/s. Ferrocene / Ferrocenium was used as an internal standard.

<sup>[b]</sup>  $\Delta E_p$ : difference between peak potentials in mV.

## 5.5. EPR Spectroscopy

The complexes **2**, **3** and **4** are paramagnetic in nature. X band EPR measurements were performed to investigate the charge distribution in these complexes. The complexes are EPR silent at room temperature; however, they show EPR signals with large  $g$  shift and anisotropy at 110 K (Figures 5.5.1-3). The EPR data for all four complexes (including **1**) are listed in Table 5.5.1.

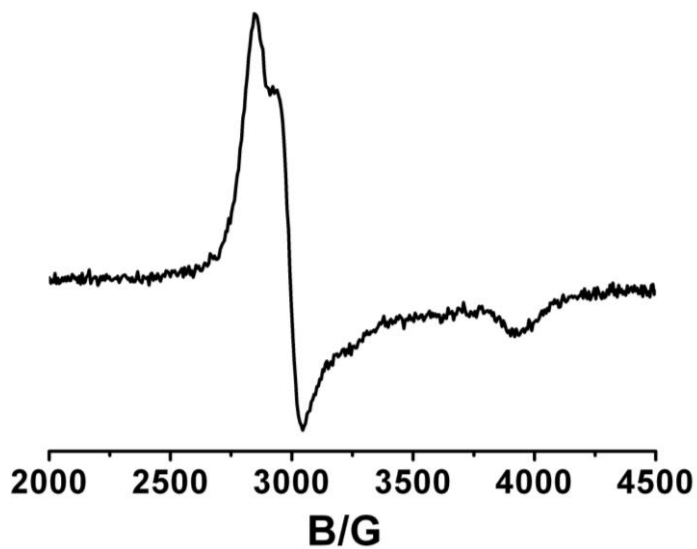


**Figure 5.5.1.** X band EPR spectrum of **2** at 110 K in  $\text{CH}_2\text{Cl}_2/0.1 \text{ M Bu}_4\text{NPF}_6$ .

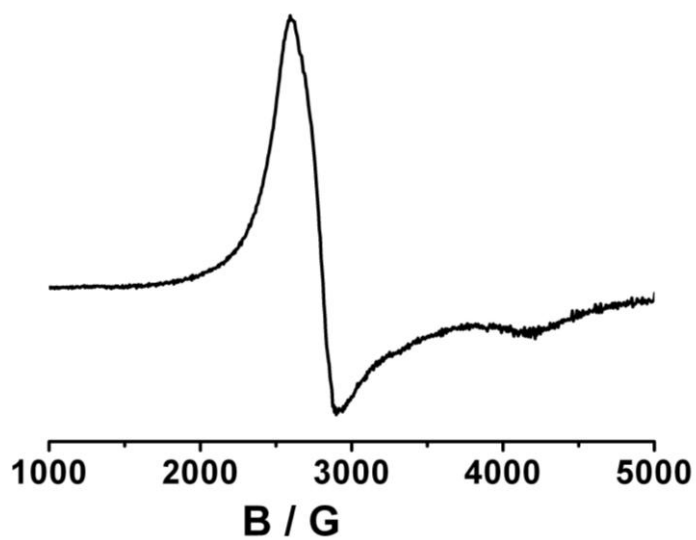


**Figure 5.5.2.** X band EPR spectrum of **3** at 110 K in  $\text{CH}_2\text{Cl}_2/0.1 \text{ M Bu}_4\text{NPF}_6$ .

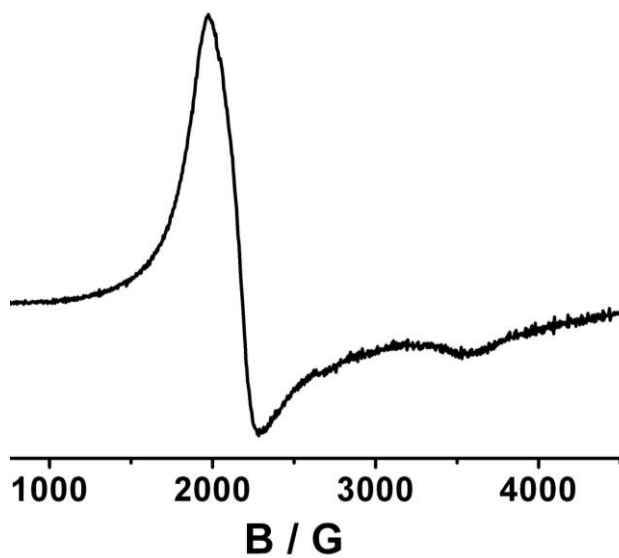


**Figure 5.5.3.** X band EPR spectrum of **4** at 110 K in  $\text{CH}_2\text{Cl}_2/0.1 \text{ M Bu}_4\text{NPF}_6$ .

**Table 5.5.1.** EPR spectroscopic data of the complexes **2**, **3** and **4**.<sup>[a]</sup>

| Complex  | $g_1$ | $g_2$ | $g_3$ | $g_{av}$ <sup>[b]</sup> | $\Delta g = g_1 - g_3$ |
|----------|-------|-------|-------|-------------------------|------------------------|
| <b>1</b> | 2.450 | 2.160 | 1.450 | 2.063                   | 1.000                  |
| <b>2</b> | 2.420 | 2.306 | 1.751 | 2.179                   | 0.669                  |
| <b>3</b> | 2.603 | 2.324 | 1.609 | 2.219                   | 0.994                  |
| <b>4</b> | 3.417 | 2.957 | 1.892 | 2.828                   | 1.525                  |

<sup>[a]</sup> EPR data of species in CH<sub>2</sub>Cl<sub>2</sub> at 110 K. <sup>[b]</sup>  $g_{av} = \sqrt{(g_1^2 + g_2^2 + g_3^2)/3}$ .

Complex **1** exhibits a ruthenium(III) type EPR signal with three  $g$  values ( $g_1 = 2.45$ ,  $g_2 = 2.16$  and  $g_3 = 1.45$ ) having  $g_{av} = 2.063$  and  $\Delta g = 1.0$ .<sup>[178]</sup> For **2**,  $g_{av} = 2.179$  and  $\Delta g = 0.669$  ( $g_1 = 2.420$ ,  $g_2 = 2.306$  and  $g_3 = 1.751$ ). Such values are typical for low-spin  $d^5$  ruthenium(III) complexes having distorted octahedral geometry. The complexes **3** and **4** also exhibit ruthenium(III) type EPR signals with very large  $g_{av}$  value and  $g$  anisotropy. The results of EPR measurements confirm the +III oxidation state of ruthenium in these complexes.

## 5.6. UV/Vis/NIR Spectroelectrochemistry

To obtain information about the electronic spectra of the complex **2**, **3** and **4** in various accessible redox processes, UV-Vis-NIR spectroscopic changes of all the three complexes were monitored using OTTLE spectroelectrochemistry. The spectral results are summarized in table 5.6.1. The UV-Vis spectral data of **1** also included for comparison. Complex **1**, [Ru<sup>III</sup>(acac)<sub>3</sub>] exhibits three absorption bands (Table 5.6.1). According to Kobayashi *et al.* the three absorption bands are assigned as ligand-to-metal charge-transfer transition and intraligand ( $\pi, \pi^*$ ) charge transfer transition.<sup>[179]</sup> The native complex **2**, [Ru<sup>III</sup>(acac)<sub>2</sub>L<sub>H</sub>] exhibits an intense band at 484 nm with a shoulder which can be assigned as mixed of LMCT (acac → Ru<sup>III</sup>) and (L<sub>H</sub> → Ru<sup>III</sup>) transitions. In addition, there are further ligand-centered transitions in the UV region (Figure 5.6.1). Upon one-electron oxidation to **2**<sup>+</sup> the LMCT bands are red-shifted to 530 nm with a substantial decrease in intensity and several shoulders in the Vis-NIR region are observed (Figure 5.6.1 and Table 5.6.1). Upon one-electron reduction to **2**<sup>-</sup>, the LMCT transitions are diminished in intensity and a new intense band appear at 685 nm which can be assigned as MLCT ( $d[\text{Ru}] \rightarrow \pi^*[\text{L}_H]$ ) transition (Figure 5.6.2).

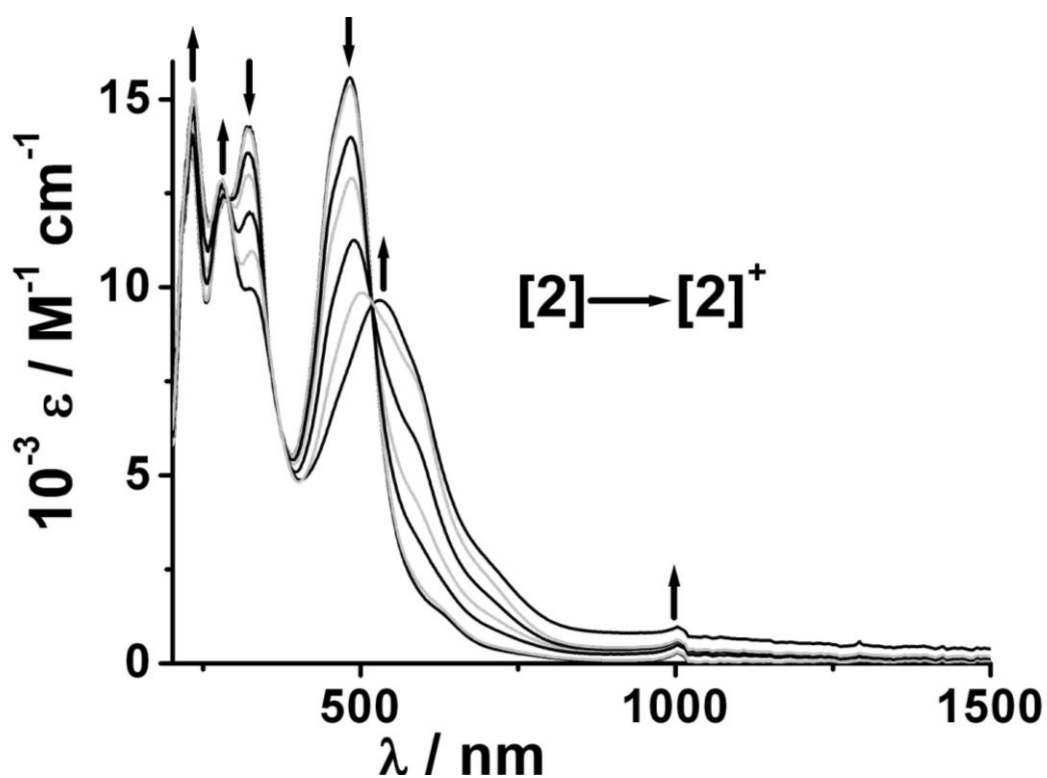


**Figure 5.6.1** UV-Vis-NIR spectroelectrochemistry of the conversion  $[2]^{(0) \rightarrow (+)}$  in  $\text{CH}_2\text{Cl}_2$  / 0.1 M  $\text{Bu}_4\text{NPF}_6$ .

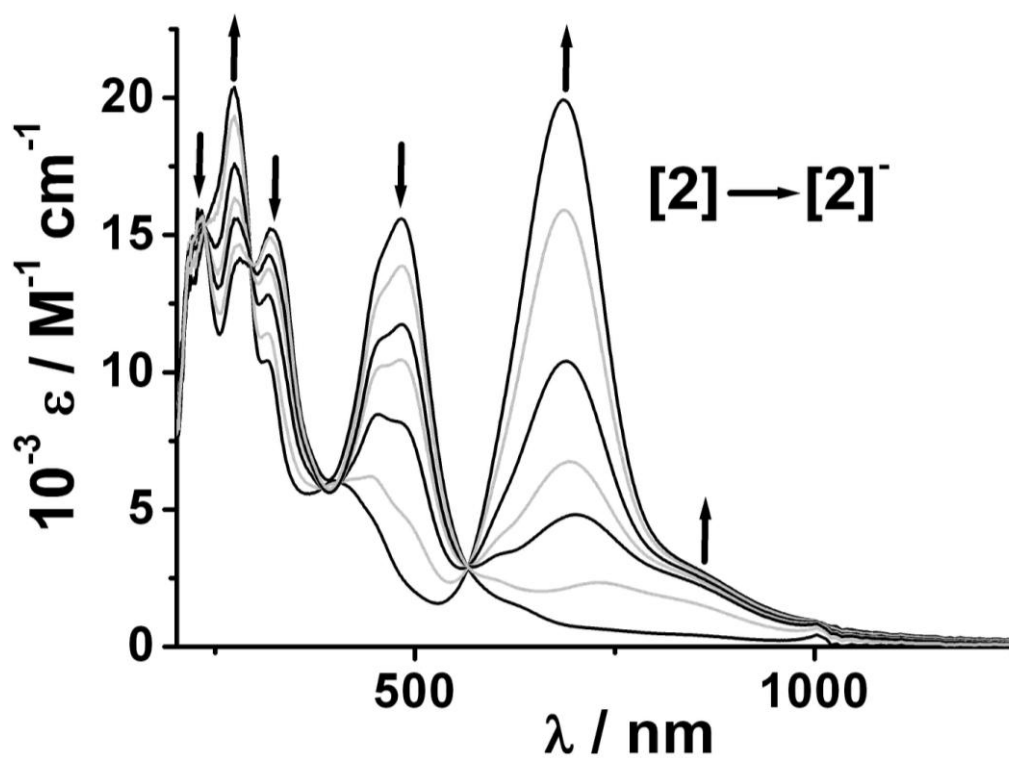


**Figure 5.6.2** UV-Vis-NIR spectroelectrochemistry of the conversion  $[2]^{(0) \rightarrow (-)}$  in  $\text{CH}_2\text{Cl}_2$  / 0.1 M  $\text{Bu}_4\text{NPF}_6$ .

The native complex **3**, [(acac)Ru<sup>III</sup>(L-H)<sub>2</sub>] exhibits an intense absorption band at 503 nm which can be assigned as a LMCT (L-H → Ru<sup>III</sup>) transition and ligand-centered transitions in the UV region (Figure 5.6.3). In the one electron oxidized form **3**<sup>+</sup> the LMCT transitions at 503 nm is blue shifted to 470 nm with a decrease in intensity and a new broad, weak band emerge at about 1100 nm (Figure 5.6.3). The broad absorption band at around 1100 nm is tentatively assigned to intervalence charge transfer (IVCT) transitions between coordinated but weakly interacting non-innocent ligands of different charge and oxidation state.<sup>[180-183]</sup> The oxidation to **3**<sup>+</sup> leads to the formation of [(acac)Ru<sup>III</sup>(L<sup>-</sup>-H)(L<sup>•</sup>-H)]<sup>+</sup> and provide formally a L<sup>-</sup>-H to L<sup>•</sup>-H transition, which can be assigned as SOMO→LUMO. Alternatively such broad weak bands would also be assigned to a *d-d* transition with a Ru<sup>IV</sup> level. This would imply a metal-centred oxidation (Ru<sup>III</sup>→Ru<sup>IV</sup>). To assign this oxidation state perfectly, DFT calculation will be required. On one electron reduction to **3**<sup>-</sup> the LMCT band at 503 nm is disappears and two new intense absorption bands emerges at 663 and 744 nm (Figure 5.6.4), those can be assigned as a MLCT transitions (Ru<sup>II</sup>→L-H) for a [(acac)Ru<sup>II</sup>(L-H)<sub>2</sub>]<sup>-</sup> formulation. Reduction of **3**<sup>-</sup> to **3**<sup>2-</sup> causes the slight change in spectrum. The intensity of the absorption band at 663 nm is decreased and the intensity of the other band at 744 nm is increased with a broad shoulder at around 1025 nm (Figure 5.6.5) suggesting the reduction of one of the two quinonoid ligands. On further reduction to **3**<sup>3-</sup>, the bands lose their intensity (Figure 5.6.6).

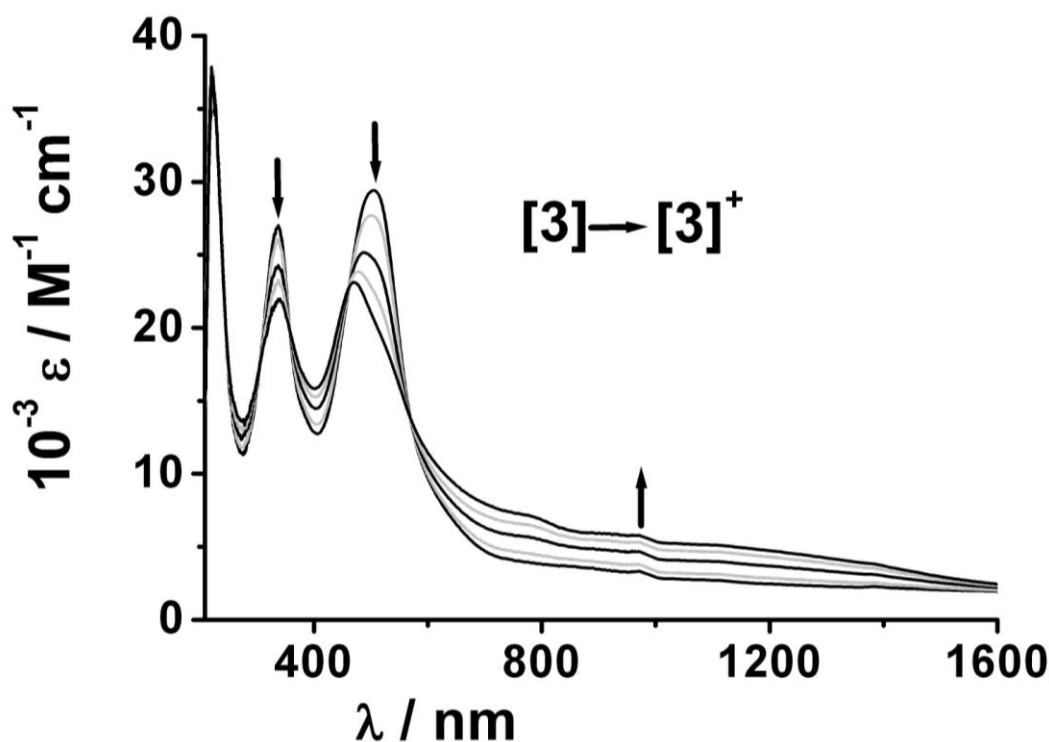


**Figure 5.6.3** UV-Vis-NIR spectroelectrochemistry of the conversion  $[3]^{(0) \rightarrow (+)}$  in  $\text{CH}_2\text{Cl}_2$  / 0.1 M  $\text{Bu}_4\text{NPF}_6$ .



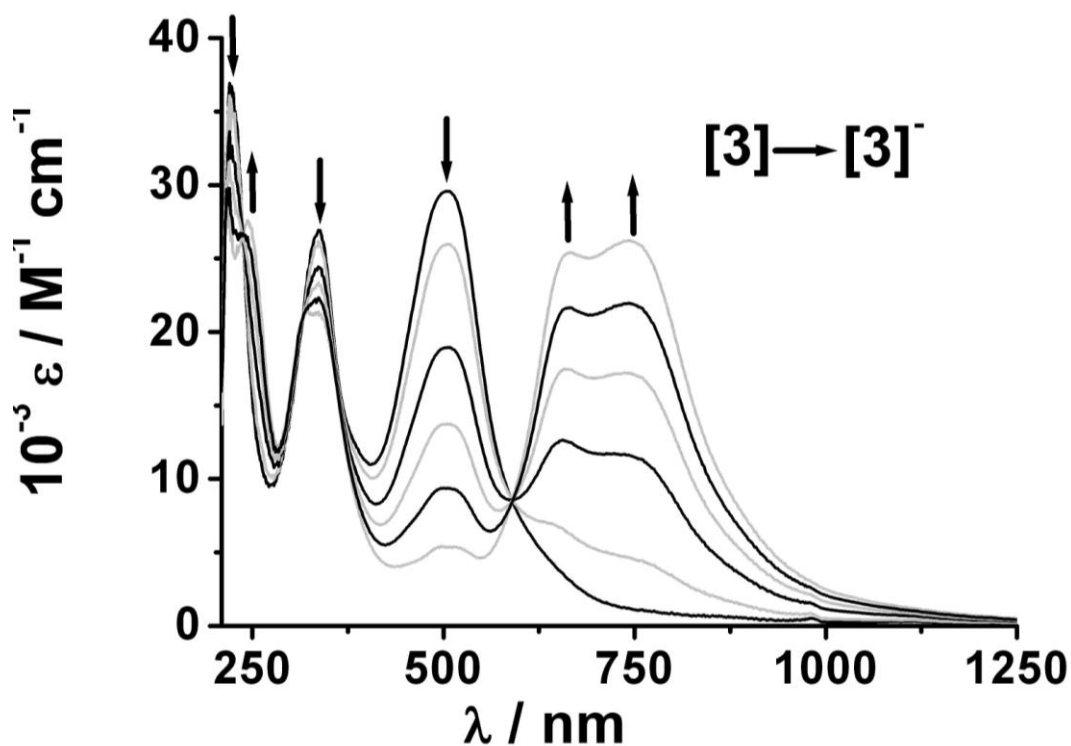


**Figure 5.6.4** UV-Vis-NIR spectroelectrochemistry of the conversion  $[3]^{(0) \rightarrow (-)}$  in  $\text{CH}_2\text{Cl}_2 / 0.1 \text{ M Bu}_4\text{NPF}_6$ .

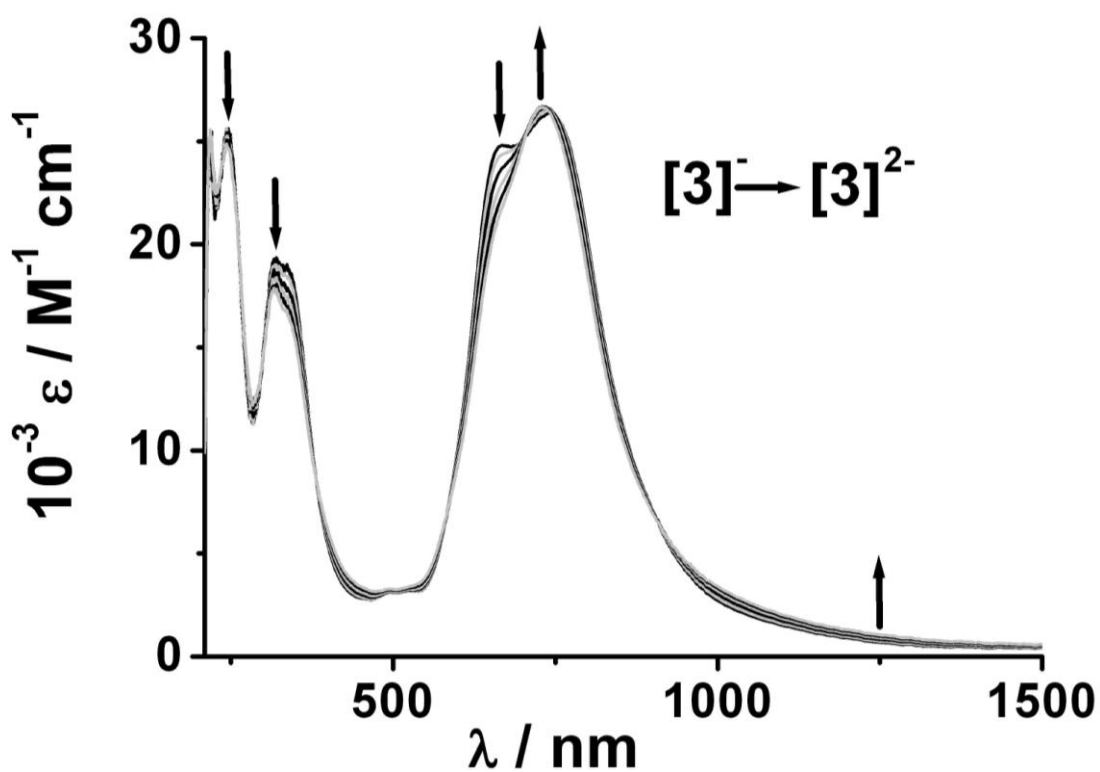


**Figure 5.6.5** UV-Vis-NIR spectroelectrochemistry of the conversion  $[3]^{(-) \rightarrow (2-)}$  in  $\text{CH}_2\text{Cl}_2 / 0.1 \text{ M Bu}_4\text{NPF}_6$ .

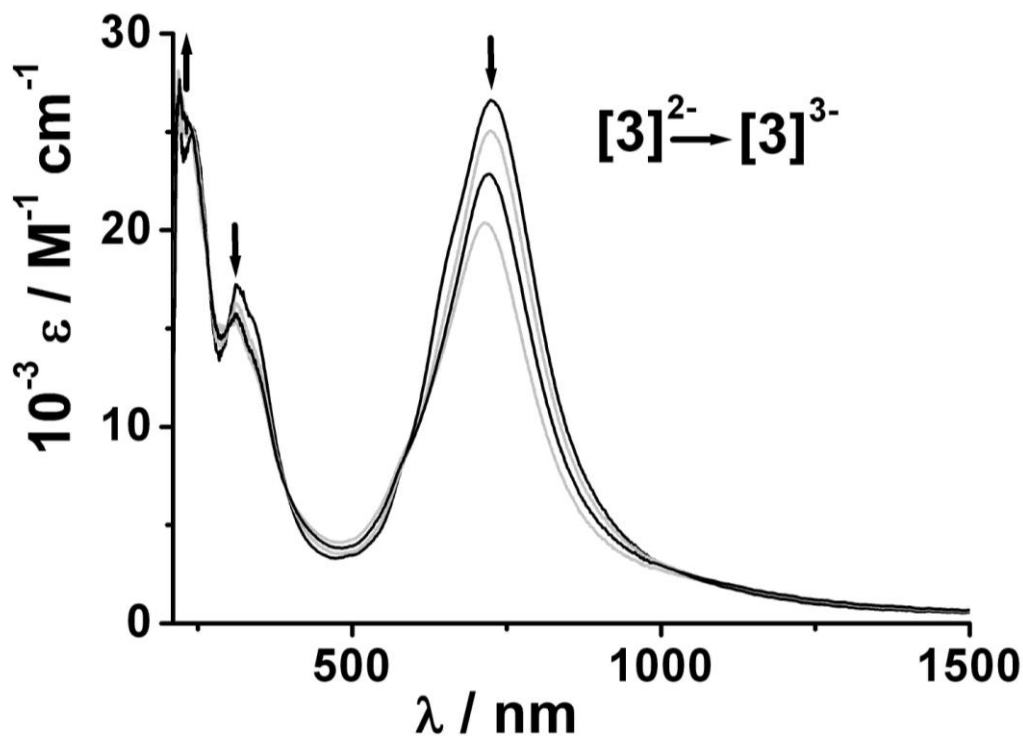


**Figure 5.6.6** UV-Vis-NIR spectroelectrochemistry of the conversion  $[3]^{(2-)\rightarrow(3-)}$  in  $\text{CH}_2\text{Cl}_2$  / 0.1 M  $\text{Bu}_4\text{NPF}_6$ .

Complex **4** shows similar charge transfer transitions like complex **3**. The native complex **4**,  $[\text{Ru}^{\text{III}}(\text{L}_{\cdot\text{H}})_3]$  exhibits an intense LMCT ( $\text{L}_{\cdot\text{H}} \rightarrow \text{Ru}^{\text{III}}$ ) transition at 501 nm and another intense band at 334 nm (Figure 5.6.7). On oxidation to  $\mathbf{4}^+$  the intensity of the band at 334 nm is decreased. The LMCT transition at 501 nm diminishes in intensity and is slightly blue shifted and a new broad, weak band emerge at about 1200 nm (Figure 5.6.7). The intense broad absorption band at around 1200 nm is tentatively assigned to SOMO $\rightarrow$ LUMO intervalence charge transfer (IVCT) transitions between  $\text{L}_{\cdot\text{H}}^-$  and  $\text{L}_{\cdot\text{H}}^\cdot$  for the formulation of  $[\text{Ru}^{\text{III}}(\text{L}_{\cdot\text{H}}^-)_2(\text{L}_{\cdot\text{H}}^\cdot)]^+$  like complex  $\mathbf{3}^+$ . Alternatively such broad weak bands can also be assigned to metal centred oxidation can also be assigned to a  $d-d$  transition with a  $\text{Ru}^{\text{IV}}$  level which would imply a metal-centred oxidation ( $\text{Ru}^{\text{III}} \rightarrow \text{Ru}^{\text{IV}}$ ). To assign this oxidation state perfectly, theoretical DFT calculation will be also required. On one electron reduction to  $\mathbf{4}^-$  the LMCT band at 501 nm disappears and two new intense absorption bands emerges at 660 and 737 nm (Figure 5.6.8), those can be assigned as a MLCT transitions ( $\text{Ru}^{\text{II}} \rightarrow \text{L}_{\cdot\text{H}}$ ) for a  $[\text{Ru}^{\text{II}}(\text{L}_{\cdot\text{H}})_3]^-$  formulation. Reduction of  $\mathbf{4}^-$  to  $\mathbf{4}^{2-}$  causes a slight change in charge transfer transitions. The intensity of the absorption band at 660 nm is decreased and the intensity of the other band at 737 nm is increased with a broad shoulder at around 1025 nm (Figure 5.6.9) suggesting the reduction of one quinonoid ligand. On further reduction to  $\mathbf{4}^{3-}$ , the bands lose intensity (Figure 5.6.10), suggesting reduction of one more quinonoid ligand.

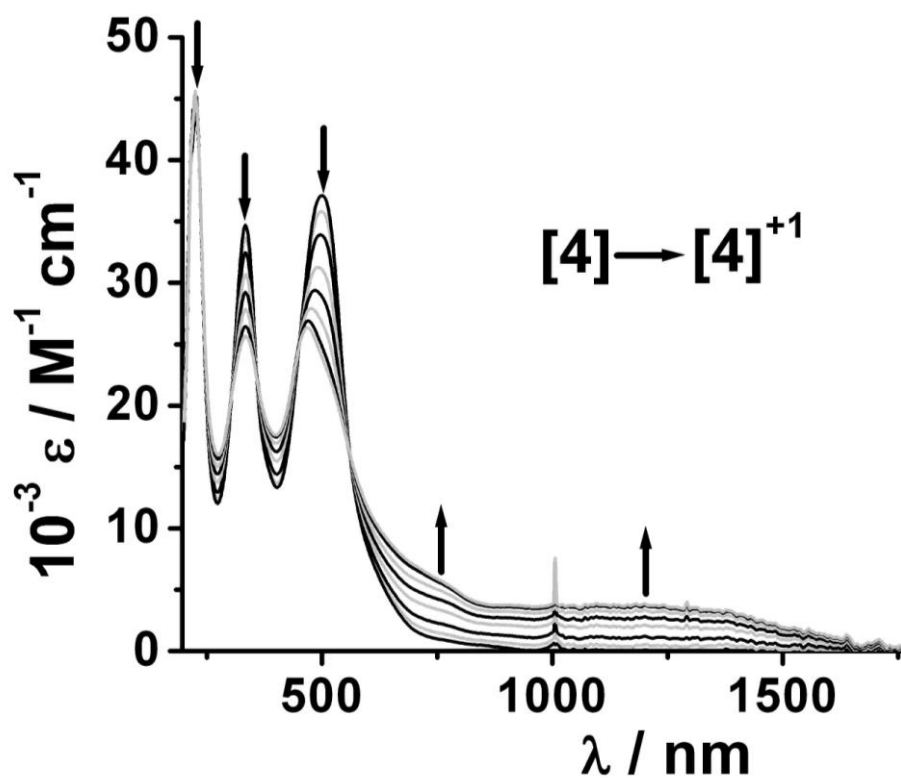


**Figure 5.6.7** UV-Vis-NIR spectroelectrochemistry of the conversion  $[4]^{(0) \rightarrow (+)}$  in  $\text{CH}_2\text{Cl}_2$  / 0.1 M  $\text{Bu}_4\text{NPF}_6$ .

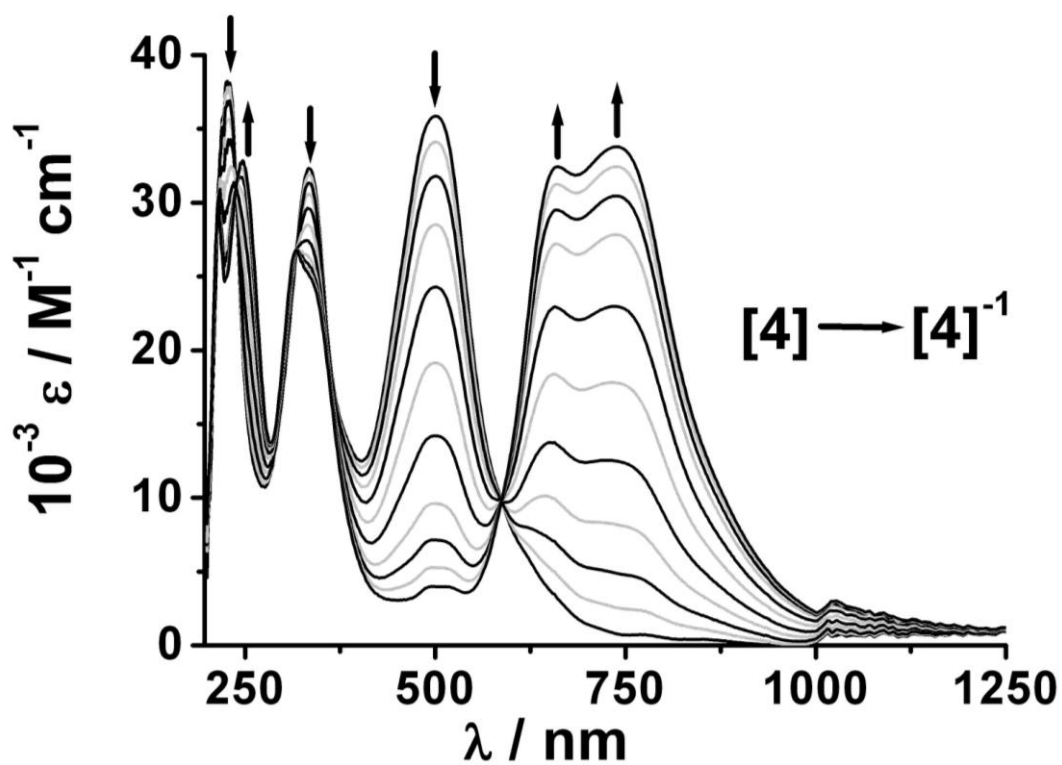


**Figure 5.6.8** UV-Vis-NIR spectroelectrochemistry of the conversion  $[4]^{(0) \rightarrow (-)}$  in  $\text{CH}_2\text{Cl}_2$  / 0.1 M  $\text{Bu}_4\text{NPF}_6$ .

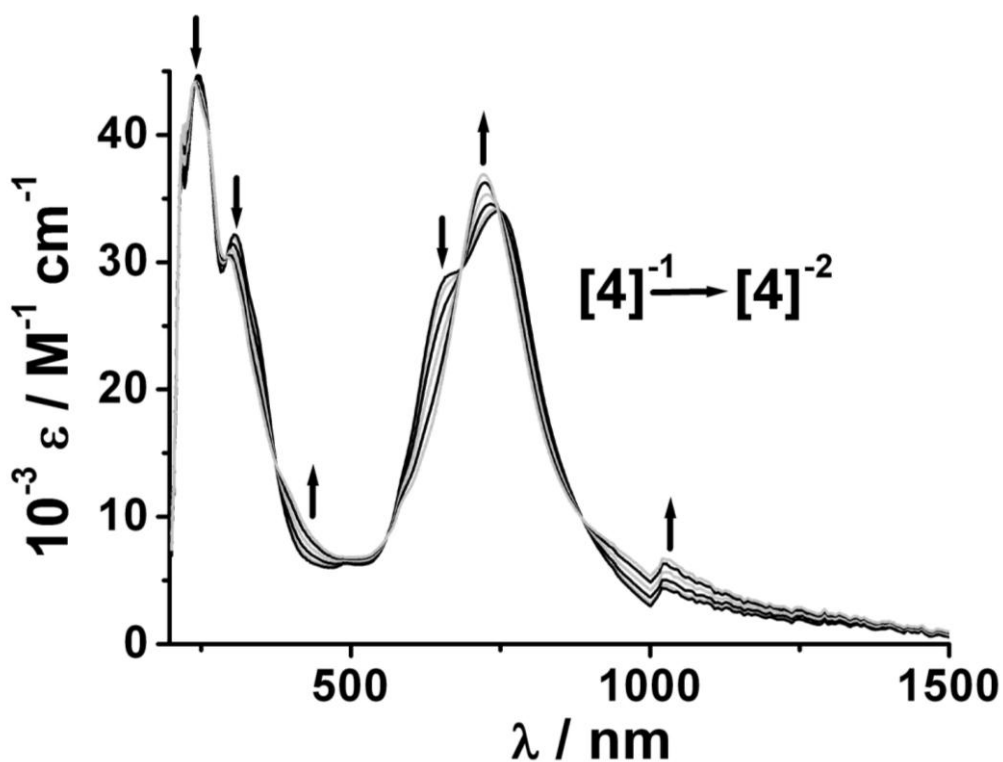


**Figure 5.6.9** UV-Vis-NIR spectroelectrochemistry of the conversion  $[4]^{(-)} \rightarrow [4]^{(2-)}$  in  $\text{CH}_2\text{Cl}_2 / 0.1 \text{ M Bu}_4\text{NPF}_6$ .

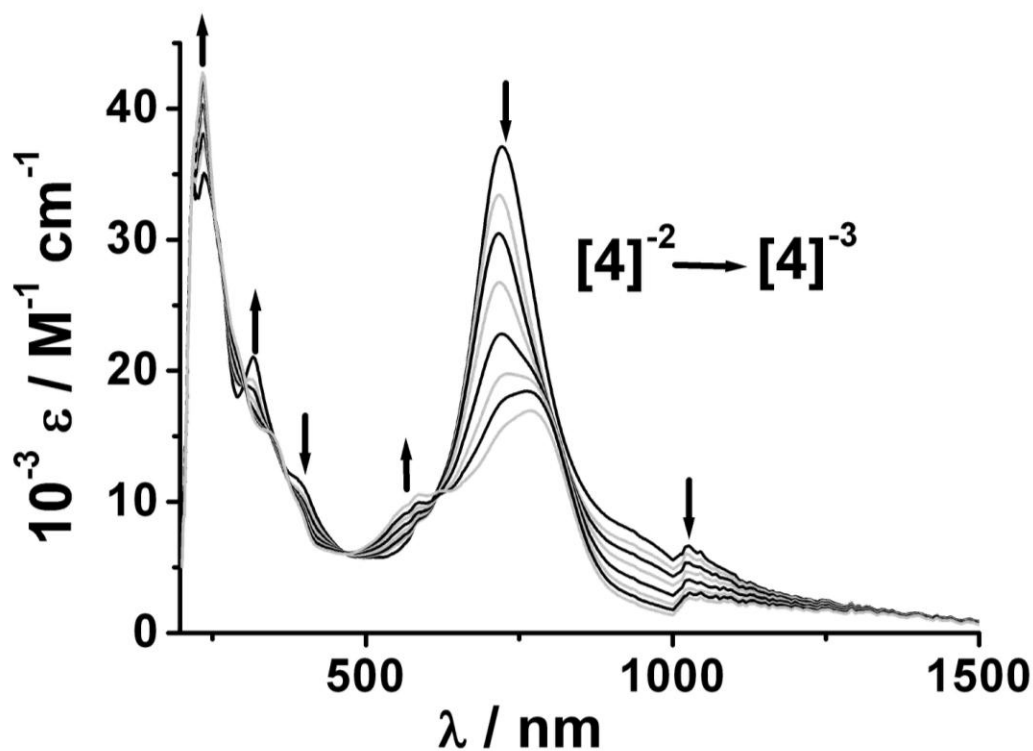


**Figure 5.6.10** UV-Vis-NIR spectroelectrochemistry of the conversion  $[4]^{(2-)} \rightarrow [4]^{(3-)}$  in  $\text{CH}_2\text{Cl}_2 / 0.1 \text{ M Bu}_4\text{NPF}_6$ .

**Table 5.6.1.** Absorption data from UV/Vis/NIR spectroelectrochemistry.<sup>[a]</sup>

| Compound              | $\lambda_{\max}$ [nm] ( $\epsilon$ [ $\text{m}^{-1}\text{cm}^{-1}$ ])          |
|-----------------------|--|
| <b>1</b>              | 272 (17.4), 349 (8.7), 506 (1.5)   |
| <b>2</b>              | 233 (13.6), 282 (12.3), 333 (14.3), 455 (sh), 484 (15.6)                       |
| <b>2<sup>+</sup></b>  | 234 (15.3), 281 (12.9), 326 (10.0), 531 (9.6), 1100 (br, 0.7)                  |
| <b>2<sup>-</sup></b>  | 273 (20.4), 315 (10.5), 400 (6.0), 458 (sh), 685 (20.0), 845 (sh)              |
| <b>3</b>              | 221 (36.9), 336 (27.1), 503 (29.7)   |
| <b>3<sup>+</sup></b>  | 219 (37.9), 339 (21.9), 470 (23.2), 1062 (br, 5.2)                             |
| <b>3<sup>-</sup></b>  | 217 (27.8), 243 (27.7), 330 (21.3), 505 (5.5), 663 (25.5), 744 (26.3)          |
| <b>3<sup>2-</sup></b> | 218 (25.5), 245 (24.8), 670 (sh), 731 (26.7)                                   |
| <b>3<sup>3-</sup></b> | 224 (27.8), 312 (15.4), 716 (20.4)   |
| <b>4</b>              | 225 (43.8), 334 (34.7), 501 (37.2)   |
| <b>4<sup>+</sup></b>  | 226 (45.3), 334 (25.7), 468 (26.4), 737 (sh), 1194 (3.9)                       |
| <b>4<sup>-</sup></b>  | 215 (29.3), 247 (32.9), 317 (26.8), 502 (4.1), 659 (32.6), 739 (33.9)          |
| <b>4<sup>2-</sup></b> | 220 (40.8), 238 (44.1), 295 (30.4), 424 (sh), 721 (37.1), 1021 (6.7)           |
| <b>4<sup>3-</sup></b> | 221 (37.8), 233 (42.8), 343 (sh), 391 (sh), 582 (10.7), 767 (17.1), 1028 (2.7) |

<sup>[a]</sup> From spectroelectrochemistry in an OTTLE cell in  $\text{CH}_2\text{Cl}_2$  / 0.1 M  $\text{Bu}_4\text{NPF}_6$  at 298 K.

## 5.7 Conclusion

A new paramagnetic substitution series  $[\text{Ru}(\text{L-H})_n(\text{acac})_{3-n}]$  (where  $n = 1-3$ ) have been synthesized and characterized in this chapter. The crystal structures of  $[\text{Ru}(\text{L-H})_1(\text{acac})_2]$  and  $[\text{Ru}(\text{L-H})_3]$  reveal the localization of the  $\pi$ -systems of the quinonoid ligand in the complexes. In addition, intermolecular non-covalent interaction involving NH- of one moiety with carbonyl oxygen of another moiety leads to the formation of polymeric framework in the crystal packing of  $[\text{Ru}(\text{L-H})_3]$ . The oxidation state of ruthenium in native complexes is +III and show EPR signals type of a low spin  $d^5$  centre at 110K with a high  $g$  anisotropy. The first oxidation of the complexes **2**, **3** and **4** could be either quinonoid centred ( $\text{L-H}$ ) or  $\text{Ru}^{\text{III}}$  centered but the  $\text{L-H}$  centered oxidation is more pronounced because the oxidation potentials are remain almost constant on successive replacement of electron donating  $\text{acac}^-$  ligands by electron withdrawing  $\text{L-H}$  ligands. In addition, the appearance of an intense broad absorption band at NIR region for the complexes  $[\text{Ru}(\text{L-H})_2(\text{acac})]^+$  and  $[\text{Ru}(\text{L-H})_3]^+$  due to the ligand contribution at the singly occupied molecular orbital (SOMO) also support  $\text{L-H}$  centered oxidation. Thus, the one electron oxidation of  $[\text{Ru}(\text{L-H})_2(\text{acac})]$  and  $[\text{Ru}(\text{L-H})_3]$  leads to ligand centred mixed-valent system. Moreover, one electron reduction of these complexes could be either  $\text{Ru}^{\text{III}}$  centered or  $\text{L-H}$  centered. However,  $\text{L-H}$  centred reduction normally occurs at higher potential than those observed here (chapter 2) and the successive decrease of reduction potential on successive replacement of electron donating  $\text{acac}^-$  ligands by electron withdrawing  $\text{L-H}$  suggest metal centered reduction. Hence the first reduction steps are assigned to metal centred reduction of  $\text{Ru}^{\text{III}}$  to  $\text{Ru}^{\text{II}}$ . The UV/Vis/NIR spectroelectrochemical results also support metal centered reduction.

## CHAPTER 6

### Isomeric Forms Separation and Their Valence and Spin Situations in Different Redox State of a $[\text{Ru}(\text{bpy})(\text{L}\cdot\text{H})_2]$ System; $\text{L} = \text{N,N}'\text{-Diisopropyl-2-amino-5-alcoholate-1,4-benzoquinonemonoiminium}$ or $2,5\text{-Bis(isopropylamino)-1,4-benzoquinone}$

#### 6.1. Introduction

Redox-active quinonoid ligands are a fascinating class molecules<sup>[184]</sup> that display non-innocent behaviour and ligand-metal orbital mixing (covalency) in their transition metal complexes.<sup>[185-188]</sup> A great deal of work has been carried out in establishing this ligand-metal orbital mixing by varying the electronic nature of the quinonoid ligands and also the ancillary ligands.<sup>[188-191]</sup> The ruthenium complexes with quinonoid ligands show such mixing considerably and thus valence ambiguities arise to assign their oxidation states.<sup>[188]</sup> The metal complexes with two or more quinonoid ligands not only show metal and ligand based frontier orbitals mixing but also show ligand-to-ligand IVCT transitions in their mixed-valence state (Chapter 5). Sometime the mononuclear complexes of quinonoid ligands such as  $\text{L}^1$  or  $\text{L}^2$  (Figure 6.1.1) are also able to show non-covalent interactions through the metal free site (Chapter 3 and 5). Such non-covalent interactions play a key role in the fields of chemistry, pharmaceutical design, supramolecular chemistry, molecular biology, materials and crystal engineering.<sup>[192-195]</sup>

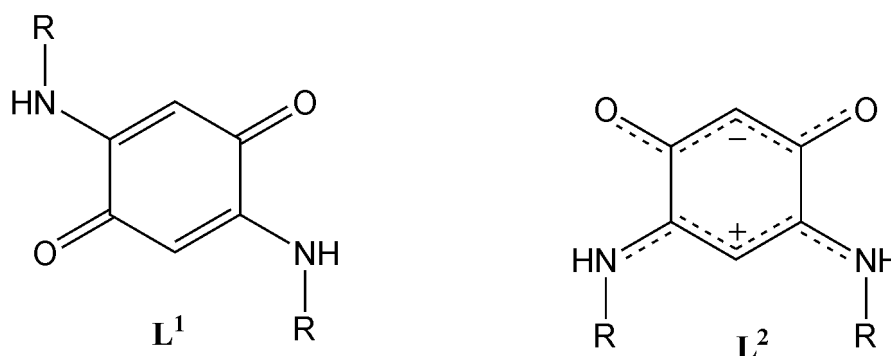


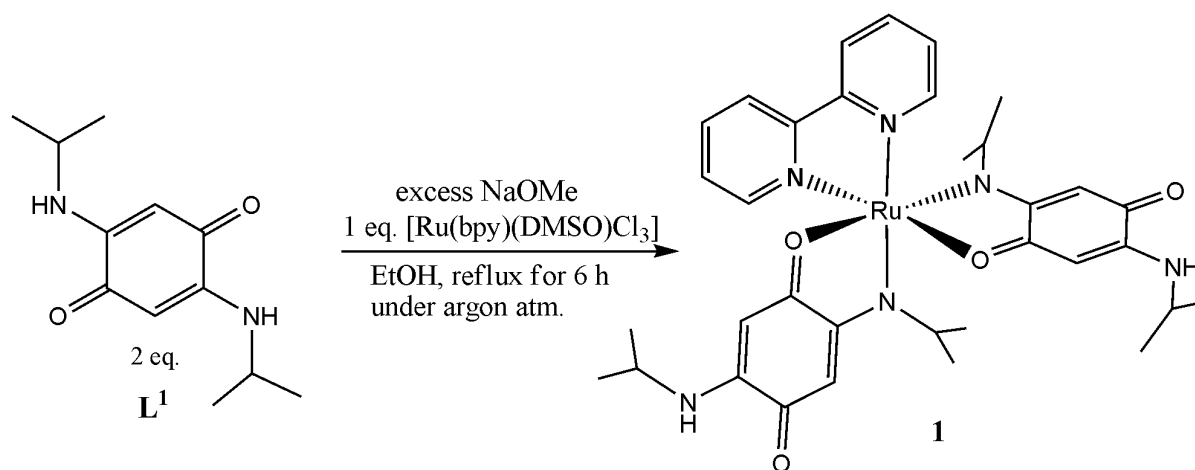
**Figure 6.1.1.** Molecular formulae of two quinonoid non-innocent ligands ( $\text{L}^1$  and  $\text{L}^2$ ).

This chapter describes the syntheses, structures, isomerism, redox properties, charge distribution and non-covalent interactions of the complexes  $[\text{Ru}(\text{bpy})(\text{L}^1\cdot\text{H})_2]$  (**1**) and  $[\text{Ru}(\text{bpy})(\text{L}^2\cdot\text{H})_2]$  (**2**) where  $\text{bpy} = 2,2'$ -bipyridine,  $\text{L}^1 = 2,5\text{-bis(isopropylamino)-1,4-}$

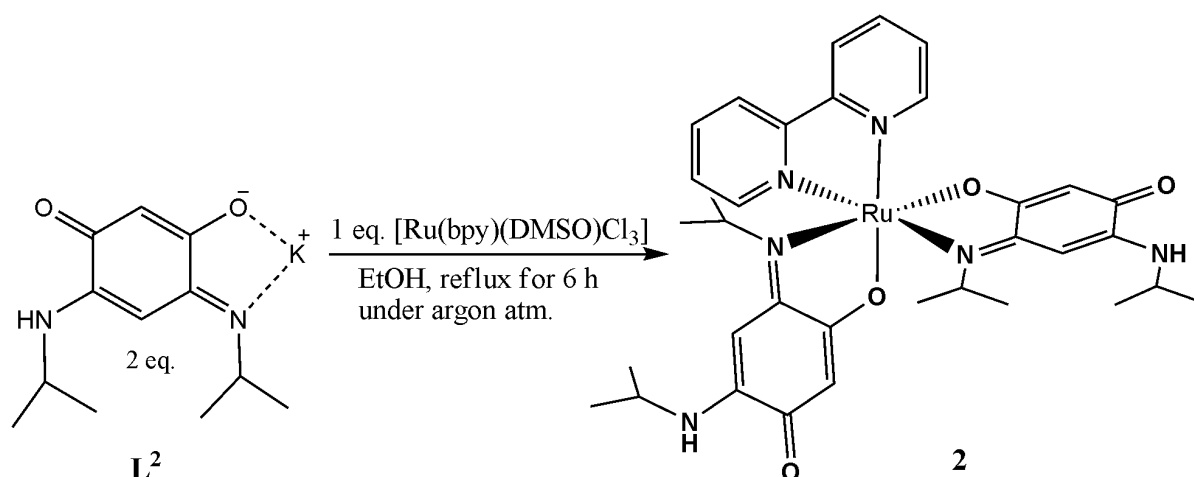
benzoquinone and  $L^2 = N,N'$ -diisopropyl-2-amino-5-alcoholate-1,4-benzoquinonemonoiminium.

## 6.2. Synthesis, characterization

The ligand  $L^1$  was prepared as depicted in chapter 3 and the ligand  $L^2$  was prepared as reported.<sup>[69]</sup> The mononuclear complex **1** was synthesized in a one-pot reaction by reacting 1 eq. of *mer*-[Ru(bpy)(DMSO)Cl<sub>3</sub>] with two eq. quinonoid ligand  $L^1$  in the presence of excess sodium methoxide in refluxing ethanol (Scheme 6.2.1), whereas complex **2** was synthesized by the reaction of 1 eq. of *mer*-[Ru(bpy)(DMSO)Cl<sub>3</sub>] with two eq. monodeprotonated form of  $L^1$ <sup>[69]</sup> in refluxing ethanol (Scheme 6.2.2). The metal precursor *mer*-[Ru(bpy)(DMSO)Cl<sub>3</sub>] was synthesized from RuCl<sub>3</sub>·xH<sub>2</sub>O by the initial synthesis of [H(DMSO)<sub>2</sub>][*trans*-RuCl<sub>4</sub>(DMSO)<sub>2</sub>].<sup>[196-197]</sup>



**Scheme 6.2.1.** Synthetic scheme for complex **1**.



**Scheme 6.2.2.** Synthetic scheme for complex **2**.



The complexes **1** and **2** were purified by column chromatography using neutral alumina column. The complexes were characterized by  $^1\text{H}$  NMR, electrospray mass spectroscopy and elemental analysis (see experimental section). Both the complexes can exist in three diastereomeric forms (Figure 6.2.1). The three diastereomers were separable only in the case of **1** (**1a** {less polar}, **1b** {medium polar}, and **1c** {more polar}) by quantitative TLC separation. In case of **2** we were able to separate only two diastereomers (**2a** {less polar} and **2b** {more polar}) by quantitative TLC separation. All the diastereomers are distinguishable in the  $^1\text{H}$  NMR (see experimental part) and  $\lambda_{\text{max}}$  in the visible region (see latter part of this chapter).

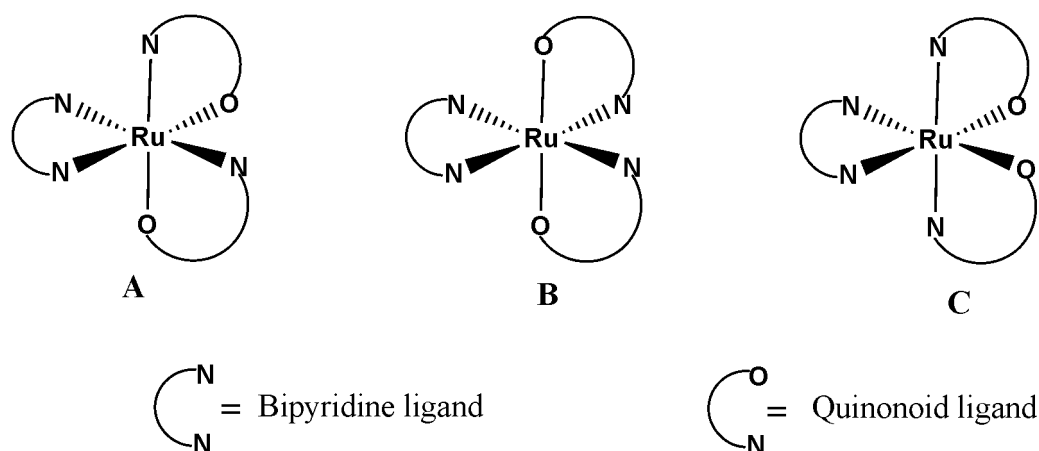


**Figure 6.2.1.** Three possible diastereomers for the system  $[\text{Ru}(\text{bpy})(\text{L-H})_2]$  ( $\text{L}$  = quinonoid ligand)

### 6.3. Crystal Structure of **1c**

We were able to get the single-crystal X-ray crystal structure of one of the diastereomer (**1c**) of the complex **1**. The single crystals of **1c** were obtained by the slow evaporation of its dichloromethane solution at 277 K. The crystal structure of the complex is depicted in Figure 6.3.1 and 6.3.2. Selected bond lengths and bond angles of the complex **1c** are listed in Tables 6.3.1 and 6.3.2, while X-ray diffraction parameters and crystallographic data are reported in Chapter 10.

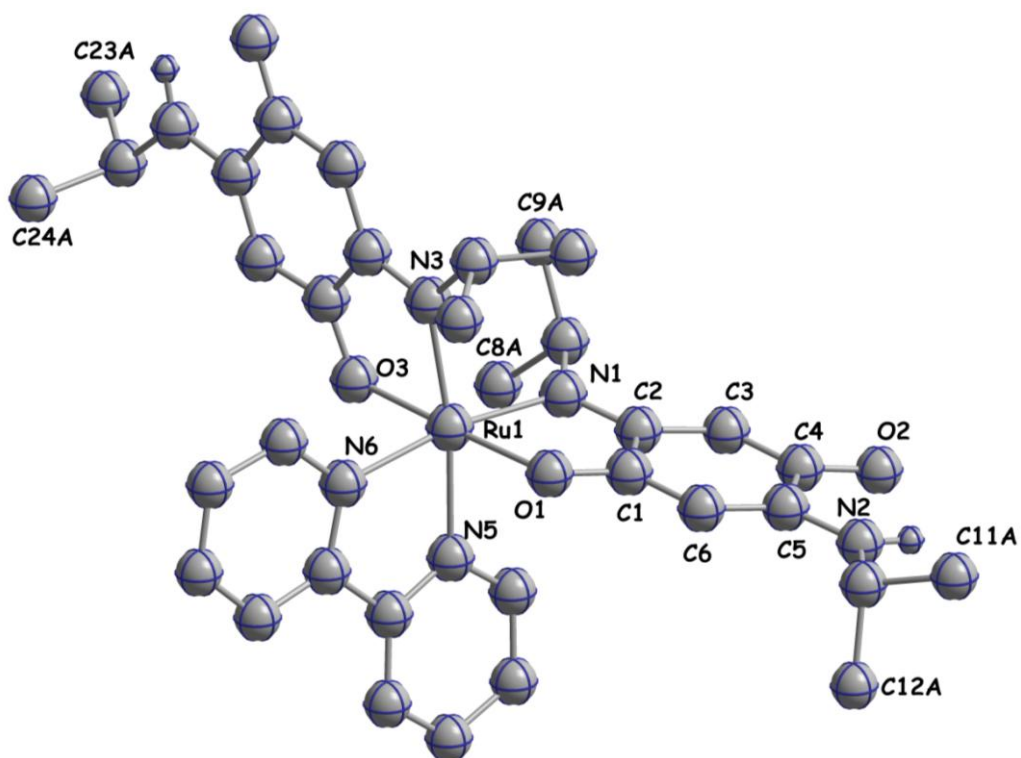


**Figure 6.3.1.** Molecular structure of the diastereomer **1c** in the crystal. Hydrogen atoms, except HN omitted for clarity.

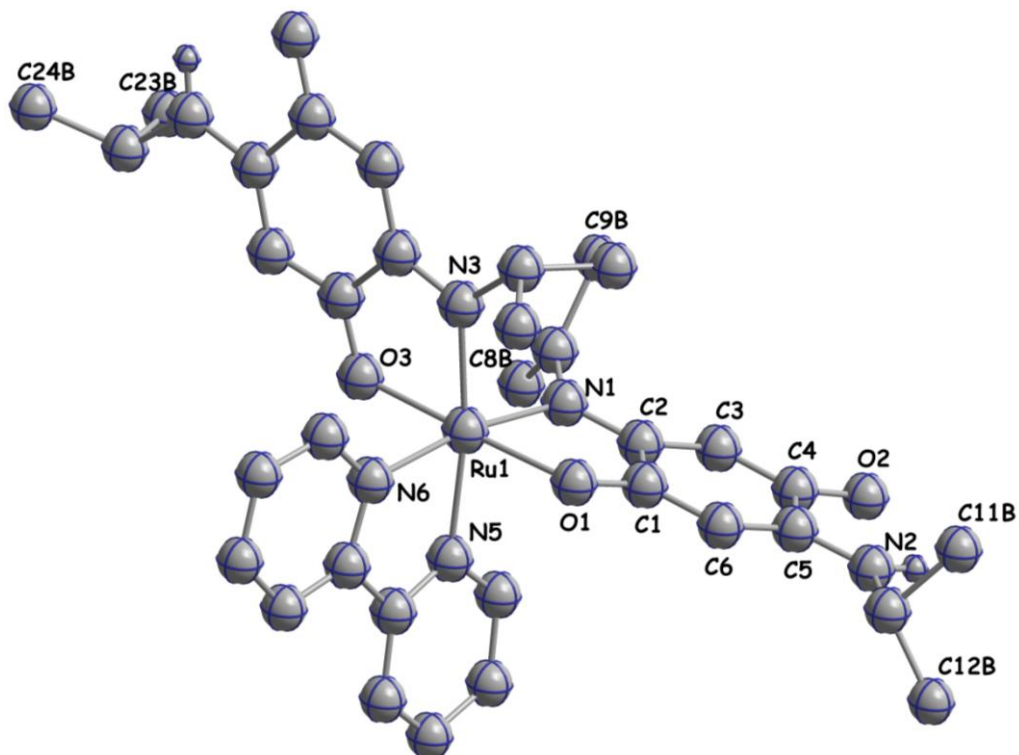


**Figure 6.3.2.** Molecular structure of the diastereomer **1c'** in the crystal. Hydrogen atoms, except HN omitted for clarity.

The crystal structure of complex **1c** reveals the distorted octahedral geometry around ruthenium metal centre. In complex **1c**, the ruthenium center is coordinated by two oxygen atoms and two nitrogen atoms from the two quinonoid ligands ( $L^1_{-H}$ ) and remaining coordination sites are occupied by two nitrogen atoms of bipyridine ligand. Each quinonoid ligand is bonded in complex **1c** in mono deprotonated form and the two coordinated nitrogen atoms of them are *trans* to each other. In the crystal lattice, complex **1c** exhibits a perfectly statistical disorder with both isopropyl groups of one coordinated quinonoid ligand and one isopropyl group in the metal free site of another coordinated quinonoid ligand.

**Table 6.3.1** Selected bond lengths [Å] for **1c**.

|       |           |        |           |
|-------|-----------|--------|-----------|
| C1-C2 | 1.465(16) | O1-C1  | 1.292(14) |
| C2-C3 | 1.441(17) | C4-O2  | 1.266(14) |
| C3-C4 | 1.396(16) | C2-N1  | 1.334(13) |
| C4-C5 | 1.511(18) | C5-N2  | 1.352(14) |
| C5-C6 | 1.386(17) | Ru1-O1 | 2.078(7)  |
| C6-C1 | 1.394(15) | Ru1-N1 | 2.049(12) |

**Table 6.3.2** Selected bond angles (°) for the complex **1c**.

|           |          |           |          |
|-----------|----------|-----------|----------|
| O1-Ru1-N1 | 78.7(4)  | N1-Ru1-N5 | 92.6(4)  |
| O1-Ru1-N6 | 97.0(4)  | N5-Ru1-O1 | 84.2(3)  |
| O3-Ru1-N6 | 84.7(4)  | N5-Ru1-N6 | 78.0(4)  |
| N1-Ru1-O3 | 99.7(4)  | N5-Ru1-O3 | 96.4(3)  |
| N1-Ru1-N3 | 95.1(5)  | N1-Ru1-N6 | 170.1(4) |
| N3-Ru1-O1 | 101.0(3) | N3-Ru1-N5 | 171.5(5) |
| N3-Ru1-O3 | 78.5(3)  | O1-Ru1-O3 | 178.3(4) |
| N3-Ru1-N6 | 94.5(4)  |           |          |

The metal–ligand ( $L^1_{-H}$ ) distances Ru–N (2.049 Å) and Ru–O (2.078 Å) in complex **1c** are of typical Ru–N and Ru–O bonds (Chapter 3). A look at the bond distances within coordinated  $L^1$  (Figure 6.3.1) shows that there is an extensive delocalization within the two  $\pi$ -systems O1-C1-C6-C5-N2 and N1-C2-C3-C4-O2 separated by authentic C–C single bonds (Table 5.3.1) compared to free ligand  $L^1_{-H}$ .<sup>[141]</sup> Such delocalization leads to  $\delta^+$  charge on the NH group and  $\delta^-$  charge on the carbonyl oxygen in the metal free site that is stabilized by strong intermolecular hydrogen bonds with the carbonyl oxygen and NH group of another moiety

(Figure 6.3.3) (hydrogen bond distance was found to be 2.161 Å, which is less than the sum of the van der Waals radii of hydrogen and oxygen (2.72 Å)), thereby leading to the formation of extended 3-D frameworks.

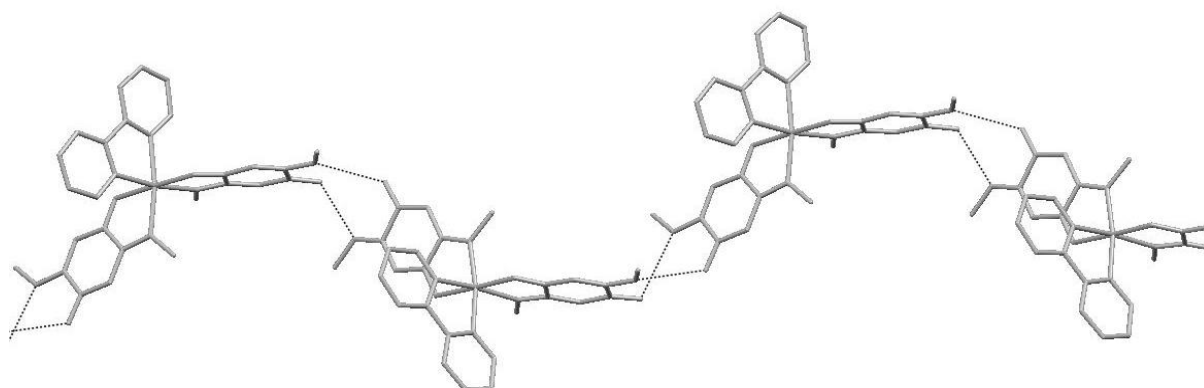


**Figure 6.3.3.** Intermolecular hydrogen bonding in the crystal structure of **1c**.

In the crystal structure of **1c**, the oxygen atoms of coordinated quinonoid ligands are also bonded with water molecules through hydrogen bonds. A repeating hexanuclear water cluster in chair form is situated in the middle of four  $[\text{Ru}(\text{bpy})(\text{L}^1\text{-H})_2]$  units connected directly with two coordinated oxygen atoms in two  $[\text{Ru}(\text{bpy})(\text{L}^1\text{-H})_2]$  units and indirectly via a water molecule with two oxygen atoms of two  $[\text{Ru}(\text{bpy})(\text{L}^1\text{-H})_2]$  units in the metal free sites (Figure 6.3.4). This type of quinonoid mediated hydrogen bonds and structure has great importance in the field of bio-inhibitors and it can also be useful for the stabilization of less stable molecules.

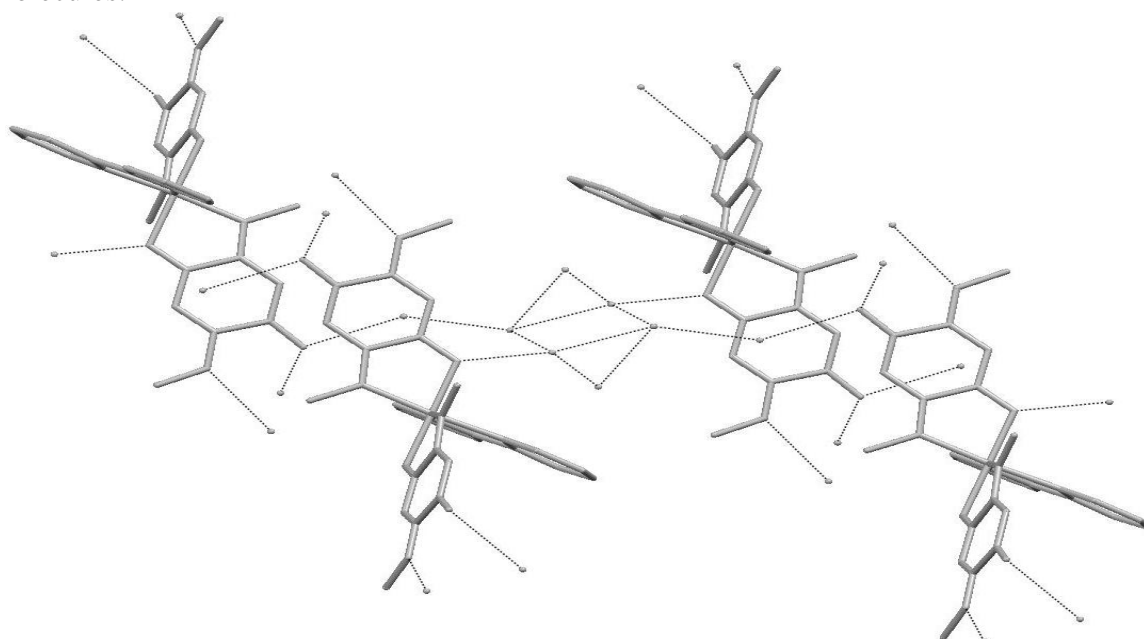


**Figure 6.3.4.** Hydrogen bonding within the crystal structure of  $[\text{Ru}(\text{bpy})(\text{L}^1\text{-H})_2]$  with a water cluster. Hydrogen atoms and methyl carbon atoms omitted for clarity.

## 6.4. Electrochemistry

The electrochemistry of the complexes **1** and **2** were studied by cyclic voltammetry in CH<sub>3</sub>CN/0.1 m Bu<sub>4</sub>NPF<sub>6</sub> at 295 K to investigate their redox properties. Ferrocene was used as an internal standard and all the redox potentials are referenced with respect to ferrocenium/ferrocene (Fc<sup>+</sup>/Fc) couple. The cyclic voltammogram of **1a** and **2a** are shown in Figure 6.4.1 while the reduction and the oxidation potential of all the isomers are summarized in Table 6.4.1.

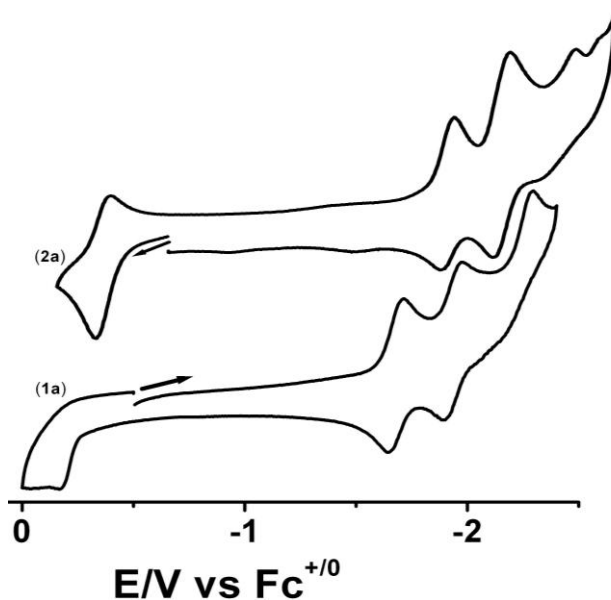


**Figure 6.4.1.** Cyclic voltammograms of **1a** and **2a** in CH<sub>3</sub>CN/0.1 m Bu<sub>4</sub>NPF<sub>6</sub> at 295 K

**Table 6.4.1.** Redox potentials of the complexes.<sup>[a]</sup>

| Complex       | $E_{1/2}^{ox1}(\Delta E_p)^{[b]}$ | $E_{1/2}^{red1}(\Delta E_p)^{[b]}$ | $E_{1/2}^{red2}(\Delta E_p)^{[b]}$ | $E_{1/2}^{red3}(\Delta E_p)^{[b]}$ |
|---------------|-----------------------------------|------------------------------------|------------------------------------|------------------------------------|
| [ <b>1a</b> ] | -0.20                             | -1.68 (64)                         | -1.94 (78)                         | -2.21 (157)                        |
| [ <b>1b</b> ] | -0.18                             | -1.67 (72)                         | -1.92 (74)                         | -2.18 (154)                        |
| [ <b>1c</b> ] | -0.15                             | -1.63 (69)                         | -1.87 (75)                         | -2.13 (168)                        |
| [ <b>2a</b> ] | -0.25 (72)                        | -1.81 (67)                         | -2.04 (76)                         | -2.33 (90)                         |
| [ <b>2b</b> ] | -0.21 (68)                        | -1.83 (71)                         | -2.10 (63)                         | -2.44 (160)                        |

<sup>[a]</sup> Electrochemical potentials in V from cyclic voltammetry in CH<sub>3</sub>CN / 0.1 M Bu<sub>4</sub>NPF<sub>6</sub> at 298 K. Scan Rate: 100 mV/s. Ferrocene / Ferrocenium was used as internal standard.

<sup>[b]</sup>  $\Delta E_p$ : difference between peak potentials in mV.

The complex **1a** and **2a** both shows three reductions and one oxidation. In case of **1a** the first two reductions are reversible whereas in case of **2a**, the first oxidation and only first reduction

are reversible. Compared to **1a**, the reduction potentials of **2a** are shifted towards higher negative potentials and oxidation potential is shifted towards lower positive potential.

### 6.5. UV-Vis-NIR spectroelectrochemistry

To assign the electronic distribution in various accessible redox processes and to compare the charge transfer transition bands in the isomers of **1** and **2** (**1a**, **1b**, **1c**, **2a** and **2b**), UV/Vis/NIR spectroelectrochemical changes of these isomers were monitored using an Optically Transparent Thin Layer Electrochemical (OTTLE) cell. The spectral changes associated with the first two reductions of **1a** and first oxidation and first reduction of **2a** are shown in Figure 6.5.1-6.5.4 and the data for all the isomers are summarized in Table 6.5.1.

The UV/Vis spectrum of the complexes **1** and **2** are dominated by an intense broad band at about 650 nm with an intense shoulder which can be assigned as mixed MLCT ( $\text{Ru}^{\text{II}} \rightarrow \text{bpy}$ ) and ( $\text{Ru}^{\text{II}} \rightarrow \text{L-H}$ ) transitions (Figure 6.5.1 and Figure 6.5.3). One-electron reduction of these complexes lead to the formation of radical mixed-valent complex  $[\text{Ru}(\text{bpy})(\text{L-H})(\text{L-H})^{\cdot-}]$ . The MLCT transitions band at about 650 nm is red shifted to about 700 nm with the decreased in intensity which can be assigned as a  $\text{Ru}^{\text{II}} \rightarrow \text{bpy}$  transition for the formulation of  $[\text{Ru}(\text{bpy})(\text{L-H})(\text{L-H})^{\cdot-}]$  and the  $\text{Ru}^{\text{II}} \rightarrow \text{L-H}$  MLCT transitions band at about 590 nm is remain almost unchanged with large decrease in intensity (Figure 6.5.1, Figure 6.5.3 and Table 6.5.1). In addition a new intense band appeared at about 460 nm which can be assigned as a LMCT transitions ( $\text{L-H}^{\cdot-} \rightarrow \text{Ru}^{\text{II}}$ ). The formation of  $[\text{Ru}(\text{bpy})(\text{L-H})(\text{L-H})^{\cdot-}]$  has been also confirmed by EPR spectroscopy (see later). The second one-electron reduction of **1** is reversible whereas the second one-electron reduction of **2** leads to slight decomposition of the product. The UV/Vis spectroelectrochemical changes for the conversion of **1<sup>-</sup>** to **1<sup>2-</sup>** are shown in the figure 6.5.2. The LMCT transitions ( $\text{L-H}^{\cdot-} \rightarrow \text{Ru}^{\text{II}}$ ) at about 460 nm are red shifted with increase in intensity that indicate the reduction of another  $\text{L-H}$  to  $\text{L-H}^{\cdot-}$  and formed  $[\text{Ru}(\text{bpy})(\text{L-H}^{\cdot-})_2]^{2-}$  species.

The one electron oxidation of complex **1** is completely irreversible whereas one electron oxidation of complex **2** is reversible, may be due to the less acidity of N-H protons in complex **2** than in complex **1** (see  $^1\text{H}$  NMR results in the experimental section). The UV/Vis spectroelectrochemical changes for the conversion of **2** to **2<sup>+</sup>** are shown in the figure 6.5.4. The MLCT transitions ( $\text{Ru}^{\text{II}} \rightarrow \text{bpy}$  and  $\text{Ru}^{\text{II}} \rightarrow \text{L-H}$ ) disappeared completely and a new intense sharp band appeared at about 460 nm. The band at about 460 nm could be  $\text{L-H} \rightarrow \text{Ru}^{\text{III}}$  LMCT

transition for the formulation of  $[\text{Ru}^{\text{III}}(\text{bpy})(\text{L}_\text{H})_2]^+$ . Thus the first oxidation of complex **2** is ruthenium centred which is further verified by EPR spectroscopy (see later).

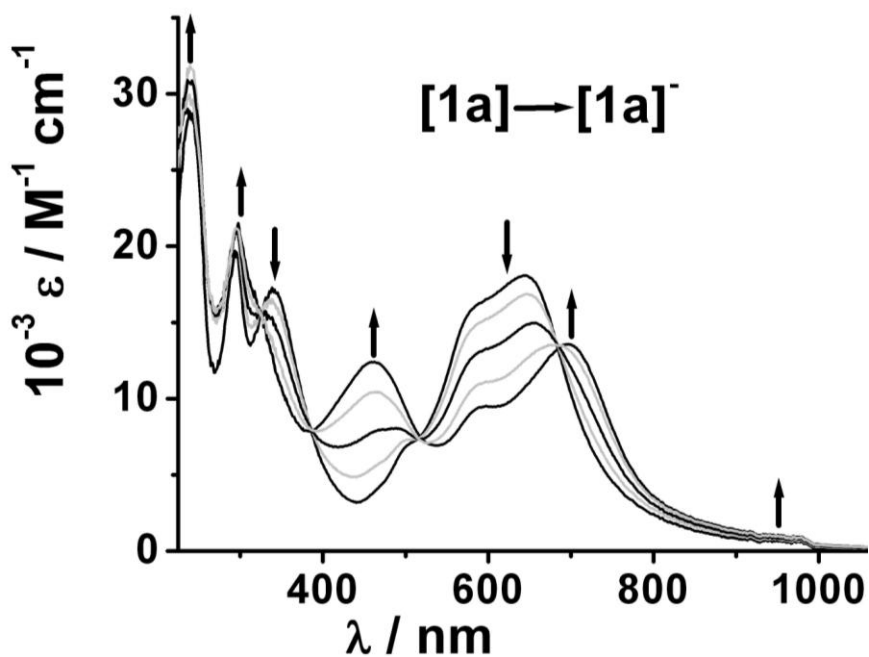


**Figure 6.5.1.** UV-Vis-NIR spectroelectrochemistry of the conversion  $[1\text{a}]^{(0)-} \rightarrow [1\text{a}]^{-}$  in  $\text{CH}_3\text{CN}$  / 0.1 M  $\text{Bu}_4\text{NPF}_6$ .

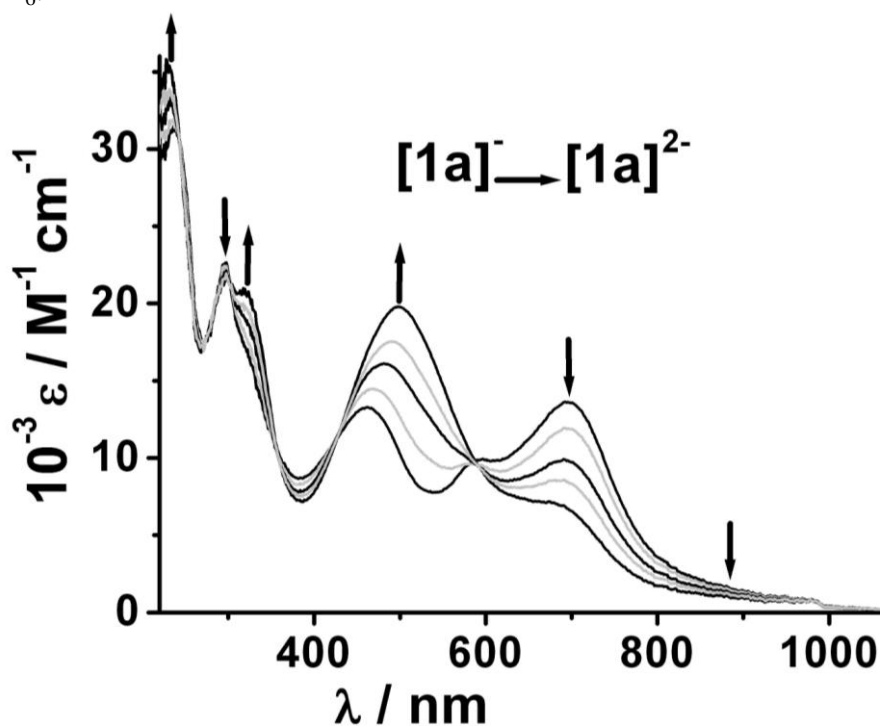


**Figure 6.5.2.** UV-Vis-NIR spectroelectrochemistry of the conversion  $[1\text{a}]^{-} \rightarrow [1\text{a}]^{2-}$  in  $\text{CH}_3\text{CN}$  / 0.1 M  $\text{Bu}_4\text{NPF}_6$ .

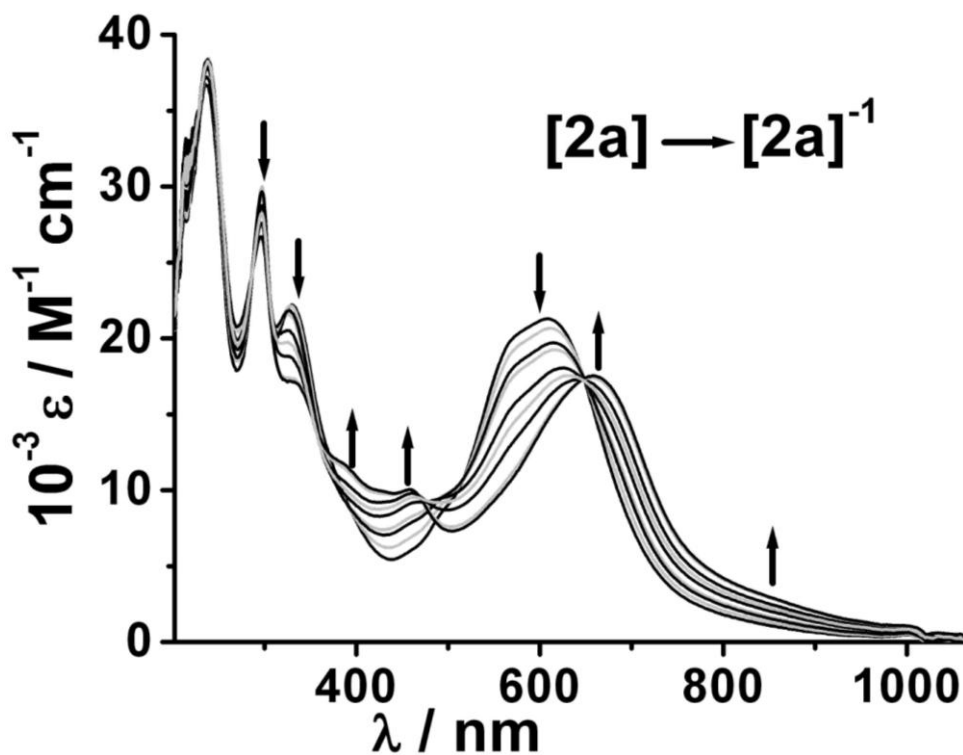


**Figure 6.5.3.** UV-Vis-NIR spectroelectrochemistry of the conversion  $[2a]^{(0) \rightarrow (-)}$  in  $\text{CH}_3\text{CN} / 0.1 \text{ M Bu}_4\text{NPF}_6$ .

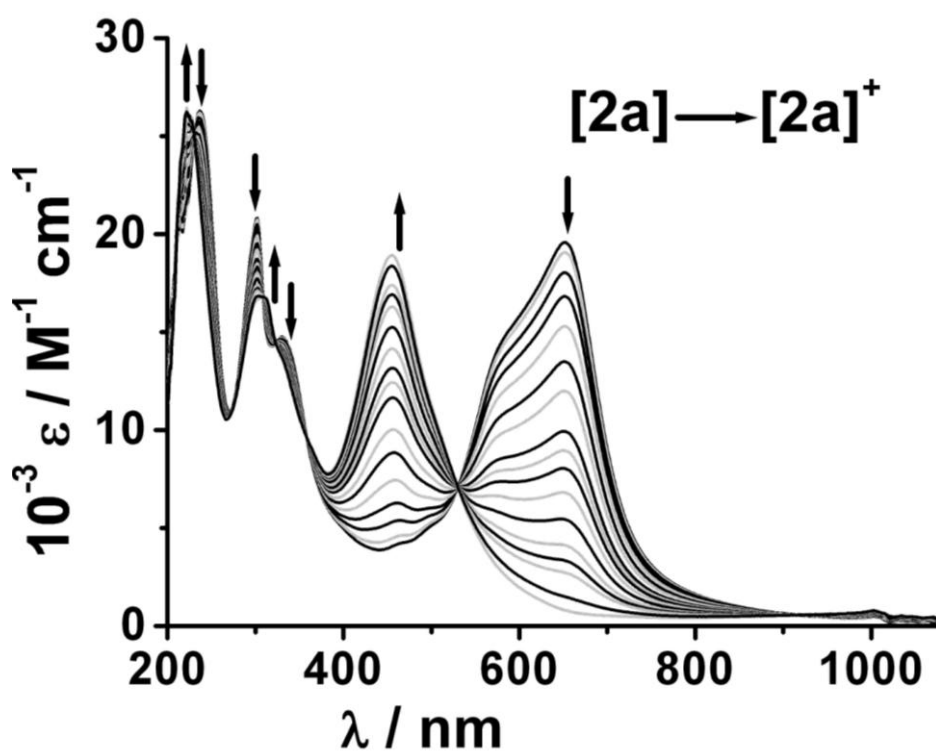


**Figure 6.5.4.** UV-Vis-NIR spectroelectrochemistry of the conversion  $[2a]^{(0) \rightarrow (+)}$  in  $\text{CH}_3\text{CN} / 0.1 \text{ M Bu}_4\text{NPF}_6$ .



**Table 5.6.1.** Absorption data from UV/Vis/NIR spectroelectrochemistry.<sup>[a]</sup>

| Compound           | $\lambda_{\max}$ [nm] ( $\epsilon$ [ $\text{m}^{-1}\text{cm}^{-1}$ ]) |
|--------------------|---|
| [1a]               | 240 (28.8), 294 (19.7), 339 (17.2), 510 (7.3), 588 (16.3), 644 (18.1) |
| [1a] <sup>-</sup>  | 239 (31.9), 298 (21.6), 460 (12.5), 590 (9.5), 695 (13.7)             |
| [1a] <sup>2-</sup> | 228 (35.8), 321 (20.9), 499 (19.9), 676 (7.2)                         |
| [1b]               | 241 (31.8), 297 (23.2), 240 (19.3), 505 (sh), 595 (18.2), 655 (19.7)  |
| [1b] <sup>-</sup>  | 241 (34.2), 298 (25.7), 461 (12.2), 592 (12.2), 704 (16.7)            |
| [1b] <sup>2-</sup> | 230 (38.8), 300 (24.6), 316 (24.1), 510 (20.2), 696 (9.7)             |
| [1c]               | 239 (39.3), 297 (27.3), 336 (21.7), 600 (19.6), 660 (21.7)            |
| [1c] <sup>-</sup>  | 234 (37.4), 298 (28.7), 457 (13.8), 594 (13.9), 703 (19.3)            |
| [1c] <sup>2-</sup> | 226 (42.5), 300 (27.2), 321 (sh), 503 (19.4), 699 (12.2)              |
| [2a]               | 235 (32.8), 296 (27.0), 332 (22.3), 500 (sh), 570 (sh), 608 (22.6)    |
| [2a] <sup>-</sup>  | 237 (36.6), 296 (26.7), 331 (17.1), 338 (sh), 458 (10.1), 658 (17.7)  |
| [2a] <sup>+</sup>  | 221.4 (32.6), 297 (22.4), 323 (21.6), 462 (27.4)                      |
| [2b]               | 237 (39.8), 299 (26.0), 329 (17.8), 498 (sh), 580 (sh), 644 (19.5)    |
| [2b] <sup>-</sup>  | 235 (38.5), 296 (23.3), 338 (sh), 458 (8.5), 664 (14.5), 760 (sh)     |
| [2c] <sup>+</sup>  | 221 (26.3), 305 (16.8), 332 (14.8), 455 (19.1)                        |

<sup>[a]</sup> From spectroelectrochemistry in CH<sub>3</sub>CN / 0.1 M Bu<sub>4</sub>NPF<sub>6</sub> at 298 K.

## 6.6. EPR spectroscopy

The reversible one-electron reduction of diamagnetic complexes **1** and **2** and the one-electron reversible oxidation of complex **1** is monitored by generating odd electron species by in situ electrolysis for EPR spectroscopy. The EPR spectra of **1**<sup>-</sup> and **2**<sup>-</sup> and **2**<sup>+</sup> are shown in Figure 6.6.1-6.6.2.

The in situ generated one-electron reduced form  $\mathbf{1}^-$  in  $\text{CH}_3\text{CN} / 0.1 \text{ M Bu}_4\text{NPF}_6$  exhibits a broad symmetrical ligand centered EPR signal with  $g_{\text{av}} = 2.00$  at 295 K (Figure 6.6.1 left). The in situ generated one-electron reduced form  $\mathbf{2}^-$  in  $\text{CH}_3\text{CN} / 0.1 \text{ M Bu}_4\text{NPF}_6$  exhibits a symmetrical line-rich highly resolved spectrum with  $g_{\text{iso}} = 2.004$  at 295 K (Figure 6.6.1 left) which is also very close to the  $g_{\text{iso}}$  of organic radical (2.0023) confirming ligand centered spin. Ms. Alexa tried to simulate this spectrum but unfortunately she failed because of the appearance of more number of lines in the spectrum of  $\mathbf{2}^-$  than the expected number of lines. The number of lines observed in the spectrum of  $\mathbf{2}^-$  is rather high compared to the expected numbers of line for an unpaired electron regionally localized on one coordinated  $\text{L}_{\text{H}}^1$  ligand. The greater number of lines appeared in the spectrum of  $\mathbf{2}^-$  may be due to the delocalization of the unpaired electron over both the coordinated  $\text{L}_{\text{H}}^1$  ligands. To explain these two EPR spectra properly, structure based DFT calculation will be require.

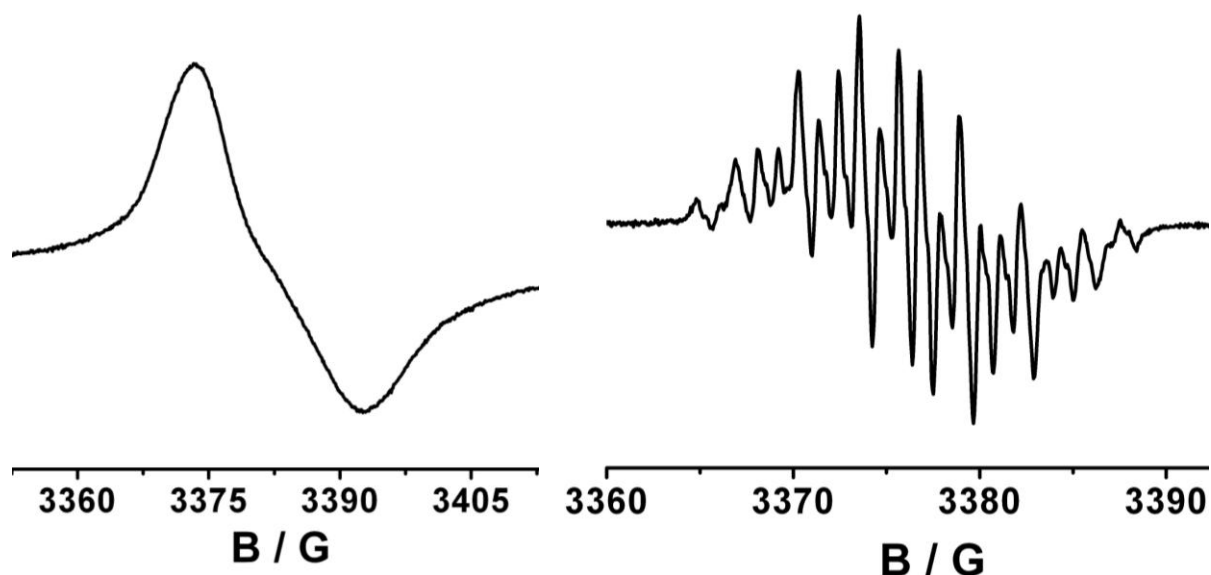


**Figure 6.6.2.** X-band EPR spectra of electrochemically generated  $\mathbf{1}^-$  (left) and  $\mathbf{2}^-$  obtained by in situ reduction in  $\text{CH}_3\text{CN} / 0.1 \text{ M Bu}_4\text{NPF}_6$  at RT.

The one-electron oxidation of diamagnetic complex  $\mathbf{2}$  in  $\text{CH}_3\text{CN}/0.1\text{M Bu}_4\text{NPF}_6$  at 110 K leads to slight decomposition and exhibits EPR signal with three  $g$  values ( $g_1 = 2.607$ ,  $g_2 = 2.171$  and  $g_3 = 2.007$ ) having  $g_{\text{av}} = 2.063$  and  $\Delta g = 1.0$  (Figure 6.6.2). Such values are typical for low-spin  $d^5$  ruthenium(III) complexes having distorted octahedral geometry. Thus the one electron oxidation is ruthenium centred.

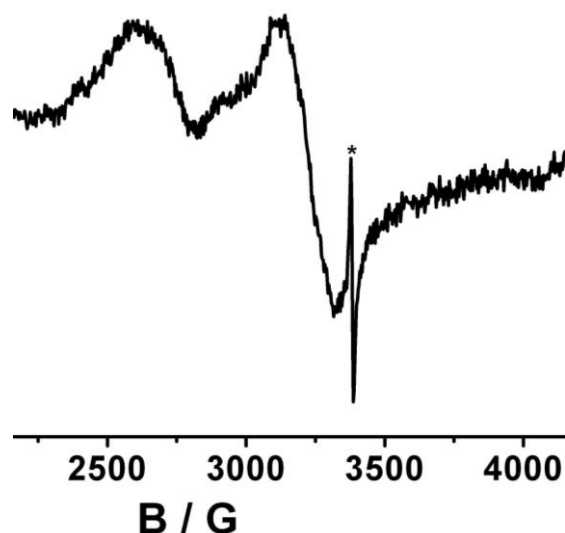


**Figure 6.6.2.** X-band EPR spectrum of electrochemically generated  $2^+$  obtained by in situ oxidation of **2** in  $\text{CH}_3\text{CN} / 0.1 \text{ M Bu}_4\text{NPF}_6$  at 110 K. \* Indicates signal from the decomposed product.

## 6.7. Conclusion

In summary, the mononuclear ruthenium complexes with one bipyridine and two quinonoid ligands have been synthesized and their isomers have been separated. The more polar isomer of the three isomers of complex  $[(\text{bpy})\text{Ru}^{\text{II}}(\text{L}^1\text{-H})_2]$  ( $\text{L}^1 = 2,5$ -bis(isopropylamino)-1,4-benzoquinone) has been structurally characterized. In the crystal structure, the two coordinated oxygen atoms are *trans* to each other. The  $\pi$ -systems of the quinonoid ligand  $\text{L}^1\text{-H}$  in complex  $[(\text{bpy})\text{Ru}^{\text{II}}(\text{L}^1\text{-H})_2]$  are more delocalized than free ligand  $\text{L}^1$ . This delocalization leads to partial charge on the NH group and carbonyl oxygen in the metal free site that stabilized by strong intermolecular hydrogen bonds involving NH- of one molecule with carbonyl oxygen of another molecule that leads to the formation of extended polymeric 3-D frameworks. In addition it is also observed that the vacant space in the crystal lattice has been occupied by several water cluster units through hydrogen bonds. The complexes **1** and **2** show three reductions and one oxidation in the solvent window. The first two reductions are reversible for complex **1** whereas the first reduction and first oxidation are reversible for complex **2**. The EPR and UV/Vis/NIR spectroscopic results imply that the first reductions of the complexes **1** and **2** are quinonoid ligand centred ( $\text{L}\text{-H}$  to  $\text{L}\text{-H}^{\cdot-}$ ) and the first oxidation of complex **2** is ruthenium centred ( $\text{Ru}^{\text{II}}$  to  $\text{Ru}^{\text{III}}$ ).

## CHAPTER 7

# Synthesis of Dinuclear Ruthenium Arene Complexes with Symmetric and Asymmetric *p*-Quinone Ligands and Their Unprecedented Substituent Induced Reactivity

## 7.1 Introduction

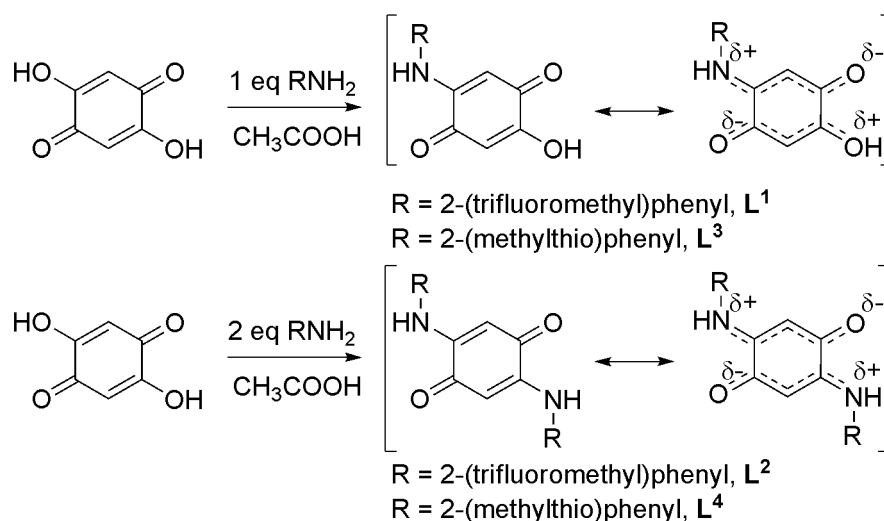
Coordination compounds with quinone ligands have been studied for a variety of reasons, such as their interesting electron transfer properties,<sup>[198-202]</sup> magnetic behavior,<sup>[203,204]</sup> valence ambiguity, mixed valency and use in homogeneous catalysis.<sup>[205,206]</sup> Hemilability of ligands is an important phenomenon in catalysis.<sup>[207]</sup> Efforts at synthesizing potentially bridging quinone ligands with additional donor atoms capable of showing hemilability have been rare until now.<sup>[206]</sup> Recently it has also been observed that arene ruthenium complexes containing potentially bridging quinone ligands units can be used to generate supramolecular assemblies that show encapsulation of different functionalities.<sup>[208-211]</sup> Ruthenium arene compounds are also considered as promising anticancer agents and many compounds have been evaluated *in vitro* and *in vivo*.<sup>[212-214]</sup>

In this chapter a one pot synthesis of new quinonoid ligands 2-[2-(trifluoromethyl)-anilino]-5-hydroxy-1,4-benzoquinone (**L**<sup>1</sup>), 2,5-di-[2-(trifluoromethyl)-anilino]-1,4-benzoquinone (**L**<sup>2</sup>),<sup>[215]</sup> 2-[2-(methylthio)-anilino]-5-hydroxy-1,4-benzoquinone (**L**<sup>3</sup>), and 2,5-di-[2-(methylthio)-anilino]-1,4-benzoquinone (**L**<sup>4</sup>)<sup>[215]</sup> are presented. **L**<sup>1</sup> and **L**<sup>3</sup> are rare examples of asymmetric *p*-quinones containing an additional OH group which are directly related to quinones that play an important role as inhibitors of tumors<sup>[216]</sup> and of hydroxyphenyl pyruvate dioxygenase.<sup>[217]</sup> **L**<sup>3</sup> and **L**<sup>4</sup> combine additional SMe donors at the nitrogen substituents, thus making these ligands potentially hemilabile, with **L**<sup>3</sup> having this feature only on one side of the molecule. These ligands were used to form complexes [ $\{\text{Cl}(\eta^6\text{-Cym})\text{Ru}\}_2(\mu\text{-L}^1\text{-2H})$ ] (**1**), [ $\{\text{Cl}(\eta^6\text{-Cym})\text{Ru}\}_2(\mu\text{-L}^2\text{-2H})$ ] (**2**), [ $\{\text{Cl}(\eta^6\text{-Cym})\text{Ru}\}_2(\mu\text{-L}^3\text{-2H})$ ] (**3**), and [ $\{\text{Cl}(\eta^6\text{-Cym})\text{Ru}\}_2(\mu\text{-L}^4\text{-2H})$ ] (**4**)<sup>[215]</sup> that contain the “[Ru(Cym)]” (Cym = *p*-Cymene = 1-isopropyl-4-methyl-benzene) fragment. These complexes were further reacted with silver salts in acetonitrile to produce [ $\{(\text{CH}_3\text{CN})(\eta^6\text{-Cym})\text{Ru}\}_2(\mu\text{-L}^1\text{-2H})$ ][ClO<sub>4</sub>]<sub>2</sub> (**5**)[ClO<sub>4</sub>]<sub>2</sub>,

$\{[(\text{CH}_3\text{CN})(\eta^6\text{-Cym})\text{Ru}]_2(\mu\text{-L}^2\text{-2H})\}[\text{ClO}_4]_2$  ( $6[\text{ClO}_4]_2$ ),  $[(\text{CH}_3\text{CN})\text{-}(\eta^6\text{-Cym})\text{Ru}(\mu\text{-L}^3\text{-2H})\text{Ru}(\text{CH}_3\text{CN})_3][\text{ClO}_4]_2$  ( $7[\text{ClO}_4]_2$ ), and  $\{[(\text{CH}_3\text{CN})_3\text{Ru}]_2(\mu\text{-L}^4\text{-2H})\}[\text{ClO}_4]_2$  ( $8[\text{ClO}_4]_2$ )<sup>[215]</sup>. In the following, a detailed synthetic and crystallographic study on these ligands and complexes is presented. Reactivity studies are reported to determine the potential hemilabile character of ligands such as  $\text{L}^3$  and  $\text{L}^4$ . Reasons for the unprecedented coordination induced release of Cym in complexes **3** and **4** to form  $7[\text{ClO}_4]_2$  and  $8[\text{ClO}_4]_2$  are stated and explained. Finally, the complex  $8[\text{ClO}_4]_2$  is used as a versatile precursor.

## 7.2. Syntheses of ligands $\text{L}^1\text{-L}^4$

The symmetric ( $\text{L}^2$  and  $\text{L}^4$ )<sup>[215]</sup> and asymmetric ( $\text{L}^1$  and  $\text{L}^3$ ) ligands were synthesized according to the procedure reported in the chapter 3 and purified by column chromatography. The ligands  $\text{L}^3$  and  $\text{L}^4$  have additional donor atoms at the nitrogen substituents, and can be crucial for hemilabile behaviour and catalysis (Scheme 7.2.1).

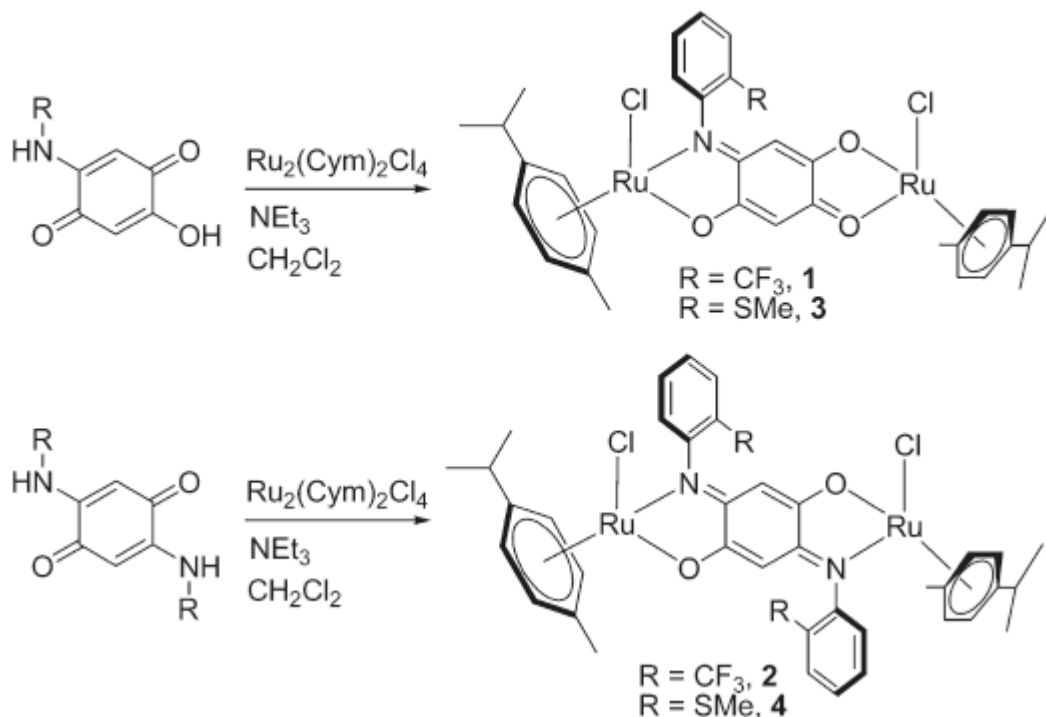


**Scheme 7.2.1.** Reaction scheme for the synthesis of ligands.

$\text{L}^1\text{-L}^4$  were characterized by  $^1\text{H}$  and  $^{13}\text{C}$  NMR spectroscopy and elemental analyses. The  $^1\text{H}$  NMR spectra of  $\text{L}^2$  and  $\text{L}^4$  show only one signal corresponding to the *p*-quinone ring C-H protons<sup>[215]</sup> but  $\text{L}^1$  and  $\text{L}^3$  show two different signals for the non-equivalent *p*-quinone ring C-H protons (see the Experimental Section). In the  $^{13}\text{C}$  NMR spectra for  $\text{L}^2$  and  $\text{L}^4$ , only one signal is seen for the “C=O” carbon,<sup>[215]</sup> for  $\text{L}^1$  and  $\text{L}^3$  two different signals are observed owing to their inequivalence.

### 7.3. Synthesis of Dinuclear Complexes 1-4

The reactions of  $L^1$ - $L^4$  with  $[Cl(\eta^6\text{-Cym})Ru(\mu\text{-Cl})_2Ru(\eta^6\text{-Cym})Cl]$  in the presence of  $NEt_3$  (base) in dichloromethane resulted in the formation of **1-4** respectively with excellent yields (Scheme 7.3.1). The analytical purity of these complexes was determined by  $^1H$  NMR spectroscopy, elemental analyses and mass spectrometry.



**Scheme 7.3.1.** Reactions scheme for the synthesis of **1-4**. The ligand  $L^2$  and  $L^4$  and the complex **4** were synthesized by Mr. D. Schweinfurth and Mr. F. Weisser.<sup>[215]</sup>

The orientation of the chloro ligands in such dinuclear complexes with respect to the *p*-quinone plane leads to the formation of two possible *syn*- and *anti*- isomers. The  $^1H$  NMR spectrum showed two sets of signals that indicate the formation of both isomers under our reaction conditions.  $^1H$  NMR spectroscopy as well as mass spectrometry showed the presence of two Cym groups in all of the complexes, including **3** and **4**, that have additional thioether donor groups on the substituent on nitrogen atoms.

## 7.4. Crystal Structure of 2

The single crystal of complex **2** could be obtained by the slow evaporation of a dichloromethane solution at room temperature and it crystallized in the  $P2_1/c$  space group. Crystallographic data are summarized in chapter 10. The ORTEP diagram of complex **2** is shown in figures 7.4.1, and selected bond lengths and bond angles are given in table 7.4.2. The bond lengths of the reported free ligand  $L^2$  are also included in the Table 8.4.2 for the comparison with complex **2**.

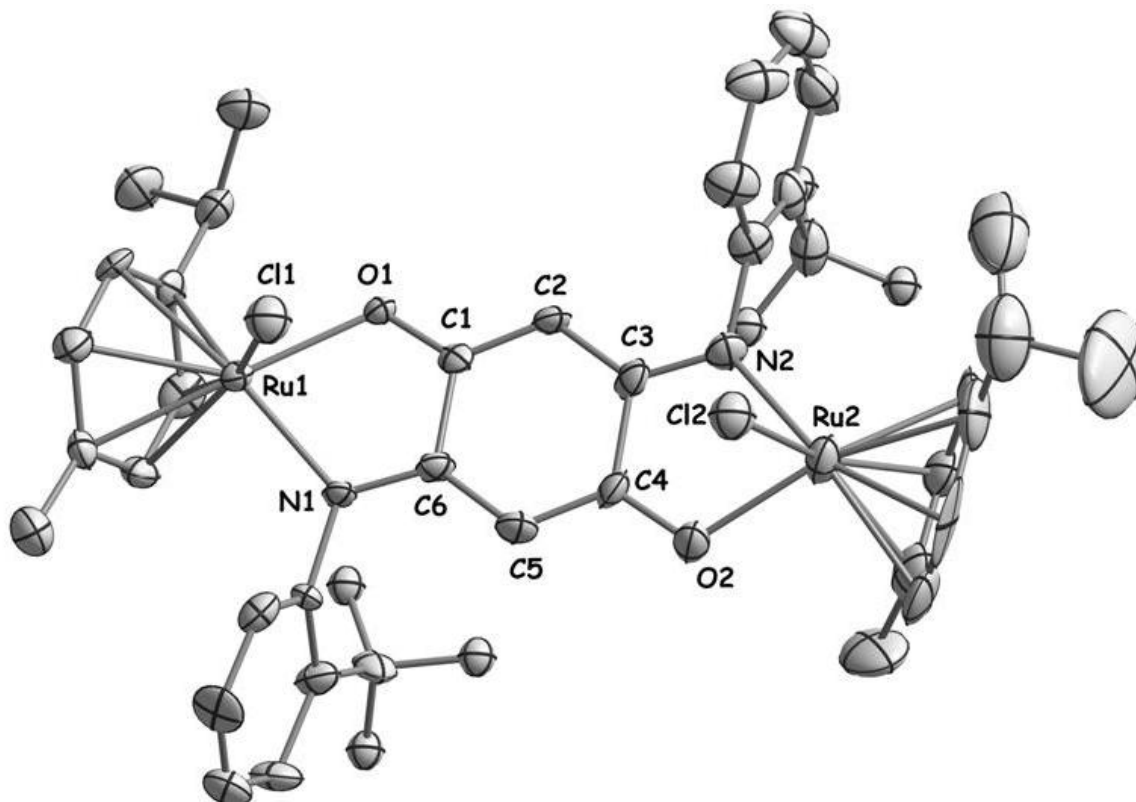


**Figure 7.4.1.** Molecular structure of complex **2** in the crystal. Ellipsoids are drawn at 50% probability. Hydrogen atoms are omitted for clarity.

The above crystal structure indicates that the cymene group binds in a  $\eta^6$  manner and it is a nice example of piano-stool structure. The orientations of the two chloro ligands are *syn* with respect to the *p*-quinone plane. The reported crystal structure of **4**<sup>[215]</sup> also confirms *syn* orientation of chloro ligands but the dinuclear complexes with similar ligands with the “Ir(Cp\*)Cl” or “Rh(Cp\*)Cl” (Cp\* = pentamethylcyclopentadienyl) fragments, showed the presence of the chloro ligands in an *anti* configuration. According to the steric interactions, normally the *anti*-isomer is more stable than the *syn*-isomer. However, in our case the *syn*-isomer crystallizes preferentially.

**Table 7.4.2.** Selected bond lengths (Å) and angles (°) for **2**.

| bond lengths             | <b>L</b> <sup>2</sup> | <b>2</b> | bond angles | <b>2</b> |
|--------------------------|-----------------------|----------|-------------|----------|
| C1-O1                    | 1.237(2)              | 1.281(8) | O1-Ru1-N1   | 76.2(2)  |
| C4-O2                    |                       | 1.294(8) | O1-Ru1-Cl1  | 83.2(1)  |
| C3-N <sup>a</sup>        | 1.337(2)              | 1.311(9) | N1-Ru1-Cl1  | 85.0(2)  |
| C6-N1                    |                       | 1.313(9) | O2-Ru2-N2   | 76.2(2)  |
| C1-C2                    | 1.418(2)              | 1.34(1)  | O2-Ru2-Cl2  | 83.6(2)  |
| C1-C3/C1-C6 <sup>b</sup> | 1.519(2)              | 1.511(9) | N2-Ru2-Cl2  | 85.0(2)  |
| C2-C3                    | 1.366(2)              | 1.39(1)  |             |          |
| C3-C4                    |                       | 1.498(9) |             |          |
| C4-C5                    |                       | 1.34(1)  |             |          |
| C5-C6                    |                       | 1.41(1)  |             |          |
| Ru1-O1                   |                       | 2.083(4) |             |          |
| Ru1-N1                   |                       | 2.083(5) |             |          |
| Ru1-Cl1                  |                       | 2.414(2) |             |          |
| Ru1-C <sup>c</sup>       |                       | 1.669(8) |             |          |
| Ru2-O2                   |                       | 2.065(5) |             |          |
| Ru2-N2                   |                       | 2.092(6) |             |          |
| Ru2-Cl2                  |                       | 2.403(2) |             |          |
| Ru2-C <sup>d</sup>       |                       | 1.669(8) |             |          |
| Ru1-Ru2                  |                       | 7.964(2) |             |          |

<sup>a</sup> C3-N refers to C3-N2 for **2**.

<sup>b</sup> The bond C1-C6 in **2** is the same as the bond C1-C3 in the **L**<sup>2</sup>. A uniform numbering is not possible because the ligand **L**<sup>2</sup> is centrosymmetric but the complex **2** is non-centrosymmetric.<sup>[215]</sup>

<sup>c</sup> Ru1-C refers to the distance between the Ru center and the centroid of the *p*-Cym ring.

<sup>d</sup> Ru2-C refers to the distance between the Ru center and the centroid of the *p*-Cym ring.

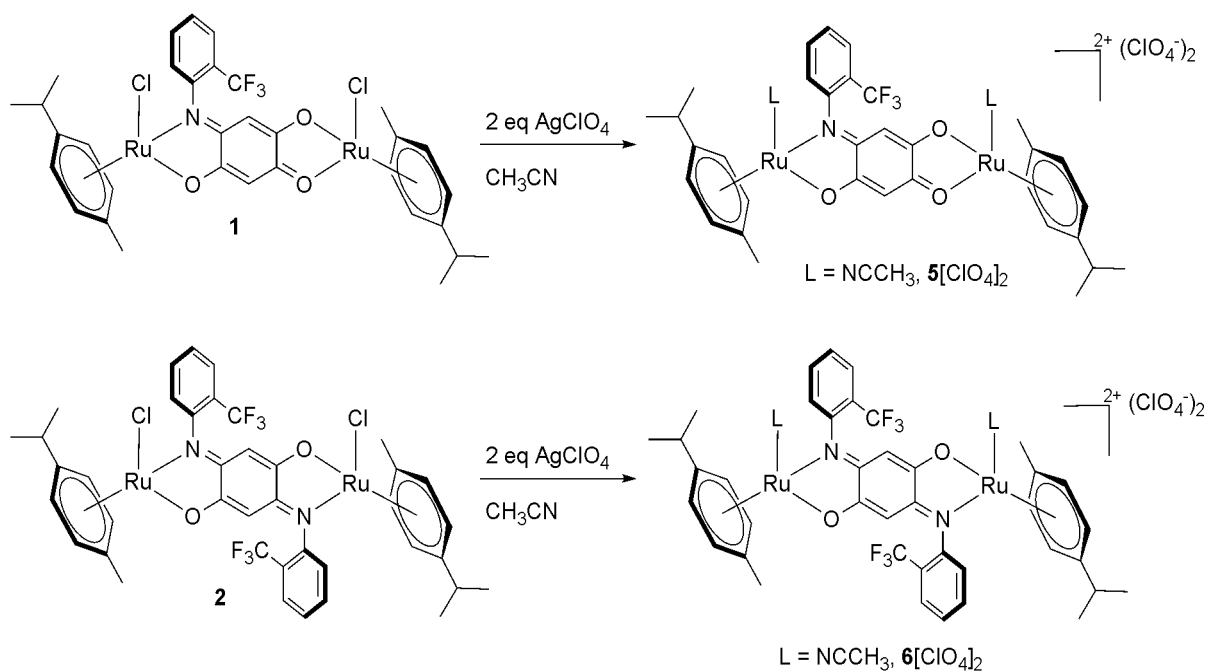
The Ru-O, Ru-N, and Ru-Cl distances are typical for values reported in the literature for such complexes (Table 3).<sup>[218-219]</sup> The  $\eta^6$  coordination mode of the Cym ligand is seen in the similar Ru-C bond distances for all six carbon atoms of the arene ring. Thus, the ruthenium centers have a piano-stool-type configuration in this complex. Analyses of the bond lengths within



the *p*-quinone ring in **2** show a tendency toward localization of the two  $\pi$ -systems O1-C1-C2-C3-N2 and O2-C4-C5-C6-N1 in contrast to the free ligands (Table 2). Thus, the C1-O1 and C3-N2 distances in **2** are 1.281(8) and 1.311(9) Å, respectively and the corresponding distances in **L**<sup>2</sup> are 1.237(2) and 1.337(2) Å, respectively.<sup>[215]</sup> Similarly, the C1-C2 and C2-C3 distances in **2** are 1.34(1) and 1.39(1) Å, respectively, and the corresponding distances in **L**<sup>2</sup> are 1.418(2) and 1.366(2) Å, respectively.<sup>[215]</sup> These results point to a localization of double bonds within the *p*-quinone ring on metal coordination and the concomitant binding of **L**<sup>2</sup>-**2H** through O<sup>-</sup> and imine nitrogen atoms like the dinuclear systems with similar ligands in chapter 3. The C1-C6 and C3-C4 distances at about 1.5 Å remain unchanged in both the free ligands and the metal complexes indicating that the two  $\pi$ -systems are separated by C—C sigma bond (Table 7.4.2). The Ru-Ru intramolecular distance is 7.964(2) Å.

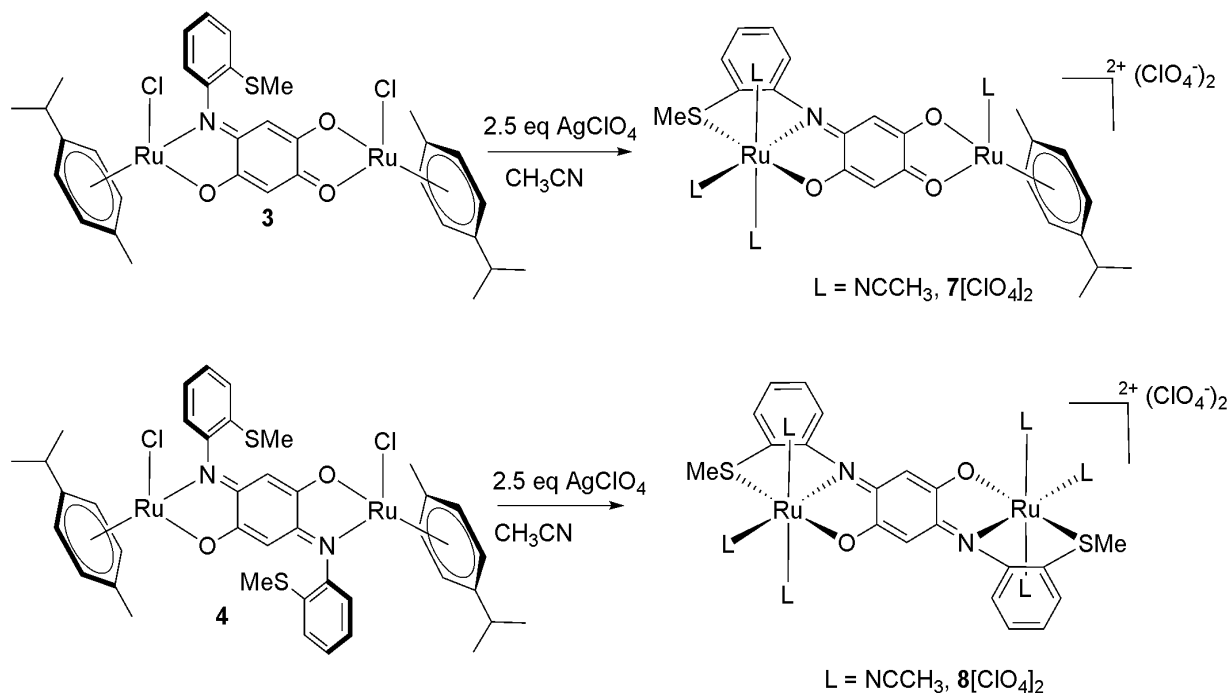
### 7.5. Reaction of dinuclear ruthenium arene complexes **1-4** with AgClO<sub>4</sub> in MeCN

Reactions of **1** or **2** with two equivalents of AgClO<sub>4</sub> in acetonitrile resulted in chloride abstraction and the expected formation of **5**[ClO<sub>4</sub>]<sub>2</sub> or **6**[ClO<sub>4</sub>]<sub>2</sub>, respectively, where the chloro ligands have been substituted by acetonitrile molecules (Scheme 8.5.1). Such reactions have been observed before, and compounds related to **5**[ClO<sub>4</sub>]<sub>2</sub> or **6**[ClO<sub>4</sub>]<sub>2</sub> are often intermediates in the formation of supramolecular assemblies.<sup>[218-219]</sup>



**Scheme 7.5.1.** Reactions scheme for the synthesis of complex **5** and **6**.

While carrying out the same reaction under identical conditions with **4**, it was observed that the cymene groups are released and replaced by acetonitrile molecules (Scheme 7.5.2).<sup>[215]</sup> There are some examples reported in the literature where the reaction takes place only either through excitation by light or because of the presence of an oxidizing agent but Schweinfurth *et al* proved that in case of **4** the cymene release reaction does not depend on the light or oxidizing agents.<sup>[215]</sup> At this point, the possible importance of the SMe groups in the side arm of the ligand **L**<sup>4</sup><sub>2H</sub> in cymene release was considered.



**Scheme 7.5.2.** Reactions scheme for the synthesis of complex **7** and **8**.<sup>[215]</sup>

In order to verify this hypothesis, we carried out the chloride abstraction reaction with the complex **3** in acetonitrile. In keeping with our hypothesis, the product **7**[ClO<sub>4</sub>]<sub>2</sub> formed in this case showed the presence of only one Cym group per molecule of **7**[ClO<sub>4</sub>]<sub>2</sub>, thus proving the importance of the SMe group since the bridging ligand **L**<sup>3</sup><sub>2H</sub> in this case has a SMe group on only one side of the molecule (Scheme 7.5.2).

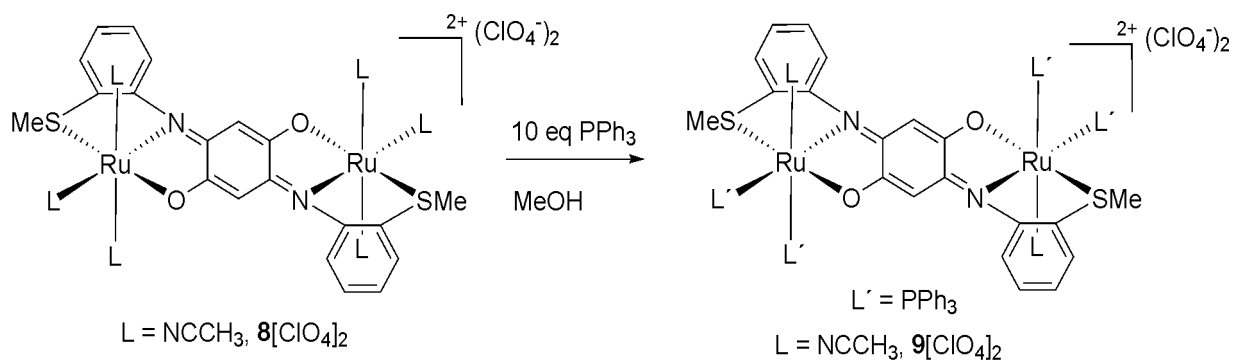
The above three complexes **5**[ClO<sub>4</sub>]<sub>2</sub>, **6**[ClO<sub>4</sub>]<sub>2</sub> and **7**[ClO<sub>4</sub>]<sub>2</sub> were characterized by <sup>1</sup>H NMR spectroscopy, elemental analyses and mass spectrometry.

## 7.6. Explanation for the release of Cymene

The  $\eta^6$ -arene ligand in a piano-stool complex dictates the facial coordination of the other three donor atoms at the metal center. In cases where ligand rigidity together with strong donation force a *meridional* coordination, a direct Cym release has been observed in the literature previously,<sup>[220]</sup> with bis(imino) pyridine ligands being an important example showing such an effect.<sup>[221]</sup> Substitution of one arene ring with another has also been studied in the context of hemilability. In our case, the isolation of chloro-complex **3** and **4**<sup>[215]</sup> proves that such a direct Cym release does not occur. The abstraction of chloride atoms from **3** and **4** causes an increase of Lewis acidity at the metal center but this increase of Lewis acidity alone is not sufficient for the binding of SMe and concomitant release of Cym, as has been proven by the observation of the  $[M-2Cl]^{2+}$  peak for **3**<sup>2+</sup> (see experimental section) and **4**<sup>2+</sup> in mass spectrometry experiments in the gas phase.<sup>[215]</sup> This indicates the requirements of suitable coordinating atoms for the substitution of Cym ligand. On carrying out these chloride abstraction reactions in a coordinating solvent such as acetonitrile, we believe there are several phenomena that occur simultaneously. Chloride abstraction increases the Lewis acidity at the metal center, and this facilitates the binding of the SMe group. However, the rigidity of the ligand **L**<sup>3</sup><sub>-2H</sub> and **L**<sup>4</sup><sub>-2H</sub> because of partial double bond character of the bonds around the donor atoms prevents the facial binding mode of the O,N,S atoms.<sup>[215]</sup> The Lewis acidic metal center, however, now wants to bind with the SMe group, which is possible only in a meridional fashion. This meridional coordination is incompatible with a piano-stool-type structure and the  $\eta^6$ -binding mode of the arene ligands. This leads to arene release and makes three vacant meridional coordinations which are saturated by coordinating acetonitrile solvents molecules. So this reaction probably occurs in a concerted step that includes simultaneous chloride abstraction, acetonitrile coordination, and Cym release. The requirement of an additional donor atom in a rigid bridging ligand for the arene release can be proved strongly by the observation of the formation of **7**[ClO<sub>4</sub>]<sub>2</sub> from **3** (Scheme 7.5.2). The bridging ligand **L**<sup>3</sup><sub>-2H</sub> has an additional SMe donor only on one side, and concomitantly Cym release is observed also from one side.

### 7.7. Substitution reactions of $\mathbf{8}[\text{ClO}_4]_2$

The coordinated acetonitrile ligands can be replaced by other ligands because the ruthenium-acetonitrile bonds are weak and it has been proven by the observation of the  $[\text{M} - 2\text{ClO}_4^- - 4\text{CH}_3\text{CN}]^{2+}$  peak for  $\mathbf{8}[\text{ClO}_4]_2$  in mass spectrometry experiments in the gas phase.<sup>[215]</sup> The reaction of  $\mathbf{8}[\text{ClO}_4]_2$  with excess  $\text{PPh}_3$  under refluxing conditions leads to the coordination of two  $\text{PPh}_3$  molecules per ruthenium center, resulting in  $\mathbf{9}[\text{ClO}_4]_2$  (Scheme 7.7.1).



**Scheme 7.7.1.** Reactions scheme for the substitution of  $\mathbf{8}[\text{ClO}_4]_2$ .

The product was characterized by  $^1\text{H}$  and  $^{31}\text{P}$  NMR spectroscopy as well as mass spectrometry. Attempts at substituting the third acetonitrile molecule from each ruthenium center by  $\text{PPh}_3$  did not meet with success even under forcing conditions. We believe this to be because of the steric bulk of the  $\text{PPh}_3$  ligands. The presence of doublets in the  $^{31}\text{P}$  NMR spectrum also confirmed the formation of a *cis* product.

## 7.8. Conclusion

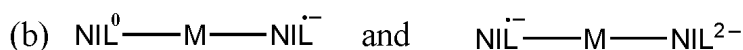
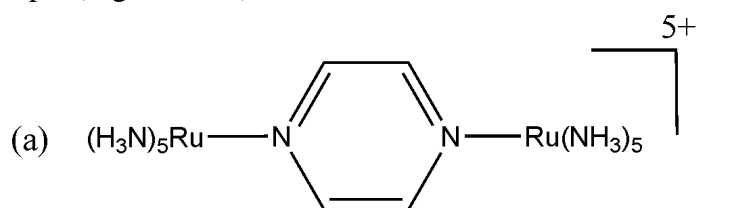
We have reported here on new symmetric and asymmetric biologically relevant *p*-quinone ligands. Some of the ligands also contain an additional SMe donor group which could act as a potentially hemilabile donor. Dinuclear complexes of the form  $[\{\text{Cl}(\eta^6\text{-Cym})\text{Ru}\}_2(\mu\text{-BL}_{2\text{H}})]$  ( $\text{BL}_{2\text{H}}$ =bridging ligand) were synthesized with the doubly deprotonated forms of all the ligands. Structural characterization of one of these complexes has shown the  $\eta^6$ -coordination mode of the arene ligand and localization of the double bonds within the *p*-quinone bridge. Reactions of these complexes with  $\text{AgClO}_4$  led to the unprecedented substituent induced release of *p*-Cym from these complexes only in cases where an additional SMe group is present in the bridging ligand. The increase in the Lewis acidity at the metal center on chloride abstraction is mainly responsible for the coordination of the SMe group, and the inability of the rigid bridging ligand to take up a facial coordination as demanded by a piano-stool configuration is suggested to induce *p*-Cym release. Such stepwise reactivity of this complex shows the possible use of the SMe groups in hemilabile behavior. The presence of the labile solvent molecules in  $\mathbf{7}[\text{ClO}_4]_2$  and  $\mathbf{8}[\text{ClO}_4]_2$  make these good starting materials for subsequent reactions, and success in that direction has been observed with the substitution of  $\text{CH}_3\text{CN}$  molecules with  $\text{PPh}_3$ . In addition, compound  $\mathbf{8}[\text{ClO}_4]_2$  provides a unique opportunity of getting at systems with the potential of multielectron reservoirs because of its inherent redox-rich nature as well as the possibility of building in additional redox-active components in place of the labile acetonitrile ligands.

## CHAPTER 8

# Molecular Coupling of Three Non-innocent Ligands and Two Redox-active Metal Centers in a Super Redox-rich System

### 8.1. Introduction

Bridge mediated molecular coupling between electroactive metal centers have contributed greatly to our understanding of redox reactivity and have helped in the advancement of currently relevant fields such as energy research<sup>[27-31]</sup> and information storage.<sup>[32-35]</sup> The prototype of such a system is the Creutz-Taube ion, a  $\pi$ -acceptor bridged mixed-valent diruthenium(II,III) complex (Figure 8.1.1a). The Creutz-Taube ion<sup>[222]</sup> and related systems have been the focus of intensive theoretical and experimental studies for several decades in order to address questions of electron transfer, electron localization versus delocalization and identification of spin bearing centers.<sup>[223]</sup> Recent efforts have seen the emergence of two other kinds of systems: One in which the bridge is redox-active, thus opening up issues of a radical-bridged homodivalent metal center versus a non-radical bridged mixed-valent case.<sup>[223]</sup> Such issues have been addressed by using a combination of various structural, electrochemical, spectroscopic and theoretical methods. The other systems turn the concept of mixed-valency around and deal with metal bridged di-ligand systems where the ligands are non-innocent.<sup>[223]</sup> Such cases thus deal with ligand centered mixed-valency (Figure 8.1.1b). In this work, we present a molecular platform that combines all of the above mentioned concepts (Figure 8.1.1).

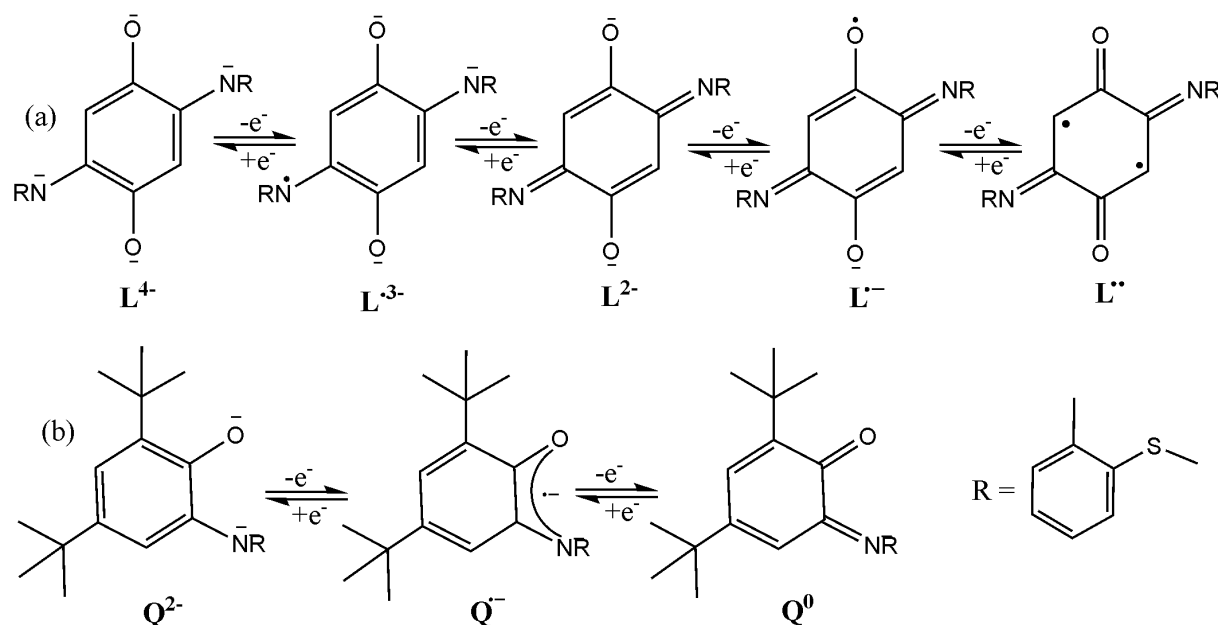


NIL = non-innocent ligands such as 1,2-dioxolene, M = transition metal

**Figure 8.1.1.** The Creutz-Taube ion (a) and metal bridged di-ligand systems (b).

The dinuclear complex that is discussed here contains the doubly deprotonated form ( $\mathbf{L}^{2-}$ ) of 2,5-di-[2-(methylthio)-anilino]-1,4-benzoquinone as the bridging ligand.  $\mathbf{L}^{2-}$  can exist in five

different oxidation states as shown in Scheme 8.1.1a. The metal center of choice is ruthenium and the available oxidation states are Ru<sup>II</sup>, Ru<sup>III</sup> and Ru<sup>IV</sup>. Finally, as a stopper co-ligand, we use the increasingly popular non-innocent ligand, 4,6-di-*tert*-butyl-*N*-(2-methylthiophenyl)-*o*-iminobenzoquinone ( $Q^0$ ), which can exist in three different oxidation states (Scheme 8.1.1b). In the metal bound form, the ligand  $Q$  is known to deliver stable radicals in the form  $Q^{\cdot-}$ . The platform  $[(Q)Ru(\mu-L)Ru(Q)]^n$  thus allows us to address questions of direct electronic and spin-spin coupling between  $Q$  and Ru as well as bridge mediated electronic and spin-spin coupling between the two  $Q$  units and between the two Ru centers. In addition, it also provides with the opportunity to address issues of site of electron transfer and spin localization because of the presence of five different redox-active sites within the same molecule.

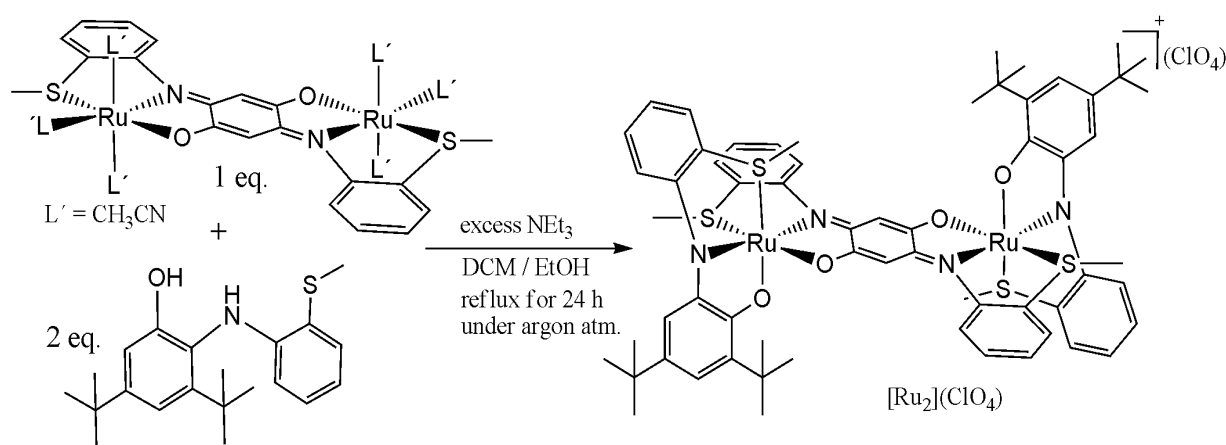


**Scheme 8.1.1.** Different redox forms of  $L^{2-}$  (doubly deprotonated form of 2,5-di-[2-(methylthio)-anilino]-1,4-benzoquinone) (a) and 4,6-di-*tert*-butyl-*N*-(2-methylthiophenyl)-*o*-iminobenzoquinone ( $Q^0$ ) (b).

In the following, we present a detailed structural, electrochemical, UV-vis-NIR and EPR spectroelectrochemical and DFT investigation on the system  $[(Q)Ru(\mu-L)Ru(Q)]^n$  in its eight different redox-states connected by reversible one-electron transfer between  $n = (+4)$  to  $(-4)$  to address the above mentioned issues. We also show the control of the position and intensity of NIR bands in the various redox forms of this molecule, an aim that is important for future opto-electronic devices.<sup>[224-227]</sup>

## 8.2. Synthesis and characterization

The super redox-rich native complex with odd outer charge (+1)  $[(Q)Ru(\mu-L)Ru(Q)](ClO_4)$   $[Ru_2](ClO_4)$  was synthesized *via* the reaction of 2 eq.  $H_2Q$  ligand and 1 eq.  $[(CH_3CN)_3Ru(\mu-L)Ru(CH_3CN)_3](ClO_4)_2$  metal precursor in the presence of  $NEt_3$  base in refluxing dichloromethane/ethanol mixture (see experimental section) (Scheme 8.2.1). The quinonoid bridged dinuclear metal precursor  $[(CH_3CN)_3Ru(\mu-L)Ru(CH_3CN)_3](ClO_4)_2$  was obtained as a product from an unprecedented reaction of corresponding quinonoid bridged dinuclear ruthenium arene complex and  $AgClO_4$  in coordinating acetonitrile solvent (Chapter 7). The ligand 2-(2-methyl)-aniline-4,6-di-tert-butylphenol ( $H_2Q$ ) was prepared as reported.<sup>[228]</sup> The one-electron oxidized species  $[Ru_2]^{2+}$  was isolated as the perchlorate salt  $[Ru_2](ClO_4)_2$  by the reaction of  $[Ru_2](ClO_4)$  and ferrocenium hexafluorophosphate in presence of excess  $NaClO_4$  (see experimental section). Both the complexes were purified by column chromatography using neutral alumina column. The native species  $[Ru_2](ClO_4)$  is paramagnetic and characterized by only electrospray mass spectroscopy and elemental analysis (see experimental section). Where as one-electron oxidized species  $[Ru_2](ClO_4)_2$  is diamagnetic in nature and characterized by  $^1H$  NMR also (see experimental section).



**Scheme 8.2.1.** Synthesis of dinuclear super redox-rich complex  $[Ru_2](ClO_4)$ .

## 8.3 Crystal structure of $[Ru_2](ClO_4)_2$

The one-electron oxidized species  $[Ru_2](ClO_4)_2$  could be crystallized as  $[Ru_2](ClO_4)_2 \cdot 2H_2O$  (Figure 8.3.1) by layering dichloromethane solution of  $[Ru_2](ClO_4)_2$  with excess *n*-hexene (1:2, slow diffusion). Crystallographic data are summarized in Chapter 10. Selected bond lengths and bond angles are listed in Table 8.3.1 and 8.3.2 respectively.



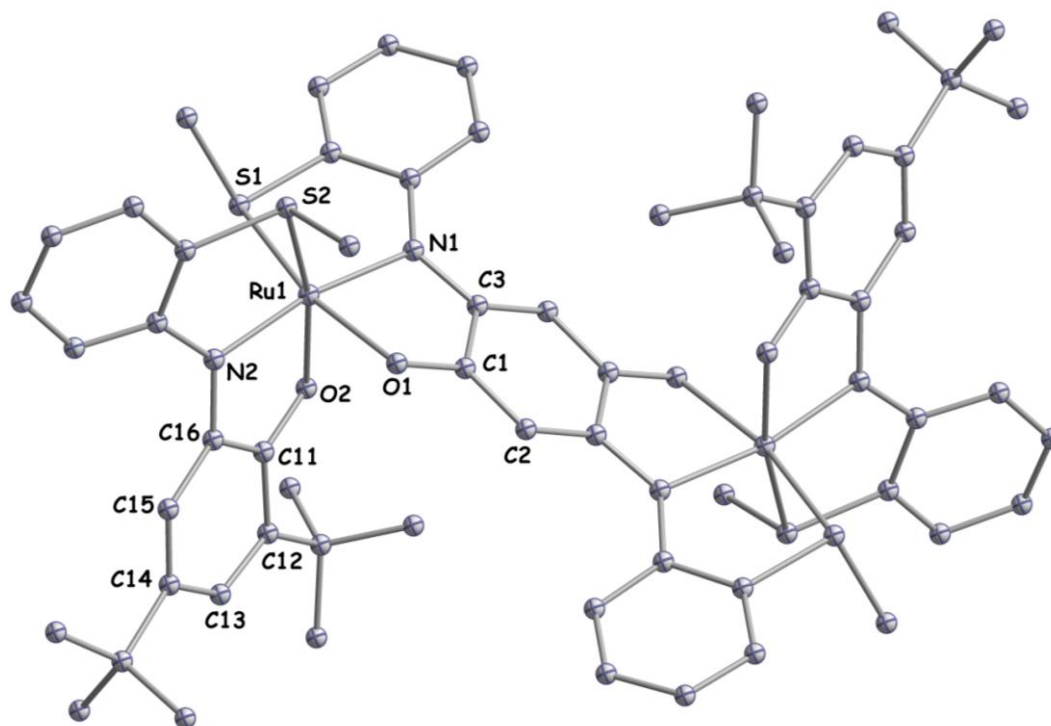


**Figure 8.3.1.** Molecular structure of the dication in the crystal structure of  $[\text{Ru}_2](\text{ClO}_4)_2 \cdot 2\text{H}_2\text{O}$ . Ellipsoids include 50% of the electron density. Hydrogen atoms are omitted for clarity.

The crystal structure analysis reveals that the two peripheral non-innocent ligands are *trans* to each other and perpendicular to the plane of quinonoid bridged diruthenium system. The ruthenium centres in the complex exhibit distorted octahedral coordination, being coordinated by six coordinating atoms, three (O, N and S) from peripheral non-innocent ligand and three (O, N, and S) from quinonoid bridging ligand. The Ru-N, Ru-O and Ru-S bond lengths are in the expected range (Table 8.3.1). Bond length analysis within the peripheral non-innocent ligands (double deprotonated form of 2-(2-methyl)-aniline-4,6-di-tert-butylphenol) show C11-O2, C15-C16 (meta) and C16-N2 bond lengths of 1.308 (13), 1.420(16) and 1.348(13). The bond lengths of these three bonds are most important than the others for the assignment of oxidation state of peripheral iminonoquinone ligands (Q) because of the transition of bond order (see Scheme 8.1.1b). The C11-O2 and C16-N2 bond distances suggest the bond order of C11-O2 and C16-N2 are greater than one but less than two. Similarly the C15-C16 bond distance suggests bond order in between 1 and 1.5 (aromatic, fully reduced system). So the analysis of bond lengths clearly suggest that the two peripheral non-innocent ligands are in semiquinone ( $\text{Q}^{\cdot-}$ ) forms in the complex  $[\text{Ru}_2](\text{ClO}_4)_2$ . The observed diamagnetism and semiquinone assignment for Q implies the best description of  $[\text{Ru}_2](\text{ClO}_4)_2$  is  $[(\text{Q}^{\cdot-})\text{Ru}^{\text{III}}(\mu\text{-L})^2\text{Ru}^{\text{III}}(\text{Q}^{\cdot-})](\text{ClO}_4)_2$  where the spin of  $\text{Q}^{\cdot-}$  and  $\text{Ru}^{\text{III}}$  are antiferromagnetically coupled at each end.

**Table 8.3.1.** Selected bond lengths [Å] for [Ru<sub>2</sub>](ClO<sub>4</sub>)<sub>2</sub>.

|         |           |         |           |         |          |
|---------|-----------|---------|-----------|---------|----------|
| C1-C2   | 1.382(14) | C14-C15 | 1.314(16) | Ru1-N2  | 1.943(8) |
| C1-C31  | 1.471(14) | C15-C16 | 1.420(16) | Ru1-O1  | 2.033(7) |
| C3-N1   | 1.345(12) | C11-C16 | 1.424(17) | Ru1-O2  | 2.038(7) |
| C1-O1   | 1.320(12) | C16-N2  | 1.348(13) | Ru1-S1  | 2.317(3) |
| C11-C12 | 1.450(15) | C11-O2  | 1.308(13) | Ru1-S2  | 2.325(3) |
| C12-C13 | 1.392(17) | Ru1-N1  | 2.014(8)  | Ru1-Ru1 | 7.738    |
| C13-C14 | 1.435(19) |         |           |         |          |

**Table 8.3.2.** Selected bond angles [Å] for [Ru<sub>2</sub>](ClO<sub>4</sub>)<sub>2</sub>.

|           |          |           |          |           |           |
|-----------|----------|-----------|----------|-----------|-----------|
| N1-Ru1-O1 | 80.1(3)  | O1-Ru1-O2 | 87.9(3)  | S1-Ru1-O2 | 90.0(2)   |
| N1-Ru1-O2 | 88.1(3)  | O1-Ru1-S2 | 92.1(2)  | S1-Ru1-S2 | 93.43(11) |
| N1-Ru1-S1 | 84.5(2)  | N2-Ru1-O2 | 81.2(3)  | N1-Ru1-N2 | 168.3(3)  |
| N1-Ru1-S2 | 105.2(2) | N2-Ru1-S1 | 100.0(2) | O1-Ru1-S1 | 164.6(2)  |
| O1-Ru1-N2 | 94.8(3)  | N2-Ru1-S2 | 85.3(3)  | O2-Ru1-S2 | 166.5(2)  |

## 8.4. Electrochemistry

The electrochemistry of the complex [Ru<sub>2</sub>](ClO<sub>4</sub>) has been studied by cyclic voltammetry to see how many redox processes are there. The cyclic voltammetry experiment was carried out in a CH<sub>3</sub>CN solution of Bu<sub>4</sub>NPF<sub>6</sub> (0.1 mol). Ferrocene was used as an internal standard and all the redox potentials are referenced with respect to ferrocenium /ferrocene (Fc<sup>+</sup>/Fc) couple. The reductions and the oxidations of the complex [Ru<sub>2</sub>](ClO<sub>4</sub>) is shown in figure 8.4.1 and the potential values are summarized in Table 8.4.1.

The native complex [Ru<sub>2</sub>](ClO<sub>4</sub>) shows three oxidations and five reductions in the solvent window of acetonitrile. All the redox processes are reversible at room temperature except third oxidation which is reversible at low temperature. The EPR, UV-Vis-NIR spectroelectrochemistry and DFT calculation were used to analyze the electronic configurations for all the accessible redox states. The preferred (in bold) and alternative interpretations at each redox state of [Ru<sub>2</sub>](ClO<sub>4</sub>) are summarized in Scheme 8.4.1.

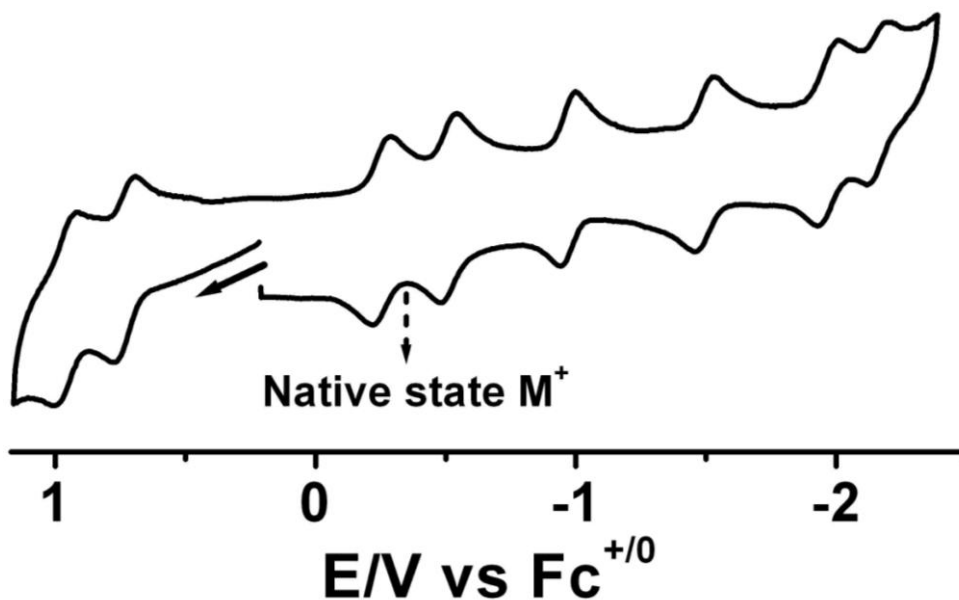


**Figure 8.4.1.** Cyclic voltammogram of  $[\text{Ru}_2](\text{ClO}_4)$  in  $\text{CH}_3\text{CN} / 0.1 \text{ M Bu}_4\text{NPF}_6$  at 295 K.

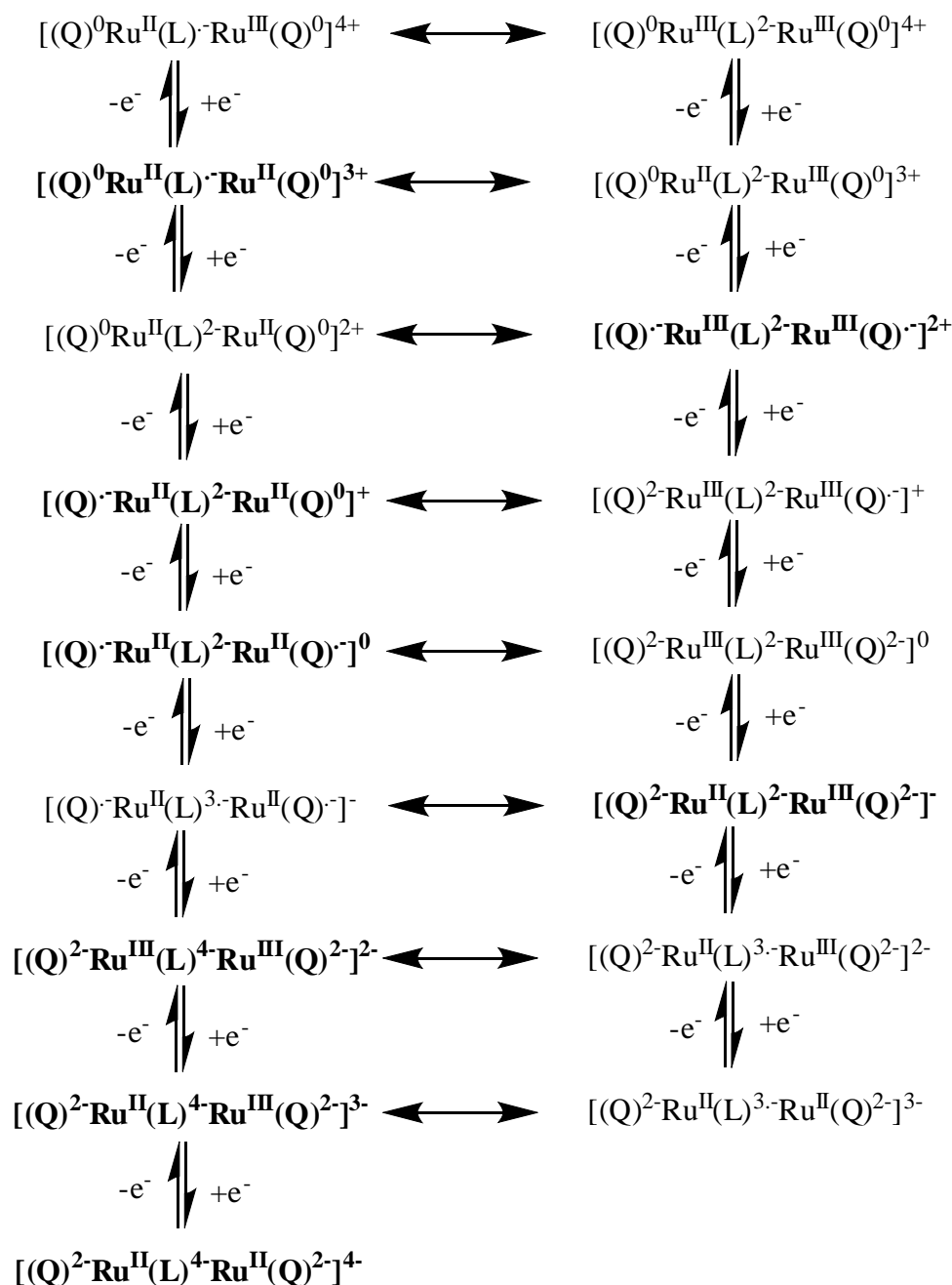
**Table 8.4.1.** Redox potentials of the complex  $[\text{Ru}_2](\text{ClO}_4)$ .<sup>[a]</sup>

| Complex        | $E_{1/2}^{\text{ox}3}$<br>( $\Delta E_p$ ) <sup>[b]</sup> | $E_{1/2}^{\text{ox}2}$<br>( $\Delta E_p$ ) <sup>[b]</sup> | $E_{1/2}^{\text{ox}1}$<br>( $\Delta E_p$ ) <sup>[b]</sup> | $E_{1/2}^{\text{red}1}$<br>( $\Delta E_p$ ) <sup>[b]</sup> | $E_{1/2}^{\text{red}2}$<br>( $\Delta E_p$ ) <sup>[b]</sup> | $E_{1/2}^{\text{red}3}$<br>( $\Delta E_p$ ) <sup>[b]</sup> | $E_{1/2}^{\text{red}4}$<br>( $\Delta E_p$ ) <sup>[b]</sup> | $E_{1/2}^{\text{red}5}$<br>( $\Delta E_p$ ) <sup>[b]</sup> |
|----------------|---|---|---|--|--|--|--|--|
| $[\text{M}]^+$ | +0.96<br>(86)   | +0.73<br>(77)   | -0.25<br>(63)   | -0.51<br>(59)  | -0.97<br>(55)  | -1.50<br>(72)  | -1.97<br>(77)  | -2.16<br>(78)  |

<sup>[a]</sup> Electrochemical potentials in V from cyclic voltammetry in  $\text{CH}_3\text{CN} / 0.1 \text{ M Bu}_4\text{NPF}_6$  at 298 K. Scan Rate: 100 mV/s. Ferrocene / Ferrocenium was used as internal standard.

<sup>[b]</sup>  $\Delta E_p$ : difference between peak potentials in mV.

**Scheme 8.4.1.** Possible oxidation state distribution of  $[\text{Ru}_2]^n$  ( $n = 4-$  to  $4+$ ). The more preferred electronic configuration at each redox state is in bold except  $n = +4$  state due to the unavailability of UV-Vis-NIR data for the assignment of electronic configuration.



## 8.5. EPR spectroscopy

The native form  $[\text{Ru}_2]^+$  two oxidized forms ( $[\text{Ru}_2]^{2+}$  and  $[\text{Ru}_2]^{3+}$ ) and three reduced forms ( $[\text{Ru}_2]^0$ ,  $[\text{Ru}_2]^{1-}$  and  $[\text{Ru}_2]^{2-}$ ) were monitored by EPR spectroscopy to get their electronic configurations. The oxidized and reduced forms were isolated by chemically using ferrocenium hexafluorophosphate (oxidant) and cobaltocene or decamethylcobaltocene (reductant). The structurally characterized one electron oxidized product  $[\text{Ru}_2]^{2+}$  with

electronic configuration  $[(Q^{\cdot-}Ru^{III}(\mu-L)^2Ru^{III}(Q^{\cdot-})^{2+}]^{2+}$  is diamagnetic and EPR silent. Oxidation of diamagnetic, EPR-silent  $[Ru_2]^{2+}$  results in the appearance of an EPR signal at  $g_{av} = 1.998$  with very small  $g$ -anisotropy (Figure 8.5.1b,  $g_1 = 2.012$ ,  $g_2 = 1.998$  and  $g_3 = 1.984$ ,  $\Delta g = 0.028$ ) at 110 K.  $Ru^{III}$  centered EPR signals usually show a large  $g$ -anisotropy and  $g_{av}$  value of much greater than 2.0023 ( $g_{av}$  for free electron), whereas radical-bound  $Ru^{II}$  species show EPR signals that have  $g$  values much closer to the free electron  $g$  value.<sup>[73,74]</sup> The present EPR spectrum of  $[Ru_2]^{3+}$  is more compatible with the electronic configuration  $[(Q^0Ru^{II}(\mu-L)^{\cdot-}Ru^{II}(Q^0)]^{3+}$  where the unpaired electron is localized over the quinonoid bridge than the alternative electronic configuration  $[(Q^0Ru^{II}(\mu-L)^2Ru^{III}(Q^0)]^{3+}$  where the unpaired electron is localized over ruthenium moiety. Thus the one electron oxidation of bridging ligand of  $[(Q^0Ru^{II}(\mu-L)^2Ru^{III}(Q^0)]^{3+}$  leads to reduction of two  $Ru^{III}$  units to  $Ru^{II}$  units and oxidation of two  $Q^{\cdot-}$  units to  $Q^0$  units. Such electron transfer is called redox-induced electron transfer (RIET).<sup>[229]</sup> The electronic configuration of paramagnetic native state  $[Ru_2]^+$  could be either  $[(Q^2Ru^{III}(\mu-L)^2Ru^{III}(Q^{\cdot-})^+]$  ( $Q^{\cdot-}$  centered reduction with respect to  $[Ru_2]^{2+}$ ) or  $[(Q^0Ru^{II}(\mu-L)^2Ru^{II}(Q^{\cdot-})^+]$  ( $Ru^{III}$  centered reduction with respect to  $[Ru_2]^{2+}$  causes RIET). The EPR spectrum of  $[Ru_2]^+$  suggests  $[(Q^0Ru^{II}(\mu-L)^2Ru^{II}(Q^{\cdot-})^+]$  electronic configuration because of the appearance of ligand centered signal with  $g_{iso} = 1.997$  (Figure 8.5.1a) at RT. Reduction to the neutral complex  $[Ru_2]^0$  results in the appearance of a ligand centered EPR signal with  $g_{iso} = 1.999$  at RT (Figure 8.5.1c). The paramagnetic nature of  $[Ru_2]^0$  and appearance of ligand centered EPR signal suggest electronic configuration  $[(Q^{\cdot-}Ru^{II}(\mu-L)^2Ru^{II}(Q^{\cdot-})^0]$  where the unpaired electrons of two  $Q^{\cdot-}$  units are not antiferromagnetically coupled. Further reduction of  $[Ru_2]^0$  to  $[Ru_2]^-$  could be either  $Q^{\cdot-}$  centered or  $L^{2-}$  centered (because the bridging ligand can potentially be reduced in this region, Chapter 3). Both possibilities will show ligand centered EPR signal. However the reduced species  $[Ru_2]^-$  shows an EPR signal (Figure 8.5.1d) with  $g$  values 2.091, 2.057, 2.002, 1.960 and  $g_{av}$  of 2.028 (much greater than  $g$  value of organic radicals) at 110 K. The  $g$  values and  $g_{av}$  value suggest low-spin  $d^5$  ruthenium(III) centered EPR signal. Thus the electronic configuration of could be more likely  $[(Q^2Ru^{II}(\mu-L)^2Ru^{III}(Q^2)]^-$  where the reduction of one  $Q^{\cdot-}$  to  $Q^{2-}$  leads to oxidation of  $Ru^{II}$  to  $Ru^{III}$  and reduction of another  $Q^{\cdot-}$  to  $Q^{2-}$ . The reduction of  $[Ru_2]^-$  to  $[Ru_2]^{2-}$  by using strong reducing agent decamethylcobaltocene results also in the appearance of  $Ru^{III}$  type EPR signal (Figure 8.5.1e,  $g_1 = g_2 = 2.125$ ,  $g_3 = 2.047$ ,  $g_{av} = 2.130$  and  $\Delta g = 0.078$ ) at 110K. Appearance of such EPR signal can be described easily with the electronic configuration of  $[(Q^2Ru^{III}(\mu-L)^4Ru^{III}(Q^2)]^{2-}$ . The EPR of other two reduced states  $[Ru_2]^{3-}$  and  $[Ru_2]^{4-}$  were not measured because of the high reduction potentials.

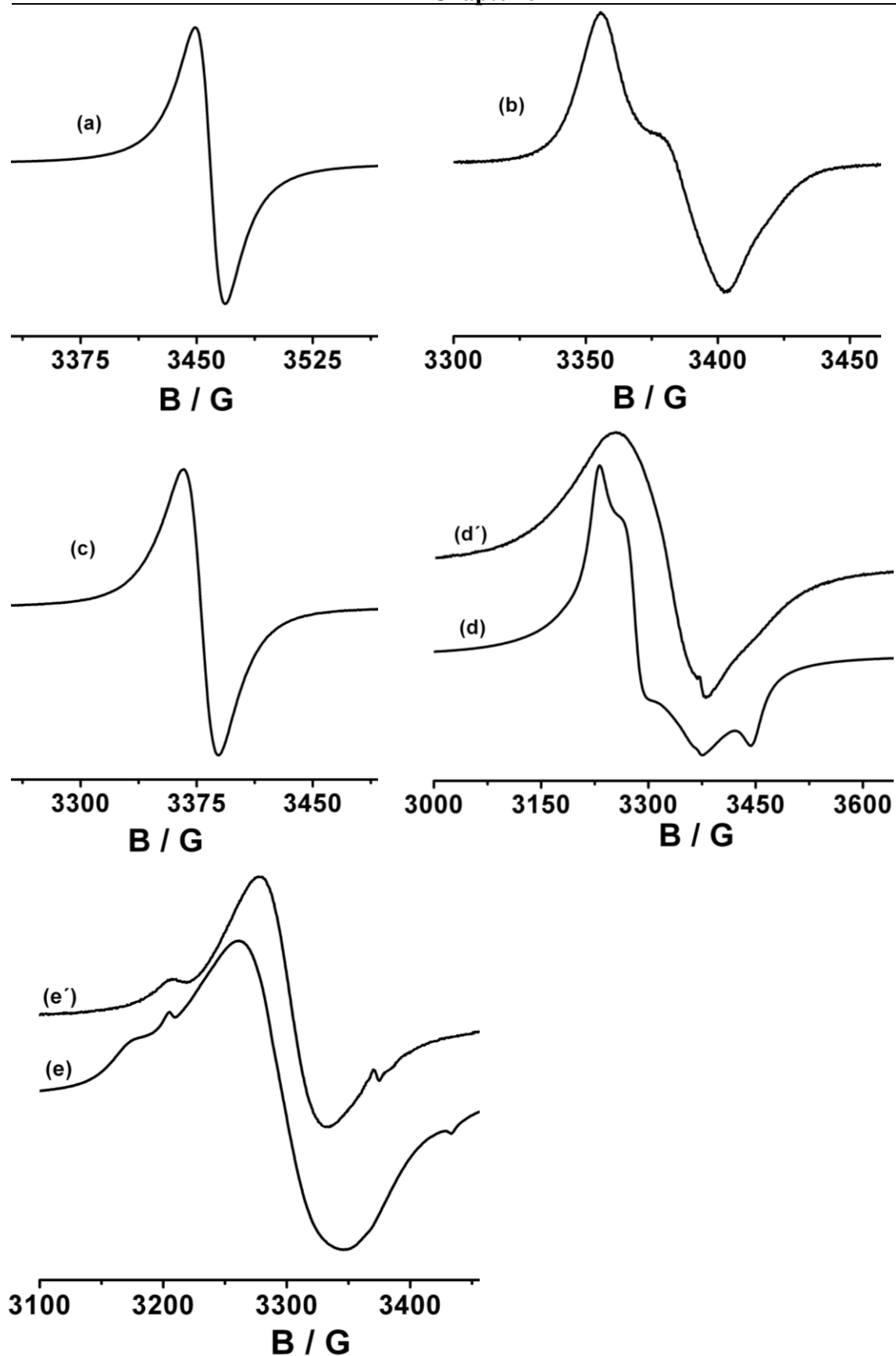


**Figure 8.5.1.** EPR spectrum of  $[\text{Ru}_2]^+$  at RT (a), EPR spectrum of  $[\text{Ru}_2]^{3+}$  at 110K (b), EPR spectrum of  $[\text{Ru}_2]^0$  at RT (c), EPR spectra of  $[\text{Ru}_2]^-$  at 110K (d) and at RT (d'), EPR spectra of  $[\text{Ru}_2]^{2-}$  at 110K (e) and at RT (e'),

## 8.6. UV/Vis/NIR spectroelectrochemistry

The preferred electronic configurations of all the redox states depicted in Scheme 8.4.1 were also verified by the analysis of UV/Vis/NIR spectroelectrochemical changes during oxidations and reductions. The UV/Vis/NIR spectroelectrochemical changes of all the redox states (except third oxidation) were monitored using an optically transparent Thin Layer Electrochemical (OTTLE) cell. The data are summarized in Table 8.6.1.

The structurally characterized electronic configuration  $[(Q)^{\cdot-}Ru^{III}(\mu-L)^2Ru^{III}(Q)^{\cdot-}]^{2+}$  of  $[Ru_2]^{2+}$  shows a lower energy transition band at 1133 nm in the NIR region and three intense bands at 778, 633 and 497 nm in the visible region (Figure 8.6.1). The bands at 1133 and 778 nm are assigned to mixed IL (inter ligand) + MLCT (metal to ligand) transitions ( $L^{2-} \rightarrow Q^{\cdot-}$  and  $Ru^{III} \rightarrow Q^{\cdot-}$ ) by time dependent DFT (TD DFT) method (see later). The TD DFT calculations of other redox states are still going on. We have assigned some transition bands of other oxidation states tentatively. The native state  $[Ru_2]^+$  shows intense NIR transition bands at 1338, and 868 nm and three transition bands at 682, 555 and 497 nm (Figure 8.6.1). The NIR transition bands at 1338, and 868 nm could be assigned tentatively to mixed IL + MLCT transitions ( $L^{2-} \rightarrow Q^0$ ,  $L^{2-} \rightarrow Q^{\cdot-}$  and  $Ru^{II} \rightarrow Q^0$  and  $Ru^{II} \rightarrow Q^{\cdot-}$ ) for the electronic configuration of  $[(Q)^0Ru^{II}(\mu-L)^2Ru^{II}(Q)^{\cdot-}]^+$ . The NIR transitions band are red shifted with respect to  $[Ru_2]^{2+}$  state suggest reduction of metals (ruthenium) or oxidation of  $Q^{\cdot-}$  to  $Q^0$ . Thus the ground state electronic configuration is more compatible with  $[(Q)^0Ru^{II}(\mu-L)^2Ru^{II}(Q)^{\cdot-}]^+$ . On one-electron  $[Ru_2]^+ \rightarrow [Ru_2]^0$ , the NIR band at around 1338 nm is red-shifted to 1678 nm with substantial increase in intensity and the NIR band at 868 nm is blue-shifted to 780 nm with substantial decrease in intensity (Figure 8.6.2). The blue-shifting of MLCT or ILCT band at 868 nm to at 780 nm suggest  $Q^0$  to  $Q^{\cdot-}$  reduction and the increase of the other NIR band intensity could be due to the increase of  $Q^{\cdot-}$  chromophores. Thus the electronic configuration  $[(Q)^{\cdot-}Ru^{II}(\mu-L)^2Ru^{II}(Q)^{\cdot-}]^0$  of  $[Ru_2]^0$  is well compatible with the experimental UV-Vis-NIR spectrum. On second reduction  $[Ru_2]^0 \rightarrow [Ru_2]^-$ , the NIR band at 1678 nm is blue-shifted to 1421 nm and a new band appears at around 961 nm (Figure 8.6.3). For the electronic configuration  $[(Q)^{2-}Ru^{II}(\mu-L)^2Ru^{III}(Q)^{2-}]^-$  of  $[Ru_2]^-$  state, the intense broad NIR band at around 1421 nm could be mixed of IVCT and intra ligands (IL) charge transfer transition. For further reduction to  $[Ru_2]^{2-}$  the intensity of the NIR band at 961 nm is decreased without shifting the position and the NIR band at 1421 nm is red-shifted to 1480 nm with marginal increase in intensity (Figure 8.6.4). For the electronic configuration  $[(Q)^{2-}Ru^{III}(\mu-L)^4Ru^{III}(Q)^{2-}]^{2-}$  ( $[Ru_2]^{2-}$ ) the band at 1480 nm can be assigned tentatively to mixed of intra ligand (IL)  $\pi \rightarrow \pi^*$  charge transfer transition and LMCT (ligand to metal charge transfer transition). On fourth reduction  $[Ru_2]^{2-} \rightarrow [Ru_2]^{3-}$ ,

the NIR band at 1480 nm is blue-shifted to 1374 nm and the NIR band at 961 nm is red-shifted to 996 nm with substantial decrease in intensity (Figure 8.6.5). After fifth reduction, the NIR bands are almost vanished (Figure 8.6.6). The five electron reduced species  $[\text{Ru}_2]^{4-}$  is compatible with the  $[(\text{Q})^2-\text{Ru}^{\text{II}}(\mu\text{-L})^4\text{Ru}^{\text{II}}(\text{Q})^{2-}]^{4-}$  formulation.

On second oxidation to  $[\text{Ru}_2]^{2+} \rightarrow [\text{Ru}_2]^{3+}$  form, the NIR band at 1133 nm is slightly blue-shifted to 1083 nm with enhanced intensity and the NIR band at 778 nm is red shifted to 821 nm with almost unchanged intensity (Figure 8.6.7). The absent of intense IVCT transition NIR band at about 1400 nm for mixed valence state (Chapter 3) suggest bridging ligand centered oxidation. The terminal semiquinone centered oxidation ( $\text{Q}^{\cdot-}$  to  $\text{Q}^0$ ) is also possible but the  $\text{Ru}^{\text{III}}-\text{Q}^0$  bonding is comparatively unstable. Thus the two electrons oxidized form  $[\text{Ru}_2]^{3+}$  is compatible with the  $[(\text{Q})^0\text{Ru}^{\text{II}}(\mu\text{-L})^{\cdot}\text{Ru}^{\text{II}}(\text{Q})^0]^{3+}$  electronic configuration. The removal of an electron from  $[\text{Ru}_2]^{2+}$  state leads to reductions of  $\text{Ru}^{\text{III}}$  units and oxidations of  $\text{Q}^{\cdot-}$  units can be verified by the red shifting of MLCT band at about 961 nm. On further oxidation the complex is partially decomposed at RT. The possible electronic configurations are  $[(\text{Q})^0\text{Ru}^{\text{II}}(\mu\text{-L})^{\cdot}\text{Ru}^{\text{III}}(\text{Q})^0]^{4+}$  and  $[(\text{Q})^0\text{Ru}^{\text{III}}(\mu\text{-L})^{2-}\text{Ru}^{\text{III}}(\text{Q})^0]^{4+}$ . The electronic configuration  $[(\text{Q})^0\text{Ru}^{\text{III}}(\mu\text{-L})^{2-}\text{Ru}^{\text{III}}(\text{Q})^0]^{4+}$  is more preferred compared to the  $[(\text{Q})^0\text{Ru}^{\text{II}}(\mu\text{-L})^{\cdot}\text{Ru}^{\text{III}}(\text{Q})^0]^{4+}$  electronic configuration because the oxidation of radical bridge similar dinuclear complexes with bipyridine ancillary ligands lead to reduction of  $\text{L}^{\cdot-}$  and oxidation of both ruthenium (Chapter 2 and 3).

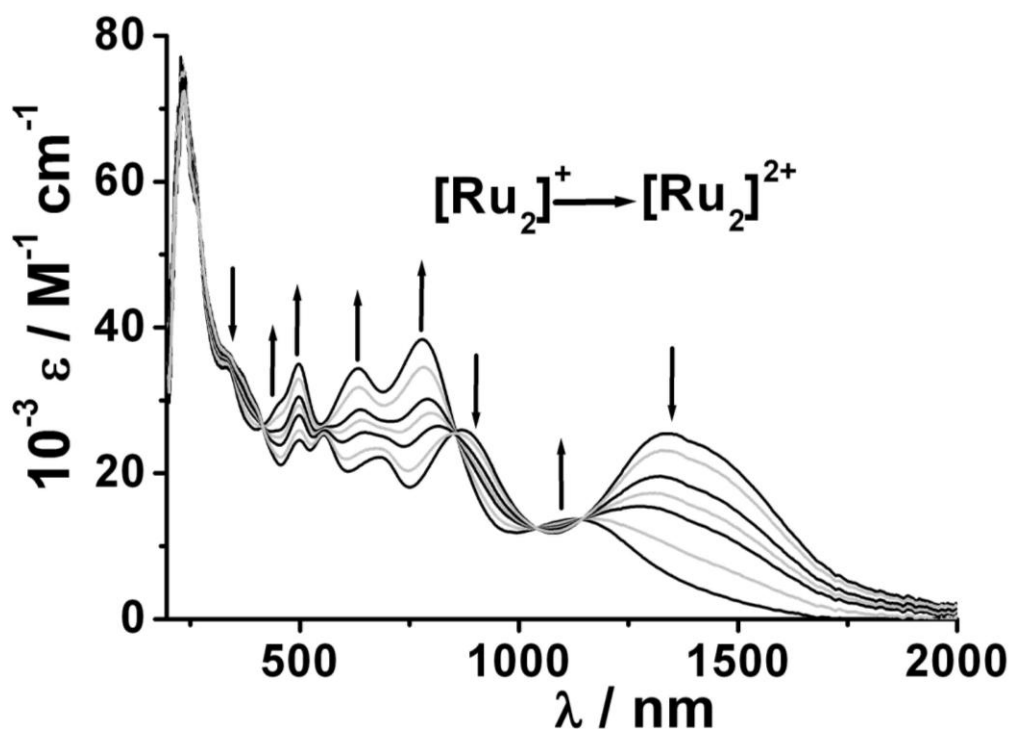


**Figure 8.6.1.** UV-Vis-NIR spectroelectrochemistry of the conversion  $[\text{Ru}_2]^{(+)\rightarrow(2+)}$  in  $\text{CH}_3\text{CN} / 0.1 \text{ M Bu}_4\text{NPF}_6$ .



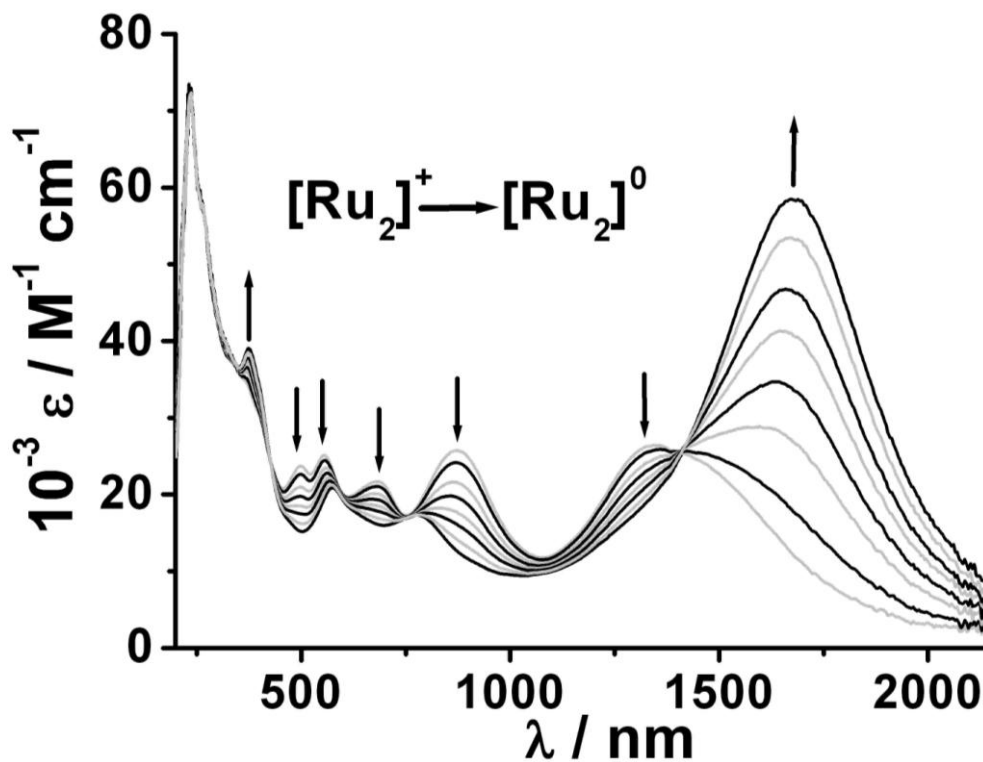


**Figure 8.6.2.** UV-Vis-NIR spectroelectrochemistry of the conversion  $[\text{Ru}_2]^{(+)\rightarrow(0)}$  in  $\text{CH}_3\text{CN} / 0.1 \text{ M Bu}_4\text{NPF}_6$ .

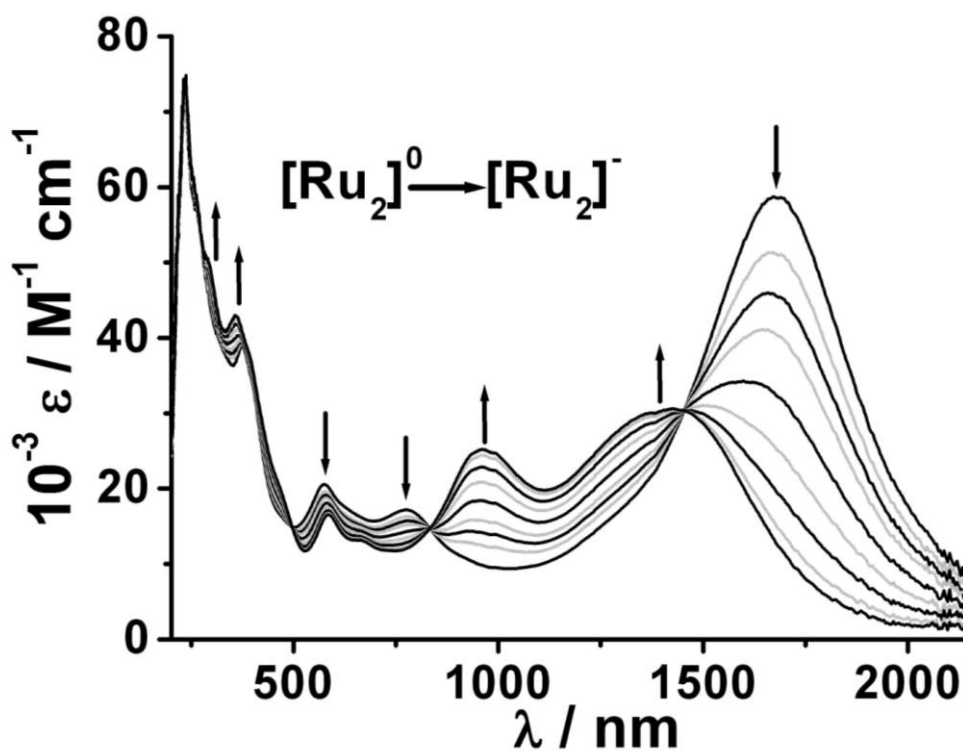


**Figure 8.6.3.** UV-Vis-NIR spectroelectrochemistry of the conversion  $[\text{Ru}_2]^{(0)\rightarrow(-)}$  in  $\text{CH}_3\text{CN} / 0.1 \text{ M Bu}_4\text{NPF}_6$ .

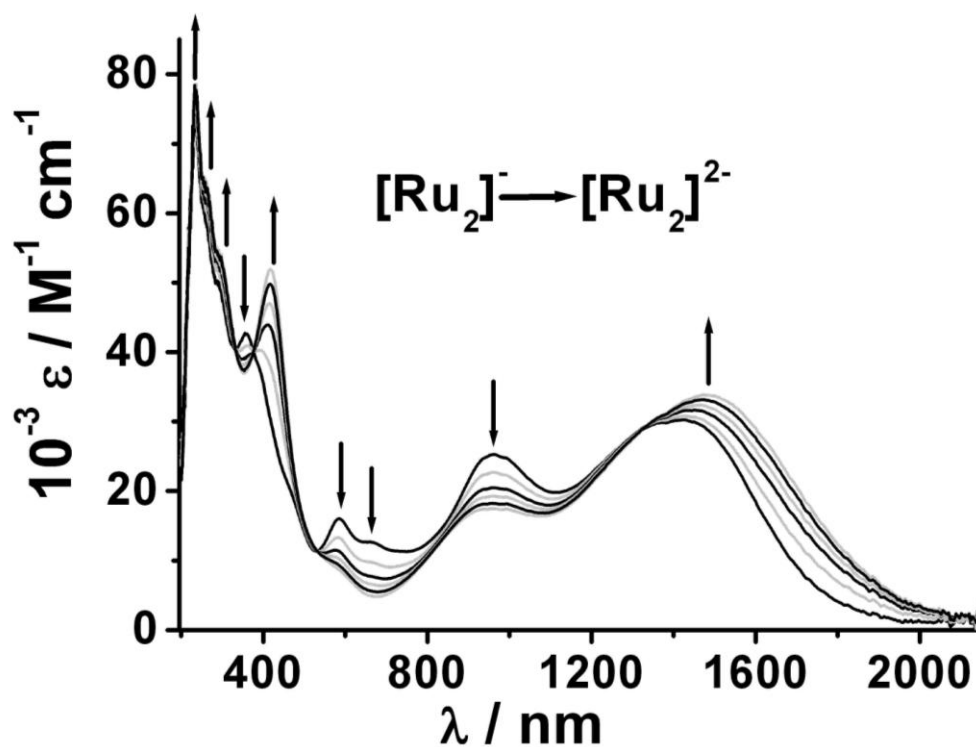


**Figure 8.6.4.** UV-Vis-NIR spectroelectrochemistry of the conversion  $[\text{Ru}_2]^{(-) \rightarrow (2-)}$  in  $\text{CH}_3\text{CN}$  / 0.1 M  $\text{Bu}_4\text{NPF}_6$ .

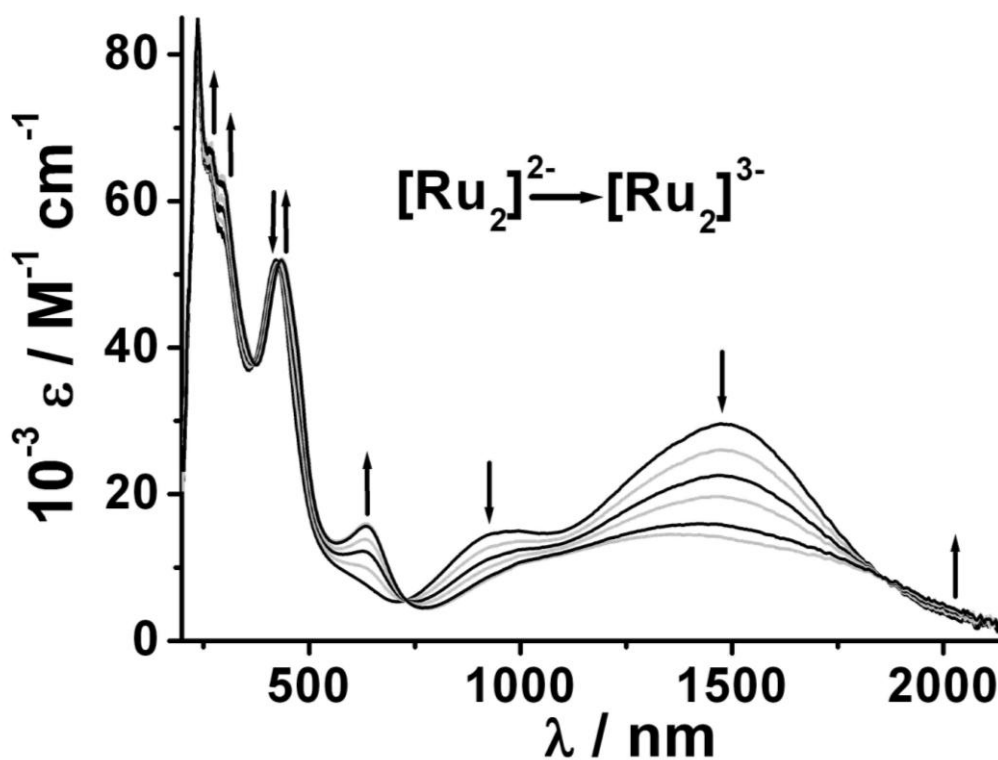


**Figure 8.6.5.** UV-Vis-NIR spectroelectrochemistry of the conversion  $[\text{Ru}_2]^{(2-) \rightarrow (3-)}$  in  $\text{CH}_3\text{CN}$  / 0.1 M  $\text{Bu}_4\text{NPF}_6$ .

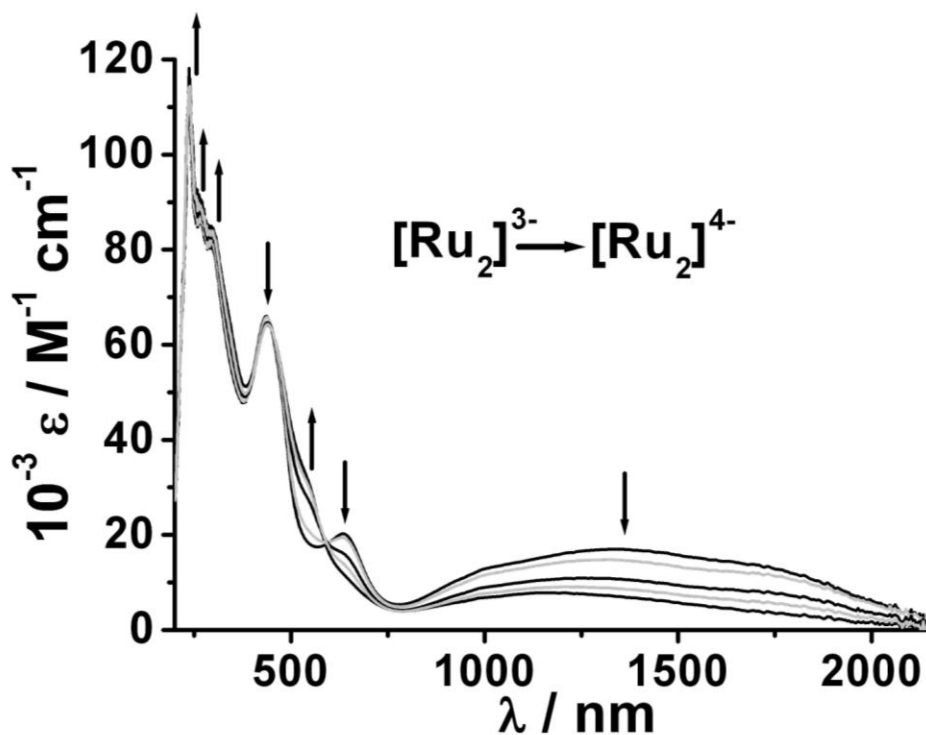


**Figure 8.6.6.** UV-Vis-NIR spectroelectrochemistry of the conversion  $[\text{Ru}_2]^{(3-)\rightarrow(4-)}$  in  $\text{CH}_3\text{CN} / 0.1 \text{ M Bu}_4\text{NPF}_6$ .

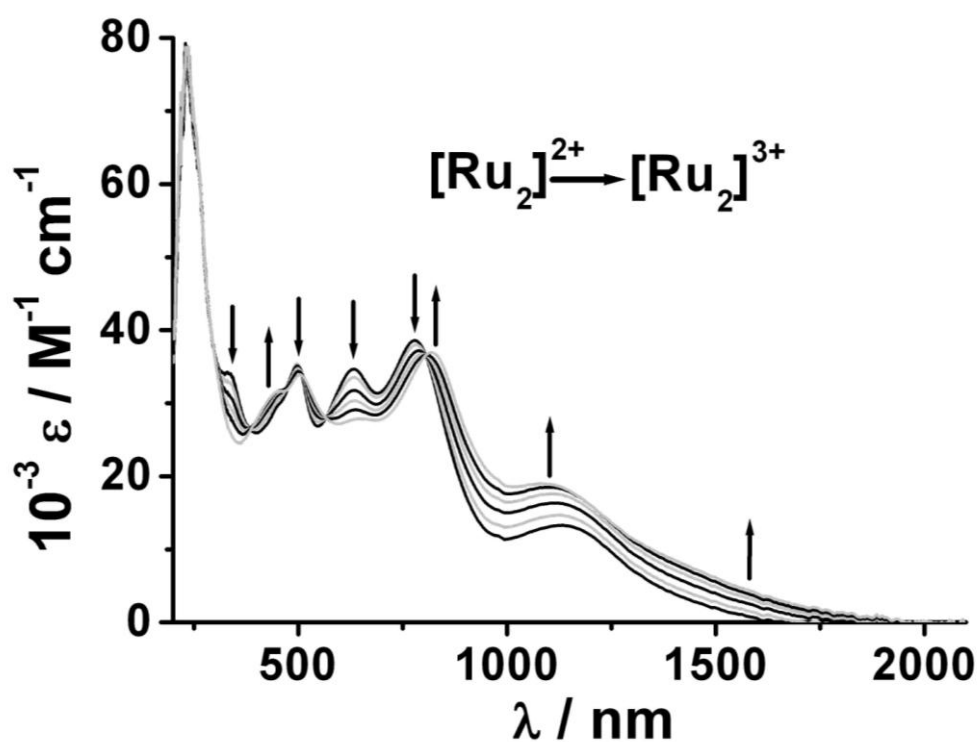


**Figure 8.6.7.** UV-Vis-NIR spectroelectrochemistry of the conversion  $[\text{Ru}_2]^{(2+)\rightarrow(3+)}$  in  $\text{CH}_3\text{CN} / 0.1 \text{ M Bu}_4\text{NPF}_6$ .

**Table 8.6.1.** Absorption data of complexes.<sup>[a]</sup>

| Compound                         | $\lambda_{\max}$ [nm] ( $10^{-3} \epsilon$ [ $M^{-1} \text{cm}^{-1}$ ])  |
|----------------------------------|--|
| [Ru <sub>2</sub> ] <sup>3+</sup> | 1083 (19.1), 821 (37.2), 647 (28.09), 505 (33.9), 452 (31.7), 426 (sh), 253 (sh), 234 (78.9)                               |
| [Ru <sub>2</sub> ] <sup>2+</sup> | 1133 (13.8), 778 (38.4), 633 (34.5), 497 (35.1), 454 (sh), 423 (sh), 334 (34.5), 256 (sh), 231 (76.7)                      |
| [Ru <sub>2</sub> ] <sup>+</sup>  | 1401 (sh), 1338 (25.5), 868 (26.1), 682 (22.4), 555 (25.1), 497 (24.8), 396 (sh), 368 (sh), 334 (sh), 258 (sh), 234 (71.6) |
| [Ru <sub>2</sub> ] <sup>0</sup>  | 1678 (58.6), 1324 (sh), 780 (17.2), 644 (sh), 572 (21.1), 398 (sh) 374 (39.2), 264 (sh), 234 (71.8)                        |
| [Ru <sub>2</sub> ] <sup>-</sup>  | 1421 (30.7), 961 (25.3), 663 (13.2), 585 (16.6), 454 (sh), 388 (sh), 359 (43.0), 288 (50.5), 258 (sh), 234 (74.4)          |
| [Ru <sub>2</sub> ] <sup>2-</sup> | 1480 (33.9), 946 (17.7), 558 (sh), 419 (52.0), 289 (sh), 262 (sh), 237 (78.6)  |
| [Ru <sub>2</sub> ] <sup>3-</sup> | 1690 (sh), 1374 (14.6), 996 (sh), 636 (16.0), 435 (52.2), 295 (63.4), 268 (67.8), 237 (85.9)                               |
| [Ru <sub>2</sub> ] <sup>4-</sup> | 1688 (sh), 1160 (8.2), 627 (sh), 537 (sh), 440 (64.2), 296 (84.9), 260 (91.8), 237 (118.0)                                 |

<sup>[a]</sup> From spectroelectrochemistry in CH<sub>3</sub>CN / 0.1 M Bu<sub>4</sub>NPF<sub>6</sub> at 298 K.

## 8.7. DFT calculation

The electronic structures of the complex [Ru<sub>2</sub>]<sup>n</sup>, n = +3,+2,+1,0,-1,-2,-3,-4, were calculated by density functional theory (DFT) methods using the Gaussian 09<sup>[230]</sup> and ADF2010.01<sup>[231,232]</sup> program packages.

For the H, C, N, O and S atoms 6-31g(d) polarized double- $\zeta$  basis sets<sup>[233]</sup> (G09) were used together with quasirelativistic effective core pseudopotentials and a corresponding optimized set of basis functions for Ru.<sup>[234]</sup> All structures were optimized without geometrical constraints using the hybrid PBE0 functional,<sup>[235,236]</sup> open shell systems within the UKS approach. The vibrational analysis was done with using structures optimized with the corresponding functional. The polarizable continuum model<sup>[240]</sup> (PCM) was used for modeling of the solvent influence. Electronic transitions were calculated by time dependent DFT (TD DFT) method.

Slater type orbital (STO) basis sets of triple- $\zeta$  quality with two polarization functions for Ru atoms and of double- $\zeta$  quality with polarization functions for the remaining atoms were employed within ADF2010.02. The inner shells were represented by the frozen core approximation (1s for C, N, O, 2s for S, 1s-3d for Ru were kept frozen). The calculations were done with the functional including Becke's gradient correction<sup>[237]</sup> to the local exchange expression in conjunction with Perdew's gradient correction<sup>[238]</sup> to the local correlation (ADF/BP). The scalar relativistic (SR) zero order regular approximation (ZORA) was used within ADF calculations. The  $g$  tensor was obtained from a spin-nonpolarized wave function after incorporating the spin-orbit (SO) coupling by the first-order perturbation theory from a ZORA Hamiltonian in the presence of a time-independent magnetic field.<sup>[239]</sup>

### 8.7.1. Results and discussions

Optimized geometrical parameters of the  $[\text{Ru}_2]^+$  complex (Table 8.7.1.1) reasonably well describe the experimental structure, only Ru-N2 bond length is overestimated by calculations. Agreement of calculated and experimental intraligand bond lengths indicates that the electron density redistribution radical cation is well described. Qualitative MO scheme of  $[\text{Ru}_2]^{2+}$  complex is depicted in Figure 8.7.1.1, this Figure also shows shapes of frontier orbitals of this complex. Almost degenerate HOMO and HOMO-1 are formed mainly by  $\pi^*$  orbitals of bridging ligand with contribution of Ru  $d_\pi$  orbital of 26 and 28%, respectively. LUMO and LUMO+1 are to large extent formed by  $\pi^*$  orbitals of side ligands, LUMO+2 is delocalized over the bridge ligand. Ru  $d_\pi$  orbitals contribute to LUMO, LUMO+1 and LUMO+2 by 12, 22 and 12%, respectively.

During reduction the lowest LUMOs are stepwise filled up and during oxidation the electrons are going out stepwise from highest HOMOs. Figure 8.7.1.2 shows spin density calculated with PCM correction for radical ions  $[\text{Ru}_2]^{\text{n}}$ . The Table 8.7.1.2 shows reasonable agreement between experimental and calculated EPR data for ions  $[\text{Ru}_2]^{\text{n}}$ .

Table 8.7.1.3 presents TD-DFT calculated allowed lowest lying transitions of  $[\text{Ru}_2]^{2+}$  complex. Experimental spectrum is qualitatively well reproduced by calculations. Intense experimental features at 778 and 1133 nm are assigned to mixed IL + MLCT transitions from the HOMO, HOMO-1 into LUMO and LUMO+1.

**Table 8.7.1.1.** The comparison of selected G09/PBE0 calculated averaged bond lengths [ $\text{\AA}$ ] of  $[\text{Ru}_2]^+$  with experimental ones.

| Bond lengths<br>( $\text{\AA}$ ) | experiment | calculated | Bond lengths<br>( $\text{\AA}$ ) | experiment | calculated |
|----------------------------------|------------|------------|----------------------------------|------------|------------|
| Ru-N1                            | 2.014      | 2.012      | C3-C2                            | 1.388      | 1.401      |
| Ru-N2                            | 1.943      | 1.994      | O2-C11                           | 1.308      | 1.295      |
| Ru-O1                            | 2.033      | 2.042      | N2-C16                           | 1.348      | 1.357      |
| Ru-O2                            | 2.038      | 2.039      | C11-C16                          | 1.424      | 1.450      |
| Ru-S1                            | 2.317      | 2.342      | N1-C4                            | 1.421      | 1.396      |
| Ru-S2                            | 2.325      | 2.342      | S1-C9                            | 1.805      | 1.798      |
| O1-C1                            | 1.320      | 1.297      | C4-C9                            | 1.385      | 1.411      |
| N1-C3                            | 1.345      | 1.347      | N2-C17                           | 1.397      | 1.390      |
| C1-C3                            | 1.471      | 1.478      | S2-C22                           | 1.799      | 1.794      |
| C1-C2                            | 1.382      | 1.391      | C17-C22                          | 1.405      | 1.414      |

**Table 8.7.1.2.** EPR data for ions  $[\text{Ru}_2]^n$ ,  $n=3, 2, 1, 0, -1, -2$ .

| complex         | Experimental |   | Calculated       |                                |
|-----------------|--------------|---|------------------|--------------------------------|
|                 | (T = 273 K)  | (T= 110 K) ( $\Delta_g$ )                         | $g_{\text{iso}}$ | $g_1, g_2, g_3$ ( $\Delta_g$ ) |
| $\text{M}^{3+}$ |              | 2.012 ( $g_1$ ), 1.998 ( $g_2$ ), 1.984 ( $g_3$ ) | 2.004            | 2.035, 2.000, 1.977            |
| $\text{M}^{2+}$ | diamagnetic  |   | -                |                                |
| $\text{M}^+$    | 1.997        | 1.997   | 2.006            | 2.050, 2.006, 1.963            |
| $\text{M}^0$    | 1.999        | 1.999   | 2.008            | 2.041, 2.005, 1.979            |
| $\text{M}^-$    | 2.033        | 2.091, 2.057, 2.002, 1.960                        | 2.007            | 2.067, 2.000, 1.954            |
| $\text{M}^{2-}$ | 2.046        | 2.125, 2.047                                      |                  |                                |

**Table 8.7.1.3.** TD-DFT (PBE0/PCM-acetonitrile) calculated lowest lying dominant transitions of  $[\text{Ru}_2]^\text{n}$  with oscillator strengths larger than 0.001 (MOs composing individual excitations are depicted in Figures 1)

| main component (%)  | transition energy<br>eV(nm) | oscillator strength | exp. absorption maximum<br>(nm) | molar extinction coefficient,<br>( $\text{mol dm}^{-3}$ ) |
|---|-----------------------------|---------------------|---------------------------------|---|
| n = 2   |                             |                     |                                 |   |
| HOMO $\rightarrow$ LUMO (39)<br>HOMO-1 $\rightarrow$ LUMO+1 (38)                                    | 1.05 (1180)                 | 0.053               | 1083                            | 13.8  |
| HOMO $\rightarrow$ LUMO (36)<br>HOMO-1 $\rightarrow$ LUMO+1 (30)<br>HOMO -2 $\rightarrow$ LUMO (18) | 1.31 (936)                  | 0.172               |                                 |   |
| HOMO -2 $\rightarrow$ LUMO (36)<br>HOMO $\rightarrow$ LUMO (18)<br>HOMO-3 $\rightarrow$ LUMO+1 (17) | 1.64 (755)                  | 0.261               |                                 |   |
| HOMO -4 $\rightarrow$ LUMO (50)<br>HOMO-1 $\rightarrow$ LUMO+1 (19)                                 | 1.85(672)                   | 0.229               | 633                             | 34.5  |
| HOMO $\rightarrow$ LUMO+2 (64)  | 2.19 (566)                  | 0.195               | 497                             | 35.1  |
| HOMO -8 $\rightarrow$ LUMO (45)   | 2.41 (514)                  | 0.203               |                                 |   |
| HOMO -5 $\rightarrow$ LUMO +1 (28)<br>HOMO -8 $\rightarrow$ LUMO (21)                               | 2.56 (484)                  | 0.299               |                                 |   |

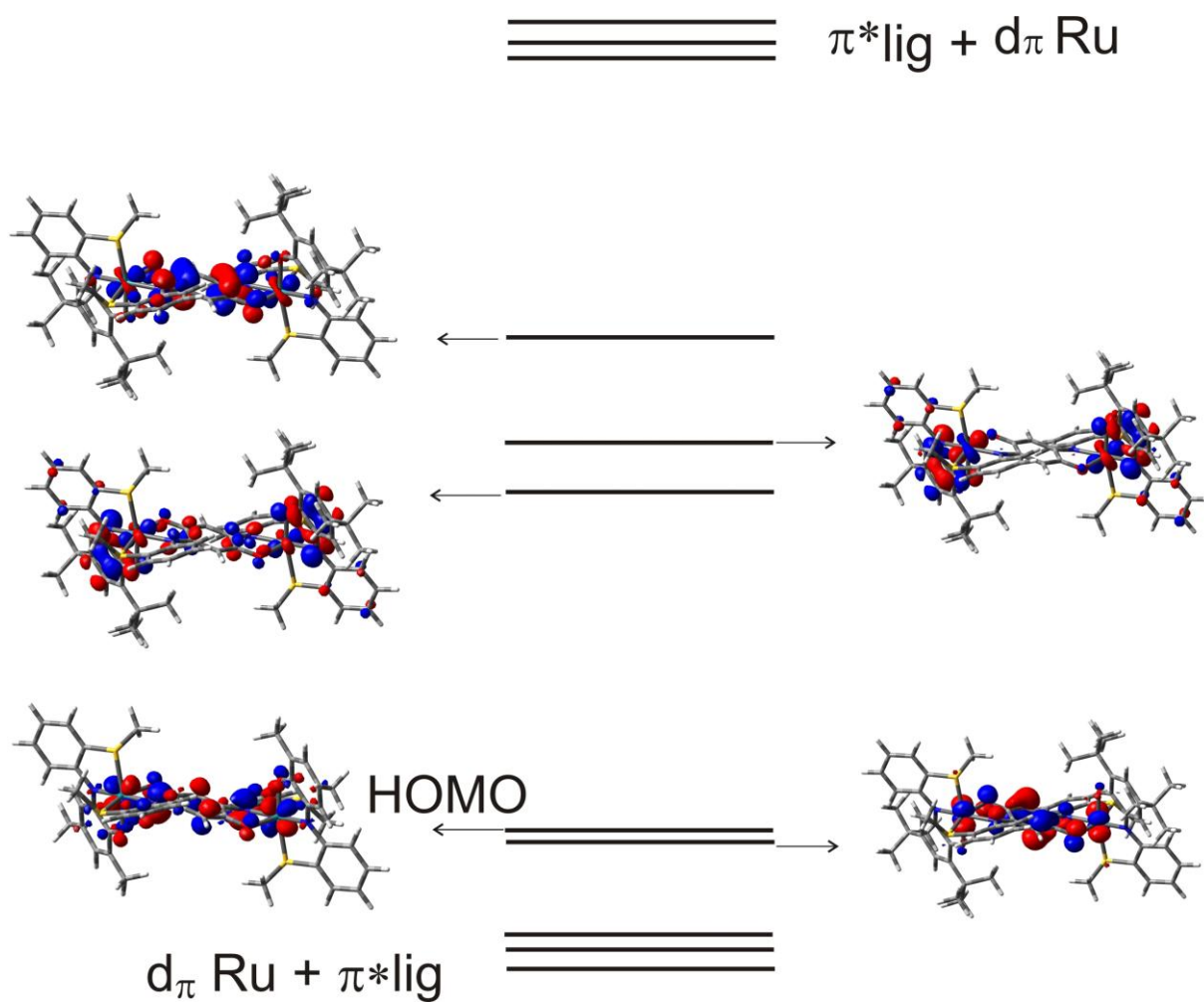


**Figure 8.7.1.1.** Qualitative DFT (G03/PBE0/PCM) calculated MO scheme of the  $[\text{Ru}_2]^{2+}$ .



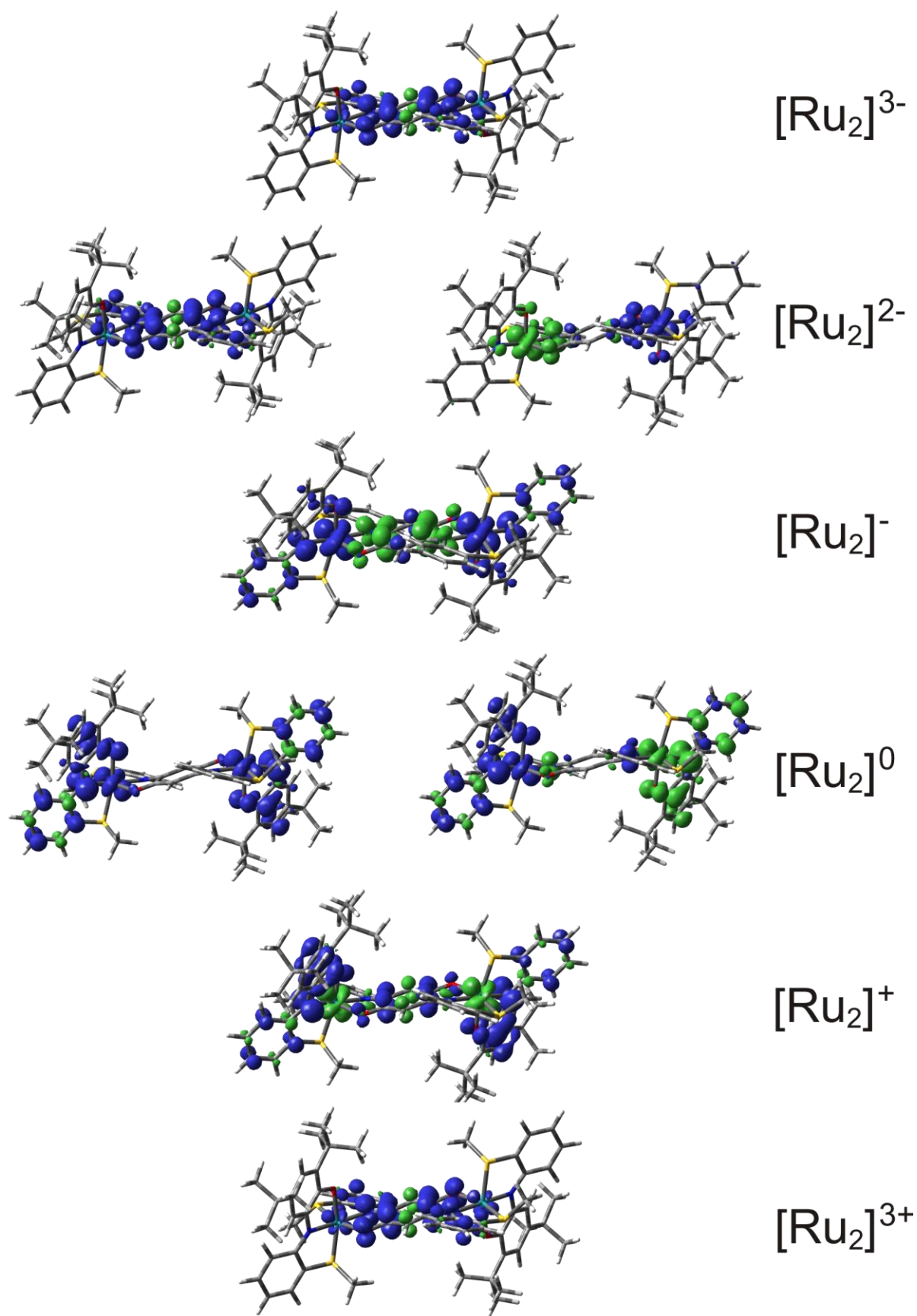


**Figure 8.7.1.2.** DFT (G09/PBE0/PCM) calculated spin density of the  $[\text{Ru}_2]^n$ ,  $n = +3, +2, +1, 0, -1, -2, -3$  and  $-4$ .

## 8.8. Conclusion

By combining the concepts of a non-innocent bridge as well as metal and co-ligand redox activity, we present here a structurally, electrochemically and spectroscopically characterized five component super redox-rich system  $[(Q)Ru(\mu-L)Ru(Q)]^n$  where  $Q^0$  is 4,6-di-*tert*-butyl-*N*-(2-methylthiophenyl)-*o*-iminobenzoquinone and  $L^{2-}$  is the doubly deprotonated form of 2,5-di-[2-(methylthio)-anilino]-1,4-benzoquinone. The available oxidation states are  $Q^{0,-,2-}$ ,  $Ru^{II,III,IV}$  and  $L^{0,-,2-,3-,4-}$ . Eight reversible one-electron transfer steps between  $n = (+4)$  to  $(-4)$  were investigated by cyclic voltammetry, UV-vis-NIR and EPR spectroelectrochemistry for the structurally characterized  $[(Q)Ru(\mu-L)Ru(Q)](ClO_4)_2$ ,  $[Ru_2](ClO_4)_2$ . These combined studies revealed that  $[Ru_2](ClO_4)_2$  is best described as  $[(Q)^{\cdot-}Ru^{III}(\mu-L)^{2-}Ru^{III}(Q)^{\cdot-}](ClO_4)_2$  with antiferromagnetic coupling between  $Q^{\cdot-}$  and  $Ru^{III}$  spins at each end. The EPR and UV-Vis-NIR spectroelectrochemical results have allowed us to identify the most appropriate oxidations state combinations for the accessible redox forms as listed in Scheme 8.4.1. The oxidation state combinations depicted in scheme 8.4.1 are also verified by quantum chemical calculations.

## CHAPTER 9

# A Mononuclear Ruthenium Complex with Noninnocent *N*-(2-Methyl-5,8-dioxo-5,8-dihydroquinolin-7-yl)acetamide Ligand and Acetylacetonato Terminal Ligands

### 9.1 Introduction

Ruthenium complexes with non-innocent ligands (NILs) such as benzoquinone, iminobenzoquinone, benzoquinonediimine and their redox derivatives exhibit delocalized electron distributions, non-integer oxidation states and interesting electronic properties due to the extensive mixing of NIL  $\pi^*$  orbitals with the ruthenium  $d\pi$  orbitals.<sup>[241,242]</sup> The electron distribution within these complexes can be modulated by altering both the ancillary ligands and the NIL, and in a few cases the resultant electron distributions are used to greatest advantage for catalysis like alcohol oxidation, water oxidation etc.<sup>[243]</sup> Recent studies have focused on mono as well as multinuclear complexes with quinones and other noninnocent ligands.<sup>[244-246]</sup> Substituted quinoline-5,8-diones have found extensive use in organic and medicinal chemistry owing to their potent antitumor, antibacterial, antifungal activity.<sup>[247-251]</sup> Such compounds which combine a *p*-quinone part condensed with a pyridine part have several binding sites available for one or more metal centres. The compound *N*-(2-methyl-5,8-dioxo-5,8-dihydroquinolin-7-yl)acetamide, **L** can bind to a metal centre either through an oxygen atom of the *p*-quinone ring and the pyridine nitrogen atom or through the N–H group (before or after deprotonation) together with the oxygen atom but usually this type of ligands bind to a metal centre through an oxygen atom of the *p*-quinone ring and the pyridine nitrogen atom.<sup>[252]</sup> This coordination produces a five-membered ring containing an unsaturated  $\alpha$ -iminoketo function which can act as a  $\pi$  acceptor towards a bound  $\pi$  electron-rich metal centre such as ruthenium(II).

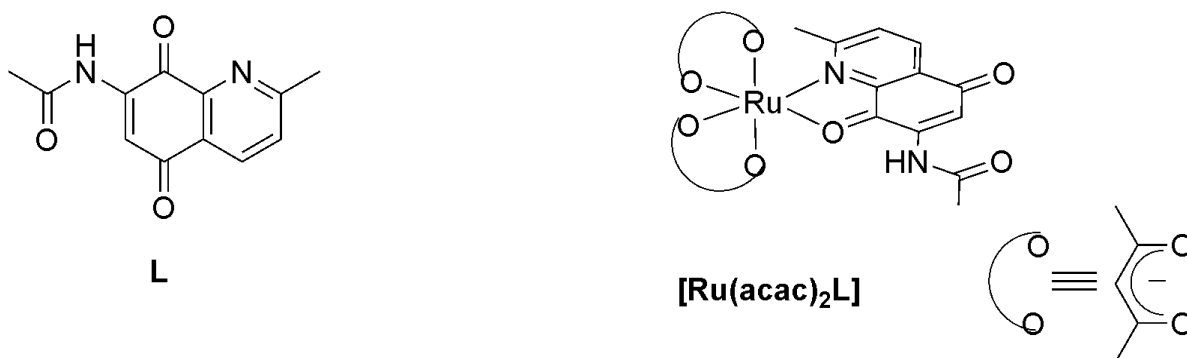
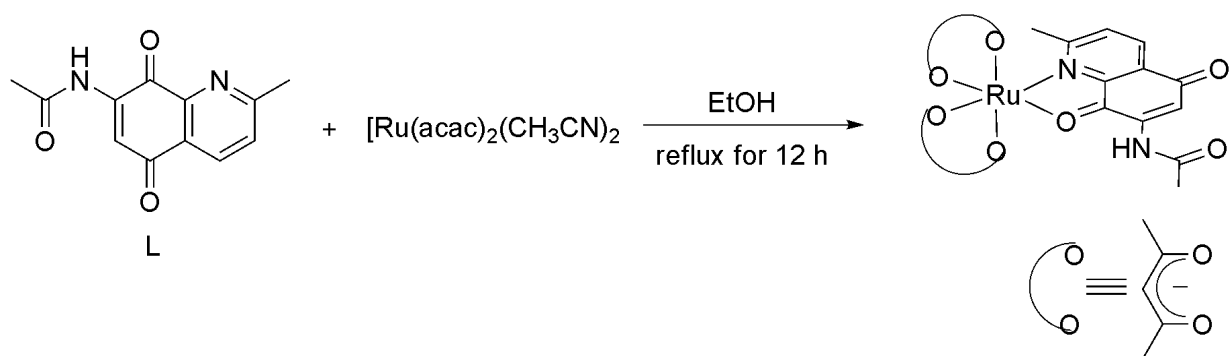


**Figure 9.1.1.** Molecular formulae of the ligand (**L**) and its metal complex **[Ru(acac)<sub>2</sub>L]**.

The *p*-quinone part is a potentially reversible electron transfer site and the presence of several carbonyl groups in **L** provides for good IR spectroscopic handles to verify bonding as well as the redox level of **L**. This is not usually the case for most of the quinone ligands used in the literature because the C–O stretching frequencies in those cases (particularly for the reduced forms of the ligands) fall in the fingerprint region and hence identifying them becomes difficult. In view of the coordination ambiguity, potentially non-innocent character, presence of convenient spectroscopic handles in **L** as well as our general interest in building up metal complexes with new quinone-based ligands,<sup>[253-256]</sup> we ventured out to probe its reactions with [Ru(acac)<sub>2</sub>(CH<sub>3</sub>CN)<sub>2</sub>] (acac = acetylacetonato). The ruthenium complexes of quinone-based ligands are known to show valence and spin ambiguity with various oxidation levels of the ligand and metal center that might occur depending on intramolecular electron transfer. Herein we report on the synthesis of [Ru(acac)<sub>2</sub>**L**]. The Ru<sup>II</sup> centers are usually prone to undergo intramolecular electron transfer when combined with the completely oxidized form of a quinone ligand. Information on such processes can be vital when trying to determine reactivity of such complexes. By using the ligand **L** we show here how the extent of this electron transfer is taking place. The “[Ru(acac)<sub>2</sub>]” component was chosen because of the relatively electron-rich nature (vide infra) of the Ru<sup>II</sup> center, kinetically stable in different oxidation states and generally show reversible electrochemical behaviour. A combination of electrochemical as well as UV/Vis/NIR, IR, and EPR (Electron Paramagnetic Resonance) spectroelectrochemical results are used to answer questions related to electron transfer and valence and spin distribution.

## 9. 2. Syntheses and characterization

The complex was synthesized by the reactions of **L** with [Ru(acac)<sub>2</sub>(CH<sub>3</sub>CN)<sub>2</sub>] in EtOH (Scheme 9.2.1). Attempts to prepare the corresponding complex with the [Ru(bpy)<sub>2</sub>(Cl)<sub>2</sub>] (bpy = 2,2'-bipyridine) precursor, even after removal of the chloride ions by Ag<sup>I</sup> salts, were not successful and showed the competition for metal dπ electrons between bpy and **L** which does not allow sufficient Ru–**L** π-bonding interaction that would stabilize coordination of the rather poor σ-donating ligand **L**.



**Scheme 9.2.1.** Synthetic scheme for  $[\text{Ru}(\text{acac})_2\text{L}]$ .

The diamagnetic complex  $[\text{Ru}(\text{acac})_2\text{L}]$  was purified by column chromatography on an alumina column and characterized by elemental analysis, electrospray mass, IR and  $^1\text{H-NMR}$  spectroscopy.

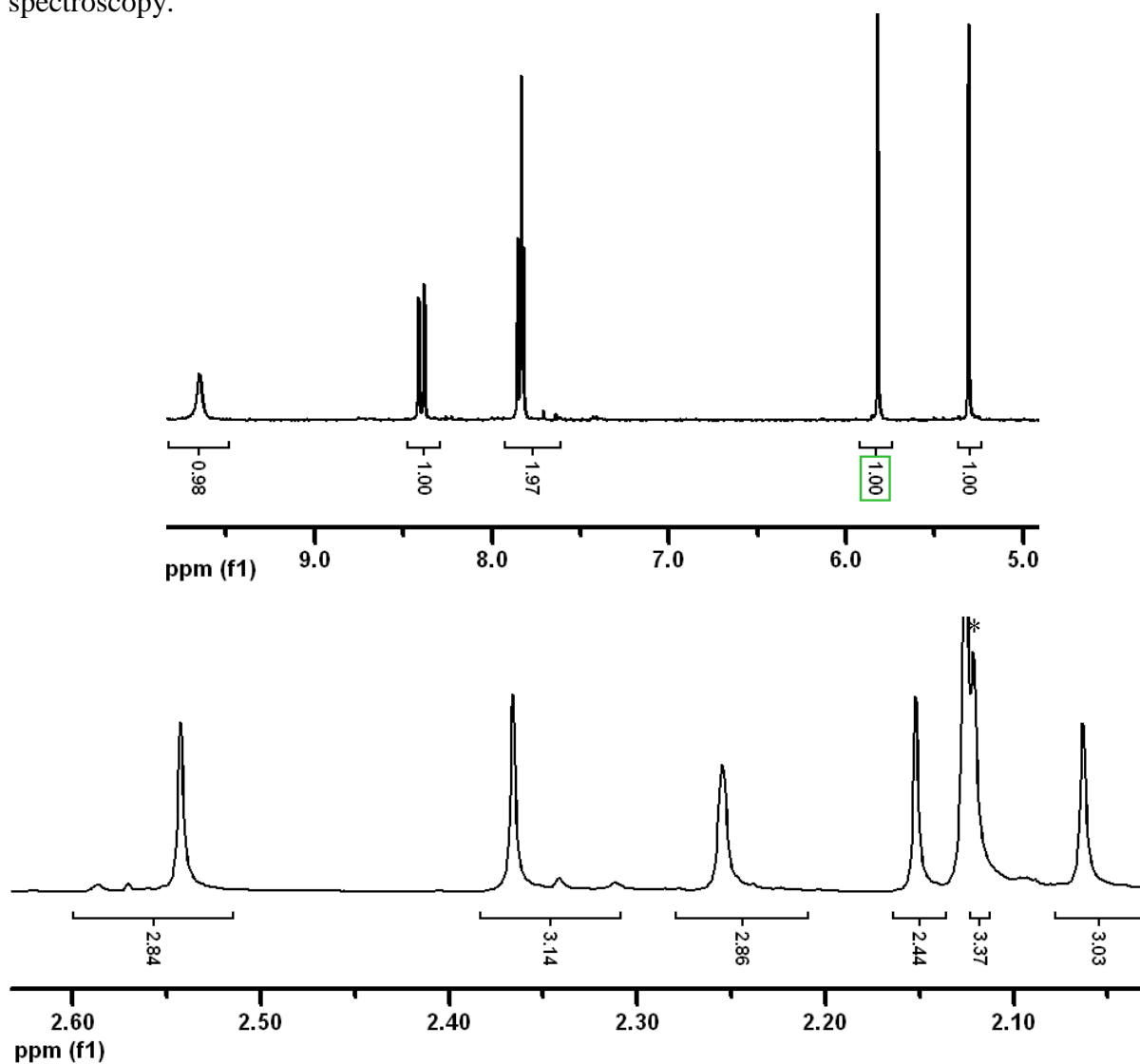


**Figure 9.2.1.**  $^1\text{H-NMR}$  spectra of the complex  $[\text{Ru}(\text{acac})_2\text{L}]$ ; CH and NH protons (top) and Me protons (bottom); \* indicates signals from the solvent.

The  $^1\text{H-NMR}$  spectrum of  $[\text{Ru}(\text{acac})_2\text{L}]$  (Figure 9.2.1), recorded in  $\text{CD}_3\text{CN}$  at room temperature, exhibits six distinct Me signals, five CH signals and one broad NH signal. The appearance of three non-equivalent carbonyl IR stretching bands at 1702, 1600 and  $1547\text{ cm}^{-1}$  with large shift compared to free ligand also supports the formation of  $[(\text{acac})_2\text{Ru}(\text{L})]$ .

### 9.3. Electrochemistry

The electrochemistry of the complex  $[\text{Ru}(\text{acac})_2\text{L}]$  and the ligand **L** has been studied by cyclic voltammetry in order to investigate their redox properties. The  $[\text{Ru}(\text{acac})_2\text{L}]$  shows one one-electron reversible oxidation and two one-electron reversible reductions in  $\text{CH}_2\text{Cl}_2/0.1\text{ m Bu}_4\text{NPF}_6$  at 295 K (Figure 9.3.1 [left]). The free ligand **L** shows only two one-electron reversible reduction processes at in  $\text{CH}_2\text{Cl}_2/0.1\text{ m Bu}_4\text{NPF}_6$  at 295 K (Figure 9.3.1 [right]).<sup>[257]</sup>

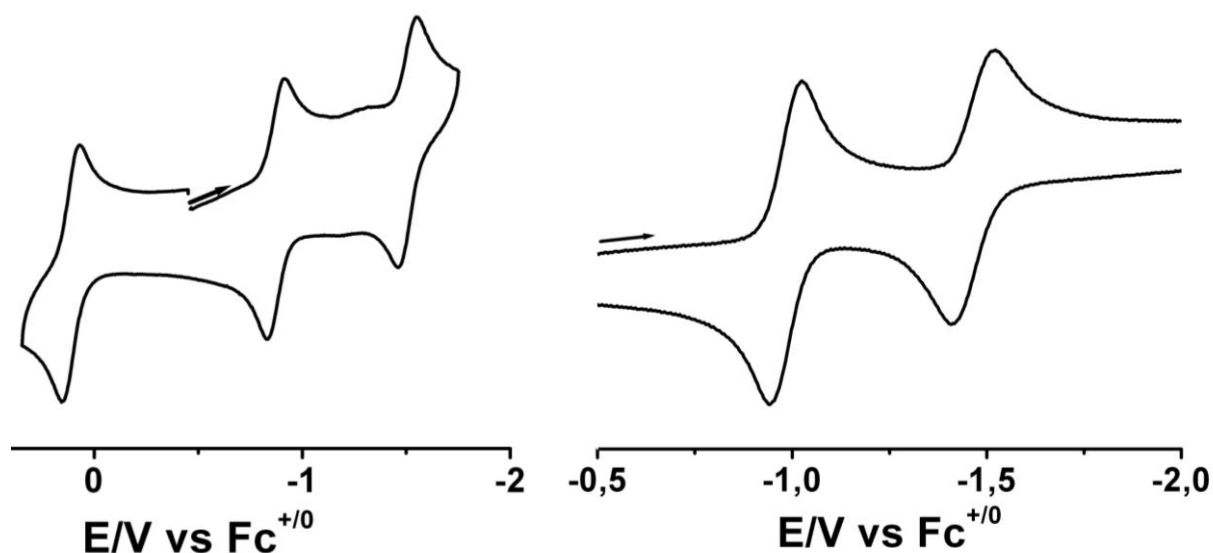


**Figure 9.3.1.** Cyclic voltammograms of  $[\text{Ru}(\text{acac})_2\text{L}]$  (left) and **L** (right) in  $\text{CH}_2\text{Cl}_2/0.1\text{ m Bu}_4\text{NPF}_6$  at 295 K

Ferrocene was used as an internal standard and all the redox potentials are referenced with respect to ferrocenium /ferrocene ( $\text{Fc}^+/\text{Fc}$ ) couple. The reductions and the oxidation potential are summarized in Table 9.3.1.

**Table 9.3.1.** Redox potentials of the complex and the ligand.

| Compound                             | $E_{1/2}(\text{ox})$ | $E_{1/2}(\text{red1})$ | $E_{1/2}(\text{red2})$ |
|--------------------------------------|----------------------|------------------------|------------------------|
| <b>L</b>                             | --                   | -0.98                  | -1.47                  |
| $[\text{Ru}(\text{acac})_2\text{L}]$ | +0.11                | -0.87                  | -1.51                  |

The reduction potentials of the complex are only slightly shifted compared to the reduction potentials of **L**. In order to gain more insight into the redox processes of the complex as well as to make a possible assignment of them we carried out a combination of UV/Vis/NIR, IR, and EPR spectroelectrochemical measurements.

## 9.4. IR Spectroelectrochemistry

The IR spectroelectrochemical investigation was performed in OTTLE cell. The IR spectroelectrochemical measurements of the complex  $[\text{Ru}(\text{acac})_2\text{L}]$  were done to investigate the change of coordinated and non-coordinated carbonyl stretching frequencies on reduction and oxidation processes. To assign the sites of the redox processes, the IR spectroelectrochemical measurements of free ligand **L** were also done.

### 9.4.1 The ligand **L**

The changes in the carbonyl stretching bands of the ligand **L** during the first reduction are shown in Figure 9.4.1 and Figure 9.4.2. The results for the **L** are summarized in Tab 9.4.1.

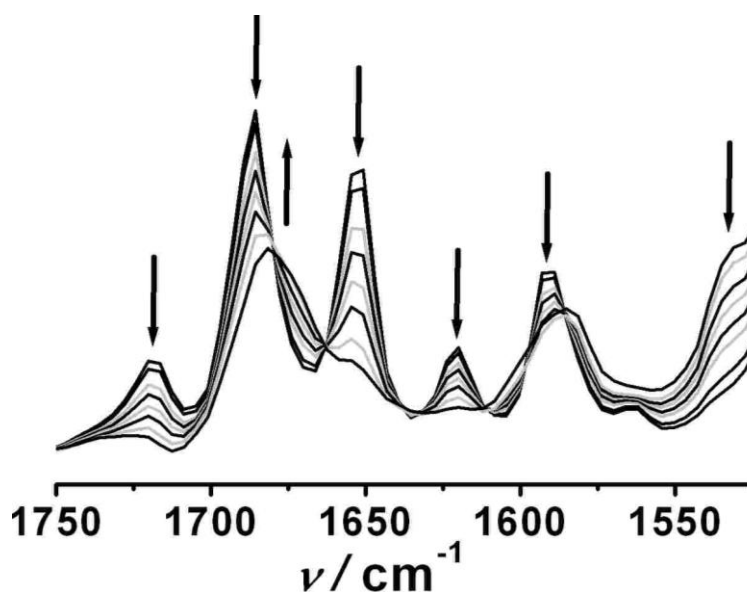


**Figure 9.4.1:** Changes in the IR spectrum (carbonyl region) of **L** during first reduction in  $\text{CH}_2\text{Cl}_2 / 0.1 \text{ M Bu}_4\text{NPF}_6$ .

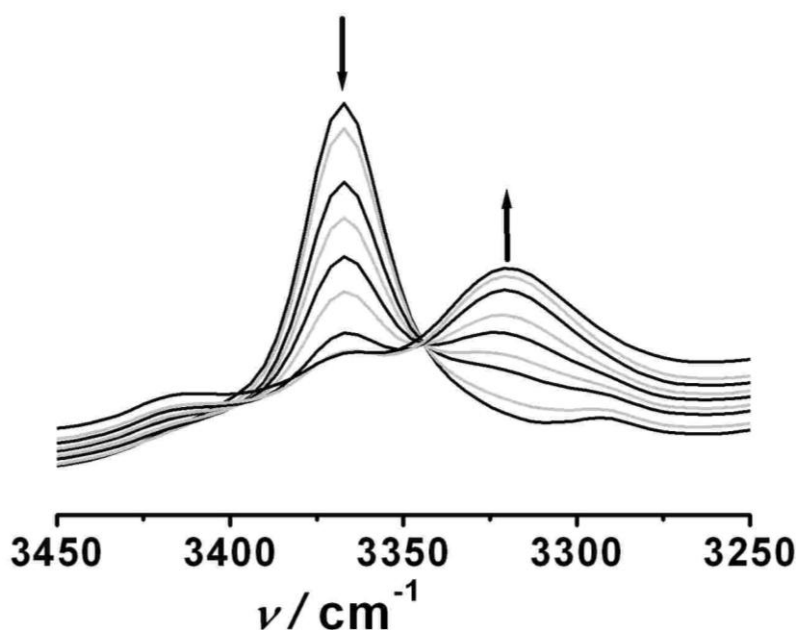


**Figure 9.4.2:** Changes in the IR spectrum (N-H region) of **L** during first reduction in  $\text{CH}_2\text{Cl}_2$  / 0.1 M  $\text{Bu}_4\text{NPF}_6$ .

The assignment of IR bands of **L** (Figure 9.4.1 and Figure 9.4.2) are complicated because of coupling of C=O stretchings with ring vibrations and possible shifts due to Fermi resonance. Furthermore, a hydrogen bond from the N–H group to neighbouring carbonyl on the quinone ring can weaken this C=O bond and shift the stretching frequency to a lower value. Tentatively we ascribe the bands  $1685$  and  $1652\text{ cm}^{-1}$  to quinone (C5, C8) C=O stretchings in analogy to the assignment for the benzoquinone molecule [ $\nu(\text{CO}) = 1686$  and  $1666\text{ cm}^{-1}$ ]. The band at higher wavenumbers  $1719\text{ cm}^{-1}$  remains almost unchanged after coordination of **L** to the  $\text{Ru}^{\text{II}}$  unit (Table 9.4.1) and can be assigned to the C=O stretching of the amide group. The N–H stretching vibration of the amide group appears at  $3367\text{ cm}^{-1}$ . On one-electron reduction to **L**<sup>•−</sup> the bands in the carbonyl and ring vibration region are shifted to lower frequencies (Figures 9.4.1 and 9.4.2, Table 9.4.1) and the overall character of the spectrum (shape, separation of bands) seems to be largely changed. The shift of the bands to lower frequencies can be explained by the population of an antibonding orbital on one-electron reduction; the dislocation of bands is probably influenced by the formation of a stronger  $\text{O}\cdots\text{H}$  hydrogen bond between the C=O (C8) group and the amide N–H group in the more electron-rich one-electron reduced species. The hydrogen bond also weakens the N–H bond which results in the shift of its stretching band to  $3319\text{ cm}^{-1}$ .



### 9.4.2. The Complex $[\text{Ru}(\text{acac})_2\text{L}]$

The changes in the carbonyl stretching bands of the complex  $[\text{Ru}(\text{acac})_2\text{L}]$  during the first oxidation and reduction are shown in Figure 7.4.2 and the results for the  $[\text{Ru}(\text{acac})_2\text{L}]$  are summarized in Table 7.4.1.

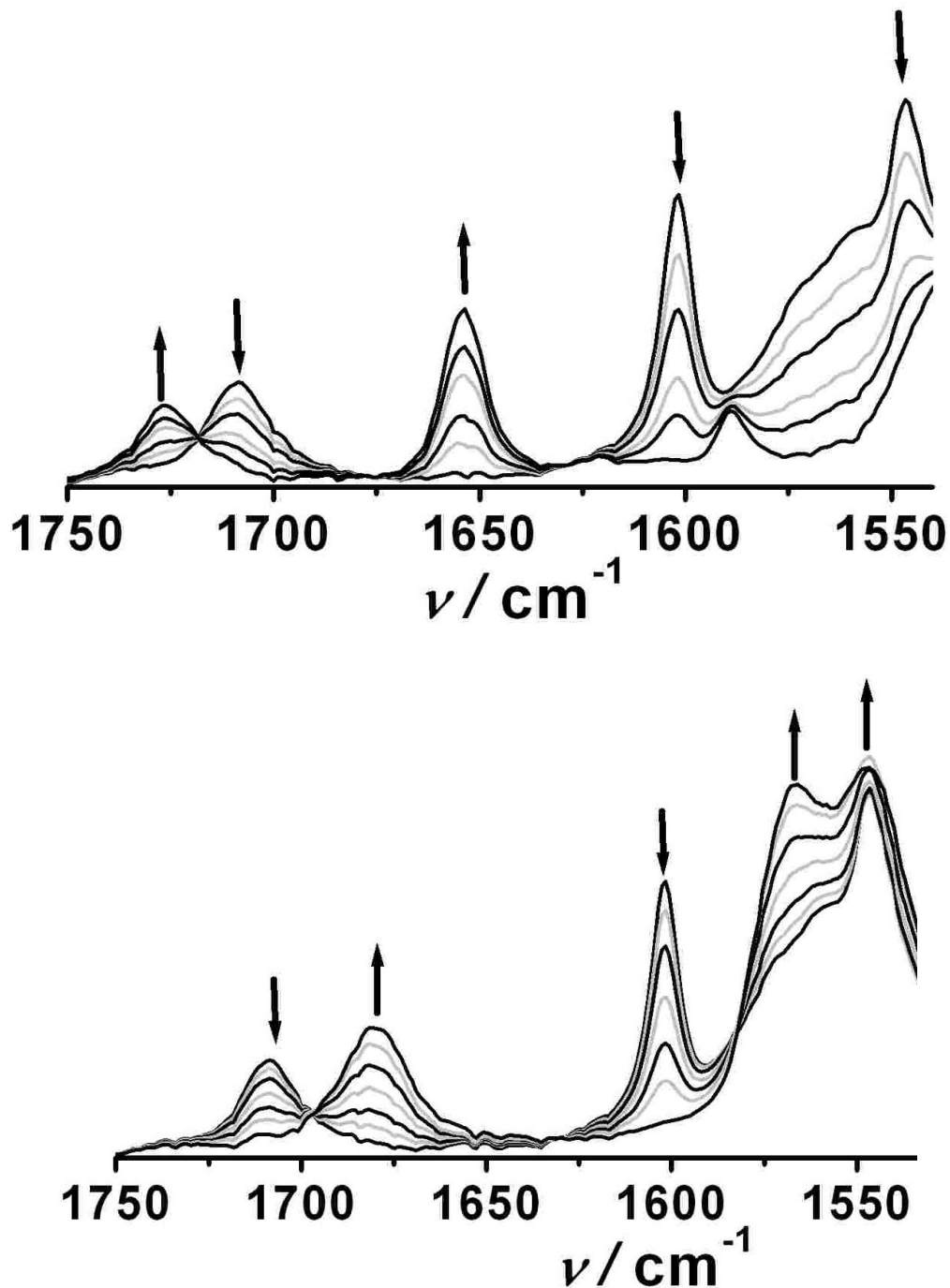


**Figure 9.4.3.** Changes in the IR spectrum of  $[\text{Ru}(\text{acac})_2\text{L}]$  during first oxidation (top) and first reduction (bottom) in  $\text{CH}_2\text{Cl}_2 / 0.1 \text{ M Bu}_4\text{NPF}_6$ .

**Table 9.4.1.** IR vibrational data obtained from spectroelectrochemistry for the ligand and complex.<sup>[a]</sup>

| Compound                                 | $\nu$ [ $\text{cm}^{-1}$ ]         |
|--|------------------------------------|
| $\mathbf{L}\cdot^-$                      | 3319, 1682, 1585, 1533             |
| $\mathbf{L}$                             | 3367, 1719, 1685, 1652, 1620, 1591 |
| $[\text{Ru}(\text{acac})_2\mathbf{L}]^-$ | 3380, 1680, 1567, 1547             |
| $[\text{Ru}(\text{acac})_2\mathbf{L}]$   | 3386, 1708, 1601, 1547             |
| $[\text{Ru}(\text{acac})_2\mathbf{L}]^+$ | 3385, 1726, 1654, 1590             |

<sup>[a]</sup> From spectroelectrochemistry in an OTTLE cell in  $\text{CH}_2\text{Cl}_2$  / 0.1 M  $\text{Bu}_4\text{NPF}_6$ ;

The complex  $[\text{Ru}(\text{acac})_2\mathbf{L}]$  shows all the stretching band at lower frequencies in comparison to free ligand. Particularly the quinone C=O frequencies at 1601 and 1547  $\text{cm}^{-1}$  are closer to frequencies of  $\mathbf{L}^-$  than to those of unreduced  $\mathbf{L}$ , the amide C=O lies at 1708  $\text{cm}^{-1}$  (Figure 9.4.3, Table 9.4.1). These values are indicative of a large back-donation from the  $\text{Ru}^{\text{II}}$  center to  $\mathbf{L}$  means strong mixing of  $d\pi$  of ruthenium based orbitals with the  $\mathbf{L}$  based  $\pi^*$  orbitals and the importance of covalency in such ruthenium complexes. Complex  $[\text{Ru}(\text{acac})_2\mathbf{L}]$  would thus be described as a resonance hybrid of  $\text{Ru}^{\text{II}}-\mathbf{L}$  and  $\text{Ru}^{\text{III}}-\mathbf{L}^-$ . Influence of the electronic spin of  $\text{Ru}^{\text{III}}$  and the radical form  $\mathbf{L}^-$  (paramagnetic shift) on the  $^1\text{H}$  NMR spectrum of  $[\text{Ru}(\text{acac})_2\mathbf{L}]$  is not observed. This is because of the antiferromagnetic coupling of the two spins which results in a diamagnetic complex. Similar situations are known in the literature for singlet diradicals. On one-electron oxidation to  $[\text{Ru}(\text{acac})_2\mathbf{L}]^+$  shifts all the C=O bands to higher wavenumbers (Figure 9.4.3 and Table 9.4.1) and these values are now closer to those of  $\mathbf{L}$ . The still lower stretching frequencies (1654 and 1590  $\text{cm}^{-1}$ ) of the two C=O (C5 and C8) groups in comparison to the values for the free ligand (1685 and 1652  $\text{cm}^{-1}$ ) can be explained by back-donation from the ruthenium center. The ruthenium center in this case is comparatively “electron rich” even in higher oxidation states because of the presence of strong  $\sigma$ -donating ligands such as acac. One-electron reduction to  $[\text{Ru}(\text{acac})_2\mathbf{L}]^-$  shifts all the C=O bands to lower energies and these values are now compatible with  $\mathbf{L}^-$  thus showing the presence of  $\mathbf{L}^-$  in  $[\text{Ru}(\text{acac})_2\mathbf{L}]^-$  (Table 9.4.1 and Figure 9.4.1 and 9.4.2). The N–H stretching bands in  $[\text{Ru}(\text{acac})_2\mathbf{L}]$ ,  $[\text{Ru}(\text{acac})_2\mathbf{L}]^-$ , and  $[\text{Ru}(\text{acac})_2\mathbf{L}]^+$  appear at almost identical frequencies showing the negligible effects of the

redox processes of  $[\text{Ru}(\text{acac})_2\text{L}]$  on the strength of the N–H bond in these complexes and probably weaker influence of the hydrogen bond  $\text{N–H}\cdots\text{O}=\text{C}$ . The lack of complete reversibility of the second reduction process in the longer time scale of the OTTLE measurement precluded the identification of IR bands for  $[\text{Ru}(\text{acac})_2\text{L}]^{2-}$ .

### 9.5. UV/Vis/NIR Spectroelectrochemistry

To obtain more information about the electronic distribution of the complex  $[\text{Ru}(\text{acac})_2\text{L}]$  in various accessible redox processes, UV-Vis-NIR spectroelectrochemical changes of the complexes  $[\text{Ru}(\text{acac})_2\text{L}]$  and also the ligand **L** were monitored using an OTTLE cell. The results are summarized in table 9.5.1.

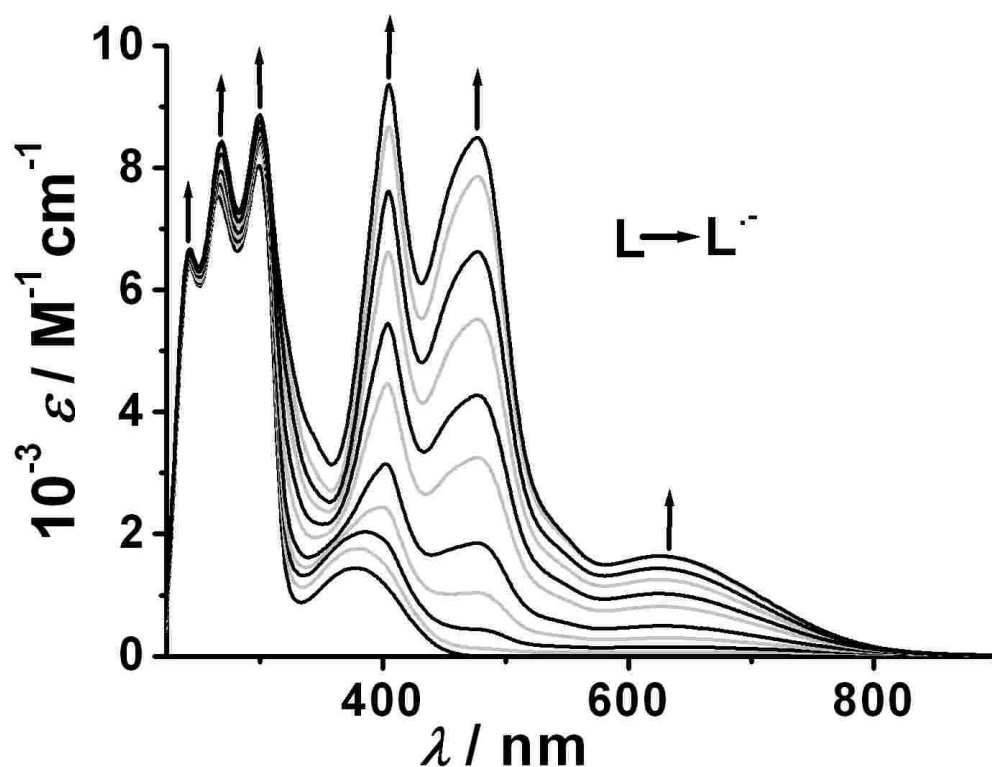


**Figure 9.5.1.** Changes in the UV-Vis-NIR spectrum of **L** during first reduction in  $\text{CH}_2\text{Cl}_2$  / 0.1 M  $\text{Bu}_4\text{NPF}_6$ .

The free ligand **L** shows absorptions in the UV region and one in the visible region at 377 nm which can be assigned to a  $\pi \rightarrow \pi^*$  transition (Table 9.5.1 and Figure 9.5.1). On reduction to  $\text{L}^{\bullet-}$  in  $\text{CH}_2\text{Cl}_2/0.1 \text{ m Bu}_4\text{NPF}_6$ , the  $\pi \rightarrow \pi^*$  transition band is red shifted with enhanced intensity and new bands show up in the visible region at 477 nm ( $8500 \text{ m}^{-1}\text{cm}^{-1}$ ) and 630 nm ( $1700 \text{ m}^{-1}\text{cm}^{-1}$ , Figure 9.5.1). Such low energy bands are typical for organic radicals because of the low energy gap between the singly occupied molecular orbital

(SOMO) generated on one-electron reduction and other close-lying higher energy empty orbitals. The bands in the UV region of **L** remain unchanged on one-electron reduction.

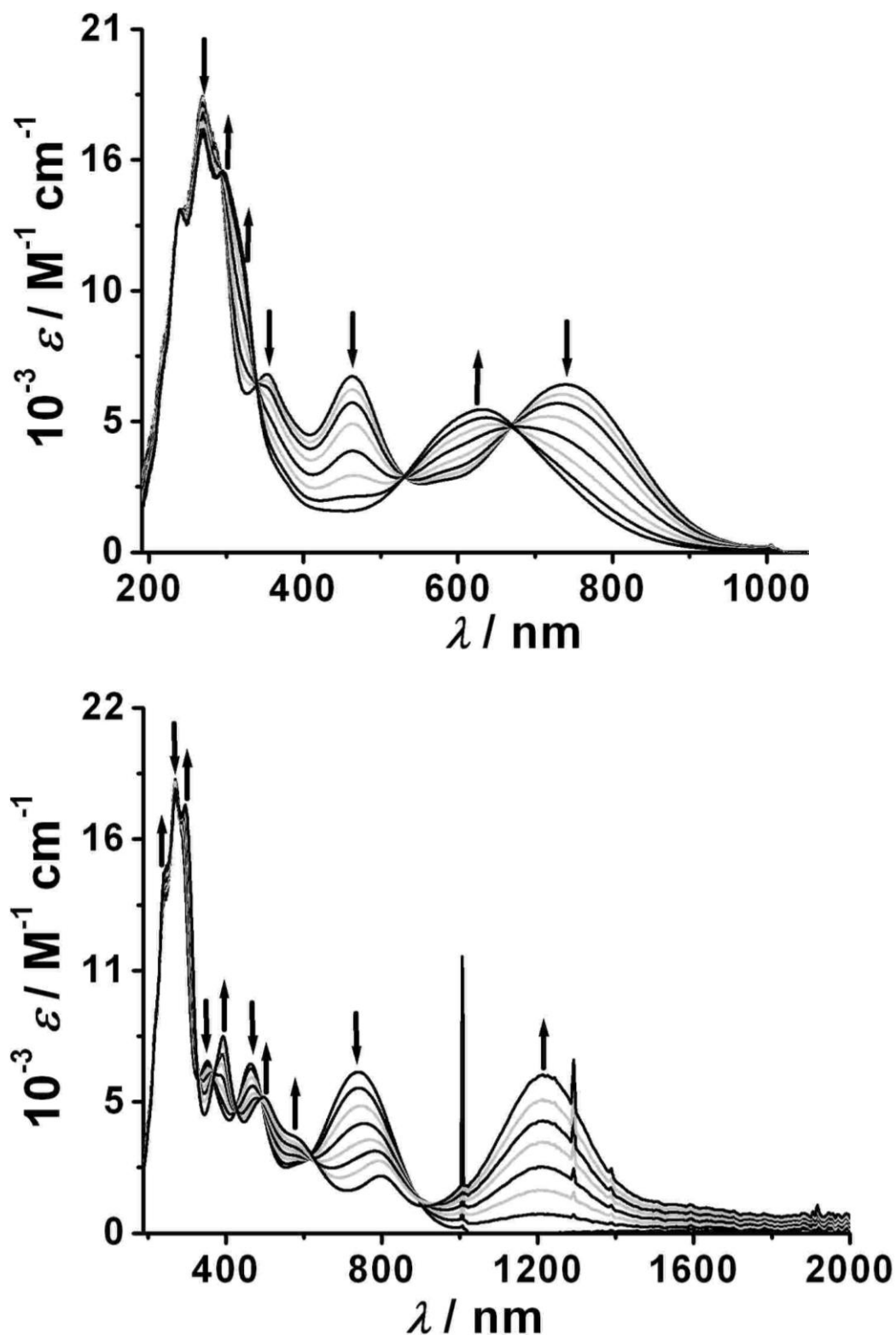


**Figure 9.5.2.** Changes in the UV-Vis-NIR spectrum of  $[\text{Ru}(\text{acac})_2\text{L}]$  during first oxidation (top) and first reduction (bottom) in  $\text{CH}_2\text{Cl}_2 / 0.1 \text{ M Bu}_4\text{NPF}_6$ .

Complex  $[\text{Ru}(\text{acac})_2\mathbf{L}]$  exhibits the expected  $d(\text{Ru}) \rightarrow \pi^*(\mathbf{L})$  MLCT band in the visible region at 743 nm ( $\varepsilon = 6700 \text{ m}^{-1}\text{cm}^{-1}$ ) and an additional band at shorter wavelengths (463 nm,  $\varepsilon = 7000 \text{ m}^{-1}\text{cm}^{-1}$ ) which we attribute to MLCT from  $\text{Ru}^{\text{II}}$  to energetically higher (in comparison to  $\mathbf{L}$ )  $\pi^*$  orbitals of acac. Upon one-electron oxidation to  $[\text{Ru}(\text{acac})_2\mathbf{L}]^+$  the MLCT band is blue-shifted to 630 nm with a substantial decrease in intensity (Figure 9.5.2 and Table 9.5.1). Upon one-electron reduction to  $[\text{Ru}(\text{acac})_2\mathbf{L}]^-$ , a new relatively intense band emerges in the NIR region at 1217 nm ( $6500 \text{ m}^{-1}\text{cm}^{-1}$ ) which is tentatively assigned to a ligand-to-metal charge transfer (LMCT) transition from  $\mathbf{L}^-$  (SOMO) to  $d(\text{Ru})$  (Figure 9.5.2 and Table 9.5.1).<sup>[254]</sup> Such low-energy LMCT bands with radical ligands have precedence in the literature. Additionally,  $[\text{Ru}(\text{acac})_2\mathbf{L}]^-$  shows bands at 570, 500, and 392 nm that are very similar with the bands observed in the case of  $\mathbf{L}^-$  and are hence assigned to intraligand (IL) transitions based on  $\mathbf{L}^-$ . The absorptions in the UV region remain unchanged in the case of all redox forms of  $[\text{Ru}(\text{acac})_2\mathbf{L}]$ . The lack of complete reversibility of the second reduction process in the longer time scale of spectroelectrochemical experiments precluded the identification of charge transfer bands for  $[\text{Ru}(\text{acac})_2\mathbf{L}]^{2-}$ .

**Table 9.5.1** UV/Vis/NIR data obtained from spectroelectrochemistry for the ligand ( $\mathbf{L}$ ) and complex  $[\text{Ru}(\text{acac})_2\mathbf{L}]$ .<sup>[a]</sup>

| Compound                                   | $\lambda_{\text{max}}$ [nm] ( $\varepsilon$ [ $\text{m}^{-1}\text{cm}^{-1}$ ])         |
|--|--|
| $[\text{Ru}(\text{acac})_2\mathbf{L}]$     | 240 (13500) 270 (18200), 353 (7100), 463 (7000), 743 (6700)                            |
| $[\text{Ru}(\text{acac})_2\mathbf{L}]^-$ , | 243 (14800), 270 (18100), 296 (17600), 392 (8100), 500 (5600), 570 (4000), 1217 (6500) |
| $[\text{Ru}(\text{acac})_2\mathbf{L}]^+$   | 239 (13600), 270 (16700), 297 (15100), 327 (11000), 630 (5700)                         |
| $\mathbf{L}$                               | 242 (6400), 265 (7500), 299 (8000), 377 (1500)   |
| $\mathbf{L}^-$                             | 242 (6700), 268 (8400), 300 (8900), 404 (9400), 477 (8500), 630 (1700)                 |

<sup>[a]</sup> From spectroelectrochemistry in an OTTLE cell in  $\text{CH}_2\text{Cl}_2$  / 0.1 M  $\text{Bu}_4\text{NPF}_6$ ;

## 9.6. EPR Spectroscopy

The complex  $[\text{Ru}(\text{acac})_2\text{L}]$  is a diamagnetic in nature but the electrochemically generated both one electron oxidized  $[\text{Ru}(\text{acac})_2\text{L}]^+$  and reduced  $[\text{Ru}(\text{acac})_2\text{L}]^-$  species are paramagnetic in nature. EPR spectroscopy was used directly to determine the electron density distribution for the paramagnetic species  $[\text{Ru}(\text{acac})_2\text{L}]^+$  and  $[\text{Ru}(\text{acac})_2\text{L}]^-$  and shows some interesting effects.

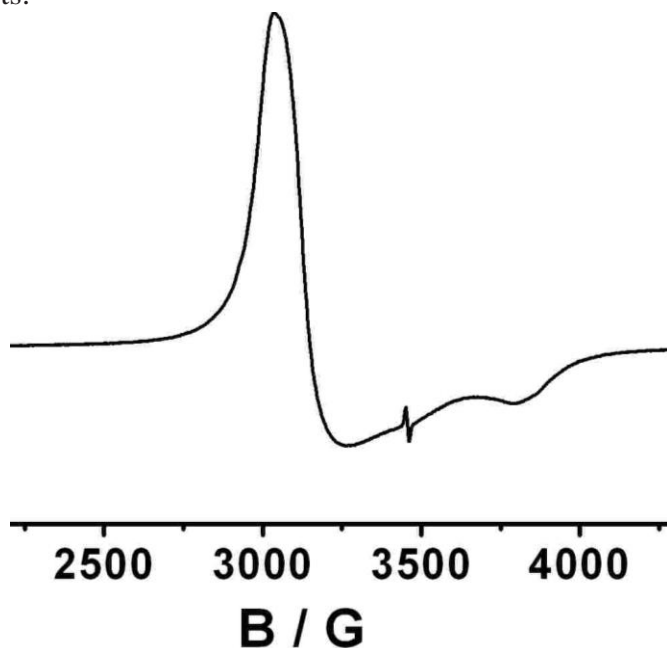


**Figure 9.6.1.** EPR spectrum of electrochemically generated  $[\text{Ru}(\text{acac})_2\text{L}]^+$  at 110 K in  $\text{CH}_2\text{Cl}_2/0.1 \text{ M Bu}_4\text{NPF}_6$ .

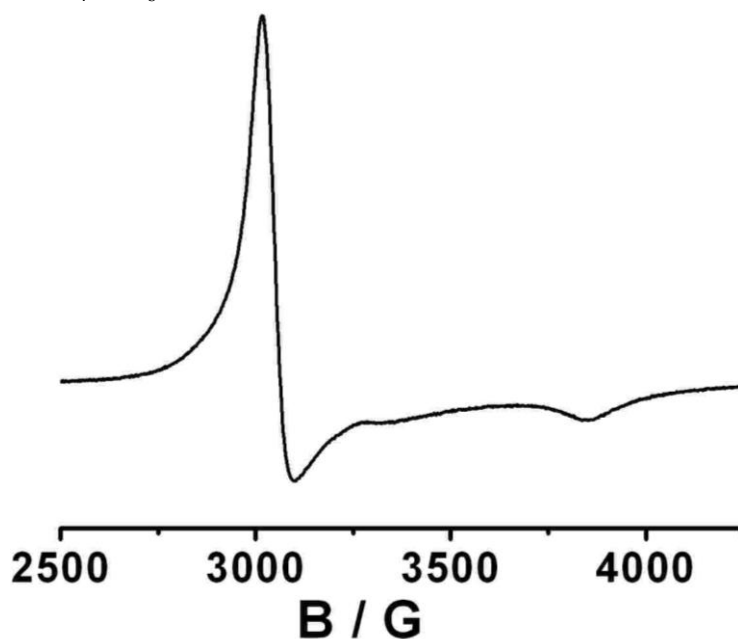


**Figure 9.6.2.** EPR spectrum of electrochemically generated  $[\text{Ru}(\text{acac})_2\text{L}]^-$  at 110 K in  $\text{CH}_2\text{Cl}_2/0.1 \text{ M Bu}_4\text{NPF}_6$ .

The one-electron oxidized form  $[\text{Ru}(\text{acac})_2\text{L}]^+$  is EPR silent at 295 K and at 110 K, an axially symmetric signal is observed with  $g_{\perp} = 2.269$  and  $g_{\parallel} = 1.798$  (Figure 9.6.1). The large  $g$  anisotropy ( $\Delta g = g_{\perp} - g_{\parallel}$ ) of 0.471 and the  $g_{\text{av}}$  value of 2.112 clearly indicate ruthenium-centered spin which is compatible with a  $[(\text{acac})_2\text{Ru}^{\text{III}}(\text{L})]^+$  description. Surprisingly, the one-electron reduced species  $[\text{Ru}(\text{acac})_2\text{L}]^-$  is also EPR silent at 295 K and at 110 K this species shows an axial symmetric signal as well with  $g_{\perp} = 2.213$  and  $g_{\parallel} = 1.809$  (Figure 9.6.2). The  $g_{\text{av}}$  is 2.078 and the  $g$  anisotropy ( $\Delta g = g_{\perp} - g_{\parallel}$ ) is 0.404. Although the  $\Delta g$  value in this case is smaller than that for  $[\text{Ru}(\text{acac})_2\text{L}]^+$ , this value as well as the  $g_{\text{av}}$  value clearly indicate significant amount of ruthenium-centered spin also for  $[\text{Ru}(\text{acac})_2\text{L}]^-$ .

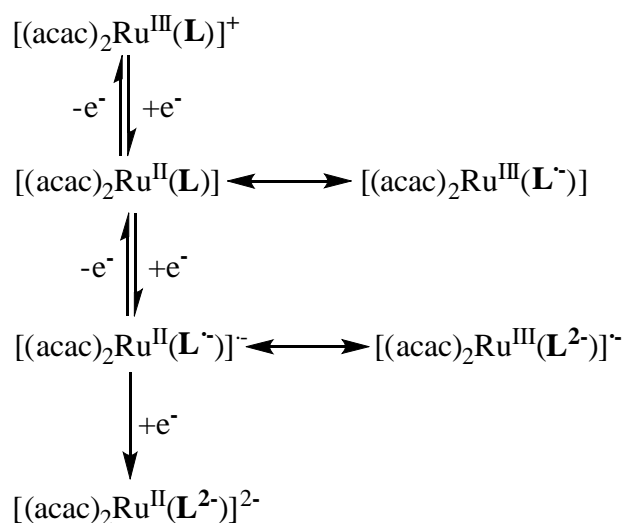
### 9.7. Discussion of Combined Spectroscopic Results

In the absence of structural data, it can be assign properly the oxidation state of the ruthenium and the ligand in different redox state by using the IR spectroscopy data together with UV/Vis/NIR spectroscopy and EPR data. The extremely large shifts to lower energy observed for the C=O stretching frequencies of the ligand **L** in  $[\text{Ru}(\text{acac})_2\text{L}]$  compared to its free form indicates a strong amount of back-bonding from the  $\text{Ru}^{\text{II}}$  center to the ligand **L**. Simple coordination-induced shifts are likely to be much smaller than what is observed in this case. The UV/Vis/NIR spectrum also shows a strong  $\text{Ru}^{\text{II}}$  to ligand **L** charge transfer band. So these data together with the EPR silence of the species till 110 K clearly indicate the electronic structure of the native complex  $[\text{Ru}(\text{acac})_2\text{L}]$  is a resonance hybrid between the forms  $[(\text{acac})_2\text{Ru}^{\text{II}}(\text{L})]$  and the spin-coupled  $[(\text{acac})_2\text{Ru}^{\text{III}}(\text{L}^-)]$ .

The one electron oxidized species is EPR silent at room temperature but shows a signal at 110K which has a large  $g$ -anisotropy and  $g_{\text{av}}$  value very different from that of the free electron value. This is a clear indication of metal-centered spin and is compatible with literature reports of  $\text{Ru}^{\text{III}}$ -based EPR signals. The UV/Vis/NIR and IR spectroscopic results also support the metal-centered oxidation. So the electronic structure of the one electron oxidized species is  $[(\text{acac})_2\text{Ru}^{\text{III}}(\text{L})]^+$ .

The UV/Vis/NIR and IR spectroscopic results of the one electron reduced species  $[\text{Ru}(\text{acac})_2\text{L}]^-$  indicate the formation of  $\text{L}^-$  means ligand centered reduction because the large low energy shifts of the C=O stretching frequencies as well as the appearance of intraligand bands with vibrational structure in the visible region. So from these data we can say that the electronic structure of  $[\text{Ru}(\text{acac})_2\text{L}]^-$  is  $[(\text{acac})_2\text{Ru}^{\text{II}}(\text{L}^-)]^-$ . However, the EPR signal for  $[\text{Ru}(\text{acac})_2\text{L}]^-$  which is observed only at 110 K is very similar to that observed for  $[\text{Ru}(\text{acac})_2\text{L}]^+$  and indicates substantial  $\text{Ru}^{\text{III}}$  character for this species. Thus, these combined

data point to a best description of  $[\text{Ru}(\text{acac})_2\mathbf{L}]^{\cdot-}$  as a resonance hybrid between  $[(\text{acac})_2\text{Ru}^{\text{II}}(\mathbf{L}^{\cdot-})]^{\cdot-}$  and  $[(\text{acac})_2\text{Ru}^{\text{III}}(\mathbf{L}^{2-})]^{\cdot-}$ . Further one-electron reduction to  $[\text{Ru}(\text{acac})_2\mathbf{L}]^{2-}$  probably produces  $[(\text{acac})_2\text{Ru}^{\text{II}}(\mathbf{L}^{2-})]^{2-}$  without much doubt (Scheme 9.7.1).



**Scheme 9.7.1.** oxidation state distribution of the complex  $[\text{Ru}(\text{acac})_2\mathbf{L}]$  in different accessible redox states.

## 9.8. Conclusions

From the synthetic point of view it is clear that the metal center should be electron rich to make a stable complex with the noninnocent *N*-(2-methyl-5,8-dioxo-5,8-dihydroquinolin-7-yl)acetamide ligand ( $\mathbf{L}$ ). The native complex  $[\text{Ru}(\text{acac})_2\mathbf{L}]$  were isolated in diamagnetic form and the amide group of the coordinated group is remained in undeprotonated form. The ruthenium complex with this noninnocent ligand ( $\mathbf{L}$ ) shows strong back donation from ruthenium center to ligand center and the redox states show a mixed type of valence situation pointing to the importance of covalency in metal complexes of ruthenium. The observed results for ruthenium complex are summarized in Scheme 9.7.1.



## CHAPTER 10

### Experimental

#### 10.1. Instrumentation

##### *Elemental analysis*

C, H, N analyses were carried out on a Perkin Elmer analyzer 240 by Ms. B. Förtsch.

##### *NMR spectroscopy*

$^1\text{H}$  and  $^{31}\text{P}$ -NMR experiments at 250 MHz and 400 MHz were carried out by Ms. K. Török on a Bruker AC 250 spectrometer and Bruker AM 400 MHz spectrometer. Tetramethylsilane (TMS) was used as external chemical shift standard.

##### *EPR spectroscopy*

EPR spectra in the X-band at about 9.5 GHz were obtained from Bruker system ESP 300 equipped with a Hewlett-Packard Frequency counter 5350B, a Bruker ER035M gaussmeter for  $g$  values determination as a Bruker system EMX and a continuous flow cryostat ESR 900 of Oxford instruments for measurements at liquid helium temperature (4 K). For measurements between 110-300K, same instrumental configuration was used with liquid nitrogen cryostat. The measurements were carried out by David Schweinfurth and Alexa Paretzki at Institut für Anorganische Chemie, Universität Stuttgart. A two-electrode capillary served to electrogenerate. The intermediates for X-band EPR were generated electrochemically by using a two-electrode capillary and chemically by ferroceniumhexafluorophosphat and cobaltocene. All the EPR spectroscopic measurements were carried out by Mr. D. Schweinfurth and Ms. A. Paretzki.

##### *ESI-mass spectroscopy*

ESI mass spectra were recorded on Bruker Daltonics-microTOF-Q by Dr. J. Opitz, Mr. J. Trinkner and Ms. K. Wohlbold.

##### *IR spectroscopy*

IR spectra were obtained using Nicolet 6700 FT-IR instrument. The solid state IR measurements were performed with an ATR unit (smart orbit with diamond crystal) and the solution measurements were performed by using  $\text{CaF}_2$  windows.

### *UV-Vis-NIR spectroscopy*

Electronic absorption studies were recorded on J&M TIDAS and Shimadzu UV 3101 PC spectrophotometers. The measurements were done in solution using quartz cuvettes of 1 cm or 1 mm path length.

### *UV-Vis-NIR and IR spectroelectrochemistry*

UV-Vis-NIR and IR Spectroelectrochemistry measurements were carried out under argon atmosphere using an optically transparent thin-layer electrode (OTTLE) cell developed by Mr. Krejčík. The windows of the cell consist of CaF<sub>2</sub> plates. Between the cell working (platinum mesh), auxiliary (platinum mesh) and reference electrodes (silver wire as pseudo reference) are melt-sealed. All the UV-Vis-NIR and IR spectroelectrochemical measurements were carried out by Dr. J. Fiedler, Mr. Fritz Weißer and Dr. Ralph Hübner

### *Cyclic voltammetry*

Cyclic voltammetry measurements were performed on an EG&G PAR 273 potentiostat. The measurements were carried out in 0.1M Bu<sub>4</sub>NPF<sub>6</sub> solutions using a three-electrode configuration (glassy-carbon working electrode, Pt counter electrode, Ag/AgCl reference) and a PAR 273 potentiostat and function generator. The ferrocene/ferrocenium (Fc/Fc<sup>+</sup>) couple served as internal reference.

## **10.2. Solvents and working conditions**

The ligands were synthesized under normal atmospheric conditions using reagent grade solvents. For the metal complexes, all manipulations were carried out using Schlenk techniques under an argon atmosphere. The solvents used for metal complex synthesis were dried by refluxing under argon over calcium hydride (dichloromethane, ethanol, methanol, acetonitrile, and hexane), calcium chloride (acetone), sodium (toluene) or lithium aluminium hydride (diethyl ether).

## 10.3 Syntheses

### 10.3.1 Commercially available compounds

$\text{RuCl}_3 \cdot n\text{H}_2\text{O}$  from Merck.

*Cis*- $\text{Ru}(\text{bpy})_2\text{Cl}_2$  from ABCR.

2,5-diaminohydroquinonedihydrochloride, 2,5-Dihydroxybenzoquinone, 3,5-di-tert-butylcatechol, 2,4,6-Trimethylaniline, Benzylamine, Isopropylamine, 2-(trifluoromethyl)aniline, 2-(methylthio)aniline, 2,2'-Bipyridine and  $\text{PPh}_3$  from Aldrich.

4,6-Diaminoresorcinol dihydrochloride, 2,4-pentanedione from Acros.

$\text{AgClO}_4$  from STREM

### 10.3.2 Syntheses of reported compounds

The ligands *N,N'*-diisopropyl-2-amino-5-alcoholate-1,4-benzoquinonemonoiminium and *N,N'*-dibenzyl-2-amino-5-alcoholate-1,4-benzoquinonemonoiminium,<sup>[258]</sup> 2,5-di-[2-(methylthio)-anilino]-1,4-benzoquinone,<sup>[259]</sup> 3,5-Di-tert-butyl-2-hydroxy-1-(2-methylthioanilido)benzene,<sup>[260]</sup> *N*-(2-methyl-5,8-dioxo-5,8-dihydroquinolin-7-yl)acetamide,<sup>[261]</sup> 2,5-Di-[2-(trifluoromethyl)-anilino]-1,4-benzoquinone<sup>[259]</sup> and the metal precursor  $[\text{Ru}(\text{acac})_2(\text{CH}_3\text{CN})_2]$ ,<sup>[262]</sup> *mer*- $[\text{Ru}(\text{bpy})(\text{DMSO})\text{Cl}_3]$ ,<sup>[263]</sup>  $\text{Na}[\text{tnns-Ru}(\text{DMSO})_2\text{C}_{14}]$ ,<sup>[264]</sup>  $[\{\text{Cl}(\eta^6\text{-Cym})\text{Ru}\}_2(\mu\text{-L}_{\text{2H}}^4)]$  and  $[\{(\text{CH}_3\text{CN})_3\text{Ru}\}_2(\mu\text{-L}_{\text{2H}})]$  $[\text{ClO}_4]_2$  ( $\text{L}=2,5\text{-di-[2-(methylthio)-anilino]-1,4-benzoquinone}$ )<sup>[259]</sup> were synthesized according to reported procedures.

### 10.3.3. Synthesis of mono- and dinuclear complexes derived from zwitterionic quinonoid ligands *N,N'*-Diisopropyl-2-amino-5-alcoholate-1,4-benzoquinonemonoiminium (L) and *N,N'*-Dibenzyl-2-amino-5-alcoholate-1,4-benzoquinonemonoiminium (L')

#### 10.3.3.1. Synthesis of mono- and dinuclear complexes with bipyridine ancillary ligands

##### $[\text{Ru}(\text{bpy})_2\text{L}_{\text{H}}](\text{ClO}_4)$

To solid  $\text{KO}^t\text{Bu}$  (0.0135 g, 0.12 mmol) in a Schlenk flask was added L (0.0266 g, 0.12 mmol) and 15 ml THF under argon atmosphere resulting immediate color change from purple to orange. The reaction mixture was stirred overnight at room temperature. The solvent was then removed under reduced pressure. In an another Schlenk flask  $[\text{Ru}(\text{bpy})_2\text{Cl}_2]$  (0.0581 g, 0.12 mmol),  $\text{AgClO}_4$  (0.0622 g, 0.3 mmol) and 25 ml ethanol was added and refluxed for 3 h under argon atmosphere. It was then filtered under argon to the previous deprotonated

ligand residue through G4 crucible containing a celite bed. The resulting mixture was refluxed for 6 h and color changed from red to pink. It was then reduced to 7-8 ml and an excess saturated aqueous solution of NaClO<sub>4</sub> was added to it. The solid precipitate thus obtained was filtered off and dried in vacuum. It was then purified on an alumina (neutral) column. The pink product was eluted with CH<sub>2</sub>Cl<sub>2</sub>/CH<sub>3</sub>CN (2:1). Evaporation of the solvent under reduced pressure afforded the pure complex. Yield: 0.022 g (25%). C<sub>32</sub>H<sub>33</sub>N<sub>6</sub>O<sub>6</sub>RuCl·1/2(CH<sub>2</sub>Cl<sub>2</sub>) (776.65): calcd. C 50.26, H 4.4, N 10.82%; found C 51.05, H 4.68, N 9.94%. <sup>1</sup>H NMR (250 MHz, CD<sub>3</sub>CN) δ/ppm: 0.29 (3H, d, <sup>3</sup>J = 6.5 Hz, CH<sub>3</sub>-CH-NH), 0.86 (3H, d, <sup>3</sup>J = 6.4 Hz, CH<sub>3</sub>-CH-NH), 1.22 (3H, d, <sup>3</sup>J = 6.4 Hz, CH<sub>3</sub>-CH-N), 1.26 (3H, d, <sup>3</sup>J = 6.7 Hz, CH<sub>3</sub>-CH-N), 3.72 (1H, m, CH<sub>3</sub>-CH-NH), 4.45 (1H, m, CH<sub>3</sub>-CH-N), 5.46 (1H, s, N-C-CH), 5.72 (1H, s, O-C-CH), 6.13 (1H, d, br, <sup>3</sup>J = 8.3 Hz, NH), 7.09-7.22 (2H, m, bpy), 7.27-7.34 (1H, m, bpy), 7.60-7.72 (2H, m, bpy), 7.74-7.89 (3H, m, bpy), 8.03-8.16 (2H, m, bpy), 8.31-8.42 (2H, m, bpy), 8.43-8.55 (3H, m, bpy), 8.60-8.68 (1H, m, bpy). ES-MS (m/z): 635 [M - ClO<sub>4</sub>]<sup>+</sup>.

### [Ru(bpy)(L-H)<sub>2</sub>]

The ligand L (0.040 g, 0.18 mmol) was deprotonated according to the above procedure by using KO<sup>t</sup>Bu (0.020 g, 0.18 mmol). Then the metal precursor [Ru(bpy)(DMSO)Cl<sub>3</sub>] (0.040 g, 0.09 mmol) was added and refluxed at 70 C° for 5 h in EtOH under argon atmosphere resulting colour changed from reddish yellow to deep-blue. The solvent of the reaction mixture was evaporated to dryness under reduced pressure and the residue was then purified on an alumina column. The deep blue product was eluted with CH<sub>2</sub>Cl<sub>2</sub>/CH<sub>3</sub>CN (2:1). On alumina TLC plate with the moving phase CH<sub>2</sub>Cl<sub>2</sub>/CO(CH<sub>3</sub>)<sub>2</sub> (6:1) the deep blue product was separated in two fractions. The two fractions were separated by cutting the TLC plate and dissolved in MeOH and filtered. Evaporation of the solvent under reduced pressure afforded the pure isomer.

**1<sup>st</sup> Fraction;** Yield 0.012 g. 19%). C<sub>34</sub>H<sub>42</sub>N<sub>6</sub>O<sub>4</sub>Ru (699.81): calcd. C 58.35, H 6.05, N 12.01%; found C 57.79, H 5.86, N 11.28%. <sup>1</sup>H NMR (250 MHz, CDCl<sub>3</sub>) δ/ppm: 0.22 (3H, d, <sup>3</sup>J = 6.9 Hz, CH<sub>3</sub>-CH-N), 0.45 (6H, d, <sup>3</sup>J = 5.5 Hz, CH<sub>3</sub>-CH-NH), 0.65 (6H, d, <sup>3</sup>J = 4.9 Hz, CH<sub>3</sub>-CH-NH), 0.69 (6H, d, <sup>3</sup>J = 6.5 Hz, CH<sub>3</sub>-CH-N), 0.74 (3H, d, <sup>3</sup>J = 6.6 Hz, CH<sub>3</sub>-CH-N), 3.04 (1H, m, CH<sub>3</sub>-CH-NH), 3.20 (1H, m, CH<sub>3</sub>-CH-NH), 4.00 (2H, sept, <sup>3</sup>J = 6.7 Hz, CH<sub>3</sub>-CH-N), 4.88 (2H, s, N-C-CH), 5.11 (2H, s, O-C-CH), 5.31 (2H, d, br, <sup>3</sup>J = 8.0 Hz, NH), 6.72 (2H, t, <sup>3</sup>J = 6.4 Hz, bpy), 7.12 (2H, t, <sup>3</sup>J = 7.9 Hz, bpy), 7.49 (2H, m, bpy), . ES-MS: m/z calcd for C<sub>34</sub>H<sub>42</sub>N<sub>6</sub>O<sub>4</sub>Ru: 700.23 [M]<sup>+</sup>; found: 700.21 [M]<sup>+</sup> and 723.21 [M+Na]<sup>+</sup>.

**2<sup>nd</sup> Fraction;** Yield 0.014 g. 22%). C<sub>34</sub>H<sub>42</sub>N<sub>6</sub>O<sub>4</sub>Ru (699.81): calcd. C 58.35, H 6.05, N 12.01%; found C 57.52, H 5.46, N 11.61%. <sup>1</sup>H NMR (250 MHz, CDCl<sub>3</sub>) δ/ppm: 0.27 (6H, d, <sup>3</sup>J = 6.4Hz, CH<sub>3</sub>-CH-NH), 0.55 (6H, d, <sup>3</sup>J = 6.8Hz, CH<sub>3</sub>-CH-NH), 0.59 (12H, d, <sup>3</sup>J = 8.5Hz, CH<sub>3</sub>-CH-N), 2.86 (2H, sept, <sup>3</sup>J = 6.5Hz, CH<sub>3</sub>-CH-NH), 3.51 (2H, sept, <sup>3</sup>J = 6.7Hz, CH<sub>3</sub>-CH-N), 4.73 (2H, s, N-C-CH), 5.24 (2H, s, O-C-CH), 5.39 (2H, d, br, <sup>3</sup>J = 7.8Hz NH), 6.73 (2H, t, <sup>3</sup>J = 6.2Hz, bpy), 7.04 (2H, t, <sup>3</sup>J = 7.8Hz, bpy), 7.40 (2H, d, <sup>3</sup>J = 8.2Hz, bpy), 7.81 (2H, d, <sup>3</sup>J = 5.7Hz, bpy), ES-MS: *m/z* calcd for C<sub>34</sub>H<sub>42</sub>N<sub>6</sub>O<sub>4</sub>Ru: 700.23 [M]<sup>+</sup>; found: 700.22 [M]<sup>+</sup> and 723.22 [M+Na]<sup>+</sup>.

### **[{Ru(bpy)<sub>2</sub>}<sub>2</sub>(μ-L<sub>H2</sub>)](ClO<sub>4</sub>)<sub>2</sub>**

In an Schlenk flask [Ru(bpy)<sub>2</sub>Cl<sub>2</sub>] (0.068 g, 0.14 mmol), AgClO<sub>4</sub> (0.0725 g, 0.35 mmol) and 25 ml ethanol were added under argon atmosphere and refluxed for 3 h. It was then filtered under argon to another Schlenk flask through G4 crucible containing a celite bed. Then L (0.0155 g 0.07 mmol) and 0.2 ml NaOMe was added to the reaction mixture and refluxed overnight under argon atmosphere resulting colour change to blue. It was then reduced to 7-8 ml and an excess saturated aqueous solution of NaClO<sub>4</sub> was added to it. The solid precipitate thus obtained was filtered off and dried in vacuum. It was then purified on an alumina (neutral) column. The deep blue product was eluted with CH<sub>2</sub>Cl<sub>2</sub>/CH<sub>3</sub>CN (2:1). Evaporation of the solvent under reduced pressure afforded the pure complex. Yield: 0.020 g (22%). C<sub>52</sub>H<sub>48</sub>N<sub>10</sub>O<sub>10</sub>Ru<sub>2</sub>Cl<sub>2</sub>·(CH<sub>2</sub>Cl<sub>2</sub>) (1331): calcd. C 47.83, H 3.79, N 10.52%; found C 47.71, H 4.09, N 9.86%. <sup>1</sup>H NMR (250 MHz, CD<sub>3</sub>CN) δ: 0.24 (6H, d, <sup>3</sup>J = 6.4Hz, CH<sub>3</sub>-CH-N), 0.78 (6H, d, <sup>3</sup>J = 6.7Hz, CH<sub>3</sub>-CH-N), 4.08 (2H, m, CH<sub>3</sub>-CH-N), 5.68 (1H, s, N-C-CH), 5.72 (1H, s, O-C-CH), 7.07-7.19 (4H, m, bpy), 7.27-7.35 (2H, m, bpy), 7.55-7.72 (4H, m, bpy), 7.74-7.88 (6H, m, bpy), 8.01-8.16 (4H, m, bpy), 8.27-8.42 (6H, m, bpy), 8.43-8.53 (4H, m, bpy), 8.68-8.78 (2H, m, bpy). ES-MS (*m/z*): 524 [M-2ClO<sub>4</sub>]<sup>2+</sup>. Two sets of signals in <sup>1</sup>H NMR spectrum clearly indicates formation of two diastereomers. Analysis of δ = 5.72 and 5.69 peaks attribute composition of about 1:1.

**[{Ru(bpy)}<sub>2</sub>(μ-L'-H<sub>2</sub>)](ClO<sub>4</sub>)<sub>2</sub>**

The compound was prepared following the procedure depicted above. Yield: 0.026 g (28%). C<sub>60</sub>H<sub>48</sub>N<sub>10</sub>O<sub>10</sub>Ru<sub>2</sub>Cl<sub>2</sub> (1342): calcd. C 53.69, H 3.60, N 10.44%; found C 52.92, H 3.28, N 9.97%. <sup>1</sup>H NMR (250 MHz, CD<sub>3</sub>CN) δ: 4.16 (2H, d, <sup>2</sup>J = 14.9 Hz, CH<sub>2</sub>-Ph), 5.22 (2H, d, <sup>2</sup>J = 15.1 Hz, CH<sub>2</sub>-Ph), 5.93 (1H, s, CH-C-N), 5.95 (1H, s, CH-C-O), 6.02 (2H, d, <sup>3</sup>J = 7.3 Hz, Ph), 6.19 (2H, d, <sup>3</sup>J = 7.8 Hz, Ph), 6.56 (2H, t, <sup>3</sup>J = 7.8 Hz, Ph), 6.60 - 6.98 (4H, m, Ph), 7.15 (4H, m, bpy), 7.39 (2H, m, bpy), 7.53 - 7.91 (15H, m, bpy), 8.07 (3H, m, bpy), 8.28-8.69 (8H, m, bpy). ES-MS (m/z): 572.11 [M-2ClO<sub>4</sub>]<sup>2+</sup>. Two sets of signals in <sup>1</sup>H NMR spectrum clearly indicates formation of two diastereomers. Analysis of δ = 5.22 and 5.04 peaks attribute composition of about 7:3.

**10.3.3.2. Synthesis of mono- and dinuclear complexes with acetylacetonato ancillary ligands****[Ru(acac)<sub>2</sub>L]**

The ligand L (0.027 g, 0.12 mmol) was deprotonated according to the above procedure by using KO<sup>t</sup>Bu (0.014 g, 0.12 mmol). Then the metal precursor [Ru(acac)<sub>2</sub>(CH<sub>3</sub>CN)<sub>2</sub>] (0.046 g, 0.12 mmol) was added and refluxed at 70 C° for 6h in EtOH under argon atmosphere resulting colour changed from reddish yellow to deep-green. The green colour changed to brown in air. The solvent of the reaction mixture was evaporated to dryness under reduced pressure and the residue was then purified on an alumina column. The reddish brown product was eluted with CH<sub>2</sub>Cl<sub>2</sub>/CH<sub>3</sub>CN (10:1). Evaporation of solvent under reduced pressure afforded the pure complex. Yield: 0.020 g (32%); elemental analysis calcd (%) for C<sub>22</sub>H<sub>31</sub>N<sub>2</sub>O<sub>6</sub>Ru: C 50.76, H 6.00, N 5.38; found: C 50.07, H 5.63, N 5.02; ES-MS: (m/z): calcd for C<sub>22</sub>H<sub>31</sub>N<sub>2</sub>O<sub>6</sub>Ru: 521.12 [M]<sup>+</sup>; found: 522.13 [MH]<sup>+</sup>, 544.11 [MNa]<sup>+</sup>.

**Synthesis of [Ru(acac)(L)<sub>2</sub>]**

The compound was prepared following the procedure for [Ru(acac)<sub>2</sub>L] by using KO<sup>t</sup>Bu (0.030 g, 0.27 mmol), L (0.060 g, 0.27 mmol) and metal precursor [Ru(acac)<sub>2</sub>(CH<sub>3</sub>CN)<sub>2</sub>] (0.041 g, 0.11 mmol). After refluxing for 24 h in argon atmosphere the reddish brown product was purified on an alumina column. The 1<sup>st</sup> reddish brown band corresponding to [Ru(acac)<sub>2</sub>L] was eluted with CH<sub>2</sub>Cl<sub>2</sub>/CH<sub>3</sub>CN (10:1), followed by the 2<sup>nd</sup> red band corresponding to compound [Ru(acac)L<sub>2</sub>] was eluted with CH<sub>2</sub>Cl<sub>2</sub>/CH<sub>3</sub>CN (5:1). Evaporation of the solvent under reduced pressure afforded the pure complex. Yield: 0.013 g (18%); elemental analysis calcd (%) for C<sub>29</sub>H<sub>41</sub>N<sub>4</sub>O<sub>6</sub>Ru: C 54.19, H 6.43, N 8.72; found: C

53.41, H 5.95, N 8.18; ES-MS: (m/z): calcd for  $C_{29}H_{41}N_4O_6Ru$ : 643.21  $[M]^+$ ; found: 644.21  $[M+H]^+$ , 666.19  $[M+Na]^+$ .

### **[{Ru(acac)<sub>2</sub>}<sub>2</sub>( $\mu$ -L-H<sub>2</sub>)]**

The ligand L (20 mg, 0.09 mmol) and excess NaH (60%) (11 mg, 3 mmol) were dissolved in THF (20 mL) and the reaction mixture was stirred for 12 h at room temperature under argon atmosphere resulting immediate color change from purple to orange. The solvent was then removed under reduced pressure and then the metal precursor  $[Ru(acac)_2(CH_3CN)_2]$  (69 mg, 0.18 mmol) and EtOH (20 mL) were added and mixture was refluxed for 16 h under argon atmosphere resulting color changed from red to redishyellow to green. The green colour changed to brown in air. The solvent of the reaction mixture was evaporated to dryness under reduced pressure and the residue was then purified on a silica column. The deep-blue product was eluted with  $CH_2Cl_2/CH_3CN$  (10:1). Evaporation of solvent under reduced pressure afforded the pure complex. On silica TLC plate with the moving phase  $CH_2Cl_2/CH_3CN$  (10:1) the deep blue product was separated in two fractions. The two fractions were separated by cutting the TLC plate and dissolved in MeOH and filtered. Evaporation of the solvent under reduced pressure afforded the pure isomer.

**1<sup>st</sup> Fraction;** Yield 0.008 g. 5%); elemental analysis calcd (%) for  $C_{32}H_{44}N_2O_{10}Ru_2$ : C 46.94, H 5.42, N 3.42; found: C 46.27, H 5.38, N 3.14; ES-MS: (m/z): calcd for  $C_{32}H_{44}N_2O_{10}Ru_2$ : 818.86  $[M]^+$ ; found: 820.11  $[M+H]^+$ , 842.10  $[M+Na]^+$ .

**2<sup>nd</sup> Fraction;** Yield 0.010 g. 7%); elemental analysis calcd (%) for  $C_{32}H_{44}N_2O_{10}Ru_2$ : C 46.94, H 5.42, N 3.42; found: C 46.32, H 5.44, N 2.97; ES-MS: (m/z): calcd for  $C_{32}H_{44}N_2O_{10}Ru_2$ : 818.86  $[M]^+$ ; found: 820.10  $[M+H]^+$ , 842.10  $[M+Na]^+$ .

### **10.3.3.3. Synthesis of mononuclear complex with three quinonoid terminal ligands**

#### **Synthesis of $RuL_3$**

The ligand L (0.060 g, 0.27 mmol) was deprotonated according to the above procedure by using  $KO^tBu$  (0.030 g, 0.27 mmol). Then the metal precursor  $[Na][Ru(DMSO)_2Cl_4]$  (0.038 g, 0.09 mmol) were added and refluxed at 70 C° for 6h in EtOH under argon atmosphere resulting colour changed from orange to deep-blue. The deep-blue colour changed to reddish brown in air after removing the solvent and the residue was

then purified on an alumina column. The reddish brown product was eluted with  $\text{CH}_2\text{Cl}_2/\text{CH}_3\text{CN}$  (10:1). Evaporation of solvent under reduced pressure afforded the pure complex. Yield: 0.032 g (46%); elemental analysis calcd (%) for  $\text{C}_{36}\text{H}_{51}\text{N}_6\text{O}_6\text{Ru}$ : C 56.53, H 6.72, N 10.99; found: C 56.38, H 6.63, N 10.28; ES-MS: (m/z): calcd for  $\text{C}_{36}\text{H}_{52}\text{N}_6\text{O}_6\text{Ru}$ : 765.29  $[\text{M}]^+$ ; found: 765.30  $[\text{MH}]^+$ .

#### 10.3.3.4. Synthesis of an asymmetric dinuclear complex with acetylacetonato and bipyridine ancillary ligands

##### **[Ru(bpy)<sub>2</sub>( $\mu$ -L-H<sub>2</sub>)Ru(acac)<sub>2</sub>]**

The complex  $[\text{Ru}(\text{bpy})_2\text{L-H}](\text{ClO}_4)$  (37 mg, 0.05 mmol) and excess NaH (60%) were dissolved in THF (20 mL) and the reaction mixture was stirred for 3 h at room temperature under argon atmosphere resulting some redish precipitate insoluble in THF. The solvent was then removed under reduced pressure and then the metal precursor  $[\text{Ru}(\text{acac})_2(\text{CH}_3\text{CN})_2]$  (19 mg, 0.05 mmol) and EtOH (20 mL) were added and mixture was refluxed for 24 h under argon atmosphere resulting color changed from red to deep-blue. The solvent of the reaction mixture was evaporated to dryness under reduced pressure and the residue was then purified on a silica column. The deep-blue product was eluted with  $\text{CH}_2\text{Cl}_2/\text{CH}_3\text{CN}$  (3:1). Evaporation of solvent under reduced pressure afforded the pure complex. Yield 0.016 g, 30%); elemental analysis calcd (%) for  $\text{C}_{42}\text{H}_{46}\text{N}_6\text{O}_{10}\text{ClRu}_2$ : C 48.86, H 4.49, N 8.14; found: C 48.52, H 4.61, N 7.58; ES-MS: (m/z): calcd for  $\text{C}_{42}\text{H}_{46}\text{N}_6\text{O}_6\text{Ru}_2$ : 934.16  $[\text{M}-\text{ClO}_4]^+$ ; found: 934.16.

#### 10.3.4 Synthesis of symmetric and asymmetric quinonoid ligands

##### *2,5-diamino 1,4-benzoquinone*<sup>[141]</sup>

2,5-diaminohydroquinonehydrochloride (213 mg, 1 mmol) was dissolved in water (20 mL) and an excess of triethylamine (1.4 mL, 10 mmol) was added while stirring the mixture in air at room temperature. The addition was followed by a slight change of colour from violet to dark red and the formation of a dark purple precipitate. The suspension was stirred for 30 minutes, the precipitate was filtered off, washed with water, methanol and finally with ether. After drying under vacuum the reaction afforded **1** in 90% yield (0.120 g). <sup>1</sup>H NMR (250 MHz,  $[\text{D}_6]$ DMSO, at 25°C, TMS):  $\delta=7.70$  (brs, 2H;  $\text{NH}_{ax}$ ), 6.96 (brs, 2H;  $\text{NH}_{eq}$ ), 5.29 (s, 2H; CH) .



### 10.3.4.1. General procedure for preparing mono- and di-alkyl derivatives of 2,5-diamino 1,4-benzoquinone

Into a flask with a mechanical stirrer was added water (20 mL), DCM (20 mL), THF (3 mL), one spatula n-tetrabutylammoniumchloride, 2,5-diaminohydroquinonedihydrochloride (213 mg, 1 mmol), and finally excess alkyl amine (11 mmol). The mixture was stirred well for 12 h at room temperature. Then the organic layer was separated, washed with water, dried over Na<sub>2</sub>SO<sub>4</sub>, and then evaporated to dryness under reduced pressure. The residue was then purified on a silica column. The product was eluted by CH<sub>2</sub>Cl<sub>2</sub>/CH<sub>3</sub>OH (100:1) mixture. The 1<sup>st</sup> red-fraction corresponding to di-alkyl derivative and 2<sup>nd</sup> red-fraction corresponding to mono-alkyl derivative of 2,5-diamino 1,4-benzoquinone. Evaporation of solvent under reduced pressure afforded the pure ligand. Depending on the reaction conditions and time, the reaction afforded different ratios of mono- and di-alkyl derivative of 2,5-diamino 1,4-benzoquinone.

#### *2-amino-5-(isopropylamino)-1,4-benzoquinone*

Yield: 45% after 12 h stirring; <sup>1</sup>H NMR (250 MHz, CDCl<sub>3</sub> at 25°C): δ=6.30 (brs, 1H; CNHCH), 5.65 (brs, 2H; CNH<sub>2</sub>), 5.50 (s, 1H; CHCNH<sub>2</sub>), 5.28 (s, 1H; CHCNH), 3.55 (heptet, *J*=7.8 Hz, 1H; CH(CH<sub>3</sub>)<sub>2</sub>), 1.25 ppm (d, *J*= 6.4 Hz, 6H; CH(CH<sub>3</sub>)<sub>2</sub>); <sup>13</sup>C{<sup>1</sup>H} NMR (60 MHz, CDCl<sub>3</sub> at 25°C): δ=21.66 (CH<sub>3</sub>), 44.17 (CH(CH<sub>3</sub>)<sub>2</sub>), 93.19 (CHCNH), 96.64 (CHCNH<sub>2</sub>), 149.27 (CHCNH), 151.81 (CNH<sub>2</sub>), 178.44 (NHCCO), 179.69 (NH<sub>2</sub>CCO); elemental analysis calcd (%) for C<sub>9</sub>H<sub>12</sub>N<sub>2</sub>O<sub>2</sub>·1/2 MeOH: C 58.14, H 7.19, N 14.27; found: C 58.44, H 7.11, N 13.94. ES-MS: *m/z* calcd for C<sub>9</sub>H<sub>12</sub>N<sub>2</sub>O<sub>2</sub>: 180.09 [M]<sup>+</sup>; found: 203.08 [MNa]<sup>+</sup>.

#### *2,5-bis(isopropylamino)-1,4-benzoquinone*

Yield: 91% after 2 days stirring; <sup>1</sup>H NMR (250 MHz, CDCl<sub>3</sub> at 25°C): δ=6.46 (brs, 2H; CNHCH), 5.29 (s, 2H; CCHC), 3.58 (heptet, *J*=8.1 Hz, 2H; CH(CH<sub>3</sub>)<sub>2</sub>), 1.25(d, *J*=6.5 Hz, 12H; CH(CH<sub>3</sub>)<sub>2</sub>); <sup>13</sup>C{<sup>1</sup>H} NMR (60 MHz, CDCl<sub>3</sub> at 25°C): δ=21.68 (CH<sub>3</sub>), 44.14 (CH(CH<sub>3</sub>)<sub>2</sub>), 92.84 (CHCO), 150.08 (CNH), 178.10 (CO); elemental analysis calcd (%) for C<sub>12</sub>H<sub>18</sub>N<sub>2</sub>O<sub>2</sub>: C 64.84, H 8.16, N 12.60; found: C 64.66, H 7.98, N 12.92.

### 10.3.4.2. General procedure for preparing symmetric and asymmetric quinonoid ligands from 2,5-dihydroxy 1,4-benzoquinone

2,5-Dihydroxybenzoquinone (300mg, 2.15 mmol) was dissolved in acetic acid (40 mL), and corresponding amine (4.30 mmol for symmetric and 2.15 mmol for asymmetric) were added dropwise. This was accompanied by a sudden color change from yellow to red. The solution was refluxed for 5 h and allowed to cool down to room temperature. After the addition of water (250 mL), a red solid precipitated and could be collected by filtration. The crude product was then washed with water and diethylether and then dried in air.

#### *2,5-bis(isopropylamino)-1,4-benzoquinone*

The crude product was purified by column chromatography on a silica column. The 1<sup>st</sup> reddish brown band corresponding to the ligand 2,5-bis(isopropylamino)-1,4-benzoquinone was eluted with CH<sub>2</sub>Cl<sub>2</sub>/CH<sub>3</sub>CN (5:1). Evaporation of the solvent under reduced pressure afforded the pure ligand. Yield: 72%; <sup>1</sup>H NMR (250 MHz, CDCl<sub>3</sub> at 25°C): δ=6.46 (brs, 2H; CNHCH), 5.29 (s, 2H; CCHC), 3.58 (heptet, *J*=8.1 Hz, 2H; CH(CH<sub>3</sub>)<sub>2</sub>), 1.25(d, *J*=6.5 Hz, 12H; CH(CH<sub>3</sub>)<sub>2</sub>); <sup>13</sup>C{<sup>1</sup>H} NMR (60 MHz, CDCl<sub>3</sub> at 25°C): δ=21.68 (CH<sub>3</sub>), 44.14 (CH(CH<sub>3</sub>)<sub>2</sub>), 92.84 (CHCO), 150.08 (CNH), 178.10 (CO); elemental analysis calcd (%) for C<sub>12</sub>H<sub>18</sub>N<sub>2</sub>O<sub>2</sub>: C 64.84, H 8.16, N 12.60; found: C 64.52, H 8.05, N 12.97.

#### *2,5-bis(benzylamino)-1,4-benzoquinone*

No further purification was required, and the pure red compound could be obtained after washing with water and diethylether. The compound is very poor soluble in organic solvents. Yield: 85%; elemental analysis calcd (%) for C<sub>40</sub>H<sub>18</sub>N<sub>2</sub>O<sub>2</sub>: C 75.45, H 5.70, N 8.80; found: C 75.14, H 5.02, N 7.93. ES-MS: *m/z* calcd for C<sub>40</sub>H<sub>18</sub>N<sub>2</sub>O<sub>2</sub>: 318.137 [M]<sup>+</sup>; found: 318.14.

#### *2,5-bis(2,4,6-trimethylanilino)-1,4-benzoquinone*

No further purification was required, and the pure orange compound could be obtained after washing with water and diethylether. The compound is very poor soluble in organic solvents. Yield: 92%; elemental analysis calcd (%) for C<sub>24</sub>H<sub>26</sub>N<sub>2</sub>O<sub>2</sub>: C 76.98, H 7.00, N 7.48; found: C 76.69, H 6.18, N 6.92. ES-MS: *m/z* calcd for C<sub>24</sub>H<sub>26</sub>N<sub>2</sub>O<sub>2</sub>: 374.199 [M]<sup>+</sup>; found: 374.2.

***2-(isopropylamino)-5-hydroxy-1,4-benzoquinone***

The crude product was purified by column chromatography on a silica column. The 1<sup>st</sup> reddish brown band corresponding to the symmetric 2,5-bis(isopropylamino)-1,4-benzoquinone ligand was eluted with CH<sub>2</sub>Cl<sub>2</sub>/CH<sub>3</sub>CN (5:1) and 2<sup>nd</sup> red-fraction corresponding to asymmetric 2-(isopropylamino)-5-hydroxy-1,4-benzoquinone ligand was eluted with CH<sub>2</sub>Cl<sub>2</sub>/MeOH (5:1). Evaporation of solvent under reduced pressure afforded the pure ligand but insoluble in organic solvents. Yield: 22%; elemental analysis calcd (%) for C<sub>9</sub>H<sub>11</sub>NO<sub>3</sub>: C 59.66, H 6.12 and N 7.73; found: C 59.08, H 5.72 and N 7.25. ES-MS: *m/z* calcd for C<sub>9</sub>H<sub>11</sub>NO<sub>3</sub>: 181.074 [M]<sup>+</sup>; found: 181.1.

***2-(benzylamino)-5-hydroxy-1,4-benzoquinone***

The compound was purified according to the above procedure. The 2<sup>nd</sup> red-fraction corresponding to asymmetric 2-(benzylamino)-5-hydroxy-1,4-benzoquinone compound was eluted with CH<sub>2</sub>Cl<sub>2</sub>/MeOH (7:1). After evaporation of solvents the compound is insoluble in organic solvents. Yield: 28%; elemental analysis calcd (%) for C<sub>13</sub>H<sub>11</sub>NO<sub>3</sub>: C 68.11, H 4.84 and N 6.11; found: C 67.55, H 4.23 and N 5.71. ES-MS: *m/z* calcd for C<sub>13</sub>H<sub>11</sub>NO<sub>3</sub>: 229.074 [M]<sup>+</sup>; found: 229.1.

***2-(2,4,6-trimethylanilino)-5-hydroxy-1,4-benzoquinone***

The compound was purified according to the above procedure. The 2<sup>nd</sup> red-fraction corresponding to asymmetric 2-(2,4,6-trimethylanilino)-5-hydroxy-1,4-benzoquinone compound was eluted with CH<sub>2</sub>Cl<sub>2</sub>/MeOH (10:1). After evaporation of solvents the compound is insoluble in organic solvents. Yield: 35%; elemental analysis calcd (%) for C<sub>15</sub>H<sub>15</sub>NO<sub>3</sub>: C 70.02, H 5.88 and N 5.44; found: C 69.54, H 5.37 and N 5.08. ES-MS: *m/z* calcd for C<sub>15</sub>H<sub>15</sub>NO<sub>3</sub>: 257.1 [M]<sup>+</sup>; found: 257.1.

***2-[2-(Methylthio)-anilino]-5-hydroxy-1,4-benzoquinone***

The compound was purified according to the above procedure. The 2<sup>nd</sup> red-fraction corresponding to asymmetric 2-(2,4,6-trimethylanilino)-5-hydroxy-1,4-benzoquinone compound was eluted with CH<sub>2</sub>Cl<sub>2</sub>/MeOH (10:1). Yield: 51.5%; elemental analysis calcd (%) for C<sub>13</sub>H<sub>11</sub>NO<sub>3</sub>S: C, 59.76; H, 4.24 and N, 5.36. Found: C, 59.28; H, 4.07 and N, 5.33. <sup>1</sup>H-NMR (250 MHz, CDCl<sub>3</sub>): δ 2.06 (s, 3H, SCH<sub>3</sub>), 5.27 (s, 1H, quinone-*H*), 5.97 (s, 1H, quinone-*H*) 7.24 (m, 2H, aryl-*H*), 7.37 (m, 2H, aryl-*H*), 8.33 (s, 1H, NH). <sup>13</sup>C{<sup>1</sup>H}-NMR (62.9

MHz, CDCl<sub>3</sub>):  $\delta$  16.6, 95.2, 103.3, 123.1, 126.84, 127.1, 129.5, 133.2, 135.1, 146.2, 158.5, 180.1, 182.7. ES-MS:  $m/z$  calcd for C<sub>13</sub>H<sub>11</sub>NO<sub>3</sub>S: 261.0 [M]<sup>+</sup>; found: 261.0.

### 10.3.5 Synthesis of mono- and dinuclear complexes of symmetric quinonoid ligands

#### 10.3.5.1. Mono-nuclear complexes with bipyridine ancillary ligand.

##### [Ru(bpy)<sub>2</sub>L<sub>-H</sub>](ClO<sub>4</sub>); L = 2,5-bis(isopropylamino)-1,4-benzoquinone

In an Schlenk flask [Ru(bpy)<sub>2</sub>Cl<sub>2</sub>] (0.068 g, 0.14 mmol), AgClO<sub>4</sub> (0.0725 g, 0.35 mmol) and 25 ml ethanol was added under argon atmosphere and refluxed for 3 h. It was then filtered under argon to another Schlenk flask through G4 crucible containing a celite bed. Then L (0.031 g 0.14 mmol) and 0.2 ml NaOMe was added to the reaction mixture and refluxed for 5 h under argon atmosphere resulting colour change to purple-red. It was then reduced to 7-8 ml and an excess saturated aqueous solution of NaClO<sub>4</sub> was added to it. The solid precipitate thus obtained was filtered off and dried in vacuum. It was then purified on an alumina (neutral) column. The purple-red product was eluted with CH<sub>2</sub>Cl<sub>2</sub>/CH<sub>3</sub>CN (1:1). Evaporation of the solvent under reduced pressure afforded the pure complex. Yield: 0.038 g (37%). C<sub>32</sub>H<sub>33</sub>N<sub>6</sub>O<sub>6</sub>RuCl (734): calcd. C 52.35, H 4.53, N 11.45%; found C 51.92, H 4.38, N 10.84%. <sup>1</sup>H NMR (250 MHz, CDCl<sub>3</sub>)  $\delta$ : 0.24 (3H, d, <sup>3</sup>J = 6.0Hz, CH<sub>3</sub>-CH-NH), 0.78 (3H, d, <sup>3</sup>J = 6.6Hz, CH<sub>3</sub>-CH-NH), 1.17 (3H, d, <sup>3</sup>J = 7.0Hz, CH<sub>3</sub>-CH-N), 1.19 (3H, d, <sup>3</sup>J = 7.0Hz, CH<sub>3</sub>-CH-N), 4.11 (1H, m, CH<sub>3</sub>-CH-NH), 4.29 (1H, sept, <sup>3</sup>J = 6.8Hz, CH<sub>3</sub>-CH-N), 5.65 (1H, s, N-C-CH), 5.77 (1H, s, NH-C-CH), 7.13-7.27 (2H, m, bpy), 7.4 (1H, d, br, <sup>3</sup>J = 8.1Hz, NH), 7.56 (2H, t, <sup>3</sup>J = 6.6Hz bpy), 7.65-7.81 (4H, m, bpy), 8.06 (2H, m, bpy), 8.36 (3H, m, bpy), 8.49 (3H, m, bpy). ES-MS: ( $m/z$ ): calcd for C<sub>62</sub>H<sub>70</sub>N<sub>4</sub>O<sub>4</sub>Ru<sub>2</sub>S<sub>4</sub>: 635.17 [M]<sup>+</sup>; found: 635.17.

##### [Ru(bpy)(L<sub>-H</sub>)<sub>2</sub>]; L = 2,5-bis(isopropylamino)-1,4-benzoquinone

In an Schlenk flask [Ru(bpy)(DMSO)Cl<sub>3</sub>] (0.040 g, 0.09 mmol) and the ligand L (0.040 g, 0.18 mmol) were dissolved in 25 ml EtOH and then excess base NaOMe was added. It was then refluxed for 6 h at 70 C° under argon atmosphere resulting colour change to deep-blue. The solvent of the reaction mixture was evaporated to dryness under reduced pressure and the residue was then purified on an alumina column. The deep blue product was eluted with CH<sub>2</sub>Cl<sub>2</sub>/MeOH (10:1). On alumina TLC plate with the moving phase CH<sub>2</sub>Cl<sub>2</sub>/MeOH (20:1) the deep blue product was separated in three fractions. The two fractions were separated by cutting the TLC plate and dissolved in MeOH and filtered. Evaporation of the solvent under reduced pressure afforded the pure isomer.

**1<sup>st</sup> Fraction;** Yield 0.012 g. (19%). C<sub>34</sub>H<sub>42</sub>N<sub>6</sub>O<sub>4</sub>Ru (699.81): calcd. C 58.35, H 6.05, N 12.01%; found C 57.86, H 5.73, N 11.44%. <sup>1</sup>H NMR (250 MHz, CDCl<sub>3</sub>) δ/ppm: -0.09 (6H, d, <sup>3</sup>J = 6.4Hz, CH<sub>3</sub>-CH-N), 0.82 (6H, d, <sup>3</sup>J = 6.5Hz, CH<sub>3</sub>-CH-NH), 1.26 (6H, d, <sup>3</sup>J = 6.4Hz, CH<sub>3</sub>-CH-NH), 1.32 (6H, d, <sup>3</sup>J = 6.4Hz, CH<sub>3</sub>-CH-N), 3.74 (2H, m, CH<sub>3</sub>-CH-NH), 3.98 (2H, sept, <sup>3</sup>J = 6.6Hz, CH<sub>3</sub>-CH-N), 5.62 (2H, s, N-C-CH), 5.86 (2H, s, NH-C-CH), 7.23 (2H, d, br, <sup>3</sup>J = 7.9Hz, NH), 7.32 (2H, t, <sup>3</sup>J = 6.0Hz, bpy), 7.66 (2H, t, <sup>3</sup>J = 7.5Hz, bpy), 8.04 (2H, d, <sup>3</sup>J = 8.0Hz, bpy), 8.36 (2H, d, <sup>3</sup>J = 5.8Hz, bpy). ES-MS: *m/z* calcd for C<sub>34</sub>H<sub>42</sub>N<sub>6</sub>O<sub>4</sub>Ru: 700.23 [M]<sup>+</sup>; found: 700.22 [M]<sup>+</sup> and 723.22 [M+Na]<sup>+</sup>.

**2<sup>nd</sup> Fraction;** Yield 0.009 g. (14%). C<sub>34</sub>H<sub>42</sub>N<sub>6</sub>O<sub>4</sub>Ru (699.81): calcd. C 58.35, H 6.05, N 12.01%; found C 57.86, H 5.62, N 11.73%. <sup>1</sup>H NMR (250 MHz, CDCl<sub>3</sub>) δ/ppm: 0.72 (3H, d, <sup>3</sup>J = 6.6Hz, CH<sub>3</sub>-CH-NH), 0.85 (3H, d, <sup>3</sup>J = 6.2Hz, CH<sub>3</sub>-CH-NH), 1.15 (3H, d, <sup>3</sup>J = 5.3Hz, CH<sub>3</sub>-CH-NH), 1.18 (3H, d, <sup>3</sup>J = 5.3Hz, CH<sub>3</sub>-CH-NH), 1.25 (3H, d, <sup>3</sup>J = 5.5Hz, CH<sub>3</sub>-CH-NH), 1.29 (3H, d, <sup>3</sup>J = 6.5Hz, CH<sub>3</sub>-CH-NH), 1.29 (3H, d, <sup>3</sup>J = 6.1Hz, CH<sub>3</sub>-CH-NH), 1.32 (3H, d, <sup>3</sup>J = 5.2Hz, CH<sub>3</sub>-CH-NH), 3.72 (2H, m, CH<sub>3</sub>-CH-NH), 4.12 (2H, m, CH<sub>3</sub>-CH-N), 5.48 (2H, s, N-C-CH), 6.01 (2H, s, NH-C-CH), 7.31 (2H, d, br, <sup>3</sup>J = 7.4Hz, NH), 7.34 (2H, m, bpy), 7.73 (1H, t, <sup>3</sup>J = 7.8Hz, bpy), 7.80 (1H, t, <sup>3</sup>J = 7.5Hz, bpy), 7.96 (1H, d, <sup>3</sup>J = 8.3Hz, bpy), 8.09 (2H, d, <sup>3</sup>J = 5.2Hz, bpy), 8.54 (1H, d, <sup>3</sup>J = 6.0Hz, bpy). ES-MS: *m/z* calcd for C<sub>34</sub>H<sub>42</sub>N<sub>6</sub>O<sub>4</sub>Ru: 700.23 [M]<sup>+</sup>; found: 700.22 [M]<sup>+</sup> and 723.22 [M+Na]<sup>+</sup>.

**3<sup>rd</sup> Fraction;** Yield 0.014 g. (22%). C<sub>34</sub>H<sub>42</sub>N<sub>6</sub>O<sub>4</sub>Ru (699.81): calcd. C 58.35, H 6.05, N 12.01%; found C 57.58, H 5.18, N 11.45%. <sup>1</sup>H NMR (250 MHz, CDCl<sub>3</sub>) δ/ppm: 1.15 (6H, d, <sup>3</sup>J = 6.2Hz, CH<sub>3</sub>-CH-N), 1.25 (6H, d, <sup>3</sup>J = 6.8Hz, CH<sub>3</sub>-CH-NH), 1.56 (12H, d, <sup>3</sup>J = 5.5Hz, CH<sub>3</sub>-CH-NH), 3.52 (2H, m, CH<sub>3</sub>-CH-NH), 3.65 (2H, m, CH<sub>3</sub>-CH-N), 5.26 (2H, s, N-C-CH), 5.67 (2H, s, NH-C-CH), 6.85 (2H, d, br, <sup>3</sup>J = 7.3Hz, NH), 7.45 (2H, t, <sup>3</sup>J = 6.4Hz, bpy), 7.66 (2H, d, <sup>3</sup>J = 6.2Hz, bpy), 7.85 (2H, m, bpy), 8.14 (2H, d, <sup>3</sup>J = 6.6Hz, bpy). ES-MS: *m/z* calcd for C<sub>34</sub>H<sub>42</sub>N<sub>6</sub>O<sub>4</sub>Ru: 700.23 [M]<sup>+</sup>; found: 700.22 [M]<sup>+</sup> and 723.22 [M+Na]<sup>+</sup>.

### 10.3.5.2. Dinuclear complexes with bipyridine ancillary ligand.

#### **[{Ru(bpy)<sub>2</sub>}<sub>2</sub>( $\mu$ -L<sub>2H</sub>)](ClO<sub>4</sub>)<sub>2</sub>; L = 2,5-bis(isopropylamino)-1,4-benzoquinone**

The ligand L<sup>1</sup> (20 mg, 0.09 mmol) and excess NaH (60%) (11 mg, 3 mmol) were dissolved in THF (20 mL) and the reaction mixture was stirred for 3 h at room temperature under argon atmosphere resulting some redish precipitate insoluble in THF. The solvent was then removed under reduced pressure. In an another Schlenk flask [Ru(bpy)<sub>2</sub>Cl<sub>2</sub>] (0.094 g, 0.18 mmol), AgClO<sub>4</sub> (0.093 g, 0.45 mmol) and 30 ml ethanol was added under argon atmosphere and refluxed for 3 h. It was then filtered under argon to the previous reaction mixture through G4 crucible containing a celite bed and refluxed overnight under argon atmosphere resulting colour change to blue. It was then reduced to 7-8 ml and an excess saturated aqueous solution of NaClO<sub>4</sub> was added to it. The solid precipitate thus obtained was filtered off and dried in vacuum. It was then purified on an alumina (neutral) column. The deep blue product was eluted with CH<sub>2</sub>Cl<sub>2</sub>/CH<sub>3</sub>CN (2:1). Evaporation of the solvent under reduced pressure afforded the pure complex. Yield: 0.036 g (32%). C<sub>52</sub>H<sub>48</sub>N<sub>10</sub>O<sub>10</sub>Ru<sub>2</sub>Cl<sub>2</sub> (1246): calcd. C 50.12, H 3.88, N 11.24%; found C 49.97, H 3.74, N 11.03%. ES-MS: (m/z): calcd for C<sub>52</sub>H<sub>48</sub>N<sub>10</sub>O<sub>2</sub>Ru<sub>2</sub>: 524.1025 [M-2ClO<sub>4</sub>]<sup>2+</sup>; found: 524.1041. <sup>1</sup>H NMR (400 MHz, CD<sub>3</sub>CN)  $\delta$ : 0.01 (6H, d, <sup>3</sup>J = 6.5 Hz, CH<sub>3</sub>-CH-N), 0.58 (6H, d, <sup>3</sup>J = 6.5 Hz, CH<sub>3</sub>-CH-N), 4.01 (2H, m, CH<sub>3</sub>-CH-N), 5.75 (2H, s, N-C-CH), 6.91-7.00 (4H, m, bpy), 7.13 (2H, m, bpy), 7.43 (2H, m, bpy), 7.50-7.68 (8H, m, bpy), 7.92 (4H, m, bpy), 8.18 (4H, m, bpy), 8.29-8.43 (6H, m, bpy), 8.50 (1H, m, bpy), 8.60-8.67 (1H, m, bpy). Two setes of signals in <sup>1</sup>H NMR spectrum clearly indicates formation of two diastereomers. Analysis of  $\delta$  = 0.58 and 0.64 peaks attribute composition of about 2:1.

#### **[{Ru(bpy)<sub>2</sub>}<sub>2</sub>( $\mu$ -L<sub>2H</sub>)](ClO<sub>4</sub>)<sub>2</sub>; L = 2,5-bis(benzylamino)-1,4-benzoquinone**

The compound was prepared according to the above procedure by using [Ru(bpy)<sub>2</sub>Cl<sub>2</sub>] (0.094 g, 0.18 mmol), and ligand L<sup>2</sup> (29 mg, 0.09 mmol). The compound was purified on an alumina (neutral) column by using CH<sub>2</sub>Cl<sub>2</sub>/CH<sub>3</sub>CN (2:1) solvents mixture. Yield: 0.042 g (35%). C<sub>60</sub>H<sub>48</sub>N<sub>10</sub>O<sub>10</sub>Ru<sub>2</sub>Cl<sub>2</sub> (1343): calcd. C 53.69, H 3.60, N 10.44%; found C 53.38, H 3.72, N 10.13%. ES-MS: (m/z): calcd for C<sub>60</sub>H<sub>48</sub>N<sub>10</sub>O<sub>2</sub>Ru<sub>2</sub>: 572.10 [M-2ClO<sub>4</sub>]<sup>2+</sup>; found: 572.11. <sup>1</sup>H NMR (250 MHz, CD<sub>3</sub>CN)  $\delta$ : 4.35 (2H, d, <sup>2</sup>J = 14.4 Hz, CH<sub>2</sub>-Ph), 5.39 (2H, d, <sup>2</sup>J = 14.4 Hz, CH<sub>2</sub>-Ph), 6.03 (2H, d, <sup>2</sup>J = 7.4 Hz, Ph), 6.12 (2H, s, CH-C-N), 6.17 (2H, d, <sup>2</sup>J = 7.5 Hz, Ph), 6.64 (2H, t, <sup>3</sup>J = 7.6 Hz, Ph), 6.75 (2H, t, <sup>3</sup>J = 7.7 Hz, Ph), 6.90 (1H, t, <sup>3</sup>J = 7.5 Hz, Ph), 6.97 (1H, t, <sup>3</sup>J = 7.4 Hz, Ph), 7.10 – 7.18 (4H, m, bpy), 7.23 – 7.29 (2H, m, bpy), 7.61 –

7.89 (16H, m, bpy), 8.09 (2H, m, bpy), 8.31 (2H, m, bpy), 8.43 (2H, m, bpy) 8.54 (2H, t,  $^3J = 5.4\text{Hz}$ , bpy), 8.64 (1H, d,  $^3J = 5.0\text{Hz}$ , bpy), 8.64 (1H, d,  $^3J = 5.7\text{Hz}$ , bpy). Two sets of signals in  $^1\text{H}$  NMR spectrum clearly indicates formation of two diastereomers. Analysis of  $\delta = 5.39$  and 5.37 peaks attribute composition of about 1:1.

**[{Ru(bpy)<sub>2</sub>]<sub>2</sub>( $\mu$ -L<sup>3</sup><sub>-2H</sub>)](ClO<sub>4</sub>)<sub>2</sub>; L = 2,5-bis(2,4,6-trimethylanilino)-1,4-benzoquinone**

The compound was prepared according to the above procedure by using [Ru(bpy)<sub>2</sub>Cl<sub>2</sub>] (0.094 g, 0.18 mmol), and ligand L<sup>3</sup> (34 mg, 0.09 mmol). The compound was purified on an alumina (neutral) column by using CH<sub>2</sub>Cl<sub>2</sub>/CH<sub>3</sub>CN (2:1) solvents mixture. Yield: 0.048 g (38%). C<sub>64</sub>H<sub>56</sub>N<sub>10</sub>O<sub>10</sub>Ru<sub>2</sub>Cl<sub>2</sub> (1398): calcd. C 54.98, H 4.04, N 10.02%; found C 54.67, H 3.83, N 9.57%. ES-MS: (m/z): calcd for C<sub>64</sub>H<sub>56</sub>N<sub>10</sub>O<sub>2</sub>Ru<sub>2</sub>: 600.13 [M-2ClO<sub>4</sub>]<sup>2+</sup>; found: 600.14.  $^1\text{H}$  NMR (250 MHz, CD<sub>3</sub>CN)  $\delta$ : 3.61 (18H, s, CH<sub>3</sub>), 5.29 (2H, s, CH-C-O), 6.23 (2H, s, aryl), 6.45 (2H, s, aryl), 6.92 (2H, m, bpy), 7.10 (2H, m, bpy), 7.37 (2H, m, bpy) 7.52 (2H, m, bpy), 7.59 (2H, m, bpy), 7.69 (4H, m, bpy), 7.79 (4H, m, bpy), 7.98-8.20 (6H, m, bpy), 8.39 (2H, m, bpy), 8.50 (2H, m,  $^3J = 6.5\text{Hz}$ , bpy), 8.85 (4H, m, bpy). Two sets of signals in  $^1\text{H}$  NMR spectrum clearly indicates formation of two diastereomers. Analysis of  $\delta = 5.29$  and 5.18 peaks attribute composition of about 6:1.

**10.3.5.3. dinuclear complex with acetylacetonato ancillary ligand.**

**[{Ru(acac)<sub>2</sub>]<sub>2</sub>( $\mu$ -L<sub>-2H</sub>)} L = 2,5-bis(isopropylamino)-1,4-benzoquinone**

The compound was synthesized according to the procedure reported in the section 10.3.3.2 and purified on a silica column. The purple-red product was eluted with CH<sub>2</sub>Cl<sub>2</sub>/CH<sub>3</sub>CN (10:1). Evaporation of solvent under reduced pressure afforded the pure complex. Yield: (24%); elemental analysis calcd (%) for C<sub>32</sub>H<sub>44</sub>N<sub>2</sub>O<sub>10</sub>Ru<sub>2</sub>: C 46.94, H 5.42, N 3.42; found: C 46.58, H 5.26, N 3.18; ES-MS: (m/z): calcd for C<sub>32</sub>H<sub>44</sub>N<sub>2</sub>O<sub>10</sub>Ru<sub>2</sub>: 818.86 [M]<sup>+</sup>; found: 820.11 [M+H]<sup>+</sup>, 842.10 [M+Na]<sup>+</sup>.

**[Ru(bpy)<sub>2</sub>( $\mu$ -L<sub>-H2</sub>)Ru(acac)<sub>2</sub>] L = 2,5-bis(isopropylamino)-1,4-benzoquinone**

The compound was synthesized according to the procedure reported in the section 10.3.3.4. Yield 0.024 g. 45%); elemental analysis calcd (%) for C<sub>42</sub>H<sub>46</sub>N<sub>6</sub>O<sub>10</sub>ClRu<sub>2</sub>: C 48.86, H 4.49, N 8.14; found: C 48.25, H 4.06, N 7.83; ES-MS: (m/z): calcd for C<sub>42</sub>H<sub>46</sub>N<sub>6</sub>O<sub>6</sub>Ru<sub>2</sub>: 934.1566 [M-ClO<sub>4</sub>]<sup>+</sup>; found: 934.1564.

### 10.3.6 Synthesis of mono- and dinuclear complexes of asymmetric quinonoid ligands

#### 10.3.6.1. Synthesis of mono-nuclear complex with bipyridine ancillary ligand.

##### [Ru(bpy)<sub>2</sub>L](ClO<sub>4</sub>); L = 2-(isopropylamino)-5-hydroxy-1,4-benzoquinone

The complex was synthesized according to the procedure depicted in section 10.3.5.1. Yield: 0.056 g (58%). C<sub>29</sub>H<sub>26</sub>N<sub>5</sub>O<sub>7</sub>RuCl (693): calcd. C 50.26, H 3.78, N 10.10%; found C 49.85, H 3.26, N 9.81%. <sup>1</sup>H NMR (250 MHz, C<sub>2</sub>D<sub>2</sub>Cl<sub>4</sub>) δ: 1.21 (6H, d, <sup>3</sup>J = 5.2 Hz, CH<sub>3</sub>-CH-NH), 3.54 (1H, sept, <sup>3</sup>J = 6.6 Hz, CH<sub>3</sub>-CH-N), 5.69 (1H, s, N-C-CH), 6.50 (3H, m, bpy), 6.63 (1H, s, NH-C-C-CH), 6.86 (1H, d, <sup>3</sup>J = 5.7 Hz, bpy), 6.91 (1H, d, <sup>3</sup>J = 5.1 Hz, bpy), 7.06 (1H, d, br, <sup>3</sup>J = 8.2 Hz, NH), 7.12 (3H, m, bpy), 7.44 (2H, m, bpy), 7.58 (2H, t, <sup>3</sup>J = 7.3 Hz, bpy), 7.72 (2H, t, <sup>3</sup>J = 7.9 Hz, bpy), 7.97 (1H, d, <sup>3</sup>J = 5.9 Hz, bpy), 8.05 (1H, d, <sup>3</sup>J = 5.9 Hz, bpy). ES-MS: (m/z): calcd for C<sub>29</sub>H<sub>26</sub>N<sub>5</sub>O<sub>3</sub>Ru: 594.12 [M]<sup>+</sup>; found: 594.12.

#### 10.3.6.2. Synthesis of dinuclear complex with bipyridine ancillary ligand.

##### [{Ru(bpy)<sub>2</sub>}<sub>2</sub>(μ-L<sub>2H</sub>)](ClO<sub>4</sub>)<sub>2</sub>; L = 2-(isopropylamino)-5-hydroxy-1,4-benzoquinone

The complex was synthesized according to the procedure depicted in the section 10.3.5.1. Yield: 0.036 g (34%). C<sub>49</sub>H<sub>41</sub>N<sub>9</sub>O<sub>11</sub>Ru<sub>2</sub>Cl<sub>2</sub> (1205): calcd. C 48.84, H 3.43, N 10.46%; found C 47.93, H 3.04, N 9.68%. ES-MS: (m/z): calcd for C<sub>49</sub>H<sub>41</sub>N<sub>9</sub>O<sub>3</sub>Ru<sub>2</sub>: 503.57 [M-2ClO<sub>4</sub>]<sup>2+</sup>; found: 503.57. <sup>1</sup>H NMR (250 MHz, CD<sub>3</sub>CN) δ: 0.25 (3H, d, <sup>3</sup>J = 7.7 Hz, CH<sub>3</sub>-CH-N), 0.82 (3H, d, <sup>3</sup>J = 6.5 Hz, CH<sub>3</sub>-CH-N), 4.28 (H, m, CH<sub>3</sub>-CH-N), 5.83 (1H, s, N-C-CH), 6.09 (1H, s, O-C-CH), 7.11-7.30 (5H, m, bpy), 7.59-7.90 (11H, m, bpy), 8.11 (4H, m, bpy), 8.24-8.52 (10H, m, bpy), 8.64-8.81 (2H, m, bpy). Two sets of signals in <sup>1</sup>H NMR spectrum clearly indicates formation of two diastereomers. Analysis of δ = 5.83 and 5.78 peaks attribute composition of about 3:2.

##### [{Ru(bpy)<sub>2</sub>}<sub>2</sub>(μ-L<sub>2H</sub>)](ClO<sub>4</sub>)<sub>2</sub>; L = 2-(isopropylamino)-5-hydroxy-1,4-benzoquinone

The complex was synthesized according to the procedure depicted in the section 10.3.5.1. Yield: 0.043 g (38%). C<sub>53</sub>H<sub>41</sub>N<sub>9</sub>O<sub>11</sub>Ru<sub>2</sub>Cl<sub>2</sub> (1253): calcd. C 50.80, H 3.30, N 10.06%; found C 50.26, H 3.17, N 9.53%. ES-MS: (m/z): calcd for C<sub>53</sub>H<sub>41</sub>N<sub>9</sub>O<sub>3</sub>Ru<sub>2</sub>: 527.57 [M-2ClO<sub>4</sub>]<sup>2+</sup>; found: 527.57. <sup>1</sup>H NMR (250 MHz, CD<sub>3</sub>CN) δ: 3.62 (2H, d, <sup>2</sup>J = 1.4 Hz, CH<sub>2</sub>-Ph), 5.90 (1H, s, N-C-CH), 6.13 (1H, d, <sup>3</sup>J = 8.9 Hz, bpy), 6.25 (1H, d, <sup>3</sup>J = 7.4 Hz, bpy), 6.42 (1H, d, <sup>3</sup>J = 8.4 Hz, bpy), 6.49 (1H, s, O-C-CH), 6.60-6.75 (2H, m, bpy), 6.87-7.23 (6H,



m, bpy), 7.43 (2H, m, bpy), 7.60-7.86 (11H, m, bpy), 7.98-8.21 (4H, m, bpy), 8.25-8.54 (6H, m, bpy), 8.67-8.87 (3H, m, bpy).

### **[[Ru(bpy)<sub>2</sub>]<sub>2</sub>(μ-L<sub>2H</sub>)](ClO<sub>4</sub>)<sub>2</sub>; L=2-(2,4,6-trimethylanilino)-5-hydroxy-1,4-benzoquinone**

The complex was synthesized according to the procedure depicted in the section 10.3.5.1. Yield: 0.048 g (41%). C<sub>55</sub>H<sub>45</sub>N<sub>9</sub>O<sub>11</sub>Ru<sub>2</sub>Cl<sub>2</sub> (1281): calcd. C 51.57, H 3.54, N 9.84%; found C 50.85, H 3.29, N 9.68%. ES-MS: (m/z): calcd for C<sub>55</sub>H<sub>45</sub>N<sub>9</sub>O<sub>3</sub>Ru<sub>2</sub>: 541.59 [M-2ClO<sub>4</sub>]<sup>2+</sup>; found: 541.60. <sup>1</sup>H NMR (250 MHz, CD<sub>3</sub>CN) δ: 0.92 (3H, s, CH<sub>3</sub>), 1.28 (3H, s, CH<sub>3</sub>), 1.59 (3H, s, CH<sub>3</sub>), 5.35 (1H, s, N-C-CH), 5.91 (1H, s, O-C-CH), 6.24 (1H, s, mes), 6.48 (1H, s, mes), 6.92-7.21 (4H, m, bpy), 7.39 (1H, m, bpy), 7.50-7.90 (13H, m, bpy), 8.00-8.21 (5H, m, bpy), 8.33 (2H, m, bpy), 8.46 (4H, m, bpy), 8.57-8.77 (3H, m, bpy).

## **10.3.7. Synthesis of Cymene complexes**

### **10.3.7.1. Dinuclear ruthenium complex with symmetric bridging ligand.**

#### **Synthesis of [[Cl(η<sup>6</sup>-Cym)Ru]<sub>2</sub>(μ-L<sub>2H</sub>)]; L = 2,5-di-[2-(trifluoromethyl)-anilino]-1,4-benzoquinone.**

Ru<sub>2</sub>(cym)<sub>2</sub>Cl<sub>4</sub> (80mg, 0.13 mmol) and the ligand symmetric-CF<sub>3</sub> (55.4 mg, 0.13 mmol) were dissolved in CH<sub>2</sub>Cl<sub>2</sub> (30 mL) under an argon atmosphere. NEt<sub>3</sub> (1.0 mL) was added and the solution was stirred over night at room temperature. The solution was concentrated and the product was precipitated by addition of hexane. The compound was filtered, washed with hexane and dried *in vacuo*. The desired product was obtained as a purple solid (yield: 114 mg, 91%). Anal. calcd. for C<sub>40</sub>H<sub>38</sub>Cl<sub>2</sub>F<sub>6</sub>N<sub>2</sub>O<sub>2</sub>Ru<sub>2</sub>: C, 49.75; H, 3.97; N, 2.90. Found: C, 49.64; H, 3.86; N, 2.82. MS (ESI): Calcd. for C<sub>40</sub>H<sub>38</sub>Cl<sub>2</sub>F<sub>6</sub>N<sub>2</sub>O<sub>2</sub>Ru<sub>2</sub> ([M - Cl]<sup>+</sup> and [M - 2 Cl]<sup>2+</sup>): m/z 931.06 and 447.44; found 931.06 and 447.56. <sup>1</sup>H-NMR (250 MHz, CD<sub>2</sub>Cl<sub>2</sub>): δ 1.09 (d, <sup>3</sup>J<sub>H-H</sub> = 7 Hz, 6H, CH(CH<sub>3</sub>)<sub>2</sub>), 1.16 (d, <sup>3</sup>J<sub>H-H</sub> = 7 Hz, 6H, CH(CH<sub>3</sub>)<sub>2</sub>), 1.86 (s, 6H, CH<sub>3</sub>), 2.31 (sept, <sup>3</sup>J<sub>H-H</sub> = 7.0 Hz, 1H, CH(CH<sub>3</sub>)<sub>2</sub>), 2.40 (sept, <sup>3</sup>J<sub>H-H</sub> = 7.0 Hz, 1H, CH(CH<sub>3</sub>)<sub>2</sub>), 4.89 (d, <sup>3</sup>J<sub>H-H</sub> = 6.5 Hz, 2H, arene-H), 4.95 (s, 2H, quinone-H), 5.19 (d, <sup>3</sup>J<sub>H-H</sub> = 6.0 Hz, 2H, arene-H), 5.31 (d, <sup>3</sup>J<sub>H-H</sub> = 6.1 Hz, 4H, arene-H), 7.46 (t, <sup>3</sup>J<sub>H-H</sub> = 7.4 Hz, 2H, aryl-H), 7.63 (t, <sup>3</sup>J<sub>H-H</sub> = 7.8 Hz, 2H, aryl-H), 7.74 (m, 4H, aryl-H).

**10.3.7.2. Dinuclear ruthenium complex with asymmetric bridging ligand.****Synthesis of  $[\{\text{Cl}(\eta^6\text{-Cym})\text{Ru}\}_2(\mu\text{-L}_{2\text{H}})]$ ; L = 2-[2-(trifluoromethyl)-anilino]-5-hydroxy-1,4-benzoquinone.**

The compound was obtained as a reddish-purple solid (92 mg, 86 %) by using the procedure depicted above. Anal. calcd. for  $\text{C}_{33}\text{H}_{34}\text{Cl}_2\text{F}_3\text{NO}_3\text{Ru}_2$ : C, 48.18; H, 4.17; N, 1.70. Found: C, 47.86; H, 4.05; N, 1.66. MS (ESI): Calcd. for  $\text{C}_{33}\text{H}_{34}\text{Cl}_2\text{F}_3\text{NO}_3\text{Ru}_2$  ( $[\text{M} - \text{Cl}]^+$ ):  $m/z$  788.03; found 788.03.  $^1\text{H-NMR}$  (250 MHz,  $\text{CDCl}_3$ ):  $\delta$  1.09 (d,  $^3J_{\text{H-H}} = 6.9$  Hz, 3H,  $\text{CH}(\text{CH}_3)_2$ ), 1.16 (d,  $^3J_{\text{H-H}} = 6.9$  Hz, 3H,  $\text{CH}(\text{CH}_3)_2$ ), 1.26 (d,  $^3J_{\text{H-H}} = 6.9$  Hz, 3H,  $\text{CH}(\text{CH}_3)_2$ ), 1.27 (d,  $^3J_{\text{H-H}} = 6.9$  Hz, 3H,  $\text{CH}(\text{CH}_3)_2$ ), 1.89 (s, 3H,  $\text{CH}_3$ ), 2.20 (s, 3H,  $\text{CH}_3$ ), 2.46 (sept,  $^3J_{\text{H-H}} = 7.9$  Hz, 1H,  $\text{CH}(\text{CH}_3)_2$ ), 2.86 (sept,  $^3J_{\text{H-H}} = 6.9$  Hz, 1H,  $\text{CH}(\text{CH}_3)_2$ ), 4.92 (s, 1H, quinone-*H*), 4.96 (d,  $^3J_{\text{H-H}} = 5.9$  Hz, 1H, arene-*H*), 5.25 (d,  $^3J_{\text{H-H}} = 5.6$  Hz, 1H, arene-*H*), 5.27 (d,  $^3J_{\text{H-H}} = 5.6$  Hz, 2H, arene-*H*), 5.40 (d,  $^3J_{\text{H-H}} = 6.0$  Hz, 2H, arene-*H*), 5.48 (d,  $^3J_{\text{H-H}} = 4.6$  Hz, 1H, arene-*H*), 5.50 (d,  $^3J_{\text{H-H}} = 4.6$  Hz, 1H, arene-*H*), 5.85 (s, 1H, quinone-*H*), 7.39 (t,  $^3J_{\text{H-H}} = 7.9$  Hz, 1H, aryl-*H*), 7.57 (t,  $^3J_{\text{H-H}} = 6.9$  Hz, 1H, aryl-*H*), 7.67 (d,  $^3J_{\text{H-H}} = 8.7$  Hz, 1H, aryl-*H*), 7.71 (d,  $^3J_{\text{H-H}} = 8.3$  Hz, 1H, aryl-*H*).

**Synthesis of  $[\{\text{Cl}(\eta^6\text{-Cym})\text{Ru}\}_2(\mu\text{-L}_{2\text{H}})]$ ; L = 2-[2-(methylthio)-anilino]-5-hydroxy-1,4-benzoquinone.**

The compound was obtained as a reddish-purple solid (96 mg, 92 %) by using the procedure depicted above. Calcd. for  $\text{C}_{33}\text{H}_{37}\text{Cl}_2\text{NO}_3\text{SRu}_2$ : C, 49.50; H, 4.66; N, 1.75. Found: C, 48.61; H, 4.35; N, 1.58. MS (ESI): Calcd. for  $\text{C}_{33}\text{H}_{37}\text{Cl}_2\text{NO}_3\text{SRu}_2$  ( $[\text{M} - \text{Cl}]^+$ ):  $m/z$  766.02; found 766.00.  $^1\text{H-NMR}$  (250 MHz,  $\text{CDCl}_3$ ):  $\delta$  1.08 (d,  $^3J_{\text{H-H}} = 6.9$  Hz, 3H,  $\text{CH}(\text{CH}_3)_2$ ), 1.16 (d,  $^3J_{\text{H-H}} = 6.9$  Hz, 3H,  $\text{CH}(\text{CH}_3)_2$ ), 1.24 (d,  $^3J_{\text{H-H}} = 1.9$  Hz, 3H,  $\text{CH}(\text{CH}_3)_2$ ), 1.27 (d,  $^3J_{\text{H-H}} = 2.0$  Hz, 3H,  $\text{CH}(\text{CH}_3)_2$ ), 2.20 (s, 3H,  $\text{CH}_3$ ), 2.41 (s, 3H,  $\text{CH}_3$ ), 2.53 (s, 3H,  $\text{SCH}_3$ ), 2.85 (sept,  $^3J_{\text{H-H}} = 6.9$  Hz, 1H,  $\text{CH}(\text{CH}_3)_2$ ), 3.70 (sept,  $^3J_{\text{H-H}} = 2.6$  Hz, 1H,  $\text{CH}(\text{CH}_3)_2$ ), 5.03 (s, 1H, quinone-*H*), 5.06 (d,  $^3J_{\text{H-H}} = 4.8$  Hz, 1H, arene-*H*), 5.25 (d,  $^3J_{\text{H-H}} = 5.8$  Hz, 2H, arene-*H*), 5.34 (d,  $^3J_{\text{H-H}} = 5.7$  Hz, 1H, arene-*H*), 5.47 (d,  $^3J_{\text{H-H}} = 5.2$  Hz, 3H, arene-*H*), 5.58 (d,  $^3J_{\text{H-H}} = 5.4$  Hz, 1H, arene-*H*), 5.83 (s, 1H, quinone-*H*), 7.12 (m, 1H, aryl-*H*), 7.21 (m, 2H, aryl-*H*), 7.36 (m, 1H, aryl-*H*).

### 10.3.8. Substitution of cym/Cl by acetonitrile solvents molecules.

#### Synthesis of $[(\text{CH}_3\text{CN})(\eta^6\text{-Cym})\text{Ru}]_2(\mu\text{-L}_{2\text{H}})[\text{ClO}_4]_2$ ; L = 2,5-di-[2-(trifluoromethyl)-anilino]-1,4-benzoquinone.

The compound was obtained as a brown-red solid (25 mg, 85 %) by using the procedure depicted above. Anal. calcd. for  $\text{C}_{44}\text{H}_{44}\text{Cl}_2\text{F}_6\text{N}_4\text{O}_{10}\text{Ru}_2$ : C, 44.94; H, 3.77; N, 4.76. Found: C, 44.53; H, 3.85; N, 4.37. HRMS (ESI): Calcd. for  $\text{C}_{44}\text{H}_{44}\text{Cl}_2\text{F}_6\text{N}_4\text{O}_{10}\text{Ru}_2$  ( $[\text{M} - 2\text{ClO}_4^- - 2\text{CH}_3\text{CN}]^{2+}$ ):  $m/z$  448.0462; found 448.0470.  $^1\text{H-NMR}$  (250 MHz,  $\text{CD}_3\text{CN}$ ):  $\delta$  1.13 (d,  $^3J_{\text{H-H}} = 6.9$  Hz, 12H,  $\text{CH}(\text{CH}_3)_2$ ), 1.78 (s, 6H,  $\text{CH}_3$ ), 2.15 (s, 6H,  $\text{CH}_3\text{CN}$ ); 2.30 (sept,  $^3J_{\text{H-H}} = 5.1$  Hz, 1H,  $\text{CH}(\text{CH}_3)_2$ ), 2.55 (sept,  $^3J_{\text{H-H}} = 6.9$  Hz, 1H,  $\text{CH}(\text{CH}_3)_2$ ), 5.01 (s, 2H, quinone-*H*), 5.08 (d,  $^3J_{\text{H-H}} = 6.0$  Hz, 1H, arene-*H*), 5.31 (d,  $^3J_{\text{H-H}} = 6.5$  Hz, 1H, arene-*H*), 5.56 (d,  $^3J_{\text{H-H}} = 7.0$  Hz, 4H, arene-*H*), 5.61 (d,  $^3J_{\text{H-H}} = 5.6$  Hz, 2H, arene-*H*), 7.44 (t,  $^3J_{\text{H-H}} = 8.2$  Hz, 1H, aryl-*H*), 7.65 (t,  $^3J_{\text{H-H}} = 7.8$  Hz, 2H, aryl-*H*), 7.80 (t,  $^3J_{\text{H-H}} = 6.7$  Hz, 1H, aryl-*H*), 7.87 (d,  $^3J_{\text{H-H}} = 6.6$  Hz, 2H, aryl-*H*), 7.93 (d,  $^3J_{\text{H-H}} = 7.4$  Hz, 2H, aryl-*H*).

#### Synthesis of $[(\text{CH}_3\text{CN})(\eta^6\text{-Cym})\text{Ru}]_2(\mu\text{-L}_{2\text{H}})[\text{ClO}_4]_2$ ; L = 2,5-di-[2-(trifluoromethyl)-anilino]-1,4-benzoquinone.

The compound was obtained as a brown solid (24 mg, 78 %) by using the procedure depicted above. Anal. calcd. for  $\text{C}_{37}\text{H}_{40}\text{Cl}_2\text{F}_3\text{N}_3\text{O}_{11}\text{Ru}_2$ : C, 43.03; H, 3.90; N, 4.07. Found: C, 42.79; H, 3.65; N, 3.88.  $^1\text{H-NMR}$  (250 MHz,  $\text{CD}_3\text{CN}$ ):  $\delta$  1.17 (d,  $^3J_{\text{H-H}} = 7.0$  Hz, 6H,  $\text{CH}(\text{CH}_3)_2$ ), 1.28 (d,  $^3J_{\text{H-H}} = 7.0$  Hz, 6H,  $\text{CH}(\text{CH}_3)_2$ ), 1.88 (s, 3H,  $\text{CH}_3$ ), 2.09 (s, 3H,  $\text{CH}_3\text{CN}$ ), 2.15 (s, 3H,  $\text{CH}_3\text{CN}$ ), 2.21 (s, 3H,  $\text{CH}_3$ ), 2.57 (sept,  $^3J_{\text{H-H}} = 6.5$  Hz, 1H,  $\text{CH}(\text{CH}_3)_2$ ), 2.80 (sept,  $^3J_{\text{H-H}} = 6.8$  Hz, 1H,  $\text{CH}(\text{CH}_3)_2$ ), 4.94 (s, 1H, quinone-*H*), 5.40 (d,  $^3J_{\text{H-H}} = 6.5$  Hz, 1H, arene-*H*), 5.59 (d,  $^3J_{\text{H-H}} = 5.0$  Hz, 1H, arene-*H*), 5.61 (d,  $^3J_{\text{H-H}} = 6.0$  Hz, 1H, arene-*H*), 5.69 (d,  $^3J_{\text{H-H}} = 4.1$  Hz, 2H, arene-*H*), 5.74 (d,  $^3J_{\text{H-H}} = 4.1$  Hz, 1H, arene-*H*), 5.85 (d,  $^3J_{\text{H-H}} = 7.2$  Hz, 2H, arene-*H*), 5.87 (s, 1H, quinone-*H*), 7.18 (t,  $^3J_{\text{H-H}} = 8.4$  Hz, 1H, aryl-*H*), 7.66 (t,  $^3J_{\text{H-H}} = 7.8$  Hz, 1H, aryl-*H*), 7.84 (d,  $^3J_{\text{H-H}} = 5.8$  Hz, 1H, aryl-*H*), 7.94 (d,  $^3J_{\text{H-H}} = 8.1$  Hz, 1H, aryl-*H*).

#### Synthesis of $[(\text{CH}_3\text{CN})(\eta^6\text{-Cym})\text{Ru}(\mu\text{-L}_{2\text{H}})\text{Ru}(\text{CH}_3\text{CN})_3][\text{ClO}_4]_2$ ; L = 2-[2-(methylthio)-anilino]-5-hydroxy-1,4-benzoquinone.

The compound was obtained as a bluish green solid (24 mg, 83 %) by using the procedure depicted above. Anal. calcd. for  $\text{C}_{31}\text{H}_{35}\text{Cl}_2\text{N}_5\text{O}_{11}\text{Ru}_2\text{S}$ : C, 38.84; H, 3.68; N, 7.30. Found: C, 38.26; H, 3.72; N, 6.94. HRMS (ESI): Calcd. for  $\text{C}_{24}\text{H}_{22}\text{N}_4\text{O}_2\text{Ru}_2\text{S}_2$  ( $[\text{M} - 2\text{ClO}_4^- - 3\text{CH}_3\text{CN}]^{2+}$ ,  $[\text{M} - 2\text{ClO}_4^- - 4\text{CH}_3\text{CN} + \text{H}_2\text{O}]^{2+}$ , and  $[\text{M} - 2\text{ClO}_4^- - 4\text{CH}_3\text{CN}]^{2+}$ ):  $m/z$  318.9876, 307.4796 and 298.4743; found 318.9881, 307.4812 and 298.4736.  $^1\text{H-NMR}$  (250

MHz, CD<sub>3</sub>CN): <sup>1</sup>H-NMR (250 MHz, CD<sub>3</sub>CN): δ 1.34 (d, <sup>3</sup>J<sub>H-H</sub> = 6.9 Hz, 6H, CH(CH<sub>3</sub>)<sub>2</sub>), 2.14 (s, 9H, CH<sub>3</sub>CN), 2.27 (s, 3H, CH<sub>3</sub>CN), 2.57 (s, 3H, CH<sub>3</sub>), 2.58 (s, 3H, SCH<sub>3</sub>), 3.15 (sept, <sup>3</sup>J<sub>H-H</sub> = 5.5 Hz, 1H, CH(CH<sub>3</sub>)<sub>2</sub>), 5.62 (d, <sup>3</sup>J<sub>H-H</sub> = 6.3 Hz, 2H, arene-H), 5.89 (d, <sup>3</sup>J<sub>H-H</sub> = 6.4 Hz, 2H, arene-H), 5.95 (s, 1H, quinone-H), 6.66 (s, 1H, quinone-H), 7.48 (m, 2H, aryl-H), 7.72 (dd, <sup>3</sup>J<sub>H-H</sub> = 10.2 Hz, <sup>4</sup>J<sub>H-H</sub> = 1.6 Hz, 1H, aryl-H), 8.03 (dd, <sup>3</sup>J<sub>H-H</sub> = 8.2 Hz, <sup>4</sup>J<sub>H-H</sub> = 1.0 Hz, 1H, aryl-H).

### 10.3.9. Substitution of coordinated acetonitrile in the complex [(CH<sub>3</sub>CN)<sub>3</sub>Ru]<sub>2</sub>(μ-L-2H)][ClO<sub>4</sub>]<sub>2</sub>.

#### 10.3.9.1. Synthesis of [(CH<sub>3</sub>CN)(PPh<sub>3</sub>)<sub>2</sub>Ru]<sub>2</sub>(μ-L-2H)][ClO<sub>4</sub>]<sub>2</sub>

The complex (103 mg, 0.10 mmol) and PPh<sub>3</sub> (262 mg, 1.00 mmol) were dissolved in MeOH (15 mL) under an argon atmosphere. The solution was refluxed over night and the solvent evaporated. The crude product was cleaned by multiple column chromatography using alumina and CH<sub>2</sub>Cl<sub>2</sub>/CH<sub>3</sub>CN (3/2) as the eluent. The first deep-blue fraction was collected and evaporated the solvent under reduced pressure afforded the pure complex (yield: 34.0 mg 18 %). Anal. calcd. for C<sub>96</sub>H<sub>82</sub>Cl<sub>2</sub>N<sub>4</sub>O<sub>10</sub>P<sub>4</sub>Ru<sub>2</sub>S<sub>2</sub>: C, 60.28; H, 4.32; N, 2.93. Found: C, 59.94; H, 4.16; N, 3.06. MS (ESI): Calcd. for C<sub>96</sub>H<sub>82</sub>N<sub>4</sub>O<sub>10</sub>P<sub>4</sub>Ru<sub>2</sub>S<sub>2</sub> ([M - 2 ClO<sub>4</sub><sup>-</sup> - 2 CH<sub>3</sub>CN]<sup>2+</sup>): m/z 816.12; found 816.13. <sup>1</sup>H-NMR (250 MHz, CD<sub>3</sub>CN): δ 2.34 (s, 6H, CH<sub>3</sub>CN), 3.62 (s, 6H, SCH<sub>3</sub>), 6.92 (s, 2H, quinone-H), 7.02 – 7.17 (m, 22H, aryl-H), 7.20 – 7.38 (m, 25H, aryl-H), 7.45 – 7.65 (m, 21H, aryl-H). <sup>31</sup>P-NMR (250 MHz, CD<sub>3</sub>CN) δ 35.45 (d, <sup>2</sup>J<sub>P-P</sub> = 30.7 Hz, 2P), 37.65 (d, <sup>2</sup>J<sub>P-P</sub> = 30.7 Hz, 2P).

#### 10.3.9.2. Synthesis of the complex [(Q)Ru]<sub>2</sub>(μ-L-2H)][ClO<sub>4</sub>].

##### Q = 4,6-di-*tert*-butyl-*N*-(*o*-methylthiophenyl)-*o*-iminobenzoquinone.

The metal precursor [Ru<sub>2</sub>(CH<sub>3</sub>CN)<sub>6</sub>L](ClO<sub>4</sub>)<sub>2</sub> (52 mg, 0.05 mol) was dissolved in 5 ml CH<sub>2</sub>Cl<sub>2</sub> in a Schlenk flask under argon atmosphere. Then 3,5-Di-*tert*-butyl-2-hydroxy-1-(2-methylthioanilido)benzene ligand (35 mg, 0.1 mol), 25 ml EtOH and 1 ml NEt<sub>3</sub> were added and refluxed for 18 h at 70 C° temperature. The solvent of the reaction mixture was evaporated to dryness under reduced pressure and the residue was then purified on a silica column. The gray-purple product was eluted with CH<sub>2</sub>Cl<sub>2</sub>/CH<sub>3</sub>CN (10:1). Evaporation of solvent under reduced pressure afforded the pure complex. Yield: (14%); elemental analysis calcd (%) for C<sub>62</sub>H<sub>70</sub>N<sub>4</sub>O<sub>8</sub>ClRu<sub>2</sub>S<sub>4</sub>: C 54.55, H 5.17, N 4.10; found: C 53.83, H 4.96, N 3.78; ES-MS: (m/z): calcd. for C<sub>62</sub>H<sub>70</sub>N<sub>4</sub>O<sub>4</sub>Ru<sub>2</sub>S<sub>4</sub>: 1266.24 [M]<sup>+</sup>; found: 1266.24.

### 10.3.9.2.1. Synthesis of the complex $[(Q)Ru]_2(\mu-L_{2H})[ClO_4]_2$ .

To a solution of the complex  $[(Q)Ru]_2(\mu-L_{2H})[ClO_4]$  (30 mg 0.022 mol) in 8 ml  $CH_3CN$  was added ferrocenium hexafluorophosphate (7.3 mg 0.022 mol). The initial gray-purple solution changed to green. Then an excess of a saturated aqueous solution of  $NaClO_4$  was added. The precipitate thus obtained was collected and dried in vacuum and then purified by column chromatography (neutral alumina). The green product was eluted with  $CH_2Cl_2/CH_3CN$  (7:1). Evaporation of the solvent under reduced pressure afforded the pure complex. Yield: (86%). elemental analysis calcd (%) for  $C_{62}H_{70}N_4O_{12}Cl_2Ru_2S_4 \cdot 2H_2O$ : C 49.63, H 4.97, N 3.73; found: C 49.94, H 4.85, N 3.62; ES-MS: (m/z): calcd. for  $C_{62}H_{74}N_4O_4Ru_2S_4$ : 633.12  $[M]^{2+}$ ; found: 633.13.  $^1H$  NMR (250 MHz,  $CD_3CN$ )  $\delta$ /ppm: 1.43 (24H, s,  $CCH_3$ ), 1.47 (12H, s,  $CCH_3$ ), 2.00 (6H, s,  $SCH_3$ ), 2.21 (6H, s,  $SCH_3$ ), 5.42 (2H, s, O-C-CH), 5.84 (2H, s,  $C(CH_3)_3$ -C-CH), 6.56 (2H, s,  $C(CH_3)_3$ -C-CH), 7.04 (2H, m, aryl), 7.33 (4H, m, aryl), 7.72 (2H, d,  $^3J_{H-H} = 7.7$  Hz, aryl), 7.8 (3H, m, aryl), 8.00 (2H, m, aryl), (3H, m, aryl)

### 10.3.10. Ruthenium complex of quinolin-5,8-dione ligand

#### Synthesis of $[Ru(acac)_2L]$ ; L = N-(2-methyl-5,8-dioxo-5,8-dihydroquinolin-7-yl)acetamide

The ligand L (23 mg, 0.1 mmol) and the metal precursor  $[Ru(acac)_2(CH_3CN)_2]$  (38 mg, 0.1 mmol) were dissolved in 20 ml ethanol and refluxed for 12 h under argon atmosphere resulting color changed from orange to dark-green. The solvent of the reaction mixture was evaporated to dryness under reduced pressure and the residue was then purified on an alumina column. The dark-green product was eluted with  $CH_2Cl_2/CH_3CN$  (9:1). Evaporation of solvent under reduced pressure afforded the pure complex (12 mg, 23%). Anal. calcd for  $C_{22}H_{24}N_2O_7Ru$ : C, 49.90; H, 4.57; N, 5.29%. Found: C, 49.58; H, 4.36; N, 5.12%.  $\lambda_{max}$  ( $CH_3CN$ )/nm 743, 462, 353, 270 and 241 ( $\epsilon/dm^{-3} mol^{-1} cm^{-1}$  6700, 7000, 7000, 18100 and 13600).  $\nu_{max}$ (solid)/ $cm^{-1}$  1702 (CO), 1600 (CO), 1547 (CO), 1510 (CN).  $\delta_H$  (300 MHz;  $CD_3CN$ ;  $Me_3Si$ ) 2.06 (3H, s, Me), 2.12 (3H, s, Me), 2.15 (3H, s, Me), 2.26 (3H, s, Me), 2.37 (3H, s, Me), 2.54 (3H, s, Me) 5.31 (1H, s, CH), 5.82 (1H, s, CH), 7.83 (1H, s, CH), 7.84 (1H, d,  $J_{HH} = 8$  Hz, CH) 8.4 (1H, d,  $J_{HH} = 8$  Hz, CH), 9.65 (1H, br s, NH). m/z (ESI) 531 ( $[M+H]^+$ ), 553 ( $[M+Na]^+$ ).

## 10.4 Crystallography

Crystallographic data collection was carried out by Dr. Wolfgang, Dr. F. Lissner and Dr. I. Hartenbach from University of Stuttgart and S. Mobin from Indian Institute of Technology, Bombay. Crystal structure solving was done by S. Hohloch, Dr. I. Hartenbach, R. Pattacini, S. Mobin and Dr. C.-Y. Su. Suitable crystal were selected under a cover of paraffin oil and sealed in capillaries for the measurements. The selected single crystals were instantly placed in a liquid nitrogen stream for the diffraction measurements.

The crystallographic reflection intensity data for  $[(Q)\text{-Ru}^{\text{III}}(\mu\text{-L}_{2\text{H}})^2\text{-Ru}^{\text{III}}(Q)]\text{-}[\text{ClO}_4]_2$  (L = 2,5-di-[2-(methylthio)-anilino]-1,4-benzoquinone and Q = 4,6-di-*tert*-butyl-*N*-(*o*-methylthiophenyl)-*o*-iminobenzoquinone),  $[\text{Ru}(\text{bpy})(\text{L}_{\text{H}})_2]$  (L = 2,5-bis(isopropylamino)-1,4-benzoquinone) and  $[\text{Ru}(\text{L}_{\text{H}})_3]$  (L = *N,N'*-Diisopropyl-2-amino-5-alcoholate-1,4-benzoquinonemonoiminium) were collected at 100 K on an Bruker Kappa Apex II duo diffractometer with the Enhance X-ray Source of Mo radiation ( $\lambda = 0.71073 \text{ \AA}$ ).

Data for complex  $[\{\text{Cl}(\eta^6\text{-Cym})\text{Ru}\}_2(\mu\text{-L}_{2\text{H}})]$  (L = 2,5-di-[2-(trifluoromethyl)-anilino]-1,4-benzoquinone),  $[\text{Ru}(\text{bpy})_2\text{L}_{\text{H}}]\text{ClO}_4$  (L = *N,N'*-Diisopropyl-2-amino-5-alcoholate-1,4-benzoquinonemonoiminium) and  $[\{\text{Ru}(\text{bpy})_2\}_2(\mu\text{-L}_{\text{H}2})](\text{ClO}_4)_2$  (L = *N,N'*-Diisopropyl-2-amino-5-alcoholate-1,4-benzoquinonemonoiminium) were collected on four circle diffractometer NONIUS Kappa-CCD with the Enhance X-ray Source of Mo radiation ( $\lambda = 0.71073 \text{ \AA}$ ).

Data for complex  $[\{\text{Ru}(\text{bpy})_2\}_2(\mu\text{-L}_{\text{H}2})](\text{ClO}_4)_2$  and  $[\text{Ru}(\text{acac})_2\text{L}_{\text{H}}]$  (L = *N,N'*-Diisopropyl-2-amino-5-alcoholate-1,4-benzoquinonemonoiminium ligand) were collected on a Kappa CCD diffractometer with the Enhance X-ray Source of Mo radiation ( $\lambda = 0.71073 \text{ \AA}$ ) at 173 K.

The selected single crystals of  $[\text{Ru}(\text{bpy})_2\text{L}_{\text{H}}]\text{ClO}_4$  and  $[\{\text{Ru}(\text{bpy})_2\}_2(\mu\text{-L}_{\text{H}2})](\text{ClO}_4)_2$  (L = 2,5-bis(isopropylamino)-1,4-benzoquinone) were measured using graphite-monochromated Mo radiation ( $\lambda = 0.71073 \text{ \AA}$ ) at 150 K in a CCD Oxford Diffraction XCALIBUR-S diffractometer equipped with an Oxford Instruments low temperature attachment.

The structure were solved via direct methods using the programme SHELXS-97.<sup>[128]</sup> Refinement was carried out by the full matrix least squares method employing the programme SHELXL-97.<sup>[129]</sup> All non-hydrogen atoms are refined anisotropically, hydrogen atoms were introduced in proper positions with coupled isotropic factors using the riding model. Absorption corrections were performed numerically using the programme HABITUS.130 The programme DIAMOND 2.1e131 was used for structure drawing.

Crystallographic parameters:

$$R = (\Sigma | |F_o| - |F_c| |) / \Sigma |F_o|$$

$$WR = \{ \Sigma [w(|F_o|^2 - |F_c|^2)^2] / \Sigma [w(F_o^4)] \}^{1/2}$$

$$GOF = \{ \Sigma w(|F_o|^2 - |F_c|^2)^2 / (n - m) \}^{1/2} \text{ where } n = \text{number of data and } m = \text{number of variables}$$

**10.4.1. [Ru(bpy)<sub>2</sub>L-H]ClO<sub>4</sub>**

**L = *N,N'*-diisopropyl-2-amino-5-alcoholate-1,4-benzoquinonemonoiminium ligand.**

Purple-red plates shaped single crystals for X-ray diffraction were obtained by slow diffusion of a solution of [Ru(bpy)<sub>2</sub>L-H]ClO<sub>4</sub> in dichloromethane layered with *n*-hexane.

**Table 10.4.1.1.** Crystallographic data and refinement parameters for [Ru(bpy)<sub>2</sub>L-H]ClO<sub>4</sub> ·CH<sub>2</sub>Cl<sub>2</sub>.

|  |   |
|--|---|
| Chemical formula   | C <sub>32</sub> H <sub>33</sub> N <sub>6</sub> O <sub>2</sub> Ru ·CH <sub>2</sub> Cl <sub>2</sub> ·ClO <sub>4</sub> |
| <i>M<sub>r</sub></i>   | 819.09  |
| Cell setting, space group  | Monoclinic, <i>P</i> 21/ <i>c</i>   |
| Temperature(K)   | 100(2)  |
| <i>a</i> , <i>b</i> , <i>c</i> (Å)   | 9.8944(2), 18.0252(2), 19.8545(3)   |
| <i>α</i> , <i>β</i> , <i>γ</i> (°)   | 90.00, 99.260(1), 90.00   |
| <i>V</i> (Å <sup>3</sup> )   | 3494.9(1)   |
| <i>Z</i>   | 4   |
| <i>D<sub>x</sub></i> (Mg m <sup>-3</sup> )   | 1.557   |
| Radiation type   | Mo <i>Kα</i>  |
| <i>μ</i> (mm <sup>-1</sup> )   | 0.73  |
| Crystal size(mm)   | 0.12 × 0.12 × 0.10  |
| Meas., indep. and obsvd refl.  | 15946, 8319, 6724   |
| <i>R</i> [ <i>F</i> <sup>2</sup> > 2σ( <i>F</i> <sup>2</sup> )], <i>wR</i> ( <i>F</i> <sup>2</sup> ), <i>S</i> | 0.037, 0.127, 1.17  |
| F000   | 1672  |
| <i>R</i> <sub>int</sub>  | 0.029   |
| θ <sub>max</sub> (°)   | 27.9  |
| Δρ <sub>max</sub> , Δρ <sub>min</sub> (e Å <sup>-3</sup> )   | 1.09, -1.43   |



**10.4.2.  $[\{\text{Ru}(\text{bpy})_2\}_2(\mu\text{-L}_{\text{H2}})](\text{ClO}_4)_2$** **L = *N,N'*-diisopropyl-2-amino-5-alcoholate-1,4-benzoquinonemonoiminium ligand.**

Black block shaped single crystals for X-ray diffraction were obtained by slow diffusion of a solution of  $[\{\text{Ru}(\text{bpy})_2\}_2(\mu\text{-L}_{\text{H2}})](\text{ClO}_4)_2$  in dichloromethane layered with *n*-hexane.

**Table 10.4.1.1.** Crystallographic data and refinement parameters for  $[\{\text{Ru}(\text{bpy})_2\}_2(\mu\text{-L}_{\text{H2}})](\text{ClO}_4)_2 \cdot 2\text{CH}_2\text{Cl}_2$ .

|   |  |
|---|--|
| Chemical formula  | $\text{C}_{52}\text{H}_{48}\text{N}_{10}\text{O}_2\text{Ru}_2 \cdot 2\text{CH}_2\text{Cl}_2 \cdot 2\text{ClO}_4$ |
| $M_r$   | 1415.90  |
| Cell setting, space group   | Triclinic, <i>P</i> -1   |
| Temperature(K)  | 173(2)   |
| $a, b, c(\text{\AA})$   | 12.8148(5), 13.9252(3), 17.7605(6)   |
| $\alpha, \beta, \gamma(^{\circ})$                                     | 68.649(2), 86.397(2), 88.834(2)  |
| $V(\text{\AA}^3)$   | 2945.97(16)  |
| <i>Z</i>  | 2  |
| $D_x(\text{Mg m}^{-3})$   | 1.596  |
| Radiation type  | Mo $K\alpha$   |
| $\mu(\text{mm}^{-1})$   | 0.85   |
| Crystal size(mm)  | $0.12 \times 0.12 \times 0.10$   |
| Meas., indep. and obsvd refl.   | 18481, 12203, 8157   |
| $R[F^2 > 2\sigma(F^2)], wR(F^2), S$                                   | 0.053, 0.151, 1.02   |
| F000  | 1432   |
| $R_{\text{int}}$  | 0.034  |
| $\theta_{\text{max}}(^{\circ})$                                       | 26.5   |
| $\Delta\rho_{\text{max}}, \Delta\rho_{\text{min}}(\text{e \AA}^{-3})$ | 1.35, -0.88  |

**10.4.3.  $[\{\text{Ru}(\text{bpy})_2\}_2(\mu\text{-L}'\text{-H}_2)](\text{ClO}_4)_2$**  **$\text{L}' = N,N'$ -dibenzyl-2-amino-5-alcoholate-1,4-benzoquinonemonoiminium.**

Black needle shaped single crystals for X-ray diffraction were obtained by slow diffusion of a solution of  $[\{\text{Ru}(\text{bpy})_2\}_2(\mu\text{-L}'\text{-H}_2)](\text{ClO}_4)_2$  in dichloromethane layered with *n*-hexane.

**Table 10.4.3.1.** Crystallographic data and refinement parameters for  $[\{\text{Ru}(\text{bpy})_2\}_2(\mu\text{-L}'\text{-H}_2)](\text{ClO}_4)_2$ .

|   |  |
|---|--|
| Chemical formula  | $\text{C}_{60}\text{H}_{48}\text{N}_{10}\text{O}_2\text{Ru}_2 \cdot 2\text{ClO}_4$ |
| $M_r$   | 1342.12  |
| Cell setting, space group   | Monoclinic, $P21/n$  |
| Temperature(K)  | 100(2)   |
| $a, b, c(\text{\AA})$   | 11.5555(2), 24.1007(4), 23.6059(4)   |
| $\alpha, \beta, \gamma(^{\circ})$                                     | 90.00, 92.412(1), 90.00  |
| $V(\text{\AA}^3)$   | 6568.31(19)  |
| $Z$   | 4  |
| $D_x(\text{Mg m}^{-3})$   | 1.357  |
| Radiation type  | Mo $K\alpha$   |
| $\mu(\text{mm}^{-1})$   | 0.601  |
| Meas., indep. and obsvd refl.   | 29610, 15602, 10646  |
| $R[F^2 > 2\sigma(F^2)], wR(F^2), S$                                   | 0.081, 0.246, 1.073  |
| F000  | 2720   |
| $R_{\text{int}}$  | 0.036  |
| $\theta_{\text{max}}(^{\circ})$                                       | 27.9   |
| $\Delta\rho_{\text{max}}, \Delta\rho_{\text{min}}(\text{e \AA}^{-3})$ | 2.11, -1.12  |

**10.4.4. [Ru(bpy)<sub>2</sub>L-H]ClO<sub>4</sub>****L = 2,5-bis(isopropylamino)-1,4-benzoquinone.**

Orange block shaped single crystals for X-ray diffraction were obtained by slow diffusion of a solution of [Ru(bpy)<sub>2</sub>L-H]ClO<sub>4</sub> in dichloromethane layered with *n*-hexane.

**Table 10.4.4.1.** Crystallographic data and refinement parameters for [Ru(bpy)<sub>2</sub>L-H]ClO<sub>4</sub>.

|   |  |
|---|--|
| Chemical formula  | C <sub>32</sub> H <sub>33</sub> N <sub>6</sub> O <sub>6</sub> ClRu |
| $M_r$   | 734.16   |
| Cell setting, space group   | Monoclinic, <i>C2/c</i>  |
| Temperature(K)  | 150(2)   |
| $a, b, c(\text{Å})$   | 22.3438(8), 17.7934(5), 17.2914(7)                                 |
| $\alpha, \beta, \gamma(^{\circ})$                                   | 90.00, 108.698(4), 90.00   |
| $V(\text{Å}^3)$   | 6511.7(4)  |
| $Z$   | 8  |
| $D_x(\text{Mg m}^{-3})$   | 1.498  |
| Radiation type  | Mo $K\alpha$   |
| $\mu(\text{mm}^{-1})$   | 0.617  |
| Crystal size(mm)  | 0.33 × 0.28 × 0.23   |
| Meas., indep. and<br>obsvd refl.                                    | 22568, 5721, 4865  |
| $R[F^2 > 2\sigma(F^2)], wR(F^2), S$                                 | 0.0385, 0.1178, 1.087  |
| F000  | 3008   |
| $R_{\text{int}}$  | 0.0317   |
| $\theta_{\text{max}}(^{\circ})$                                     | 25.00  |
| $\Delta\rho_{\text{max}}, \Delta\rho_{\text{min}}(\text{e Å}^{-3})$ | 1.056, -0.583  |

**10.4.5.  $[\{\text{Ru}(\text{bpy})_2\}_2(\mu\text{-L}_{\text{H2}})](\text{ClO}_4)_2$** **L = 2,5-bis(isopropylamino)-1,4-benzoquinone.**

Black block shaped single crystals for X-ray diffraction were obtained by slow diffusion of a solution of  $[\{\text{Ru}(\text{bpy})_2\}_2(\mu\text{-L}_{\text{H2}})](\text{ClO}_4)_2$  in dichloromethane layered with *n*-hexane.

**Table 10.4.5.1.** Crystallographic data and refinement parameters for  $[\{\text{Ru}(\text{bpy})_2\}_2(\mu\text{-L}_{\text{H2}})](\text{ClO}_4)_2$ .

|   |  |
|---|--|
| Chemical formula  | $\text{C}_{52}\text{H}_{48}\text{N}_{10}\text{O}_{10}\text{Cl}_2\text{Ru}_2$ |
| $M_r$   | 1246.04  |
| Cell setting, space group   | Monoclinic, $P2_1/n$   |
| Temperature(K)  | 150(2)   |
| $a, b, c(\text{\AA})$   | 11.9202(8), 25.997(3),<br>17.5434(10)  |
| $\alpha, \beta, \gamma(^{\circ})$                                     | 90.00, 99.753(7),<br>90.00   |
| $V(\text{\AA}^3)$   | 5357.9(7)  |
| $Z$   | 4  |
| $D_x(\text{Mg m}^{-3})$   | 1.545  |
| Radiation type  | Mo $K\alpha$   |
| $\mu(\text{mm}^{-1})$   | 0.731  |
| Crystal size(mm)  | $0.33 \times 0.28 \times 0.23$   |
| Meas., indep. and<br>obsvd refl.                                      | 41215, 9405, 2646  |
| $R[F^2 > 2\sigma(F^2)], wR(F^2), S$                                   | 0.0951, 0.3034, 0.2526   |
| F000  | 2528   |
| $R_{\text{int}}$  | 0.1546   |
| $\theta_{\text{max}}(^{\circ})$                                       | 25.00  |
| $\Delta\rho_{\text{max}}, \Delta\rho_{\text{min}}(\text{e \AA}^{-3})$ | 0.838, -0.518  |

**10.4.6. [Ru(bpy)(L-H)<sub>2</sub>]****L = 2,5-bis(isopropylamino)-1,4-benzoquinone.**

Red block shaped single crystals for X-ray diffraction were obtained by slow diffusion of a solution of [Ru(bpy)(L-H)<sub>2</sub>] in dichloromethane layered with *n*-hexane.

**Table 10.4.6.1.** Crystallographic data and refinement parameters for [Ru(bpy)(L-H)<sub>2</sub>].

|  |  |
|--|--|
| Chemical formula   | C <sub>34</sub> H <sub>42</sub> N <sub>6</sub> O <sub>6.5</sub> Ru |
| <i>M<sub>r</sub></i>   | 739.81   |
| Cell setting, space group  | Monoclinic, P2/c   |
| Temperature(K)   | 100(2)   |
| <i>a</i> , <i>b</i> , <i>c</i> (Å)   | 12.972(3), 19.839(4), 14.561(3)                                    |
| α, β, γ(°)   | 90.00, 107.788(5), 90.00   |
| <i>V</i> (Å <sup>3</sup> )   | 3568.2(14)   |
| <i>Z</i>   | 4  |
| <i>D<sub>x</sub></i> (Mg m <sup>-3</sup> )   | 1.377  |
| Radiation type   | Mo <i>K</i> α  |
| μ(mm <sup>-1</sup> )   | 0.492  |
| Crystal size(mm)   | 0.34 × 0.20 × 0.10   |
| Meas., indep. and obsvd refl.  | 30408, 6156, 2722  |
| <i>R</i> [ <i>F</i> <sup>2</sup> > 2σ( <i>F</i> <sup>2</sup> )], <i>wR</i> ( <i>F</i> <sup>2</sup> ), <i>S</i> | 0.0993, 0.2772, 1.022  |
| <i>F</i> 000   | 1536   |
| <i>R</i> <sub>int</sub>  | 0.1401   |
| θ <sub>max</sub> (°)   | 25.00  |
| Δρ <sub>max</sub> , Δρ <sub>min</sub> (e Å <sup>-3</sup> )   | 0.994, -0.755  |

**10.4.7. [Ru(acac)<sub>2</sub>L<sub>H</sub>]****L = N,N'-diisopropyl-2-amino-5-alcoholate-1,4-benzoquinonemonoiminium ligand.**

Red needle shaped single crystals for X-ray diffraction were obtained by slow evaporation of a solution of [Ru(acac)<sub>2</sub>L<sub>H</sub>] in dichloromethane.

**Table 10.4.7.1.** Crystallographic data and refinement parameters for [Ru(acac)<sub>2</sub>L<sub>H</sub>].

|  |  |
|--|--|
| Chemical formula   | C <sub>22</sub> H <sub>31</sub> N <sub>2</sub> O <sub>6</sub> Ru |
| <i>M<sub>r</sub></i>   | 520.56   |
| Cell setting, space group  | Monoclinic,P21/c   |
| Temperature(K)   | 173(2)   |
| <i>a</i> , <i>b</i> , <i>c</i> (Å)   | 14.5139(17), 31.258(4), 20.987(3)                                |
| $\alpha$ , $\beta$ , $\gamma$ (°)  | 90.00, 112.244(3),<br>90.00                                      |
| <i>V</i> (Å <sup>3</sup> )   | 2336.61(19)  |
| <i>Z</i>   | 4  |
| <i>D<sub>x</sub></i> (Mg m <sup>-3</sup> )   | 1.480  |
| Radiation type   | Mo <i>K</i> α  |
| $\mu$ (mm <sup>-1</sup> )  | 0.710  |
| Crystal size(mm)   | 0.13 × 0.05 × 0.05   |
| Meas., indep. And<br>obsvd refl.   | 8766, 4778, 3397   |
| <i>R</i> [ <i>F</i> <sup>2</sup> > 2σ( <i>F</i> <sup>2</sup> )], <i>wR</i> ( <i>F</i> <sup>2</sup> ), <i>S</i> | 0.0481, 0.1088, 1.036  |
| F000   | 1076   |
| <i>R</i> <sub>int</sub>  | 0.0397   |
| $\theta$ <sub>max</sub> (°)  | 26.40  |
| $\Delta\rho$ <sub>max</sub> , $\Delta\rho$ <sub>min</sub> (e Å <sup>-3</sup> )                                 | 1.613, -0.833  |

**10.4.8. [Ru(L-H)<sub>3</sub>]**

**L = N,N'-diisopropyl-2-amino-5-alcoholate-1,4-benzoquinonemonoiminium ligand.**

Red-brown needle shaped single crystals for X-ray diffraction were obtained by slow evaporation of a solution of [Ru(L-H)<sub>3</sub>] in dichloromethane.

**Table 10.4.8.1.** Crystallographic data and refinement parameters for [Ru(L-H)<sub>3</sub>].

|  |  |
|--|--|
| Chemical formula   | C <sub>72</sub> H <sub>101</sub> N <sub>12</sub> O <sub>12</sub> Ru <sub>2</sub> |
| <i>M<sub>r</sub></i>   | 1528.79  |
| Cell setting, space group  | Monoclinic,P21/c   |
| Temperature(K)   | 100(2)   |
| <i>a</i> , <i>b</i> , <i>c</i> (Å)   | 8.4202(2), 20.047(1), 14.9552(8)   |
| $\alpha$ , $\beta$ , $\gamma$ (°)  | 90.00, 106.002(7), 90.00   |
| <i>V</i> (Å <sup>3</sup> )   | 9152.3(19)   |
| <i>Z</i>   | 4  |
| <i>D<sub>x</sub></i> (Mg m <sup>-3</sup> )   | 1.110  |
| Radiation type   | Cu <i>K</i> α  |
| $\mu$ (mm <sup>-1</sup> )  | 3.115  |
| Crystal size(mm)   | 0.19 × 0.11 × 0.03   |
| Meas., indep. And<br>obsvd refl.   | 76159, 14714, 10343  |
| <i>R</i> [ <i>F</i> <sup>2</sup> > 2σ( <i>F</i> <sup>2</sup> )], <i>wR</i> ( <i>F</i> <sup>2</sup> ), <i>S</i> | 0.0692, 0.1912, 1.065  |
| F000   | 3204   |
| <i>R</i> <sub>int</sub>  | 0.0636   |
| $\theta$ <sub>max</sub> (°)  | 66.38  |
| $\Delta\rho$ <sub>max</sub> , $\Delta\rho$ <sub>min</sub> (e Å <sup>-3</sup> )                                 | 1.089, -0.963  |

**10.4.9.  $\{[\text{Ru}(\text{acac})_2]_2(\mu\text{-L}_{\text{H}2})\}$** **L = 2,5-bis(isopropylamino)-1,4-benzoquinone.**

Red needle shaped single crystals for X-ray diffraction were obtained by slow evaporation of a solution of  $[\text{Ru}(\text{acac})_2\text{L}_{\text{H}}]$  in dichloromethane.

**Table 10.4.9.1.** Crystallographic data and refinement parameters for  $[\text{Ru}(\text{acac})_2\text{L}_{\text{H}}]$ .

|   |  |
|---|--|
| Chemical formula  | $\text{C}_{32}\text{H}_{44}\text{N}_2\text{O}_{10}\text{Ru}_2$ |
| $M_r$   | 818.83   |
| Cell setting, space group   | Monoclinic, $P2_1/c$   |
| Temperature(K)  | 150(2)   |
| $a, b, c(\text{\AA})$   | 8.4154(1), 21.6986(3), 9.8276(2)                               |
| $\alpha, \beta, \gamma(^{\circ})$                                     | 90.00, 95.729(2), 90.00  |
| $V(\text{\AA}^3)$   | 1785.6(5)  |
| $Z$   | 2  |
| $D_x(\text{Mg m}^{-3})$   | 1.523  |
| Radiation type  | Cu $K\alpha$ ( $\lambda = 1.54178 \text{ \AA}$ )               |
| $\mu(\text{mm}^{-1})$   | 1.54   |
| Crystal size(mm)  | $0.28 \times 0.24 \times 0.18$                                 |
| Meas., indep. and obsvd refl.   | 7723, 2680, 2126   |
| $R[F^2 > 2\sigma(F^2)], wR(F^2), S$                                   | 0.052, 0.144, 1.009  |
| No. of parameters   | 406  |
| $R_{\text{int}}$  | 0.036  |
| $\theta_{\text{max}}(^{\circ})$                                       | 60.8   |
| $\Delta\rho_{\text{max}}, \Delta\rho_{\text{min}}(\text{e \AA}^{-3})$ | 1.11, -0.71  |



**10.4.10.  $[\{\text{Cl}(\eta^6\text{-Cym})\text{Ru}\}_2(\mu\text{-L}_{2\text{H}})]$** **L = 2,5-di-[2-(trifluoromethyl)-anilino]-1,4-benzoquinone.**

Black platetlet shaped single crystals for X-ray diffraction were obtained by slow evaporation of a solution of  $[\{\text{Cl}(\eta^6\text{-Cym})\text{Ru}\}_2(\mu\text{-L}_{2\text{H}})]$  in dichloromethane.

**Table 10.4.10.1.** Crystallographic data and refinement parameters for  $[\{\text{Cl}(\eta^6\text{-Cym})\text{Ru}\}_2(\mu\text{-L}_{2\text{H}})]$ .

|   |  |
|---|--|
| Chemical formula  | $\text{C}_{40}\text{H}_{38}\text{C}_{12}\text{F}_6\text{N}_2\text{O}_2\text{Ru}_2$ |
| $M_r$   | 965.76   |
| Cell setting, space group   | Monoclinic, $P2_1/c$   |
| Temperature(K)  | 100(2)   |
| $a, b, c(\text{\AA})$   | 17.592(4) 12.234(2) 19.212(4)  |
| $\alpha, \beta, \gamma(^{\circ})$                                     | 90.00, 107.35(3)90.00  |
| $V(\text{\AA}^3)$   | 3946.8(1)  |
| $Z$   | 4  |
| $D_x(\text{Mg m}^{-3})$   | 1.625  |
| Radiation type  | Mo $K\alpha$   |
| $\mu(\text{mm}^{-1})$   | 0.711  |
| Crystal size(mm)  | $0.23 \times 0.21 \times 0.08$   |
| Meas., indep. and obsvd refl.   | 15417, 8011, 4924  |
| $R[F^2 > 2\sigma(F^2)], wR(F^2), S$                                   | 0.078, 0.175, 1.286  |
| F000  | 1936   |
| $R_{\text{int}}$  | 0.075  |
| $\theta_{\text{max}}(^{\circ})$                                       | 26.37  |
| $\Delta\rho_{\text{max}}, \Delta\rho_{\text{min}}(\text{e \AA}^{-3})$ | 2.677, -0.972  |

**10.4.11. [(Q)<sup>-</sup>Ru<sup>III</sup>(μ-L<sub>2H</sub>)<sup>2-</sup>Ru<sup>III</sup>(Q)<sup>-</sup>](ClO<sub>4</sub>)<sub>2</sub>****L = 2,5-di-[2-(methylthio)-anilino]-1,4-benzoquinone.****Q = 4,6-di-*tert*-butyl-*N*-(*o*-methylthiophenyl)-*o*-iminobenzoquinone.**

Black block shaped single crystals for X-ray diffraction were obtained by slow diffusion of a solution of [(Q)<sup>-</sup>Ru<sup>III</sup>(μ-L<sub>2H</sub>)<sup>2-</sup>Ru<sup>III</sup>(Q)<sup>-</sup>](ClO<sub>4</sub>)<sub>2</sub> in dichloromethane layered with *n*-hexane.

**Table 10.4.11.1.** Crystallographic data and refinement parameters for [(Q)<sup>-</sup>Ru<sup>III</sup>(μ-L<sub>2H</sub>)<sup>2-</sup>Ru<sup>III</sup>(Q)<sup>-</sup>](ClO<sub>4</sub>)<sub>2</sub>.

|  |   |
|--|---|
| Chemical formula   | C <sub>62</sub> H <sub>70</sub> N <sub>4</sub> O <sub>4</sub> S <sub>4</sub> Ru <sub>2</sub> ·2H <sub>2</sub> O·2ClO <sub>4</sub> |
| <i>M<sub>r</sub></i>   | 1496.50   |
| Cell setting, space group  | Monoclinic, <i>P</i> 21/ <i>n</i>   |
| Temperature(K)   | 100(2)  |
| <i>a</i> , <i>b</i> , <i>c</i> (Å)   | 8.6405(12), 23.239(3), 16.703(2)  |
| α, β, γ(°)   | 90.00, 95.989(5), 90.00   |
| <i>V</i> (Å <sup>3</sup> )   | 3335.6(8)   |
| <i>Z</i>   | 2   |
| <i>D<sub>x</sub></i> (Mg m <sup>-3</sup> )   | 1.490   |
| Radiation type   | Mo <i>K</i> α   |
| μ(mm <sup>-1</sup> )   | 0.723   |
| Crystal size (nm)  | 0.23 × 0.21 × 0.16  |
| Meas., indep. and obsvd refl.  | 14499, 4907, 3315   |
| <i>R</i> [ <i>F</i> <sup>2</sup> > 2σ( <i>F</i> <sup>2</sup> )], <i>wR</i> ( <i>F</i> <sup>2</sup> ), <i>S</i> | 0.0873, 0.1895, 1.101   |
| <i>F</i> 000   | 1536  |
| <i>R</i> <sub>int</sub>  | 0.0598  |
| θ <sub>max</sub> (°)   | 25.08   |
| Δρ <sub>max</sub> , Δρ <sub>min</sub> (e Å <sup>-3</sup> )   | 0.830, -0.762   |

## CHAPTER 11

### Summary

Redox active quinonoid ligands and their metal complexes are gaining increasing attention because of their wide importance in inorganic, organic, physical and even in biochemistry. In this doctoral thesis structural and electronic properties of mono- and dinuclear ruthenium complexes of non-innocent quinonoid bridging ligands have been investigated. Additionally, the thesis covers the straightforward, one-pot and green synthesis of symmetrically and rare asymmetrically substituted biologically relevant *p*-quinone ligands with different steric and electronic properties. The *N*-substituents in the ligands are used to tune the structural and electronic properties of their metal complexes.

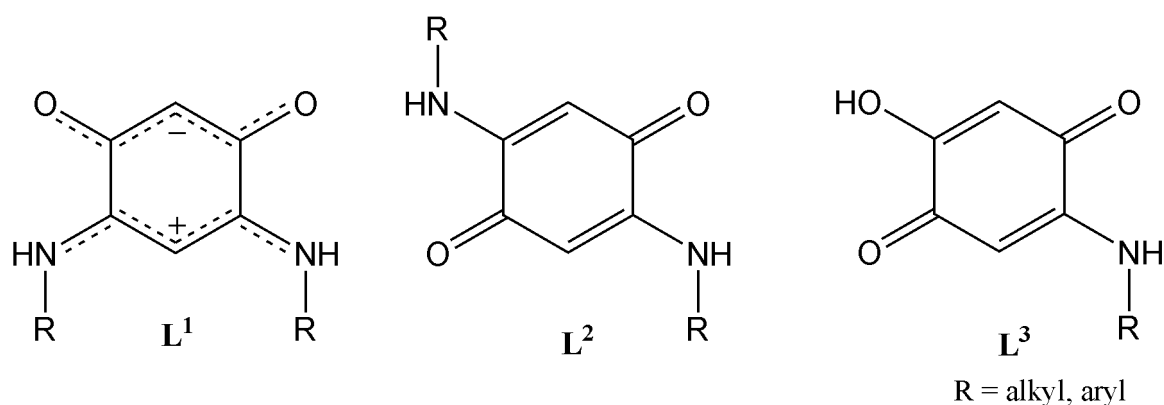


**Figure 11.1.** Molecular formulae of *N*-substituted sym. *m*-[O,O,N,N] zwitterionic ( $\mathbf{L}^1$ ), sym. *p*-[O,N,O,N] ( $\mathbf{L}^2$ ) and asym. *p*-[O,O,O,N] ( $\mathbf{L}^3$ ) quinonoid ligands.

The properties of these symmetric and asymmetric ligand systems ( $\mathbf{L}^1$ ,  $\mathbf{L}^2$  and  $\mathbf{L}^3$ ) such as redox, electron transfer, structures, bonding and delocalization of the  $\pi$ -systems have been investigated in their mono- and dinuclear metal complexes.

Chapter 2 describes the structural, electrochemical and spectroscopic properties of mono- and dinuclear ruthenium bipyridine complexes with *N*-substituted *m*-[O,O,N,N] zwitterionic ligands ( $\mathbf{L}^1$ ). The mononuclear complex  $[\text{Ru}^{\text{II}}(\text{bpy})_2(\mathbf{L}^1)](\text{ClO}_4)$  and dinuclear complexes  $[\{\text{Ru}^{\text{II}}(\text{bpy})_2\}_2(\mu\text{-}\mathbf{L}^1)](\text{ClO}_4)_2$  have been structurally characterized (Figure 11.2). Crystal structure analysis confirms that successive metallation of the zwitterionic ligand  $\mathbf{L}^1$  leads first to a localization of the  $\pi$ -system in the mononuclear complex  $[\text{Ru}^{\text{II}}(\text{bpy})_2(\mathbf{L}^1)](\text{ClO}_4)$  and further 're'-delocalization in the dinuclear complex  $[\{\text{Ru}^{\text{II}}(\text{bpy})_2\}_2(\mu\text{-}\mathbf{L}^1)](\text{ClO}_4)_2$ .

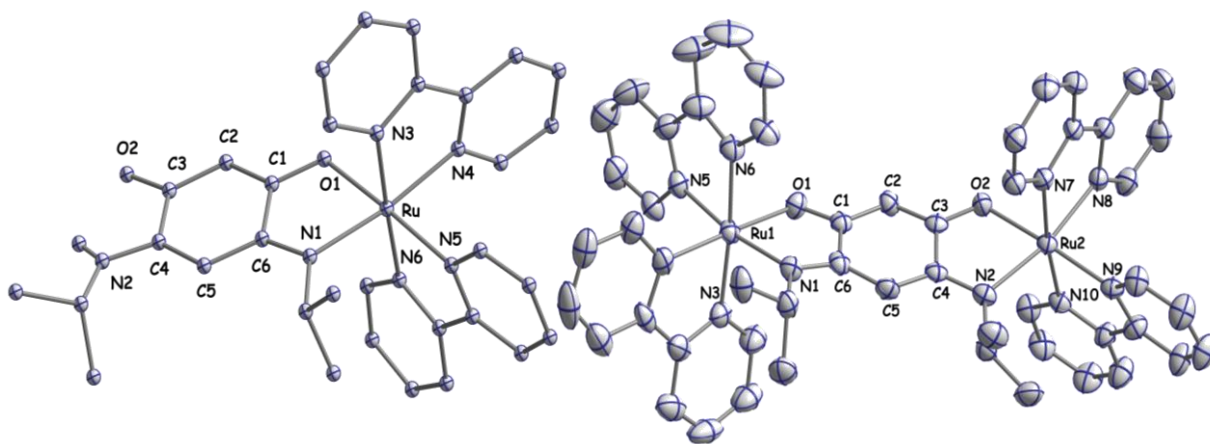


**Figure 11.2.** Molecular structure of the cations in  $[\text{Ru}^{\text{II}}(\text{bpy})_2(\text{L-H}^1)](\text{ClO}_4)$  (left) and *meso*- $[\{\text{Ru}^{\text{II}}(\text{bpy})_2\}_2(\mu\text{-L-2H}^1)](\text{ClO}_4)_2$  (right).

Both of the above complexes show redox rich chemistry. The dinuclear complex  $[\{\text{Ru}^{\text{II}}(\text{bpy})_2\}_2(\mu\text{-L-2H}^1)](\text{ClO}_4)_2$  shows two reversible oxidation and several reduction steps. The comproportionation constant  $K_c$  for the one-electron oxidized species  $[\{\text{Ru}(\text{bpy})_2\}_2(\mu\text{-L-2H}^1)]^{3+}$  is exceptionally large (order of  $10^{13}$ ). The large  $K_c$  value can be explained in terms of the delocalization of the quinonoid  $\pi$ -systems. Spectroelectrochemical oxidation of  $[\{\text{Ru}^{\text{II}}(\text{bpy})_2\}_2(\mu\text{-L-2H}^1)](\text{ClO}_4)_2$  generates a species with an EPR signal with  $g_{\text{av}} = 2.070$  and a small  $g$ -anisotropy of 0.135 (Figure 11.3 {right}). Such values are typical for a SOMO with mixed ruthenium quinone character. The emergence (on first oxidation) and subsequent disappearance (on second oxidation) of an intense broad NIR band at about  $1670\text{ cm}^{-1}$ , together with the EPR data strongly suggests a mixed-valent configuration (Figure 11.3 {left}). The experimental line-width of the IVCT band ( $\Delta\nu_{1/2}$ ) of about  $1670\text{ cm}^{-1}$  for the IVCT band at  $1560\text{ nm}$  is much smaller than that calculated using the Hush formula  $\Delta\nu_{1/2}(\text{calc}) = (2310\nu_{\text{IVCT}})^{1/2} \approx 3850\text{ cm}^{-1}$ . These results point to a valence averaged situation and hence the species  $[\{\text{Ru}(\text{bpy})_2\}_2(\mu\text{-L-2H}^1)]^{3+}$  belongs to the strongly coupled Class III mixed-valent systems. Similarly the EPR and UV-Vis-NIR results imply that the first reduction of  $[\{\text{Ru}^{\text{II}}(\text{bpy})_2\}_2(\mu\text{-L-2H}^1)](\text{ClO}_4)_2$  is bridging ligand centred as confirmed by the appearance of a quintet signal in EPR due to the presence of two equivalent  $^{14}\text{N}$  ( $I = 1/2$ ) nuclei in  $\text{L}^1$ . The redox potentials and metal-metal coupling of the quinonoid bridge dinuclear complex can be tuned remarkably by varying the R groups in  $\text{L}^1$ .

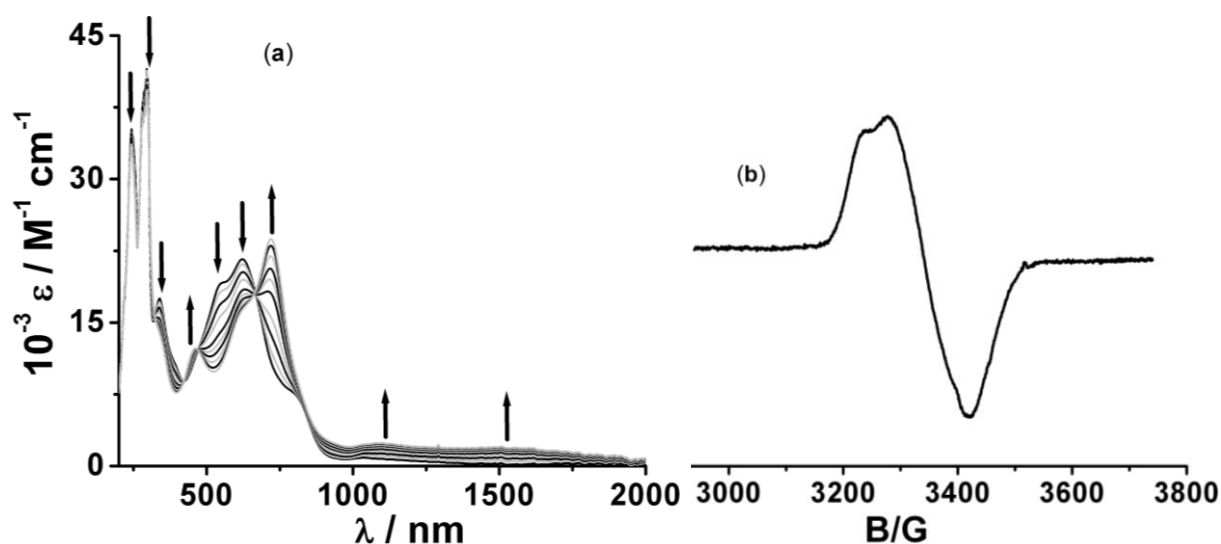
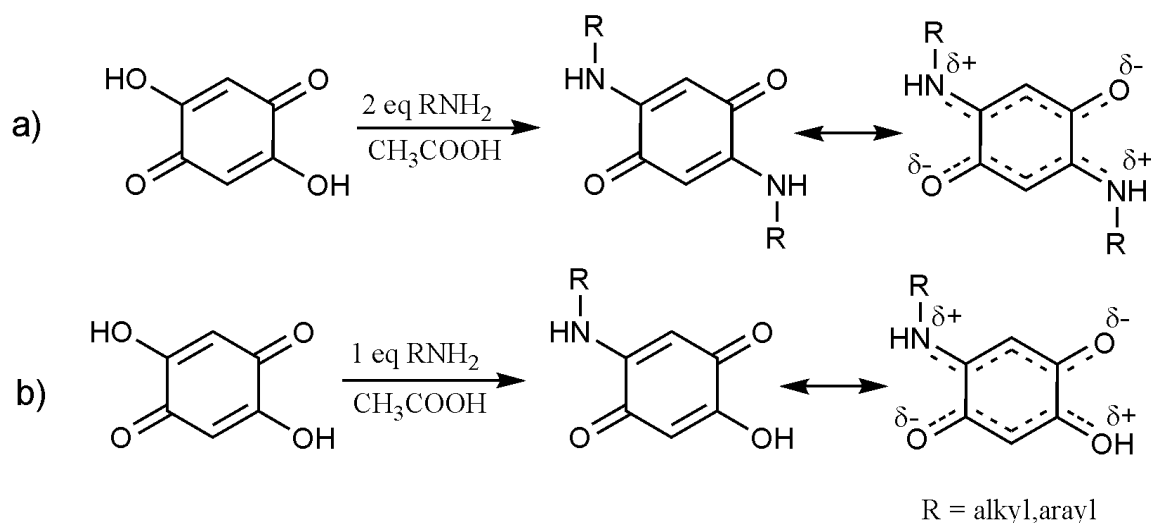
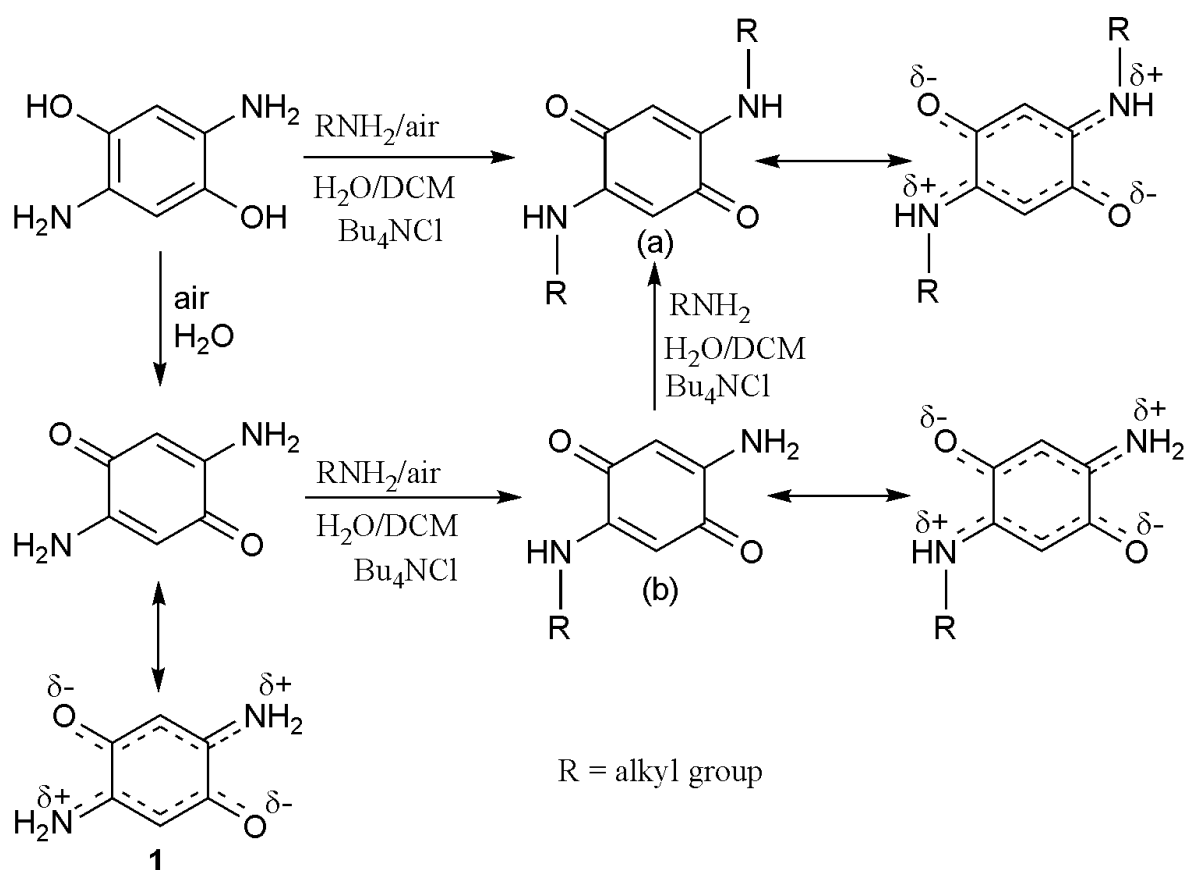


**Figure 11.3.** (a) UV/Vis/NIR-spectroelectrochemical changes of  $[\{\text{Ru}^{\text{II}}(\text{bpy})_2\}_2(\mu\text{-L-2H}^1)]^{2+}$  on oxidation in  $\text{CH}_3\text{CN}/0.1 \text{ M Bu}_4\text{NPF}_6$ , (b) EPR spectrum of electrogenerated  $[\{\text{Ru}(\text{bpy})_2\}_2(\mu\text{-L-2H})]^{3+}$  (a, 110 K).

Chapter 3 describes straightforward, one-pot and green synthesis of substituted *p*-quinone ligands and their use as bridging ligands for mono- and dinuclear polypyridyl ruthenium complexes. The replacement of ‘O’ atoms of 2,5-dihydroxy-1,4-benzoquinone *p*-[O,O,O,O] leads to symmetrically *p*-[O,N,O,N] ( $\text{L}^2$ ) and rare asymmetrically *p*-[O,N,O,O] ( $\text{L}^3$ ) *N*-substituted biologically relevant *p*-quinone ligands (Scheme 11.1). The one pot synthesis of *N*-substituted symmetric *p*-quinonoid ligands from 2,5-Diamino-1,4-benzoquinone and the isolation of a key intermediate of this reaction have also been reported (Scheme 11.2).



**Scheme 11.1.** One pot synthesis of symmetric (a) and asymmetric (b) quinonoid ligands.



**Scheme 11.2.** One pot synthesis of symmetric ligands (a) and its key intermediate (b).

The mono- and dinuclear complexes of symmetric *p*-[O,N,O,N] ( $\text{L}^2$ ) *N*-isopropyl substituted quinonoid ligand have been structurally characterized (Figure 11.4). From the X-ray crystal structure it is seen that the  $\pi$ -systems of bridging ligand in dinuclear complex  $[\{\text{Ru}^{\text{II}}(\text{bpy})_2\}_2(\mu\text{-L}_{-2\text{H}}^2)]^{2+}$  are localized and the double negative charge are localized more on oxygen atoms. Whereas the  $\pi$ -systems in mononuclear complex  $[\text{Ru}^{\text{II}}(\text{bpy})_2(\text{L}_{-\text{H}}^2)]^+$  are localized in such a way as to generate a phenolate and imminium part in the quinone ligand which is stabilized by strong hydrogen bond with an adjacent molecule (Figure 11.5 a).

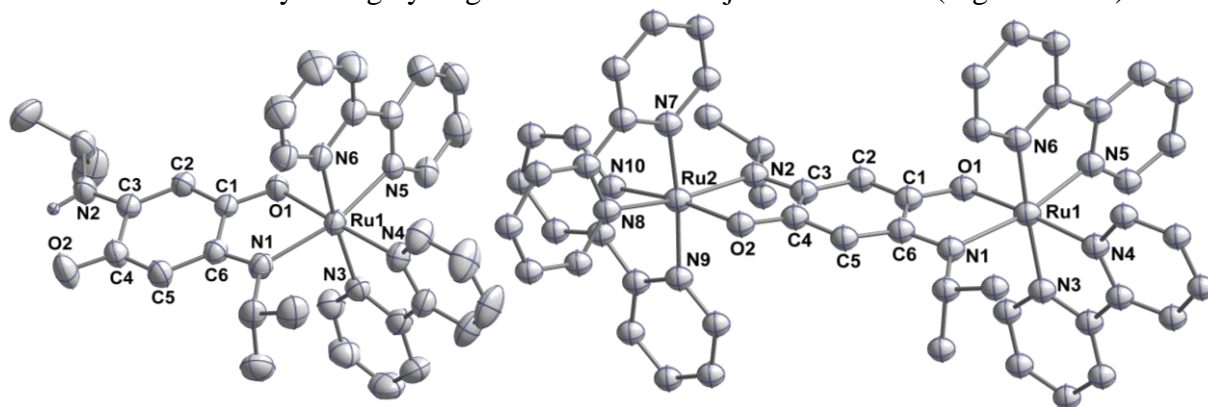


**Figure 11.4.** Molecular structure of the cations in  $[\text{Ru}^{\text{II}}(\text{bpy})_2(\text{L}_{-\text{H}}^2)](\text{ClO}_4)$  (left) and  $[\{\text{Ru}^{\text{II}}(\text{bpy})_2\}_2(\mu\text{-L}_{-2\text{H}}^2)](\text{ClO}_4)_2$  (right).

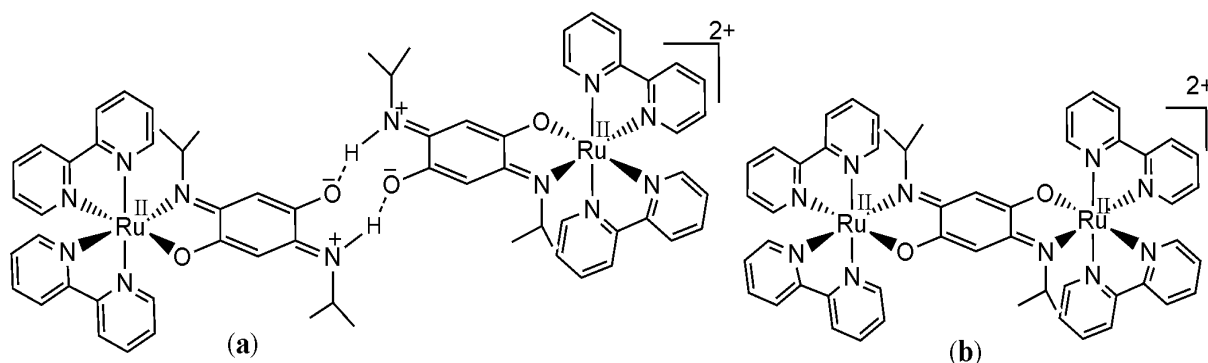


**Figure 11.5.** Molecular formula of the complexes  $[\text{Ru}^{\text{II}}(\text{bpy})_2(\text{L}\cdot\text{H})]^+$  with intermolecular H-bonding (a) and  $[\{\text{Ru}^{\text{II}}(\text{bpy})_2\}_2(\mu\text{-L}\cdot\text{2H})]^{2+}$  showing orientation of  $\pi$ -systems in coordinated quinonoid ligand.

The mono- and dinuclear complexes with symmetric *p*-[O,N,O,N] ( $\text{L}^2$ ) and asymmetric *p*-[O,N,O,O] ( $\text{L}^3$ ) *N*-substituted quinonoid ligands show redox rich chemistry like the complexes with zwitterionic *m*-[O,O,N,N] ( $\text{L}^1$ ) *N*-substituted ligands. The  $K_c$  of one electron oxidized species  $[\{\text{Ru}^{\text{II}}(\text{bpy})_2\}_2(\mu\text{-L}\cdot\text{2H}^2)]^{3+}$  and  $[\{\text{Ru}^{\text{II}}(\text{bpy})_2\}_2(\mu\text{-L}\cdot\text{2H}^3)]^{3+}$  with *N*-isopropyl substituted bridging ligands are of the order of  $10^8$  and  $10^9$  respectively which are less than the corresponding *m*-[O,O,N,N] *N*-substituted quinonoid bridge complex  $[\{\text{Ru}^{\text{II}}(\text{bpy})_2\}_2(\mu\text{-L}\cdot\text{2H}^1)]^{3+}$  ( $K_c = 10^{13}$ , Chapter 2). These effects can be explained by the localization of  $\pi$ -systems in the *para* form [O,N,O,N] and [O,O,O,N] of these ligands in their metal complexes vs. completely delocalized in the *meta* form [O,O,N,N] ligand in these complexes. The one electron oxidized form of the dinuclear complexes show properties that are typical of valence-averaged mixed-valent  $\text{Ru}^{2.5}\text{-Ru}^{2.5}$  species. The inter valence charge transfer (IVCT) band in the mixed-valent state can be tuned remarkably by the replacement of oxygen atoms in 2,5-dihydroxy-*p*-quinone with isoelectronic NR groups and also by changing the R groups (Figure 11.6.).

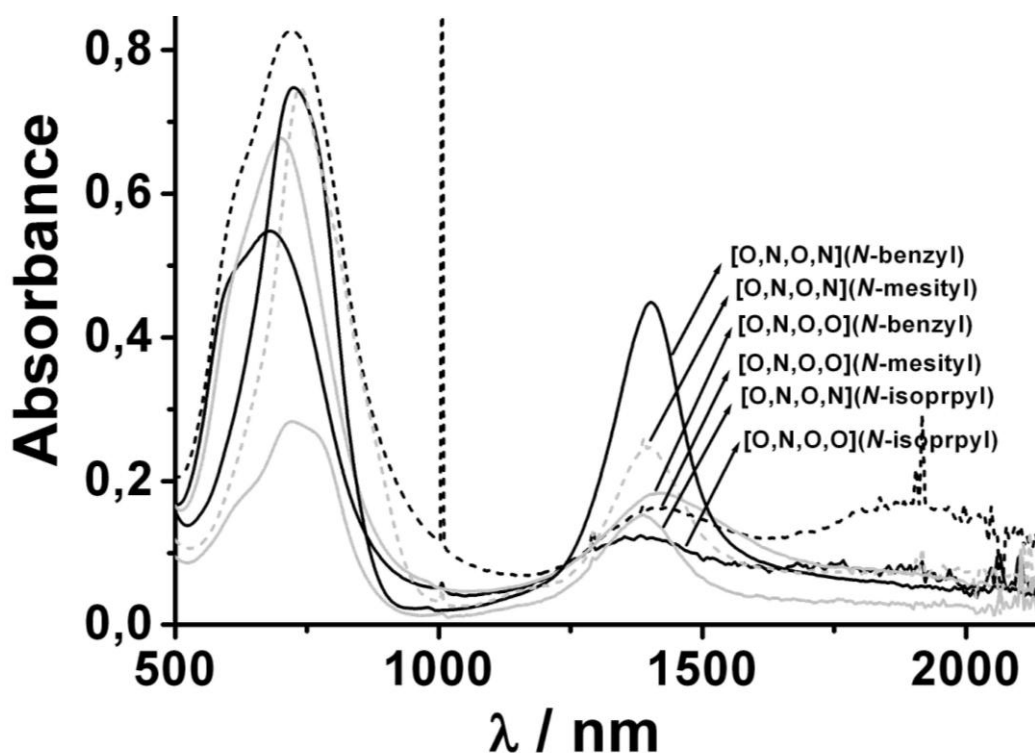


**Figure 11.6.** Change of NIR band on replacement of bridging ligands.

In chapter 4 quinonoid bridge symmetric dinuclear complexes of the type  $\{[(\text{acac})_2\text{Ru}^{\text{III}}]\}_2(\mu\text{-L}_{-2\text{H}})$  ( $\text{Ru}^{\text{III}}\text{-Ru}^{\text{III}}$ ) and rare asymmetric dinuclear mixed-valent complexes of the type  $[(\text{bpy})_2\text{Ru}^{\text{II}}(\mu\text{-L}_{-2\text{H}})\text{Ru}^{\text{III}}(\text{acac})_2]^+$  ( $\text{Ru}^{\text{II}}\text{-Ru}^{\text{III}}$ ) have been synthesized and the *m*-[O,O,N,N] ( $\text{L}_{-2\text{H}}^1$ ) vs. *p*-[O,N,O,N] ( $\text{L}_{-2\text{H}}^2$ ) bridges have been compared in terms of their electron transfer properties. The one-electron oxidation of the symmetric compounds ( $\text{Ru}^{\text{III}}\text{-Ru}^{\text{III}}$ ) leads to  $\text{Ru}^{\text{III}}\text{-Ru}^{\text{IV}}$  mixed-valent species and shows strong metal-metal IVCT transition in the NIR region, whereas reduction leads to a quinonoid radical bridge-containing  $\text{Ru}^{\text{III}}\text{-Ru}^{\text{III}}$  species. The native asymmetric mixed-valent  $\text{Ru}^{\text{III}}\text{-Ru}^{\text{II}}$  species does not show metal-metal IVCT transition in the NIR region. One-electron oxidation of the native asymmetric mixed-valent  $\text{Ru}^{\text{III}}\text{-Ru}^{\text{II}}$  complexes leads to quinonoid radical-containing  $\text{Ru}^{\text{III}}\text{-Ru}^{\text{II}}$  species while one electron reduction of these complexes leads to  $\text{Ru}^{\text{II}}\text{-Ru}^{\text{II}}$  species. The substitution of localized *p*-[O,N,O,N] quinonoid ligand by delocalized *m*-[O,O,N,N] quinonoid ligand in these complexes governed the redox properties, metal-metal coupling and charge distributions in different oxidation states substantially.

In chapter 5 the redox properties, structures and bonding of a new paramagnetic substitution series  $[\text{Ru}(\text{L}_{-2\text{H}}^1)_n(\text{acac})_{3-n}]$  (where  $n = 1\text{-}3$  and  $\text{L}_{-2\text{H}}^1 = N,N'$ -diisopropyl-*m*-[O,O,N,N] ligand) are described. The crystal structures of  $[\text{Ru}(\text{L}_{-2\text{H}}^1)(\text{acac})_2]$  and  $[\text{Ru}(\text{L}_{-2\text{H}}^1)_3]$  reveal the localization of the  $\pi$ -systems of the quinonoid ligand in the complexes (Figure 11.7). In



addition, intermolecular non-covalent interaction involving NH- of one moiety with carbonyl oxygen of another moiety leads to the formation of polymeric framework in the crystal packing of *mer*-[Ru(L-H<sup>1</sup>)<sub>3</sub>]. The metal-quinone distances of [Ru(L-H<sup>1</sup>)(acac)<sub>2</sub>] and [Ru(L-H<sup>1</sup>)<sub>3</sub>] are comparatively shorter than in the mono-nuclear complex [(bpy)<sub>2</sub>Ru<sup>II</sup>(L-H<sup>1</sup>)](ClO<sub>4</sub>) because of the oxidation state change from Ru<sup>II</sup> to Ru<sup>III</sup> in these complexes.

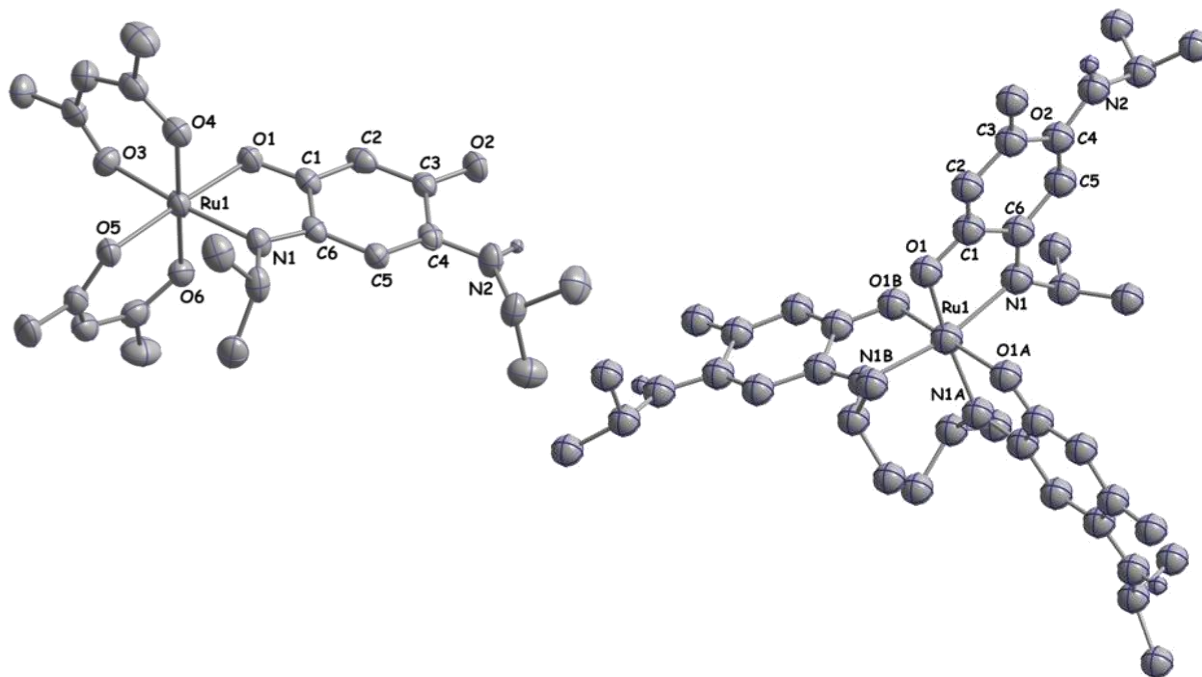


**Figure 11.7.** Molecular structure of the complex [Ru(L-H<sup>1</sup>)<sub>1</sub>(acac)<sub>2</sub>] (left) and *mer*-[Ru(L-H<sup>1</sup>)<sub>3</sub>] (right).

The oxidation state of ruthenium center in these complexes is +III as confirmed by the appearance of EPR signals typical of a low spin  $d^5$  centre at 110K with large (in the range of 1 to 1.5)  $g$  anisotropy. The complexes with two or three quinonoid ligands undergo one oxidation and several reduction processes. In contrast the other complexes in this series with one or without any quinonoid ligands show one oxidation and one reduction in the solvent window. One electron oxidation of the native complexes to [Ru(L-H<sup>1</sup>)<sub>2</sub>(acac)]<sup>+</sup> and [Ru(L-H<sup>1</sup>)<sub>3</sub>]<sup>+</sup> produces an intense broad absorption band in the NIR region (Figure 11.8). This charge transfer transition suggests ligand contribution at the singly occupied molecular orbital (SOMO). Thus, the one electron oxidation of [Ru(L-H<sup>1</sup>)<sub>2</sub>(acac)] and [Ru(L-H<sup>1</sup>)<sub>3</sub>] leads to ligand centred mixed-valent system. Moreover, one electron reduction of these complexes could be either Ru<sup>III</sup> centred or L-H centred. However L-H centred reduction normally occurs at higher potential than these observed here (chapter 2). Hence the first reduction steps are assigned to metal centred reduction of Ru<sup>III</sup> to Ru<sup>II</sup> which is confirmed by the results obtained from UV-Vis-NIR spectroscopy.

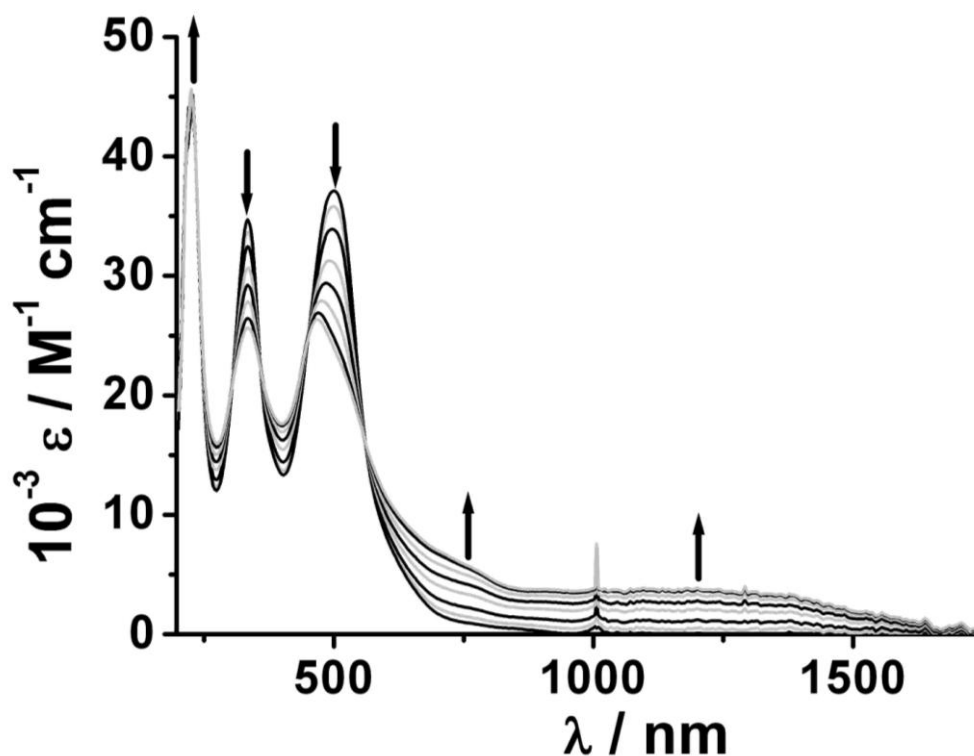


**Figure 11.8.** UV-Vis-NIR spectroelectrochemistry of the conversion of  $[\text{Ru}(\text{L-H}^1)_3]$  to  $[\text{Ru}(\text{L-H}^1)_3]^+$  in  $\text{CH}_2\text{Cl}_2 / 0.1 \text{ M Bu}_4\text{NPF}_6$ .

Chapter 6 describes the isomeric forms, structure, noncovalent interactions and charge distribution of mono-nuclear ruthenium systems of the form  $[(\text{bpy})\text{Ru}^{\text{II}}(\text{L-H})_2]$  ( $\text{L} = m$ -[O,O,N,N] ( $\text{L}^1$ ) and  $p$ -[O,N,O,N] ( $\text{L}^2$ )  $N$ -isopropyl substituted quinonoid ligands). In the crystal structure of  $[(\text{bpy})\text{Ru}^{\text{II}}(\text{L-H}^2)_2]$ , the two coordinated oxygen atoms are trans to each other (Figure 11.9). The  $\pi$ -systems of the quinonoid ligand are more delocalized than in the free ligand state thus leading to partial charge on the NH group and carbonyl oxygen in the metal free site. These charges are stabilized by strong intermolecular hydrogen bonds  $\{2.161 \text{ \AA} \ll 2.72 \text{ \AA}$  (sum of the van der waals radii of hydrogen and oxygen)}, thereby leading to the formation of extended 3-D frameworks (Figure 11.9). It is also observed that the vacant space in the crystal lattice has been occupied by several water molecules through hydrogen bonds. The complexes show one quasireversible oxidation and two reversible reductions. The EPR and UV/Vis/NIR spectroscopic results of one-electron oxidized and reduced species imply the oxidation is ruthenium centred ( $\text{Ru}^{\text{II}} \rightarrow \text{Ru}^{\text{III}}$ ) and the reduction is quinonoid centred ( $(\text{L-H}^2) \rightarrow (\text{L-H}^2)^-$ ).

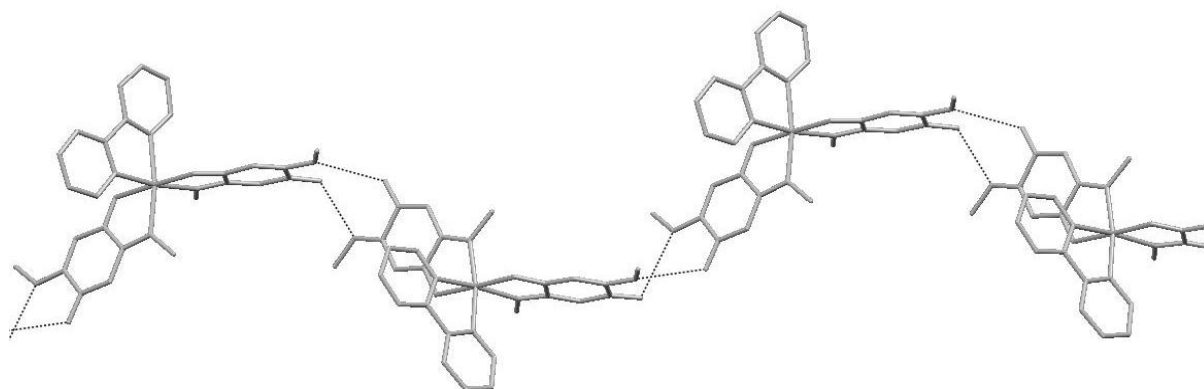


**Figure 11.9.** Intermolecular hydrogen bonding in the crystal structure of  $[(\text{bpy})\text{Ru}^{\text{II}}(\text{L}_2\text{H})_2]$ . The hydrogen atoms and the methyl carbon atoms are omitted for clarity.

Chapter 7 describes the syntheses of dinuclear ruthenium arene complexes with symmetric ( $\text{L}^2$ ) and asymmetric ( $\text{L}^3$ ) *p*-quinone ligands and unprecedented substituent induced reactivity. One of the dinuclear complexes of the form  $[\{\text{Cl}(\eta^6\text{-Cym})\text{Ru}\}_2(\mu\text{-L}_2\text{H})]$  (Cym = *p*-cymene) was structurally characterized and shows  $\eta^6$ -coordination mode of the arene ring (figure 11.10).

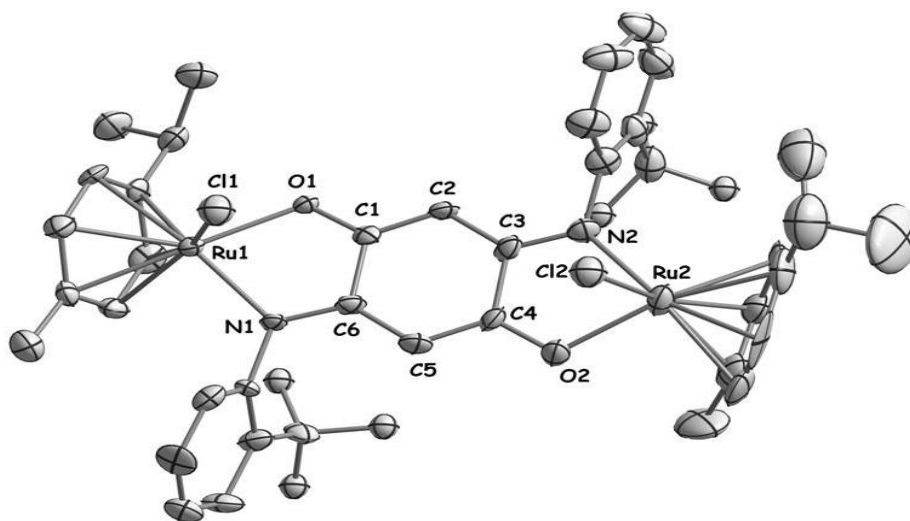
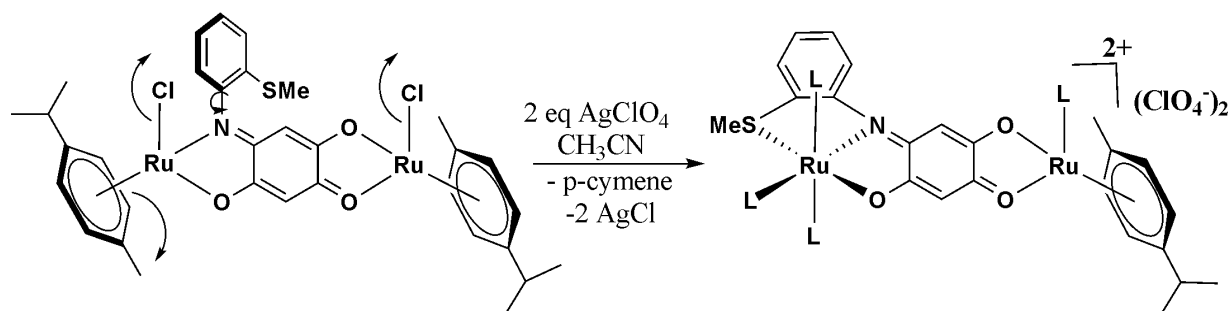


**Figure 11.10.** Molecular structure of the complex  $[\{\text{Cl}(\eta^6\text{-Cym})\text{Ru}\}_2(\mu\text{-L}_2\text{H})]$ .

Reactions of these complexes with  $\text{AgClO}_4$  led to normal chloride abstraction as expected whereas complexes with an additional -SMe group present at the bridging ligand ( $\text{L}^2$  and  $\text{L}^3$ ) led to unprecedented substituent induced *p*-Cym release (Scheme 11.3). The increase in the Lewis acidity at the metal center on chloride abstraction is mainly responsible for the coordination of the -SMe group, and the inability of the rigid bridging ligand to take up a facial coordination as demanded by a piano-stool configuration is suggested to induce *p*-Cym release.



**Scheme 11.3.** Chloride abstraction reaction led to release of cymene group.

Chapter 8 describes the synthesis, structural, electrochemical and spectroscopic properties of five component super redox-rich system  $[(Q)Ru(\mu-L)Ru(Q)]^n$  where  $Q^0$  is 4,6-di-*tert*-butyl-*N*-phenyl-*o*-iminobenzoquinone and  $L^{2-}$  is the doubly deprotonated form of 2,5-di-[2-(methylthio)-anilino]-1,4-benzoquinone. The available oxidation states are  $Q^{0,-,2-}$ ,  $Ru^{II,III,IV}$  and  $L^{0,-,2-,3-,4-}$ . The complex was synthesized from a dinuclear metal precursor of 2,5-di-[2-(methylthio)-anilino]-1,4-benzoquinone  $[(MeCN)_3Ru(\mu-L)Ru(MeCN)_3]^{2+}$ , obtained from the above reaction (Scheme 11.3) and shows eight reversible one-electron transfer steps between  $n = (+4)$  to  $(-4)$  which have been investigated by cyclic voltammetry (Figure 11.12), UV-vis-NIR and EPR spectroelectrochemistry for the structurally characterized  $[(Q)Ru(\mu-L)Ru(Q)](ClO_4)_2$ ,  $M(ClO_4)_2$  (Figure 11.11). These combined studies revealed that  $M(ClO_4)_2$  is best described as  $[(Q)^-Ru^{III}(\mu-L)^{2-}Ru^{III}(Q)^-](ClO_4)_2$  with antiferromagnetic coupling between  $Q^-$  and  $Ru^{III}$  spins at each end.

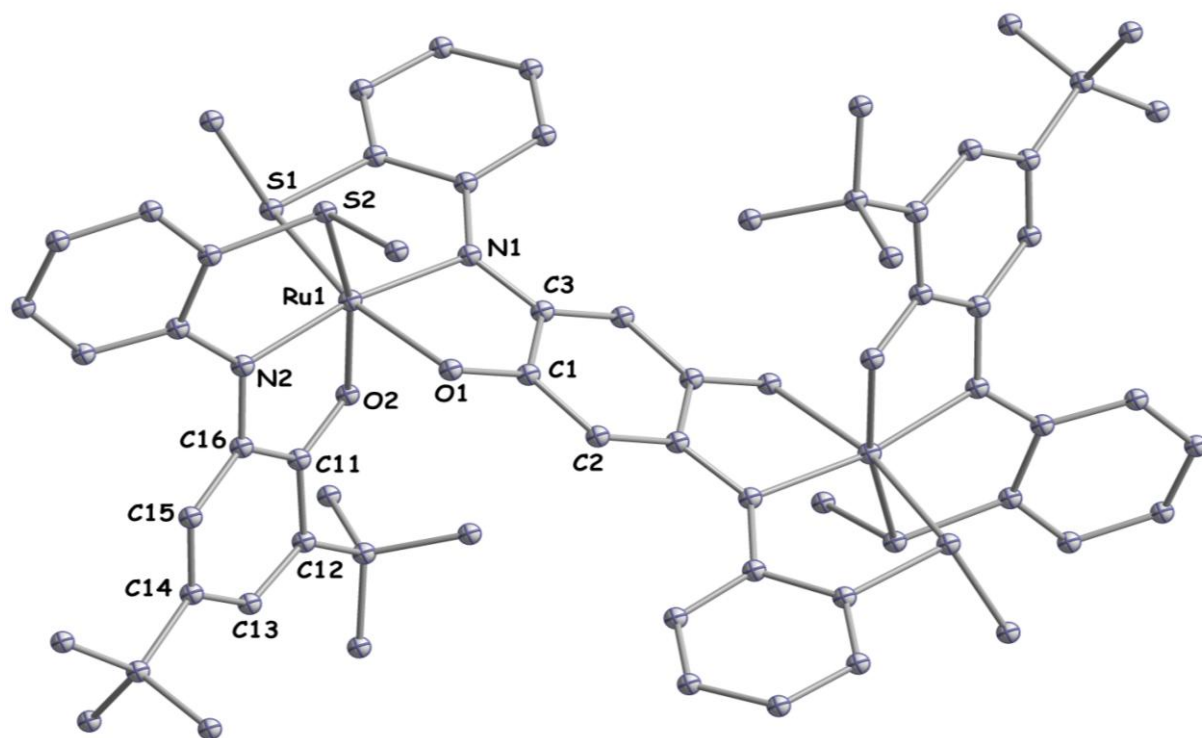


**Figure 11.11.** Molecular structure of the dication in the crystal of  $[(Q)Ru(\mu-L)Ru(Q)](ClO_4)_2$ .

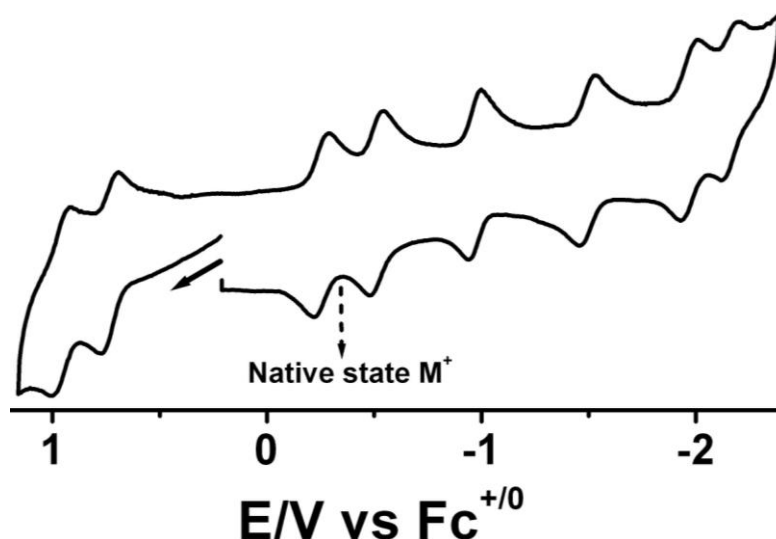


**Figure 11.12.** Cyclic voltammogram of  $(Q)Ru(\mu-L)Ru(Q)](ClO_4)$  in  $CH_3CN/0.1\text{ m } Bu_4NPF_6$  at 295 K.

The last chapter 9 describes the requirement of electron rich ruthenium centre to make stable complex with the noninnocent *N*-(2-methyl-5,8-dioxo-5,8-dihydroquinolin-7-yl)acetamide ligand ( $L^5$ ). A ruthenium complex of  $L^5$  with strong  $\sigma$ -donating  $acac^-$  ligand  $[Ru^{II}(acac)_2L^5]$  has been synthesized and isolated in the diamagnetic form for the investigation of  $d\pi(Ru)-p\pi^*(L^5)$  mixing in the accessible redox states. The complex with  $L^5$  shows strong  $d\pi(Ru)-p\pi^*(L^5)$  mixing that leads to a mixed type of valence situation in the redox states pointing to the importance of covalency in metal complexes of ruthenium. Such mixing has great importance in the field of water oxidation and stabilization of metal coordinated reactive radicals.

## KAPITEL 11

### Zusammenfassung

Redoxaktive chinoider Liganden und deren Metallkomplexe gewinnen zusehends an Aufmerksamkeit aufgrund ihrer umfangreichen Wichtigkeit in Anorganischer, Organischer, Physikalischer und sogar Biochemie. In dieser Doktorarbeit wurden strukturelle und elektronische Eigenschaften von ein- und zweikernigen Rutheniumkomplexen mit 'nicht-unschuldigen' chinoiden Brückenliganden untersucht. Zusätzlich deckt diese Arbeit die direkte, 'grüne' Eintopfreaktion von symmetrisch und seltenen asymmetrisch substituierten, biologisch relevanten *p*-Chinon-Liganden mit unterschiedlicher Sterik und elektronischen Eigenschaften ab.

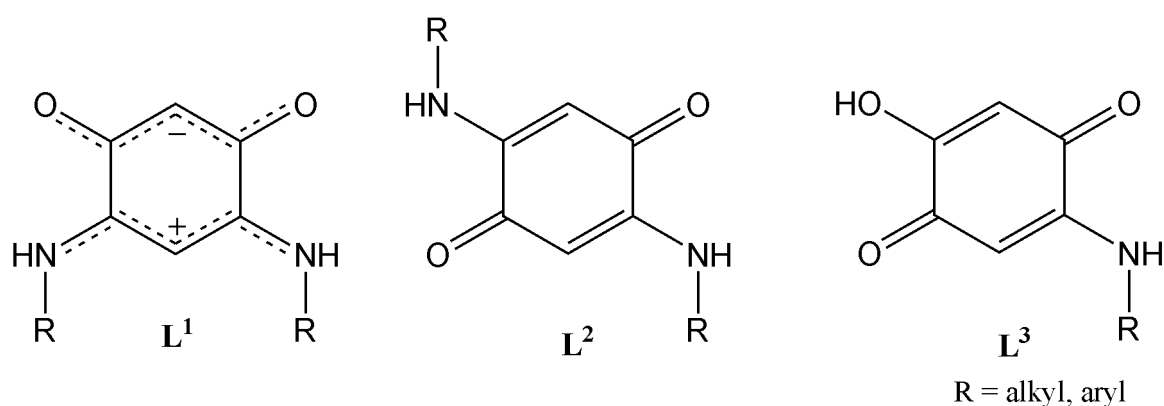


**Abbildung 11.1:** Molekülstrukturen von *N*-substituierten sym. *m*-[O,O,N,N]-zwitterionischen (L<sup>1</sup>), sym. *p*-[O,N,O,N] (L<sup>2</sup>) und asym. *p*-[O,O,O,N] (L<sup>3</sup>) chinoider Liganden.

Die Eigenschaften dieser symmetrischen und asymmetrischen Ligandensysteme (L<sup>1</sup>, L<sup>2</sup> und L<sup>3</sup>), wie Elektronenübertragung, Strukturen, Bindung und Delokalisierung der  $\pi$ -Systeme, wurden untersucht in Form ihrer Ein- und Zweikernmetallkomplexe.

Kapitel 2 beschreibt die strukturellen, elektrochemischen und spektroskopischen Eigenschaften ein- und zweikerniger Rutheniumbipyridin-Komplexe mit *N*-substituiertem *m*-[O,O,N,N] zwitterionischem Liganden (L<sup>1</sup>). Der Einkernkomplex [Ru<sup>II</sup>(bpy)<sub>2</sub>(L<sub>H</sub><sup>1</sup>)](ClO<sub>4</sub>) und die Zweikernkomplexe [{Ru<sup>II</sup>(bpy)<sub>2</sub>]<sub>2</sub>( $\mu$ -L<sub>2H</sub><sup>1</sup>)](ClO<sub>4</sub>)<sub>2</sub> wurden strukturell charakterisiert (Abbildung 11.2). Die Kristallstrukturanalyse beweist, dass sukzessive Metallierung des zwitterionischen Liganden L<sup>1</sup> zuerst zu einer Lokalisierung des  $\pi$ -Systems im Einkernkomplex [Ru<sup>II</sup>(bpy)<sub>2</sub>(L<sub>H</sub><sup>1</sup>)](ClO<sub>4</sub>) und weiterhin wiederum zur Delokalisierung im Zweikernkomplex [{Ru<sup>II</sup>(bpy)<sub>2</sub>]<sub>2</sub>( $\mu$ -L<sub>2H</sub><sup>1</sup>)](ClO<sub>4</sub>)<sub>2</sub> führt.

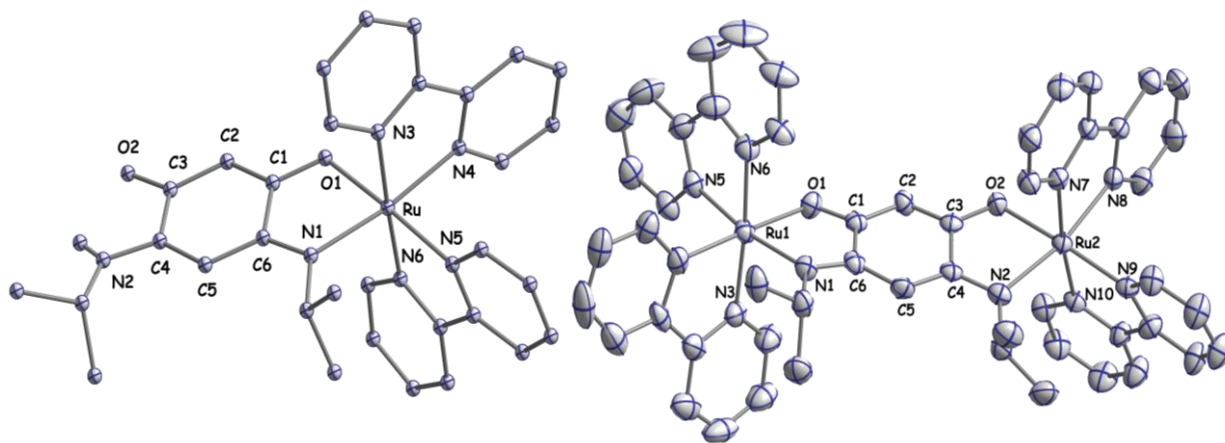


**Abbildung 11.2.** Molekülstruktur der Kationen von  $[\text{Ru}^{\text{II}}(\text{bpy})_2(\text{L-H}^1)](\text{ClO}_4)$  (links) und  $\text{meso}-[[\text{Ru}^{\text{II}}(\text{bpy})_2]_2(\mu\text{-L-2H}^1)](\text{ClO}_4)_2$  (rechts).

Beide der oben dargestellten Komplexe zeigen 'redoxreiche' Chemie. Der Zweikernkomplex  $[[\text{Ru}^{\text{II}}(\text{bpy})_2]_2(\mu\text{-L-2H}^1)](\text{ClO}_4)_2$  zeigt zwei reversible Oxidationen und zahlreiche Reduktionsschritte. Die Komproportionierungskonstante  $K_c$  der einfach oxidierten Spezies  $[[\text{Ru}(\text{bpy})_2]_2(\mu\text{-L-2H}^1)]^{3+}$  ist außergewöhnlich hoch (Größenordnung  $10^{13}$ ). Der große  $K_c$ -Wert kann hinsichtlich der Delokalisierung des chinoiden  $\pi$ -Systems erklärt werden. Spektroelektrochemische Oxidation von  $[[\text{Ru}^{\text{II}}(\text{bpy})_2]_2(\mu\text{-L-2H}^1)](\text{ClO}_4)_2$  erzeugt eine Spezies mit einem EPR-Signal von  $g_{\text{av}} = 2.070$  und einer kleinen  $g$ -Anisotropie von 0.135 (Abbildung 11.3 {rechts}). Solche Werte sind typisch für ein SOMO mit gemischtem Ruthenium Chinin Charakter. Das Auftauchen (während der ersten Oxidation) und anschließendem Verschwinden (während der zweiten Oxidation) einer intensiv breiten NIR-Bande bei ungefähr  $1670 \text{ cm}^{-1}$ , zusammen mit den EPR-Daten, lässt stark auf eine gemischtvalente Konfiguration (Abbildung 11.3 {links}) schließen. Die experimentelle Linienbreite der IVCT-Bande ( $\Delta\nu_{1/2}$ ) von ca.  $1670 \text{ cm}^{-1}$  für die IVCT-Bande von  $1560 \text{ nm}$  ist viel kleiner als die mit der Hush-Formel  $\Delta\nu_{1/2}(\text{calc}) = (2310\nu_{\text{IVCT}})^{1/2} \approx 3850 \text{ cm}^{-1}$  berechnete. Diese Ergebnisse deuten auf eine gemittelte Valenzsituation hin und demzufolge gehört die Spezies  $[[\text{Ru}(\text{bpy})_2]_2(\mu\text{-L-2H}^1)]^{3+}$  zur stark gekoppelten Klasse III gemischtvalenter Systeme. Gleichermassen implizieren die EPR- und UV-Vis-NIR-Ergebnisse, dass die erste Reduktion von  $[[\text{Ru}^{\text{II}}(\text{bpy})_2]_2(\mu\text{-L-2H}^1)](\text{ClO}_4)_2$  Brückenligand-zentriert ist, was durch das Auftreten eines Quintett-Signals in EPR aufgrund des Vorhandenseins zweier äquivalenter  $^{14}\text{N}$  ( $I = 1/2$ ) Kerne in  $\text{L}^1$  bewiesen wird. Die Redoxpotentiale und die Metall-Metall-Kopplung des chinoid verbrückten Zweikernkomplexes können außergewöhnlich abgestimmt werden durch die Variation der R-Gruppen in  $\text{L}^1$ .

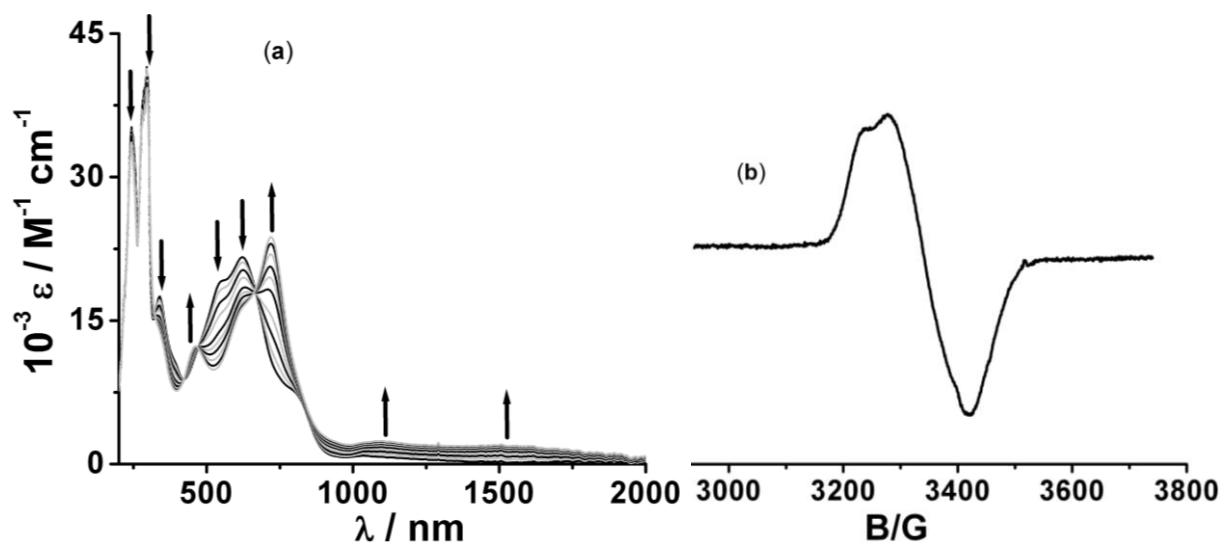
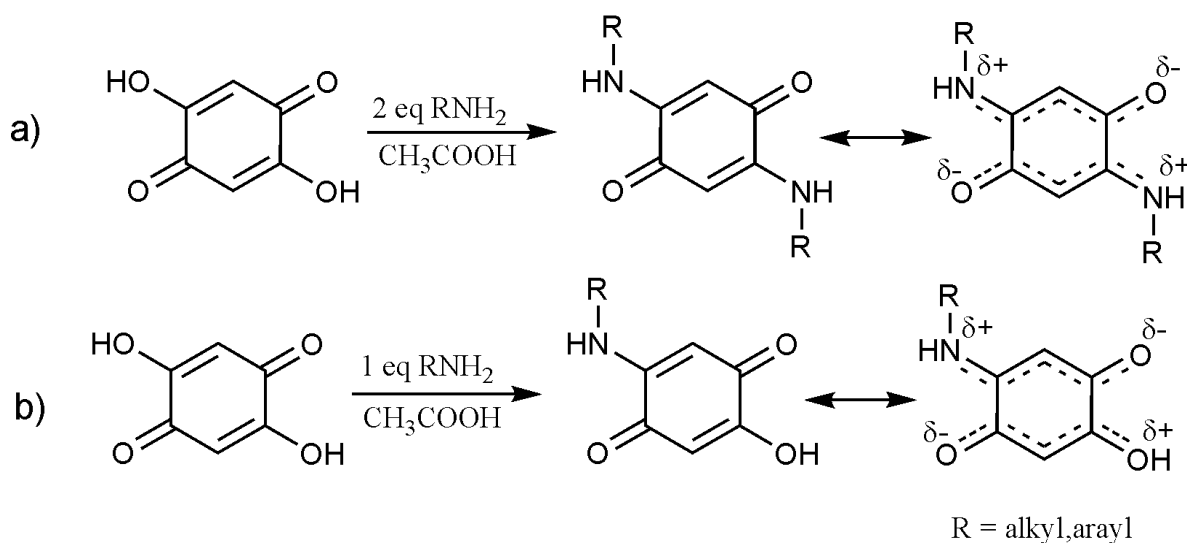


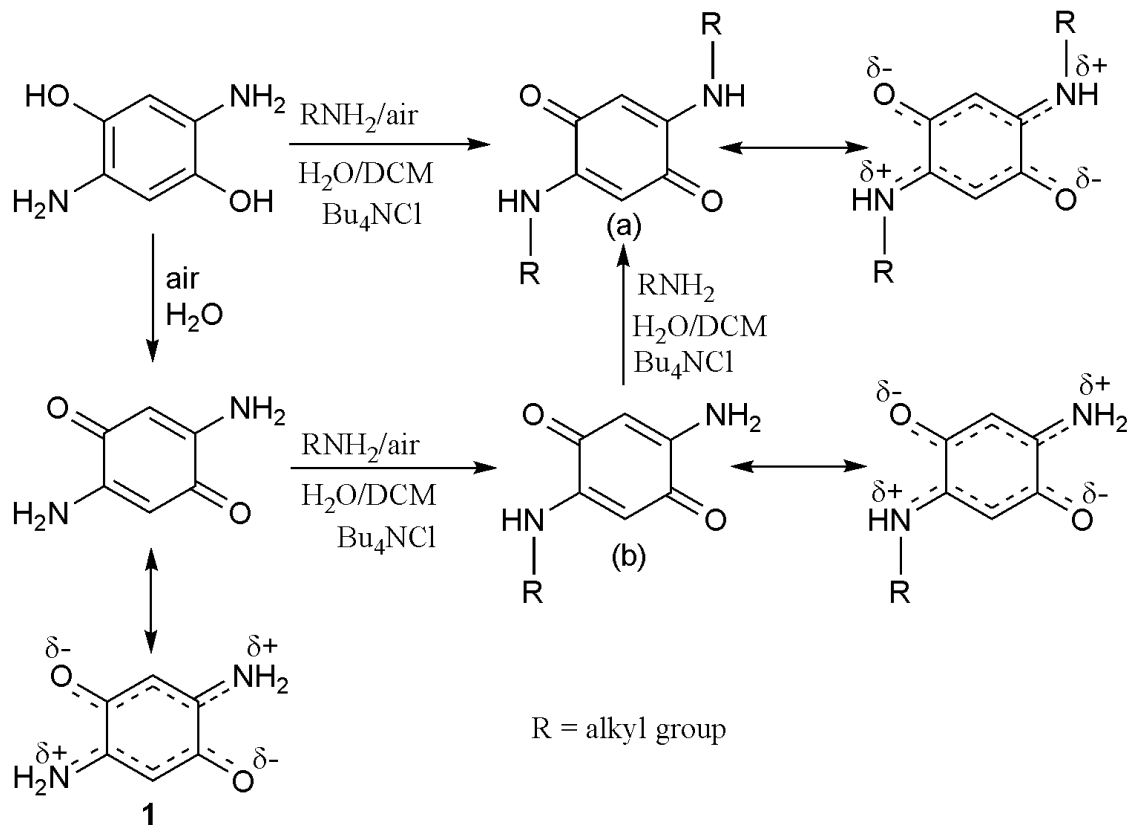
**Abbildung 11.3.** (a) UV/Vis/NIR-spektroelektrochemische Veränderungen von  $[\{\text{Ru}^{\text{II}}(\text{bpy})_2\}_2(\mu\text{-L-2H}^1)]^{2+}$  während Oxidation in  $\text{CH}_3\text{CN}/0.1 \text{ M Bu}_4\text{NPF}_6$ , (b) EPR-Spektrum von elektrochemisch erzeugtem  $[\{\text{Ru}(\text{bpy})_2\}_2(\mu\text{-L-2H})]^{3+}$  (a, 110 K).

Kapitel 3 beschreibt die direkte, 'grüne' Eintopfreaktion von substituierten *p*-Chinon-Liganden und ihre Verwendung als Brückenligand für ein- und zweikernige Polypyridylrutheniumkomplexe. Das Ersetzen von 'O'-Atomen bei 2,5-Dihydroxy-1,4-benzochinon *p*-[O,O,O,O] führt zu symmetrischen *p*-[O,N,O,N] ( $\text{L}^2$ ) und seltenen asymmetrischen *p*-[O,N,O,O] ( $\text{L}^3$ ) *N*-substituierten biologisch relevanten *p*-chinoiden Liganden (Schema 11.1). Die Eintopfreaktion von *N*-substituierten symmetrischen *p*-chinoiden aus 2,5-Diamino-1,4-benzochinon und von der Isolierung eines Schlüsselintermediates dieser Reaktion wurde ebenfalls berichtet (Schema 11.2).



**Schema 11.1.** Eintopfreaktion von symmetrischen (a) und asymmetrischen (b) chinoider Liganden.





**Schema 11.2.** Einpottreaktion symmetrischer Liganden (a) und dessen Schlüsselintermediat (b).

Die Ein- und Zweikernkomplexe der symmetrisch  $p$ -[O,N,O,N] ( $\text{L}^2$ )  $N$ -Isopropyl substituierten chinoiden Liganden wurden strukturell charakterisiert (Abbildung 11.4). Anhand der Röntgenstruktur kann man erkennen, dass die  $\pi$ -Systeme des Brückenliganden im Zweikernkomplex  $[\{\text{Ru}^{\text{II}}(\text{bpy})_2\}_2(\mu\text{-L-2H}^2)]^{2+}$  lokalisiert sind und die zweifach negative Ladung mehr an den Sauerstoffatomen lokalisiert sind. Wohingegen die  $\pi$ -Systeme im Einkernkomplex  $[\text{Ru}^{\text{II}}(\text{bpy})_2(\text{L-H}^2)]^+$  in solch einem Weg lokalisiert sind, dass ein Phenolat und Imminium Teil im Chinon-Liganden generiert wird, der stabilisiert wird durch starke Wasserstoffbindungen zum benachbarten Molekül (Abbildung 11.5 a).

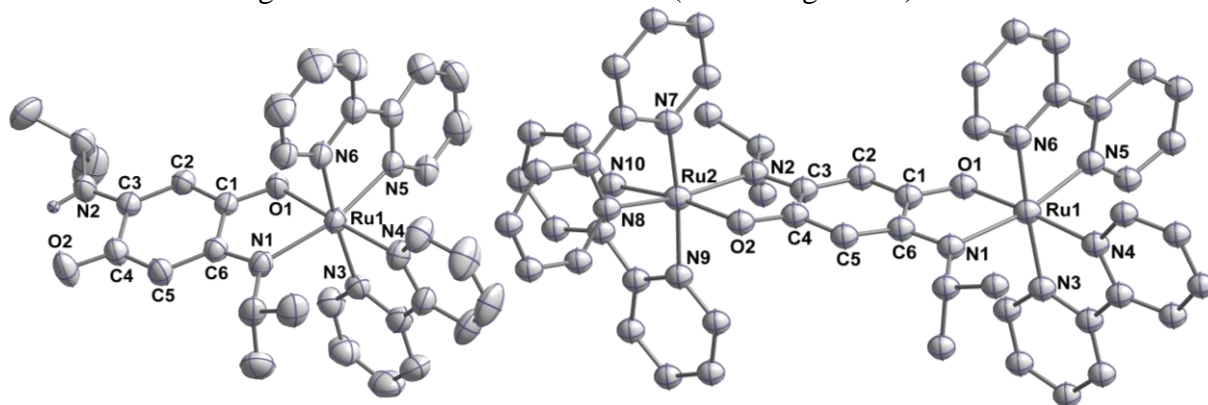


**Abbildung 11.4.** Molekülstruktur der Kationen von  $[\text{Ru}^{\text{II}}(\text{bpy})_2(\text{L-H})](\text{ClO}_4)$  (links) und  $[\{\text{Ru}^{\text{II}}(\text{bpy})_2\}_2(\mu\text{-L-2H})](\text{ClO}_4)_2$  (rechts).

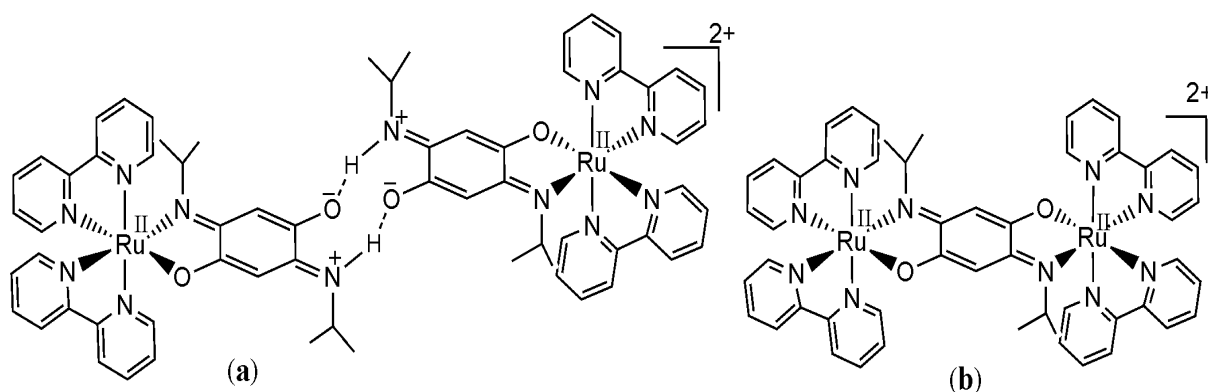


**Abbildung 11.5.** Molekülformel der Komplexe  $[\text{Ru}^{\text{II}}(\text{bpy})_2(\text{L-H}^2)]^+$  mit intermolekularer H-Bindung (a) und  $[\{\text{Ru}^{\text{II}}(\text{bpy})_2\}_2(\mu\text{-L-2H}^2)]^{2+}$  der die Orientierung der  $\pi$ -Systeme im koordinierten chinonoiden Liganden zeigt.

Die Ein- und Zweikernkomplexe mit symmetrischen  $p$ -[O,N,O,N] ( $\text{L}^2$ ) und asymmetrischen  $p$ -[O,N,O,O] ( $\text{L}^3$ )  $N$ -substituierten chinonoiden Liganden zeigen 'redoxreiche' Chemie wie die Komplexe mit zwitterionischen  $m$ -[O,O,N,N] ( $\text{L}^1$ )  $N$ -substituierten Liganden. Die  $K_c$ -Werte der monooxidierten Spezies  $[\{\text{Ru}^{\text{II}}(\text{bpy})_2\}_2(\mu\text{-L-2H}^2)]^{3+}$  und  $[\{\text{Ru}^{\text{II}}(\text{bpy})_2\}_2(\mu\text{-L-2H}^3)]^{3+}$  mit  $N$ -Isopropyl substituierten Brückenliganden haben eine Größe von  $10^8$  bzw.  $10^9$ , welche kleiner sind als die des entsprechenden  $m$ -[O,O,N,N]  $N$ -substituierten chinonoiden Brückenkomplexes  $[\{\text{Ru}^{\text{II}}(\text{bpy})_2\}_2(\mu\text{-L-2H}^1)]^{3+}$  ( $K_c = 10^{13}$ , Kapitel 2). Diese Effekte können durch die Lokalisierung des  $\pi$ -Systems in der *para*-Form [O,N,O,N] und [O,O,O,N] dieser Liganden in ihren Metallkomplexen im Gegensatz zu komplett delokalisiert in den *meta*-Form [O,O,N,N]-Liganden in diesen Komplexen. Die monooxidierete Form der Zweikernkomplexe zeigen Eigenschaften, die typisch sind für Valenz-gemittelte gemischtvalente  $\text{Ru}^{2.5}\text{-Ru}^{2.5}$ -Spezies. Die IVCT-Bande im gemischtvalenten Zustand kann bemerkenswert verändert werden durch Ersetzen der Sauerstoffatome in 2,5-Dihydroxy-*p*-chinon mit isoelektronischer NR-Gruppen und zusätzlich durch Änderung der R-Gruppen (Abbildung 11.6.).

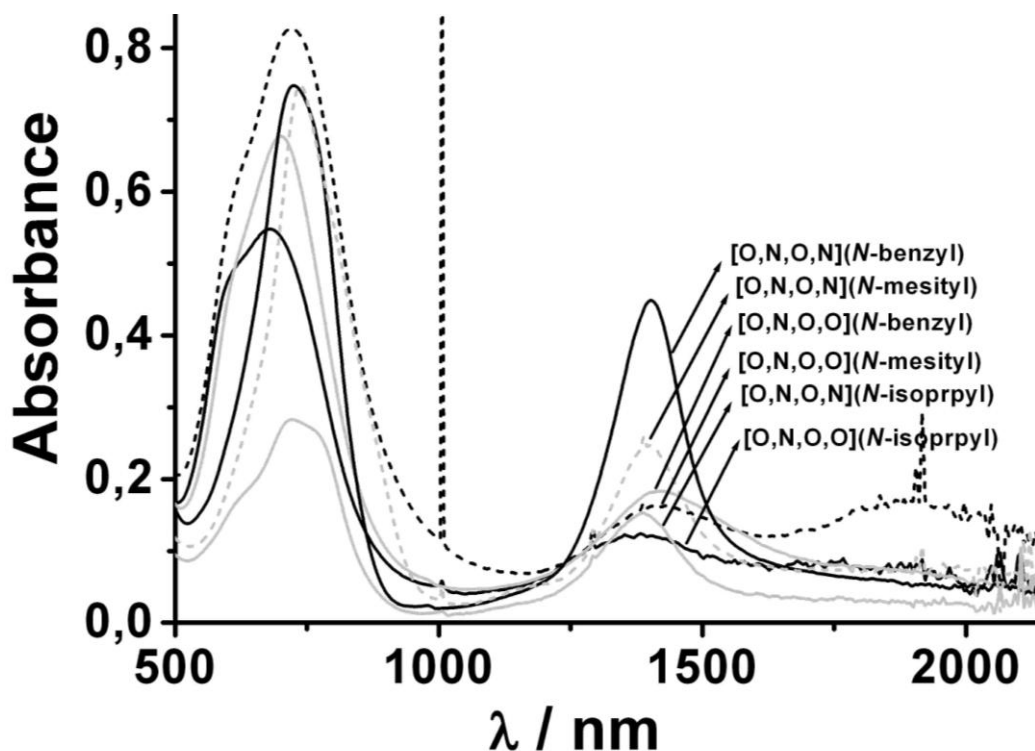


**Abbildung 11.6.** Veränderung der NIR-Bande durch Veränderung des Brückenligandes.

In Kapitel 4 wurden Zweikernkomplexe mit chinoiden symmetrischen Brückenliganden der Form  $[(\text{acac})_2\text{Ru}^{\text{III}}]_2(\mu\text{-L}_{-2\text{H}})$  ( $\text{Ru}^{\text{III}}\text{-Ru}^{\text{III}}$ ), sowie seltene asymmetrische Zweikern-gemischivalente Komplexe des Typs  $[(\text{bpy})_2\text{Ru}^{\text{II}}(\mu\text{-L}_{-2\text{H}})\text{Ru}^{\text{III}}(\text{acac})_2]^+$  ( $\text{Ru}^{\text{II}}\text{-Ru}^{\text{III}}$ ) synthetisiert und  $m\text{-[O,O,N,N]}$  ( $\text{L}_{-2\text{H}}^1$ ) im Gegensatz zu  $p\text{-[O,N,O,N]}$  ( $\text{L}_{-2\text{H}}^2$ )-Brücken verglichen hinsichtlich ihrer Elektronenübertragungseigenschaften. Einelektronenoxidation der symmetrischen Verbindung ( $\text{Ru}^{\text{III}}\text{-Ru}^{\text{III}}$ ) führt zu  $\text{Ru}^{\text{III}}\text{-Ru}^{\text{IV}}$  gemischvalenter Spezies und zeigt starke Metall-Metall IVCT-Übergänge in der NIR-Region, wohingegen Reduktion zu einer chinoiden, Radikal-Brücke beinhaltenden  $\text{Ru}^{\text{III}}\text{-Ru}^{\text{III}}$ -Spezies führt. Der ursprünglich asymmetrisch gemischvalente  $\text{Ru}^{\text{III}}\text{-Ru}^{\text{II}}$ -Spezies zeigt keine Metall-Metall-IVCT-Übergänge in NIR-Region. Einelektronenoxidation der ursprünglich asymmetrisch gemischvalenten  $\text{Ru}^{\text{III}}\text{-Ru}^{\text{II}}$ -Spezies führt zu chinoiden-Radikal-enthaltenden  $\text{Ru}^{\text{III}}\text{-Ru}^{\text{II}}$ -Spezies während Einelektronenreduktion dieser Komplexe zu  $\text{Ru}^{\text{II}}\text{-Ru}^{\text{II}}$ -Spezies führt. Die Substitution von lokalisierten  $p\text{-[O,N,O,N]}$  chinoider Liganden durch delokalisierte  $m\text{-[O,O,N,N]}$  chinoider Liganden in diesen Komplexen steuert die Redoxseigenschaften, Metall-Metall-Wechselwirkungen und Ladungsverteilung in verschiedenen Oxidationszuständen maßgeblich.

In Kapitel 5 sind Redox Eigenschaften, Strukturen und Bindungsverhältnisse einer neuen paramagnetischen Substitutionsreihe  $[\text{Ru}(\text{L}_\text{H}^1)_n(\text{acac})_{3-n}]$  (mit  $n = 1-3$  und  $\text{L}_\text{H}^1 = N,N'$ -Diisopropyl-*m*-[O,O,N,N Ligand]) beschrieben. Die Kristallstrukturen von  $[\text{Ru}(\text{L}_\text{H}^1)(\text{acac})_2]$  und  $[\text{Ru}(\text{L}_\text{H}^1)_3]$  verdeutlichen die Lokalisierung des  $\pi$ -Systems des chinoiden Liganden in den Komplexen (Abbildung 11.7). Zusätzlich dazu führen intermolekulare nicht-kovalente Wechselwirkungen zwischen NH- des einen Teils mit dem Carbonyl-Sauerstoff des anderen Teils zur Bildung eines polymeren Gerüsts in der Kristallpackung von *mer*- $[\text{Ru}(\text{L}_\text{H}^1)_3]$ . Die Metall-Chinon-Abstände von  $[\text{Ru}(\text{L}_\text{H}^1)(\text{acac})_2]$  und  $[\text{Ru}(\text{L}_\text{H}^1)_3]$  sind vergleichsweise kürzer als im Einkernkomplex  $[(\text{bpy})_2\text{Ru}^{\text{II}}(\text{L}_\text{H}^1)](\text{ClO}_4)$  aufgrund des Oxidationsstufenwechsels von  $\text{Ru}^{\text{II}}$  zu  $\text{Ru}^{\text{III}}$  in diesen Komplexen.

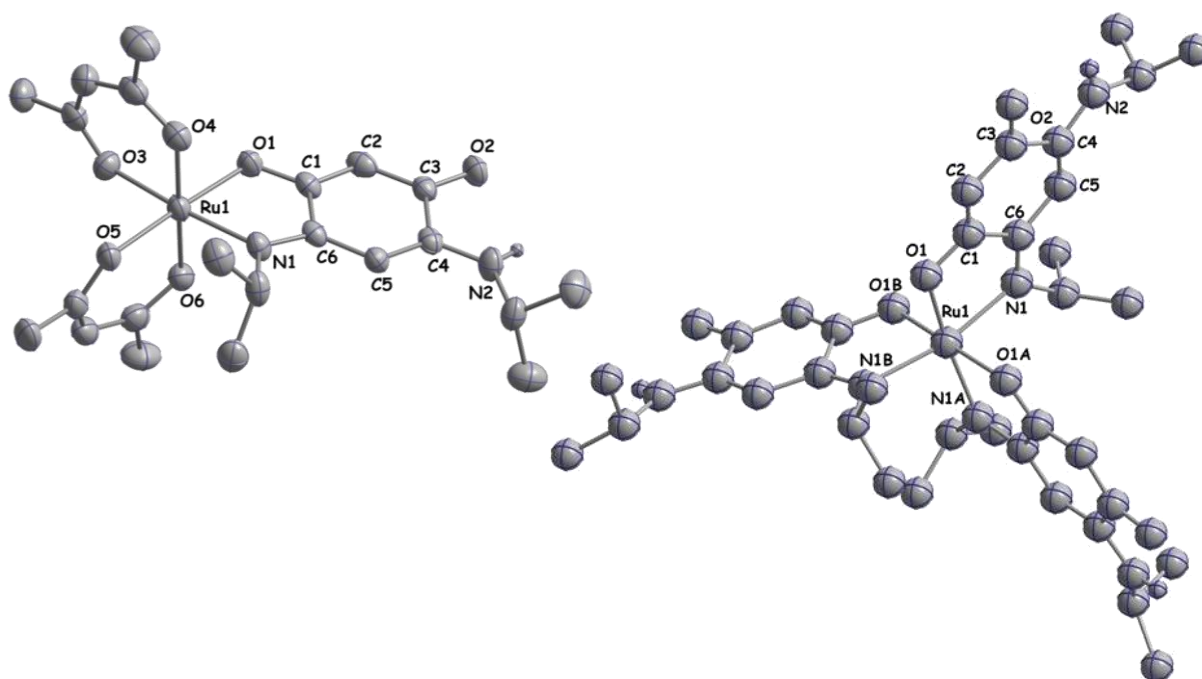


**Abbildung 11.7.** Molekülstruktur des Komplexes  $[\text{Ru}(\text{L}_\text{H}^1)_1(\text{acac})_2]$  (links) und *mer*- $[\text{Ru}(\text{L}_\text{H}^1)_3]$  (rechts).

Die Oxidationsstufe des Rutheniumzentrums in diesen Komplexen ist +III, wie durch das Auftreten eines typischen EPR-Signals für low-spin  $d^5$ -Zentren bei 110 K mit hoher (im Bereich von 1 bis 1.5) g-Anisotropie bewiesen wurde. Die Komplexe mit zwei oder drei chinoiden Liganden lassen sich einmal oxidieren und mehrfach reduzieren. Im Gegensatz dazu weisen die anderen Komplexe dieser Serie mit einem oder keinem chinoiden Liganden eine Oxidation und eine Reduktion im Lösungsmittelfenster auf. Einelektronenoxidation der Komplexe zu  $[\text{Ru}(\text{L}_\text{H}^1)_2(\text{acac})]^+$  und  $[\text{Ru}(\text{L}_\text{H}^1)_3]^+$  erzeugt eine intensive, breite Bande in der NIR-Region (Abbildung 11.8). Dieser charge-transfer-Übergang lässt auf eine

Ligandenbeteiligung im SOMO schließen. Deswegen führt die Einelektronenoxidation von  $[\text{Ru}(\text{L-H}^1)_2(\text{acac})]$  und  $[\text{Ru}(\text{L-H}^1)_3]$  zu ligandenzentrierten gemischtvalenten Systemen. Darüber hinaus könnte die Einelektronenreduktion dieser Komplexe entweder  $\text{Ru}^{\text{III}}$ -zentriert oder  $\text{L-H}$ -zentriert verlaufen. Jedoch verlaufen  $\text{L-H}$ -zentrierte Reduktionen normalerweise bei höherem Potential als das hier beobachtete (Kapitel 2). Deshalb sind die ersten Reduktionsschritte einer metallzentrierten Reduktion von  $\text{Ru}^{\text{III}}$  zu  $\text{Ru}^{\text{II}}$  zugeordnet, was durch die erhaltenen UV-Vis-NIR-Spektroskopie-Ergebnisse bestätigt wird.

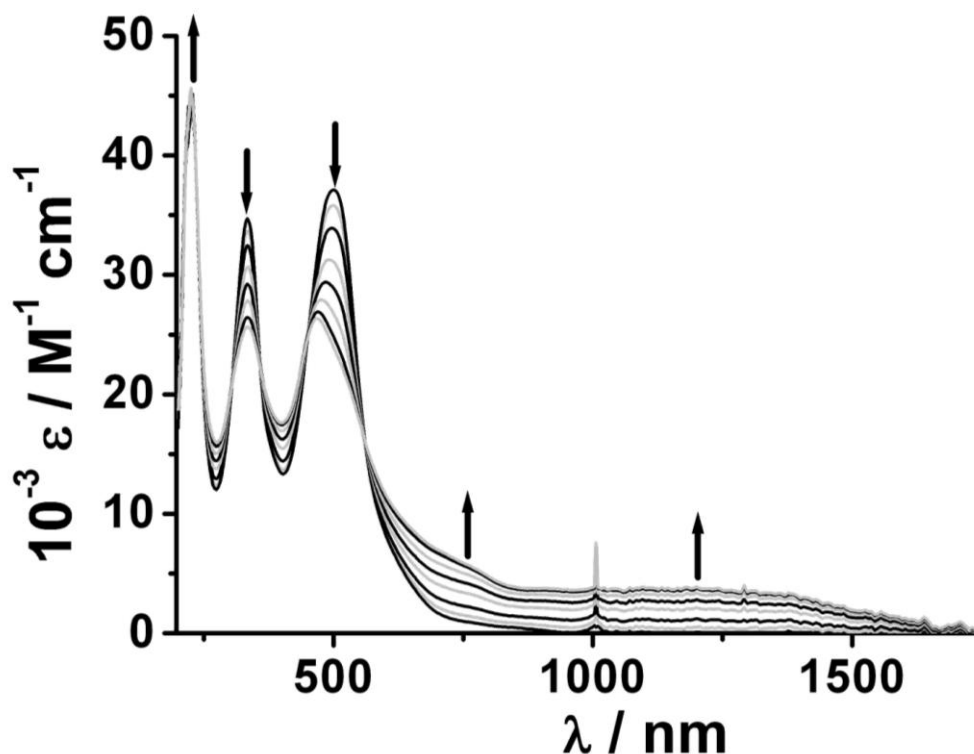


**Abbildung 11.8.** UV-Vis-NIR-Spektroelektrochemie der Umsetzung von  $[\text{Ru}(\text{L-H}^1)_3]$  zu  $[\text{Ru}(\text{L-H}^1)_3]^+$  in  $\text{CH}_2\text{Cl}_2 / 0.1 \text{ M Bu}_4\text{NPF}_6$ .

Kapitel 6 beschreibt die isomeren Formen, Struktur, nicht-kovalente Wechselwirkungen und die Ladungsverteilung von Rutheniumeinkernsystemen der Form  $[(\text{bpy})\text{Ru}^{\text{II}}(\text{L-H})_2]$  ( $\text{L} = m\text{-}[\text{O},\text{O},\text{N},\text{N}] (\text{L}^1)$  und  $p\text{-}[\text{O},\text{N},\text{O},\text{N}] (\text{L}^2)$  *N*-Isopropyl-substituierten chinoiden Liganden). Bei der Kristallstruktur von  $[(\text{bpy})\text{Ru}^{\text{II}}(\text{L-H}^2)_2]$  stehen die zwei koordinierten Sauerstoffatome *trans* zueinander (Abbildung 11.9). Die  $\pi$ -Systeme des chinoiden Liganden sind mehr delokalisiert als im Zustand des freien Liganden, was demnach zu teilweiser Ladung an der NH-Gruppe und am Carbonyl-Sauerstoff der metallfreien Seite führt. Diese Ladungen sind durch starke intermolekulare Wasserstoffbindungen stabilisiert  $\{2.161 \text{ \AA} \ll 2.72 \text{ \AA} (\text{Summe der Van-der-Waals-Radien von Wasserstoff und Sauerstoff})\}$ , was dadurch zur Bildung eines ausgedehnten 3-D-Gerüsts

führt (Abbildung 11.9). Es wird auch beobachtet, dass der freie Platz im Kristallgitter von einigen Wassermolekülen durch Wasserstoffbindungen belegt wurde. Die Komplexe zeigen eine quasireversible Oxidation und zwei reversible Reduktionen. Die EPR- und UV/Vis/NIR-spektroskopischen Ergebnisse der einelektronenoxidierten/reduzierten Spezies implizieren, dass die Oxidation Ruthenium-zentriert ( $\text{Ru}^{\text{II}} \rightarrow \text{Ru}^{\text{III}}$ ) und die Reduktion Chinoid-basiert ( $\{\text{L}\cdot\text{H}^2\} \rightarrow \{\text{L}\cdot\text{H}^2\}^-$ ) verläuft.

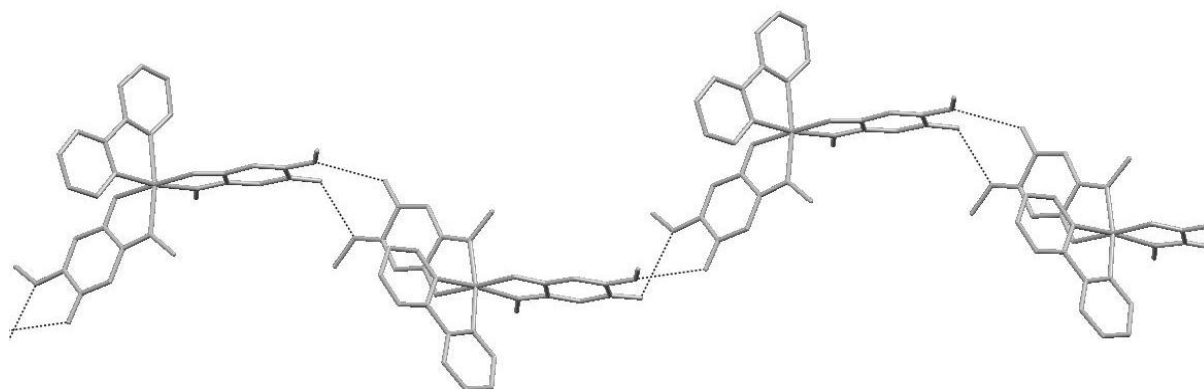


**Abbildung 11.9.** Intermolekulare Wasserstoffbindung der Kristallstruktur von  $[(\text{bpy})\text{Ru}^{\text{II}}(\text{L}\cdot\text{H}^2)_2]$ . Die Wasserstoffatome und die Methyl-Kohlenstoffatome sind der Übersichtlichkeit wegen weggelassen.

Kapitel 7 beschreibt die Synthese zweikerniger Ruthenium-Aren-Komplexe mit symmetrischen ( $\text{L}^2$ ) und asymmetrischen ( $\text{L}^3$ ) *p*-Chinon Liganden und beispiellosen substituentinduzierter Reaktivität. Einer der Zweikernkomplexe mit der Form  $[\{\text{Cl}(\eta^6\text{-Cym})\text{Ru}\}_2(\mu\text{-L}\cdot 2\text{H}^2)]$  (Cym = *p*-Cymen) wurde strukturell charakterisiert und zeigt  $\eta^6$ -Koordination des Aren-Rings (11.10).

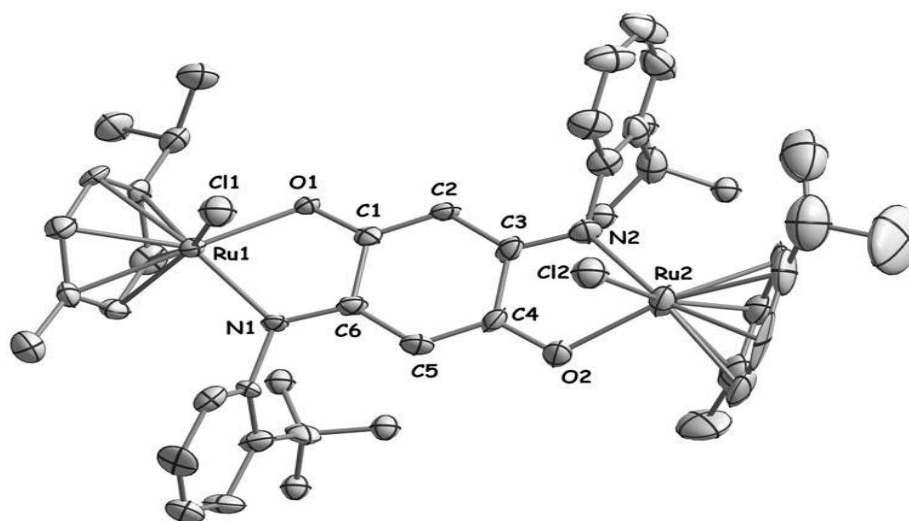
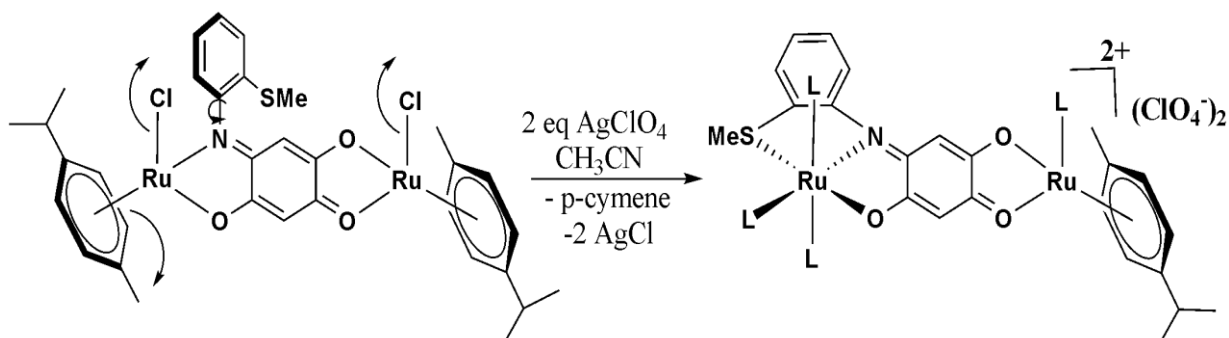


**Abbildung 11.10.** Kristallstruktur des Komplexes  $[\{\text{Cl}(\eta^6\text{-Cym})\text{Ru}\}_2(\mu\text{-L}\cdot 2\text{H})]$ .

Reaktionen dieser Komplexe mit  $\text{AgClO}_4$  führen wie erwartet zu normaler Chlorid-Abstraktion, wohingegen Komplexe mit einer zusätzlichen -SMe Gruppe am Brückenligand ( $\mathbf{L}^2$  and  $\mathbf{L}^3$ ) zur beispiellosen substituenteninduzierten Abspaltung des *p*-Cym-Liganden führte (Abbildung 11.3). Die Erhöhung der Lewis-Acidität am Metallzentrum aufgrund der Chlorid-Abstraktion ist hauptsächlich verantwortlich für die Koordination der -SMe Gruppe, sowie desweiteren die Unfähigkeit des starren Brückenliganden einer facialen Koordination, welche für eine Klavierstuhl-Konfiguration benötigt wird, die Abspaltung des *p*-Cym zu herbeizuführen.



**Scheme 11.3.** Chloride abstraction reaction led to release of cymene group.

Kapitel 8 beschreibt die Synthese, strukturelle, elektrochemische und spektroskopische Eigenschaften des fünf Komponenten enthaltenden 'super'-Redoxsystems  $[(\text{Q})\text{Ru}(\mu\text{-L})\text{Ru}(\text{Q})]^n$  mit  $\text{Q}^0 = 4,6\text{-Di-}i\text{-tert-butyl-N-phenyl-}o\text{-iminobenzochinon}$  und  $\mathbf{L}^{2-}$  stellt die doppelt deprotonierte Form von 2,5-Di-[2-(methylthio)-anilino]-1,4-benzochinon dar. Die zugänglichen Oxidationsstufen sind  $\text{Q}^{0,-,2-}$ ,  $\text{Ru}^{\text{II,III,IV}}$  und  $\mathbf{L}^{0,-,2-,3-,4-}$ . Der Komplex wurde synthetisiert aus dem Zweikernvorläufer 2,5-Di-[2-(methylthio)-anilino]-1,4-benzochinon  $[(\text{MeCN})_3\text{Ru}(\mu\text{-L})\text{Ru}(\text{MeCN})_3]^{2+}$  nach der oben gezeigten Reaktionsgleichung (Abbildung 11.3) erhalten und zeigt acht reversible Eielektronenübertragungsschritte zwischen  $n = (+4)$  bis  $(-4)$ , was anhand Cyclovoltammetrie (Abbildung 11.12), UV-Vis-NIR- und EPR-Spektroelektrochemie am strukturell charakterisierten  $[(\text{Q})\text{Ru}(\mu\text{-L})\text{Ru}(\text{Q})](\text{ClO}_4)_2$ ,  $\mathbf{M}(\text{ClO}_4)_2$  (Abbildung 11.11) untersucht wurde. Diese kombinierten Untersuchungen zeigten, dass  $\mathbf{M}(\text{ClO}_4)_2$  am besten beschrieben wird als  $[(\text{Q})^-\text{Ru}^{\text{III}}(\mu\text{-L})^2\text{-Ru}^{\text{III}}(\text{Q})^-](\text{ClO}_4)_2$  mit antiferromagnetischer Kopplung zwischen den Spins von  $\text{Q}^-$  und  $\text{Ru}^{\text{III}}$  am jeweiligen Ende.

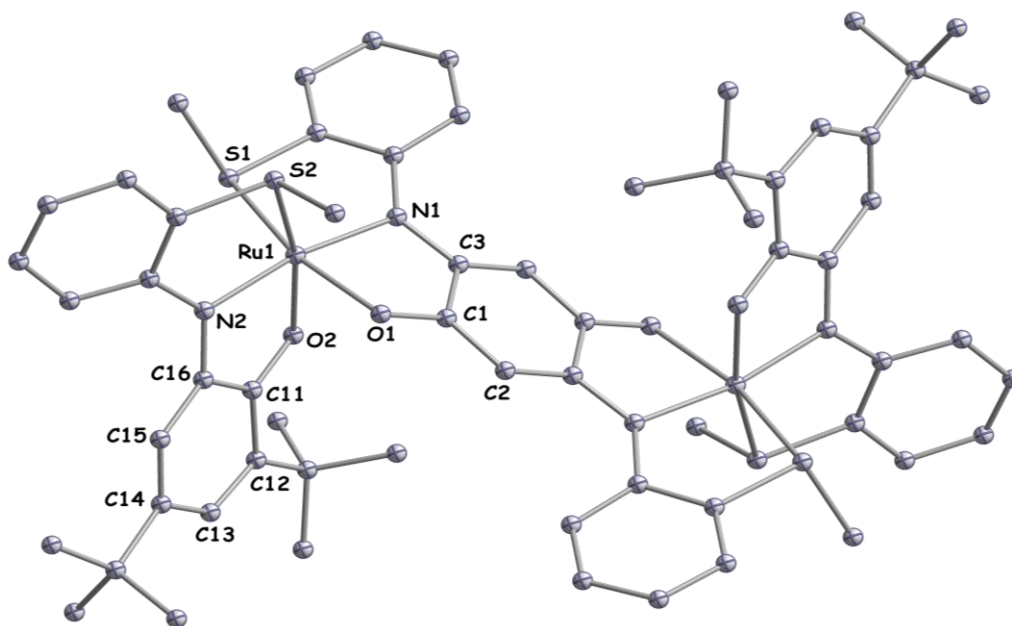


Abbildung 11.11. ORTEP-Darstellung der Kationen von  $[(Q)Ru(\mu-L)Ru(Q)](ClO_4)_2$ .

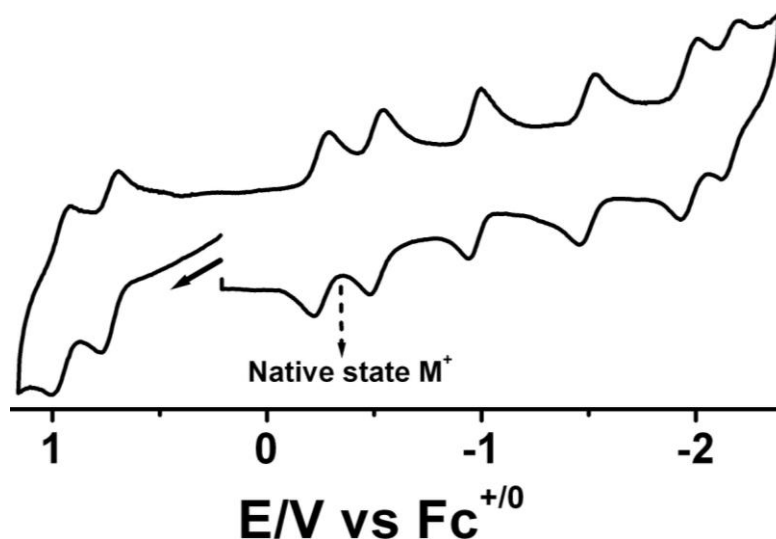


Abbildung 11.12. Cyclovoltammogramm von  $(Q)Ru(\mu-L)Ru(Q)](ClO_4)$  in  $CH_3CN/0.1 M Bu_4NPF_6$  bei 295 K.

Das letzte Kapitel 9 beschreibt die Notwendigkeit eines elektronenreichen Rutheniumzentrums einen stabilen Komplex mit dem 'nicht-unschuldigen' *N*-(2-Methyl-5,8-dioxo-5,8-dihydrochinolin-7-yl)acetamid-Liganden ( $L^5$ ) zu bilden. Ein Rutheniumkomplex von  $L^5$  mit starken  $\sigma$ -donierenden *acac*<sup>-</sup>-Liganden  $[Ru^{II}(acac)_2L^5]$  wurde in der diamagnetischen Form synthetisiert und isoliert um  $d\pi(Ru)-p\pi^*(L^5)$  Mischung in den zugänglichen Redoxstufen zu untersuchen. Der Komplex mit  $L^5$  zeigt starke  $d\pi(Ru)-p\pi^*(L^5)$  Mischung, was zu einer gemischten Art der Valenzsituation der Redoxzustände führt und die Wichtigkeit von Kovalenz in Rutheniummetallkomplexen andeutet. Solche Mischung besitzt große Wichtigkeit im Bereich der Wasseroxidation und bei der Stabilisierung von metallkoordinierten reaktiven Radikalen.



## APPENDIX

### *Bibliography*

- [1] S. D. Thomson, *Naturally Occuring Quinones: IV*, Springer: The Netherlands, **1996**.
- [2] D. Zhang, G.-X. Jin, *Organometallics* **2003**, 22, 2851.
- [3] W.-G. Jia, Y.-F. Han, Y.-J. Lin, L.-H. Weng, G.-X. Jin, *Organometallics* **2009**, 28, 3459.
- [4] J. Mattson, P. Govindaswamy, A. K. Renfrew, P. J. Dyson, P. Stepnicka, G. S.-Fink, B. Therrien, *Organometallics* **2009**, 28, 4350.
- [5] S. Kitagawa, S. Kawata, *Coord. Chem. Rev.* **2002**, 224, 11.
- [6] G. Margraf, T. Kretz, F. F. d. Biani, F. Laschi, S. Losi, P. Zanello, J. W. Bats, J. Wolf, K. Removic-Langer, M. Lang, A. Prokofiev, W. Assmus, H.-W. Lerner, M. Wagner, *Inorg. Chem.* **2005**, 45, 1277-1288.
- [7] R. H. Thompson, *Naturally Occurring Quinones IV, Recent Advances*, 4<sup>th</sup> ed., Chapman and Hall, London, **1997**.
- [8] Q.-Z. Yang, O. Siri, P. Braunstein, *Chem. Eur. J.* **2005**, 11, 7237.
- [9] A. Caneschi, A. Dei, *Angew. Chem. Int. Ed.* **1998**, 37, 3005.
- [10] P. Gütllich, A. Die, *Angew. Chem. Int. Ed.* **1997**, 36, 2734.
- [11] D.M. Adams, A. Dei, A. L. Rheingold, D.N. Hendrickson *J. Am. Chem. Soc.* **1993**, 115, 8221.
- [12] D. Kumbhakar, B. Sarkar, S. Maji, S. M. Mobin, J. Fiedler, R. J.-Aparicio, W. Kaim, G. K. Lahiri, *J. Amer. Chem. Soc.* **2008**, 130, 17575.
- [13] T. E. Keyes, R. J. Forster, P. M. Jayaweera, C. G. Coates, J. J. McGarvey, J. G. Vos, *Inorg. Chem.* **1998**, 37, 5925.
- [14] S. Kar, B. Sarkar, S. Ghumaan, D. Janardanan, J. v. Slageren, J. Fiedler, V. G. Puranik, R. B. Sunoj, W. Kaim, G. K. Lahiri, *Chem-Eur. J.* **2005**, 11, 4901.
- [15] H. Masui, A. L. Freda, M. C. Zerner, A. B. P. Lever, *Inorg. Chem.* **2000**, 39, 141.
- [16] S. B. Braun-Sand, O. Wiest, *J. Phys. Chem. B* **2003**, 107, 9624.
- [17] S. B. Braun-Sand, O. Wiest, *J. Phys. Chem. A* **2003**, 107, 285.
- [18] Y. Wang, M. Lieberman, *IEEE Trans. Nanotech.* **2004**, 3, 368.
- [19] A. F. Heyduk, D. G. Nocera, *Science* **2001**, 293, 1639.
- [20] A. J. Esswein, A. S. Veige, P. M. B. Piccoli, A. J. Schultz, D. G. Nocera, *Organometallics* **2008**, 27, 1073.
- [21] C. Creutz, *Prog. Inorg. Chem.* **1983**, 30, 1.

- [22] R. J. Crutchley, *Adv. Inorg. Chem.* **1994**, *41*, 273.
- [23] K. D. Demadis, C. M. Hartshorn, T. J. Meyer, *Chem. Rev.* **2001**, *101*, 2655.
- [24] D. M. D'Alessandro, F. R. Keene, *Chem. Soc. Rev.* **2006**, *35*, 424.
- [25] F. Weisser, R. Huebner, D. Schweinfurth, B. Sarkar *Chem. Eur. J.* **2011**, *17*, 5727.
- [26] S. Kar, B. Sarkar, S. Ghumaan, D. Janardanan, J. V. Slageren, J. Fiedler, V. G. Puranik, R. B. Sunoj, W. Kaim, G. K. Lahiri, *Chem. Eur. J.* **2005**, *11*, 4901.
- [27] A. F. Heyduk, D. G. Nocera, *Science* **2001**, *293*, 1639.
- [28] A. J. Esswein, A. S. Veige, P. M. B. Piccoli, A. J. Schultz, D. G. Nocera, *Organometallics* **2008**, *27*, 1073.
- [29] E. Amouyal, *Sol. Energy Mater. Sol. Cells* **1995**, *38*, 249.
- [30] R. Argazzi, C. A. Bignozzi, G. M. Hasselman, G. J. Meyer, *Inorg. Chem.* **1998**, *37*, 4533.
- [31] G. Qian, Z.Y. Wang, *Chem. Asian J.* **2010**, *5*, 1006.
- [32] J. Fabian, H. Nakazumi, M. Matsuoka, *Chem. Rev.* **1992**, *92*, 1197.
- [33] K.J. Thorley, J.M. Hales, H.L. Anderson, J.W. Perry, *Angew. Chem. Int. Ed.* **2008**, *47*, 7095.
- [34] M.D. Ward, J.A. McCleverty, *J. Chem. Soc., Dalton Trans.* **2002**, 275.
- [35] S. Kar, B. Sarkar, S. Ghumaan, D. Janardanan, J. V. Slageren, J. Fiedler, V. G. Puranik, R. B. Sunoj, W. Kaim, G. K. Lahiri, *Chem. Eur. J.* **2005**, *11*, 4901.
- [36] S. Patra, B. Sarkar, S. Ghumaan, J. Fiedler, W. Kaim, G. K. Lahiri, *Inorg. Chem.* **2004**, *43*, 6108.
- [37] B. Sarkar, W. Kaim, A. Klein, B. Schwederski, J. Fiedler, C. Duboc-Toia, G. K. Lahiri, *Inorg. Chem.* **2003**, *42*, 6172.
- [38] S. Patra, T. A. Miller, B. Sarkar, M. Niemeyer, M. D. Ward, G. K. Lahiri, *Inorg. Chem.* **2003**, *42*, 4707.
- [39] T. Ling, E. Poupon, E. J. Rueden, S. H. Kim, E. A. Theodorakis, *J. Am. Chem. Soc.* **2002**, *124*, 12261.
- [40] G. Meazza, B. E. Scheffler, M. R. Tellez, A. M. Rimando, J. G. Romagni, S. O. Duke, D. Nanayakkara, I. A. Khan, E. A. Abourashed, F. E. Dayan, *Phytochemistry* **2002**, *59*, 281.
- [41] M. Aguilar-MartVnez, J. A. Bautista-MartVnez, N. MacVas-Ruvalcaba, I. GonzWles, E. Tovar, T. M. d. Alizal, O. Collera, G. Cuevas, *J. Org. Chem.* **2001**, *66*, 8349.
- [42] J. Mattsson, P. Govindaswamy, J. Furrer, Y. Sei, K. Yamaguchi, G. Süß-Fink, B. Therrien, *Organometallics* **2008**, *27*, 4346.

- [43] J. Mattsson, P. Govindaswamy, A. K. Renfrew, P. J. Dyson, P. Stepnicka, G. Süß-Fink, B. Therrien, *Organometallics* **2009**, *28*, 4350.
- [44] A. Paretzki, H. S. Das, F. Weisser, T. Scherer, D. Bubrin, J. Fiedler, J. E. Nycz, B. Sarkar, *Eur. J. Inorg. Chem.* **2011**, 2413.
- [45] B. Podeszwa, H. Niedbala, J. Polanski, R. Musiol, D. Tabak, J. Finster, K. Serafin, M. Milczarek, J. Wietrzyk, S. Boryczka, W. Mol, J. Jampilek, J. Dohnal, D. S. Kalinowski, D. R. Richardson, *Bioorg. Med. Chem. Lett.* **2007**, *17*, 6138.
- [46] M. Hassani, W. Cai, D. C. Holley, J. P. Lineswala, B. R. Maharjan, G. R. Ebrahimian, H. Seradj, M. G. Stocksdale, F. Mohammadi, C. C. Marvin, J. M. Gerdes, H. D. Beall, M. Behforouz, *J. Med. Chem.* **2005**, *48*, 7733.
- [47] M. Behforouz, J. Haddad, W. Cai, M. B. Arnold, F. Mohammadi, A. C. Sousa, M. A. Horn, *J. Org. Chem.* **1996**, *61*, 6552.
- [48] M. Behforouz, W. Cai, F. Mohammadi, M.G. Stocksdale, Z. Gu, M. Ahmadian, D.E. Baty, M.R. Etling, H. ChAl-Anzi, T.M. Swiftney, L.R. Tanzer, R.L. Merrimanb, N.C. Behforouz, *Bioorg. Med. Chem.* **2007**, *15*, 495.
- [49] R. Hargreaves, C.L. David, L. Whitesell, E.B. Skibo, *Bioorg. Med. Chem. Lett.* **2003**, *13*, 3075.
- [50] M. D. Ward, J. A. McCleverty, *J. Chem. Soc., Dalton Trans.* **2002**, 275.
- [51] D. Herebian, E. Bothe, F. Neese, T. Weyhermüller, K. Wieghardt, *J. Am. Chem. Soc.* **2003**, *125*, 9116.
- [52] F. Paul, C. Lapinte, *Coord. Chem. Rev.* **1998**, *431*, 178.
- [53] M. D. Ward, *Chem. Ind.* **1997**, 640.
- [54] M. D. Ward, *Chem. Ind.* **1996**, 568.
- [55] M. D. Ward, *Chem. Soc. Rev.* **1995**, 121.
- [56] C. Creutz, *Prog. Inorg. Chem.* **1983**, *30*, 1.
- [57] R. J. Crutchley, *Adv. Inorg. Chem.* **1994**, *41*, 273.
- [58] K. D. Demadis, C. M. Hartshorn, T. J. Meyer, *Chem. Rev.* **2001**, *101*, 2655.
- [59] D. M. D'Alessandro, F. R. Keene, *Chem. Soc. Rev.* **2006**, *35*, 424.
- [60] W. Kaim, G. K. Lahiri, *Angew. Chem., Int. Ed.* **2007**, *46*, 1778.
- [61] J. C. Salsman, C. P. Kubiak, *J. Am. Chem. Soc.* **2005**, *127*, 2382.
- [62] J. Maurer, R. F. Winter, B. Sarkar, J. Fiedler, S. Zalis, *Chem. Commun.* **2004**, 1900.
- [63] S. Bhattacharya, P. Gupta, F. Basuli, C. G. Pierpont, *Inorg. Chem.* **2002**, *41*, 5810.
- [64] M. D. Ward, *Inorg. Chem.* **1996**, *35*, 1712.
- [65] H. Masui, A. L. Freda, M. C. Zerner, A. B. P. Lever, *Inorg. Chem.* **2000**, *39*, 141.

- [66] P. Braunstein, D. Bubrin, B. Sarkar, *Inorg. Chem.* **2009**, *48*, 2534.
- [67] F. A. Cotton, J.-Y. Jin, Z. Li, C. A. Murillo, J. H. Reibenspies, *Chem. Commun.* **2008**, 211.
- [68] Q.-Z. Yang, A. Kermagoret, M. Agostinho, O. Siri, P. Braunstein *Organometallics*, **2006**, *25*, 5519.
- [69] Q.-Z. Yang, O. Siri, P. Braunstein, *Chem. Eur. J.* **2005**, *11*, 7237.
- [70] D. E. Richardson, H. Taube, *Coord. Chem. Rev.* **1984**, *60*, 107.
- [71] S. Kar, B. Sarkar, S. Ghumaan, D. Janardanan, J. v. Slageren, J. Fiedler, V. G. Puranik, R. B. Sunoj, W. Kaim, G. K. Lahiri, *Chem.–Eur. J.* **2005**, *11*, 4901.
- [72] N. S. Hush, *Prog. Inorg. Chem.* **1967**, *8*, 391.
- [73] S. Patra, B. Sarkar, S. M. Mobin, W. Kaim, G. K. Lahiri, *Inorg. Chem.* **2003**, *42*, 6469.
- [74] W. Kaim, S. Ernst, V. Kasack, *J. Am. Chem. Soc.* **1990**, *112*, 173.
- [75] Morton, R. A. *The Biochemistry of Quinones*, Academic Press: New York: **1965**.
- [76] Patai, S.; Rappoport, Z. *The Chemistry of Quinonoid Compounds*, Wiley and Sons: New York, **1988**; Vols. 1 and 2.
- [77] H. Nohl, W. Jordan, R. J. Youngman, *Adv. Free Radical Biol. Med.* **1986**, *2*, 211.
- [78] S. D. Thompson, *Naturally Occuring Quinones IV*; Springer: The Netherlands, **1996**.
- [79] Y. Izumi, H. Sawada, N. Sakka, N. Yamamoto, T. Kume, H. Katsuki, S. Shimohama, A. Akaike, *J. Neurosci. Res.* **2005**, *79*, 849.
- [80] M. He, P. J. Sheldon, D. H. Sherman, *Proc. Natl. Acad. Sci. USA* **2001**, *98*, 926–931.
- [81] A. J. Lin, L. A. Cosby, A. C. Sartorelli, *Cancer Chemother. Rep. Part 2* **1974**, *4*, 23.
- [82] J. J. Inbaraj, R. Gandhidasan, R. Murugesan, *Free Radical Biol. Med.* **1999**, *26*, 1072.
- [83] N. U. Frigaard, S. Tokita, K. Matsuura, *Biochim. Biophys. Acta* **1999**, *1413*, 108.
- [84] N. R. Bachur, S. L. Gordon, M. V. Gee, *Cancer Res.* **1978**, 1745.
- [85] P. Stahl, L. Kissau, R. Matzischek, A. Giannis, H. Waldmann, *Angew. Chem., Int. Ed.* **2002**, *41*, 1174.
- [86] G. Meazza, B. E. Scheffler, M. R. Tellez, A. M. Rimando, J. G. Romagni, S. O. Duke, D. Nanayakkara, I. A. Khan, E. A. Abourashed, F. E. Dayan, *Phytochemistry* **2002**, *59*, 281.
- [87] T. Ling, E. Poupon, E. J. Rueden, S. H. Kim, E. A. Theodorakis, *J. Am. Chem. Soc.* **2002**, *124*, 12261.
- [88] M. Aguilar-Martinez, J. A. Bautista-Martinez, N. Macias-Ruvalcaba, I. Gonzalez, E. Tovar, T. M. d. Alizal, O. Collera, G. Cuevas, *J. Org. Chem.* **2001**, *66*, 8349.

- [89] N. Subbarayudu, Y. D. Satyanarayana, E. Vankata-Rao, D. Venkata-Rao, *Ind. J. Pharm. Sc.* **1978**, *40*, 173.
- [90] B. S. Joshi, V. S. Kamat, *Indian J. Chem.* **1975**, *13*, 795.
- [91] M. K. Manthey, S. G. Pyne, R. J. W. Trusscot, *Aust. J. Chem.* **1989**, *42*, 365.
- [92] P. D. Mize, P. W. Jeffs, K. Boelkelheide, *J. Org. Chem.* **1980**, *45*, 3540.
- [93] P. Braunstein, O. Siri, J.-P. Taquet, Q.-Z. Yang, *Chem.;Eur. J.* **2004**, *10*, 3817.
- [94] A.-M. Osman, *J. Am. Chem. Soc.* **1957**, *79*, 966.
- [95] R. N. Harger, *J. Am. Chem. Soc.* **1924**, *46*, 2540.
- [96] S. Bayen, N. Barooah, R. J. Sarma, T. K. Sen, A. Karmakar, J. B. Baruah, *Dyes Pigm.* **2007**, *75*, 770.
- [97] H. B. Mereyala, M. V. Chary, S. Kantevari, *Synthesis* **2007**, 187.
- [98] Q.-Z. Yang, O. Siri, P. Braunstein, *Chem. Commun.* **2005**, 2660.
- [99] Q.-Z. Yang, O. Siri, P. Braunstein, *Chem. Eur. J.* **2005**, *11*, 7237.
- [100] S. Scheuermann, T. Kretz, H. Vitze, J. W. Bats, M. Bolte, H.-W. Lerner, M. Wagner, *Chem. Eur. J.* **2008**, *14*, 2590.
- [101] W.-G. Jia, Y.-F. Han, Y.-J. Lin, L.-H. Weng, G.-X. Jin, *Organometallics* **2009**, *28*, 3459.
- [102] J. S. Miller, K. S. Min, *Angew. Chem.* 2009, *121*, 268–278; *Angew. Chem. Int. Ed.* **2009**, *48*, 262.
- [103] W. Kaim, *Inorg. Chem.* **2011**, *50*, 9752.
- [104] J. L. Boyer, J. Rochford, M.-K. Tsai, J. T. Muckerman, E. Fujita, *Coordination Chemistry Reviews* **2010**, *254*, 309.
- [105] H. Masui, A. L. Freda, M. C. Zerner, A. B. P. Lever, *Inorg. Chem.* **2000**, *39*, 141.
- [106] S. Bhattacharya, P. Gupta, P. Basuli, C. G. Pierpont, *Inorg. Chem.* **2002**, *41*, 5810.
- [107] M. D. Ward, *Inorg. Chem.* **1996**, *35*, 1712.
- [108] W. I. Dzik, J. I. van der Vlugt, J. N. H. Reek, B. de Bruin, *Angew. Chem. Int. Ed.* **2011**, *50*, 3356.
- [109] T. Wada, K. Tsuge, K. Tanaka, *Angew. Chem. Int. Ed.* **2000**, *39*, 1479.
- [110] H. C. Zhao, J. P. Harney, Y.-T. Huang, J.-H. Yum, Md. K. Nazeeruddin, M. Grätzel, M.-K. Tsai, J. Rochford, *Inorg. Chem.* **2012**, *51*, 1.
- [111] S. Kitagawa, S. Kawata, *Coord. Chem. Rev.* **2002**, *224*, 11.
- [112] M. Leschke, M. Welter, H. Lang, *Inorg. Chim. Acta* **2003**, *350*, 114.
- [113] J. S. Miller, K. S. Min, *Angew. Chem.* **2009**, *121*, 268; *Angew. Chem. Int. Ed.* **2009**, *48*, 262.

- [114] M. Ueda, N. Sakai, Y. Makromol. Imai, *Chem.* **1979**, *180*, 2813.
- [115] D. Zhang, G.-X. Jin, *Organometallics* **2003**, *22*, 2851.
- [116] *Sigma Aldrich Safety Data Sheet (MSDS), Regulation (EC) No. 1907/2006*, version 3.0, Revision Date Dec. 28, 2008; Sigma Aldrich: St. Louis, MO.
- [117] J. P. Klinman, *Proc. Natl. Acad. Sci. U.S.A.* **2001**, *98*, 14766.
- [118] H. S. Das, F. Weisser, D. Schweinfurth, C.-Y. Su, L. Bogani, J. Fiedler, B. Sarkar *Chem. Eur. J.* **2010**, *16*, 2977.
- [119] Q.-Z. Yang, O. Siri, P. Braunstein, *Chem. Commun.* **2005**, 2660.
- [120] Q.-Z. Yang, O. Siri, P. Braunstein, *Chem. Eur. J.* **2005**, *11*, 7237.
- [121] C. Xing, E. B. Skibo, *Biochemistry* **2000**, *39*, 10770.
- [122] F. Weisser, R. Huebner, D. Schweinfurth, B. Sarkar, *Chem. Eur. J.* **2011**, *17*, 5727.
- [123] M. D. Ward, *Inorg. Chem.* **1996**, *35*, 1712.
- [124] M. B. Robin, P. Day, *Adv. Inorg. Chem.* **1967**, *10*, 247.
- [125] K. D. Demadis, C. M. Hartshorn, T. J. Meyer, *Chem. Rev.* **2001**, *101*, 2655.
- [126] D. M. DMAlessandro, F. R. Keene, *Chem. Soc. Rev.* **2006**, *35*, 424.
- [127] S. F. Nelsen, *Chem. Eur. J.* **2000**, *6*, 581.
- [128] V. Balzani, A. Zuris, M. Venturi, S. Campagna, S. Serroni, *Chem. Rev.* **1996**, *96*, 759.
- [129] E. Amouyal, *Sol. Energy Mater. Sol. Cells* **1995**, *38*, 249.
- [130] A. Kay, M. Grätzel, *Sol. Energy Mater. Sol. Cells* **1991**, *44*, 99.
- [131] V. Balzani, F. Scandola, *Supramolecular photochemistry*, **1991** (New York: Ellis Horwood).
- [132] A. Hatzidimitriou, A. Gourdon, J. Devillers, J.-P. Launay, E. Mena, E. Amouyal, *Inorg. Chem.* **1996**, *35*, 2212.
- [133] K. E. Erkkila, D. T. Odom, J. K. Barton, *Chem. Rev.* **1999**, *29*, 2777.
- [134] J. K. Barton, A. T. Danishefsky, J. M. Goldberg, *J. Am. Chem. Soc.* **1984**, *106*, 2172.
- [135] J. Kelly, A. Tossi, D. McConnel, C. Ohuigin, *Nucleic Acids Res.* **1985**, *13*, 6017.
- [136] S. Patra, B. Sarkar, S. Ghumaan, J. Fiedler, W. Kaim, G. K. Lahiri, *Inorg. Chem.* **2004**, *43*, 6108.
- [137] N. Chanda, B. Sarkar, S. Kar, J. Fiedler, W. Kaim, G. K. Lahiri, *Inorg. Chem.* **2004**, *43*, 5128.
- [138] S. Kar, N. Chanda, S. M. Mobin, A. Datta, F. A. Urbanos, V. G. Puranik, R. Jimenez - Aparicio, G. K. Lahiri, *Inorg. Chem.* **2004**, *43*, 4911.
- [139] S. Chakraborty, R. H. Laye, R. L. Paul, R. G. Gonnade, V. G. Puranik, M. D. Ward, G. K. Lahiri, *J. Chem. Soc. Dalton Trans.* **2002**, 1172.

- [140] S. Chakraborty, R. H. Laye, P. Munshi, R. L. Paul, M. D. Ward, G. K. Lahiri, *J. Chem. Soc. Dalton Trans.* **2002**, 2348.
- [141] H. S. Das, F. Weisser, D. Schweinfurth, C.-Y. Su, L. Bogani, J. Fiedler, B. Sarkar, *Chem. Eur. J.* **2010**, *16*, 2977.
- [142] S. Dähne, D. Leupold, *Angew. Chem.* **1966**, *78*, 1029; *Angew. Chem. Int. Ed.* **1966**, *5*, 984.
- [143] A. Dei, D. Gatteschi, L. Pardi, *Inorg. Chem.* **1990**, *29*, 1442.
- [144] S. Kar, B. Sarkar, S. Ghumaan, D. Janardanan, J. von Slageren, J. Fiedler, V. G. Puranik, R. B. Sunoj, W. Kaim, G. K. Lahiri, *Chem. Eur. J.* **2005**, *11*, 4901.
- [145] C. Creutz, *Prog. Inorg. Chem.* **1983**, *30*, 1.
- [146] I. A. Miller, E. R. Offenbacher, *Phys. Rev.* **1968**, *166*, 269.
- [147] A. Bencini, D. Gatteschi, *EPR of Exchange Coupled Systems*, Springer, Heidelberg, **1990**.
- [148] S. Kar, B. Sarkar, S. Ghumaan, D. Janardanan, J. von Slageren, J. Fiedler, V. G. Puranik, R. B. Sunoj, W. Kaim, G. K. Lahiri, *Chem. Eur. J.* **2005**, *11*, 4901.
- [149] K.J. Thorley, J.M. Hales, H.L. Anderson, J.W. Perry, *Angew. Chem. Int. Ed.* **2008**, *47*, 7095.
- [150] M.D. Ward, J.A. McCleverty, *J. Chem. Soc., Dalton Trans.* **2002**, 275.
- [151] M.D. Ward, *J. Solid State Electrochem.* **2005**, *9*, 778.
- [152] S. Ghumaan, B. Sarkar, S. Patra, K. Parimal, J. V. Slageren, J. Fiedler, W. Kaim, G. K. Lahiri, *Dalton Trans.* **2005**, 706.
- [153] Q.-Z. Yang, O. Siri, P. Braunstein, *Chem. Commun.* **2005**, 2660.
- [154] Q.-Z. Yang, O. Siri, P. Braunstein, *Chem. Eur. J.* **2005**, *11*, 7237.
- [155] D. Kumbhakar, B. Sarkar, S. Maji, S. M. Mobin, J. Fiedler, R. J. Aparicio, W. Kaim, G. K. Lahiri, *J. Am. Chem. Soc.* **2008**, *130*, 17575.
- [156] O. Kahn, *Molecular Magnetism*, VCH, Weinheim, **1993**.
- [157] F. Fabrizi de Biani, A. Dei, C. Sangregorio, L. Sorace, *Dalton Trans.* **2005**, 3868.
- [158] M. Haga, E. S. Dodsworth, A. B. P. Lever, *Inorg. Chem.* **1986**, *25*, 447.
- [159] H. Masui, A. B. P. Lever, P. Auburn, *Inorg. Chem.* **1991**, *30*, 2402.
- [160] C. G. Pierpont, *Coord. Chem. Rev.* **2001**, *415*, 219.
- [161] S. Ernst, P. Hänel, J. Jordanov, W. Kaim, V. Kasack, E. Roth, *J. Am. Chem. Soc.* **1989**, *111*, 1733.
- [162] Q.-Z. Yang, O. Siri, P. Braunstein, *Chem. Eur. J.* **2005**, *11*, 7237.
- [163] C. G. Pierpont, C. W. Lange, *Inorg. Chem.* **1994**, *41*, 331.

- [164] D. Das, A. K. Das, B. Sarkar, T. K. Mondal, S. M. Mobin, J. Fiedler, S. Zalis, F. A. Urbanos, R. J.-Aparicio, W. Kaim, G. K. Lahiri, *Inorg. Chem.* **2009**, *48*, 11853.
- [165] D. Kalinina, C. Dares, H. Kaluarachchi, P. G. Potvin, A. B. P. Lever, *Inorg. Chem.* **2008**, *47*, 10110.
- [166] J. L. Boyer, J. Rochford, M.-K. Tsai, J. T. Muckerman, E. Fujita, *Coord. Chem. Rev.* **2010**, *254*, 309.
- [167] T. Ling, E. Poupon, E. J. Rueden, S. H. Kim, E. A. Theodorakis, *J. Am. Chem. Soc.* **2002**, *124*, 12261.
- [168] G. Meazza, B. E. Scheffler, M. R. Tellez, A. M. Rimando, J. G. Romagni, S. O. Duke, D. Nanayakkara, I. A. Khan, E. A. Abourashed, F. E. Dayan, *Phytochemistry* **2002**, *59*, 281.
- [169] B. S. Joshi, V. N. Kamat, *J. Chem. Soc. Perkin Trans. 1* **1975**, 327.
- [170] P. Stahl, L. Kissau, R. Mazitschek, A. Giannis, H. Waldmann, *Angew. Chem.* **2002**, *114*, 1222.
- [171] R. H. Thompson, *Naturally Occurring Quinones IV, Recent Advances*, 4th ed., Chapman and Hall, London, **1997**.
- [172] T. Ling, E. Poupon, E. J. Rueden, S. H. Kim, E. A. Theodorakis, *J. Am. Chem. Soc.* **2002**, *124*, 12261.
- [173] P. stahl, L. Kissau, R. Mazitschek, A. Giannis, H. Waldmann, *Angew. Chem.* **2002**, *114*, 1222.
- [174] T. Kobayashi, Y. Nishina, K. G. Shimizu, G. P. Sato, *Chem. Lett.* **1988**, 1137.
- [175] P. Chaudhuri, R. Wagner, U. Pieper, B. Biswas, T. Weyhermüller, *Dalton Trans.* **2008**, 1286.
- [176] S. Mukherjee, T. Weyhermüller, E. Bill, K. Wieghardt, P. Chaudhuri, *Inorg. Chem.* **2005**, *44*, 7099.
- [177] R. R. Gagne, C. A. Koval, G. C. Lisensky, *Inorg. Chem.* **1980**, *19*, 2855.
- [178] R. E. DeSimone, *J. Am. Chem. Soc.* **1973**, *95*, 6238.
- [179] H. Kobayashi, H. Matsuzawa, Y. Kaizu, A. Ichidat, *Inorg. Chem.* **1987**, *26*, 4318.
- [180] S. Bhattacharya, S. R. Boone, G. A. Fox, C. G. Pierpont, *J. Am. Chem. Soc.* **1990**, *112*, 1088.
- [181] C. G. Pierpont, *Coord. Chem. Rev.* **2001**, *219-221*, 415.
- [182] S. Chakraborty, R. H. Laye, R. L. Paul, R. G. Gonnade, V. G. Puranik, M. D. Ward, G. K. Lahiri, *J. Chem. Soc., Dalton Trans.*, **2002**, 1172.



- [183] R. A. Metcalfe, L. C. G. Vasconcellos, H. Mirza, D. W. Franco, A. B. P. Lever, *J. Chem. Soc., Dalton Trans.* **1999**, 2653.
- [184] S. D. Thomson, *Naturally Occuring Quinones: IV*, Springer, Amsterdam, **1996**.
- [185] M. Haga, E. S. Dodsworth, A. B. P. Lever, *Inorg. Chem.* **1986**, 25, 447.
- [186] D. Kalinina, D. Dares, H. Kaluarachchi, P. G. Potvin, A. B. P. Lever, *Inorg. Chem.* **2008**, 47, 10110.
- [187] S. Patra, B. Sarkar, S. Ghumaan, J. Fiedler, S. Zalis, W. Kaim, G. K. Lahiri, *J. Chem. Soc., Dalton Trans.* **2004**, 750.
- [188] S. Ye, B. Sarkar, C. Duboc, J. Fiedler, W. Kaim, *Inorg. Chem.* **2005**, 44, 2843.
- [189] C. G. Pierpont, R. M. Buchanan, *Coord. Chem. Rev.* **1981**, 38, 45.
- [190] Pierpont, C.G. *Coord. Chem. Rev.* **2001**, 216, 99.
- [191] A. I. Poddelsky, V. K. Cherkasov, G. A. Abakumov, *Coord. Chem. Rev.* **2009**, 253, 291.
- [192] C. Bissantz C, B. Kuhn, M. Stahl, *J. Med. Chem.* **2010**, 53, 5061.
- [193] H. J. Schneider, *Angew. Chem. Int Ed.* **2009**, 48, 3924.
- [194] B. Moulton, M. J. Zaworotko, *Chem. Rev.* **2001**, 101, 1629.
- [195] C. B. Aakeroy, K. R. Seddon, *Chem. Soc. Rev.* **1993**, 22, 397.
- [196] E. Alessio, G. Balducci, M. Calligaris, G. Costa, W. M. Attia, G. Mestroni, *Inorg. Chem.* **1991**, 30, 609.
- [197] R. S. Srivastava, F. R. Fronczek, N. R. Tarver, R. S. Perkins, *Polyhedron*, **2007**, 26, 5389.
- [198] A. B. P. Lever, *Coord. Chem. Rev.* **2010**, 254, 1397.
- [199] C. G. Pierpont, *Coord. Chem. Rev.* **2001**, 216-217, 95.
- [200] M. D. Ward, *Inorg. Chem.* **1996**, 35, 1712.
- [201] M. Leschke, M. Melter, H. Lang, *Inorg. Chim. Acta* **2003**, 350, 114.
- [202] O. Siri, J.-P. Taquet, J.-P. Collin, M.-M. Rohmer, M. Benard, P. Braunstein, *Chem. Eur. J.* **2005**, 11, 7247.
- [203] S. Ye, B. Sarkar, F. Lissner, T. Schleid, J. v. Slageren, J. Fiedler, W. Kaim, *Angew. Chem., Int. Ed.* **2005**, 44, 2103.
- [204] C. Carbonera, A. Dei, J.-F. Letard, C. Sangregorio, L. Sorace, *Angew. Chem., Int. Ed.* **2004**, 43, 3136.
- [205] J.-P. Taquet, O. Siri, P. Braunstein, R. Welter, *Inorg. Chem.* **2004**, 43, 6944.
- [206] Q.-Z. Yang, A. Kermagoret, M. Agostinho, O. Siri, P. Braunstein, *Organometallics* **2006**, 25, 5518.

- [207] P. Braunstein, F. Naud, *Angew. Chem., Int. Ed.* **2001**, *40*, 680.
- [208] S. Korn, W. S. Sheldrick, *J. Chem. Soc., Dalton Trans.* **1997**, 2191.
- [209] K. Yamanari, R. Ito, S. Yamamoto, T. Konno, A. Fuyuhiko, K. Fujioka, R. Arakawa, *Inorg. Chem.* **2002**, *41*, 6824.
- [210] Z. Grote, S. Bonazzi, R. Scopelliti, K. Severin, *J. Am. Chem. Soc.* **2006**, *128*, 10382.
- [211] C. Olivier, R. Scopelliti, K. Severin, *Eur. J. Inorg. Chem.* **2009**, 207.
- [212] Y. K. Yan, M. Melchart, A. Habtemariam, P. J. Sadler, *Chem. Commun.* **2005**, 4764.
- [213] L. Ronconi, P. J. Sadler, *Coord. Chem. Rev.* **2007**, *251*, 1633.
- [214] C. G. Hartinger, P. J. Dyson, *Chem. Soc. Rev.* **2009**, *38*, 391.
- [215] D. Schweinfurth, H. S. Das, F. Weisser, D. Bubrin, B. Sarkar, *Inorg. Chem.* **2011**, *50*, 1150.
- [216] P. Stahl, L. Kissau, R. Matzischek, A. Giannis, H. Waldmann, *Angew. Chem., Int. Ed.* **2002**, *41*, 1174.
- [217] G. Meazza, B. E. Scheffler, M. R. Tellez, A. M. Rimando, J. G. Romagni, S. O. Duke, D. Nanayakkara, I. A. Khan, E. A. Abourashed, F. E. Dayan, *Phytochemistry* **2002**, *59*, 281.
- [218] J. Mattsson, P. Govindaswamy, A. K. Renfrew, P. J. Dyson, P. Stepnicka, G. Süß-Fink, B. Therrien, *Organometallics* **2009**, *28*, 4350.
- [219] J. Mattsson, P. Govindaswamy, J. Furrer, Y. Sei, K. Yamaguchi, G. Süß-Fink, B. Therrien, *Organometallics* **2008**, *27*, 4346.
- [220] P. Braunstein, F. Naud, A. Pfaltz, S. J. Rettig, *Organometallics* **2000**, *19*, 2676.
- [221] B. Cetinkaya, E. Cetinkaya, M. Brookhart, P. S. White, *J. Mol. Cat. A: Chem.* **1999**, *142*, 101.
- [222] C. Creutz, *Prog. Inorg. Chem.* **1983**, *30*, 1.
- [223] W. Kaim, *Coordination Chemistry Reviews* **2011**, *255*, 2503.
- [224] S. Rigaut, J. Perruchon, L.L. Pichon, D. Touchard, P.H. Dixneuf, *Organomet. Chem.* **2003**, *670*, 37.
- [225] Q. Hang, Y. Wang, M. Lieberman, G.H. Bernstein, *J. Vac. Sci. Technol. B* **2003**, *21*, 227.
- [226] A. Barbieri, B. Ventura, L. Flamigni, F. Barigelletti, G. Fuhrmann, P. Bauerle, S. Goeb, R. Ziessel, *Inorg. Chem.* **2005**, *44*, 8033.
- [227] H. Tannai, K. Tsuge, Y. Sasaki, *Inorg. Chem.* **2005**, *44*, 5206.
- [228] S. Ye, B. Sarkar, F. Lissner, T. Schleid, J. V. Slageren, J. Fiedler, W. Kaim, *Angew. Chem. Int. Ed.* **2005**, *44*, 2103.

- [229] J. S. Miller, K. S. Min, *Angew. Chem.* **2008**, *Angew. Chem. Int. Ed.* **2008**, *48*, 262.
- [230] M. J. Frisch, G. W. Trucks, H. B. Schlegel, G. E. Scuseria, M. A. Robb, J. R. Cheeseman, G. Scalmani, V. Barone, B. Mennucci, G. A. Petersson, H. Nakatsuji, M. Caricato, X. Li, H. P. Hratchian, A. F. Izmaylov, J. Bloino, G. Zheng, J. L. Sonnenberg, M. Hada, M. Ehara, K. Toyota, R. Fukuda, J. Hasegawa, M. Ishida, T. Nakajima, Y. Honda, O. Kitao, H. Nakai, T. Vreven, J. A. Montgomery, Jr., J. E. Peralta, F. Ogliaro, M. Bearpark, J. J. Heyd, E. Brothers, K. N. Kudin, V. N. Staroverov, R. Kobayashi, J. Normand, K. Raghavachari, A. Rendell, J. C. Burant, S. S. Iyengar, J. Tomasi, M. Cossi, N. Rega, J. M. Millam, M. Klene, J. E. Knox, J. B. Cross, V. Bakken, C. Adamo, J. Jaramillo, R. Gomperts, R. E. Stratmann, O. Yazyev, A. J. Austin, R. Cammi, C. Pomelli, J. W. Ochterski, R. L. Martin, K. Morokuma, V. G. Zakrzewski, G. A. Voth, P. Salvador, J. J. Dannenberg, S. Dapprich, A. D. Daniels, Ö. Farkas, J. B. Foresman, J. V. Ortiz, J. Cioslowski, and D. J. Fox, Gaussian 09, Revision B.01, Gaussian, Inc., Wallingford CT, 2009.
- [231] G. te Velde, F. M. Bickelhaupt, S. J. A. van Gisbergen, C. Fonseca Guerra, E. J. Baerends, J. G. Snijders and T. Ziegler, *J. Comput. Chem.* **2001**, *22*, 931.
- [232] ADF 2010.01, SCM, Vrije Universiteit, Amsterdam, <http://www.scm.com>, Amsterdam, The Netherlands, Editon edn. **2005**.
- [233] P. H. Hariharan and J. A. Pople, *Theor. Chim. Acta* **1973**, *28*, 213.
- [234] D. Andrae, U. Haeussermann, M. Dolg, H. Stoll and H. Preuss, *Theor. Chim. Acta* **1990**, *77*, 123.
- [235] J. P. Perdew, K. Burke and M. Enzerhof, *Phys. Rev. Lett.* **1996**, *77*, 3865.
- [236] C. Adamo and V. Barone, *J. Chem. Phys.* **1999**, *110*, 6158.
- [237] Becke A. D. *J. Chem. Phys.* **1993**, *98*, 5648.
- [238] (a) Becke, A. D. *Phys. Rev. A* **1988**, *38*, 3098. (b) Perdew, J. P.; Wang, Y. *Phys. Rev. B* **1992**, *45*, 13244. (c) Perdew, J. P. *Phys. Rev. B* **1986**, *33*, 8822.
- [239] (a) van Lenthe, E.; van der Avoird, A.; Wormer, P.E.S. *J. Chem. Phys.* **1998**, *108*, 4783. (b) van Lenthe, E.; van der Avoird, A.; Wormer, P.E.S. *J. Chem. Phys.* **1997**, *107*, 2488.
- [240] M. Cossi, N. Rega, G. Scalmani and V. Barone, *J. Comput. Chem.* **2003**, *24*, 669.
- [241] S. Bhattacharya, P. Gupta, F. Basuli, C. G. Pierpont, *Inorg. Chem.* **2002**, *41*, 5810.
- [242] A. B. P. Lever, *Coord. Chem. Rev.* **2010**, *254*, 1397.
- [243] T. Wada, K. Tsuge, K. Tanaka, *Angew. Chem. Int. Ed.* **2000**, *39*, 1479.

- [244] H. Masui, A. L. Freda, M. C. Zerner, A. B. P. Lever, *Inorg. Chem.* **2000**, *39*, 141.
- [245] S. Kar, B. Sarkar, S. Ghumaan, D. Janardanan, J. v. Slageren, J. Fiedler, V. G. Puranik, R. B. Sunoj, W. Kaim, G. K. Lahiri, *Chem. Eur. J.* **2005**, *11*, 4901.
- [246] D. Kumbhakar, B. Sarkar, S. Maji, S. M. Mobin, J. Fiedler, F. A. Urbanos, R.-J. Aparicio, W. Kaim, G. K. Lahiri, *J. Am. Chem. Soc.* **2008**, *130*, 17575.
- [247] B. Podeszwa, H. Niedbala, J. Polanski, R. Musiol, D. Tabak, J. Finster, K. Serafin, M. Milczarek, J. Wietrzyk, S. Boryczka, W. Mol, J. Jampilek, J. Dohnal, D. S. Kalinowski, D. R. Richardson, *Bioorg. Med. Chem. Lett.* **2007**, *17*, 6138.
- [248] M. Hassani, W. Cai, D. C. Holley, J. P. Lineswala, B. R. Maharjan, G. R. Ebrahimian, H. Seradj, M. G. Stocksdale, F. Mohammadi, C. C. Marvin, J. M. Gerdes, H. D. Beall, M. Behforouz, *J. Med. Chem.* **2005**, *48*, 7733.
- [249] M. Behforouz, J. Haddad, W. Cai, M. B. Arnold, F. Mohammadi, A. C. Sousa, M. A. Horn, *J. Org. Chem.* **1996**, *61*, 6552.
- [250] M. Behforouz, W. Cai, F. Mohammadi, M.G. Stocksdale, Z. Gu, M. Ahmadian, D.E. Baty, M.R. Etling, H. ChAl-Anzi, T.M. Swiftney, L.R. Tanzer, R.L. Merrimanb, N.C. Behforouz, *Bioorg. Med. Chem.* **2007**, *15*, 495.
- [251] R. Hargreaves, C.L. David, L. Whitesell, E.B. Skibo, *Bioorg. Med. Chem. Lett.* **2003**, *13*, 3075.
- [252] B. Machura, A. Switlicka, M. Wolff, D. Tabak, R. Musiol, J. Polanski, R. Kruszynski, *J. Organomet. Chem.* **2011**, *696*, 3150
- [253] H. S. Das, A. K. Das, R. Pattacini, R. Huebner, B. Sarkar, P. Braunstein, *Chem. Commun.* **2009**, 4387.
- [254] H. S. Das, F. Weisser, D. Schweinfurth, C.-Y. Su, L. Bogani, J. Fiedler, B. Sarkar, *Chem. Eur. J.* **2010**, *16*, 2977.
- [255] P. Braunstein, D. Bubrin, B. Sarkar, *Inorg. Chem.* **2009**, *48*, 2534.
- [256] S. Patra, B. Sarkar, S. M. Mobin, W. Kaim, G. K. Lahiri, *Inorg. Chem.* **2003**, *42*, 6469.
- [257] A. Paretzki, H. S. Das, F. Weisser, T. Scherer, D. Bubrin, J. Fiedler, J. E. Nycz, B. Sarkar, *Eur. J. Inorg. Chem.* **2011**, 2413
- [258] P. Braunstein, D. Bubrin, B. Sarkar, *Inorg. Chem.* **2009**, *48*, 2534.
- [259] D. Schweinfurth, H. S. Das, F. Weisser, D. Bubrin, B. Sarkar, *Inorg. Chem.* **2011**, *50*, 1150.
- [260] S. Ye, B. Sarkar, F. Lissner, T. Schleid, J. V. Slageren, J. Fiedler, W. Kaim, *Angew. Chem. Int. Ed.* **2005**, *44*, 2103.

- [261] M. Behforouz, Z. Gu, W. Cai, M. A. Horn, M. Ahmadian, *J. Org. Chem.* **1993**, *58*, 7089.
- [262] T. Kobayashi, Y. Nishina, K. G. Shimizu, G. P. Sato, *Chem. Lett.* **1988**, 1137.
- [263] R. S. Srivastava, F. R. Fronczek, N. R. Tarver, R. S. Perkins, *Polyhedron* **2007**, *26*, 5389.
- [264] E. Alessio, G. Balducci, M. Calligaris, G. Costa, W. M. Attia, G. Mestroni, *Inorg. Chem.* **1991**, *30*, 609.

## ***ABBREVIATIONS***

|                                  |  |
|----------------------------------|--|
| A                                | hyperfine coupling constant            |
| $a_0$                            | isotropic hyperfine constant           |
| A                                | ampere                                 |
| abb.                             | abbildung                              |
| acac <sup>-</sup>                | acetylacetonato                        |
| asym                             | asymmetric                             |
| av                               | average                                |
| B                                | magnetic field                         |
| bpy                              | bipyridine                             |
| br                               | broad                                  |
| Bu <sub>4</sub> NPF <sub>6</sub> | tetrabutylammonium hexafluorophosphate |
| calc.                            | calculated                             |
| cm                               | centimetre                             |
| Cl                               | chloro                                 |
| Cym                              | cymene                                 |
| d                                | doublet                                |
| $\delta$                         | chemical shift                         |
| E <sub>pa</sub>                  | anodic peak potential                  |
| E <sub>pc</sub>                  | cathodic peak potential                |
| $\epsilon$                       | molar extinction coefficient           |
| EPR                              | electron paramagnetic resonance        |
| eq.                              | equivalent                             |
| expt                             | experimental                           |
| DCM                              | dichloromethane                        |
| Fc <sup>0/+</sup>                | ferrocene / ferrocenium                |
| g                                | gram                                   |
| GHz                              | gigahertz                              |
| HOMO                             | highest occupied molecular orbital     |
| Hz                               | hertz                                  |
| I                                | nuclear spin                           |
| IR                               | infrared                               |

|           |  |
|-----------|--|
| Ir        | irreversible   |
| Iso       | isotropic  |
| isp       | isopropyl  |
| IVCT      | inter valence charge transfer                              |
| k         | rate constant  |
| Kc        | comproportionation constant                                |
| L         | ligand   |
| $\lambda$ | wavelength   |
| LLCT      | ligand to ligand charge transfer                           |
| LMCT      | ligand to metal charge transfer                            |
| LUMO      | lowest unoccupied molecular orbital                        |
| m         | meta   |
| M         | mol / liter  |
| Me        | methyl   |
| MeCN      | acetonitrile   |
| MeOH      | methanol   |
| mg        | milligram  |
| MHz       | megahertz  |
| ml        | milliliter   |
| MLCT      | metal to ligand charge transfer                            |
| mm        | millimeter   |
| mmol      | milimole   |
| MO        | molecular orbital  |
| mol       | mole   |
| mT        | militesla  |
| mV        | milivolt   |
| $\nu$     | wavenumbers  |
| NIR       | near infrared  |
| nm        | nanometer  |
| NMR       | nuclear magnetic resonance                                 |
| °         | degree   |
| °C        | degree centigrade  |
| OTTLE     | cell optically transparent thin layer electrochemical cell |

|          |  |
|----------|--|
| Ox       | oxidized   |
| <i>p</i> | para   |
| Ph       | phenyl   |
| ppm      | parts per million  |
| Q        | 4,6-di- <i>tert</i> -butyl-N-phenyl- <i>o</i> -iminobenzoquinone |
| red      | reduced  |
| RT       | room temperature   |
| s        | singlet  |
| S        | electron spin  |
| SCE      | standard calomel electrode                                       |
| sh       | shoulder   |
| SOMO     | singly occupied molecular orbital                                |
| Sym      | symmetric  |
| t        | triplet  |
| T        | temperature / Tesla  |
| THF      | tetrahydrofuran  |
| UV       | ultra violet   |
| V        | volt   |
| vs.      | versus   |
| vis      | visible  |
| $\omega$ | dihedral angle   |
| Z        | atomic number  |



## ◆ Curriculum Vitae ◆

---

### *Personal Information*

Name: Hari Sankar Das

Sex: Male

Date of birth: 1st Jan 1986

Nationality: Indian

Address: Hari Sankar Das

Institut für Anorganische Chemie

Universität Stuttgart

Pfaffenwaldring 55

70569 stuttgart, Germany

E-mail: [iachsdas@iac.uni-stuttgart.de](mailto:iachsdas@iac.uni-stuttgart.de) / [haridasiitk@gmail.com](mailto:haridasiitk@gmail.com)

---

### *Education*

**1996 to 2001:** *Saora Union High School*, Hooghly, Westbengal, India

**2001 to 2003:** *Dhaniakhali Mahamaya Vidyamandir*, Hooghly, Westbengal, India

**2003 to 2006:** *Calcutta University*, Kolkata, Westbengal, India

Degree obtained: B.Sc. in Chemistry

**2006 to 2008:** *Indian Institute Of Technology-Kanpur*, U.P., India

Degree obtained: M.Sc. in Chemistry

Thesis Title: "Synthesis of water soluble corrole complex and joining of two corroles via imine, amide, ester bond" under Prof. S. Sarkar at IIT-Kanpur

**October 2008 to March 2012:** Doctoral research at the *Institute für Anorganische Chemie der Universität Stuttgart* under the guidance of Prof. Dr. Biprajit Sarkar

Thesis title: "Ruthenium complexes with non-innocent Quinonoid, Quinoline-5,8-dione and Iminoquinone Ligands: Synthesis, Structure, Redox properties and electron distribution"

---

### *Positions Held*

**October 2008 to 2012:** Graduate Lab Assistant for the UT-VT Practical.

**2010 to 2012:** Graduate Teaching Assistant, Inorganic Chemistry-WASTE, Air Quality Control, Solid Waste water Process Engineering.

---

## List of Publications

1. “First structurally Characterized *mono*- and *di*-nuclear Ruthenium Complexes Derived from Zwitterionic Quinonoid Ligands”, **H. S. Das**, A. K. Das, R. Pattacini, R. Hübner, B. Sarkar, and P. Braunstein, *Chem. Commun.*, **2009**, 4387–4389.
2. “Straightforward Synthesis of Substituted *p*-Quinones: Isolation of a Key Intermediate and Use as a Bridging Ligand in a Diruthenium Complex”, **H. S. Das**, F. Weisser, D. Schweinfurth, C.-Y. Su, L. Bogani, J. Fiedler, and B. Sarkar, *Chem. Eur. J.*, **2010**, *16*, 2977–2981.
3. “One-pot Synthesis of Symmetric und Asymmetric *p*-Quinone Ligands and Unprecedented Substituent Induced Reactivity in a Dinuclear Ruthenium Complex”, David Schweinfurth, **H. S. Das**, F. Weisser, D. Bubrin, S. Zalis and B. Sarkar, *Inorg. Chem.*, **2011**, *50*, 1150–1159.
4. “Invariant Oxidation State of Copper but not of Ruthenium in complexes with Noninnocent *N*-(2-Methyl-5,8-dihydroquinolin-7-yl)acetamide: A Combined Structural, Electrochemical and Spectroelectrochemical Investigation”, Alexa Paretzki, **H. S. Das**, F. Weisser, T. Scherer, D. Bubrin, J. Fiedler, J. E. Nycz and B. Sarkar, *Eur. J. Inorg. Chem.*, **2011**, *15*, 2413-2421.